Rudra Narayan Dash ·
Akshay Kumar Rathore ·
Vinod Khadkikar · Ranjeeta Patel ·
Manoj Debnath   *Editors*

Smart Technologies for Power and Green Energy

Proceedings of STPGE 2022

Springer

Lecture Notes in Networks and Systems

Volume 443

The series "Lecture Notes in Networks and Systems" publishes the latest developments in Networks and Systems—quickly, informally and with high quality. Original research reported in proceedings and post-proceedings represents the core of LNNS.

Volumes published in LNNS embrace all aspects and subfields of, as well as new challenges in, Networks and Systems.

The series contains proceedings and edited volumes in systems and networks, spanning the areas of Cyber-Physical Systems, Autonomous Systems, Sensor Networks, Control Systems, Energy Systems, Automotive Systems, Biological Systems, Vehicular Networking and Connected Vehicles, Aerospace Systems, Automation, Manufacturing, Smart Grids, Nonlinear Systems, Power Systems, Robotics, Social Systems, Economic Systems and other. Of particular value to both the contributors and the readership are the short publication timeframe and the world-wide distribution and exposure which enable both a wide and rapid dissemination of research output.

The series covers the theory, applications, and perspectives on the state of the art and future developments relevant to systems and networks, decision making, control, complex processes and related areas, as embedded in the fields of interdisciplinary and applied sciences, engineering, computer science, physics, economics, social, and life sciences, as well as the paradigms and methodologies behind them.

Indexed by SCOPUS, INSPEC, WTI Frankfurt eG, zbMATH, SCImago.

All books published in the series are submitted for consideration in Web of Science.

For proposals from Asia please contact Aninda Bose (aninda.bose@springer.com).

Rudra Narayan Dash · Akshay Kumar Rathore ·
Vinod Khadkikar · Ranjeeta Patel · Manoj Debnath
Editors

Smart Technologies
for Power and Green Energy

Proceedings of STPGE 2022

Editors
Rudra Narayan Dash
School of Electrical Engineering
KIIT University
Bhubaneswar, India

Vinod Khadkikar
Khalifa University
Abu Dhabi, United Arab Emirates

Manoj Debnath
Department of Electrical and Electronics
Engineering
ITER, Siksha 'O' Anusandhan
Bhubaneswar, India

Akshay Kumar Rathore
Concordia University
Montreal, QC, Canada

Ranjeeta Patel
School of Electrical Engineering
KIIT University
Bhubaneswar, India

Preface

As per the present scenario of climate change, the globe needs a revolution on green power in a smarter way. The power system with power electronics really enhanced the electrical system. The fusion of smart technologies such as Artificial Intelligence (AI), Machine Learning (ML), Internet of Things (IoT) with green power generation, transmission, distribution and control leads to the future development of our society. Along with this, the emergence of electric vehicles using green energy is a gift to the globe. Continuous research in all these domains with proper dissemination leads to global improvement.

The First International conference entitled "Smart Technologies for Power and Green Energy", (STPGE—2022) is organized by School of Electrical Engineering, Kalinga Institute of Industrial Technology (Deemed to be University), Bhubaneswar, Odisha, India, on 12–13 February 2022. The conference is focused on the direction of basic research into applied investigation and converting applied investigation into practice in the field of Power System and Power Electronics, Application of Smart Technologies and Green Energy. This conference also creates awareness about the importance of basic scientific research in different fields matching the current trends. More than 100 numbers of articles have been received online related to the scope of the conference area. Out of these submissions, the editors have chosen only 37 high-quality articles after a thorough rigorous peer-review process. In the peer-review process, several highly knowledgeable researchers/professors with expertise in single/multi-domain assisted the editors in unbiased decision-making of the acceptance of the selected articles. Moreover, valuable suggestions from the advisory, programme and technical committee also help the editors for smoothing the peer-review process. The complete review process is based on several criteria, such as major contribution, technicality, clarity and originality of some latest findings. The whole process starting from initial submission to the acceptance notification to authors is done electronically.

The first international conference STPGE—2022 gives a platform for sharing research and ideas among different academicians, researches and scientists from throughout the world with an intention of global development. The conference includes various keynote addresses by world-renowned researchers particular on the

scope of STPGE research topics. The sessions including (presentation of author's contribution and keynote address) are principally organized in accordance with the significance and interdependency of the articles with reference to the basic concept and motivation of the conference.

The accepted manuscripts (original research and survey articles) have been well organized to emphasize the cutting-edge technologies applied in Power System, Power Electronics and Green Energy domains. We appreciate the authors' contribution and value the choice that is 'STPGE' for disseminating the output of their research findings. We are also grateful for the help received from each individual reviewer and the Program Committee members regarding peer-review process.

We are highly thankful to the KIIT Deemed to be University and each faculty member of the School of Electrical Engineering, for their constant support and motivation for making the conference successful. The editors would also like to thank Springer Editorial Members for their constant help and for publishing the proceedings in "Lecture Notes in Networks and Systems" series.

Bhubaneswar, India   Rudra Narayan Dash
Montreal, Canada   Akshay Kumar Rathore
Abu Dhabi, United Arab Emirates   Vinod Khadkikar
Bhubaneswar, India   Ranjeeta Patel
Bhubaneswar, India   Manoj Debnath

Contents

Editors and Contributors

About the Editors

Dr. Rudra Narayan Dash is working as Assistant Professor and Program Head of the School of Electrical Engineering, Kalinga Institute of Industrial Technology (KIIT DU), Bhubaneswar. He received his Ph.D. in Electrical Engineering from KIIT DU, Bhubaneswar, in 2018, M.Tech. in Electrical Engineering from National Institute of Technology, Rourkela, in 2010 and B.Tech. Degree in Electrical Engineering from KIIT University in the year 2005. At present, he has more than Fourteen years of teaching experience in the field of Electrical Engineering. He is Life Member IE (India), Member IET, Member IEEE and Life member ISTE. His research areas are applications of soft computing and signal processing techniques in electrical machines, power systems, fault diagnosis and evolutionary algorithms. He has published more than 18 research papers in various reputed peer-reviewed international journals, conferences and book chapters. He is currently guiding two Ph.D. scholars.

Dr. Akshay Kumar Rathore is Associate Professor, Graduate Program Director and Chair of Graduate Awards in the department of electrical and computer engineering, Concordia University, Montreal, Canada. He is an IEEE Fellow, Awards Department Chair and Prominent Lecturer of the IEEE Industry Applications Society and an elected AdCom Member-at-Large of the IEEE Industrial Electronics Society. He received the 2013 IEEE IAS Andrew W. Smith Outstanding Young Member Achievement Award, 2014 Isao Takahashi Power Electronics Award, 2017 IEEE IES David J Irwin Early Career Award, 2020 IEEE Bimal Bose Award for Industrial Electronics Applications in Energy Systems, and 2020 IEEE IAS Outstanding Area Chair Award. He published above 270 research papers in international journals and conferences including 92 IEEE Transactions. His research is mainly focused on current-fed converters and multilevel inverters. He is leading the area of current-fed power electronics and contributed to the analysis, and design of two new classes of snubberless current-fed converters. To his credit, he has one approved European

patent and three book chapters. Dr. Rathore is Associate Editor of IEEE TRANS-ACTIONS ON SUSTAINABLE ENERGY and Paper Review Chair of IEEE Transactions on Industry Applications for Renewable and Sustainable Energy Conversion Systems. He was Distinguished Lecturer (2017–2018) and Executive Board Member-at-Large (2017-2019) of the IEEE Industry Applications Society. He received his M.Tech. degree from the Indian Institute of Technology (BHU), Varanasi, India, in 2003, and the Ph.D. degree from the University of Victoria, BC, Canada, in 2008. He had two postdoctoral research appointments with the University of Wuppertal, Germany, and University of Illinois at Chicago, USA. He received the Gold Medal during his M.Tech. degree for securing highest academic standing among all electrical engineering specializations. He was a recipient of University Ph.D. Fellowship and Thouvenelle Graduate Scholarship during his Ph.D.

Dr. Vinod Khadkikar (S'06, M'09, SM'15) received the M.Tech. in power electronics, electrical machines and drives from the Indian Institute of Technology (IITD), New Delhi, India, in 2002, and Ph.D. degree in electrical engineering from the École de Technologie Supérieure, Montréal, QC, Canada, in 2008. From December 2008 to March 2010, he was Postdoctoral Fellow at the University of Western Ontario, London, ON, Canada. In 2010, he was Visiting Faculty at Massachusetts Institute of Technology (MIT), Cambridge, MA, USA. He is currently Professor with the Department of Electrical Engineering and Computer Science, Khalifa University, Abu Dhabi, United Arab Emirates. His research interests include applications of power electronics in distribution systems and renewable energy resources, grid interconnection issues, power quality enhancement, active power filters and electric vehicles. Dr. Khadkikar is currently Associate Editor for the IEEE Transactions on Industrial Electronics, IEEE Transactions on Industry Applications and IET Power Electronics. Affiliation: Vinod Khadkikar is with the Advanced Power and Energy (APEC) and Khalifa University Space Technology and Innovation (KUSTIC) centers, Electrical Engineering and Computer Science Department, Khalifa University, Abu Dhabi 127788, UAE.

Dr. Ranjeeta Patel is presently working as Assistant Professor (II) in the School of Electrical Engineering, KIIT Deemed to be University, Bhubaneswar, India. She received her Ph.D. degree from National Institute of Technology Rourkela, India in 2017, M.Tech. degree from KIIT University, India in 2009 and Bachelor's degree in Electrical Engineering from affiliated BPUT, Rourkela, India, in 2006. She worked in various institutes and has 11 years of teaching experience. She served for various administrative positions like HoD, EE, FIC of library, disciplinary committee, anti-ragging committee etc. during the stay in SIT, Sambalpur, India. Her research areas are power quality, renewable energy integration, active power filter, fuzzy controller, etc. She has various published papers in reputed journals and has been a presenter at various FDPs and conferences, etc. Currently, 2 Ph.D. scholars are working under her guidance. She has been continuing giving service as a reviewer to reputed journals of IEEE, IET, Springer, Wiley, Taylor & Francis, etc. She is Senior Member of IEEE and presently holding the position of IEEE officials as Treasurer of IEEE PELS

and IEEE CTSoc joint chapters IEEE Bhubaneswar Sub-sec IEEE Kolkata section. She is also the co-organizer of IEEE CTSoc joint chapter, IEEE Bhubaneswar sub-section and IEEE section. She organized successfully two international conferences SPRINGER ETAEERE 2020 KIIT DU and IEEE ICPEE 2021 and also acted as Technical Program Chair for both the conference. She is also Editor of the Springer LNEE Series book consisting of select proceedings of ETAEERE 2020.

Dr. Manoj Debnath is working as Assistant Professor in the Department of Electrical Engineering under the Faculty of Engineering and Technology, Siksha 'O' Anusandhan University, Bhubaneswar. He received his Ph.D. in Electrical Engineering, M.Tech. in Power System and Power Electronics and B.Tech. in Electrical engineering in 2017, 2013 and 2007, respectively. He has published more than 70 research papers in various reputed peer-reviewed international journals, conferences and book chapters. He has served as reviewers for various reputed Journal publishers such as Springer, IEEE, Elsevier, Willey and Inderscience. At present, he has more than 14 years of teaching experience in the field of electrical engineering. He is a senior member of IEEE, member of Institute of Engineers (India) and life member of ISTE. He is currently guiding 5 Ph.D. scholars. His area of interest includes power system control, artificial intelligence, optimal control, fuzzy logic, bioinspired algorithm, optimization and renewable energy. He has served as organizing chair for many international conferences.

Contributors

Afreen Neda Department of Computer Engineering, Jamia Millia Islamia, New Delhi, India

Ashish Apurva Kalinga Institute of Industrial Technology Deemed to Be University, Bhubaneswar, India

Badar Altaf Q. H. Department of Electrical Engineering, National Institute of Technology Warangal, Telangana, India

Bapurao Kanjune Akshay Department of EEE, NIT Goa, Ponda, Goa, India

Barik Prasanta Kumar Department of MEE, CAET, OUAT, Bhubaneswar, Odisha, India

Behera Badri Narayan Department of Electrical Engineering, CET, Bhubaneswar, India

Behera Bruti Kumar Department of Electrical Engineering, Institute of Technical Education & Research, Siksha 'O' Anusandhan Deemed to be Univesity, Bhubaneswar, India

Bhatnagar Maanvi Department of Electrical Engineering, National Institute of Technology, Raipur, India

Bhende Chandrashekhar Narayan School of Electrical Sciences, IIT Bhubaneswar, Bhubaneswar, Odisha, India

Bonthagorla Praveen Kumar Department of EEE, NIT Goa, Ponda, Goa, India

Chandel Aseem Department of Electrical Engineering, Rajkiya Engineering College Mainpuri, Mainpuri, UP, India

Chatterjee Biswapriya Aliah University, Newtown, Kolkata, WB, India

Chavan Vinaya Chandrakant Electrical and Electronics Engineering, National Institute of Technology Goa, Ponda, Goa, India

Choudhury Abhijeet Department of Electrical Engineering, Institute of Technical Education & Research, Siksha 'O' Anusandhan Deemed to be University, Bhubaneswar, India

Daniya T. Research Scholar, Sathyabama Institute of Science and Technology, Chennai, India

Das Bikramaditya Department of Electronics & Telecommunication Engineering, VSS University of Technology, Burla, Odisha, India

Das Sunanda Department of Computer Science and Engineering, Jain University, Bangalore, India

Dash Rudra Narayan School of Electrical Engineering, Kalinga Institute of Industrial Technology Deemed to Be University, BBSR, Bhubaneswar, Odisha, India

Dei Geetanjali School of EE, KIIT Deemed to Be University, Bhubaneswar, India

Fernandes B. G. Department of Electrical Engineering, IIT Bombay, Mumbai, India

Gantayat Janmajaya Department of Electrical Engineering, Institute of Technical Education & Research, Siksha 'O' Anusandhan Deemed to Be University, Bhubaneswar, India

Gayatri Sarman K. V. S. H. Department of ECE, Vishnu Institute of Technology, Bhimavaram, Andra Pradesh, India

Ghatak Sriparna Roy School of Electrical Engineering KIIT Deemed to Be University Bhubaneswar, Bhubaneswar, India

Godwal Shanker Institute of Technology, Nirma University, Ahmedabad, India

Goswami Arup Kumar Electrical Engineering Department NIT, Silchar, India

Gupta Deepak Kumar School of Electrical Engineering KIIT, Deemed to Be University, Bhubaneswar, India

Jabirullah Mohammad Department of ECE, Lords Institute of Engineering and Technology Hyderabad, Telangana, India

Jena Chitralekha School of Electrical Engineering, KIIT Deemed to be University, Bhubaneswar, Odisha, India

Kanojia Sarika Institute of Technology, Nirma University, Ahmedabad, India

Kar Sanjeeb Kumar Department of Electrical Engineering, Institute of Technical Education and Research, Siksha 'O' Anusandhan Deemed to Be University, Bhubaneswar, India

Kishore Shradha Birla Institute of Technology, Patna Off-Campus, Patna Extension Centre, Mesra, India

Kumar Ajay School of Electrical Engineering KIIT Deemed to Be University Bhubaneswar, Bhubaneswar, India

Lokesh Tandra Bachelor of Technology, CSE, GMRIT, Rajam, India

Maharana Manoj Kumar School of Electrical Engineering, KIIT Deemed to Be University, Bhubaneswar, India

Mangaraj Mrutyunjaya Department of Electrical & Electronics Engineering, Lendi Institute of Engineering and Technology, Vizianagaram, India

Manikandan R. UGC-Dr D. S. Kothari Post-doctoral Fellow, Department of Applied Mathematics, Bharathiar University, Coimbatore, Tamil Nadu, India

Mansani Swapna Electrical Engineering Department NIT, Silchar, India

Maram Balajee Department of CSE, GMRIT, Rajam, India;
Dept of CSE, Chitkara University Institute of Engineering and Technology, Chitkara University, Baddi, Himachal Pradesh, India

Mathew Lini Department of Electrical Engineering, National Institute of Technical Teachers Training & Research, Chandigarh, India

Mikkili Suresh Department of EEE, NIT Goa, Ponda, Goa, India

Mishra Anshul Kumar Department of Electrical Engineering, Rajkiya Engineering College Mainpuri, Mainpuri, UP, India

Mishra Prajna Parimita School of Electrical Engineering, KIIT Deemed to be University, Bhubaneswar, India

Mishra Sanhita KIIT Deemed to Be University, BBSR, India

Mishra Sanjoy Kumar Department of Electrical Engineering, G H Raisoni University Amaravati, Maharashtra, India

Mishra Subhendu Kalinga Institute of Industrial Technology, Bhubaneswar, India;
Indian Institute of Technology, Bombay, India

Mohanty Madhusmita Odisha Power Transmission Corporation Limited, Bhubaneswar, Odisha, India

Mohanty Soumya Department of Electrical Engineering, Institute of Technical Education and Research, Siksha 'O' Anusandhan Deemed to Be University, Bhubaneswar, India

Mohapatra Alivarani School of Electrical Engineering, KIIT Deemed to be University, Bhubaneswar, Odisha, India

Mohapatra Bijaya Kumar School of Electrical Engineering KIIT, Deemed to Be University, Bhubaneswar, India

Mohapatra Sushree Shataroopa School of Electrical Engineering, KIIT Deemed to Be University, Bhubaneswar, India

Muleta Negasa Department of Electrical Engineering, National Institute of Technology Warangal, Telangana, India

Muthria Ashok Department of Electrical Engineering, National Institute of Technical Teachers Training & Research, Chandigarh, India

Nanda Lipika School of Electrical Engineering, KIIT Deemed to be University, Bhubaneswar, Odisha, India

Nayak B. K. Kalinga Institute of Industrial Technology, Bhubaneswar, India

Nayak Byamakesh School of Electrical Engineering, KIIT Deemed to be University, Bhubaneswar, Odisha, India

Nimje Akhilesh Institute of Technology, Nirma University, Ahmedabad, India

Padhee Subhransu Department of Electrical and Electronics Engineering, Sambalpur University Institute of Information Technology, Burla, Odisha, India

Panda Babita School of Electrical Engineering, KIIT Deemed to be University, Bhubaneswar, Odisha, India

Pani Smarak SoEE, KIIT DU, Bhubaneswar, Odisha, India

Panigrahi Chinmoy Kumar School of Electrical Engineering KIIT, Deemed to Be University, Bhubaneswar, India

Panigrahi P. K. School of Engineering and Technology, GIETU, Gunupur, Odisha, India

Patel Debasis Kumar Electrical Engineering Department NIT, Silchar, India

Patel Ranjeeta Electrical Engineering Department, Kalinga Institute of Industrial Technology Deemed to Be University, Bhubaneswar, India

Patel Ravindu Institute of Technology, Nirma University, Ahmedabad, India

Pati Akshaya Kumar School of Electronics Engineering, KIIT Deemed to be University, Bhubaneswar, India

Pati Bibhuti Bhusan Department of Electrical Engineering, VSS University of Technology, Burla, Odisha, India

Pati Swagat Department of Electrical Engineering, Institute of Technical Education & Research, Siksha 'O' Anusandhan Deemed to be Univesity, Bhubaneswar, India

Patra Anil Kumar Department of Electrical & Electronics Engineering, Kalam Institute of Technology, Berhampur, Odisha, India

Phukan Hillol Electrical Engineering Department NIT, Silchar, India

Prabhakara Rao Amarana Department of ECE, Vishnu Institute of Technology, Bhimavaram, Andra Pradesh, India

Pradhan Abhilash GIET University, Gunupur, Odisha, India

Pradhan Arjyadhara School of Electrical Engineering, KIIT Deemed to be University, Bhubaneswar, Odisha, India

Prakash Satya Department of Electrical Engineering, Parala Maharaja Engineering College, Brahmapur, Odisha, India

Prusty R. C. Department of Electrical Engineering, VSSUT, Burla, Odisha, India

Prusty Soubhagya Ranjan School of Electrical Engineering, KIIT Deemed to be University, Bhubaneswar, Odisha, India

Ranjan Mrinal National Institute of Technology, Patna, India

Raut Usharani Department of Electrical Engineering, IIIT Bhubaneswar, Bhubaneswar, Odisha, India

Rout Kamalesh Chandra Department of Electrical Engineering, VNIT, Nagpur, India

Routray Aurobinda IIT, Kharagpur, India

Roy Subhadeep IISC, Bangalore, India

Sabat Jogeswara Department of Electrical & Electronics Engineering, Lendi Institute of Engineering and Technology, Vizianagaram, India

Sahoo Sarada Prasanna Department of Electrical Engineering, VSS University of Technology, Burla, Odisha, India

Sahu Binod Kumar SOA Deemed to Be University, Bhubaneswar, India

Sahukari Jitendra Bachelor of Technology, CSE, GMRIT, Rajam, India

Saiprakash Chidurala School of Electrical Engineering, KIIT Deemed to be University, Bhubaneswar, Odisha, India

Sakthivel Rathinasamy Professor, Department of Applied Mathematics, Bharathiar University, Coimbatore, Tamil Nadu, India

Samal Sarita School of Electrical Engineering, KIIT Deemed to be University, Bhubaneswar, Odisha, India

Shankar Ravi National Institute of Technology, Patna, India

Sharma Archana Bhabha Atomic Research Centre, Trombay, Mumbai, India; Department of Electrical Engineering, Rajkiya Engineering College Bijnor, Bijnor, India

Sharma Renu Department of Electrical Engineering, Institute of Technical Education & Research, Siksha 'O' Anusandhan Deemed to be Univesity, Bhubaneswar, India

Siddique Md. Shabaaz Hussain Aliah University, Newtown, Kolkata, WB, India

Singh Jiwanjot Electrical Engineering Department NIT, Silchar, India

Somarajan Sreeja Department of EEE, College of Engineering-Poonjar, Kottayam, Kerala, India

Sreejith S. Electrical Engineering Department NIT, Silchar, India

Srinadh V. Department of Computer Science and Engineering, GMR Institute of Technology, Rajam, Andhra Pradesh, India

Swain Sarat Chandra KIIT Deemed to Be University, BBSR, India

Swetapadma Aleena School of Computer Engineering, KIIT Deemed to Be University, Bhubaneswar, India

Thakur Rohan Vijay Department of Electrical Engineering, G H Raisoni University Amaravati, Maharashtra, India

Virat Aditya Kalinga Institute of Industrial Technology Deemed to Be University, Bhubaneswar, India

Wankhede Ashok K. HBNI Anushaktinagar, Mumbai, India

Yadav Anamika Department of Electrical Engineering, National Institute of Technology, Raipur, India

Non-traditional Algorithms for Offshore Engineering Systems

Sreeja Somarajan , **R. Manikandan** , **and Rathinasamy Sakthivel**

Abstract Brushlike Direct Current Motors (BLDCM) are the most extensively used machine in a wide range of oceanic applications such as operation of offshore wind turbines, including robotics, food technology, and aviation. PID controllers exceed other linear controllers in terms of performance. This controller is typically utilized for controlling the motor's speed. In computing, the traditional approach for adjusting PID parameters is indirect. In this paper, two non-traditional algorithms such as genetic algorithm and ant colony optimization are proposed for tuning PID parameters in order to control the speed of BLDC motor. With the goal of constructing a speed regulation controller, these algorithms were applied and assessed on a second-order plant model of a BLDC motor. The GA- and PSO-based control algorithms were implemented using MATLAB-Simulink interfaces. For each technique, the resulting system performance was compared.

Keywords BLDC motor · Controls · Optimization · Ant colony optimization · Particle swarm optimization

1 Introduction

Offshore electrical dynamical systems (OEDS) are cited in a severe environment and experienced large loads [1, 9]. OEDS are offshore wind turbines, marine robots, and under water vehicles. These systems are using permanent magnet brushless motor [2–4]. Brushless direct current (BLDC) motors are popular device in oceanic appli-

S. Somarajan
Department of EEE, College of Engineering-Poonjar, Kottayam 686582, Kerala, India

R. Manikandan (✉)
UGC-Dr D. S. Kothari Post-doctoral Fellow, Department of Applied Mathematics, Bharathiar University, Coimbatore 641046, Tamil Nadu, India
e-mail: manikandan.pdf@buc.edu.in

R. Sakthivel
Professor, Department of Applied Mathematics, Bharathiar University, Coimbatore 641046, Tamil Nadu, India

cations like fixed and floating sustainable offshore wind turbines. The brushless DC motor is used to run the loads at the regular speed, by achieving the same a suitable control algorithm is mandatory [5–8]. The investigations of offshore electrical dynamical system associated with controls carried out and the following things were located.

– The Routh-Hurwitz criteria, pole placement methodology, root locus approach, and Ziegler-Nichols (ZN) tuning formula are commonly used to produce traditional PID controller gains.
– Concepts related with the optimal settings need a dynamic weighting matrix.
– Advance control concepts based on Artificial Intelligence along with soft computing techniques are mandate for improving the overall performance of the system.

So the outcome of the literature study, the research work focused on developing the suitable control technique to improve the performance of BLDC motor. The current research work speaks the controller concept for BLDC motor which are developed from genetic algorithm and ACO-based PID mechanism. Numerical simulations are conducted and results were discussed. The paper is organized as follows: system descriptions are reported in Sect. 2, PID controller mechanism described in Sect. 4, GA and PSO details were in Sect. 5, and the end like discussions, results were in Sect. 6.

2 Mathematical Model of BLDC Motors

A brushless DC motor's mathematical model is typically similar to that of a normal DC motor [10–12]. The phases involved in the BLDC motor have a significant impact on the overall results. The resistive and inductive properties of the BLDC configuration are affected by the phases' peculiarities. A basic design with a symmetrical three-phase and internal "wye" link, for example, might provide a quick overview of the complete phase idea (Fig. 1). The mechanical and electrical constants are, respectively, $\tau_m = \frac{J.\,3R}{K_e K_t}$ and $\tau_e = \frac{L}{3.\,R}$. By the introduction effects, one can derive the transfer function BLDC motor systems and same can be

Fig. 1 Schematic illustration of a Brushless DC Motor
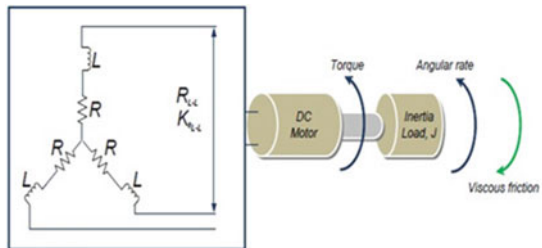
$$G(s) = \frac{\frac{1}{K_e}}{\tau_m \tau_e . S^2 + \tau_m S + 1} \tag{1}$$

where J is the inertia of motor, R is the internal resistance, and K_e and K_t are the back EMF and torque constant correspondingly.

3 PID Control Algorithm

The concept of controller variant is P-I-D, which is readily available industry-based controller and same is utilized in this study for achieving the response control of sustainable marine machine applications. In the vast majority of applications, the PID algorithm is employed to regulate feedback loops. The primary objective is to maintain the demand in highly stochastic load in offshore scenario and maintain the stable operation under Morison-type wave loads. The preliminary details along with operation are shown in Fig. 2.

The controller is responsible for providing the system with the necessary excitation and for controlling the system's overall behavior. The structural configurations of the PID controller are divided into numerous groups. The series and parallel structures are the most prevalent, while hybrid forms of the series and parallel structures exist in some circumstances.

In Fig. 2, the error term e as required demand R versus output Y of the system in offshore scenario. The addition of errors such as K_p proportional error signal, K_i the integral error, and K_d the derivative error are given as an input to the controller module. That is,

$$u = K_p + K_i \int edt + K_d \frac{de}{dt} \tag{2}$$
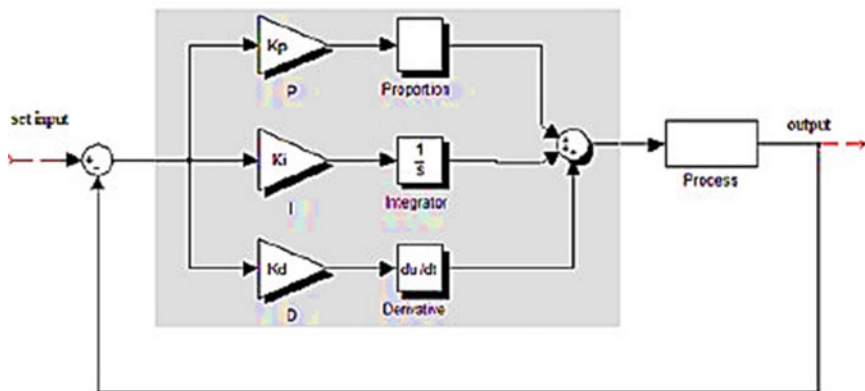
Fig. 2 PID control block

4 Non-traditional Optimization Techniques

4.1 GA—Genetic Algorithm

This variant of AI uses approaches inspired by natural processes including selection, inheritance, mutation, and crossover to solve optimization issues. GA concept is used to achieve the best pair of optimized controller variables to engineering dynamical systems cited in offshore scenario. John Holland deployed this variant in early decades of 1970 and the reason is to locate the best pair solutions to unsolvable engineering and real-time problems. The variant has the theory, often known as the fundamental hypothesis of hereditary calculations, which is widely accepted as the foundation for elucidating the force of hereditary calculations. It claims that in progressive periods, brief, low-request schemata with above-normal health increase rapidly.

Genetic algorithm is deployed to yield the best globally converged parameters for controller to improve the overall performance of the offshore sustainable systems. Figure 3 demonstrates the genetic algorithm process design flowchart. It populates a beginning set of PID controller settings at that point. The populace is hastily assembled, encompassing the whole spectrum of possible scenarios. Chromosomes make up the population. Every chromosome has a competing solution to the problem. The controller variables are packed into the fundamental chromosomal structure. In the offshore dynamical marine system, the chromosomes are linked, and the system dynamic execution characteristics are resolved for each chromosome. After that, the target capacity is used to measure the wellness value of each chromosome. Based on the original quality estimates, a group of the best chromosomes is picked to create the next population. The first stage in GAs is to create the first population. The population is made up of chromosomes that are connected together in a parallel pattern.

4.2 Ant Colony Optimization

ACO is a meta-heuristic algorithm under development that is based on the combined activities arising from the hybrids of many search threads and has shown to be successful in handling hybrid optimization problems. The PID controller gains (G) are modified using a trial-and-error technique based on the prior experiment and system behavior. The gains are maximized using the ACO, and the results are sent into the system's controller. This algorithm's goal is to optimize the PID controller's gains for the provided systems. The controller responds to the loss by using the error proportional gain. The controller benefits from reducing steady-state error and minimizing overshooting of the integral derivative gain. ACO is a meta-heuristic algorithm design approach for combinatorial optimization issues. Ant colonies' natural behaviors of searching out food sources and returning it to their nest by creating a one-of-a-kind path activate the ACO.

Fig. 3 A Flowchart for
Genetic algorithm operations
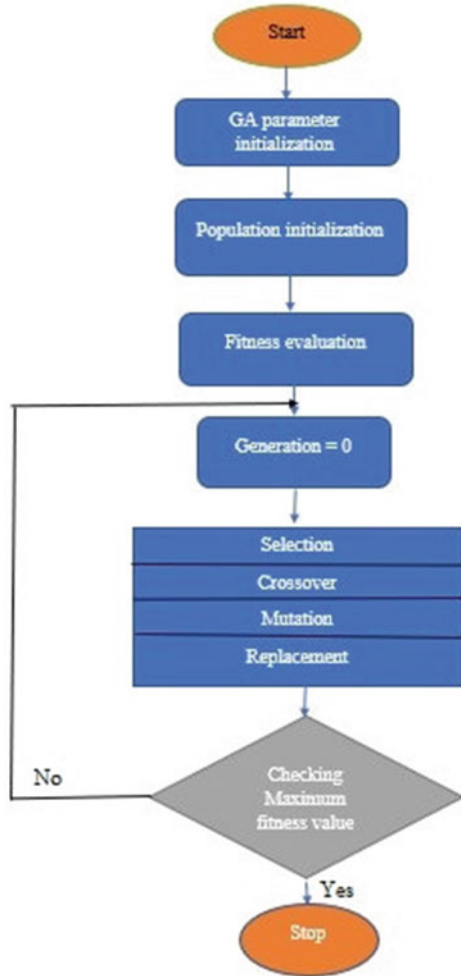
The distance between each city is adjusted based on its own pheromone level and the pheromone level of the other ant. The standard fixed gain PID controller is extensively used in various control processes. Proportional gain (KP), integral constant (Ki), and derivative constant (Kd) are the parameters used to develop the controller (Kd). The primary goal of ACO is to describe the issue as a search for the cheapest path in a graph using an evolutionary meta-heuristic algorithm. Artificial ants' behavior is based on that of real ants. They leave pheromone trails and use transition probability to select their course. Ants like to go to nodes with short edges and a high concentration of pheromone. The pheromone matrix is essential for ACO.

5   Results and Discussions

The results of a typical PID controller for high-performance control system design of BLDC motor systems are not ideal. Similarly, the use of genetic algorithms with ACO-based PID controllers yields the most appropriate optimized coefficient values for the controller. The steady and dynamic performances of a certain BLDC motor control system will be linked using a simulation software. The model is used for building Simulink transfer functions, which makes simulation easier. The parameters used are given in Table 1. Table 2 gives the genetic algorithm parameters and Table 3 gives the ACO parameters used.

The parameter seeding details of genetic algorithm and ant colony optimizations are reported in the tables correspondingly.

Figure 4 shows a system with control algorithm implementations. The model controller optimizes the PID gain parameters by minimizing the error and achieving the global minima of objective function designed. The numerical simulations are carried out for a range of parameters and the best performance is reported in the paper (Figs. 6 and 7).

The numerical results are presented in Table 4 using various parameters choosing ways for the controller variable. Figure 4 shows the output speed response of the system using regular PID controller. Figure 5 shows the simulation results for AI tools-based controller concepts.

Table 1 BLDC motor specifications

Parameters	Value	Units
Winding resistance	0.014	Ohms
Winding inductance	0.0001	H
Moment of inertia of rotor	0.0002	
Coefficient of viscous function	0.004586	
Motor torque constant	0.0275	
Back EMF constant	0.0275	
Load torque	10	Nm
Reference speed	1500	rpm

Table 2 Input details of genetic algorithms

Parameters	Values
Population size	15
Maximum number of iterations	20
Selection rate	0.25
Mutation rate	0.1

Table 3 Input details of ant colony optimization

Parameters	Values
Maximum number of iterations	20
Number of ants	40
Pheromone exponential weight	1
Number of nodes	500
Evaporation factor	0.7
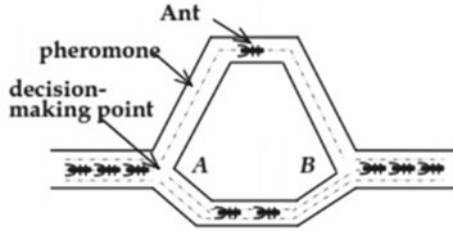
Fig. 4 Decision-making process of ACO

Table 4 Numerical results

Parameters	GA	ACO
Kp	5.9564	2.7856
Ki	95.4084	54.7094
Kd	0.1604	0.9579
Rise time	19.425 ms	17.969 ms
Settling time	19.2 ms	17.4 ms
Overshoot	48.529	22.619
Undershoot	1.99	0
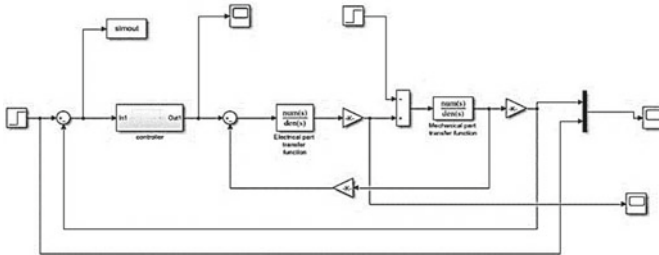
Fig. 5 MATLAB-Simulink diagram model of the BLDC motor
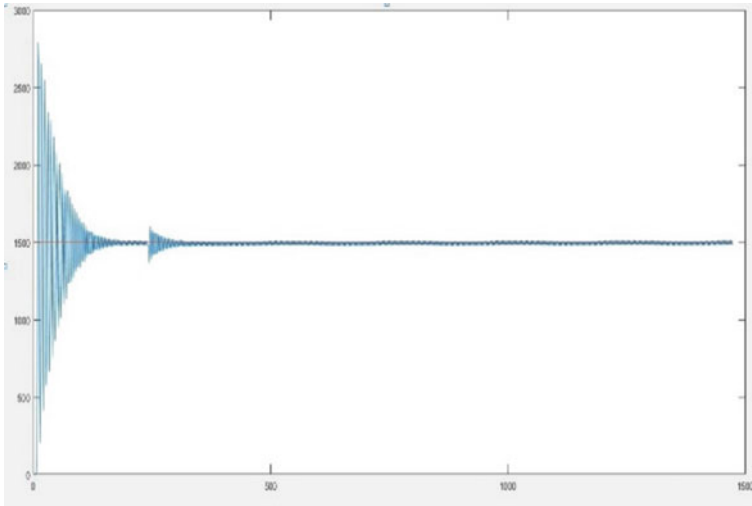
Fig. 6 Output speed versus time response of BLDC motor using PID controller without optimization
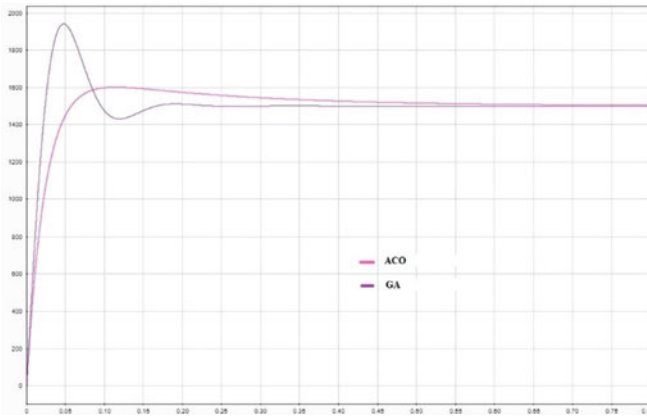
Fig. 7 Speed response of motor with GA- and ACO-based PID controller

6 Closure

In this work, we proposed the advanced artificial intelligence technique-based PID mechanism proposed for BLDC motors in marine green energy applications. The proposed methods were validated with readily available techniques such as conventional modeling for performance evaluation and same has been visualized via simulation outputs. From the results, the proposed method performs well in over-

all performances of the machine and the better time-domain characteristics are also achieved simultaneously. The steady-state responsiveness and performance indices of the ACO-tuned machine are excellent. The same can be plugged into the real-time higher order experimental systems in ocean-based applications.

References

1. D.H. Kim, J.C. Hoon, Biologically inspired intelligent PID controller tuning for AVR systems. Int. J. Control. Autom. Syst. **4**(5), 624–636 (2006)
2. D.H. Kim, A. Abraham, A hybrid genetic algorithm and bacterial foraging approach for global optimization and robust tuning of PID controller with disturbance rejection. Stud. Comput. Intell. **75**, 171–199 (2007)
3. K.M. Passino, Bio mimicry of bacterial foraging for distributed optimization and control. IEEE Control Syst. Mag. **17**(08), 52–67 (2002)
4. S. Ying, C. Zengqiang, Y. Zhuzhi, Adaptive constrained predictive PID controller via PSO, in *Proceedings of the 26th Chinese Control Conference*. (Zhangjiajie, Hunan, China, 2007), pp. 729–733
5. M.R. Alrashidi, A survey of PSO applications in electric power system. IEEE Trans. Evol. Comput. **13**(4), 913–918 (2009)
6. K. Ogata, *Modern Control Systems Engineering* (Prentice Hall India, Prentice, 2010)
7. R. Manikandan, N. Saha, Soft computing based optimum parameter design of PID controller in rotor speed control of wind turbines (2011)
8. R, Manikandan, N. Saha, On the elimination of destabilizing motions of guyed offshore wind turbines using geometrical control mechanism, in *ICCES'14* (Tech Science press, Changwon, Korea, 2014/3)
9. R. Manikandan, N, Saha, A control algorithm for nonlinear offshore structural dynamical systems, in *Proceedings of the Royal Society A: Mathematical* (2015)
10. R. Manikandan, N, Saha, Modeling and PI control of spar offshore floating wind turbine, in *IFAC-PapersOnLine* (2016)
11. R, Manikandan, N, Saha, Dynamic modelling and non-linear control of TLP supported offshore wind turbine under environmental loads. Mar. Struct. (2019)
12. R. Vanchinathan, Improvement of time response for sensorless control of BLDC motor drive using ant colony optimization technique. Int. J. Appl. Eng. Res. (2005)

A Critical Analysis of Control Approach for DSTATCOM

Anshul Kumar Mishra, Archana Sharma, and Aseem Chandel

Abstract With the emergence of the smart grid, the need for a reliable and pure power supply to the customer arises. The problem of power quality of the power system has to be addressed at the distribution side itself, so that the remaining power grid remains clean. In this work, a critical analysis of the recent control algorithms proposed for extenuation of power quality problems at the distribution side will be analysed. The maximum Versoria criteria and affine projection sign-based control algorithms will be analysed thoroughly. The algorithm is adaptive and can work for reference current generation through estimation of reactive and active power of load current. The results of the algorithms will be compared in MATLAB/SIMULINK for various aspects.

Keywords Affine projection sign algorithm · Distribution side · Harmonics · Maximum Versoria criteria · Power quality

1 Introduction

The emergence of power electronic converters has provided a wide range of control ability in power system operation. The converters solve the problems related to the controlling of the devices as well as save the power that was wasted due to the use of conventional control methods [1]. The power electronic converters find application in the equipment commonly used in residential and industrial works. But its enormous use increases the pollution of the current [2]. The current that is flowing through the devices gets polluted due to the injection of harmonics and inter-harmonics. This polluted current then flows through other devices and causes the heating effect in

A. K. Mishra · A. Chandel
Department of Electrical Engineering, Rajkiya Engineering College Mainpuri, Mainpuri 205001, UP, India

A. Sharma (✉)
Department of Electrical Engineering, Rajkiya Engineering College Bijnor, Bijnor, India
e-mail: archana.ee@recb.ac.in

the equipment, thereby reducing the life of the equipment and causes a loss of the millions of dollars [3].

For the mitigation of harmonics injected by the power electronic converters, many Flexible AC Transmission System (FACTS) devices are used. Some of them are STATCOM, UPQC, DVR, SVC, etc. Among these Distribution Static Synchronous Compensator (DSTATCOM) is used for extenuation of distribution-side power quality problems. The working procedure of the device mainly depends on the control algorithm that is used to drive the device [4]. The control algorithm for DSTATCOM can be bifurcated into conventional and adaptive. The conventional schemes are Synchronous Reference Frame (SRF), power balance theory, Instantaneous Reference Frame (IRP) theory, etc. The adaptive control algorithms work on the principle of reference current generation by weight updated algorithm. Some of the recent adaptive algorithms are Euclidean Directional Search Algorithm [5], Affine Projection Algorithm [6], Echo State Network Algorithm [7] and many more [8–13].

In this work, two very recent adaptive algorithms: Maximum Versoria Criteria (MVC) [14] and Affine Projection Sign Algorithm (APSA) [15] have been critically analysed in various aspects. The crucial bases of analysis are the reduction in harmonics from source current, the stability of the algorithm, speed of response and many more. MVC and APSA algorithms are known to operate in noisy condition. Due to enormous data flow in the smart grid, the requirement of algorithm to work in noisy condition has emerged. MVC algorithm can prove to be a boon for the smart grid power quality mitigation. On the other hand, the integration of many devices in the smart grid makes the stability of the grid questionable. The advantages of MVC and APSA algorithm in noise cancellation in smart grid approach motivate the comparison of the algorithms' performance.

The management of the paper is as follows: (2) the power system distribution network under consideration for power quality improvement is discussed, (3) the process of adaptive filtering is explained with the weight update equations of MVC and APSA algorithms and (4) the results obtained from each algorithm are discussed critically on the basis as described above.

2 Power System Distribution Network

The network used in power distribution generally consists of a source, the transformers and various loads that are connected to the system. In this work, the network that is under attention is shown in Fig. 1. The source is feeding power to the load which consists of the rectifier and the R-L load. The load is non-linear in nature and injects the components of the current that are of non-fundamental frequencies, also known as harmonics. The load also requires the reactive power, which is supplied by the DSTATCOM.
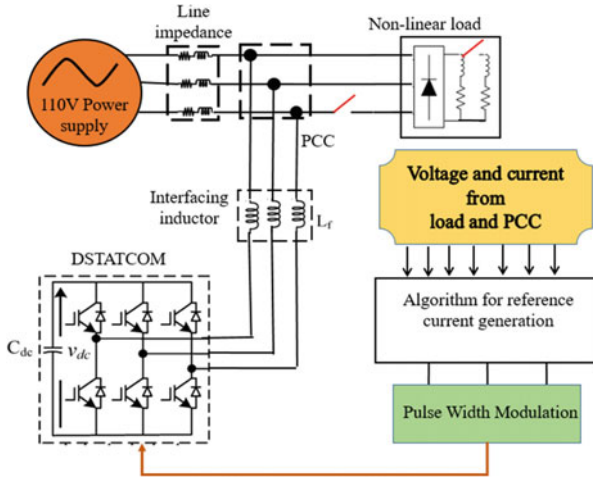
Fig. 1 Distribution side power network under consideration

Table 1 Power system parameters

Parameters	Simulation
AC line voltage, frequency	415 V(L–L), 50 Hz
Source impedance	$R_s = 0.06\ \Omega$, $L_s = 3$ mH
Load	$R_l = 30\ \Omega$, $L_l = 200$ mH
DC bus voltage	700 V
Interfacing inductor	$L_f = 2.3$ mH
Max. switching frequency	20 kHz

Moreover, some other real-time situations are under consideration of the work: load balancing and system balance during faulty condition are also considered in the work. The parameters of the network devices are mentioned in Table 1.

The system is designed at the distribution voltage level of 415 V, with source impedances R_s and L_s as mentioned. The source is feeding the load of R_l and L_l. DSTATCOM used a DC capacitor to inject anti-harmonics and fulfil the need of reactive power of the load. The major drive of the DSTATCOM is the control approach that is used for generation of the pulses. The frequency of switching for the DSTATCOM is kept at 20 kHz.

3 Comparative Analysis of Adaptive Control of DSTATCOM Through MVC and APSA

A three-step procedure is used in the adaptive algorithm-based control approach. Firstly, the unit vectors which are in-phase and in-quadrature to the voltage of the Point of Common Coupling (PCC) are calculated by the procedure shown below. The figure shows the calculation of the terminal voltage v_{tP}, which is further used for the calculation of the in-phase unit templates for three phases of the power system ($uT_{spa}, uT_{spb}, uT_{spc}$) and in-quadrature unit templates ($uT_{sqa}, uT_{sqb}, uT_{sqc}$) as shown in Fig. 2. The purpose of the calculation of the templates is to align the reference current that is extracted from the control algorithm to the PCC voltage. Secondly, the cost of charging and discharging of DC capacitor in the form of active power is to be calculated. The loss in active power is calculated in the form of weight component which is updated with each iteration. The change in voltage is converted to equivalent weight through the PI controller having gain as k_{pdc} and k_{idc} as mentioned in (1). The demand of reactive power in regulating the voltage at PCC is computed by using another PI controller with gains k_{pr} and k_{ir}. The gain is adjusted to represent the change in voltage to equivalent weight component of reactive power as mentioned in (2).

$$w_{pdc}(n) = w_{pdc}(n-1) + K_{pdc}\{V_{de}(n) - V_{de}(n-1)\} + K_{idc}V_{de}(n) \qquad (1)$$

where V_{de} is the DC voltage of DSTATCOM.
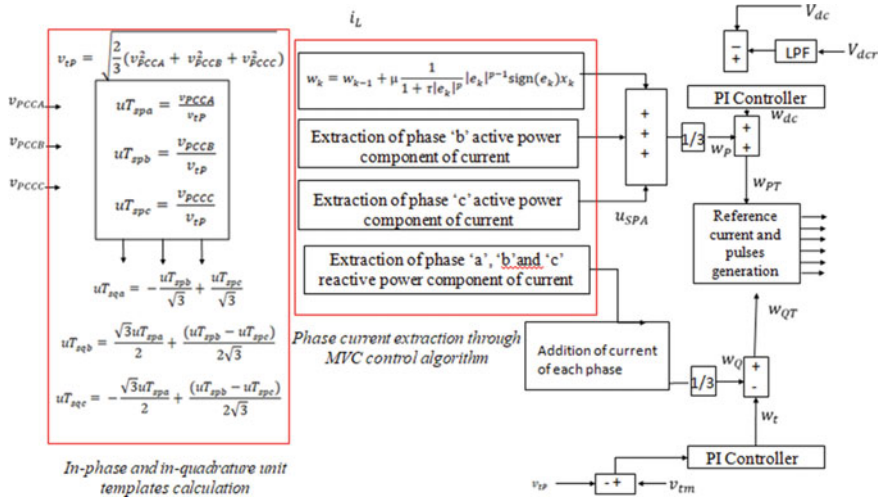
Fig. 2 Detailed block diagram of control algorithm

$$w_{qr}(n) = w_{qr}(n-1) + K_{pr}\{V_{tp}(n) - V_{tp}(n-1)\} + K_{ir}V_{tr}(n) \qquad (2)$$

where V_{tp} is the terminal voltage at the PCC.

After the calculation of other losses, next task is the calculation of the reference current. The adaptive algorithms generally use weight update equations for the calculation of the reference current. The motive behind the algorithms is continuously updating the weight in each iterations to minimize the error between the calculated reference current and the actual reference current. In this work, two recent algorithms MVC and APSA are analysed.

The weight update equation for the MVC control algorithm is given in (3). The analysis of the equation reveals that the signum of the error e_k between the estimated and actual load current is calculated in each iteration. If the error is affected from the impulsive noise, the value of $\text{sign}(e_k)$ will be zero. Hence, the algorithm is not affected by the impulsive noise. The constant μ decides the time of one iteration and hence it should be low, whereas the constant τ decides the area of the Versoria curve. The calculative burden of the algorithm is calculated as the weight equation has three multiplicative terms and one division term and a few additive and subtractive terms.

$$w_k = w_{k-1} + \mu \frac{1}{1 + \tau|e_k|^p}|e_k|^{p-1}\text{sign}(e_k)x_k \qquad (3)$$

The reactive and active power weight equation of individual phases will be calculated and averaged to predict the total reactive and active power component of load current.

The weight update equation used in APSA algorithm is given in (4). The analysis of the equation shows that the value of $\text{sign}(e_k)$ will be zero in the presence of impulsive noise. Hence, the algorithm can work satisfactorily in the presence of impulsive noise in the smart grid. The number of constant is one, δ which determines the step size of the algorithm. The calculative burden of the APSA algorithm is heavier in comparison to the MVC algorithm, which makes the time for settling the weight larger in comparison to MVC. The stability of the APSA algorithm is a bit less than the MVC due to large time taken in the settling of the weight equation.

$$w_{k+1} = w_k + \frac{\delta X(k) * \text{sgn}(e(k))}{\sqrt{\text{sgn}(e^T(k)) * X^T(k) * X(k) * \text{sgn}(e(k))}} \qquad (4)$$

The reference current calculated from the weight update equations of the algorithm is further used to bring about the pulses for DSTATCOM. Hysteresis current controller or pulse width modulation can be used for the generation of the pulses.

4   Results and Discussions

The analysis of MVC and APSA algorithm is carried out in this section under harmonics, stability and other power system operating conditions using MATLAB/Simulink 2017a, power system toolbox. The performance of MVC algorithm during sudden increase in the load is shown in Fig. 3. The figure has the waveforms of the source voltage, source current, load current, compensating current and DC voltage. The waveform of load current is highly non-linear in nature due to the presence of harmonics.

The compensating current is supplied by the DSTATCOM. The value of the compensating current is increased at t = 0.4 s which shows that as the load current is increasing, suddenly so the compensating current. The DC voltage level has also experienced a dip at the point when the load has suddenly changed and the DC level is maintained at a different point.

The performance of MVC during a single-phase fault condition is shown in Fig. 4. The figure shows that the system experienced a faulty condition at t = 0.8 s.

Fig. 3 Performance of MVC algorithm during sudden load increase: **a** voltage at the terminals of PCC, **b** three-phase source current, **c** three-phase load current, **d** single-phase compensating current and, **e** voltage at the DC link under varying load conditions

Fig. 4 Performance of MVC algorithm during single-phase fault: **a** voltage at the terminals of PCC, **b** three-phase source current, **c** three-phase load current, **d** single-phase compensating current and, **e** voltage at the DC link under varying load conditions

Fig. 5 Performance of MVC algorithm during power factor control mode: **a** voltage at the terminals of PCC, **b** single-phase source current, **c** single-phase load current, **d** single-phase compensating current and, **e** voltage at the DC link and, **f** voltage at PCC under varying load conditions

During the fault, the current of one of the phases becomes zero, and at that point DSTATCOM supplies the current to maintain the balanced condition of the system. The balanced condition is achieved at a lower magnitude than the original. The DC value is perturbed during the faulty condition but again maintains the constant value after 0.5 s, which shows the stable operation of the algorithm during faulty condition also. The power factor control mode of operation needs the analysis of the terminal voltage during different operating conditions of the power system. From Fig. 5. the performance of MVC algorithm during power factor control mode can be observed. The PCC voltage magnitude remains constant which reveals that the algorithm is able to maintain the voltage at PCC by supplying the required reactive power to the load.

The fast Fourier transform of the load source current before supplying the DSTATCOM is shown in Fig. 6a. The total harmonics distortion present in the load current is 22.99%, which is far more than the allowable harmonics limit of 5% mentioned by the IEEE 519 standards. After providing the compensation from DSTATCOM, the harmonics content in the source current has been reduced as shown in Fig. 6b. The value of the total harmonic distortion of the source current after injecting anti-harmonics from DSTATCOM is reduced to 2.35% which is below the prescribed limit. The performance of the APSA algorithm is shown in Fig. 7. The waveforms of the source voltage, source current, load current, compensating current and DC voltage are shown in the figure. The sudden increase in the load current at t = 0.4 s shows the negligible effect in the DC link voltage of the DSTATCOM. The perturbation is very minor during load change condition which was 0.5 s in case of MVC. It shows that the APSA algorithm has better stability and accuracy. The operation of single-phase fault in case of APSA algorithm has been shown in Fig. 8. The algorithm shows better performance during single-phase fault in maintaining the

(a)   (b)
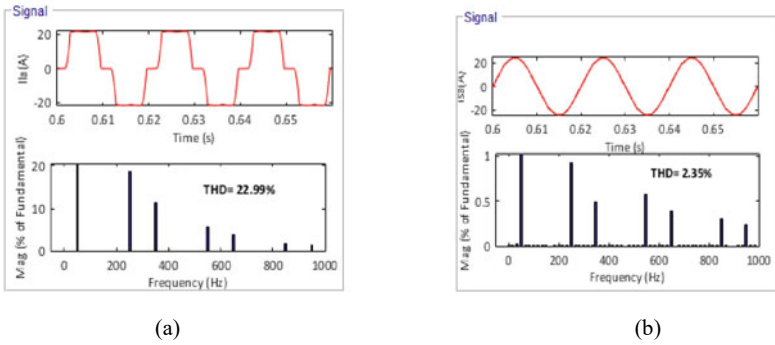
Fig. 6 Fast Fourier transform analysis of **a** source current before compensation and **b** source current after compensation

Fig. 7 Performance of APSA algorithm during sudden load increase **a** voltage at the terminals of PCC, **b** three-phase source current, **c** three-phase load current, **d** single-phase compensating current and, **e** voltage at the DC link under varying load conditions
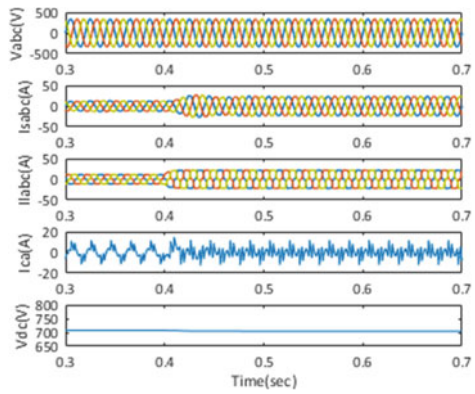
Fig. 8 Performance of APSA algorithm during single-phase fault: **a** voltage at the terminals of PCC, **b** three-phase source current, **c** three-phase load current, **d** single-phase compensating current and, **e** voltage at the DC link under varying load conditions
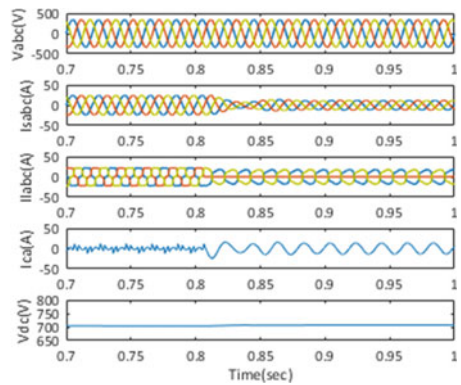
balance of the system as well as the stability of the system due to negligible change in the magnitude of DC voltage during the faulty condition.

This shows that APSA works better than MVC in case of fault operations.

The operation of power factor correction mode for APSA algorithm is shown in Fig. 9. The algorithm works better than MVC in this mode also by maintaining the accuracy and stability of the system.

The fast Fourier transform of the source current after compensation through APSA is shown in Fig. 10. The total harmonic distortion is reduced from 22.99% to 1.56% which is below the IEEE 519 standards and also lower than the MVC algorithm. The lower magnitude of harmonics in the source current gives large window to use many non-linear devices together with the maintenance of harmonics level.

Fig. 9 Performance of APSA algorithm during power factor control mode: **a** voltage at the terminals of PCC, **b** three-phase source current, **c** three-phase load current, **d** single-phas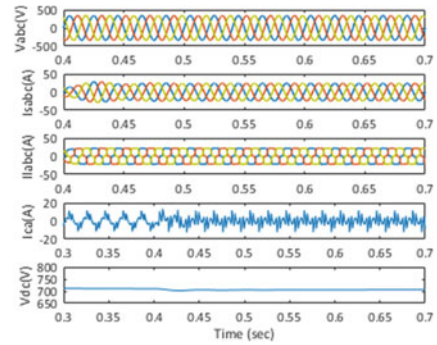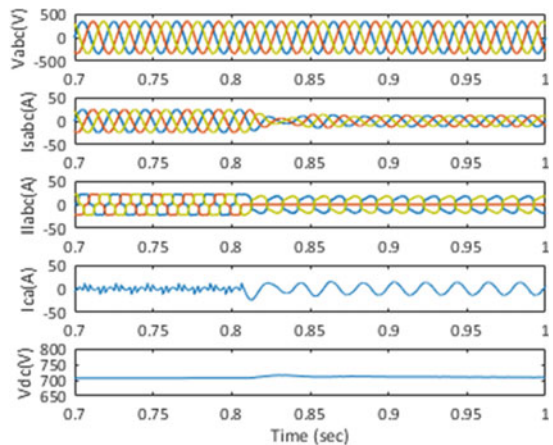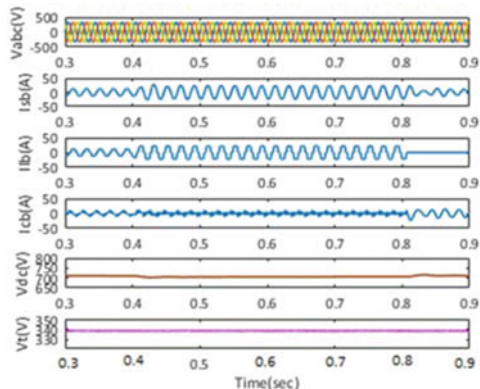e compensating current and, **e** voltage at the DC link and, **f** voltage at the terminals of PCC under varying load conditions
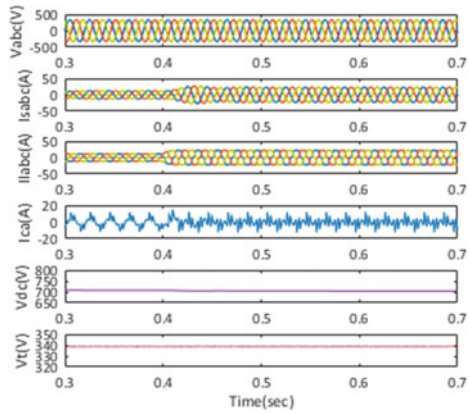
Fig. 10 Fast Fourier transform analysis of source current after compensation using APSA
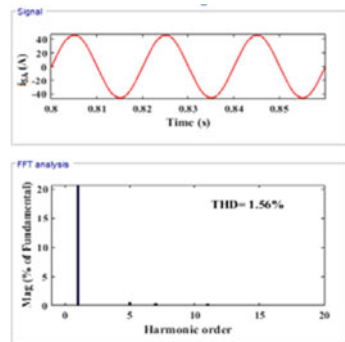
5 Conclusions

The work includes a comparative analysis of the Maximum Versoria Criteria (MVC)- and Affine Projection Sign Algorithm (APSA)-based control algorithm for DSTATCOM. The algorithms are briefly discussed with the method used in adaptive control of the DSTATCOM. The algorithm is tested for power system operating conditions like sudden load increase, single-phase faulty condition and reactive power condition. The APSA algorithm is more accurate due to the presence of only one constant that is to be predicted in weight update equation while MVC has two constants. Moreover, the deviation in the DC voltage during above-mentioned cases is minimal in APSA in comparison to the MVC algorithm which shows the better stability of the APSA algorithm. The Fourier analysis of the source current after compensation shows the total harmonic reduction is 2.35% in MVC while 1.56% in APSA algorithm. Both algorithms are able to reject the impulsive noise in the system and can work in the noisy environment.

References

1. N.G. Hingorani, L. Gyugyi, Understanding FACTS (Wiley, New Jersey, 2000)
2. B. Singh, A. Chandra, K. Al-Haddad, *Power Quality: Problems and Mitigation Techniques* (Wiley, U.K, 2015)
3. A. Sharma, B.S. Rajpurohit, S.N. Singh, A review on economics of power quality: impact, assessment and mitigation. Renew. Sustain. Energy Rev. **88**, 363–372 (2018)
4. A. Ghosh, G. Ledwich, *Power Quality Enhancement Using Custom Power Devices* (Springer International Edition, Delhi, 2009)
5. M. Badoni, A. Singh, B. Singh, Power quality enhancement using euclidean direction search based control technique. IEEE Trans. Industr. Electron. **67**(3), 2231–2240 (March 2020)
6. M. Badoni, A. Singh, B. Singh, Power quality improvement using DSTATCOM with affine projection algorithm. IET Gener. Transm. Distrib. **12**, 3261–3269 (2018)
7. M. Badoni, A. Singh, B. Singh, Implementation of echo-state network-based control for power quality improvement. IEEE Trans. Industr. Electron. **64**(7), 5576–5584 (July 2017)
8. T. Penthia, A.K. Panda, S.K. Sarangi, M. Mangaraj, ADALINE based LMS algorithm in a three phase four wire distribution system for power quality enhancement, in *2016 IEEE 6th International Conference on Power Systems (ICPS)* (2016), pp. 1–5
9. M. Srinivas, I. Hussain, B. Singh, Combined LMS–LMF-based control algorithm of DSTATCOM for power quality enhancement in distribution system. IEEE Trans. Industr. Electron. **63**(7), 4160–4168 (July 2016)
10. S. Gautam, M. Aeidapu,Sine cosine algorithm based shunt active power filter for harmonic compensation, in *2019 3rd International conference on Electronics, Communication and Aerospace Technology (ICECA)* (2019), pp. 1051–1056
11. I.A. Nassar, M.A. Omara, M.M. Abdella, Enhancement of voltage profile in power systems by using genetic algorithm, in *2019 21st International Middle East Power Systems Conference (MEPCON)* (2019), pp. 459–464
12. S. Gomathi, S. Tharanya, T. Venkatesan, Enhancement of power quality on grid connected dual voltage source inverter, in *2015 Online International Conference on Green Engineering and Technologies (IC-GET)* (2015), pp. 1–6

13. A. Sharma, A.K. Mishra, B.S. Rajpurohit, K.N. Srivastava, Power quality enhancement at PCC for PMSM based adjustable speed drive load, in *2017 7th International Conference on Power Systems (ICPS)* (2017), pp. 364–369
14. A. Sharma, B.S. Rajpurohit, Maximum versoria criteria based adaptive filter algorithm for power quality intensification, in *2020 IEEE 9th Power India International Conference (PIICON)* (2020), pp. 1–5
15. A. Sharma, B.S. Rajpurohit, S. Agnihotri, Affine projection sign algorithm based control for mitigation of distribution side power quality problems. Energy Convers. Econ. **2**, 79–90 (2021)

Matrix Magic Shifting to Extract Maximum Power Under Partial Shading Conditions

Vinaya Chandrakant Chavan and Suresh Mikkili

Abstract In PV array, Mismatch losses and power losses are the critical issues created under partial shading conditions. It can be effectively minimized by applying PV array reconfiguration. This paper compares two newly proposed physical reconfiguration methods, Novel shade Dispersion (NSD) and Matrix Magic Shifting (MMS) with conventional configurations (CC). The performance has been evaluated in MATLAB/Simulink environment under six partial conditions. P–V curve, I-V curve, Global maximum power point (GMPP), mismatch loss (ML), fill factor (FF) and efficiency are the parameters used for performance evaluation.

Keywords Maximum power · Partial shading condition · Reconfiguration

1 Introduction

To dwindle depleting nonrenewable energy sources and fulfil the worlds growing energy demand, solar energy is the most efficient, abundant, ecofriendly and promising source of energy [1]. Solar energy is currently used for a variety of operations, including building heating and cooling, industrial heat generation, food refrigeration, water heating, distillation, drying, cooking and power generation. To improve the solar industry's future prospect, continued research is going on [2]. Therefore, the output of the PV array is primarily dependent on irradiance and power generation. Partial shading created by light poles, chimneys, trees, nearby constructions, etc. inserts a major drawback in the power generation of PV array [3]. As a result, the panels are exposed to several irradiations, which create multiple peaks in P-V and I-V curves, and thereby cause power losses. One of the main drawbacks of traditional

V. C. Chavan · S. Mikkili (✉)
Electrical and Electronics Engineering, National Institute of Technology Goa, Ponda 403401, Goa, India
e-mail: mikkili.suresh@nitgoa.ac.in

V. C. Chavan
e-mail: chavanvinaya19@gmail.com

MPPT algorithms like perturb and observe, hill climbing, and incremental conductance is that they can get stuck at one of the Local Peaks of the P-V curves. To handle this issue, an advanced and complex MPPT technique is required [4]. The losses that occurred due to partial shading condition (PSC) do not only depend upon the pattern and time of shade occurrence, but also on the connection configuration of the PV array [5]. Various conventional configurations like series parallel (SP), total cross tide (TCT), bridge link (BL), honeycomb (HC) and various hybrid configurations have been addressed in the literature [6, 7]. Regardless of the fact that the TCT connection has a better potential for obtaining maximum power, it faces a number of challenges, including no shadow dispersion and the appearance of many peaks. To reduce panel violations and boosting the PV array's energy production, reconfiguration is one of the best solutions. Reconfiguration can be done either electrically or physically. In electrical array reconfigurations, electrical connections are changed through the sensor, switching matrix control through different algorithms. It increases the cost and complexity of the PV system [8]. To address this issue, [9] reviews different physical or static array reconfiguration methods. Here, the physical location of panels is changed while the electrical connection remains the same. [10]presented a Sudoku-based improvised physical reconfiguration to solve this problem. To relocate the PV panel, [11] proposes a magic square technique of reconfiguration. [12] proposes a skyscraper-based approach of physical reconfiguration based on clues. The major important constraints of these approaches include array size and power dependence on logic, clue dependency, sophisticated reasoning, implementation complexity and so on.

This paper proposes Matrix Magic Shifting (MMS), a groundbreaking row current equalization-based physical array reconfiguration, which has TCT electrical connection base. It disperses the shadow throughout the whole array and increases the output power by lowering power losses. The investigation has been done on 213 W, 6×6 PV array structure in MATLAB/Simulink environment. The performance has been investigated on P-V curve, I-V- curve, GMPP, FF, ML and efficiency under six PSCs.

2 Modelling of Sudoku and Optimal Sudoku Static PV Array Reconfiguration Techniques

The shadow falling on the panel reduces the energy generated from solar PV. The shadow causes less current generation. To increase the output power, the reconfiguration techniques are used which helps in reducing the effect of shadow. In reconfiguration techniques, either the panel is changed from its location or the electrical connection of the panel is changed. Changing the panel from its location is called static reconfiguration. Changing the electrical connection of the PV panel is called Dynamic reconfiguration. There are various types of static and dynamic techniques.

2.1 Basic Sudoku Reconfiguration Technique

This paper compares two matrix shifting-based physical array reconfiguration methods, where the physical location is changed and electrical connections remain unaltered similar to TCT connection. To do this, two components of a novel algorithm were developed. It applies reconfiguration within the column base [13]. The sub-matrices formation is the first step and forming the primary matrix is the second step. The proposed approach contributes to the research of PV array reconfiguration and improves power extraction under PSC as a result of its originality. In earlier stages, Novel shade dispersion (NSD) method was developed [14]. Based on the location of panels, the required wire length and respective wiring losses are more for NSD. Also, it gives less power generation than conventional TCT configuration under PSC6. Therefore, the MMS method has been proposed to reduce the losses and enhance the power output and overall performance under all the PSCs. The panel location for TCT, NSD and MMS is shown in Fig. 1. The flowchart for the MMS method is given in Fig. 2. This paper considers a 6×6 main PV array. The steps to form MMS reconfiguration are:

1. Submatrix of 3×2 size has been selected with 2 folds in the main matrix.
2. In the next step, the submatrix has been shifted with one row in the same fold till the filling of all places, as shown in Fig. 1c.
3. To modify the submatrix, shift the column by 1 and repeat the process till filling of all the elements as shown in Fig. 1c.

3 Partial Shading Conditions and Shade Dispersion for Proposed Methods

Shade accumulates in a certain location of the panel in a traditional arrangement, however, with reconfiguration, the PSC has spread throughout the whole PV array. This paper considers six realistic shading conditions PSC1, PSC2, PSC3, PSC4, PSC5, and PSC6. The PSCs and shade dispersion has discussed in this section.
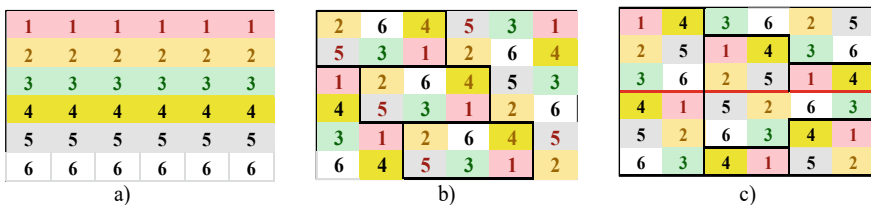
Fig. 1 PV panel position for: **a** CC **b** NSD **c** MMS

Fig. 2 Flowchart for MMS
method
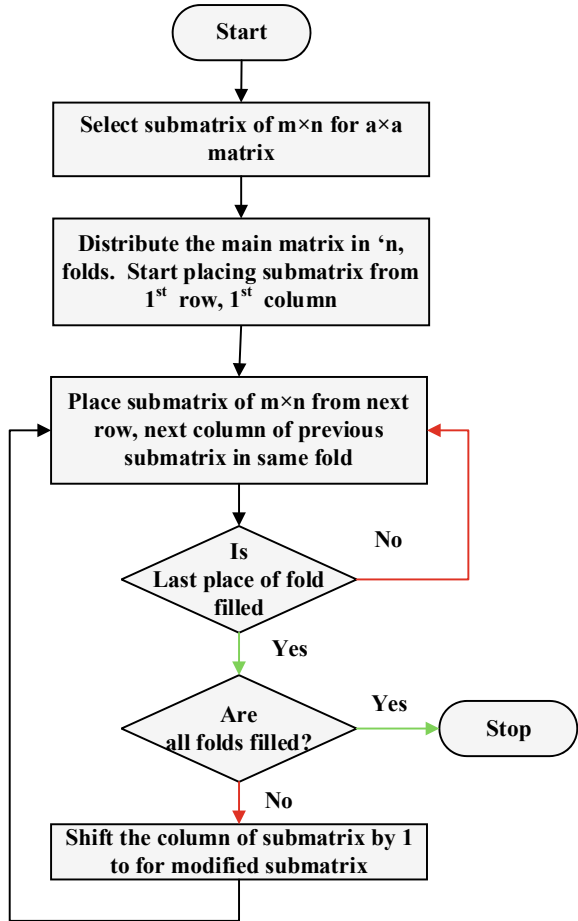
3.1 *PSC 1(Horizontal)*

Illustrated in Fig 3a, In the fourth row, the first and second columns' have 700 W/m^2
irradiances. The final two panels of the 3rd and 4th columns' fourth row have 500
W/m^2, and the last two columns of the same row have 200 W/m^2. With the suggested
reconfiguration approach, the PSC has scattered across an array, as illustrated in
Fig. 3b.
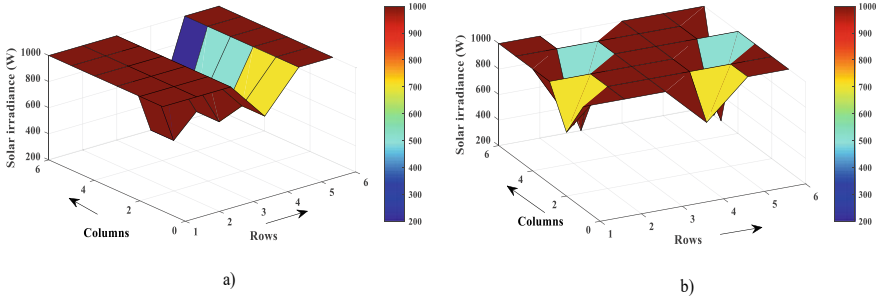
Fig. 3 PSC 1 shade pattern for **a** CC, **b** MMS
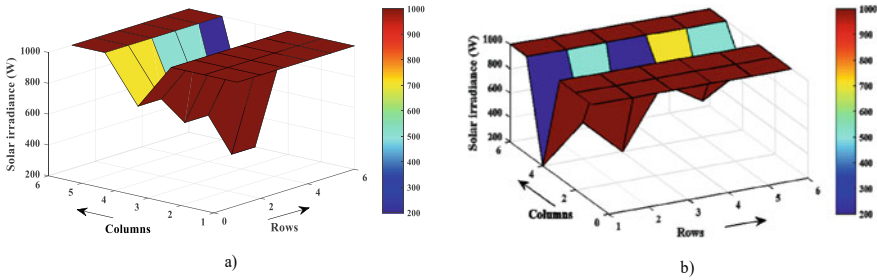
Fig. 4 PSC 2 shade pattern for **a** CC, **b** MMS

3.2 PSC 2 (Vertical)

The fourth column of the PV array has been darkened with three degrees of shading under this shading condition, as illustrated in Fig. 3a. The irradiance of 700, 500, and 200 W/m^2 have been seen on two rows of each shade from top to bottom in the considered column as shown in Fig. 4a. As demonstrated in Fig. 4, the suggested MMS approach spreads the shadow throughout the same columns (b).

3.3 PSC 3 (L shape)

Figure 5a highlights that in this pattern; the first four panels in the first columns are shaded with 700 W/m^2. The last two panels of the second column and the last panel of the third column of the array have been shaded with 500 W/m^2 and the last module of the third array is irradiated with 200 W/m^2. In Fig. 5b, the shade has dispersed on an array by the proposed MMS method.

a)   b)
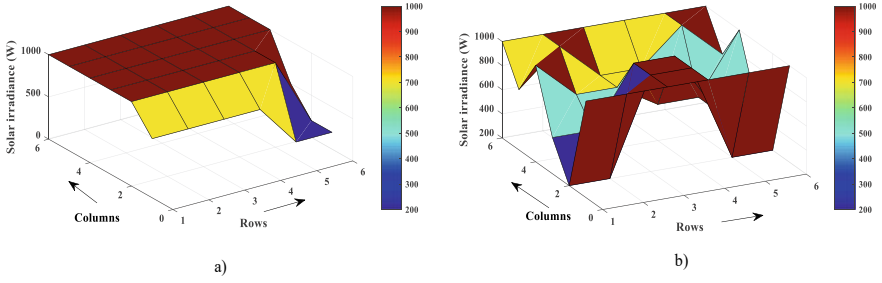
Fig. 5 PSC 3 shade pattern for **a** CC, **b** MMS

a)   b)
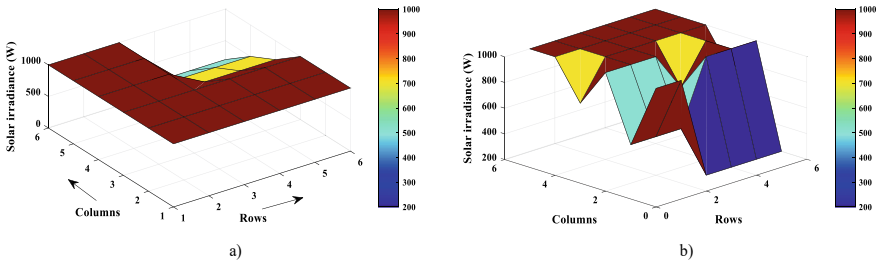
Fig. 6 PSC 4 shade pattern for **a** CC, **b** MMS

3.4 *PSC 4 (Bottom Corner)*

This pattern has developed in the bottom right of the array, with three consistent degrees of column shading. As illustrated in Fig. 8, the final three rows are shaded with the 4, 5 and 6th columns, respectively, with 700, 500 and 200 W/m² (a). As seen in Fig. 6b, it exhibits shadow distribution due to the proposed method in the final three columns of the array.

3.5 *PSC 5 (Center)*

As shown in Fig. 7a, the middle four panels of the second column are irradiated with 200 W/m², the middle four panels of the third column and third and fourth row of the fourth column are shaded with 500 W/m² and the fifth column's middle four panels, as well as the fourth and fifth rows of the fourth column, are tinted with 500 W/m². Here, the first, and last rows and columns remain none shaded. The shade scattering by the proposed method is as seen in Fig. 7b.
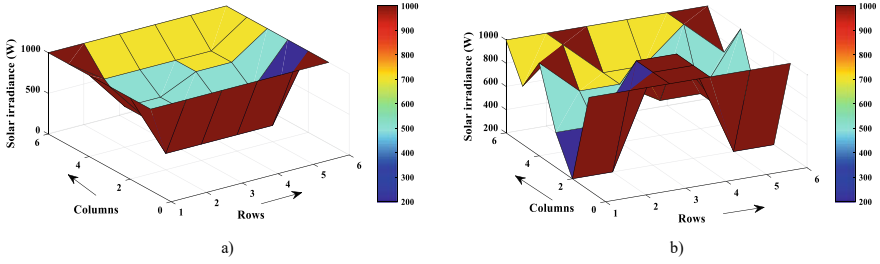
Fig. 7 PSC 5 shade pattern for **a** CC, **b** MMS
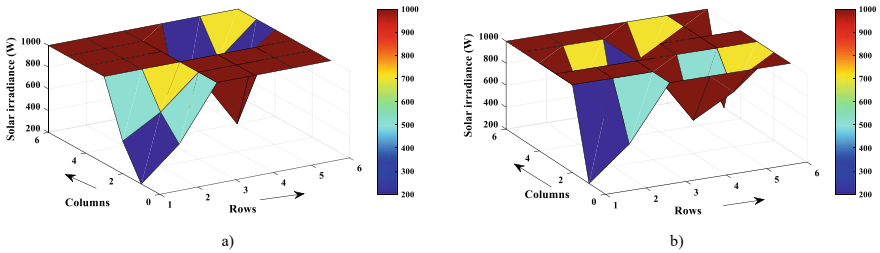
Fig. 8 PSC6 shade pattern for **a** CC, **b** MMS

3.6 PSC 6 (Random)

This shade has random shade distribution. Here, first row first column, fourth row fifth column and fifth row fifth column modules are shaded with 200 W/m^2; first row second column and second row first column are shaded with 500 W/m^2 and the diagonal location of the second, fourth and fifth columns have 700 W/m^2 irradiances as displayed in Fig. 6a. With the application of the proposed method, the shade has been distributed in array as displayed in Fig. 6b.

4 Result Discussion

4.1 PV-IV Curve Profile

Figure 9 compares the traditional configurations SP, TCT, BL, HC, and the newly proposed MMS method of reconfiguration under six PSCs. It highlights that reconfiguration reduces the number of peaks on P-V and I-V curves and also on the nature of the curves. Under the first three PSCs, both proposed and considered reconfiguration methods are giving greater power output compared to conventional configurations. The nature of the PV curve is also improved. As portrayed in Fig. 9d under PSC 4,
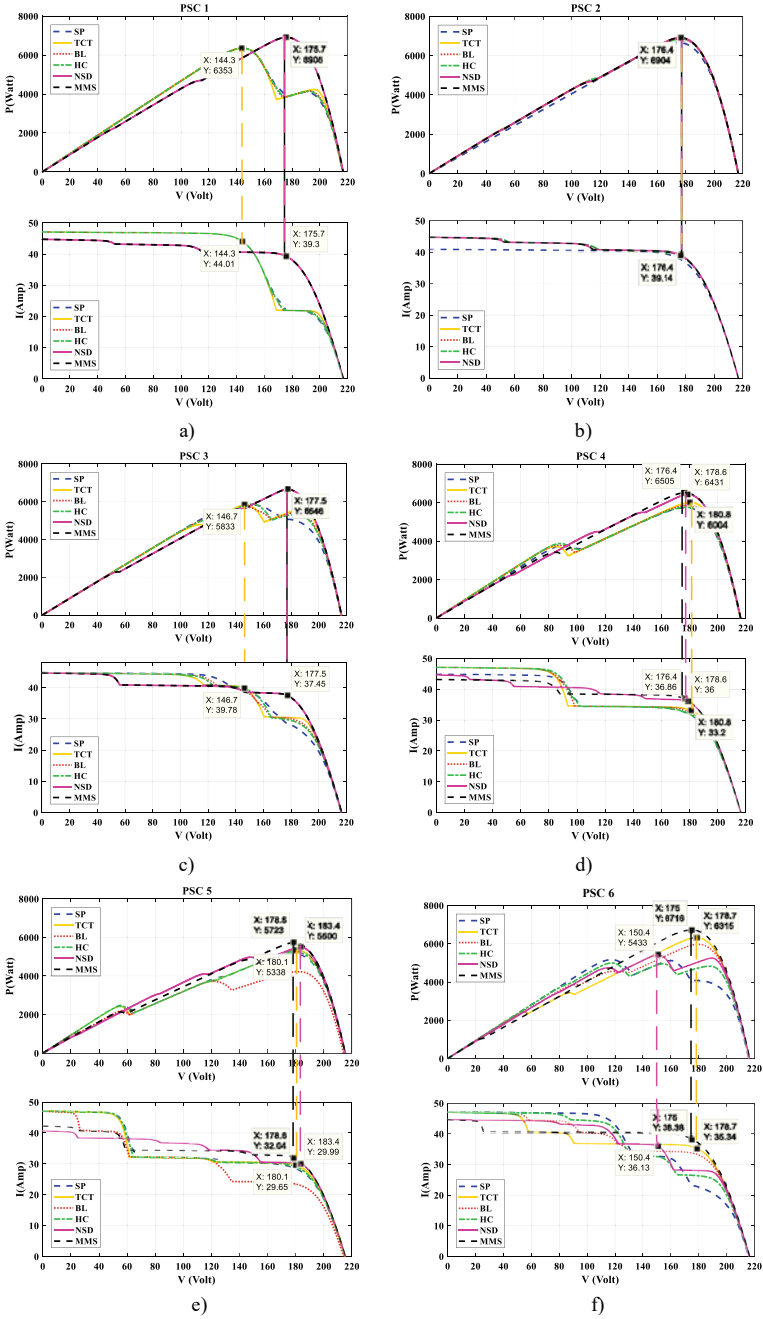
Fig. 9 IV-PV profile under considered PSCs for conventional and proposed reconfiguration: **a** PSC1, **b** PSC2, **c** PSC3, **d** PSC4, **e** PSC5, **f** PSC6

Table 1 GMPP for proposed MMS method and CC under PSCs

Array connection	PSC1	PSC2	PSC3	PSC4	PSC5	PSC6
SP	6352.8	6660.01	5818.1	5737.3	5128.7	5168.6
TCT	6352.8	6904.9	5833.8	6003.9	5338.8	6315
BL	6352.8	6842.6	5706	5854	4224.8	5966.6
HC	6352.8	6844.7	5873.3	5756.7	5238.3	4993.4
NSD	6904.9	6904.9	6645.7	6430.7	5499.7	5433.5
MMS	6904.9	6904.9	6645.7	6504.7	5723	6716.3

both NSD and MMS reconfiguration are giving improved performance compared to CC. Here, the proposed method is giving 427, 223 and 1283 W more power generation compared to the NSD method under PSC4, PSC5 and PSC6, respectively.

4.2 Global Maximum Power Point (GMPP)

Table 1 compares the traditional configurations SP, TCT, BL, HC, considered NSD reconfiguration and the proposed MMS method. Here,under the first three PSCs, both the reconfiguration methods, NSD and MMS, are giving the same highest GMPP at 6904.9, 6904.9 and 6645.7 W. Under PSC4 and PSC5, NSD shows improvement in GMPP compared to CC while MMS is giving higher GMPP than NSD at 6545.7 and 5723 W. Under PSC6, NSD was giving 881.5 W lessor power generation than conventional TCT configuration. This issue is handled by the MMS method with a hike of 401.3 W than TCT. The outer layer of the graph in Fig. 10. highlights that, under all the shading conditions, the MMS method is superior to the rest CC and NSD method.

4.3 % Mismatch Power Loss (% MPL)

% MPL is the power losses caused by PSC relative to GMPP power. Under all shading circumstances, Table 2 and Fig. 11 radar graph show that MMS has the innermost track near zero showing the lowest %MPL. In CC, TCT has the lowest %MPL. MMS has 7.2, 0, 10.59, 6.53, 5.01 and 5.23 reduced %MPL compared with TCT.

4.4 Fill Factor (FF)

The FF refers to the region that gives the active area of PV array for power generation. In Fig. 12, the performance track at the outside border of the radar chart implies that
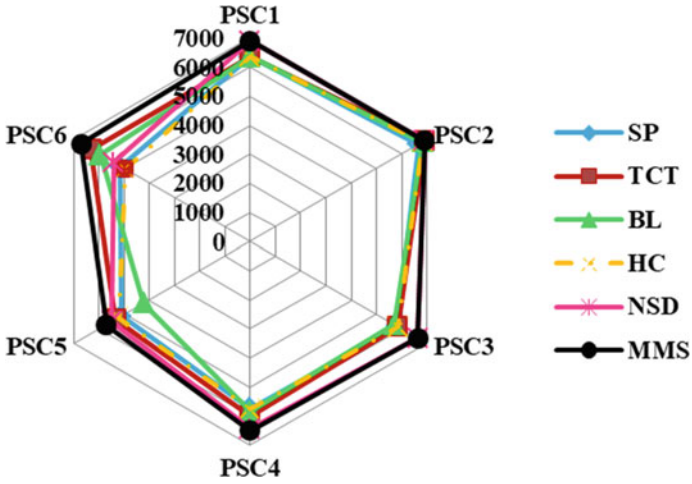
Fig. 10 GMPP analysis under six PSCs

Table 2 %MPL for proposed MMS method and CC under PSCs.

Array connection	PSC1	PSC2	PSC3	PSC4	PSC5	PSC6
SP	17.13	13.12	24.10	25.16	33.10	32.58
TCT	17.13	9.93	23.90	21.68	30.36	17.62
BL	17.13	10.74	25.57	23.63	44.89	22.17
HC	17.13	10.71	23.38	24.90	31.67	34.86
NSD	9.93	9.93	13.31	16.11	28.26	29.12
MMS	17.13	13.12	24.10	25.16	33.10	32.58
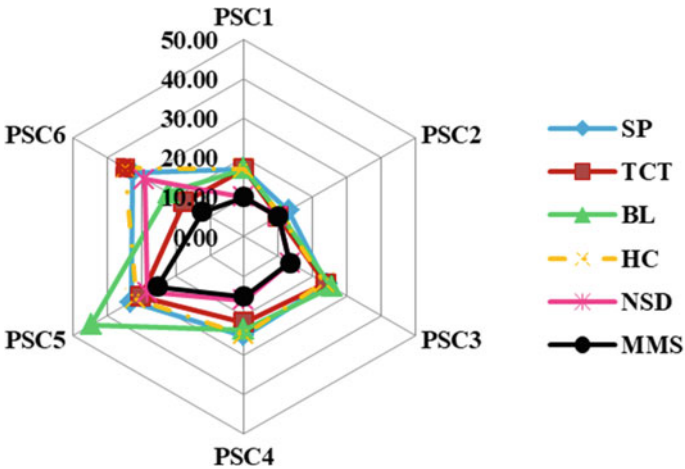
Fig. 11 %MLP analysis under six PSCs
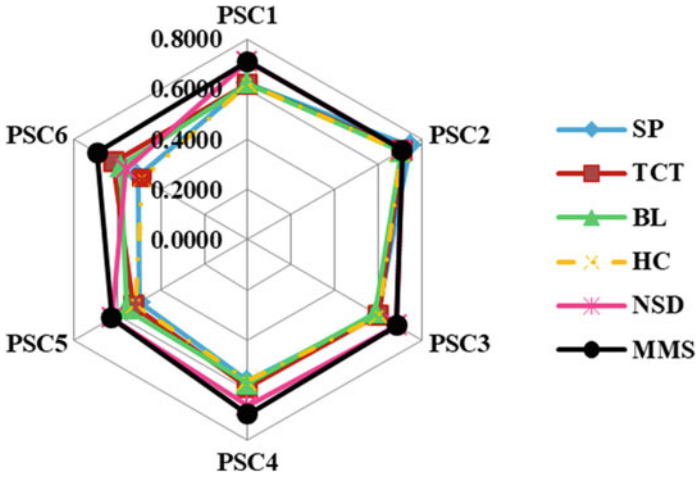
Fig. 12 FF analysis under six PSCs

Table 3 FF for proposed MMS method and CC under PSCs

Array connection	PSC1	PSC2	PSC3	PSC4	PSC5	PSC6
SP	0.6222	0.7492	0.6003	0.5657	0.4993	0.5075
TCT	0.6218	0.7111	0.6015	0.5889	0.5264	0.6193
BL	0.6221	0.7046	0.5886	0.5743	0.5581	0.5848
HC	0.6221	0.7047	0.6058	0.5648	0.5163	0.4900
NSD	0.7111	0.7111	0.6853	0.6644	0.6259	0.5613
MMS	0.7111	0.7111	0.6853	0.6957	0.6272	0.6934

MMS has the highest FF value under all shading circumstances. In CC, the TCT shows the highest FF. Table 3. Highlights that, both the reconfiguration gives 0.71, 0.71 and 0.68 FF under PSC1, PSC2 and PSC3. Under PSC4, PSC5 and PSC6, MMS gives 3, 1 and 13% more than NSD.

4.5 % Efficiency (%η)

The term efficiency has been used to describe the PV array's efficacy. The efficiency of traditional designs and reconfigurations under various PSC ranges from 15% to 21% as resulted in Table 4. In Fig. 13, the outer ring of the graph indicates the effectiveness of the MMS method compared with NSD and CC under six PSCs. It is on an average of 21% under all PSC.

Table 4 Efficiency for proposed MMS method and CC under PSCs

Array connection	PSC1	PSC2	PSC3	PSC4	PSC5	PSC6
SP	19.37	20.30	18.24	17.94	18.32	16.30
TCT	19.37	21.05	18.29	18.78	19.07	19.92
BL	19.37	20.86	17.89	18.31	15.09	18.82
HC	19.37	20.87	18.41	18.00	18.71	15.75
NSD	21.05	21.05	20.83	20.11	19.64	17.14
MMS	21.05	21.05	20.83	20.34	20.44	21.19
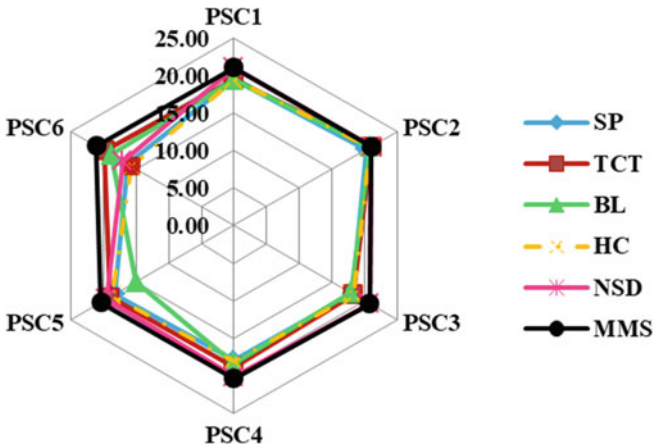
Fig. 13 FF analysis under six PSCs

5 Conclusion

The performance of traditional PV array structures such as SP, TCT, BL and HC has been evaluated and compared to NSD and the proposed MMS approach of static PV array reconfiguration in this work. On a 6 × 6 array layout, it has been done in MATLAB/Simulink. MMS reconfiguration minimizes the number of peaks and enhances the array's P-V and I-V profile for all PSCs studied. MMS has the largest GMPP of 6716W, the highest FF of 0.71, lowest mismatch losses of 9.93% and highest efficiency of 21.19%. All the Simulink results analysis of CC, NSD and MMS conclude that the MMS method is superior to the rest all CC and NSD under all considered PSC.

References

1. S.K. Sahoo, Renewable and sustainable energy reviews solar photovoltaic energy progress in India: a review. Renew. Sustain. Energy Rev. **59**, 927–939 (2016). https://doi.org/10.1016/j.rser.2016.01.049
2. N. Kannan, D. Vakeesan, Solar energy for future world: - A review (2016). https://doi.org/10.1016/j.rser.2016.05.022
3. V. Madhava, R. Tatabhatla, A. Agarwal, T. Kanumuri, Parameter enhancement of solar array under partial shading conditions (2020)
4. M. Seyedmahmoudian, B. Horan, T.K. Soon, R. Rahmani, A.M. Than Oo, S. Mekhilef, A. Stojcevski, State of the art artificial intelligence-based MPPT techniques for mitigating partial shading effects on PV systems—a review. Renew. Sustain. Energy Rev. **64**, 435–455 (2016). https://doi.org/10.1016/j.rser.2016.06.053
5. J. Ahmed, H. Nabipour-Afrouzi, M.F.N. Tajuddin, S. Kashem, Modified series-parallel photovoltaic configuration to enhance efficiency under partial shading. Int. J. Integr. Eng. **11**, 207–215 (2019). https://doi.org/10.30880/ijie.2019.11.03.021
6. C. Saiprakash, A. Mohapatra, B. Nayak, S.R. Ghatak, Analysis of partial shading effect on energy output of different solar PV array configurations. Mater. Today: Proc. **39**, 1905–1909 (2021). https://doi.org/10.1016/j.matpr.2020.08.307
7. S.R. Pendem, V.V. Katru, S. Mikkili, Hybrid PV Array configurations for mitigating the mismatching power loss and number of peaks in the output characteristics under various PSCs, in *IECON Proceedings (Industrial Electronics Conference)* (2019), pp. 2377–2382 https://doi.org/10.1109/IECON.2019.8927367
8. S. Malathy, R. Ramaprabha, Reconfiguration strategies to extract maximum power from photovoltaic array under partially shaded conditions. Renew. Sustain. Energy Rev. **81**, 2922–2934 (2018). https://doi.org/10.1016/j.rser.2017.06.100
9. C.V. Chandrakant, S. Mikkili, A typical review on static reconfiguration strategies in photovoltaic array under non-uniform shading conditions. CSEE J. Power Energy Syst. https://doi.org/10.17775/cseejpes.2020.02520.
10. M. Horoufiany, R. Ghandehari, Optimization of the Sudoku based reconfiguration technique for PV arrays power enhancement under mutual shading conditions. Sol. Energy **159**, 1037–1046 (2018). https://doi.org/10.1016/j.solener.2017.05.059
11. G. Madhusudanan, N. Rakesh, S. Senthil Kumar, S. Sarojini Mary, Solar photovoltaic array reconfiguration using Magic Su–Do–Ku algorithm for maximum power production under partial shading conditions. Int J Ambient Energy 1–29. https://doi.org/10.1080/01430750.2019.1691654
12. G. Meerimatha, B.L. Rao, Novel reconfiguration approach to reduce line losses of the photovoltaic array under various shading conditions. Energy **196**, 117120 (2020). https://doi.org/10.1016/j.energy.2020.117120
13. V.C. Chavan, S. Mikkili, Repositioning of series-parallel, total-cross-tide, bridge-link, and honey-comb PV array configurations for maximum power extraction. IETE J. Res. (2021). https://doi.org/10.1080/03772063.2021.1986151
14. C. Vinaya, M. Suresh, B. Praveen Kumar, Novel shade dispersion method to extract maximum power under partial shading condition, in *IECON 2021—47th Annual Conference of the IEEE Industrial Electronics Society* (IEEE, Tranto, Canada, 2021), p. 6

Simulation Result Analysis of a Proposed Cross Connected Switch Capacitor Multi Level Inverter Topology

Lipika Nanda [ORCID]**, Chitralekha Jena, Babita Panda, Arjyadhara Pradhan, and Rudra Narayan Dash**

Abstract The MLI is developed by combining cross-switched MLI (main circuit) with switched-capacitor MLI (auxiliary circuit). For different combinations of input DC voltage sources, the proposed inverter is analyzed and the general equations of different quantities have been found. As the switched-capacitor circuit is interconnected with the cross-switched MLI, it reduces the number of power supplies, switching devices, and further boosted the input voltage. A detailed comparison study has been presented. Half-height (HH) Pulse width modulation scheme has been chosen as the switching scheme in order to reduce the switching loss of the multi level inverter.

Keywords Cross connected source inverter · Switch capacitor inverter · THD · Symmetric configuration · Voltage stress

1   Introduction

A multi level inverter is a power electronic converter which leads to a desired AC output from several levels of input DC voltages [1]. Basically multi level inverters also have many advantages with respect to hard switched two-level inverter topology. Multi level inverters can be switched at low as well as high switching frequencies than pulse width modulation controlled inverters [2–4]. The two-level conventional

L. Nanda (✉) · C. Jena · B. Panda · A. Pradhan · R. N. Dash
KIIT Deemed to Be University, BBSR, Bhubaneswar, Odisha, India
e-mail: lnandafel@kiit.ac.in

C. Jena
e-mail: chitralekha.jenafel@kiit.ac.in

B. Panda
e-mail: babitapfel@kiit.ac.in

A. Pradhan
e-mail: arjyadhara.pradhanfel@kiit.ac.in

R. N. Dash
e-mail: dash.rudranarayan@gmail.com

inverter topologies [5, 6] have many demerits which have been overcome by multi level inverters. However switched capacitor MLI has a lesser number of dc supply compared to other existing topologies. It can operate both in symmetrical and asymmetrical modes [7–10]. In this paper comparison of switched-capacitor multi level inverters with other already existing topologies has been carried out. The comparison basically depends on the number of dc sources, switches, TSV, etc. of various topologies with respect to the proposed topology. The main feature of the proposed topology is its voltage balancing capacity of the capacitor. Compared to all the classical topologies, there is a massive decrease in device count as the output level increases [8, 11–17]. This leads to complexity in control, bulky systems, and inevitably expensive. The proposed topology offers high-energy conversion quality using little number of active and passive devices as compared to CHBs, which leads to low production cost and reduced switching losses.

2 Working Principle

The working principle of the proposed topology with two DC sources in the main circuit is presented in Fig. 1.

2.1 Modes of Operation

The auxiliary circuit as stated in the proposed topology has a fixed number of dc sources, and the values of the dc supplies are also the same. The value of the dc source voltage is one-fourth of the main circuit. To generate zero level as in Fig. 2 either all the seven switches from upper switches or seven switches from lower switches are turned on.
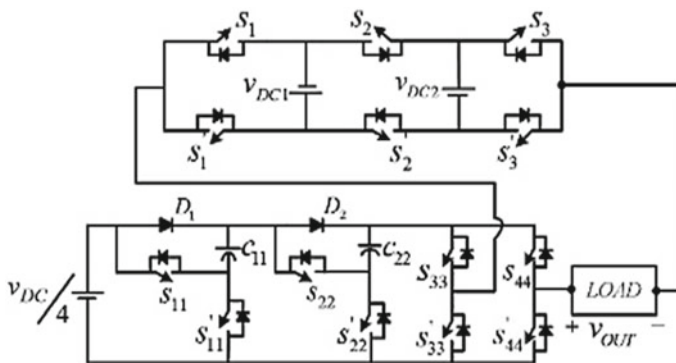
Fig. 1 Proposed topology
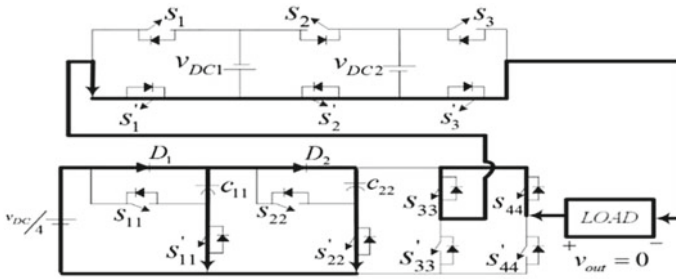
Fig. 2 Zero output level voltage for n = 2
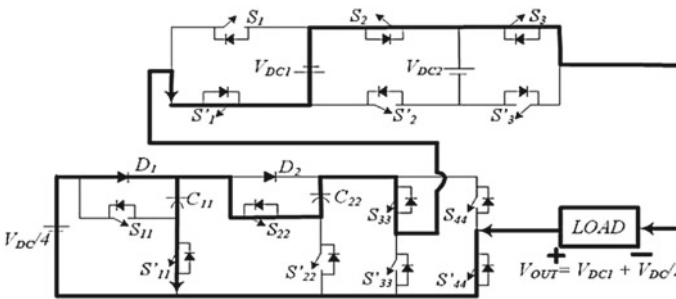
Fig. 3 Average voltage output level for n = 2

For generating $+3V_{DC}/2$ as in Fig. 3 S'_1, S_2, and S3 are in the on state of the CCS-inverter (main circuit). In the auxiliary circuit, switches S'_{11}, S_{22}, S_{33}, and S'_{44} are in the conducting mode. As S'_{11} is on, capacitor C_{11} remains in the charging mode. As S_{22} is on, the auxiliary source goes through that path. This leaves the diode D_2 in reverse bias mode, allowing for discharging of capacitor C_{22} to the load.

To generate maximum output voltage $+11V_{DC}/4$ across the load, i.e. in Fig. 4 switches S_1', S_2, and S'_3 are in the on state in the main circuit. S_{11} and S_{22} are in the on state in the auxiliary circuit. This ensures that diode D1 and D2 are reversed biased to prevent capacitors C_{11} and C_{22} from discharging to the source rather than to the load. For the negative half cycle, the switching patterns remain the same as described.

Table 1 explains the various switching schemes of the proposed converter. A positive sign indicates charging of the capacitors, and a negative sign indicates discharging of capacitors.
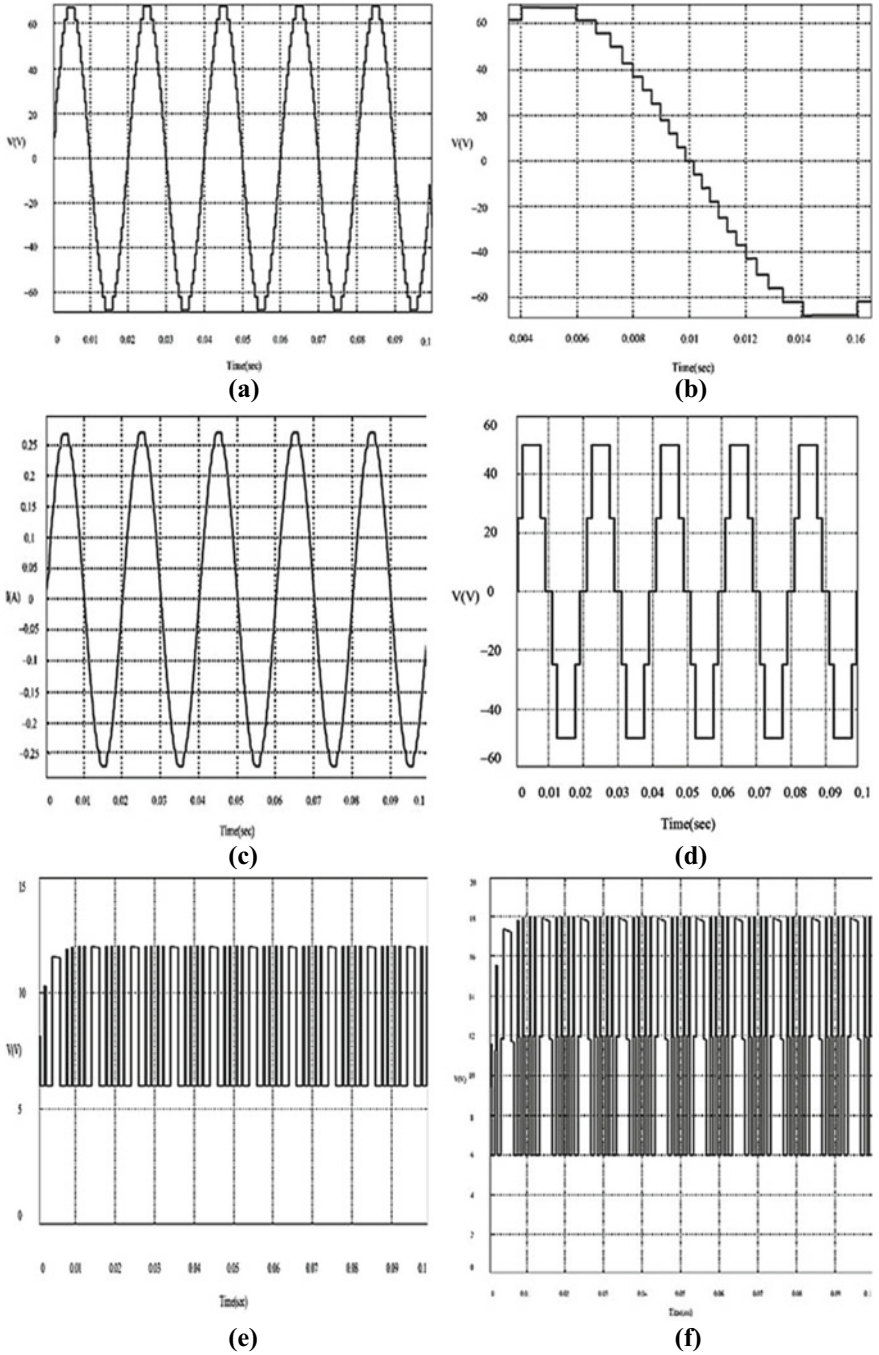
Fig. 4 RL condition with R $= 250\Omega$ **a** voltage output **b** voltage output showing all 23-steps **c** current output **d** main circuit output **e** *SSCC*1 output waveform **f** *SSCC*2 output waveform

Table 1 Various switching schemes

State	Output voltage level V_o	Switch states; 1 = On; 0 = Off							Capacitor states	
		S1	S2	S3	S11	S22	S33	S44	C11	C22
1	0	1	1	1	0	0	1	1	+	+
2	0	0	0	0	0	0	0	0	+	+
3	$+ V_{DC}/4$	0	0	0	0	0	1	0	+	+
4	$+ V_{DC}/2$	0	0	0	0	1	1	0	+	−
5	$+ 3 V_{DC}/4$	0	0	0	1	1	1	0	−	−
6	$+ V_{DC}$	0	1	1	0	0	1	1	+	+
7	$+ 5 V_{DC}/4$	0	1	1	0	0	1	0	+	+
8	$+ 3 V_{DC}/2$	0	1	1	0	1	1	0	+	−
9	$+ 7 V_{DC}/4$	0	1	1	1	1	1	0	−	−
10	$+ 2V_{DC}$	1	0	1	0	0	1	1	+	+
11	$+ 9 V_{DC}/4$	0	1	0	0	0	1	0	+	+
12	$+ 5 V_{DC}/2$	0	1	0	0	1	1	0	+	−
13	$+ 11 V_{DC}/4$	0	1	0	1	1	1	0	−	−
14	$- V_{DC}/4$	0	0	0	0	0	0	1	+	+
15	$- V_{DC}/2$	0	0	0	0	1	0	1	+	−
16	$- 3 V_{DC}/4$	0	0	0	1	1	0	1	−	−
17	$- VDC$	1	0	0	0	0	1	1	+	+
18	$- 5 V_{DC}/4$	1	0	0	0	0	0	1	+	+
19	$- 3 V_{DC}/2$	1	0	0	0	1	0	1	+	−
20	$- 7 V_{DC}/4$	1	0	0	1	1	0	1	−	−
21	$- 2 V_{DC}$	1	0	1	0	0	1	1	+	+
22	$- 9 V_{DC}/4$	1	0	1	0	0	0	1	+	+
23	$- 5 V_{DC}/2$	1	0	1	0	1	0	1	+	−
24	$- 11 V_{DC}/4$	1	0	1	1	1	0	1	−	−

2.2 Modulation Technique (Half-Height)

As much as reducing device count is of paramount interest for all modern-day MLIs, the power quality (PQ) of the output waveform is as well very essential. A means of achieving a better PQ is by reducing the total harmonic distortion (THD) to a minimum.

As already mentioned, to accomplish a good PQ of AC voltage output (which is something not done by many MLIs), the THD must be reduced to a minimum. Reducing THD means carefully arranging the switching angles of each level. The switching angle is the moment of voltage level change. Different methods are available in helping attain the best switching angles.

In the proposed topology nn = 2, twenty-three levels (steps) of output voltage is generated. With the HH method, only a reference sine signal is required (no carrier waves are needed). Since twenty-three steps are at the output, the positive half of the output will have $23-1/2 = 11$ steps. Each step is one of eleven 1/11. All that Half Height (HH) does is to determine the angle to switch, that angle is the height of the step i.e. $1/11 \div 2 = 1/22$. This signifies the generation of a pulse at every half a step. Employing Boolean operations on these pluses helps in producing the different switching patterns for the proposed twenty-three level topology.

3   Simulation Result Analysis

Figure 4a is the output waveform with a reduced resistance. The outcome is as calculated.

Figure 4b is a zoom version of the output voltage; it clearly shows the number of steps, 23-steps in total. Figure 4c is the current output waveform. Figure 4d shows the output waveform of the main circuit (CCS-MLI). Figure 4e depicts $SSCC_1$ output waveform, which correctly reads 6V as per calculations. Figure 4f represents the $SSCC_2$ voltage output waveform, which shows a change in voltage of 12V, and this accords with the earlier calculations.

Figure 5 is a display of the stress voltage of selected switches. Figure 5a shows the value of the voltage stress of switch SS_1, 25v, which matches the calculated amount. Figure 5b shows the amount of stress voltage switch SS_2 has to withstand, the combination of both main voltage sources, equating to 50 v.

Figure 6a, b shows the FFT analysis of the output current and voltage respectively. The peak value of the fundamental component of output current is 0.24 A with a THD of 1.15%. The apex amplitude of the fundamental component of the output voltage is observed to be 60.57 V with a THD of 3.55%. This value is within limits of the
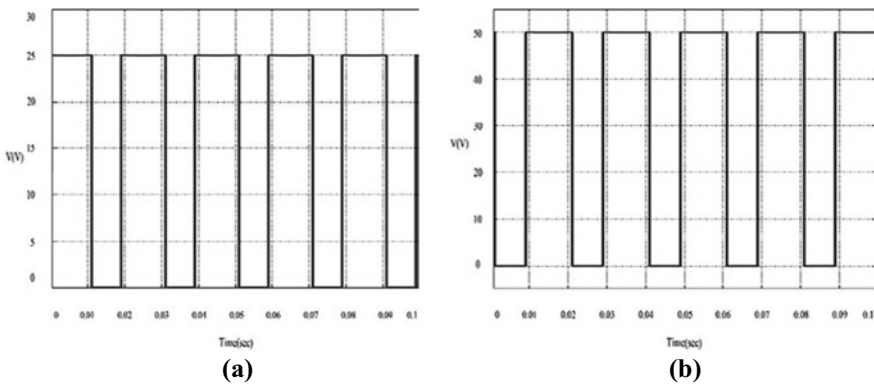
Fig. 5   a. Voltage stress of switch SS1 b.Voltage stress of switch SS2
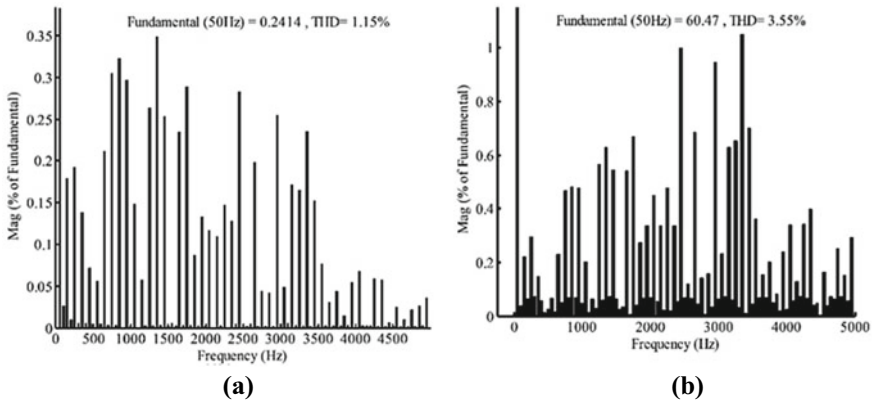
Fig. 6 **a** FFT analysis of the output current **b** FFT analysis of the output voltage

international standards set for the amount of THD acceptable. As the number of output levels increases, the THD should reduce further.

4 Conclusion

The main circuit has been looked at with a symmetric configuration of the sources and in asymmetric cases as well. The symmetric configuration in (*main circuit*) compared to other topologies in symmetric configuration did better in all aspects, including device count and output voltage level. Proposed topology as shown in fig. 1

References

1. K.K. Gupta, A. Ranjan, L. Bhatnagar, Multilevel inverter topologies with reduced device count: a review. IEEE Trans. Power Electron. **31**(1), 135–151 (2016)
2. L.G. Franquelo, J. Rodriguez, J.I. Leon, The age of multilevel converters arrives. IEEE Ind. Electron. Mag. **2**(2), 28–39 (2008)
3. J. Rodriguez, J. Lai, Multilevel inverters: a survey of topologies, controls, and applications. IEEE Trans. Industr. Electron. **49**(4), 724–738 (2002)
4. J. Lai, F. Peng, Multilevel converters-a new breed of power converters. IEEE Trans. Indus. Appl. **32**(3), 509–517 (1996)
5. L. Nanda, A. Dasgupta, U.K. Rout, A comparative analysis of symmetrical and asymmetrical cascaded multilevel inverter having reduced number of switches and DC sources. Int. J. Power Electron. Drive Syst. **8**(4), 1595–1602 (2017)
6. L. Nanda, A. Dasgupta, A comparative studies of cascaded multilevel inverters having reduced number of switches with R and RL-load. Int. J. Power Electron. Drive Syst. (IJPEDS) **8**(1), 40–50 (2017)
7. M.F. Kangarlu, E. Babaei, Cross-switched multilevel inverter: an innovative topology. IET Power Electron. **6**(4), 642–651 (2013)

8. S. Thamizharasan, J. Baskaran, S. Ramkumar, Cross-switched multilevel inverter using auxiliary reverse-connected voltage sources. IET Power Electron. **7**(6), 1519–1526 (2014)
9. Y.H. Liao, C.M. Lai, Newly-constructed simplified single-phase multistring multilevel inverter topology for distributed energy resources. IEEE Trans. Power Electron. **26**(9), 2386–2392 (2011)
10. L. Nanda, A. Dasgupta, U.K. Rout, A comparative analysis of modified cascaded multilevel inverter having reduced number of switches and DC sources. Int. J. Appl. Eng. Res. **12**(20), 10121–10126 (2017)
11. L. Nanda, A. Dasgupta, U.K. Rout, A comparative analysis of symmetrical and asymmetrical cascaded multilevel inverter having reduced number of switches and DC sources. Int. J. Power Electron. Drive Syst. (IJPEDS) **8**(4), 1595–1602 (2017)
12. P. Palanivel, S.S. Dash, Analysis of THD and output voltage performance for cascaded multi-level inverter using carrier pulse width modulation techniques. Power Electron. IET **4**(8), 951–958 (2011)
13. L. Nanda, et al., A comparative studies of different topologies of multi level inverter with SIMULINK, in *2017 International Conference on Inventive Systems and Control (ICISC)* (2017), pp.1–7
14. M.W. Tesfay, T. Roy, S.K. Swain, L. Nanda, A novel step-up 7L switched-capacitor multilevel inverter and its extended structure, in *2021 1st International Conference on Power Electronics and Energy (ICPEE)* (2021), pp. 1–6
15. L. Nanda, C. Jena, S. Samal, Symmetrical and asymmetrical conventional cascaded multilevel inverter with SPWM technique, in *2021 International Conference on Intelligent Technologies (CONIT)* (2021), pp. 1–5. https://doi.org/10.1109/CONIT51480.2021.9498417
16. L. Nanda, Analysis of a new hybrid multilevel inverter topology with reduced device count, in *2020 International Conference on Smart Electronics and Communication (ICOSEC)* (2020), pp. 1117–1122
17. L. Nanda, S. Mohapatra, A. Pradhan, S.R. Prusty, Hybridized symmetrical multilevel inverter topology with reduced number of switches and DC sources. Int. Conf. Artif. Intell. Smart Syst. (ICAIS) **2021**, 1499–1503 (2021)

Smart Grid Communication and Information Technologies: A Review

Debasis Kumar Patel, Hillol Phukan, Swapna Mansani, Jiwanjot Singh, S. Sreejith, Arup Kumar Goswami, and Ranjeeta Patel

Abstract As a result of the old-style electric grid's inability to handle the extensive incorporation of renewable energy resources and distributed renewable energy resources into the electric grid. In the twenty-first century, smart grid technology has entered the picture. Because smart grids operate on two-way communication, communication and information technology are critical to the smart grid's effective operation. The advanced version of the smart grid structure is presented in this article. Furthermore, this article discusses existing and advanced communication and information technology. Finally, the manuscript discusses future research advancements in communication and the most crucial information technologies, such as the Internet of Things (IoT), cloud computing, fog and edge computing, and blockchain in the smart grid. So, the smart grid can manage the massive integration of renewable energy resources while providing customers with efficient, sustainable, and reliable power.

Keywords IoT-Internet of Thing · ICT-Information and Communication Technology · CC: Cloud Computing

1 Introduction

Due to the vast increase in the population and the substantial electrical power demand, there is extensive use of fossil fuels to generate electricity, which causes environmental pollution and global warming due to greenhouse gas production and the decaying of fossil fuels. Therefore, plug-in hybrid electric vehicles and renewable

D. K. Patel (✉) · H. Phukan · S. Mansani · J. Singh · S. Sreejith · A. K. Goswami
Electrical Engineering Department NIT, Silchar, India
e-mail: debasispatel89@gmail.com

R. Patel
Electrical Engineering Department, Kalinga Institute of Industrial Technology, Bhubaneswar, India

energy sources are being integrated into the electrical grid system to reduce the pollution of the environment and fossil fuel decay. This integration increases the operational tasks like Demand Response (DR) and Demand Side Management (DSM) for the operational system engineer [1–5]. Due to this integration, achieving reliable, efficient, flexible, safe power system operation is essential. In order to achieve the most significant and challenging task effectively in complex power systems, electrical engineers introduced the intelligent two-way communication smart grid. The smart grid includes vital communication technology, information technology, and control infrastructure with two-way communication features for the power system to ensure proper monitoring, control, and optimise the whole power system [6, 7].

The critical components of the SG are the Phasor measurement unit (PMU), smart metres, recloser, circuit breakers and protective relays, which are required a smart communication infrastructure to exchange the information and control instruction inefficient automated manner [2].

Communication technology having many hierarchical levels. According to the architecture point, communication technologies are divided into three types: communication for information transfer in short-range, medium, and long-range [3]. Again, each type has a mixed combination of wired and wireless technology with different standards fit for the smart grid operation and specific needs like bandwidth, data rate, latency, frequency range, and security [3].

In each domain of the intelligent grid (SG), having the various object and monitoring, handling all the information of the objects is a very challenging task. Therefore to handle all the information and exchange the information between the object the IoT (Internet of Things). All smart grid devices exchange information through IoT, leading to the proper generation, transmission, distribution, and end local consumer level [2].

Moreover, the IoT alone is insufficient to handle the vast data monitoring and storage for proper operation and decision-making. Therefore, Cloud Computing and Big Data technology comes into the picture to handle the extensive data handling, accessibility for the computing resource, and help the many IoT operate the different objects of the intelligent grid. The use of clod and Big data with IoT increases the capability of SG to add more new information and devices. At the same time, the combination helps to expand the electricity market [4].

In the current review, papers such as [1, 3, 4] discussed the current SG communication technologies, communication technology in the smart grid, challenges of the communication technology. Also, cover the emerging information technology IoT and Cloud computing and Big Data usage in the Smart Grid. However, a clear picture of the current communication technology with the grid is missing.

Therefore, this article focuses on the clear picture of communication and information technology in the smart grid. The feature, standard, uses of communication technology are represented in an innovative way for better understanding. The comprehensive details of the future research scope are presented in the manuscript.

The remaining part of the article is organised as follows. In Sect. 2, the complete description of the smart grid is presented. The features of communication infrastructure are illustrated in Sect. 3. In Session 4, the different smart grid standards are

reported, the next Session 5 is for future research scope, and the last Session 6 is for the conclusion.

2 Description of Smart Grid

The primary motivation for information and communication technology is the high penetration of renewable energy, dynamically changing energy demand, the ageing of the electric grid, the decay of fossil fuels, and air pollution. This adversity motivates the intelligent smart grid prepared with communication and information technology (ICT) to manage and operate the intelligent grid smoothly. The ICT's play a prime part in the monitoring, control and operation of the SG. The critical elements of ICT are the smart metres, communication link, sensors, data acquisition and process system and data centre (i.e., IoT, Cloud Computing) [2].

The availability of the critical element in the smart grid enables it to be self-healing and self-monitoring. It provides two-way communication compared to the old traditional electric grid [1]. The intelligent grid (SG) achieves faster system analysis and system responses, and in the adequate management of renewable energy resources, renewable energy resources consist of solar, tidal, wind and geothermal [3]. This renewable resource helps in decreasing greenhouse gas and CO_2 emission. Due to the automatic specialties of the SG, it can monitor and control distributed renewable energy's outlying areas, making it simple to examine the system's current state with the unpredictable nature of the renewable energy resource [2]. In addition to that, it is easy to do Demand Side Management (DSM) with the help of the Advanced Metering Infrastructure (AMI) [3]. The DSM program focuses on the two-way communication in between the utility and the consumer to use and shift load demand [3] effectively. Due to the above reason, the smart grid can enhance efficiency, sustainability, security and reliability in the overall system. The article's primary focus is to extend the survey work of the previous article and explorer the ICT architecture of the SG and the future challenges of the SG.

2.1 Description of System Architecture

Previously, the NITS proposed the intelligent grid (SG) architecture. Which has seven domains, each of which is related to the others [2]. In this article, the new Smart grid model is discussed, which consists of four layers: information technologies (IoT, cloud computing), communication technologies, physical layer (Generation, Transmission, and Consumer) and sensor and automatic device layer [2]. The power flow from the generating station to the customer is represented by the physical layer, including the transmission and distribution stages. The generating station uses both conventional and renewable energy sources, and the distributed system includes distributed renewable energy resources [2]. All sensors, smart metres, cameras,

RFID, fault current indicators, remote terminal units and the load control switch are considered in the second layer [3, 4]. The second layer is responsible for gathering current system status data via automated and sensing devices. The Internet of Things (IoT) is also present to collect data and transport it to the upper communication layer. The information is communicated to the communication layer via the second layer in various ways (i.e., Enterprise, home and access gateway).

Communication technologies in the communication layer are in two groups. (i.e., wired and wireless.). Wi-Fi, Wi-max, ZigBee, satellite, fibre optics and other communication technologies aid in transporting data to the information technology layer, where it is stored, analysed and provided to the system engineer and other power control stations for proper decision-making. Cloud computing and Big Data are used to store and manage large amounts of data. To regulate, protect, demand side management (DSM), and demand response (DR), signals are delivered to the physical layer via the third and second layers or directly to the generation station, depending on the final choice. The smart grid's four-layer architecture is depicted in Fig. 1.
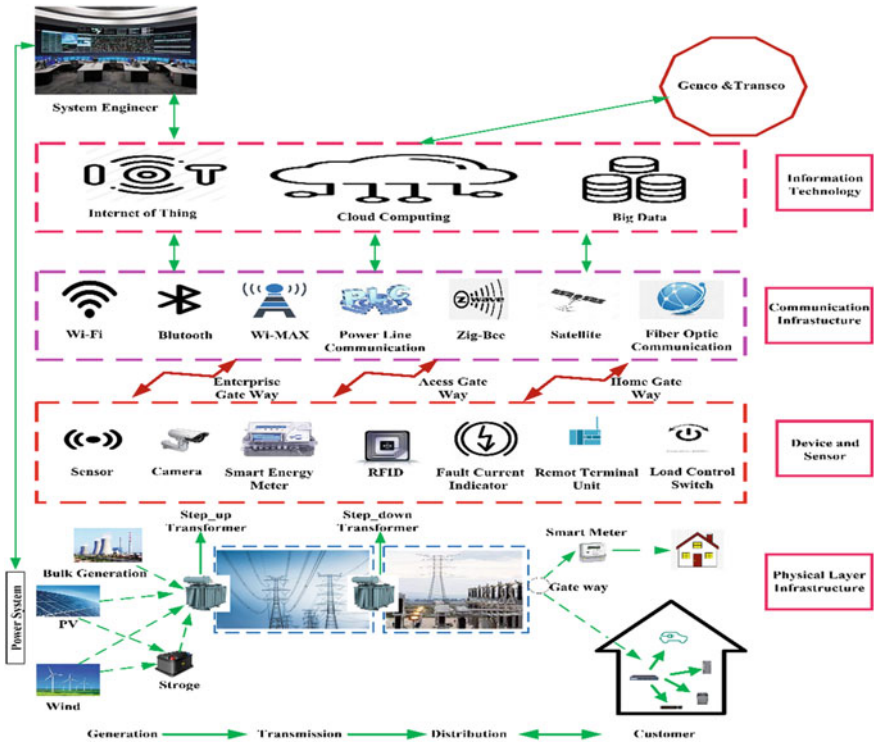
Fig. 1 Four layers of smart grid system structure

3 Communication Infrastructures

This section presents the communication architecture and communication technologies concerning the different aspects and features. The communication technologies are distributed in the different areas of the smart grid (i.e., HAN, NAN and WAN). According to data rate, coverage area and functionality of the communication technologies, the communication technologies are divided into three groups (i.e., short, medium and long ranges). The short ranges are the HAN (Home Area Network), Industrial Area Network and Building Area Network, whereas Medium range technologies are the Neighbour Area Network (NAN) and Field Area Network (FAN). Long-range technologies are the Wide Area Network (WAN). The communication technologies classification according to different ranges and corresponding communication technology application area, data rate, coverage area, communication technologies, power system level and power consumption are illustrated in Table 1.

The Home Area Network (HAN) is required at the consumer and at end-user level in the SG to make the communication capacity for the smart metre (i.e., AMI), DSM and automation of the building and industry area. The communication capability at the customer level should have lower power consumption, high efficiency with a short coverage distance of 100 m and 100 Kbps data rate.

In the SG, NAN deliver communication services for distribution systems. The most significant challenges at this level are communication services for distribution-level functions, for example, outage management (OM), DR execution, supervisory

Table 1 Taxonomy of communication technology and its feature

Different ranges CN	Application	Data rate	Coverage area	Technologies	Power system level	Power consumption
Short range	AMI, DER, DR, PHEV, HAN, BAN, IAN, Automation	Up to 100 kbps	Up to 100 m	ZigBee, Wi-Fi, Z-Wave, PLC, Bluetooth, Ethernet	Customer	Low
Medium range	Smart Metering, DR, DGMA and Electric Transportation, PHEV, NAN Control	100 Kbps–10 Mbps	Up to 10 km	ZigBee, PLC, Cellular, DSL, Wi-Max	Distribution system	Medium
Long range	WAN control, monitor, control, protection	10 Mbps –1 Gbps	Up to 100 km	Optical, Cellular, Wi-max, Satellite	Generating system, transmission system	High

control and data acquisition (SCADA), smart metering, distributed energy resources (DER) and PEV station monitoring and control in the systems. To offer a communication facility for many consumers and data concentrators, the communication infrastructure at this level must deliver reliable and secure data transmission over wider coverage areas (up to 10 km) with more excellent data transmission rates (100 kb/s–10 Mb/s).

WANs serve as communication backbones, connecting several disparate small communication networks. The WAN assists communication for power generation, transmission and distribution systems in the SG and various components such as PMUs, protection systems and compensators. This level of communication structure should deliver communication for significant coverage areas (up to 100 km) with high data transmission rates (10 Mbps–1 Gbps) securely and reliably. The most critical functions of the communication system at this level are to help wide-area control, monitoring, and protection.

To organise the presentation of the existing and the advanced communication technologies used in the SG communication structure is divided into two parts, i.e., wireline and wireless categories [1–4].

This section presents the traditional and recent communication technologies used in the SG, with their characteristics like data rate, coverage area, spectrum and uses, in Table 2.

Each communication technology is having some characteristics requirements, which are as follows.

Latency—The each communication technology take time to transfer data from the source to the destination station or vice versa.
Bandwidth—The communication technology should have an acceptable frequency range for transferring the data.
Coverage area—The communication technology should have the physical range of distance where communication is possible.
Data rate—The communication technology should transfer the data at a particular speed between the two stations or the volume transmitted within a definite duration.
Reliability—Communication technology should have a data transfer system that is available and capable of exchanging data.
Security—To provide a fair data transfer condition, the communication structure should withstand physical and cybersecurity attacks. Security is concerned with concepts such as audibility, authenticity, accessibility, confidentiality, integrity, non-reputability, privacy, third-party protection and trust [1–3].

4 Standards

Several guidelines for developing the SG, particularly the communication and information infrastructures, have been offered. After the Energy Independence and Security Act of 2007 provided the first official definition of the SG in 2007, numerous

Table 2 Existing and the advanced communication technologies in smart grid

Technology			Data Rate	Coverage	Spectrum	Application
Wireless	Cellular Network	GPRS	Up to 170 Kbps	1–10 km	900–1800 MHz	AMI, DR, HAN, NAN, WAN
		LTE	300 Mbps	30	900 MHz	NAN, WAN
		2G-GSM	Up to 14.4 Kbps	1–10 km	900–1800 MHz	AMI, DR, HAN, NAN, WAN
		3G-UTMS-CDMA	384 Kbps–7.2 Mbps	5–75 km	385 MHz	AMI, DR, HAN, NAN, WAN
		4G-LTE	3.3 Gbps	3–12 km	700, 850, 900, 1800, 2100, 2300, 2600 MHz	AMI, NAN, WAN
		5G	20 Gbps	3–12 km	Below 6, 24–86 GHz	DR, information acquisition, storage, analysis, and communication
		6G	1 Tbps		0.1 to 10 THz	Holographic communication, IoT-enabled smart city
	Bluetooth		721 Kbps	Up to 100 m	2.4 GHz	AMI, DR, HAN

Table 2 (continued)

Technology		Data Rate	Coverage	Spectrum	Application
	ZigBee	250 Kbps	Up to 100 m	2.4 GHz, 868–915 MHz	AMI, DR, HAN
	6LoWPAN	250 Kbps	10–100 m	2.4 GHz	AMI, DR, HAN
	Z-Wave	40 Kbps	Up to 100 m		HAN
	Wi-Fi	2–600 Mbps	20 m–1 km	2.5 and 5 MHz	Automatic Metre Reading
	Cognitive Radio (WRAN)	18 Mbps–24 Mbps	10–100 km	54–862 MHz	AMI, DR, HAN, NAN, WAN
	Microwave communication	155 Mbps	60 km	2–40 GHz	AMI, DR, HAN
	WiMAX	Up to 75 Mbps	10-50 km,1–5 km	2.5 GHz, 3.5 GHz, 5.8 GHZ	AMI, DR, NAN, WAN
	Satellite Communications	2.4 Kbps–100 Mbps	100–6000 km	1–40 GHz	HAN, NAN, WAN
	LoRaWAN	0.3–50 Kbps	2–15 km	430, 433, 868, 915 MHz	HAN, NAN
	SIGFOX	600 Bps	Up to 50 km	868, 902 MHz	NAN, WAN
Wired	DSL	256 Kbps to 10 Mbps	3 miles	240 kHz–1.5 MHz	HAN, NAN, WAN
	Fibre Optics	10 Gbps to 1600 Gbps	Unlimited	3*108 GHz	NAN, WAN
	PLC	2–45 Mbps	1–3 km	1–30 MHz	AMI

entities began standardising efforts. IEEE 2030 was published in 2011 as the SGs' roadmap and guidance, while NIST published ITU-T G. HNEM as a standard for high-speed communications via power lines, coaxial cables and phone lines. Organisations like IEEE, NIST, American National Standards Institute (ANSI), International Electrotechnical Commission (IEC), International Telecommunication Union-Telecommunication Standardisation Sector (ITU-T) and others have been gradually developing and completing guidelines for ICT in recent years [3]. This article highlights some essential standardised studies connected to the SG's communication and information structures in Table 3.

Table 3 Different standards of the information and communication technologies structure

Standard	Standard types	Description and application
IEEE	P1901	This standard defines PLC with high-speed standards for residential, utility and SG applications
	P2030	The first IEEE standard contributes to the SG's direction and standards by considering power systems, communication and information technology (IT) as three combined architectural outlooks
	C37.1	This standard establishes communication and information criteria for SCADA and automation systems in power substations
	1379	This standard specifies execution guidelines and directions for IED and RTU communication in power system substations
	1547	(1) Standards for SGs with interconnected renewable distributed resources are provided. (2) This standard examines the SG's three aspects: the power system, information exchange and compliance testing. (3) From the standpoint of communication, this standard considers information exchange and its power system monitoring and control requirements
	1646	This standard addresses the communication necessities of various types of electric substations. The most critical parameters in this standard are the information delivery time and delay
IEC	60,870	This guideline is concerned with the standardisation of definitions and requirements for communication systems used for power system control
	61,850	The automatic control of substations is the subject of this guideline. This standard takes data modelling and transfer, system management functions, and communication requirements for monitoring, control and security applications into account

Table 3 (continued)

Standard	Standard types	Description and application
	61,968	This standard establishes standards for information interchange between various SG devices and networks
	61,970	This standard establishes for information exchange between the SG's various devices and networks
	62,351	It establishes the SG's cybersecurity standards. This standard reports the requirements for providing security for power system control and management and information interchange issues
NIST	1108	This standard defines the SG's conceptual reference model and focuses on the SG's communication infrastructure requirements and application
	7628	This standard reports the SG's information security concerns
ANSI	C12.18	This guideline establishes a standard for two-way communication between smart metres
	C12.19	This specification explains a table structure for data transfer between computers and measurement devices
	C12.22	This standard describes a procedure for moving table data to improve the interoperability and control of smart metres and communication infrastructure
ITU-T	G.HNEM	This standard considers as narrowband PLC technology standards
	G.9955 and G.9956	This standard specifies direct and alternating current power line communication for low and medium voltage electric power lines operating at less than 500 kHz
SAE	J2293	This guideline is concerned with the transfer of electricity between an electric utility and an EV
	J2836	This guideline is known as standardised communication between electric utilities and EVs
	J2847	This standard is used to improves PEV-to-power-grid communication messaging

5 Future Research Scope

Several areas of the smart grid need to be improved for the smart grid to operate more sustainably. SDN, 6G communication, cognitive radio, Big Data, Cloud Computing, Edge and Fog and blockchain are the future research fields. The following is a short description of the fields mentioned above.

5.1 Software-Defined Networking

Suppose you have complete knowledge of the network and its configuration. In that case, you can use the software defined network to increase network efficiency and flexibility, perform dynamic resource allocation, as well as enable SG traffic routing communication networks. As a result, nowadays, computational and processing problems are used to improve livability to solve management, security and resilience issues. The SDN is integrated with SCADA, IoT and Edge computing to enhance the quality of service (QoS) for customers of intelligent cities, health care centres and smart grids [8–11]. Furthermore, the advancement of SDN aided SCDA in improving the resiliency of the Smart Grid [12].

5.2 6G of Cellular Mobile Networks

The 6G communication networks have ultrahigh capacity, ultra-large bandwidths, ultra-dense sites, ultra-reliability and interoperability with a wide range of current ICT technologies. The next-generation communication technology, 6G, is expected to overcome the shortcomings of 5G [13]. The 6G CT assists IoT, SDN, Cloud Computing and blockchain in the operation of overcoming cyberattacks, effective grid management, overcoming IoT limitations and adding more opportunities to the IoT [14–17].

5.3 Cognitive Radio

In SG communication, CR technology is used to protect frequency resources by accessing unlicensed radio spectrum and intercommunicating many different information types based on various criteria (such as security, QoS requirements and dependability). The CR technology improves the quality of service provided by a CN by overcoming spectrum limitations and interference challenges [18] and by utilising the IoT, Mitigating Jamming Attack [19], providing efficient and stable communications in the IoT environment, and reducing communication outages in the DSM [20] in the smart grid environment.

5.4 Big Data

It's impossible to make sense of the vast data collected by the IoT without big data analytics in the smart grid. Therefore with the help of Big Data, IoT, wireless

communication and SDN; the Smart grid achieve to solve the problem like analysis of the enormous data, privacy-preserving and extensive data management [21–24].

5.5 *Cloud Computing*

As in modern electrical power systems, the need for resources and storage increases, which cloud computing can deal with. It is a promising technology with the functionality of using computing resources in a scalable and virtualised manner. Cloud computing provides decentralised energy management features to the smart grid with the help of Cloud IoT technology [25]. Similarly, in the field of Demand Side Management (DSM), security and speed of task management, the CC play a crucial role like optimal resource allocation for DSM, proven secure in a robust security model, and capable of meeting a variety of security requirements and reduce the execution time in intelligent grid [26–28].

5.6 *Edge and Fog*

Data collected by IoT components may contain sensitive information, and various threats attempt to exploit insufficient IoT infrastructures. Further, the existing centralised network structure causes communication delays, necessitating massive data handling. Adding Edge and fog computing technology to IoT and Cloud technology provides a better advantage over only IoT and cloud computing. Edge and Fog computing provides a decentralised control facility, giving more security to the data, faster data operation, and reduced latency [29–32]. Therefore, proper integration of edge-fog technology into the smart grid is a challenging task.

5.7 *Blockchain*

In the field of IoT research, a new technology known as blockchain has been used. In reality, the blockchain connects the IoT ecosystem, allowing it to be distributed, trustless and secure as the blockchain has the facility of storing the data and its security [33, 34]. The blockchain is used for smart grid transactions and provides energy producers and customers with a secure distributed environment. The blockchain ensures transaction immutability, ensuring that every transaction between generators and consumers is always carried out [35–37].

6 Conclusion

This article provides detailed descriptions of the role of communication and information technologies in the smart grid, including their application and characteristics in various areas of the smart grid. It also covers advanced communication technology and its applications. Finally, the research article discusses the scope of future research advancements in communication and information technology, such as SDN, 6G communication, cognitive radio, Big Data, Cloud Computing, Edge and Fog and blockchain in the smart grid, with the intention of efficiently manage the smart grid and provide customers with efficient, sustainable and dependable power.

References

1. M. Faheem, S.B.H. Shah, R.A. Butt, et al., Smart grid communication and information technologies in the perspective of Industry 4.0: Opportunities and challenges. Comput. Sci. Rev. **30**, 1–30 (2018)
2. Y. Saleem, N. Crespi, M.H. Rehmani, R. Copeland, Internet of Things-Aided Smart Grid: Technologies, Architectures, Applications, Prototypes, and Future Research Directions. IEEE Access. **7**, 62962–63003 (2019)
3. A.A. Eladl, M.E. El-Afifi, M.M. El-Saadawi, Communication technologies requirement for energy hubs: a survey, in *21st International Middle East Power Systems Conference (MEPCON)* (2019), pp 821–827
4. L. Bagherzadeh, H. Shahinzadeh, H. Shayeghi, A. Dejamkhooy, R. Bayindir, M. Iranpour, Integration of cloud computing and IoT (CloudIoT) in smart grids: benefits, challenges, and solutions, in *International Conference on Computational Intelligence for Smart Power System and Sustainable Energy (CISPSSE)* (2020), pp 1–8
5. M. Ghorbanian, S.H. Dolatabadi, M. Masjedi, P. Siano, Communication in smart grids: a comprehensive review on the existing and future communication and information infrastructures. IEEE Syst. J. **13**(4), 4001–4014 (2019)
6. A.A. Gde Agung, R. Handayani, Blockchain for smart grid. J. King Saud Univ.—Comput. Inf. Sci. 1–10 (2020)
7. E. Munsing, J. Mather, S. Moura, Blockchains for decentralised optimisation of energy resources in microgrid networks, in *Proceedings of IEEE Conference Control Technology* (2017), pp. 2164–217
8. AAZ Soares, Y. Lopes, D. Passos, N.C. Fernandes, D.C. Muchaluat-Saade, 3AS: authentication, authorisation, and accountability for SDN-based smart grids. IEEE Access (2021)
9. M. Rahouti, K. Xiong, Y. Xin, Secure software-defined networking communication systems for smart cities: current status, challenges, and trends. IEEE Access **9**, 12083–12113 (2020)
10. A. Zilberman, Y. Haddad, S. Erlich, Y. Peretz, A. Dvir, SDN wireless controller placement problem-the 4G LTE-U case. IEEE Access **9**, 16225–16238 (2021)
11. J. Li, J. Cai, F. Khan, A. Ur Rehman, V. Balasubramaniam, J. Sun, P. Venu, A secured framework for sdn-based edge computing in IOT-enabled healthcare system. IEEE Access **8**, 135479–135490 (2020)
12. A.H.M. Jakaria, M.A. Rahman, A. Gokhale, Resiliency-aware deployment of SDN in smart grid SCADA: a formal synthesis model. IEEE Trans. Netw. Service Manag. 1–14 (2021)
13. L.U. Khan, I. Yaqoob, M. Imran, Z. Han, C.S. Hong, 6G wireless systems: a vision, architectural elements, and future directions. IEEE Access (8), 147029–147044 (2020)
14. M. Tariq, M. Ali, F. Naeem, H.V. Poor, Vulnerability assessment of 6G-enabled smart grid cyber-physical systems. IEEE Internet Things J. **8**(7), 5468–5475 (2021)

15. S. Borenius, H. Hämmäinen, M. Lehtonen, P. Ahokangas, Smart grid evolution and mobile communications—Scenarios on the Finnish power grid. Electr. Power Syst. Res. **199**, 107367 (2021)

16. A. Kumari, R. Gupta, S. Tanwar, Amalgamation of blockchain and IoT for smart cities underlying 6G communication: a comprehensive review. Comput. Commun. **172**(1), 102–118 (2021)

17. B. Barakat, A. Taha, R. Samson, A. Steponenaite, S. Ansari, P.M. Langdon, I.J. Wassell, Q.H. Abbasi, M.A. Imran, S. Keates, 6G opportunities arising from internet of things use cases: a review paper. Future Internet. **13**(6), 159 (2021)

18. E. Ogbodo, D. Dorrell, A. Abu-Mahfouz, Energy-efficient distributed heterogeneous clustered spectrum-aware cognitive radio sensor network for guaranteed quality of service in smart grid. Int. J. Distribut. Sens. Netw. **17**(7), 1–9 (2021)

19. D. Das, D.K. Rout, Adaptive algorithm for optimal real-time pricing in cognitive radio enabled smart grid network. ETRI J. **42**, 585–595 (2020)

20. N. Nurelmadina, M.K. Hasan, I. Memon, R.A. Saeed, K.A. Zainol, E.S. Ali, R.A. Mokhtar, S. Islam, E. Hossain, M.A. Hassan, A Systematic review on cognitive radio in low power wide area network for industrial IoT applications. Sustainability **13**(1), 338 (2021)

21. D. Syed, A. Zainab, A. Ghrayeb, S.S. Refaat, H. Abu-Rub, O. Bouhali, Smart grid big data analytics: Survey of technologies, techniques, and applications. IEEE Access **9** (2020)

22. Z. Guan et al., A differentially private big data nonparametric bayesian clustering algorithm in smart grid. IEEE Trans. Netw. Sci. Eng. **7**(4), 2631–2641 (2020)

23. R. Chaudhary, G.S. Aujla, N. Kumar, J.J.P.C. Rodrigues, Optimised big data management across multi-cloud data centers: Software defined network based analysis. IEEE Commun. Mag. **56**(2), 118–126 (2018)

24. K. Wang et al., Wireless big data computing in smart grid. IEEE Wirel Commun. **24**(2), 58–64 (2017)

25. Z. Cao, J. Lin, C. Wan, Y. Song, Y. Zhang, X. Wang, Optimal cloud computing resource allocation for demand side management in smart grid. IEEE Trans. Smart Grid **8**(4), 1943–1955 (2017)

26. H. Zhang, J. Shi, B. Deng, G. Jia, G. Han, L. Shu, MCTE: minimizes task completion time and execution cost to optimise scheduling performance for smart grid cloud. IEEE Access **7**, 134793–134803 (2019)

27. D. He, N. Kumar, S. Zeadally, H. Wang, Certificateless provable data possession scheme for cloud-based smart grid data management systems. IEEE Trans. Indus. Inf. **14**(3), 1232–1241 (2018)

28. M.R. Sarker, J. Wang, Z. Li, K. Ren, Security and cloud outsourcing framework for economic dispatch. IEEE Trans. Smart Grid **9**(6), 5810–5819 (2018)

29. Akira.AI(Homepage) https://www.akira.ai/blog/difference-between-cloud-edge-and-fog-computing/. Last accessed 28 Aug 2021

30. M.Y. Mehmood, A. Oad, M. Abrar, H.M. Munir, S.F. Hasan, H. Abd ul Muqeet, N.A. Golilarz, Edge computing for IoT-enabled smart grid. Secur. Commun. Netw. **2021**, 1–16 (2021)

31. Liu, J. Weng, A. Yang, Y. Chen, X. Lin, Enabling efficient and privacy-preserving aggregation communication and function query for fog computing-based smart grid. IEEE Trans. Smart Grid **11**(1), 247–257 (2020)

32. S. Zhao et al., Smart and practical privacy-preserving data aggregation for fog-based smart grids. IEEE Trans. Inf. Forensics Secur. **16**, 521–536 (2021)

33. S. Aggarwal, R. Chaudhary, G.S. Aujla, A. Jindal, A. Dua, N. Kumar, Energychain: Enabling energy trading for smart homes using blockchains in smart grid ecosystem, in *Proceedings of 1st ACM MobiHoc Workshop Netw Cybersecurity Smart Cities* (2018), pp 1–6

34. A. Jindal, G.S. Aujla, N. Kumar, Survivor: a blockchain based edge-as-a-service framework for secure energy trading in SDN-enabled vehicle-to-grid environment. Comput. Netw. **153**, 36–48 (2019)

35. M.B. Mollah et al., Blockchain for future smart grid: a comprehensive survey. IEEE Internet Things J. **8**(1), 18–43 (2021)

36. J. Wang, L. Wu, K.R. Choo, D. He, Blockchain-based anonymous authentication with key management for smart grid edge computing infrastructure. IEEE Trans. Indus. Inf. **16**(3), 1984–1992 (2020)
37. K. Gai, Y. Wu, L. Zhu, L. Xu, Y. Zhang, Permissioned blockchain and edge computing empowered privacy-preserving smart grid networks. IEEE Internet Things J. **6**(5), 7992–8004 (2019)

A Framework for Glaucoma Diagnosis Prediction Using Retinal Thickness Using Machine Learning

Balajee Maram, Jitendra Sahukari, and Tandra Lokesh

Abstract The project mainly focuses to detect a Glaucoma percentage in a person's eye. Glaucoma is an eye disease which is mainly responsible for vision impairment. So it is necessary to detect the presence of Glaucoma in the early stages. If detected in the early stage we can control our intra ocular pressure by adopting lifestyle changes and by using some other medications. The lifestyle changes may include exercising regularly and reducing stress. Hence the early detection of Glaucoma can help people from losing their vision. A machine learning model has been proposed which tells the Glaucoma percentage of the eye. In this we are giving a fundus image as the input to the model and it tells the Glaucoma percentage. This Glaucoma percentage can be detected using two things that are optic cup and optic disk. To measure the Glaucoma percentage it is necessary to find the optic cup ratio to optic disk ratio. Generally health eye optic cup ratio to optic disk ratio is less than 0.5. In Glaucoma eye the optic cup ratio to optic disk ratio is greater than 0.5. By using this concept we are going to develop the model.

Keywords Glaucoma · Intraocular · Optic cup · Optic disk · Fundus image

1 Introduction

The important parts of the human body are the eyes. These are responsible for getting the information to our brain. Glaucoma is an optic nerve disease that is responsible for loss of vision [1]. It is a combination of eye diseases that damages the optic nerve and the optic nerve cells which reflects in loss of vision. This leads to wide blindness in the human eye. Due to Glaucoma, the eye is filled with an aqueous fluid, which pressures the eye (IOP). Intra ocular pressure will be increased in the eye because of the continuous flow of fluid. In some cases, this may occur in normal

B. Maram (✉)
Department of CSE, GMRIT, Rajam, India
e-mail: maram.balajee@gmail.com

J. Sahukari · T. Lokesh
Bachelor of Technology, CSE, GMRIT, Rajam, India

eye pressure because of poor blood circulation. It should be detected in the earlier stage of the disease and treated to keep our vision safe [2]. So artificial intelligence (AI) systems are necessary to prevent Glaucoma in the early stages of a patient [3]. Manual analysis takes more time and also differs in inaccuracy. Machine learning has recently become one of the core technologies in the fields of science and technology. Classification is a major technology used in medical applications because it can be applied to prediction (diagnosis). The machine learning approach is also useful for predicting glaucoma. So machine learning is the essential tool for predicting and treating glaucoma [4–8]. For the detection of glaucoma there are two techniques that can be used. One technique is segmentation, and another technique is image-based feature extraction [9, 10]. Localization is a process used to outline a sub-image. Now that outlined image is Region of Interest. The purpose of segmentation is to identify the Optic Nerve Head from the background of the Glaucoma image [9].

2   Literature Survey

In detecting glaucoma, first of all, retinal images play a vital role in capturing the digitalized retinal images. Pre-processing is required for finding the irregularities and equalization in images. The feature extraction involves and simplifies the number of resources required to classify the required data set. Classification refers to the analysis and property verification of the images. Depending upon the analysis, the data set is divided into different classes i.e. glaucoma affected area or normal area [1].

Open-point glaucoma is the most basic type of glaucoma, representing in any event 90% of all glaucoma cases against angle-closure glaucoma. Glaucoma is caused because of eye pressure. Open-angle glaucoma has a wide point among IRIS and cornea, through point closure glaucoma has limited point among IRIS and cornea. Open-angle glaucoma increases slowly whereas angle-closure glaucoma increases quickly and is able to notice symptoms [2]. The character of glaucoma is described using structural damage and functional defects of the eye [3]. As the rise of glaucoma continues, researchers are confronted with the age-old problem to reduce the risk factor and preserve vision in glaucoma. In this we have studied 46 eyes of 46 glaucoma patients (19 NTG + 27 HPG) and 25 control eyes (CTRL) of 25 subjects. OCT progressive testing is conducted using hospitalized methods to notice the progression of the disease [4].

This survey mainly focuses on the visual fields of open-angle glaucoma patients and visual fields of health using deep learning. Open-angle glaucoma visual fields are diagnosed before the treatment. In total, we have examined 171 open-angle glaucoma visual fields from 53 eyes in 51 OAG patients and 108 visual fields are healthy from 87 glaucoma patients who were analyzed using a Humphery field analyzer. The 53 total deviations, mean deviations, and pattern standard deviations values were used to predict the output in the deep learning classifier as feed-forward neural networks [5].

This study included the untrained data set or pre-training data set of 431 images from 137 eyes with open-angle glaucoma that includes all stages of glaucoma and 19 normal eyes to obtain desirable output in the clinical method [6].

"Machine learning applied to retinal image processing for glaucoma detection: Review and perspective" is a review which is done on the important algorithms by using machine learning for detection and diagnosis of glaucoma. The methods which use the classification process were only considered and then the results were shown by doing the systematic analysis [7].

"Feasibility of simple machine learning approaches to support detection of non-glaucomatous visual fields in future automated glaucoma clinics" has been pointing out the effects caused to the glaucomatous people by pituitary diseases. This work shows that ML can perform well in diagnosis in automated glaucoma clinics with increased safety of the patient [8].

"Machine learning models based on the dimensionality reduction of standard automated perimetry data for glaucoma diagnosis" used dimensionality reduction and composite variables techniques to increase the performance of the classification. In results it is shown that dimensionality reduction improving classification performance by reducing input space dimensions [9].

"Classification of glaucoma using simplified-multiclass support vector machine" proposed multi class support vector technique (MSVM) for better classification. In many MSVM's data loss during training phase may occur. To prevent data loss, classification technique which consists of naive bayes binary classifier is proposed in the primary level and normalized multiclass SVM is proposed in the secondary level [10].

"Automated detection of glaucoma with interpretable machine learning using clinical data and multi-modal retinal images" proposed individual DL models for every imaging modal. The retinal OCT DL model will take only one retinal optical coherence tomography image as input and give probability that the given image is a glaucoma image as output. It requires individual B-scans and 128 B-scan images will be there in each retinal OCT [11].

3 Methodology

The methodology that we are using in this project is CDR methodology and taken 255 retinal image data set. CDR stands for Cup to Disc Ratio. This method mainly requires the disc and cup outline boundaries of the human retina as shown in Fig. 1.

3.1 Glaucoma Detection Using CDR

See Fig. 2.

Fig. 1 Human Retina

Optic Cup

Optic Disc

Neuro Retinal Rim

Retinal Nerve
Fiber Layer
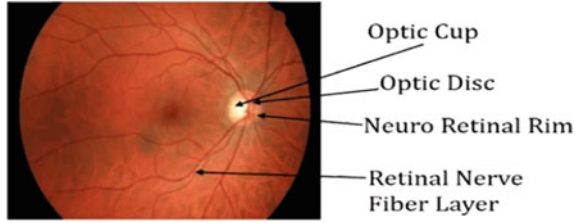
Human Retina

Fig. 2 Glaucoma detection
using CDR

Image
Acquistion

Localization of
Optic Disc

SuperPixel
Segmentation of
optic disc

Superpixel
Segmentation of
optic disc

CDR Calculation
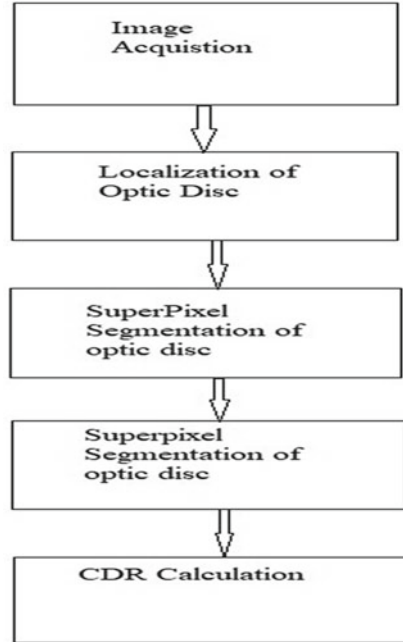
3.2　Preprocessing

See Fig. 3.

3.3　Image Enhancement

See Fig. 4.
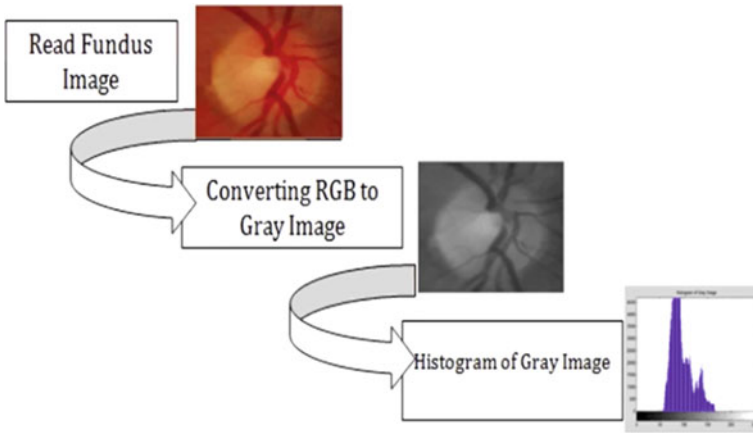
Fig. 3 Preprocessing
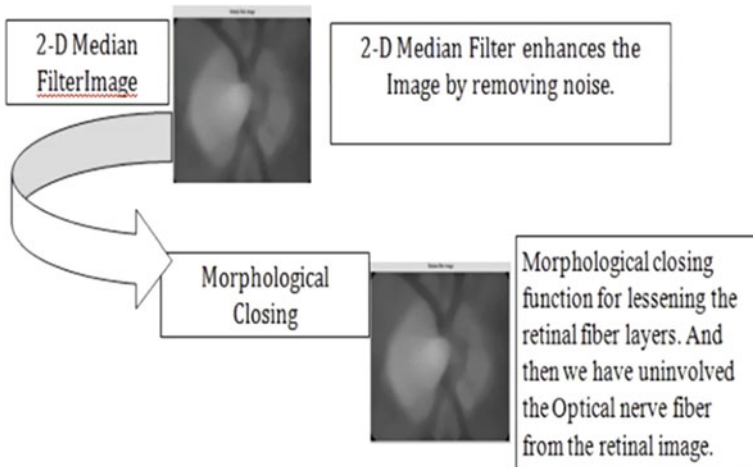
Fig. 4 Noise Removal

4 Feature Extraction

Multi Thresholding

Multiple thresholds can be applied many times on the same image. The technique sub-divides the image into two categories. One is lower, and the other one is superior limits of Region Of Interest (ROI). The optic cup is the first sub-image formed with boundary, and the optic disc is the second sub-image formed with boundary.

Region Of Interest can be calculated using the following algorithm

Step 1: Calculate the Threshold.

Step 2: By Applying Threshold identify the brighter regions.

Step 3: By Applying some of morphological operations (closing, opening, area open) identify the ROI.

Step 4: Stop.

Estimation of Threshold

The brighter regions within the retinal images are identified. The occupied pixels of the Optic disc can be calculated as

$$P_{count} = estimated\ OD\ pixel\ count\ = \frac{\pi \times (D/2)^2}{7.33 \times 8}$$

Here D indicates the diameter of the retinal image.

Optic Disc Localization

The thresholding technique is employed for locating the optic disc. The value of threshold is predicated on pixel count. The color image is regenerated into the red channel image. Then the diameter of membrane is found. The red channel image is regenerated into a binary image (Fig. 5).
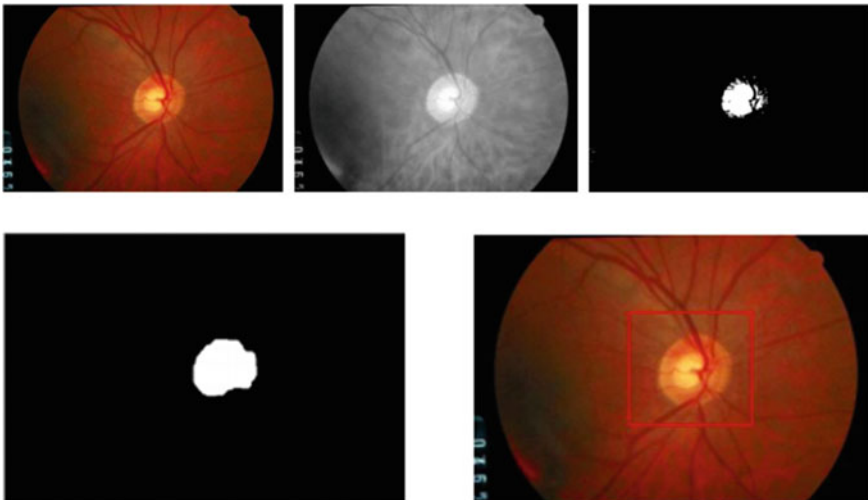
Fig. 5 Image Enhancement
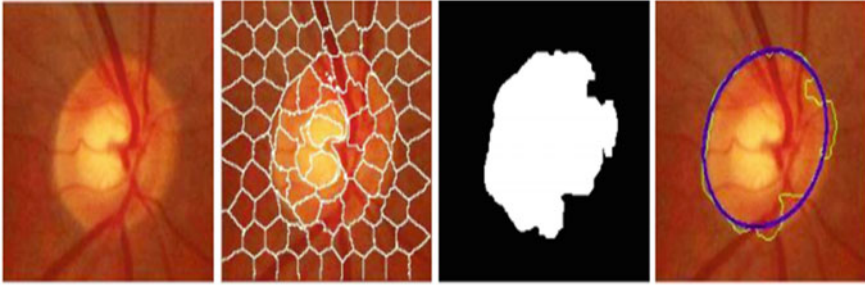
Fig. 6 Classification and Segmentation of Optic Disc
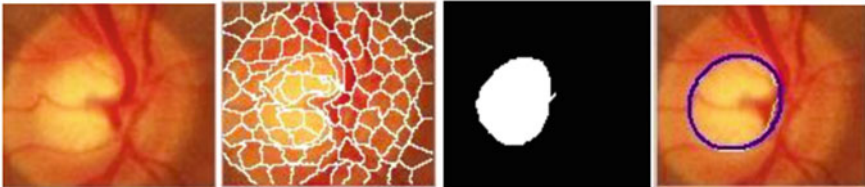
Fig. 7 Classification and Segmentation of Optic Cup

The opening operation is employed for the removing unwanted clusters outside the most cluster. Finally the most cluster has remained within the image. This can be the region of interest, and it is extracted from the color image.

Classification and Segmentation of Optic Disc

The Super pixel Segmentation method can be used on the region of interest to identify and get the disc boundary. Here the number of super pixels, the accuracy, and the time required for the evaluation increases (Fig. 6).

Classification and Segmentation of Optic Cup

The super pixel Segmentation method can be applied to the disc to identify and get the cup boundary. Parameter values are the same as disc segmentation (Fig. 7).

CDR Ratio

CDR ratio = ratio of Vertical cup diameter: vertical disc diameter. The CDR value for a healthy eye is less than the threshold otherwise it may be glaucomatous (Fig. 8).

5   Proposed Methodology

Here in our project, the document space is a database consisting of several numerical data sets of the retinal image.

Fig. 8 CDR Ratio
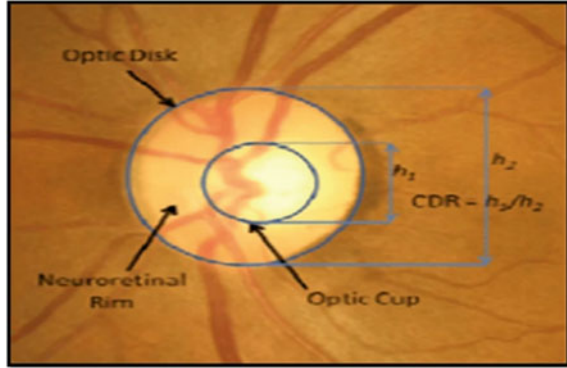
Data Set

We have taken 255 retinal image data sets and performed our classification operations on that image. We have used 70% of the image data set for training our model and left 30% for testing the model. The features are extracted from the fundus images using image processing techniques—kurtosis, k-stat, mean, median, standard deviation, and the obtained numerical features are stored in a dataset.

5.1 Overview of Proposed Algorithm

The proposed algorithm consists of the following sub-sections.

i. **K-Nearest Neighbor Algorithm for Glaucoma w Detection**

It is Classification Algorithm. Classification is determining what group something belongs in. In order for KNN to work we need some examples with correct row data. This is used to predict feature groups i.e. in what group the feature data is in. We normally refer to it as Reference data. That means we need some reference data for KNN Algorithm. For example if you say k = 5 then the data record sees five closest data records in the reference data (Fig. 9).
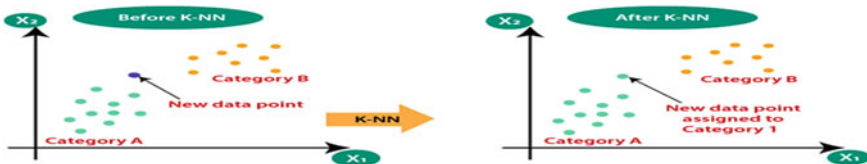
Fig. 9 KNN Classification
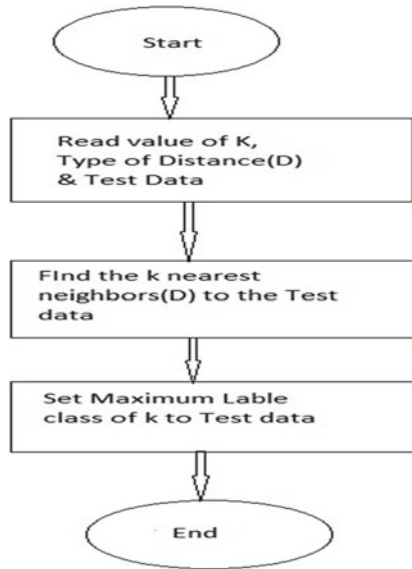
Fig. 10 K-NN algorithm flowchart

K-NN Algorithm flowchart

See Fig. 10.

ii. **Support vector machine Algorithm for Glaucoma Detection**
Support vector machine algorithms can perform very well with both linearly separable and non-linearly separable datasets. It is a representation of different classes that can be separated by a hyperplane in N dimensionality space. This hyperplane can be generated in a continuous manner so that errors can be minimized. The aim of SVM is to separate the dataset into different classes to find a maximum marginal hyperplane (Fig. 11).
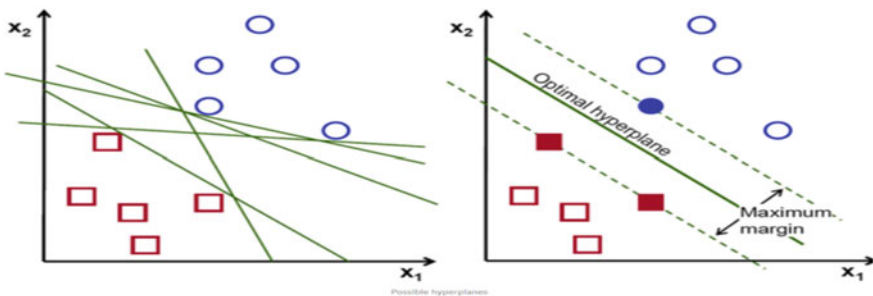
Fig. 11 SVM Classification and Maximum Marginal Hyperplane

Types of SVM

Linear SVM

A single straight line that separates the data into two classes is called Linear SVM.

Non-linear SVM

A single straight line that can not separate the data into two classes is called Non-Linear SVM.

iii. **Random Forest Algorithm for Glaucoma Detection**
      Random forest is constructed from many decision tree algorithms. It could be a methodology that operates by constructing many decision trees throughout the training phase. The maximum of the decision trees is selected by the random forest. It gives an effective way of handling the missing data.

Random forest Algorithm flowchart

See Fig. 12.

Fig. 12 Random forest Algorithm flowchart
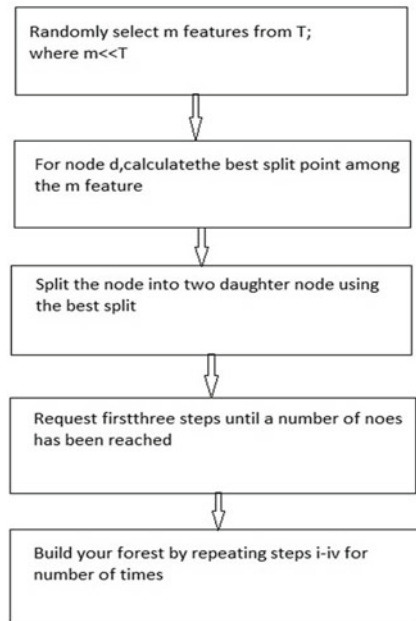
5.2 Classification Metrics

It is used to know the performance of a machine learning model after training the dataset.

Confusion Matrix

It is one type of table which shows the performance of a classification model and the table contains true values (Fig. 13).

Accuracy

The accuracy of a machine learning classification algorithmic program is a way to measure however typically the algorithmic program classifies a data point accurately. Accuracy is that the range of correctly predicted data points out of all the info data points (Fig. 14).

Precision

Precision is that the fraction of relevant instances among the retrieved instances (Fig. 15).

Recall

Recall (also called sensitivity) is that the fraction of relevant instances that were retrieved (Fig. 16).

Fig. 13 Confusion Matrix

Fig. 14 Accuracy

Fig. 15 Precision

Fig. 16 Recall
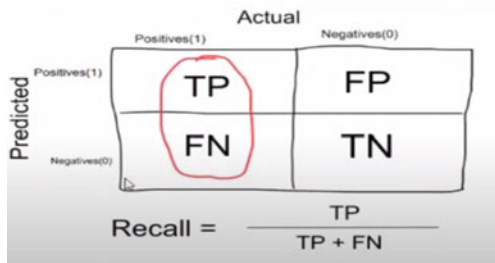
6 Experimental Results and Discussion

6.1 Result of Implementation of K-NN Algorithm Program on Eye Disease Glaucoma Data Set

We applied the KNN algorithm to glaucoma data set consisting of 255 images, and the results we got are (Fig. 17).

True Positive (TP) = 162

False negative (FN) = 14

Fig. 17 KNN metrics bar graph
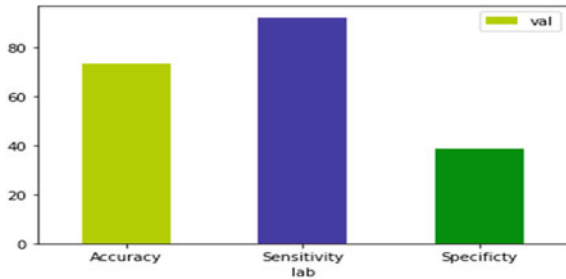
Fig. 18 SVM metrics bar graph
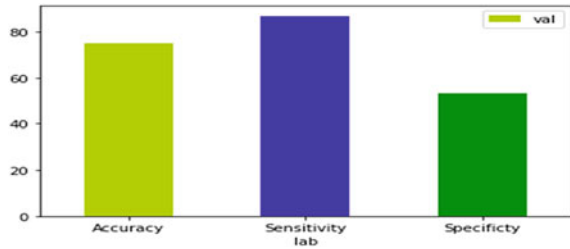
False positive (FP) = 59

True Negative (TN) = 37.

Accuracy (%) = (TP + TN/N)*100 = 73.1%

Specificity (%) = (TN/TN + FP)*100 = 38.5%

Sensitivity (%) = (TP/TP + FN)*100 = 92%

6.2 Result of Implementation of SVM Algorithm Program on Eye Disease Glaucoma Data Set

We applied the Support Vector Machine Algorithm to glaucoma data set consisting of 255 images, and the results we got are (Fig. 18).

True Positive (TP) = 153

False negative (FN) = 23

False positive (FP) = 45

True Negative (TN) = 51

Accuracy (%) = (TP + TN/N)*100 = 75%

Specificity (%) = (TN/TN + FN)*100 = 53.1%

Sensitivity (%) = (TP/TP + FN)*100 = 86.9%

6.3 Result of Implementation of Random Forest Algorithm Program on Eye Disease Glaucoma Data Set

We applied the Random Forest algorithm to glaucoma data set consisting of 255 images, and the results we got are (Fig. 19).

True Positive (TP) = 106

Fig. 19 Random forest metrics bar graph
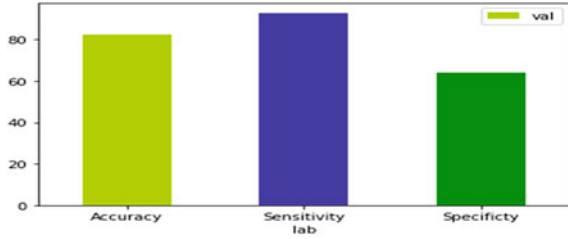
Table 1 Accuracy, Sensitivity, and Specificity of proposed algorithms

S.no	Algorithm	Accuracy(%)	Sensitivity(%)	Specificity(%)
1	KNN	73	92	38
	Input1: TestSet1			
2	SVM	75	86	53
	Input2: TestSet2			
3	Random Forest	82	92	64
	Input3: TestSet3			

False negative (FN) = 8

False positive (FP) = 24

True Negative (TN) = 4

Accuracy (%) = (TP + TN/N)*100 = 82.3%

Specificity (%) = (TN/TN + FP)*100 = 64.1%

Sensitivity (%) = (TP/TP + FN)*100 = 92.9%

6.4 Comparative Discussion with Proposed Algorithm

Table 1 shows how accurately the proposed algorithms are performed.

6.5 Comparison of Proposed Algorithm with Existing Algorithms

See Figs. 20, 21 and 22 and Table 2.

Fig. 20 Graphical representation of Accuracy of Table 2
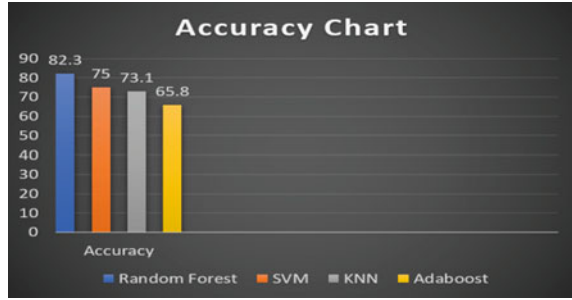
Fig. 21 Graphical representation of Sensitivity of Table 2
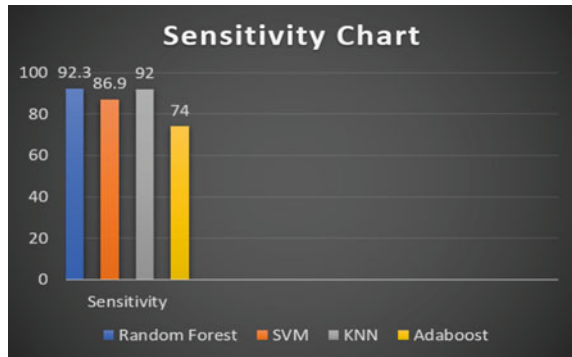
Fig. 22 Graphical representation of Specificity of Table 2
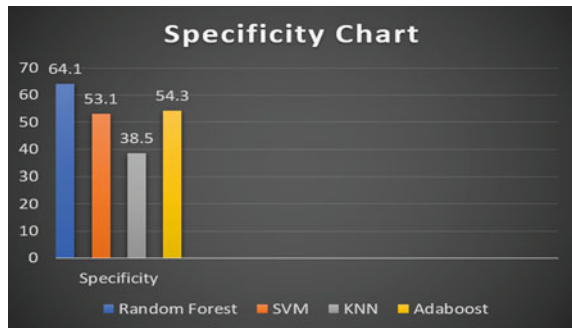
Table 2 List of algorithms with Accuracy, Sensitivity, and Specificity

Algorithm	Accuracy	Sensitivity	Specificity
Adaboost	0.65	0.74	0.54
KNN	0.73	0.92	0.38
SVM	0.75	0.86	0.53
Random forest	0.82	0.92	0.64

Further Improvements and Future Scopes

In our eye disease dataset, we tend to achieve an accuracy of 82.3% find the unwellness and in the future we are going to increase the accuracy to a higher extent. We will use algorithms like Convolutional Neural Network to extend the accuracy rate. Presently we tend to use numerical information sets as our input for classification and that we can directly take image information sets as input in the future. Advances in image process and its classification are going to be useful in designation of medical conditions properly. It will be helpful in recognizing people, performing surgery, reprogramming, defects in human DNA, etc.

7   Conclusion

We applied three algorithms to our glaucoma dataset, and we found that the random forest algorithm has the highest accuracy level of 82.3% in detecting glaucoma diseases. Also we found that the Random algorithm has the highest Specificity and Sensitivity value. All these algorithms can be used for better medical diagnosis of diseases like cancer, eye disease, etc. It can also be used for biometric purposes such as identity, face, and fingerprint documentation.

References

1. R. Asaoka, H. Murata, A. Iwase, M. Araie, Detecting preperimetric glaucoma with standard automated perimetry using a deep learning classifer. Google Sch. **123**, 1974–1980 (2016)
2. R. Asaoka, H. Murata, K. Hirasawa, Y. Fujino, M. Matsuura, A. Miki, T. Kanamoto, Y. Ikeda, K. Mori, A. Iwase et al., Using deep learning and transfer learning to accurately diagnose early-onset glaucoma from macular optical coherence tomography images. Google Sch. **198**, 136–145 (2019)
3. M. Christopher, C. Bowd, A. Belghith, M.H. Goldbaum, R.N. Weinreb, M.A. Fazio, C.A. Girkin, J.M. Liebmann, L.M. Zangwill, Deep learning approaches predict glaucomatous visual field damage from optical coherence tomography optic nerve head enface images and retinal nerve fiber layer thickness maps. Google Sch. **127**, 346–356 (2020)
4. F. Badalà, K. Nouri-Mahdavi, D.A. Raoof, N. Leeprechanon, S.K. Law, J. Caprioli, Optic disk and nerve fiber layer imaging to detect glaucoma. Am. J. Ophthalmol. Google Sch. **144**, 724–732 (2007)
5. A. Issac, M. ParthaSarathi, M.K. Dutta, An adaptive threshold-based image processing technique for improved glaucoma detection and classification. Google Sch. **122**, 229–244 (2015)
6. K.E. Kim, J.W. Jeoung, K.H. Park, D.M. Kim, S.H. Kim, Diagnostic classification of macular ganglion cell and retinal nerve fiber layer analysis. Ophthalmology Google Sch. **122**, 502–510 (2015)
7. H. Liu, L. Li, I.M. Wormstone et al., Development and validation of a deep learning system to detect glaucomatous optic neuropathy using fundus photographs. Google Sch. **137**, 1353–1360 (2019)

8. C. Muramatsu, T. Nakagawa, A. Sawada et al., Automated segmentation of optic disc region on retinal fundus photographs: comparison of contour modeling and pixel classification methods. Google Scholar **101**, 23–32 (2011)
9. R. Asaoka, K. Hirasawa, A. Iwase et al., Validating the usefulness of the "random forests" classifier to diagnose early glaucoma with optical coherence tomography. Am. J. Ophthalmol. Google Sch. **174**, 95–103 (2017)
10. D.S.W. Ting, C.Y. Cheung, G. Lim et al., Development and validation of a deep learning system for diabetic retinopathy and related eye diseases using retinal images from multiethnic populations with diabetes. Google Sch. **318**, 2211–2223 (2017)
11. P. Wang, J. Shen, R. Chang, M. Moloney, M. Torres, B. Burkemper, X. Jiang, D. Rodger, R. Varma, G.M. Richter, Machine learning models for diagnosing glaucoma from retinal nerve fiber layer thickness maps. Google Sch. **2**, 422–428 (2019)

Contingency Analysis: A Tool to Improve Power System Security

Ravindu Patel, Akhilesh Nimje, Shanker Godwal, and Sarika Kanojia

Abstract Contingency analysis is a mathematical method for predicting equipment failure or a specific line's failure and taking corrective action before the system enters an unstable state. Insertion or removal of one or more elements in an electrical network could be one of the contingencies. As a result of these adjustments, the power system is no longer in the safe operating range. Corrective action should be taken as soon as possible; otherwise, the system may enter an unstable region. Contingency ranking selection is an effective method of providing a power system safety assessment. This article summarizes the research work in the field of contingency analysis and how to find various performance indicators and classify them according to their severity. A small system consisting of 14 buses has been tested for various emergencies. After solving the emergency, it was found that the number of violations was reduced and most of the parameters were within reach to ensure the safe operation of the electrical system.

Keywords Contingency analysis · Contingency ranking · Security performance indices · Outages · Multiple contingencies

1 Introduction

The grid is a complex network that includes various expensive equipment. Any sudden outage or short circuit in these devices during their operation can harm the system and hence leads to outages. This can be further harmful to the employees working on the system. The word used to define this outage is contingency. The analysis is useful for governing, originating, scrutinizing, and revealing the lists of possible outages and associated failures or disturbances in the network. The security constraints should be within the operating point. If violated, it further gives rise to other serious problems. Hence a proper understanding of transmission management is necessary to develop an effective way of providing economic power [1]. The method

R. Patel · A. Nimje (✉) · S. Godwal · S. Kanojia
Institute of Technology, Nirma University, Ahmedabad, India
e-mail: 20meee11@nirmauni.ac.in

is useful to determine its maximum loadability for an electric utility [2–4]. To avoid a blackout, the load applied should be limited to limit the line flow in the network [5, 6]. To perform contingency analysis, line outage distribution factors (LODFs) are used. For multiple contingencies and the improvement in speed of LODFs, the simple formation of a matrix is utilized in the power transfer of distribution factors [7, 8]. To find the maximum loading factor, contingency power flow is implemented [9]. Contingency analysis is performed using two common methods: (1) Ranking Method and (2) Screening Method. The screening method is used to identify the most harmful contingencies but here the limits are violated. Cascading failure or higher-order contingency events often cause a blackout [10]. The reasons for such failures are as follows:

(1) The hidden failure happens during which the outages are not visible to users.
(2) Inadequate backup protection and relay settings
(3) Switching operation in which a system may respond to a fault but may not remove it.
(4) Interference or mismatch in communication during which the relay may unable to trip the circuit breaker while identifying the fault.
(5) External factors in which the line gets sagged because of expansion in summer [11].

2   Literature Survey

With the help of V-Q curves, the voltage stability and reactive power reserve of load buses are determined [12, 13]. The voltage stability index (VSI) margin can be calculated by examining each line in the system and determining its line stability indices when there is a branch outage. The VSI estimates the maximum load that can be connected to a bus in order to preserve system stability before an outage occurs [14]. Over the past few years, the existing distributed systems are relying on Distributed Energy Resources (DER) to meet the needs of increasing power demands. DER helps in improving power quality and reliability. An islanding is a situation where distributed generators continue to supply power to a given location even if power is removed from the grid. There are two variations of islanding namely accidental islanding and intentional islanding. In accidental islanding, the voltage and frequency are controlled without interfacing with DER equipment. In intentional islanding, the system is pre-planned and is accordingly designed to cope up with the situation [15]. When there is a disturbance or outage in a Distributed Generation (DG) system, the frequency and voltage are altered. The stability can be determined using the islanding method for different types of contingency [16]. Many researchers have tried to make improvements to this method. Using AC power flow, the contingency ranking of PI with that of distribution factors is carried out for different bus systems. This provides more stability and accuracy when compared to the standard performance index [17]. It is based on a realistic approach. It is revealed that the precise ranking method is accurate than the exact ranking method. It is a fast-based method

and can be used on a complex power system network [18]. In Analytical Hierarchy Process, the weighing factors are properly adjusted. The fast decoupled method is used to determine contingency ranking [19]. The addition of the performance index of active power and voltage performance is done, and the highest values are ranked first with subsequently the other lines in descending order. If the line ranks first, then it can make the system operate beyond its power limit [20–23]. Using a sensitivity vector, the changes in bus voltage and line flow can be determined when there is an event of a possible fault. The sensitivity vector linearizes the ac load flow. During contingency, the changes in voltage and its angle can be calculated using sensitivity vectors. The AC load flow provides better accuracy when combined with sensitivity factors. The contingencies may increase or decrease the flow of active power. Hence, contingencies should be ranked based on the active and reactive power limits [24]. Whenever a fault occurs in a transmission line, there occurs variation in voltage collapse. This is due to the change in load margin. To obtain a steady stable margin, a method called a nose curve is implemented. This method is applied and tested on single and multiple contingencies of 118 bus system. The change in load margin is estimated using linear and quadratic equations. The linear estimate proves to be faster than the quadratic equation [25]. For an accurate ranking of N-1 contingency, it is necessary to have a current-based power network system. To measure line flows, distribution factors are used. This is done using phasor measurement units which also predict the sensitivities in a system. The equations of total active and total reactive power are taken in polynomial form. The contingency ranking is performed using performance in which the summation of the total line and total voltage-based performance index is taken into consideration [26]. The method applied also improves the system's computational performance [27]. In a network, violations in a bus can happen. Radial Bus voltage violations can be used to rank the contingencies. A method called unsupervised learning is used to identify disturbances in the system. A new performance index method is proposed in which it applies to buses in the limitations of its violation. The results reveal that the neural network-based RBF (Radial Bus Function) takes less time when compared to the MLP model. The voltage performance index applied in this is faster than the conventional one. The RBF-based method can handle contingency easily on undesirable loading conditions. It can also be tested for large contingencies [28]. The results show that the post contingency voltage stability can be improved by reserve-based contingency constrained optimal power flow (RCCOPF). This can also reduce the number of iterations when there is an increase in reactive reserve while applying sensitivity [29]. Both the powers are observed, and their similarities and differences are evaluated to the solution. This real-time method has fewer steps required and can provide good voltage stability in a network system [30]. Another real-time assessment-based method is implemented by redefining contingency. This method determines the number of breakers required to isolate the system containing any possible outage. The contingency is ranked by opening the circuit breakers [31]. The method has certain limitations such as AC load flow feasibility, complexity, and the ability to handle large power networks. The desired switching is achieved using three heuristic algorithms along with parallel

computing. These algorithms provide solutions in a short time. The corrective transmission switching (CTS) reduces post contingency violations in AC load flow. The CTS is further analyzed, and the output promises more than 99% accuracy [32]. To identify possible N-K contingencies, a time-domain simulation method is used. The system first identifies the list of less severe contingencies. Then it progresses towards more severe contingencies. With every contingency ranking, simulation results are displayed. If the response is unstable, then there is a possibility of contingency. It is further evaluated on N-(K + 1) contingencies. This method was used on IEEE Nordic system. It was revealed that it identifies N-2 contingencies very early [32, 33]. It is seen that the capability of the system gets increased because the performance index of active power is greater than the overloading condition in the transmission line [34]. A three-stage fuzzy interference system is designed. The frequency deviation on three-phase fault in line and generator outage is noted. The index alerts the control operator of any possible risk that might harm the system's performance. The frequency improves after some time and reaches its expected value. There occur variations in load flow and voltage but still, the post contingency analysis drives the system into stability. Hence, dynamic security assessment is a helpful phenomenon in contingency ranking [35]. It can also be used on SCADA-based systems [36, 37]. An algorithm called Random Chemistry is developed to identify multiple contingencies which are responsible for causing large cascading failures. The method is applied to minimal branch contingencies which can cause large failures. The algorithm first initiates the power flow in the system. When the contingencies are introduced, it checks for possible system failure. The relays are then updated. It advances time until there is an occurrence of the next failure. The branches are tripped, and it is repeated for further analysis. According to the findings, the frequency with which the separate branches interact to cause big blackouts follows a power-law distribution. With the increase in the K value, the possibility of such interactions can also increase [38]. In any power system network, the main concern is always its huge computational load. Various methods of contingency analysis have been developed which provide decent results. A new method called recursion-based contingency analysis works on a particular contingency sorting. The algorithm selects its first contingency. It moves to its next contingency only after analyzing the first. It continues till the size of simultaneously failing elements reaches its maximum size. The restoration procedure begins when one of the elements is switched back on. When all of the items have been restored, the recursion-based contingency is said to have been completed. When compared to the traditional contingency sorting process, the results showed a twofold gain in computing efficiency [39]. In a deregulated environment, a heavily loaded power system is used extensively. Voltage collapse may occur if reactive power management is not accurate. First, the approach determines a list of all probable situations. For each contingency, it calculates the minimum reactive power margin. The advantage of using this method is that it does not leave out any contingency and it can work even for generator outages [40]. The method used in reference [27] can be improved if it is in a distributed computing environment. In distributed computing, a single large program can be divided into several smaller programs. The programs divided can be communicated over a common network. This speeds up the

process of contingency ranking, and the results can be obtained much earlier [41]. Contingencies were ranked by comparing their loadability to the system's maximum loadability using an appropriate screening approach and a bespoke application. The acceptable Contingency Category is used when the maximum loadability is greater than the contingency. Significant Contingencies are contingencies that fall between the acceptable and unacceptable categories and are listed in the third category. An IEEE 118-bus Test System is used to verify the approach. More than 95% of all conceivable situations are accompanied by an appropriate category, according to the technique. Unacceptable contingencies have a negative MW machine, while Significant contingencies have a MW machine that is less than 90% of the maximum MW machine. The algorithm is time-saving and provides smaller output results [42]. The composite index is used which ranks the contingencies based on the changes in the system parameters and not on independent parameters. A modified IEEE 9 bus system was implemented. First, it was done using the standard IEEE system. The second system was based on renewables connected to the weakest bus, and the third was by replacing synchronous generators with renewables. The pre and post contingencies of this bus system are done, and the contingencies were ranked on the bases at their maximum power. The results obtained were in real-time, and the time taken for computation was less [43]. Various indicators can be combined to identify critical case and fault scenarios. The stability analysis can be improved for determining the contingency through indicators derived from stability assessments. The indicators are critical clearing time, angle index, and voltage ride-through index. The indicators identify the severe contingencies, and hence it improves the performance on stability analysis in different simulation conditions. These scenarios lead to the formation of tuples which are defined here as contingencies [44]. The holomorphic embedded simulator provides a guarantee of theoretical convergence. It discards the use of numerical issues. A partitioned is developed by interfacing partitioning of Holomorphic Embedding (HE) formulation. This method also neglects the numerical issues and hence burden is reduced while analyzing large-scale contingency. The Parallel Holomorphic Embedding (PHE) method is then improved by computation of parallel or distributed method so it becomes parallel PHE [45].

3 Contingency

3.1 Single Outage Contingency (N-1)

The criterion N-1 is the interruption due to any of the following unexpected events:

(a)   The outage of an individual overhead transmission line.
(b)   Transformer failure.
(c)   Generator failure.

(d) There is a loss of Shunt devices such as capacitors and reactors. If there is a single element failure as mentioned above, it is said to have satisfied the N-1 criterion such that

(a) There is no breach of the limiting values for network operation variables (i.e. operating voltage, frequency) that could jeopardize the power system's security or cause equipment damage, destruction, or an unacceptably shortening of its life.

(b) There is no transmission line equipment or loading that has surpassed its operational thermal limit capacity.

(c) There will be no power outages.

3.2 N-K Contingency

Here, N is the number of a specific element, and K denotes the corresponding contingency applied to the power system network, with K = 0, 1, 2,… N. K = 0 indicates that the system is in good working order. A pre-contingency condition is an alternate term used for it. If K is equal to 1, only one element is out of commission. The N-1 criteria is another name for it. The N-1 criterion is a mathematical abstraction that represents a single circumstance. Due to a three-phase short circuit fault, it causes one element to trip. The nature of their combinations makes studying N-K situations challenging. Depending on the level of analysis, the number of elements (N), and the amount of contingency, the number of contingencies may vary. N-1 represents the first level contingency, N-2 represents the second level contingency, and so on. Traditionally, the system's dynamic security analysis is performed for a few minutes in response to a few pre-determined contingencies. The harmful implications of contingencies are frequently overlooked until they occur, owing to the low probability of their occurrence. However, a number of eventualities will arise, and the ramifications for analyzing high-risk N-k contingencies for online secured operation assessment could be disastrous.

3.3 Contingency Creation

Because of high precision, Newton Raphson's load flow approach is adopted. The following are the equations for real power, reactive power, and voltage magnitude:

$$P_i = \sum_{j=1}^{n} |Vi||Vj||Yij|cos(\theta ij - \delta i + \delta j) \tag{1}$$

$$Q_i = -\sum_{j=1}^{n} |Vi||Vj||Yij|sin(\theta ij - \delta i + \delta j) \tag{2}$$

$$|V_i| = (P_i - jQ_i) / \left[\sum_{j=1}^{n} |Vj||Yij|(cos(\theta ij - \delta i + \delta j) + sin(\theta ij - \delta i + \delta j)) \right]$$

(3)

where n represent the total number of buses; $|Vi|$ is the voltage magnitude at ith bus; $|Vj|$ is the voltage magnitude at j bus; $|Pi|$ is the real power; $|Qi|$ is the reactive power; $|Yij|$ and θij are bus admittance voltage and the angle at bus i and j respectively; and δi and δj are voltage angles at bus i and j respectively.

4 Performance Indices

4.1 Real Power Performance Index (PIp)

$$PI_p = \sum_{l=1}^{nl} \frac{w_p}{2N} \left\{ \frac{P_{ij}}{P_{ij}^{max}} \right\}^{2N}$$

(4)

$$P_{ij}^{max} = \frac{v_i v_j}{x_{ij}}$$

(5)

where wp is the active (real) power positive weighting factor $= 1$; N is the exponent of penalty function (N $= 1$ is preferred); Pij is the real power flow on line i-j; nl is the number of lines; and Xij is the transmission reactance between bus i and j.

4.2 Voltage Performance Index (PIv)

$$PI_v = \sum_{i=1}^{n} \frac{w_v}{2N} \left\{ \frac{|v_i| - |v_i^{spec}|}{\Delta v_i^{limit}} \right\}^{2N}$$

(6)

where $\left| v_i^{spec} \right|$ is the bus i known voltage magnitude; wv is the real positive weighing factor; n is the number of buses; and Δv_i^{limit} is the maximum voltage ceiling. If it exceeds further then voltage becomes unacceptable.
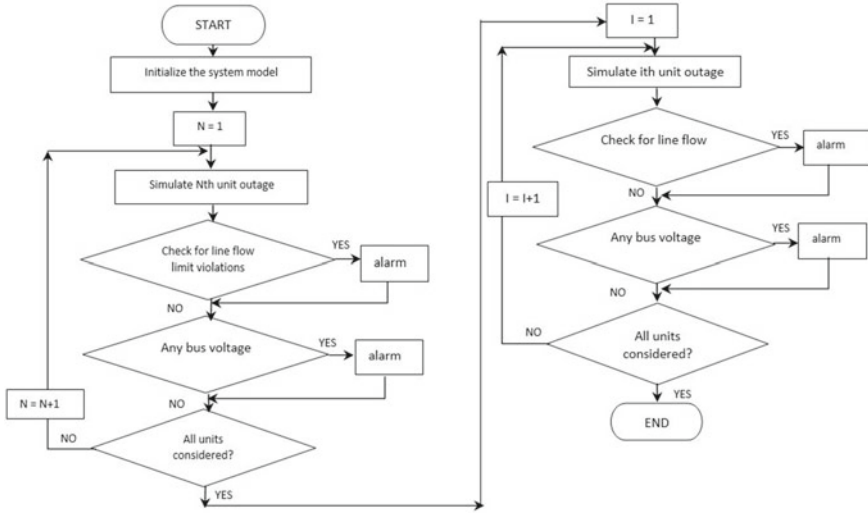
Fig. 1 Contingency analysis using simple method

Fig. 2 Contingency analysis
using Newton Raphson
method
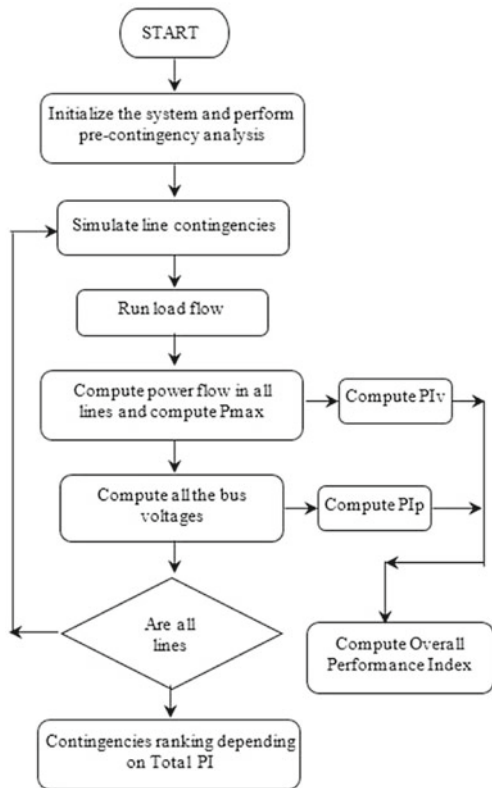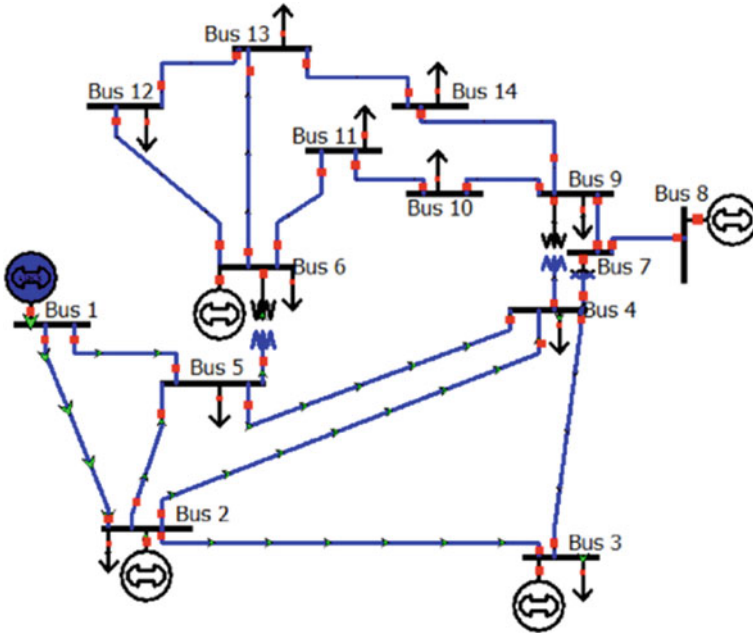
Fig. 3 IEEE 14 bus system

4.3 Reactive Power Performance Index (PIq)

$$PI_q = \sum_{l}^{ng} \frac{w_Q}{2N} \left\{ \frac{Q_i}{Q_i^m} \right\}^{2N} \tag{7}$$

where w_Q is a real positive weighting factor; ng is the number of generators; Q_i reactive power at bus i; and Q_i^m is the reactive power limit at bus i.

5 Algorithm for Contingency Analysis

See Figs. 1, 2, and 3.

6 Results and Discussion

The simulation was performed using power world simulator software on IEEE 14 bus testing network. Table 1 shows the effects of the application of contingencies. There were 65 number of severe violations found. The violations represent the total number

Table 1 Applied contingency for 14 bus system

Line number	From line	To line	Violations	Max branch%
1	1	2	4	318.6
2	1	5	5	161.0
3	2	3	6	170.6
4	2	4	5	138.5
5	2	5	3	129.8
6	3	4	2	130.5
7	4	5	7	156.8
8	4	7	4	158.3
9	4	9	1	142.1
10	5	6	8	269.9
11	6	11	2	122.5
12	6	12	1	130.1
13	6	13	3	132.0
14	7	8	2	135.7
15	7	9	5	167.1
16	9	10	1	136.6
17	9	14	2	140.6
18	10	11	1	126.3
19	12	13	1	130.4
20	13	14	2	125.1

Table 2 Limit violations when line 1–2 open

Line number	From line	To line	Violations	Max branch%
1	1	2	–	–
2	1	5		
3	2	3		318.6
4	2	4		–
5	2	5		–
6	3	4		–
7	4	5		195.3
8	4	7		–
9	4	9		–
10	5	6		162.6
11	6	11		–
12	6	12		–
13	6	13		–

Table 2 (continued)

Line number	From line	To line	Violations	Max branch%
14	7	8		–
15	7	9		–
16	9	10		–
17	9	14		–
18	10	11		102.1
19	12	13		–
20	13	14		–

of contingencies which is the summation of bus, thermal, and interface violations that were caused when introduced contingency. While solving the contingencies, when they are individually introduced, the number of violations gets reduced. As seen from Table 2, if the transmission line between bus 1 and bus 2 is switched off, the bus voltages are recomputed. The branch violations get reduced to a limit. If these limits are still higher than the threshold values, they can be further reduced by eliminating or taking corrective actions based on the performance indices. The steps are repeated till the system is achieved without any violations. For example, when the transmission lines are perfectly loaded, it will not indicate any violation thus ensuring a secured transmission system. A similar exercise can be replicated for various contingencies such as addition or removal of load and generators.

7 Conclusion

It is the foremost requirement of the power system to operate smoothly under steady-state conditions. In the event of a contingency, the irregularities and disturbance occur because it causes a severe threat to the power system. This distorts the state of equilibrium. The contingency analysis accurately identifies the violations in transmission lines, generators, transformers, etc. Thus the system can be pre-analyzed and solved even before the occurrence of the contingencies. The violations associated with the system elements can be reduced which is helpful for the economic assessment of the power flow of the system. Thus, contingency analysis provides a medium of safety and the failure of the system can be avoided.

References

1. R.D. Christie, B.F. Wollenberg, I. Wangensteen, Transmission management in the deregulated environment. Proc. IEEE **88**(2), 170–195 (2000)

2. I. Musirin, T.K. Abdul Rehman, Estimating maximum loadability for weak bus identification using FVSI. IEEE Power Eng. **22**(11), 50–52 (2002)

3. N. Shekhawat, A. K. Gupta and A. K. Sharma, "Voltage Stability Assessment Using Line Stability Indices," *3rd International Conference and Workshops on Recent Advances and Innovations in Engineering*, Jaipur, India, May 2019

4. Ismail Musirin and T. K. Abdul Rahnian, "Fast Automatic Contingency Analysis and Ranking Technique for Power System Security Assessment," *Student Conference on Research and Development*, Putrajaya, Malaysia, July 2005.

5. P. Ramanaiah, J. Srinivasa Rao, Contingency analysis under deregulated power systems using FACTS device. Int. J. Eng. Res. Dev., Ongole, India **10**(10), 44–64 (2014)

6. N. Amjady, M. Esmaili, Application of a new sensitivity analysis framework for voltage contingency ranking. IEEE Trans. Power Syst. **20**(2), 973–983 (2005)

7. J. Guo, Y. Fu, Z. Li, M. Shahidehpour, Direct calculation of line outage distribution factors. IEEE Trans. Power Syst. **24**(3), 1633–1634 (2009)

8. R. Vykuka, L. Nohacova, "Sensitivity Factors for Contingency Analysis," *International Scientific Conference on Electric Power Engineering*, Kouty and Desnou, Czech Republic, May 2015.

9. D. Asija, P. Choudekar, K.M. Soni, S.K. Sinha, Power flow study and contingency status of WSCC 9 bus test system using MATLAB, in *International Conference on Recent Developments in Control Automation and Power Engineering (RDCAPE)*, Noida, India (2015)

10. S. Soman, P. Thomas, J. George, M. Ganesh, Prevention of blackout by an effective forced islanding and restoration scheme, in *International Conference on Emerging Research in Electronics, Computer Science and Technology*, Mandya, India (2015)

11. F. Li, A. Chegu, X. Xu, An overview of the analysis of cascading failures and high-order contingency events, in *Asia Pacific Power and Energy Engineering Conference*, Chengdu, China (2010)

12. P.W. Sauer, Post-contingency equilibrium analysis of power systems, in *Proceedings of the 35th Hawaii International Conference on System Sciences,* Big Island, HI, USA (2002)

13. P.A. Upadhyay, D.R. Dobariya, S.K. Joshi, Contingency analysis and weakest bus ranking by reactive power reserve margin, in *IEEE International Conference on Computer, Communication and Control*, Indore, India (2015)

14. C. Subramani, S.S. Dash, M. Arun Bhaskar, M. Jagadeeshkumar, K. Balaji, Soft computing for voltage stability analysis and contingency ranking in power system, in *International Conference on Advances in Computing, Control, and Telecommunication Technologies*, Bangalore, India (2009)

15. M.V. Kirthiga, P. Muppiddi, A case study for controlled islanding based on line contingency ranking in autonomous micro-grids, in *Africon*, Pointe aux Piments, Mauritius (2013)

16. K. Kanimozhi, M.V. Kirthiga, Stability analysis of islanded micro- grids, in *IEEE International Conference on Power Electronics, Drives and Energy Systems (PEDES),* Trivandrum, India (2016)

17. M. Dwivedi, A. Dhandhia, V. Pandya, Optimization of weighing factors of performance index to improve contingency ranking*, 7th International Conference on Power Systems*, Pune India (2017)

18. Z. Hussain, Z. Chen, P. Thogersen, Fast and precise method of contingency ranking in modern power system, in *IEEE Jordan Conference on Applied Electrical Engineering and Computing Technologies*, Amman, Jordan (2011)

19. M. Abedi, M. Ehsan, Z.G. Jahromi, M.M. Jamei, Utilization of analytical hierarchy process in contingency ranking, in *IEEE/PES Power Systems Conference and Exposition*, Seattle, USA (2009)

20. S.R. Gongada, T.S. Rao, P.M. Rao, S. Salima, Power system contingency ranking using fast decoupled load flow method, in *International Conference on Electrical, Electronics, and Optimization Techniques*, Chennai, India (2016)

21. P. Sekhar, S. Mohanty, Power system contingency ranking using newton Raphson load flow method, in *Annual IEEE India Conference*, Mumbai, India (2013)

22. M.R. Siddappaji, K. Thippeswamy, Contingency ranking and optimal placement of DG for line loss reduction in distribution system to enhance reliability, in *International Conference on Energy, Communication, Data Analytics and Soft Computing*, Chennai, India (2017)
23. H. Jmii, A. Meddeb, S. Chebbi, Newton Raphson load flow method for contingency ranking, in *15th International Multi- Conference on Systems, Signals and Devices (SSD)*, Yasmine Hammamet, Tunisia, Mar. 2018.
24. P. Murali, G. Gajjar, S.A. Soman, Sensitivity vectors and contingency ranking using linearised AC load flow, in *IEEE/PES Innovative Smart Grid Technologies Asia*, Chengdu, China (2019)
25. S. Greene, I. Dobson, F.L. Alvarado, Contingency ranking for voltage collapse via sensitivities from a single nose curve. IEEE Trans. Power Syst. **14**(1), 232–240 (1999)
26. H. Retty, J.S. Thorp, V. Centeno, The effect of load model composition on N-1 contingency ranking, in *IEEE Power & Energy Society Innovative Smart Grid Technologies Conference*, Washington, DC, USA, 2015
27. Z. Jia, B. Jeyasurya, Contingency ranking for on-line voltage stability assessment. IEEE Trans. Power Syst., Yokohoma (2002)
28. T. Jain, L. Srivastava, S.N. Singh, Fast voltage contingency screening using radial basis function neural network. IEEE Trans. Power Syst. **18**(4), 1359–1366 (2003)
29. H. Song, B. Lee, S.H. Kwon, V. Ajjarapu, Reactive reserve-based contingency constrained optimal power flow (RCCOPF) for enhancement of voltage stability margins. IEEE Trans. Power Syst. **18**(4), 1538–1546 (2003)
30. L. Baozhu, L. Bolong, A novel static voltage stability index based on equilibrium solution region of branch power flow, in *Third International Conference on Electric Utility Deregulation and Restructuring and Power Technologies*, Nanjing, China, 2008
31. M. Chen, Contingency redefinition and its application to power system security analysis, in *IEEE/PES Conference on Power Systems Conference and Exposition*, Phoenix, USA (2011)
32. X. Li, P. Balasubramanian, M. Sahraei-Ardakani, M. Abdi-Khorsand, K.W. Hedman, R. Podmore, Real-time contingency analysis with corrective transmission switching. IEEE Trans. Power Syst. 32(4), 2604–2617 (2016)
33. T. Van Cutsem, T. Weckesser, Searching for plausible N-K contingencies endangering voltage stability, in *IEEE PES Innovative Smart Grid Technologies Conference Europe*, Turin, Italy (2018)
34. S.B. Daram, P.S. Venkataramu, M.S. Nagaraj, Performance index based contingency incorporating IPFC, in *IEEE International Conference on Electrical, Electronics and Optimization Techniques*, Chembarambakkam, Tamil Nadu (2016)
35. U. Kerin, E. Lerch, Dynamic security assessment to improve system stability, in *EPU-CRIS International Conference on Science and Technology*, Hanoi, Vietnam (2011)
36. I. Chychykina, Z.A. Styczynski, C.O. Heyde, R. Krebs, Power system instability prevention and remedial measures with online dynamic security assessment, in *IEEE Eindhoven PowerTech*, Eindhoven, Netherlands (2015)
37. P.A. Ruiz, P.W. Sauer, Voltage and reactive power estimation for contingency analysis using sensitivities. IEEE Trans. Power Syst. **22**(2), 639–647 (2007)
38. M. Eppstein, P. Hines, A random chemistry algorithm for identifying collections of multiple contingencies that initiate cascading failure. IEEE Trans. Power Syst. **27**(3), 1698–1705 (2012)
39. S. Gusev, V. Oboskalov, Recursion based contingency analysis of an electrical power system, in *International Symposium on Industrial Electronics*, Banja Luka, Bosnia and Herzegovina (2016)
40. F. Fatehi, M. Rashidinejad, A.A. Gharaveisi, Contingency ranking based on a voltage stability criteria index, in *Large Engineering Systems Conference on Power Engineering*, Montreal, Canada (2007)
41. S. Varshney, L. Srivastava, M. Pandit, M. Sharma, Voltage stability based contingency ranking using distributed computing environment, in *International Conference on Power, Energy and Control (ICPEC)*, Dindigul, India (2013)
42. M. Poshtan, P. Rastgoufard, B. Singh, Contingency ranking for voltage stability analysis of large- scale power systems, in *PES Power Systems Conference and Exposition*, New York, USA (2004)

43. L. Liyanarachchi, N. Hosseinzadeh, A. Mahmud, A. Gargoom, E.M. Farahani, Contingency ranking selection using static security performance indices in future grids, in *Australasian Universities Power Engineering Conference*, Hobart, Australia (2020)
44. S. Samaan, M. Momeni, M. Knittel, C. Meier, M. M.S. Winck, A. Moser, Approach to the identification of critical contingencies for the stability analysis of innovative operational concepts, in *ETG- Congress*, Berlin, Offenbach (2021)
45. R. Yao, F. Qiu, K. Sun, Contingency analysis based on partitioned and parallel holomorphic embedding. IEEE Trans. Power Syst. (2021)
46. A. Doroudi, A.M. Nasrabadi, R. Razani, Two novel static and dynamic voltage stability based indexes for power system contingency ranking, in *IET Generation, Transmission & Distribution* (2017)

LFC of a Deregulated Power System Using Opposition Based Novel Arithmetic Optimization Algorithm Based Fraction Order Cascade Controller

Mrinal Ranjan and **Ravi Shankar**

Abstract Several changes have occurred in the electrical power system during the previous decade, owing to continually growing load demand, quick diminution of fossil fuels, rapid industrialization, and newly implemented electrical-deregulation policies. Several reviews of literature on the topic of Load Frequency regulation (LFC), which copes with varied and modern controller techniques for the effective functioning of the power system, have been produced in the last few years. This research article discusses the Novel utilization of opposition-based Airhmetic Optimization Algorithm (OAOA) for twin areas, multiple-source of linked power system considering Thermal and Hydro in one zone and Thermal and Gas in another zone. For a practical approach, non-linear constraints such as boiler agitation (BD) effects, Time-delay, and generation-rate-constraint (GRC) have been included for each unit. A Novel cascade combination of 2-Degree-of Freedom PI controller (2DOF-PI) and Fraction order Proportional-derivative controller considering filter (FOPDN) is used as a proposed controller in the scheme. The gain parameters of the (2DOF-PI) with FOPDN controller have been improved by the opposition-based Arithmetic Optimization Algorithm (OAOA). Later, the supremacy of the suggested algorithm is verified among the other well-known meta-heuristic approaches like particle-swarm-optimization (PSO), Wild-horse-optimization (WHO), and Artificial-bee-colony (ABC) by evaluating under the same test conditions. To ensure the efficiency of the prospective work the progressive response of the suggested controller to load interuption is correlated to the schematics of current controllers.

Keywords Load frequency control · Opposition-based arithmetic optimization algorithm · Deregulated power system · (2DOF-PI-FOPDN) controller

M. Ranjan (✉) · R. Shankar
National Institute of Technology, Patna, India
e-mail: mrinalr.phd19.ee@nitp.ac.in

R. Shankar
e-mail: ravi@nitp.ac.in

1   Introduction

The efficient procedure of multi-zone electrical systems involves that the total genera-
tion must be identical to the total demand for power by load plus transmission losses.
Technology day by day will be advanced, and the power system becomes more
complex and interdependent for any interest. The functioning of an interconnected
power system has evolved through time, and as a result, the power system's rated
frequency and electrical energy exchange between the two zones of the interdepen-
dent power system may vary [1, 2]. In a multizone power system, a considerable fluc-
tuation in frequency, as well as an interchange of electrical power, can harm devices,
report device instability, extend equipment life, and finally lead to failure [3–7]. To
solve this challenge, an LFC approach to two-area power systems is presented. LFC
is important to create a superior control to get less deviation on change in frequency
of the system and tie-line power swap of the distinct control areas [4–10].

Although a linearized framework for load frequency management is built, non-
linearity is continually existing in the inter-connected power system in the real script,
allowing for further processing. Under diverse loading situations and system non-
linearity, a double-area interconnected hybrid system is offered as an exploratory
structure [11]. Previously, in a multiple-area correlated conventional power system,
power reproduction, transmission, and distribution were obtained by a particular
entity known as a vertical unified-utility[12]. A vertically integrated service provides
a certain amount of power to its customers at a set charge. In today's restruc-
tured power environment, the traditional power structure is being upgraded and
harmonized with the traditional LFC strategy. Restructure power-scheme definitions
and estimates for DISCO, GENCO, TRANSCO, and organized structure operators
were improved, and the LFC approach was effectively implemented. In the article,
the author proposes a novel meta-heuristic approach called the Opposition-Based
Arithmetic Optimization Algorithm (OAOA), depending on the nature of the distri-
bution of the arithmetic operator [13]. Owing to the occurrence of gradient-free
approach and high local optimal prevention capability approach of the suggested
algorithm, it overcomes conventional optimization algorithms. To show dominance,
the suggested algorithm is correlated with the traditional meta-heuristic approach.
In the paper, the author has designed a 2-degree of freedom PI-FOPDN Controller
and optimized its parameters using the opposition-based Arithmetic Optimization
Algorithm (OAOA) approach [14]. The tuning parameter of the proposed controller
optimized by the OAOA algorithm in a deregulated environment of a dual-zone
power system is verified by comparing with various meta-heuristic procedures like
Wild horse optimization (WHO), particle-swarm-optimization (PSO) algorithm, and
Artificial-bee-colony [15, 16]. The detailed description of the research works are as
follows:

(1)   A double-area restructure power structure having thermal constraints with a
      non-linearity effect is proposed.
(2)   For the secondary LFC, a 2DOF-PI-FOPDN Controller is proposed.

(3) Opposition-based Arithmetic Optimization Algorithm (OAOA) is recommended to get the best gain constraints of the Secondary controller.
(4) The achievement characteristic of the 2DOF-PI-FOPDN approach is linked with different controllers such as PID, FOPID, and PD(1 + PI) controller.
(5) The recommended algorithm's superiority is demonstrated by comparing it to other meta-heuristic methods.

2 Proposed System

LFC of a multiple-source double-area power scheme in the restructured environment is proposed in the paper [17, 18]. Area-1 consists of the thermal power system (GENCO-1) and Hydro Unit (GENCO-2) whereas it also includes two DISCOs, namely DISCO-1 and DISCO-2.On the other hand, Area-2 comprises the thermal power system (GENCO-4) and gas power system (GENCO-5) where it also includes two DISCOs, namely DISCO-3 and DISCO-4. Figure 1 depicts the overall comprehensive transfer-function structure of the proposed two-area power plan in a deregulated environment. The objective function deliberated is Integral-time-square error (ITSE). That is written as follows:

$$F_{ITSE} = \int_0^{T_{sim}} \left\{ |\Delta f_1|^2 + |\Delta f_2|^2 + |\Delta P_{tie}|^2 \right\} \cdot t dt \qquad (1)$$

3 Restructuring of AGC Mechanism

Deregulation relates to the procedures governing economic engagement between utilities to ensure healthy competition in the free market. The proposed two area AGC mechanism in the deregulated environment containing double GENCO and double DISCO in each zone is explained [19, 20]. The contract participation factor (cpf) parameter is used to correlate GENCO and DISCO in the Disco-participation-matrix (DPM). This reflects the correlation of the distribution of the load between the production and distribution companies. The DPM of the transmission companies having a distribution of two generating and distributing companies in each area can be given by:

$$DPM = \begin{bmatrix} cpf_{11} & \cdots & cpf_{14} \\ \vdots & \ddots & \vdots \\ cpf_{41} & \cdots & cpf_{44} \end{bmatrix} \qquad (2)$$
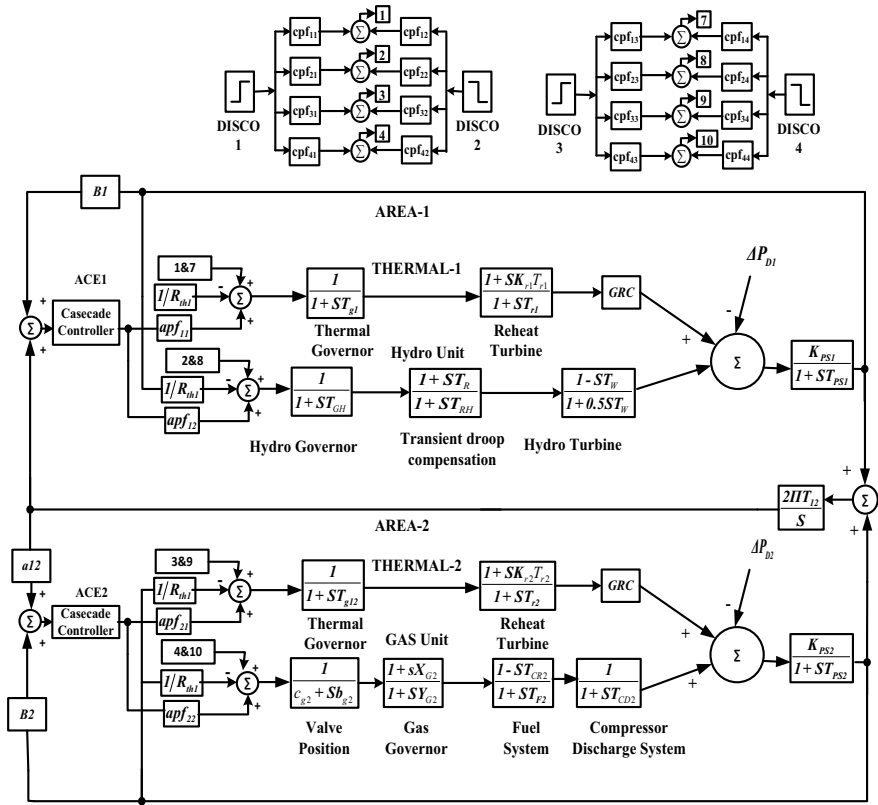
Fig. 1 Transfer function structure of a twin-area scheduled system in restructure the environment

where cpf$_{ij}$ indicates the agreement among ith GENCO and jth DISCO. It provides the value of a power-sharing agreement between the two associated electrical utilities in this area.

Tie-line power scheduling in twin areas is described as follows:

$\Delta P_{\text{tie-schedule}}$ = (Demand of active power from the distribution company in zone-j to generation company in zone-i—load demand of electrical power from the distribution company in zone-i to a distribution company in zone-j)

$$\Delta P_{\text{tie-schedule}} = P_{\text{exp}} - P_{\text{imp}} \tag{3}$$

Now the tie-line active power deviation

$$\Delta P_{\text{tie-error}} = \Delta P_{\text{tie-actual}} - \Delta P_{\text{tie-schedule}} \tag{4}$$

Therefore, Area-Control-Error (ACE) becomes

$$ACE = B\Delta f + \Delta P_{tie-error} \tag{5}$$

4 The Proposed Controller

A fractional order (FO) controller has various advantages over an integral order (IO) conventional controller. An FO controller has more degree of freedom than an IO controller as it has more tuning parameters [21, 22]. The filter coefficient (N) in competition with a derivative controller is used to diminish the noise in the system. This paper is discussed with the 2-DOF-PI-FOPDN controller to improve overall time domain specification [23]. Also the other various advantages of the proposed controller over classical integral and FOPID have been briefly elaborated in Sect. 6. The proposed controller includes a cascade structure of 2-degree of freedom proportional-integral controller and fraction order proportional derivative controller with filter coefficient, which is termed as the 2-DOF-PI-FOPDN controller [24, 25]. It has two input signals R(s) and Y(s). R(s) is the first mentioned input signal which contains Area Control Error (ACE) whereas Y(s) is the second input signal that measures the output signal indicated by area frequency deviation in the two-area system.

Figure 2 explains the basic structure of a 2-DOF-PI-FOPDN controller. Equation (6) shows the transfer function of the FOPDN controller.

$$FOPDN\ (s) = K_{p2} + K_d\left(\frac{s^m N}{s^m + N}\right) \tag{6}$$

The recommended 2-DOF-PI-FOPDN controller consists of seven tuning gain parameters in twin areas of the considered system. All the seven gain parameters are improved by the opposition-based Arithmetic Optimization Algorithm exposed.

$$K_{p1Min} < K_{p1} < K_{p1Max}, K_{IMin} < K_I < K_{IMax}, K_{dMin} < K_d < K_{dMax},$$
$$b_{Min} < b < b_{Max}, N_{Min} < N < N_{Max}, K_{p2Min} < K_{p2} < K_{p2Max}, m_{Min} < m < m_{Max}$$

where K_p, K_I, K_d, b, m, and N signifies the tuning parameters of the suggested controller.

5 Optimization

A novel Arithmetic-Optimization-Algorithm (AOA) is proposed by Seyedali Mirjalili [26]. The distribution methodology of the main arithmetic operations such as (Addition (A), subtraction (S), Division (D), and Multiplication (M)) is used by

Fig. 2 a Diagram of 2-DOF topography. **b** Suggested controller topography

(a)

(b)
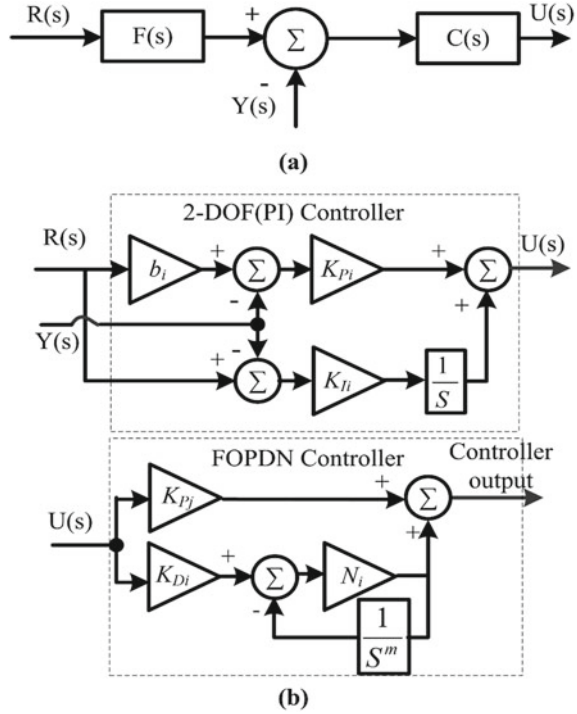
the AOA Algorithm. A mathematical model of the suggested algorithm is used to perform the optimization technique in a wide range of search spaces. The intuitive and general procedure of AOA is presented in Fig. 3.

5.1 Opposition Based Learning (OBL)

The opposite point is a reflected image of the point from the middle point of the search space ($x_{max} + x_{min}/2$). The contradictory point $\bar{x}$ for any point x in the search space, within the bounded limits can be written as

$$\bar{x} = x^{max} + x^{min} - x \tag{7}$$

Correspondingly, $\overline{X} = (\overline{x_1}, \overline{x_2}, \ldots \overline{x_d})$. is expressed as the reverse set of solutions for the present result $X = (x_1, x_2, \ldots .x_d)$. where d is represented as the range of search space and $\overline{X}$ can be written as

$$\overline{x_i} = x_{max,i} + x_{min,i} - x_i \tag{8}$$
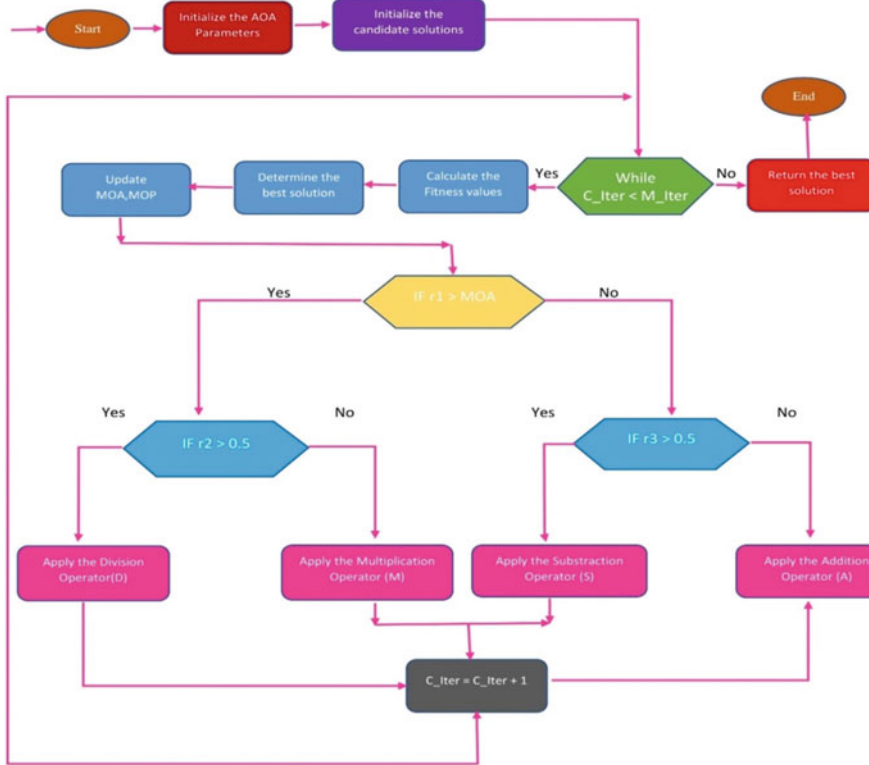
Fig. 3 Flowchart of the suggested AOA

6 Results and Discussion

To study the dynamic response of the system, that is, the frequency deviation and the power of the connecting line in two areas of the deregulated system, a step load disturbance (SLD) of 0.1 per unit in zone 1 is considered keeping zone 2 undisturbed. The DPM for deregulation is considered to be a pool-based transaction (PBT) in which the DISCO of a zone is limited to the purchase of electricity from the GENCO associated with the same zone. The disco participation matrix is given as

$$DPM_P = \begin{bmatrix} 0.5 & 0.5 & 0 & 0 \\ 0.5 & 0.5 & 0 & 0 \\ 0 & 0 & 0 & 0 \\ 0 & 0 & 0 & 0 \end{bmatrix} \tag{9}$$

The simulation was accomplished by MATLAB & SIMULINK R2020a Toolbox. The optimal gains parameters of the 2-DOF-PI-FOPDN controller have been tuned

using the Opposition Based Arithmetic Optimization Algorithm (OAOA) considering ITSE as a function of cost. The no. of initial search agents and maximum iterations are taken as 20 and 20 respectively. The achieved dynamic response is compared in two different ways as follows.

Case 1: Comparison of the dynamic response of suggested controllers with different Optimization Algorithms.

The system dynamic response and convergence curve employing the Opposition Based Arithmetic Optimization Algorithm (OAOA) are compared to other well-known evolutionary procedures like particle-swarm-optimization (PSO), wild hours optimization (WHO), and artificial-bee-colony (ABC) with the same condition on the system studied. The 2-DOF-PI-FOPDN controller optimized by the Opposition Based Arithmetic Optimization Algorithm (OAOA) showed improved transient and
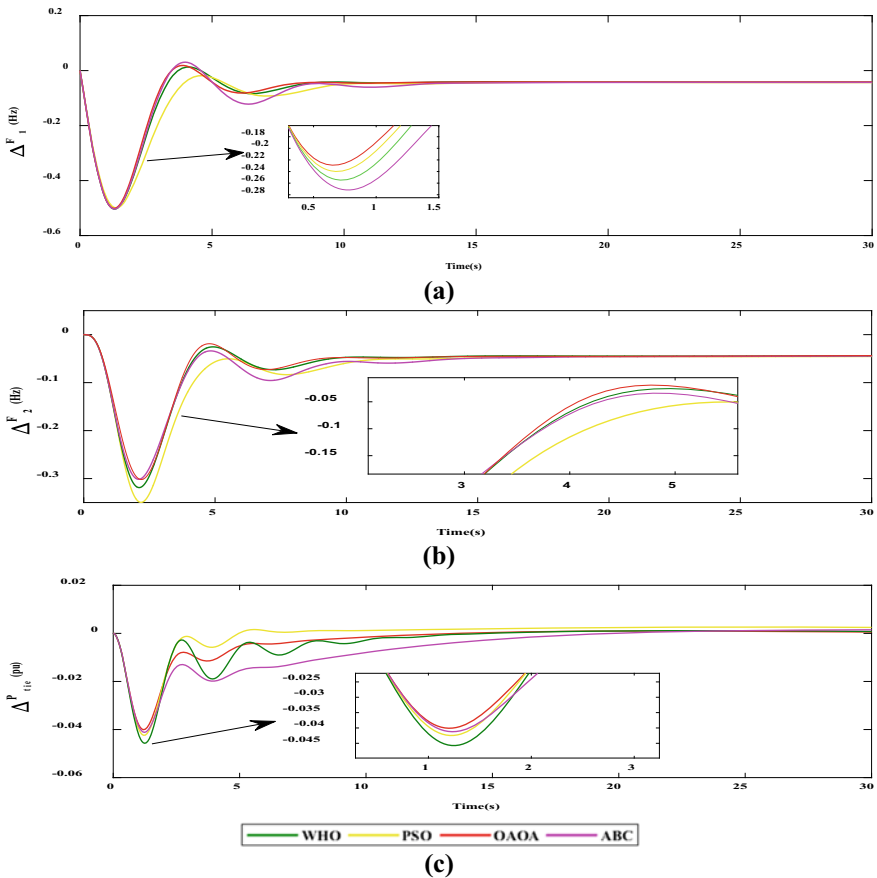
Fig. 4 a Frequency fluctuation versus time in area-1. **b** Frequency fluctuation versus time in area-2. **c** Power flow deviation in tie-line versus time

stable response with reduced settling time, undershoot, and overshoot for obtaining frequency regulation in addition to controlling the transfer of power in tie-line connection. Against the convergence curve, we can also conclude that the proposed optimization algorithm converges very quickly compared to other evolutionary techniques. The dynamic response and convergence curve for suggested algorithm schemes as well as other evolutionary methods are illustrated in Figs. 4 and 5. The dynamic response of recommended controller with a distinct algorithm is shown in comparison Tables 1 and 2.

Case 2 Comparison of the dynamic response of different controllers.

The optimal gain parameters of the 2-DOF-PI-FOPDN controller have been tuned using the Opposition Based Arithmetic Optimization Algorithm (OAOA) considering ITSE as a function of cost. The no. of initial search agents and maximum no iterations are taken as 20 and 20 respectively. The response collected is compared with (OAOA) optimized PID, FOPID, and PD(1 + PI) controllers. The suggested OAOA optimized 2-DOF-PI-FOPDN controller indicates upgraded transient and stable response with reduced settling time, undershoot and overshoot for obtaining frequency regulation in addition to controlling the transfer of power in tie-line connection. The dynamic response for popular controller schemes along with the suggested 2-DOF-PI-FOPDN is shown in Fig. 6.
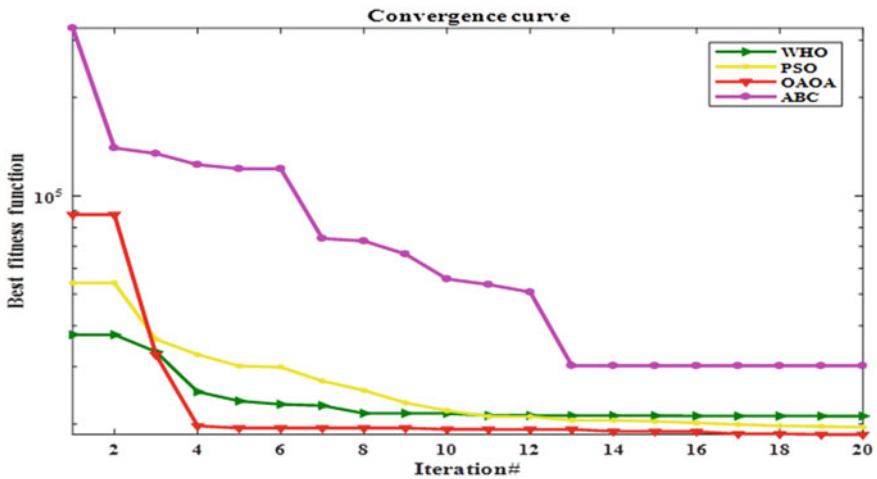
Fig. 5 Best fitness versus number of iterations
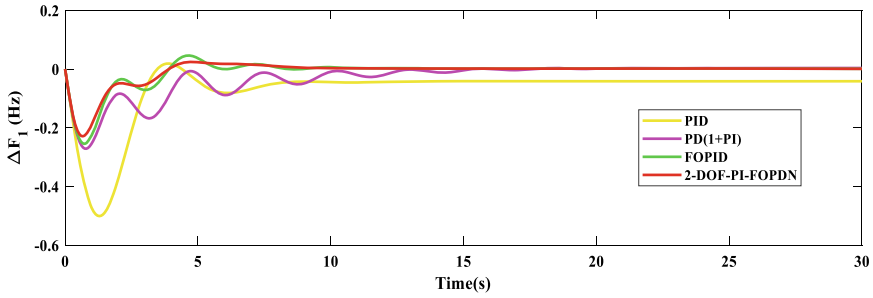
(a)
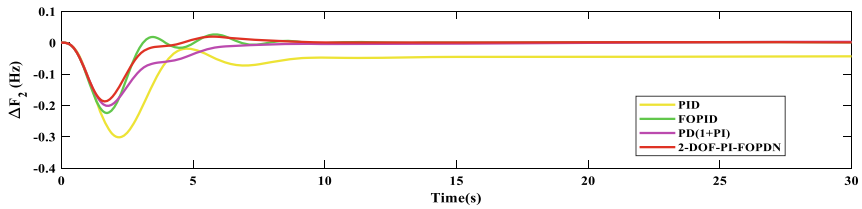
(b)
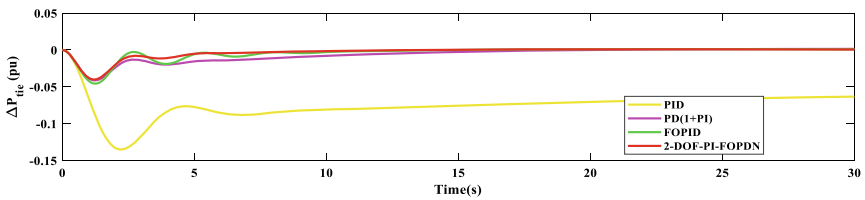
(c)

Fig. 6 **a** Frequency variation versus time in zone-1. **b** Frequency variation versus time in zone-2. **c** Power flow deviation in tie-line versus time

Table 1 Comparison of dynamic response of suggested controller with different Algorithm

Maximum deviation	ΔF_1	ΔF_2	ΔP_{tie}
OAOA optimization	−0.211	−0.291	−0.0389
PSO optimization	−0.232	−0.431	−0.0418
WHO optimization	−0.251	−0.299	−0.0423
ABC optimization	−0.279	−0.287	−0.0392
% improvement of proposed algorithm w.r.t PSO algorithm	9.00	32.71	6.93

Table 2 Optimal gain values of PID Controller obtained by OAOA algorithm with different performance indices of the system

Gains	IAE		ISE		ITAE		ITSE	
	Area-1	Area-2	Area-1	Area-2	Area-1	Area-2	Area-1	Area-2
K_P	0.7867	0.7622	0.3149	0.6838	0.0319	0.8677	0.0043	0.7279
K_I	0.4604	0.3426	0.4422	0.5887	0.5090	0.7950	0.4608	0.7032
K_D	0.6369	0.1674	0.6084	0.4740	0.2941	0.9881	0.7888	0.0087

7 Conclusion

A novel idea has been created to introduce the dynamic response of various restructure power systems using an opposition-based arithmetic optimization (OAOA) algorithm based on 2-DOF-PI-FOPDN. The influence of non-linearity such as GDB and GRC is also deliberated in dynamic response. The controller gain parameter of the recommended controller is optimized with the OAOA algorithm. The suggested optimization algorithm correlates with other algorithms for 1% SLP in zone-1 to show its supremacy. It is indicated from the dynamic response curve of the system that in zone 1, the frequency deviation is improved by 9% and by 32.7% in zone 2, while the power of the connection line is improved by 6.93%. Concerning the above convergence curve, we can also expect that the suggested optimization algorithm converges very quickly compared to other evolutionary approaches. One step forward the recommended control scheme is compared with other standard conventional controllers like PID, FOPID, and PD(1 + PI) to show its supremacy. The suggested study could be continued up to a three-zone power system integrated with non-conventional energy resources such as solar power, wind power, and biomass.

References

1. D. Sarkar, A. Kumar, P.K. Sadhu, A survey on development and recent trends of renewable energy generation from BIPV systems **37**(258–280) (2019). https://doi.org/10.1080/02564602.2019.1598294.
2. R. Shankar, S.R. Pradhan, K. Chatterjee, R. Mandal, A comprehensive state of the art literature survey on LFC mechanism for a power system. Renew. Sustain. Energy Rev. **76**, 1185–1207 (2017). https://doi.org/10.1016/j.rser.2017.02.064
3. N. Pathak, T.S. Bhatti, A. Verma, I. Nasiruddin, AGC of two area power system based on different power output control strategies of thermal power generation. IEEE Trans. Power Syst. **33**, 2040–2052 (2018)
4. S. Mir, S. Bhasin, N. Senroy, Decentralized nonlinear adaptive optimal control scheme for enhancement of power system stability. IEEE Trans. Power Syst. **35**(2), 1400–1410 (2020)

5. S. Prasad, S. Purwar, N. Kishor, Electrical power and energy systems load frequency regulation using observer based non-linear sliding mode control. Electr. Power Energy Syst. **104**, 178–193 (2019)

6. E. Sahin, Design of an optimized fractional high order differential feedback controller for load frequency control of a multi-area multi-source power system with nonlinearity. IEEE Access **8**, 12327–12342 (2020)

7. A. Latif, S.M.S. Hussain, D.C. Das, T.S. Ustun, Double-stage controller optimization for load frequency stabilization in hybrid wind-ocean wave energy based maritime microgrid system. Appl. Energy **282**(Part A), 0306–2619 (2021). https://doi.org/10.1016/j.apenergy.2020.116171

8. A. Prakash, K. Kumar, S.K. Parida, PIDF(1+FOD) controller for load frequency control with SSSC and AC–DC tie-line in a deregulated environment. IET: The Inst. Eng. Technol. **14**(14), 2751–2762 (2020). https://doi.org/10.1049/iet-gtd.2019.1418

9. Y. Arya, A novel CFFOPI-FOPID controller for AGC performance enhancement of single and multi-area electric power systems. ISA Trans. **100**, 126–135 (2020)

10. P. Jood, S.K. Aggarwal, V. Chopra, Performance assessment of a neuro-fuzzy load frequency controller in the presence of system non-linearities and renewable penetration. Comput. Electr. Eng. **74**, 362–378 (2019)

11. M. Elsisi, M. Aboelela, M. Soliman, W. Mansour, Design of optimal model predictive controller for LFC of nonlinear multi-area power system with energy storage devices. Electr. Power Compon. Syst. **46**(11–12), 1300–1311 (2018)

12. T.P. Kumar, N. Subrahmanyam, M. Sydule, CMBSNN for power flow management of the hybrid renewable energy – storage system-based distribution generation. IETE Tech. Rev. **36**(3), 258–280 (2019)

13. S. Mahdavi, S. Rahnamayan, K. Deb, Opposition based learning: a literature review. Swarm Evolut. Comput. 39(1–23) (2018). https://doi.org/10.1016/j.swevo.2017.09.010

14. A.K. Barik, D.C. Das, Expeditious frequency control of solar photovoltaic/biogas/biodiesel generator based isolated renewable microgrid using a grasshopper optimization algorithm. Inst. Eng. Technol. **12**(14), 1659–1667 (2018). https://doi.org/10.1049/iet-rpg.2018.5196

15. R. Shankar, A. Kumar, U. Raj, K. Chatterjee, Fruit fly algorithm-based automatic generation control of multi-area interconnected power system with FACTS and AC/DC links in deregulated power environment. Int. Trans. Electr. Energy Syst. **29**(1), 1–25 (2021). https://doi.org/10.1002/etep.2690

16. N. Nayak, S. Mishra, D. Sharma, B.K. Sahu, Application of modified sine cosine algorithm to optimally design PID/fuzzy-PID controllers to deal with AGC issues in deregulated power system IET Gener. Transm. Distrib. **13**(12), 2474–2487 (2019). https://doi.org/10.1049/iet-gtd.2018.6489

17. P. Aryan, R. Shankar, M. Ranjan, Equilibrium optimized AGC of multi-area restructured power system using cascaded fractional fuzzy controller, in *International Conference on Emerging Frontiers in Electrical and Electronic Technologies* (2020). https://doi.org/10.1109/ICEFEET49149.2020.9187014

18. P. Aryan, R. Shankar, M. Ranjan, Deregulated LFC scheme using equilibrium optimized type-2 fuzzy controller, in *Proceeding of International Conference on Innovative Development in Engineering Application (IDEA), WEENTECH, Bodhgaya*, pp. 495–501, 8–10 Feb 2021 (2021). https://doi.org/10.32438/WPE.442021

19. J. Morsali, K. Zare, M.T. Hagh, A novel dynamic model and control approach for SSSC to contribute effectively in AGC of a deregulated power system. Electr. Power Energy Syst. **95**, 239–253 (2018). https://doi.org/10.1016/j.ijepes.2017.08.033

20. U. Raj, R. Shankar, Deregulated automatic generation control using novel opposition-based interactive search algorithm cascade controller including distributed generation and electric vehicle. Iran. J. Sci. Technol. - Trans. Electr. Eng. (2020) https://doi.org/10.1007/s40998-019-00306-3

21. B. Khokhar, S. Dahiya, P.K.S. Parmar, A novel fractional order proportional integral derivative plus second-order derivative controller for load frequency control. Int. J. Sustain. Energy **40**, 235–252 (2020). https://doi.org/10.1080/14786451.2020.1803861

22. P. Sharma, A. Prakash, R. Shankar, S.K. Parida, A novel hybrid salp swarm differential evolution algorithm based 2DOF tilted-integral-derivative controller for restructured AGC. Electr. Power Compon. Syst. **47**(19–20), 1775–1790 (2019). https://doi.org/10.1080/15325008.2020.1731870

23. A. Prakash, S. Murali, R. Shankar, Bhushan R (2019) HVDC tie-link modeling for restructured AGC using a novel fractional order cascade controller. Electr. Power Syst. Res. **170**, 244–258 (2019). https://doi.org/10.1016/j.epsr.2019.01.021

24. D. Mohanty, S. Panda, A modified moth flame optimisation technique tuned adaptive fuzzy logic PID controller for frequency regulation of an autonomous power system. Int. J. Sustain. Energy **40**(1), 41–68 (2021). https://doi.org/10.1080/14786451.2020.1787412

25. M. Bhuyan, A.K. Barik, D.C. Das, GOA optimised frequency control of solarthermal/seawave/biodiesel generator based interconnected hybrid microgrids with DC link. Int. J. Sustain. Energy **39**(7), 615–633 (2020). https://doi.org/10.1080/14786451.2020.1741589

26. A. Abualigah, A. Diabat, S. Mirjalili, M.A. Elaziz, A.H. Gandomi, The arithmetic optimization algorithm. Comput. Methods Appl. Mech. Eng. **376**, 113609 (2021). https://doi.org/10.1016/j.cma.2020.113609

Study of Renewable Energy Resources Distribution and Its Challenges in Case of Ethiopia

Negasa Muleta and Altaf Q. H. Badar

Abstract Ethiopia has an energy generating capacity of up to 60GW. This energy can be generated from different Renewable Energy Sources (RES). The country is still experiencing an energy crisis as a result of insufficient existing power systems in terms of reliability and flexibility, high investment costs, financial constraints, population dispersion in rural areas, high electricity demand in urban areas, government energy production and distribution policies, and so on. The existing supply system in the country has the following components: Hydropower (87%), Wind (7%), and Biomass (6%). In the future, based on current trends, the cost of RES components may further decrease and the efficiency would improve due to new emerging technologies in power electronics. The main challenge of renewable energy power systems is the stability problem with frequency and voltage, due to intermittent properties of resources such as solar and wind. In this paper, different RES are discussed in detail along with the challenges involved. The resources selected for discussion are based on their availability in a country. The power contribution is likewise solely hydropower-based and needs to give attention to other resources to increase the system reliability and efficiency.

Keywords Renewable energy resources · Hydropower · Solar PV · Wind Turbine · Geothermal · Challenges

N. Muleta and A. Q. H. Badar both authors contributed equally to this work.

N. Muleta (✉) · A. Q. H. Badar
Department of Electrical Engineering, National Institute of Technology Warangal, Telangana, India
e-mail: negasam@student.nitw.ac.in

A. Q. H. Badar
e-mail: altafbadar@nitw.ac.in

1   Introduction

The share of renewables in the electricity supply increased from 26% in 2019 to 28% in 2020 [1]. RES such as Wind, solar, biomass, tidal, geothermal, etc., are continuously replenished through natural processes at a rate greater than or equal to the rate at which they are consumed, cheaper in operation cost, and do not pollute the environment [2]. RE generation has been increasing at a faster pace as compared to coal-fired energy production and has firmly established itself as the cheapest, at-scale, proven energy option available. According to a report released by the International Renewable Energy Agency (IRENA) in May 2020, utility-scale solar photovoltaic is the most widely deployed, cost-effective, and widely adaptable technology in the market. The onshore and offshore wind costs declined by 39% and 29%, respectively, whereas solar PV power declined 82% since 2010, respectively [3]. The RE installation doubled from 9% in 2000 to 17% in 2019 and is expected to exceed 30% by 2030 in the US [4].

There is an assertion of achieving 100% RE penetration regarding possibilities, prospects, and challenges as discussed in [5] and they conclude that there are advocates of a 100% RE grid and illustrated the possibility of achieving it as well. Some countries have achieved 100% or near 100% RE penetration. Iceland—100% RE penetration level, Paraguay—99%, Norway—97%, Uruguay—95%, Costa Rica—93%, Brazil—76%, and Canada—62% [6]. The feasibility of exploiting hybrid renewable energy resources, their operation, and planning need to be studied based on different parameters. Economic cost, reliability, and environmental effects are the constraints that are considered in RE. The main drawback of renewable energy is characterized by the high Levelized Cost of Energy (LCOE) due to the high investment/capital cost for construction. The average values of cost to generate 1MWh energy: Wind turbines cost $26, combined cycle gas $28, and utility-scale solar $31 [7]. The other drawback of renewable energy resources is their uncertainty due to stochastic behavior. Power Quality and Voltage stability issues are the major hurdles while increasing the penetration level of RE in power systems. To minimize such problems, the revolution of power electronics and control systems has a great role in adjusting and monitoring the system according to its requirements.

2   Renewable Energy Potential in Ethiopia

Besides Ethiopia, all power generation that is connected to the grid is generated from RES. Hydropower generation covers more percentile to other energy sources.

2.1 Hydro Power Energy

Hydropower is harnessed energy from fast-running or falling water. Ethiopia is often referred to as "water tower" of Africa because of its abundant water resources, the greatest in the whole of Africa, including the Nile River. The amount of power generated from hydropower is calculated using Eq. (1).

$$P_h = QHg\eta \qquad (1)$$

where Q : water flow rate, (m^3/s) H: water head, (m)

g : gravitational acceleration, (9.81 m/s^2)

η: total efficiency Power plant. The potential of Hydropower generation in Ethiopia is listed in Table 1.

Challenges of Hydropower Generation [9]

- Comparatively higher investment costs with higher risks associated with a large plant
- Susceptible to risks concerning environmental degradation and climate change
- Most environmental and social sensitive power generation technologies.

Table 1 Hydropower electric generation capacity [8]

Power plant	Dam height(m)	Installed cap(MW)	Aver energy(GWh)	Completed date
Genale Dawa III	110	254	–	2020
Gilgel Gibe III	243	1870	6500	2016
Beles	35	460	1867	2010
Tekeze	188	300	1393	2009
Gibe II	46.5	420	1635	2009
Gibe I	41	184	722	2004
Melka Wakena	42	153	543	1988
Fincha	22.2	134	760	1972
Fincha Amerti	38	97	–	2011
Tis Abay I	Weir	11.4	33.7	1953
Tis Abay II	Weir	73	359	2001
Koka	23.8	43.2	110	1960
Awash 2	10	32	182	1965
Awash 3	20	32	192	1971
Grand total		4063.6	14,296.7	

2.2 Wind Energy

Wind energy is originated from solar energy due to a combination of three concurrent events: Sun unevenly heats the atmosphere, irregularities in the earth's surface, and rotation of the earth. Wind turbines generate electricity from wind movements by turning the propeller-like blades of a turbine around a rotor which in turn operates the generator using the aerodynamic force.

The power generated from wind speed is formulated in Eq. (2).

$$Pwt_t = \begin{cases} 1/2\rho A_t V^3 & for \ V_c \leq V < V_r \\ 1/2\rho A_t V_r^3 & for \ V_r \leq V \leq V_f \\ 0, & otherwise \end{cases} \tag{2}$$

where A: turbine diameter area, (m^2)

V_c: cut-in speed, (m/s)

V_r: rated speed, (m/s)

V_f : cut-off wind speed, (m/s)

The wind turbine technology is increasing gradually in the power capacity from small kW to large MW as explained in [10]. Ethiopia is currently generating 324 MW of electricity from three different wind farms: Adama I with 51MW, Adama II with 153MW, and Ashegoda with 120MW. The potential of electric power generation from Wind Turbine in Ethiopia is summarized in Table 2.

Table 2 The wind power farms in Ethiopia

Project	Generating cap(MW)	Energy (GWh/yr)	Status
Adama I WPP	51	157	Commissioned
Adama II WPP	153	479	Commissioned
Ashegoda WPP	120	450	Commissioned
Ayisha WPP	300	592	Test stage
Assela WPP I	100	300	Under construction
Assela WPP II	150	450	Feasibility study
Messobo WPP	42	104	Planning stage
Debre Birhan WPP	100	19	Planning stage
Grand total	1016	2729	

The following are the Challenges of Wind Turbine Power Generation [11] :

- Efficiency maximization
- Cost reduction for a zero-incentive situation
- Mechanical load attenuation
- Extreme weather conditions
- Large-scale grid integration and penetration
- Airborne wind energy systems
- Offshore wind turbines

2.3 Solar Energy

The sun is a source of energy for other types of energy that emit enough energy to satisfy the global demand. Solar energy is used in electricity production as a form of Photovoltaic (PV) and heat collector. A PV cell is a semiconductor that produces electricity when photons strike PV cells. The electrons are dislodged from the material's atoms when the semiconductor material absorbs enough sunlight (solar energy) and free electrons migrate to the surface of the cells. Electrical power output (P_t) from the solar PV system is determined by the solar insulation (G_t), (w/m^2) and environmental temperature (T_a), (°C) as formulated in Eq. (3) [12].

$$P(t) = \frac{Gt}{Go}\left(Po + \mu a\left(Tt + Gt\left(\frac{NOCT - 20}{800}\right) - Tm\right)\right) \qquad (3)$$

where G_o: insulation at rated power, (w/m^2)

P_o: maximum power generated from the panel, (W) NOCT: normal operating cell temperature, (°C)

T_m: module temperature at the standard condition, (°C).

The efficiency at which PV cells convert sunlight to electricity varies depending on the type of material of the semiconductor and the technology used for PV cell. The efficiency of commercially available PV modules averaged approximately 23% in 2020 rising from 10% in the mid-1980s. The efficiency of the experimental PV cell for niche markets used for space satellites has reached approximately 50% [13]. There is a large solar PV power plant potential of 100 MW found near Metahara town and planned to connect to the grid system. Different potentials and statuses of electric power from solar PV are listed in Table 3.

Challenges of Solar Power [11]:

- Optimal and hybrid control algorithms
- Optimal robust control techniques
- Modes and methods for forecasting solar radiation using heterogeneous information

Table 3 Solar PV projects in Ethiopia [14]

Project	Capacity (MW)	Region	Status
Dicheto Solar (Phase I)	125	Afar	Scaling
Gad Solar (Phase I)	125	Somali	Scaling
Mekele Solar	100	Tigray	RFP Pending
Humera Solar	100	Tigray	RFP Pending
Weranso Solar PV	150	Afar	RFP Pending
Welenchiti Solar	150	Oromia	RFP Pending
Hurso Solar PV	125	Diredawa	Wait approval
Metema Solar PV	125	Amhara	Wait approval
Grand total	1000		

- Fault detection and isolation in solar power plants.
- Algorithms to estimate main process variables and parameters from heterogeneous and distributed measurements

2.4 Geothermal Energy

Geothermal energy produced heat within the sub-surface of the earth. Water steam carries the geothermal energy toward the earth's surface used to harness clean electricity. For harnessing dry steam, geothermal power, binary cycle, and flash steam techniques are used.

The main advantage of geothermal energy is its availability at all-time relative to solar and wind which are available only about 1/3rd of the time. The price of geothermal energy varies between 5 and 10 cents/kWh. This price is quite competitive as compared to other energy sources. [15]. The Aluto-Langano Geothermal field is being enhanced up to 70 MW by the Ethiopian Government. Dofan Fantale, Abaya, Tulu Moye, and Corbetti, areas are surface explored for future geothermal prospects as summarized in Table 4.

The Following are the Challenges in Geothermal Power Generation [17]:

- Its prices are heavily increased by the long project development times
- Environmental impacts
- High investment costs
- Waters from it has offensive smelling due to different chemicals
- Risk of exploratory drilling geographically limited to appropriate sites
- Low efficiencies

Table 4 Geothermal potential in ethiopia[16]

Project	Location	Installed Cap(MW)	Status
Aluto Langano	Riftvalley	75	Construction
Dofan Fantale	Riftvalley	60	Analysis stage
Abaya	Riftvalley	100	Analysis stage
Tulu Moye	Riftvalley	40	Analysis stage
Corbetti	Riftvalley	70–300	Analysis stage
Tendaho	Riftvalley	100	Analysis stage
Grand total		450–675	

2.5 Biomass Energy

Electrical power is generated by burning biomass components and converting the heat energy to electricity through the stream of water or air. The output power from biomass (P_{bm}) is formulated in Eq. (4).

$$Pbm = \frac{Totalbio \times 1000 \times CVbio \times \eta bio}{8760 \times Otime} \tag{4}$$

where CV_{bio} : the calorific value of organic material, (MJ/kg) $Total_{bio}$: total organic material of biomass, (tone/yr)

η_{bio} : biomass efficiency, 24% and

O_{time} : operating hours, (hr/day).

More than 89% of total rural energy consumption is based on biomass to fulfill the basic requirement of household energy [18] in Ethiopia in the traditional way. A rapid growth in RE power plant installations shall be carried out which will be complemented by about 500 MW of biomass capacity in 2025 [19]. In Ethiopia, the biomass power plant's statuses with their power generating capacities are presented in Table 5. Except Reppie power plant, all power plants from biomass are available at a sugar factory to supply the demand of the company load.

The Following are the Challenge in Biomass Power Generation [20]:

- Raw material transportation and its delivery from the farm to the power generation unit
- A complicated process of Gasification is depended on numerous operating parameters
- Pretreatment of raw material is an energy and labor-intensive process
- The cleaning or removal of syngas from unwanted particles and ashes is not only complex, but also cost-intensive

Table 5 Biomass power plant in Ethiopia from waste and Bagasse

Project	Location	Installed Cap(MW)	Status
Reppie energy plant	Addis Ababa	25	Commissioned
Fincha Sugar Factory	Finchaa	31	Commissioned
Wonji Sugar Factory	Metehara	31.5	Commissioned
Omo Kuraz II	Kuraz	60	commissioned
Tendaho Sugar Factory	Asaita	60	Commissioned
Omo Kuraz III	Kuraz	60	Commissioned
Tana Beles I	Agew Awi	30	Construction
Omo Kuraz I	Kuraz	45	Construction
Omo Kuraz V	Kuraz	120	Construction
Tana Beles II	Agew Awi	30	Construction
Grand total		492.5	

3 Accessibility of Renewable Energy Ethiopia

In Ethiopia, the RES is available in abundance, the potential is approximated to 60GW. The total exploited power capacity is less than 10% of total capacity by 2020. More than 75% of the population live in rural areas and out of the rural population, only 45% were electrified. According to the Ethiopian Ministry of water, irrigation, and electricity, the per capita consumption of electricity was 70 kWh by 2014 and has increased to approximately 100 kWh by 2017. However, this level of electricity consumption is significantly lower than the average level of per capita energy consumption in other African countries (500 kWh per capita) [19]. Solar radiation and wind are abundantly available during the dry season and are scarce during the wet season when more water availability increases. Complementary usage of solar sources and wind along with hydro sources is increasing the reliability of the system, efficiency, and production curtailment [21]. The Hydropower handles more than 87% of total generation in Ethiopia as current status indicated in Fig. 1. With the current status in the country, wind turbines and biomass are ranked second and third respectively. The power generated from biomass is also available on the third rank that most of them designed to supplying sugar factor except Reppie power plant that generates electricity from the waste product in Addis Ababa. So we conclude that it needs more attention to generate electricity from those different sources, which not only increases the reliability by having different resources, but also reduces the Eastern African water resources crisis.

Fig. 1 Distribution RE in Ethiopia @ 2021
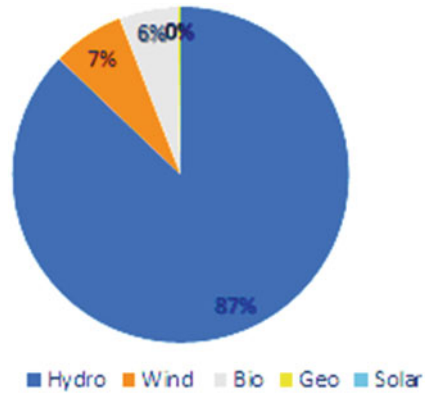
4 The Challenges of RE Generation in Ethiopia

As explained in Sect. 3, the country has a huge amount of RES. But yet more than half of the total population cannot get electricity due to:

- Finance limitation for project
- The dispersed distribution of population in the rural area
- High demand for electricity in urban areas
- Government policy for energy production and distribution
- Poor performance of current power system

The energy sector needs a huge amount of investment, especially since the capital cost is high for RE relative to other resources. So the problem of financing for RE will be solved when all respective body is giving attention and investing in electric production. In addition to satisfying electricity demand, investing in renewable energy reduces green gas emissions and creates job opportunities for the community. If a government decides to subsidize and give support to the RE production sector, coverage of electric demand will increase. As a country, there is a plan to electrify all population 100% using universal electric access programs by utilizing different sources of energy [22]. As planned, the start was on good progress, but due to scattered distribution of population in a rural area, it is difficult to achieve the planned goal at a specified period. Even it is not feasible as the current situation of population distribution in a rural area without collecting them to gather. It is more feasible if the community is collected together and forms a village for all basic infrastructure including electricity. So the Utility is stressed by supplying those demands having poor power quality rather than electrifying the rural area. The government policy on power generation is also one bottleneck in this sector; all power system (generation, transmission, and distribution) is monopolized by the government. Due to this, there is no competition in this sector. But at this time, there is a clue that the government starts to invite investors to participate in the production of electric energy [23].

The total transmission and distribution loss of power in Ethiopia is approximated up to 20% (acceptable levels approximately 5–10%) [24]. At distribution, power loss is greater than the specified figure due to the poor network and power theft. Especially on the low voltage side, the customers take the power from a long distance more than the limit which leads to more voltage drop. The accumulation of this voltage drop has an impact on the performance of the power system. At distribution, power loss is greater than the specified figure due to the poor network and power theft. The interruption is whether planned or not, but affects the customer repeatedly. As stated in the paper [25], 55% of the number of interruptions and 46% of the total duration of interruptions are in Addis Ababa, the capital city of Ethiopia.

There is a time when overload happens due to resource unavailability or beyond the capacity of substation and transmission lines. In 2019, for almost the whole year, the country was supplied with electricity on shift basis due to scarcity of resources (water) [26]. In some cities, the substation transformers are fully loaded beyound their capacity. To overcome this problem, as a temporary solution, some loads were shaded by turning off the feeders, which is not recommended in the electrical supply system. In general, there is a scarcity of switching sections that are used to isolate the required load from the system. For any fault that happened in networks, it is adapted to control from substation only in terms of sectionalizing the affected routine. Applying the section switch at the proper place in the network will reduce the interruption rate and improve the reliability profile.

The generation of power from renewable resources is not a simple issue regarding stability and reliability. The optimal operating point is attained using different techniques. Forecasting the availability of RE using different methods and managing the load accordingly will increase the reliability of the system. Maximum tracking power point (MPPT) is common in solar and wind power harvesting methods. It used to utilize the resources in an efficient way to a load by adjusting the generation plant by harvesting at the optimal operation point.

During planning, the power system has to be the modern system, democratized, decentralized, and decarbonized which are also known as '3 D's' [27]. The purpose of these trends is to optimize power system reliability, resiliency, CO_2 emission, cost of electricity, etc. Using only RES sources is not feasible due to its unavailability of intermittent properties. Using a storage system will improve the system's performance. Fuel Cells (FC) and Battery Storage (BS) are commonly used in RES industries. In Ethiopia, BS is widely used for backup service for sensitive loads like telecommunication where data storage and processing are required. Different energy storage technology is available and served in different applications. Diesel generators are used as a backup in industries, commercial, and institutes during emergency times. The fuel consumption by diesel generators has an influence on the country next to the transport sector. It has also negative impacts on the environment due to pollutant gas production from it. In the transport sector, it is better to adopt modern transportation types like trains and electric vehicles that use electric power. Using such technology reduces GHG emissions by decreasing fuel consumption.

5 Conclusion

There is abundance in renewable energy resources and, on the other hand, the overall power system in the country is poor in reliability and high power loss. To improve generation capacity and electric deficiency, integrating different renewable energy at a required place is the option. The investment cost of renewable energy resources is decreasing gradually. When the respective body got initiation, especially from the police maker, it is a feasible and the better option to encourage the satisfaction of high energy demand. In renewable energy production, the consumer can participate. They can generate electricity and sell it back to the utility when the resource is available abundant and use the utility's power at its peak hour or low tariff. So the police maker has to give an opportunity to any interested investors to generate electricity and sell it back to grid police. Promoting the prosumer to use renewable energy or a standalone system can reduce the energy crisis in the country. So having a different type of renewable energy resource increases reliability, improves power quality, and reduces environmental impacts.

References

1. P. IEA., Global energy review (2020). https://www.iea.org/reports/global-energy-review-2020
2. T.-H. Le, Y. Chang, D. Park, Renewable and nonrenewable energy consumption, economic growth, and emissions: international evidence. Energy J. **41**(2) 2020
3. M. Lempriere, Solar PV costs fall 82% over the last decade, says Irena (2020). https://www.solarpowerportal.co.uk/news/solarpvcostsfall82overthelastdecadesayirena
4. D.E. Renewable, Renewable energy is the cheapest energy option (2020). https://www.dukeenergy.com/renewableenergy/resources/top5renewableenergysources
5. B.B. Adetokun, C.M. Muriithi, J.O. Ojo, Voltage stability assessment and enhance- ment of power grid with increasing wind energy penetration. Int. J. Electr. Power Energy Syst. **120**, 105988 (2020)
6. B. Kroposki, B. Johnson, Y. Zhang, V. Gevorgian, P. Denholm, B.-M. Hodge, B. Han-negan, Achieving a 100% renewable grid: operating electric power systems with extremely high levels of variable renewable energy. IEEE Power Energy Mag. **15**(2), 61–73 (2017)
7. K. Brigham, The rise of wind power in the u.s (2021). https://www.youtube.com/watch?v=b5GOsZCWRv4
8. W. Kruger, S. Fezeka, A. Olakunle, Ethiopia country report (2019)
9. C.S. Kaunda, C.Z. Kimambo, T.K. Nielsen, Hydropower in the context of sustainable energy supply: a review of technologies and challenges. Int. Sch. Res. Not. (2012)
10. N. Josh Bauer, The leading edge: April 2020 wind energy newsletter. https://www.nrel.gov/wind/newsletter-202004.html
11. E.F. Camacho, T. Samad, M. Garcia-Sanz, I. Hiskens, Control for renewable energy and smart grids. Impact Control Technol. Control Syst. Soc. **4**(8), 69–88 (2011)
12. G. Fathi, N. Ghadimi, A. Akbarimajd, A.B. Dehkordi, Stochastic-based energy management of dc microgrids, in *Risk-Based Energy Management* (Elsevier, 2020), pp. 31–47
13. Photovoltaics and electricity (2020). https://www.eia.gov/energyexplained/solar/photovoltaics-and-electricity.php
14. K. Whyte, Ethiopia seeks to install four solar pv projects (2021). https://www.esi-africa.com/industry-sectors/renewable-energy/ethiopia-seeks-to-install-four-solar-pv-projects/

15. J.W. Lund, A.N. Toth, Direct utilization of geothermal energy 2020 worldwide review, *Geothermics* (2020), p. 101915
16. S. Kebede, Geothermal exploration and development in ethiopia: status and future plan (2013)
17. A. Evans, V. Strezov, T.J. Evans, Assessment of sustainability indicators for renew- able energy technologies. Renew. Sustain. Energy Rev. **13**(5), 1082–1088 (2009)
18. S.L. Tesema, G. Bekele et al., High wind power penetration large scale hybrid renew- able energy system design for remote off-grid application. J. Power Energy Eng. **7**(03), 11 (2019)
19. A.D. Hailu, D.K. Kumsa, Ethiopia renewable energy potentials and current state [j]. AIMS Energy **9**(1), 1–14 (2021)
20. S. Sansaniwal, M. Rosen, S. Tyagi, Global challenges in the sustainable development of biomass gasification: an overview. Renew. Sustain. Energy Rev. **80**, 23–43 (2017)
21. U. Bagalini, T. Batu, M. Armiento, Integration of variable renewable energy in the national electric system of Ethiopia (2019)
22. I. Pappis, A. Sahlberg, T. Walle, O. Broad, E. Eludoyin, M. Howells, W. Usher, Influence of electrification pathways in the electricity sector of ethiopia—policy implications linking spatial electrification analysis and medium to long-term energy planning. energies 2021, 14, 1209 (2021)
23. A. Richter, Government of Ethiopia approves ppas with private geothermal developers newsletter (2020). https://www.nrel.gov/wind/newsletter-202004.html
24. T. Bank, Electric power transmission and distribution losses (% of output), in *IEA: Paris, France* (2016)
25. D.H. Gebremeskel, G.B. Worku, Study on power distribution network automation to mitigate power outages. Zede J. **35**, 38–46 (2017)
26. M. Xuequan, Ethiopia encounters energy deficit amid water shortages in major plants. http://www.xinhuanet.com
27. M. Negasa, A.Q. Badar, Study of energy management system and IoT integration in smart grid, in *2021 1st International Conference on Power Electronics and Energy (ICPEE).* (IEEE, 2021), pp. 1–5

Shunt Active Power Filter Integrated Hybrid Energy System for Harmonics Mitigation Under Different Load Perturbation

Sarita Samal, Smarak Pani, Byamakesh Nayak, Babita Panda, Alivarani Mohapatra, and Prasanta Kumar Barik

Abstract The harmonics level of a hybrid power system based on solar PV (SPV) and wind system is measured using a shunt active power filter (SAPF) in this study. For reference current generation, the SAPF uses a modified synchronous reference frame technology, an adaptive hysteresis current controller scheme, and a traditional proportional and integral-based voltage regulator. Under various loading conditions, the suggested SAPF performs remarkably well in suppressing harmonics. The suggested model was developed in MATLAB/Simulink, and the results show that it outperforms previous methods in terms of harmonic mitigation and dc-link voltage stability. The SAPF can minimize harmonics of the source current from 26.74% to 1.52% and reduces the ripples from the dc-link capacitor voltage from 22 to 8 V under steady-state condition, respectively, based on the numerical comparison of findings.

Keywords Active filter · Harmonics · Power quality · SPV · Wind energy

1 Introduction

The current planet is in the grip of a massive power crisis. Conventional energy sources are scarce, and their prices are rising by the day. It is also harmful to the environment [1]. The modern world requires unrestricted access to energy sources that are clean, uncontaminated, and plentiful. As a result of their inevitable benefits, the globe is gravitating towards renewable sources. Renewable sources are safe for the environment, abundant in nature, and costless [2]. There are various sorts of renewable sources accessible. Solar, wind, and fuel cells are examples of renewable sources [3]. Solar energy is highly pure, and it is freely available all throughout the planet. It also has a lower carbon footprint and produces no greenhouse gases

S. Samal (✉) · S. Pani · B. Nayak · B. Panda · A. Mohapatra
SoEE, KIIT DU, Bhubaneswar, Odisha, India
e-mail: ssamalfel@kiit.ac.in

P. K. Barik
Department of MEE, CAET, OUAT, Bhubaneswar, Odisha, India

[4]. New inventive strategies are developed to improve the system's execution and effectiveness while lowering startup costs. To increase its efficiency, the solar system must be linked to electronic equipment. The MPPT strategy is used to collect the most power from solar panels [5]. Wind energy has several advantages, including the fact that it does not harm the water, air, or soil. It makes no emissions of greenhouse gases. It doesn't use nearly as much water as other energy sources do [6]. Unlike SPV, which is limited during bad weather and at night, it has a steady supply. Electricity generated by a wind power plant is less expensive than electricity provided by other sources [7]. PMSG-based wind turbine systems with a fixed pitch angle are the most effective WES methods [8]. The energy generated by the WES is first converted to dc and then fed to a boost converter through a diode rectifier. The system's power is optimized by using a boost converter with an MPPT controller. An inverter can be employed at the boost converter's terminals to give optimal power to three-phase customers' loads [9]. The missing energy can be given via a battery energy storage system [10] if the user load raises or the wind speed drops suddenly. Active power filter (APF) technology was developed in response to the need to mitigate harmonics. APFs are also employed for load balancing, reduction of flickering, and correction of neutral current, among other things [11]. APFs address the limitations of PFs due to the use of switching devices. For harmonic current and reactive power adjustment, the SAPF is linked at the PCC [12]. SAPFs are also employed in both voltage and current waveforms to correct reactive power and current harmonics. For SAPF, a variety of time domain-based control approaches such as the instantaneous "p-q" theory method, SRF, MSRF method, and so on are cited in references [13]. SAPFs in current harmonic compensation based on instantaneous reactive power theory and the SRF method are applied in domestic, commercial, and industrial applications [14–16]. The design/simulation and experimental investigations on a SAPF for harmonics and reactive power compensation are carried out in [17]. In majority of the literature, the generation of theta angle method is implemented using basic SRF and modified SRF (MSRF) schemes which minimize the inherent drawbacks of the SRF method [18]. Hence, in this work, MSRF technique is implemented for the SAPF control algorithm. In this control stage, switching PWM pulses are obtained by the error signals generated from the comparison of reference current and sensed actual currents. Various gating signal generation methods are reported in the literature. Authors in [19] proposed a hysteresis current controller (HCC) based PWM current control method for generating pulses for SAPF. This method achieves constant switching and is easy to implement. However, the disadvantage of HCC is that the change in the frequency of the switch is unequal within a specific band. An adaptive hysteresis current controller (AHCC) [20] was designed to circumvent these constraints where the hysteresis band can be adjusted according to supply and load parameters to improve the PWM inverter performance. Moreover, As explained in [21], the dc side voltage of SAPF should be regulated to ensure transient stability of the distribution system. DC side capacitor in SAPF is used to maintain the power balance in the system. If the load is suddenly increased, the capacitor discharges and delivers power to the load so that the source and load power balance will be made. Similarly, if the load is suddenly removed, the capacitor overcharges and maintains

power balance. To achieve this operation, the voltage across the DC side capacitor needs to be regulated. The DC voltage controller generates desired charging current reference which will be given to the inner current loop. Following a disturbance in source or load, the DC voltage controller generates desired shift of reference current. So under transient conditions also, the SAPF compensates for reactive and harmonic currents. Authors in [9] have proposed a linear control method for regulating the DC side voltage of SAPF. A PI controller is designed and implemented for controlling DC voltage. The controller is designed based on the plant model and parameters. Conventionally, SAPF uses PI controllers to compute the active power losses and reactive power compensation control loops. As per the literature survey, in this study, the author has used MSRF-based control methodology for generating reference signal, AHCC technique for switching signal, and for DC bus voltage, the PI controller is used.

The following are the primary objectives of this study:

- To develop a hybrid Energy system (HES) using solar panels and wind energy in a MATLAB/SIMULINK environment.
- Modelling of SAPF by using MSRF, AHCC, and PI controller-based control technique.
- Integrating a SAPF with HES and to analyze PQ issues under different nonlinear load conditions.

The article is organized as follows. The suggested hybrid energy system having MPPT and boost converter is modelled in Sect. 2. The SAPF's setups and control scheme are examined in Sect. 3. In Sect. 4, the suggested hybrid system is subjected to a SAPF-based harmonics analysis under nonlinear load conditions. A brief conclusion finishes Sect. 5 of the study.

2   Hybrid Energy System Model

2.1   Modelling of SPV

Solar energy is highly pure, and it is freely available all throughout the planet. It also has a lower carbon footprint and produces no greenhouse gases. Solar energy is a superb alternative source for electric power generation because it is pollution-free and abundant in nature. In the following section, we'll go through the specifics of the SPV system's design.

2.1.1 Modelling of Solar Panel

This proposed system uses a PV array as shown in Fig. 1, which is simulated using a model based on literature. The nonlinear output characteristics of a SPV model are written as an Eq. (1). The P&O MPPT flowchart is shown in Fig. 2. Table 1 contains the parameters of the SPV system. The BC's design is shown in Fig. 3. The output DC voltage is determined using the duty ratio D. SPV system with BC and MPPT is presented in Fig. 4, while Fig. 5 depicts the output voltage.

Fig. 1 SPV model
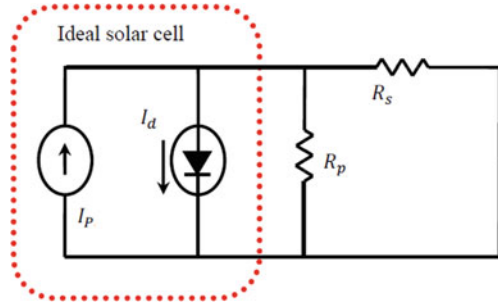
Fig. 2 MPPT flowchart
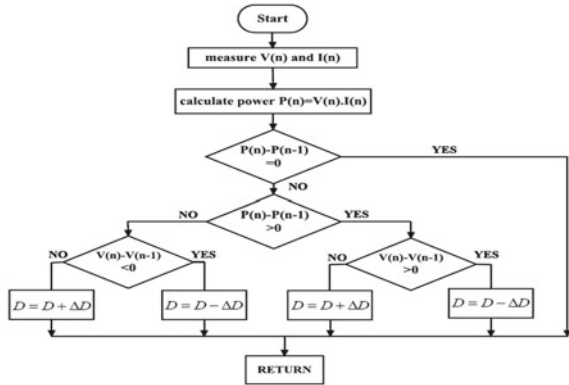
Table 1 SPV Parameters

Parameters	Ratings
V_{mp}	81.5 V
I_{mp}	8.6A
I_{sc}	10.2A
V_{oc}	90.5 V
	72
	01
V_0	230 V
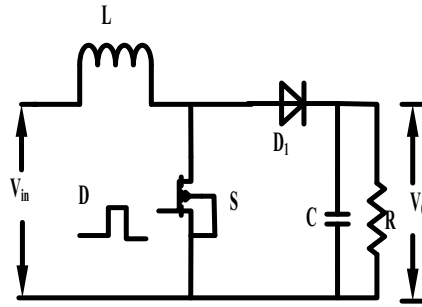
Fig. 3 Step-up converter
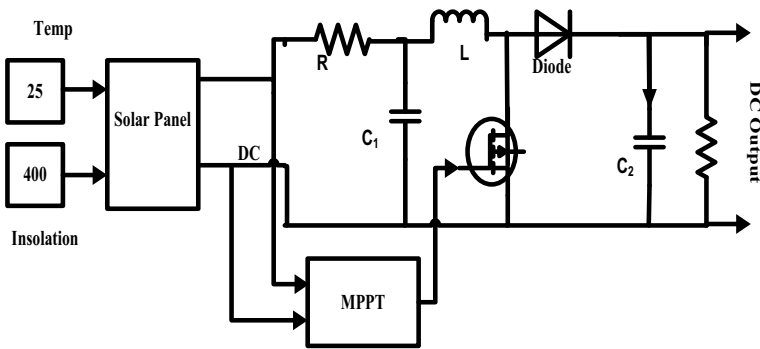
Fig. 4 SPV model block diagram

Fig. 5 Output waveform of SPV system
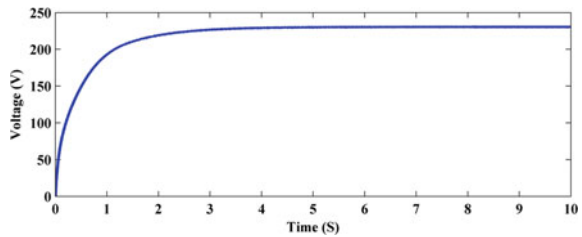
$$I_{PV} = N_P \times I_{Ph} - N_P \times I_0 \left[\exp\left\{ \frac{q \times V_{PV} + I_{PV}R_{se}}{N_S \times AkT} \right\} - 1 \right] \qquad (1)$$

2.2 Modelling of WES

In the hybrid source's structure, the wind system is another DG. To generate energy, a PMSG-based WEC is implemented using Eq. (2) as given below.

$$P_0 = \frac{1}{2} \pi \rho C_P(\lambda, \beta) R^2 V^3 \tag{2}$$

The fundamental WEC system is depicted in Fig. 6. Figures 7 and 8 show the overall model and output waveform.
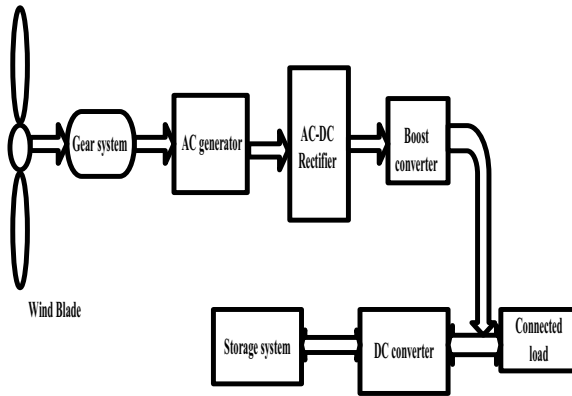
Fig. 6 Block diagram of WES
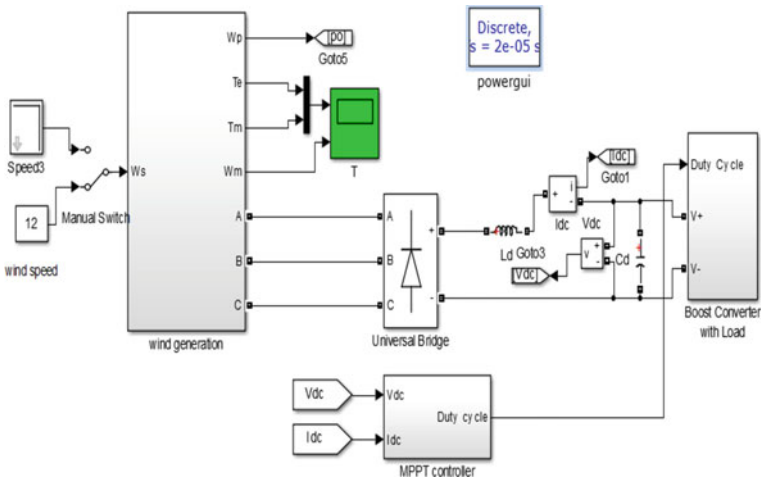
Fig. 7 Overall, WES model

Fig. 8 Output waveform of WES
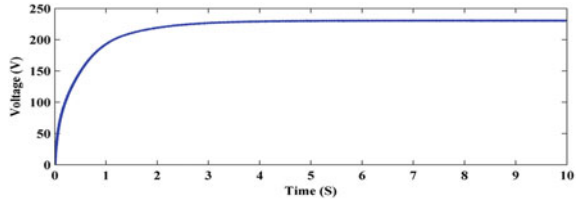
3 Design of SAPF

3.1 Components of SAPF

To cancel out the nonlinear load's harmonic currents and compensate for reactive power, the SAPF system responds by supplying/drawing a harmonic current to/from the supply. As a result, the current generated by the utility grid is sinusoidal and harmonic-free. Figure 9 shows a block diagram of the SAPF.

(a) **VSI**

To generate the compensating current, six IGBTs are employed to handle the charging and discharging of the DC-link capacitor. This converter's switching operation is entirely dependent on the control block's design.

(b) DC-Link Capacitor

This capacitor provides the load with the reactive power it requires. Large capacitors are typically used to maintain a steady DC voltage.

(c) Control Block

SAPF's overall performance is determined by the control block. The reference current and Vdc are used to create control signals for the power switches. SAPF
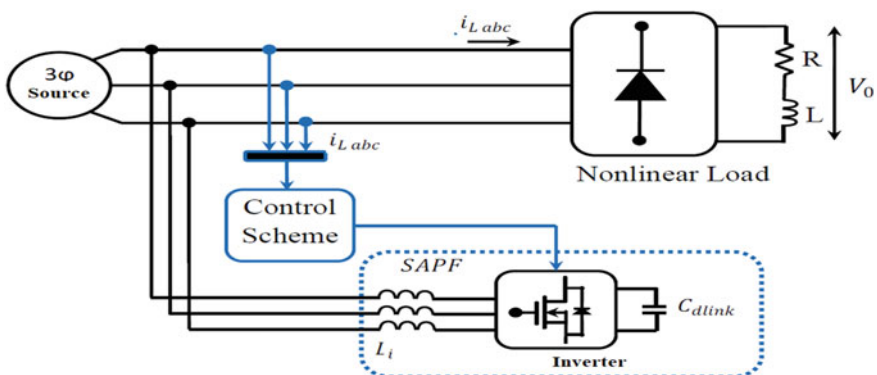
Fig. 9 Basic structure of SAPF

injects an appropriate amount of compensating current i_c in the opposite phase of the harmonic current to eliminate harmonics from the source current (i_s).

The following equation is the fundamental equation for recognizing SAPF functionality:

$$i_c(t) = i_s(t) - i_l(t) \tag{3}$$

$$v_s(t) = V_s \sin \omega t \tag{4}$$

In case of nonlinear load

$$i_l(t) = i_1 \sin(\omega t + \varphi 1) + \sum_{n=2}^{\infty} i_n sin(n\omega t + \varphi n) \tag{5}$$

$i_s(t)$ = source current.

$i_l(t)$ = load current.

$i_c(t)$ = compensating current and φ_1 is angle between current and fundamental voltage.

3.2 SAPF Control Schemes

3.2.1 Reference Current Generation

(a) **SRF control technique**

The basic SRF scheme model is revealed in Fig. 10, where the load current (i_{la}, i_{lb} and i_{lc}) and transfer to $i_d - i_q$ as acknowledged in Eq. (6). The load current is then passed via an LPF to filter out the harmonic components, leaving only the fundamental component. Finally, the inverse park-transformation approach

Fig. 10 SRF method
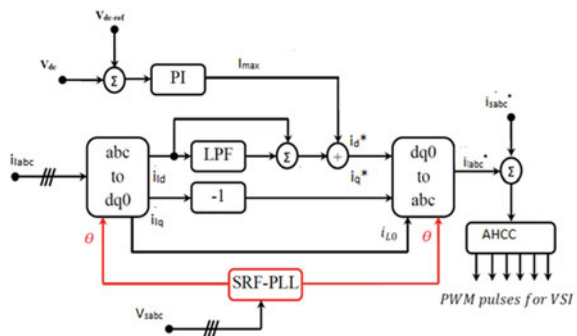
is used to convert this $i_d - i_q$ current to a three-phase stationary frame.

$$\begin{bmatrix} i_0 \\ i_d \\ i_q \end{bmatrix} = \begin{bmatrix} \cos(\theta) & \cos(\theta - 120) & \cos(\theta + 120) \\ \sin(\theta) & \cos(\theta - 120) & \cos(\theta + 120) \\ \frac{1}{2} & \frac{1}{2} & \frac{1}{2} \end{bmatrix} \begin{bmatrix} i_{lc} \\ i_{lb} \\ i_{la} \end{bmatrix} \qquad (6)$$

(b) **MSRF method**

Instead of using a PLL circuit like in the SRF approach, the MSRF method uses a simplified unit vector generating scheme to accomplish synchronization [19]. Figure 11 shows a block diagram illustration of the MSRF design. In this scheme, the synchronization angle is fed as an input for the transformation of concerned signals to reference frame (i.e. and). Thereafter, LPF is used for reducing the voltage harmonics of the corresponding signals. The block diagram of the reference current generation scheme is shown in Fig. 12. The process for generation theta angle is defined by (7)–(8).

$$\cos\theta = \frac{V_\alpha}{\sqrt{\left(V_{s\alpha}^2\right) + \left(V_{s\beta}^2\right)}} \qquad (7)$$

Fig. 11 MSRF based control scheme
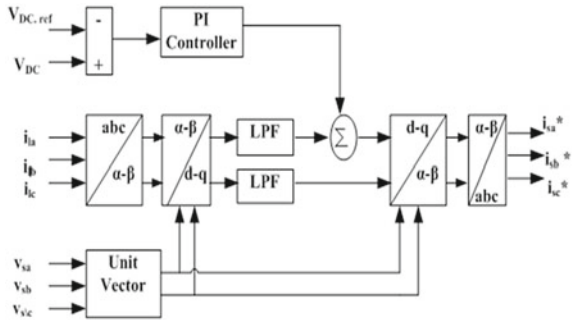
Fig. 12 Unit vector generation technique
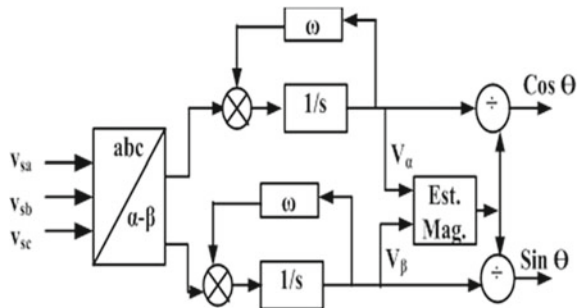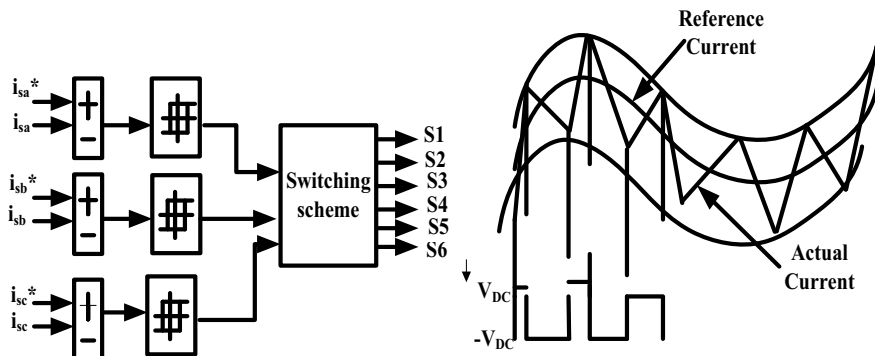
Fig. 13 HCC switching scheme

$$\sin\theta = \frac{V_\beta}{\sqrt{\left(V_{s\alpha}^2\right) + \left(V_{s\beta}^2\right)}} \tag{8}$$

3.2.2 Switching Pulses Generation Scheme

Due to its simplicity, the HCC current control technique is chosen in this paper.

(a) **HCC Scheme**

In the literature, lots of ways have been documented, but an HCC strategy has proven to be more advantageous for SAPF. Figure 13 shows the HCC's detail control mechanism in action.

(b) **AHCC Scheme**

Due to the drawbacks of the fixed-band HCC mentioned above, AHCC has been recommended, it builds the hysteresis bandwidth which is calculated instantaneously according to the instantaneous compensation current variation and voltage, hence the switching speed becomes smooth and the frequency switching will be fixed considerably. According to system topology, shown in Fig. 14, the relation between hysteresis band and f_s is presented by Eq. (9).

$$HB = \frac{0.125 V_{dc}}{f_c L_i}\left[1 - \frac{4L_i^2}{V_{dc}^2}\left(\frac{V_s}{L_i} + \frac{di_{sa}^*}{dt}\right)\right] \tag{9}$$

where, f_s is the modulation frequency.

3.2.3 DC Side Voltage Regulation

The SAPF is connected primarily to inject into the PCC, lowering the harmonic content and necessary reactive power. PI controller-based V_{dc} regulation is implemented in this scheme, which is presented below.

Fig. 14 AHCC switching scheme
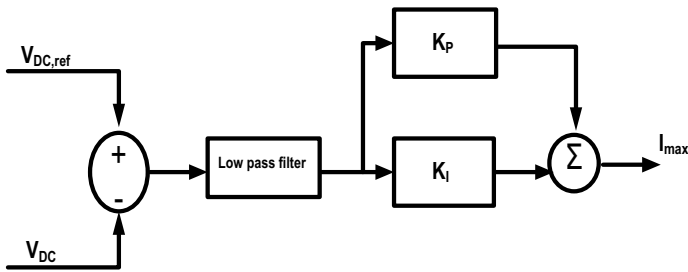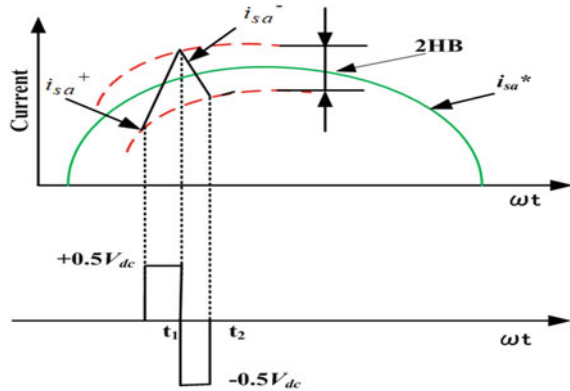
Fig. 15 PI control scheme

PI controller

The classic PI controller is typically used to manage the in the SAPF. Maintaining a steady is essential in order to achieve the SAPF's desired compensating performance. If the active power is reduced to the point where the converter is unable to compensate for its losses, the active power will not remain constant. The measured is compared to the , as shown in Fig. 15. With the use of PI controller parameters and , the PI controller regulates the error that is generated.

4 Result analysis

As shown in Fig. 16, the suggested hybrid DG was integrated with SAPF. The performance of the proposed approach is examined in a variety of scenarios, which are outlined below:
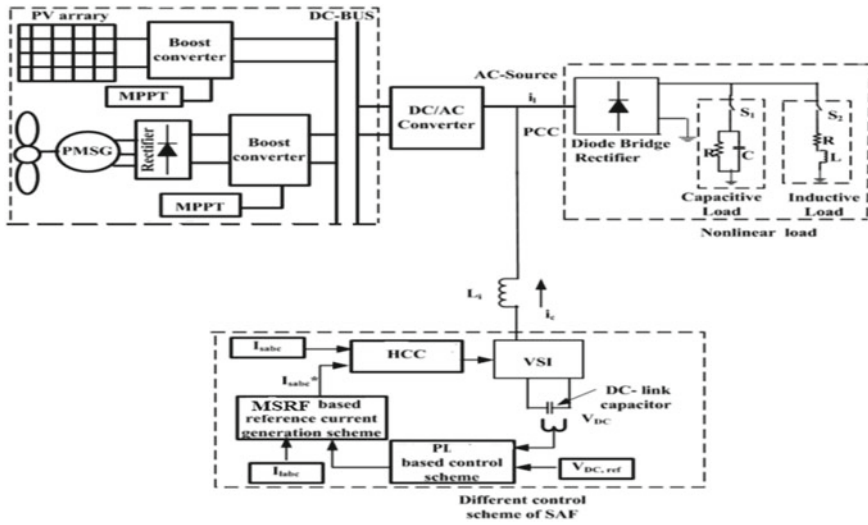
Fig. 16 Proposed system

(a)   Scenario 1: Evaluation of performance under various nonlinear loads without SAPF.
(b)   Scenario 2: Comparative performance analysis of SRF-PI-HCC scheme with proposed MSRF-PI-AHCC scheme.

4.1 Analysis Under Scenario 1

Under scenario-1, the model is simulated with the inductive/capacitive type nonlinear load without connecting the SAPF and the wave shape of the source current and its harmonic spectrum of source current are presented in Fig. 17a and b for the inductive
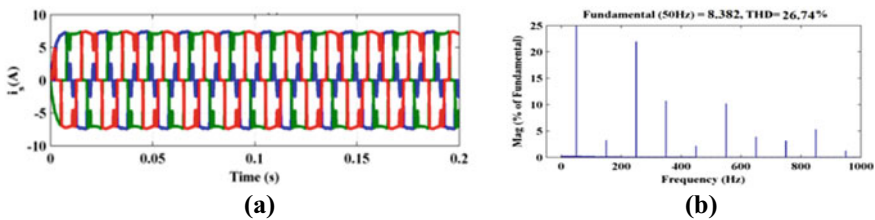
Fig. 17 Inductive load **a** i_s without SAPF, **b** THD of i_s

case and Fig. 18a and b for capacitive case, respectively. It is viewed from Fig. 17a andb that the source current waveform is non-sinusoidal and has a very high THD value of 26.74 percent. Similarly, the source current for a capacitive load is also non-sinusoidal, with a THD of 20.25 percent, as shown in Fig. 18a and b, respectively.

(a)　　　　　　　　　　　　　　　**(b)**
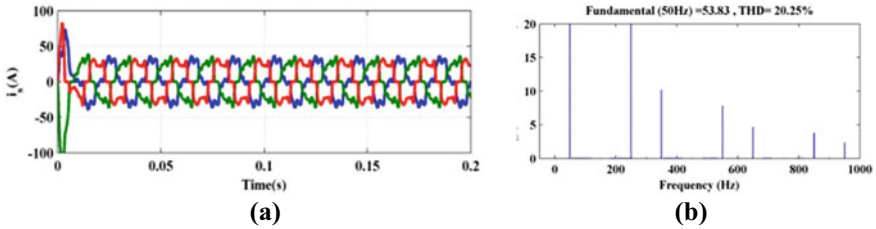
Fig. 18 Capacitive load **a** i_s without SAPF, **b** THD of i_s
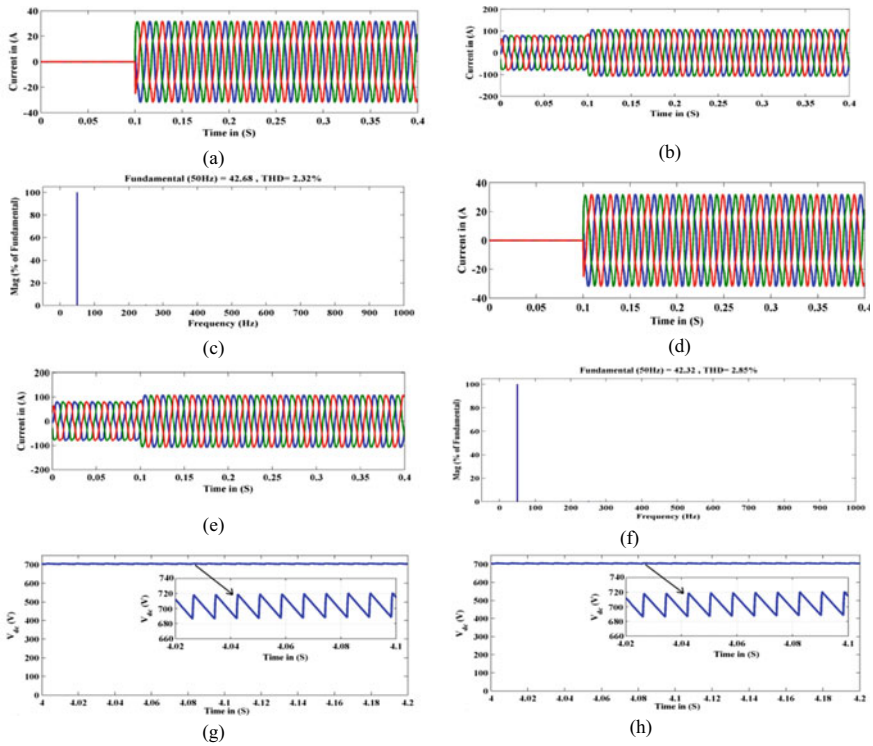
Fig. 19 SAPF With SRF-PI-HCC scheme-based compensation **a** i_c, **b** i_s, **c** Inductive case-THD level, **d** i_c, **e** i_s, **f** Capacitive case-THD level, **g** waveform (for inductive case), **h** waveform (for capacitive case)

4.2 Performance Evaluation Under Scenario 2

Under scenario 2, the SAPF (using SRF-PI-HCC)-based control scheme is turned on to make the source current sinusoidal, and at t = 0.1 s, it injects compensated current at the PCC point as shown in Fig. 19a. As a consequence, the THD level drops to 2.32 percent as shown in Fig. 19c and the source current waveform becomes almost sinusoidal after 0.1 s as shown in Fig. 19b. Similarly, the comparable waveforms for capacitive load are given in Fig. 19d–f. The compensatory current created by the SAPF is illustrated in Fig. 19d, which reduces the THD level to 2.85 percent as seen in Fig. 19f.

It is observed from the waveform, as shown in Fig. 19g and h, that the ripples in the waveform is nearly 22v for both the case. However, it is concluded from the above study that there is a scope for further reduction of THD source current and ripples in the waveform. Hence, the proposed controller is tested in similar way in using the proposed MSRF-PI-AHCC control scheme. The waveform for both the
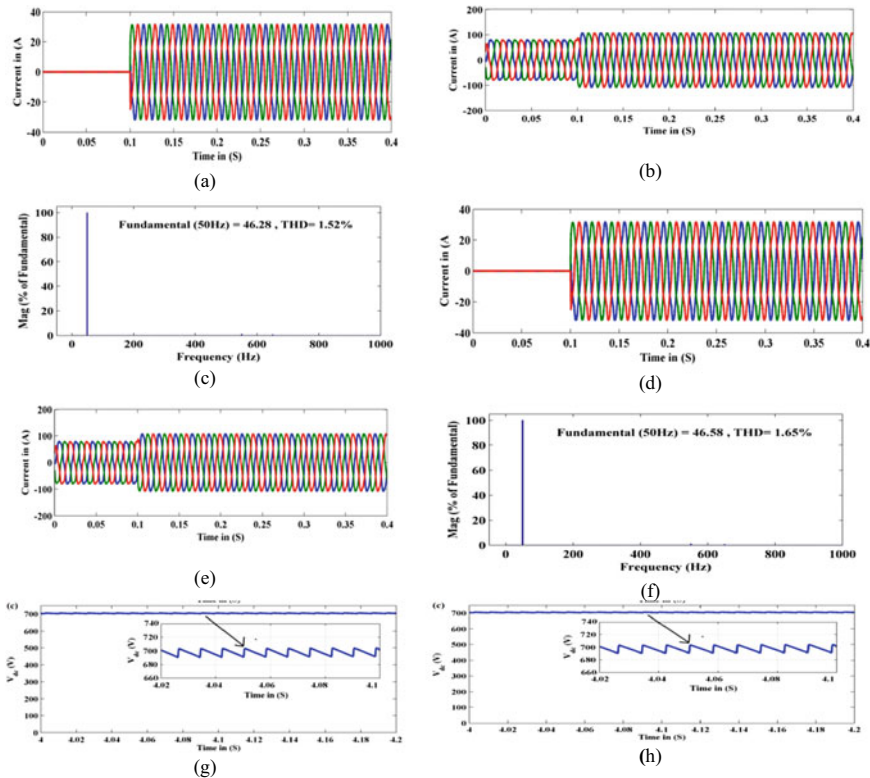
Fig. 20 SAPF With MSRF-PI-AHCC scheme-based compensation **a** i_c, **b** i_s, **c** inductive case-THD level, **d** i_c, **e** i_s, **f** (for capacitive case-THD level **g** waveform (for inductive case), **h** waveform (for capacitive case)

loads are shown in Fig. 20g and h, respectively. It is viewed from the below figures that the THD is reduced to 1.52% and 1.65% for inductive and capacitive load case. Moreover, the ripples in the waveform is reduced to nearly 8 V in both the case. Hence, it is clear from the study that the SAPF shows superior performance with MSRF-PI-AHCC-based control technique.

5 Conclusion

Harmonics issues in a hybrid power system are explored in depth by ingratiating a SAPF under various loading conditions. The suggested SAPF works remarkably well in suppressing harmonics under various loading conditions, as evidenced by the outcomes of a number of simulation-based studies. The SAPF can reduce the source current harmonics by around 1.52% and 1.65% and ripples in the waveform is reduced to nearly 8 V for inductive and capacitive loads, respectively, based on the numerical comparison of findings. Investigations into the employment of the hybrid filter and the design of its control loop may be conducted in order to improve the system's PQ in many ways.

References

1. L. Suganthi, A. Williams, Renewable energy in India-a modelling study for 2020–2021. Energy Policy **28**(15), 1095–1109 (2000)
2. S.R. Sinsel, R.L. Riemke, V.H. Hoffmann, Challenges and solution technologies for the integration of variable renewable energy sources-a review. Renew. Energy **145**, 2271–2285 (2020)
3. J. Jurasz, F.A. Canales, A. Kies, M. Guezgouz, A. Beluco, A review on the complementarity of renewable energy sources: concept, metrics, application and future research directions. Sol. Energy **195**, 703–724 (2020)
4. Y. Zhang, J. Ren, Y. Pu, P. Wang, Solar energy potential assessment: A framework to integrate geographic, technological, and economic indices for a potential analysis. Renew. Energy **149**, 577–586 (2020)
5. P.K. Pathak,, A.K. Yadav, P.A. Alvi, Advanced solar MPPT techniques under uniform and non-uniform irradiance: a comprehensive review. J. Sol. Energy Eng. **142**(4) (2020)
6. O. Kuik, F. Branger, P. Quirion, Competitive advantage in the renewable energy industry: Evidence from a gravity model. Renew. Energy **131**, 472–481 (2019)
7. D. Gielen, F. Boshell, D. Saygin, M.D. Bazilian, N. Wagner, R. Gorini, The role of renewable energy in the global energy transformation. Energ. Strat. Rev. **24**, 38–50 (2019)
8. B. Yang, T. Yu, H. Shu, Y. Han, P. Cao, L. Jiang, Adaptive fractional-order PID control of PMSG-based wind energy conversion system for MPPT using linear observers. Int. Trans. Electr. Energy Syst. **29**(1), e2697 (2019)
9. S. Samal, P.K. Hota, P.K. Barik, Performance improvement of a distributed generation system using unified power quality conditioner. Technol. Econ. Smart Grids Sustain. Energy **5**(1), 1–16 (2020)
10. S. Samal, P.K. Hota, Design and analysis of solar PV-fuel cell and wind energy based microgrid system for power quality improvement. Cogent Eng. **4**(1), 1402453 (2017)

11. B. Singh, K. Al-Haddad, A. Chandra, A review of active filters for power quality improvement. IEEE Trans. Industr. Electron. **46**(5), 960–971 (1999)
12. S. Samal, P.K. Hota, P.K. Barik, Harmonics mitigation by using shunt active power filter under different load condition, in *2016 International Conference on Signal Processing, Communication, Power and Embedded System (SCOPES)* (2016), pp. 94–98
13. A.B. Nassif, W. Xu, W. Freitas, An investigation on the selection of filter topologies for passive filter applications. IEEE Trans. Power Deliv. **24**(3), 1710–1718 (2009)
14. R. Davoodnezhad, D.G. Holmes, B.P. McGrath, A novel three-level hysteresis current regulation strategy for three-phase three-level inverters. IEEE Trans. Power Electron. **29**(11), 6100–6109 (2013)
15. O. Bamisile, Q. Huang, J. Li, M. Dagbasi, A.D. Kemena, M. Abid, W. Hu, Modelling and performance analysis of an innovative CPVT, wind and biogas integrated comprehensive energy system: an energy and exergy approach. Energy Convers. Manag. **209**, 112611 (2020)
16. P.K. Pathak, A.K. Yadav, Design of battery charging circuit through intelligent MPPT using SPV system. Sol. Energy **178**, 79–89 (2019)
17. A.O. Baba, G. Liu, X. Chen, Classification and evaluation review of maximum power point tracking methods. Sustain. Futur. **2**, 100020 (2020)
18. Y. Ouberri, H. Yatimi, E. Aroudam, Design of a robust sliding mode controller for MPPT based on automation PLC for PV applications. Int. Trans. Electr. Energy Syst. **30**(4), e12296 (2020)
19. S. Samal, P.K. Hota, P.K. Barik, Power quality assessment of a solar PV and fuel cell-based distributed generation system using unified power quality conditioner. Int. J. Ambient Energy 1–11 (2020)
20. P.K. Barik, G. Shankar, P.K. Sahoo, Power quality assessment of microgrid using fuzzy controller aided modified SRF based designed SAPF. Int. Trans. Electr. Energy Syst. **30**(4), e12289 (2020)
21. P.K. Barik, G. Shankar, P.K. Sahoo, DC-link capacitor voltage stabilization of a shunt active power filter using fuzzy logic controller under dynamic loading condition, in *Proceedings of Symposium on Power Electronic and Renewable Energy Systems Control* (Springer, Singapore, 2021), pp. 403–414

A Fault Discrimination Scheme for Transmission Systems Using Positive Sequence Complex Power

Md. Shabaaz Hussain Siddique and Biswapriya Chatterjee

Abstract The intent of this work is to develop a fault discrimination scheme between internal and external faults for transmission systems (TS). Positive sequence (PS) voltage and current data have been utilized to compute complex power. A fault threshold (*FT*) has been defined using the complex power of the two ends of a transmission line (TL). A threshold has been established to properly identify the nature of the fault (internal/external). Diversified simulations have been performed in MATLAB/Simulink environment. Outcomes of simulation results confirm that this scheme is robust and can be applied for practical engineering applications.

Keywords Positive sequence complex power · Transmission line · Internal fault detection · External fault detection

1 Introduction

The steady growth of power is inevitable across the globe due to many reasons like the advancement of technologies, rapid urbanization, etc. The existing power system networks need to be expanded to meet the escalated power demand. On the other side, the necessity of a continuous power supply is a very important aspect for power engineers. Fault, which is a natural phenomenon, is mainly responsible for the interruption of the power supply. In the actual scenario, PS networks are highly complex and interconnected. To run the power systems with minimum outage time, one must be very prompt to detect a fault. It's quite a challenging task to identify the zone of fault in a highly interconnected TS.

An integrated TL protection strategy has been suggested in [1], where discrete Fourier transform (DFT) has been used to identify and classify faults. Moreover, PS voltage and fuzzy inference system (FIS) have been used to estimate the location of the fault. A discrete wavelet transform (DWT) and FIS-based fault interception strategy for a wind farm fed TL has been reported in [2]. DWT with the aid of a

Md. S. H. Siddique · B. Chatterjee (✉)
Aliah University, Newtown, Kolkata, WB 700160, India
e-mail: bchatterjee.ee@aliah.ac.in

neural network has been utilized to propose a protection scheme for a multi-terminal TL using voltage and current data [3]. A protection scheme for shunt compensated TS has been proposed in [4] using DWT and a deep neural network. The S-transform and its derivatives have been used successfully in a variety of fault applications. A fast discrete S-transform (FDST)-based fault location scheme has been described for thyristor controlled series capacitor (TCSC) compensated line with a wind farm connected at the one end of it [5]. A TL and an underground cable were considered to be a hybrid line, on which a complete fault protection scheme has been implemented using fast discrete orthonormal S-transform (FDOST) and support vector machine (SVM) [6]. A Hilbert transform-based fault location scheme for distribution network has been proposed in [7] utilizing the energy of voltage waveform. A Hilbert Huang transform-based online fault interception strategy for a shunt compensated TL has been suggested in [8].

A correlation-based fault detection and classification method have been proposed in [9] using current signals only. Cross-correlation (CC) is a feature extraction technique that can be applied in many areas of fault application [10, 11]. In [10], a faulty phase identification scheme for a TL with a wind farm connected at one end of the line has been proposed using CC and FIS. Utilizing one-end voltage data, a single-line fault location strategy for a single-circuit TL has been discussed using CC and neural networks [11]. An analytical approach has been proposed to determine the faulty phase and fault location for TS utilizing differential admittance parameters [12]. A compact approach for fault detection, identification of faulty circuit and location estimation of the fault has been described in [13] for double circuit TL utilizing voltage and current signals. During swing condition, a novel strategy of fault detection and classification has been proposed for a hybrid line using the Lissajous pattern [14].

Besides the above mentioned techniques, sequence component analysis (SCA) is widely implemented on fault applications. A non-iterative fault location strategy for an untransposed TL has been discussed using PS and negative sequence (NS) voltage and current signals [15]. A method for identifying the faulty zone and its location estimation has been reported in [16] for a unified power flow controller (UPFC) compensated double circuit TL using PS and NS voltage and current data. A NS current phasor-based fault detection and location scheme has been reported in [17] for a UPFC compensated TL. A PS admittance-based fault detection and location methodology have been proposed for different transmission networks [18].

In this work, an approach for determining the zone of the fault has been presented using PS voltage and current data. A thorough simulation study has been performed to determine the threshold. The unique idea of this paper is to develop a *FT* from PS complex power. The two end measurement has been adopted in this study. The remaining parts of this manuscript are oriented in the subsequent sections. Section 2 illustrates the algorithm of the proposed work along with the system considered. Sections 3, 4 and 5 report results, discussions and conclusions, respectively. At last of this paper, the references have been enlisted.

2 Proposed Algorithm

A TL has been represented in Fig. 1. The physical length of the line is considered to be 300 km, which is split into two parts. The line joining bus M, N and bus N, P is 200 and 100 km long, respectively. Any fault that occurs between bus M and N, is considered to be an internal fault. On the other side, the external fault is considered to be any fault that occurs between bus N and P. Other system parameters are reported in Table 1 [18]. The voltage rating and frequency of the TL are 400 kV, 50 Hz, respectively. All the measuring has been done from bus M and N. Sampling frequency has been considered to be 4 kHz. In this work, an analytical approach has been proposed, in which the detection of fault can be identified and external faults or no fault conditions can be effectively segregated from internal fault cases.
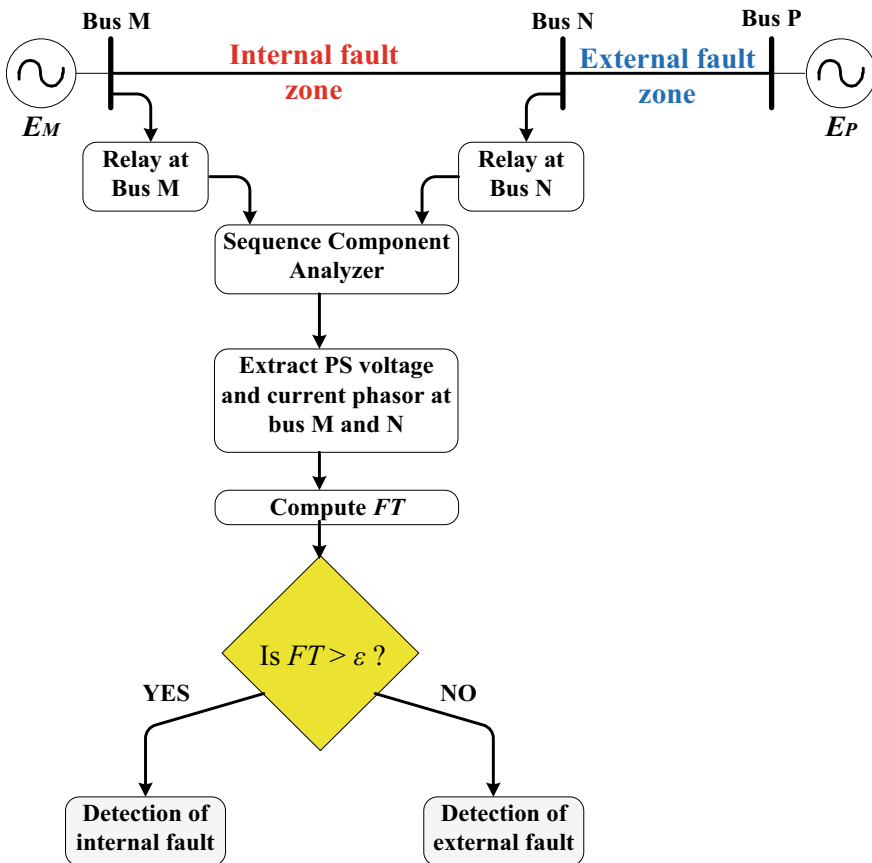
Fig. 1 Single line diagram of power system and relaying algorithm

Table 1 Source and system parameters

Source parameter	Nominal voltage, kV	400
	Frequency, Hz	50
	Three-phase short circuit level, MVA	1000
	X/R ratio	10
Transmission line parameter	Length of section MN, km	200
	Length of section NP, km	100
	PS impedance, Ω/km	$0.02979 + j0.3318$
	Zero sequence impedance, Ω/km	$0.16192 + j0.6113$
	PS capacitance, nF/km	12.74
	Zero sequence capacitance, nF/km	7.75

(a)

(b)
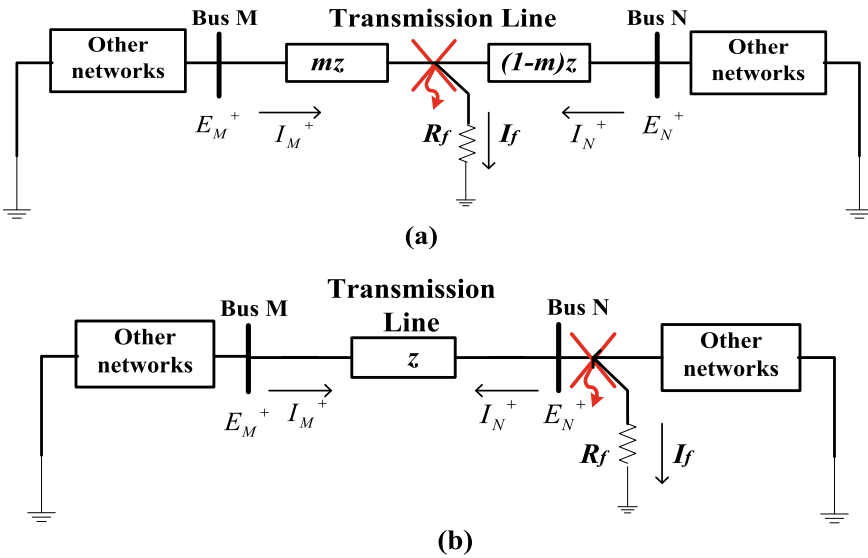
Fig. 2 Equivalent network of the proposed power system during **a** Internal fault condition, **b** external fault condition

2.1   Detection of Internal Fault

Figure 2a depicts the equivalent network of the proposed power system during internal fault conditions [16]. On applying Kirchhoff's voltage law (KVL) between bus M and N, we get

$$
\begin{aligned}
\tilde{E}_{M+} - mz \cdot \tilde{I}_{M+} &= \tilde{E}_{N+} - \overline{(1-m)z} \cdot I_{N+} \\
\tilde{E}_{M+} &= \tilde{E}_{N+} + mz \cdot \tilde{I}_{M+} - \overline{(1-m)z} \cdot I_{N+}
\end{aligned}
\tag{1}
$$

where, E_M^+, I_M^+, E_N^+, I_N^+ are the PS voltages and currents at bus M and N, respectively. Moreover, z is the total series impedance of the TL and m is the length from bus M at which fault occurs.

From Eq. (1), complex power at bus M can be computed as

$$
\tilde{S}_{M+} = \left(\tilde{E}_{M+}\right) \cdot \left(\tilde{I}_{M+}\right)^* = \left(\tilde{E}_{N+} \cdot \tilde{I}_{M+}\right) + \left(mz \cdot \left(|I_{M+}|^2\right)\right) - \left(\overline{(1-m)z} \cdot \tilde{I}_{M+} \cdot \tilde{I}_{N+}\right)
\tag{2}
$$

Similarly, complex power at bus N can be computed as

$$
\tilde{S}_{N+} = \left(\tilde{E}_{N+}\right) \cdot \left(\tilde{I}_{N+}\right)^* = \left(\tilde{E}_{M+} \cdot \tilde{I}_{N+}\right) + \left(\overline{(1-m)z} \cdot \left(|I_{N+}|^2\right)\right) - \left(mz \cdot \tilde{I}_{M+} \cdot \tilde{I}_{N+}\right)
\tag{3}
$$

Now, a new *FT* can be defined as

$$
\text{FT} = \frac{\left|\tilde{S}_{M+} + \tilde{S}_{N+}\right|}{\left|\tilde{S}_{M+} - \tilde{S}_{N+}\right|} = \frac{\left|\tilde{k}_1\right|}{\left|\tilde{k}_2\right|}
\tag{4}
$$

where,

$$
\tilde{k}_1 = \left(\tilde{E}_{M+}\tilde{I}_{N+} + \tilde{E}_{N+}\tilde{I}_{M+}\right) + mz \cdot \left(\left|\tilde{I}_{M+}\right|^2 - \left|\tilde{I}_{N+}\right|^2\right) + z \cdot \tilde{I}_{N+} \cdot \left(\tilde{I}_{N+} - \tilde{I}_{M+}\right)
\tag{5a}
$$

$$
\tilde{k}_2 = \left(\tilde{E}_{N+}\tilde{I}_{M+} - \tilde{E}_{M+}\tilde{I}_{N+}\right) + mz \cdot \left(\tilde{I}_{M+} + \tilde{I}_{N+}\right) + z \cdot \tilde{I}_{N+} \cdot \left(\tilde{I}_{M+} + \tilde{I}_{N+}\right)
\tag{5b}
$$

2.2 Detection of External Fault

Figure 2b depicts the equivalent network of the power system during external fault conditions [16]. On applying KVL between bus M and N, we get

$$\tilde{I}_{M^+} = \frac{\tilde{E}_{M^+} - \tilde{E}_{N^+}}{z} \tag{6}$$

Similarly,

$$\tilde{I}_{N^+} = \frac{\tilde{E}_{N^+} - \tilde{E}_{M^+}}{z} \tag{7}$$

From Eq. (6), complex power at bus M can be computed as

$$\tilde{S}_{M^+} = \left(\tilde{E}_{M^+}\right) \cdot \left(\tilde{I}_{M^+}\right)^* = \left(\tilde{E}_{M^+}\right) \cdot \left(\frac{\tilde{E}_{M^+} - \tilde{E}_{N^+}}{z}\right) = \frac{E_{M^{+2}} - E_M + E_{N^+}}{z} \tag{8}$$

Similarly, complex power at bus N can be computed as

$$\tilde{S}_{N^+} = \frac{E_{N^{+2}} - E_{M^+} E_{N^+}}{z} \tag{9}$$

Thus, *FT* can be computed during external fault situations as

$$\text{FT} = \frac{\left|\tilde{S}_{M^+} + \tilde{S}_{N^+}\right|}{\left|\tilde{S}_{M^+} - \tilde{S}_{N^+}\right|} = \frac{\left|\tilde{E}_{M^+} + \tilde{E}_{N^+}\right|}{\left|\tilde{E}_{M^+} - \tilde{E}_{N^+}\right|} \tag{10}$$

3 Result

In this section, the result of this proposed strategy has been illustrated in two distinct stages. The setting of an appropriate threshold is very important to detect fault accurately. Thus in the first stage, the method of selection of threshold has been described. In the next stage, the detection mechanism of different fault cases (internal/external) has been illustrated. The different fault parameters were selected as: fault resistance (FR), fault inception angle (FIA), different fault locations, and load angle. In case of FR, four different values including high impedance faults were considered. Three different FIAs and different fault locations (in a step of 10 km along the entire length of the TL) were chosen. Moreover, a study for different load angles has also been

Table 2 Different fault parameters

Internal fault	FR, Ω	0.0001, 10, 50, 100
	FIA, °	0, 45, 90
	Fault location from BUS M in MN section, *km*	10, 20, 30, …, 180, 190
	Load angle, °	10, 20, 30, −10, −20
External fault	FR, Ω	0.0001, 10, 50
	FIA	0, 45, 90
	Fault location from BUS N in NP section, *km*	10, 20, 30, …, 80, 90

conducted. Table 2 depicts the different values that were chosen for different fault parameters.

3.1 Selection of Threshold

The criterion to detect internal fault has been set as $FT > \varepsilon$, where ε is the threshold. On the other hand, if $FT < \varepsilon$, it will be considered an external fault. From Eqs. (4) and (10), it is observed that all the *FT* values for internal fault cases stay above the threshold line. Likewise, all *FT* values stay below the threshold for external fault cases. Most importantly, the data set for internal fault cases never overlap with that of external ones.

The above mentioned facts have been illustrated in Fig. 3. Figure 3a–d depicts the trajectory of *FT* values along the section MN with FIA = 0° for AG, BC, BCG, and symmetrical (ABCG) fault, respectively. Further, the same approach has been adopted for external fault cases, and trajectory of *FT* values with $FR = 0.0001\ \Omega$ and $FIA = 0°$ are reported in Fig. 4 for all fault kinds. From Figs. 3 and 4, it is revealed that the overlap between internal and external fault cases does not occur. By thorough analysis of the entire data set, the threshold (ε) has been chosen as 1.0.

3.2 Internal and External Fault Detection

In this study, the fault detection scheme has been evaluated by varying the fault parameters, viz. FR, FIA, load angle and fault location. The dependency of fault location on the detection of various faults has already been discussed in the preceding section. The dependency of the proposed algorithm on other parameters has been discussed in the following subsections.

Effect of FR

To assess the robustness of the method, the performance of the scheme has been tested. Four different values of FR have been considered for internal fault cases
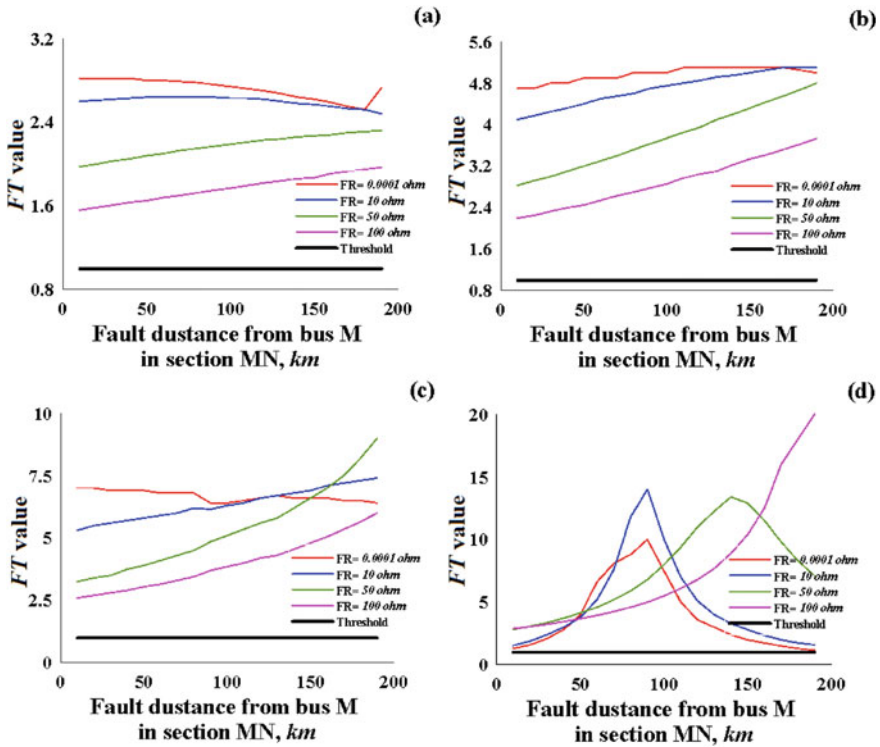
Fig. 3 Variation of *FT* for **a** AG, **b** BC, **c** BCG, **d** Symmetrical fault with FIA = 0°

Fig. 4 Variation of *FT* for
external fault with FR =
0.0001 Ω, FIA = 0
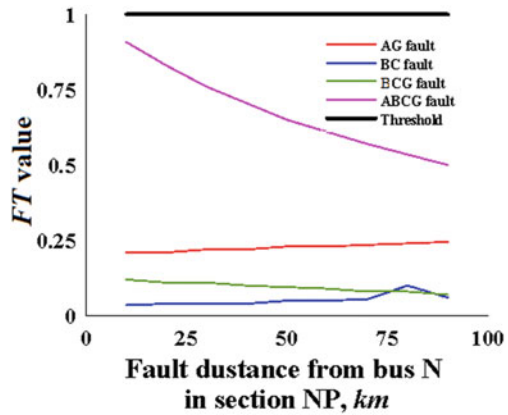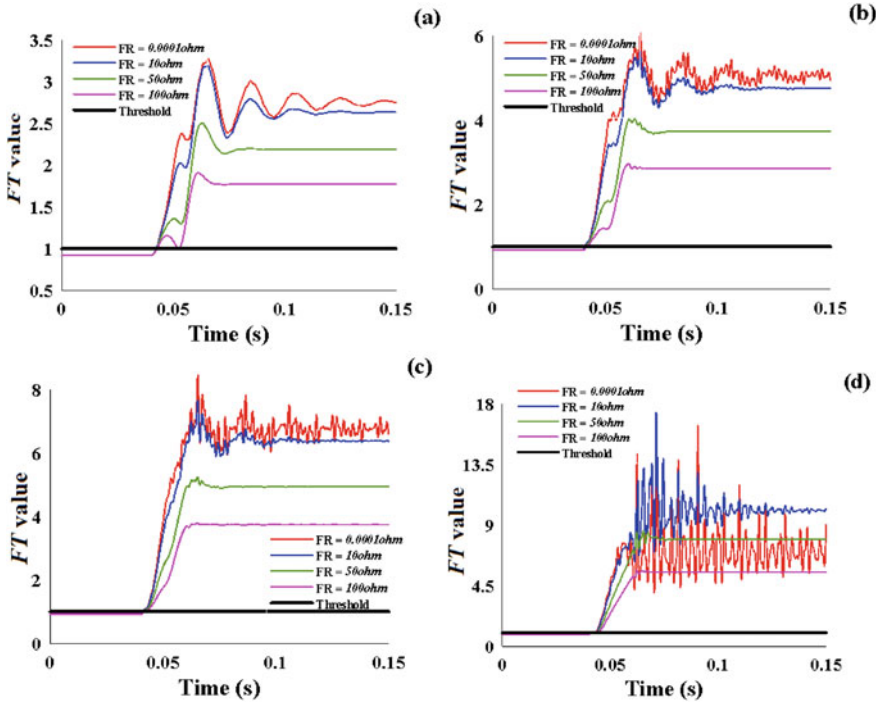
Fig. 5 Internal fault detection with varying FR, FIA $= 0°$ for **a** AG, **b** BC, **c** BCG, **d** Symmetrical faults

(reported in Table 2). The different faults, viz. AG, BC, BCG, symmetrical faults were simulated at $t = 0.04$ s with FIA $= 0°$ at the midpoint of the line section MN. The trajectories of FT for AG, BC, BCG, symmetrical faults have been reported in Fig. 5a–d, respectively. It is seen that the *FT* curve goes over the threshold line since the moment of fault inception. In addition to this, different faults (AG, BC, BCG, ABCG) have been created in the external fault zone (at 10 km from bus N in the line section NP). The trajectory of *FT* for external faults has been plotted in Fig. 6a with $FR = 0.0001\ \Omega$. In every fault case, it is seen that the *FT* curve stays below the threshold line.

Effect of FIA

The influence of FIA on the accuracy of the scheme has also been performed in this study. The AG fault was simulated at the midpoint of the line section of MN with different values of FIAs (reported in Table 2). The trajectory of *FT* curve has been plotted in Fig. 6b which shows the accurateness of the algorithm.

Effect of Load Angle

Since this algorithm mainly relies on power, hence load angle plays a key role, and to assess the performance of this scheme on the variation of load angle, the different
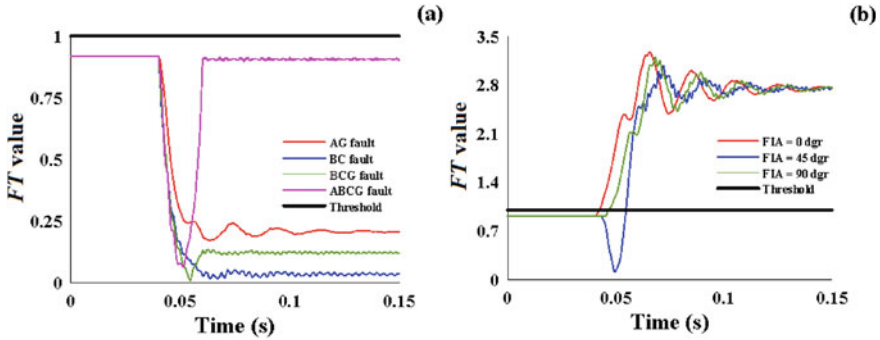
Fig. 6 **a** Detection of external fault with FR = 0.0001 Ω, **b** effect of FIA

Table 3 Different threshold values for different loading conditions

Load angle (°)	Threshold
10	1.0
20	0.5
30	0.35
−10	1.1
−20	0.6

load angles are considered. It is seen that the algorithm is much more sensitive to the variation of load angle. To attain acceptable accuracy, an adaptive selection of threshold was chosen. Table 3 shows several threshold values for various loading scenarios.

4 Discussion

In this work, an approach has been illustrated of segregating the internal faults from no fault or external fault cases. A new *FT* has been defined that can effectively serve the objective of this work. As per Eq. (4), the *FT* is a function of voltage and current for internal faults, where current quantities seem to be quite large. Thus, it is quite evident that, *FT* values for internal fault cases would yield a large number. On the other hand, as per Eq. (10), the *FT* is found to be a function of voltage only. Most importantly, the numerator of the Eq. (10) would yield a very small quantity that is close to zero, as voltages measured at two buses during no fault or external fault situations are almost the same. Thus, *FT* values during no fault or external fault situation are significantly lesser as compared to those values for internal fault cases. As a consequence of this, a threshold line can be determined that can decide the type of fault (internal/external).

In this simulation study, different fault parameters were chosen. This approach is found to be very sensitive to the load angle variation. Moreover, the effect of FR, FIA and location on the accuracy of this algorithm is negligible. This approach can sense the fault even with very high impedance value. Moreover, this method works absolutely fine for different fault occurring instances. In addition to this, the variety of fault locations does not impact much on the performance of this scheme. This algorithm stands to be simple, robust and free from heavy computation.

5   Conclusion

In this work, a fault discrimination mechanism has been illustrated between the faults in the sections MN (internal) and NP (external) of the TL. This scheme utilizes the PS voltage and current data from the two ends of the TL. A new *FT* has been defined using PS complex power from local and remote terminals. The new *FT* has been effectively utilized to detect internal and external faults. The diversified simulations have been performed by varying several fault parameters. The result confirms the merit of the scheme, as this algorithm successfully detects all fault cases with 100% accuracy. This scheme can further be implemented on more realistic TS, viz. series compensated line, double circuit line and interconnected power networks.

References

1. B. Chatterjee, S. Debnath, Fuzzy based relaying scheme for transmission line based on unsynchronized voltage measurement. IETE J Res (2020). https://doi.org/10.1080/03772063.2020.1754934
2. M. Paul, S. Debnath, Fault detection and classification scheme for transmission lines connecting wind farm using single end impedance. IETE J Res (2021). https://doi.org/10.1080/03772063.2021.1886601
3. B. Rathore, A.G. Shaik, Wavelet-alienation based protection scheme for multi-terminal transmission line. Electr Power Syst Res **161**, 8–16 (2018)
4. M. Mirzaei, B. Vahidi, S.H. Hosseinian, Accurate fault location and faulted section determination based on deep learning for a parallel-compensated three-terminal transmission line. IET Gener Transm Distrib. **13**(13), 2770–2778 (2019)
5. B. Sahoo, S.R. Samantaray, An enhanced fault detection and location estimation method for TCSC compensated line connecting wind farm. Int J Electr Power Energy Syst **96**, 432–441 (2018)
6. B. Patel, A new FDOST entropy based intelligent digital relaying for detection, classification and localization of faults on the hybrid transmission line. Electr Power Syst Res **157**, 39–47 (2018)
7. T.F. Moraes, L. Lovisolo, L.F.C. Monteiro, Fault location in distribution systems from analysis of the energy of sequence component waveforms. IET Gener Transm Distrib **12**(9), 1951–1960 (2018)
8. S. Biswal, M. Biswal, O.P. Malik, Hilbert Huang transform based online differential relay algorithm for a shunt-compensated transmission line. IEEE Trans Power Deliv **33**(6), 2803–2811 (2018)

9. A. Mukherjee, K. Chatterjee, P.K. Kundu, A. Das, Application of Poincare analogous time-split signal-based statistical correlation for transmission line fault classification. Electr Eng (2021). https://doi.org/10.1007/s00202-021-01369-4
10. B. Chatterjee, S. Debnath, Cross-correlation aided fuzzy based relaying scheme for fault classification in transmission lines. Eng Sci Technol Int J. **23**, 534–543 (2020)
11. B. Chatterjee, S. Debnath, Cross-correlation based single-phase fault location scheme for transmission lines using one-end voltage. IET Conf Proc MFIIS **2020**, 149–154 (2021)
12. S. Gangolu, P. Raja, M.P. Selvan, V.K. Murali, Effective algorithm for fault discrimination and estimation of fault location in transmission lines. IET Gener Transm Distrib **13**(13), 2789–2798 (2019)
13. V.K. Gaur, B. Bhalja, New fault detection and localization technique for double-circuit three-terminal transmission line. IET Gener Transm Distrib **12**(8), 1687–1696 (2018)
14. B. Patel, A new technique for detection and classification of faults during power swing. Electr Power Syst Res **175**, 105920 (2019)
15. A.S. Dobakhshari, Noniterative parameter-free fault location on untransposed single-circuit transmission lines. IEEE Trans Power Deliv **32**(3), 1636–1644 (2017)
16. B. Chatterjee, S. Debnath, Sequence component based approach for fault discrimination and fault location estimation in UPFC compensated transmission line. Electr Power Syst Res **180**, 106155 (2020)
17. M. Kundu, S. Debnath, Fault location in UPFC compensated double circuit transmission line using negative sequence current phasors. Electr Power Syst Res **184**, 106347 (2020)
18. B. Chatterjee, S. Debnath, A new protection scheme for transmission lines utilizing positive sequence fault components. Electr Power Syst Res **190**, 106847 (2021)

Impedance Matching of Photovoltaic System Using DC-DC Converter

Madhusmita Mohanty, Satya Prakash, and Subhransu Padhee

Abstract Selection of proper converter topology for photovoltaic-based application is one of the major design challenges faced by power electronics design professional. Impedance matching is one of the necessary and sufficient conditions which transfer power from photovoltaic source to load. Impedance matching achieved by the right DC-DC converter topology improves the utilization efficiency of the photovoltaic system. This paper studies the principle of impedance matching in photovoltaic system using different classical DC-DC converter topologies and finds the right converter topology which transfers maximum power from photovoltaic source to load.

Keywords Photovoltaic system · DC-DC converter · Impedance matching

1 Introduction

Interconnection of rooftop PV modules with a DC bus network is carried out using different approaches. In the first approach, a string of PV modules are connected with a centralized power electronic converter. In the second approach, each of the PV modules is connected to an individual power electronic converter. The second approach has several advantages such as (a) higher flexibility, (b) lower sensitivity to shading, (c) better protection of PV panels, (d) redundancy, and (e) easier maintenance [1]. The maximum power which can be extracted from a PV module is dependent on solar irradiance, temperature, and operating point of energy

M. Mohanty (✉)
Odisha Power Transmission Corporation Limited, Bhubaneswar, Odisha, India
e-mail: welcome2twinkle@gmail.com

S. Prakash
Department of Electrical Engineering, Parala Maharaja Engineering College,
Brahmapur, Odisha, India

S. Padhee
Department of Electrical and Electronics Engineering, Sambalpur University Institute
of Information Technology, Burla, Odisha, India

conversion system. PV system has nonlinear (*V-I*) and (*P-V*) characteristics. Power of PV system is maximum at a knee point of (*P-V*) characteristics. The point at which PV power is maximum is called maximum power point (MPP). When a PV panel is connected to a load resistance R_L, the operating point on the *V-I* curve of PV panel changes with change in load resistance which is a deviation from the MPP. Maximum power transfer from PV module to load occur when impedance of PV panel and load are equal. This phenomenon is known as impedance matching. Due to impedance matching, conversion as well as utilization efficiency of the system increases [2, 3]. Any changes in solar power due to change in environmental condition also change the solar voltage and internal impedance of solar cell. As the MPP keeps on changing with change in solar irradiance, MPPT algorithm are used to track the MPP of the system [4–8].

DC-DC converter is the intermediate element between PV panel and load. Varying duty cycle (by PWM method) of DC-DC converter, the input impedance of converter can be controlled. Selection of right converter topology, sizing of the converter parameters are utmost important aspects in design of photovoltaic system. The proper selection and sizing of converter not only improves the conversion efficiency of the system, but also improves the utilization efficiency of the system. Different design and integration aspects of PV-fed non-isolated DC-DC converter can be found in [9–12].

This paper provides study of impedance matching of photovoltaic system using different DC-DC converters (buck, boost, and inverting buck-boost). The condition of maximum power transfer from PV panel to load has been derived. Along with that the role of the above-mentioned DC-DC converters in impedance matching have been evaluated.

Section 2 provides preliminary idea about photovoltaic cell, Sect. 3 provides details of impedance matching of PV panel with different DC-DC converter topologies, and Sect. 4 concludes the paper.

2   Preliminary of Photovoltaic System

A comprehensive approach to model PV cell (Fig. 1a) has been outlined in [13, 14]. From Fig. 1a,

$$I_{pv} = I_{ph} - I_o \left[\exp \left(\frac{qV + qR_s I_{pv}}{N_s nKT} \right) - 1 \right] - \frac{V + R_s I_{pv}}{R_{sh}} \qquad (1)$$

where Boltzmann's constant is denoted as K, Temperature is denoted as T (Kelvin), Charge of electron is q, photocurrent is represented as I_{ph}, Saturation current is represented as I_o, Diode ideality factor is n, N_s represents number of series connected PV cells, R_{sh}, R_s are shunt and series resistance of PV cell, respectively.
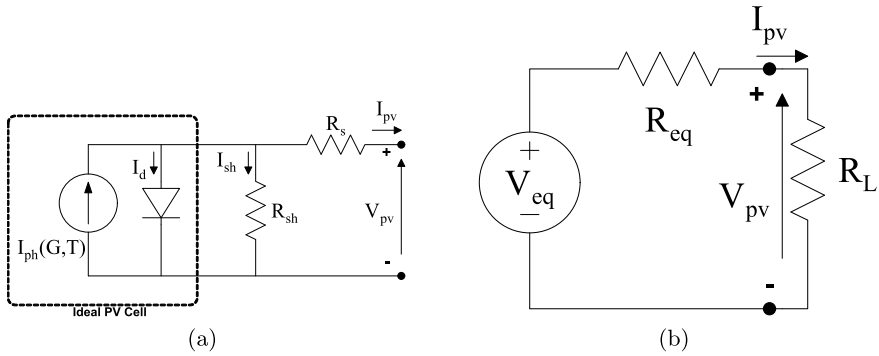
Fig. 1 **a** Equivalent circuit diagram of single diode model of PV cell. **b** Thevenin equivalent circuit of PV cell

Figure 1b presents Thevenin's equivalent circuit of PV cell where V_{eq} is Thevenin's equivalent voltage of PV cell, R_{eq} is Thevenin's equivalent resistance of PV cell and R_L is the load resistance.

The power delivered to load can be calculated as

$$P_L = I_{pv}^2 R_L = \left(\frac{V_{eq}}{R_{eq} + R_L} \right)^2 R_L \tag{2}$$

Making the differentiation of 2 to zero, $\frac{dP_L}{dR_L} = 0$

$$\frac{dP_L}{dR_L} = \frac{\left(R_{eq} + R_L\right)^2 V_{eq}^2 - 2V_{eq}^2 R_L \left(R_{eq} + R_L\right)}{\left(R_{eq} + R_L\right)^4} = 0 \tag{3}$$

which yields $R_L = R_{eq}$.

For simulation purpose, a PV module (Specification summarized in Table 1) is considered. The *P–V* and *V–I* characteristics of the considered PV module is represented in Fig. 2a, b, respectively.

Table 1 Specification of PV module used for simulation

Parameters	Values
(P_{STC})	228.735 W
(V_{oc})	37.1 V
(I_{sc})	8.18 A
(V_{mpp})	29.9 V
(I_{mpp})	7.65 A
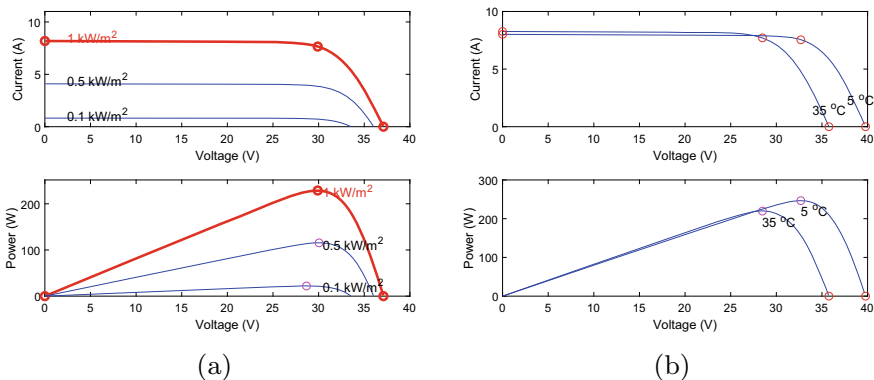
Fig. 2 **a** PV module characteristics with variable solar irradiance. **b** Characteristics of PV module with variable temperature

3 Impedance Matching of PV Panel

3.1 Impedance Matching Without Converter

PV panel with specification summarized in Table 1 transfers maximum power to a resistive load when $R_L = 4.53\ \Omega$. At $R_L = 4.53\ \Omega$, impedance matching is achieved, i.e., $V_{in} = V_o = 32V$ and $I_{in} = I_o = 7$ A as shown in Fig. 3.
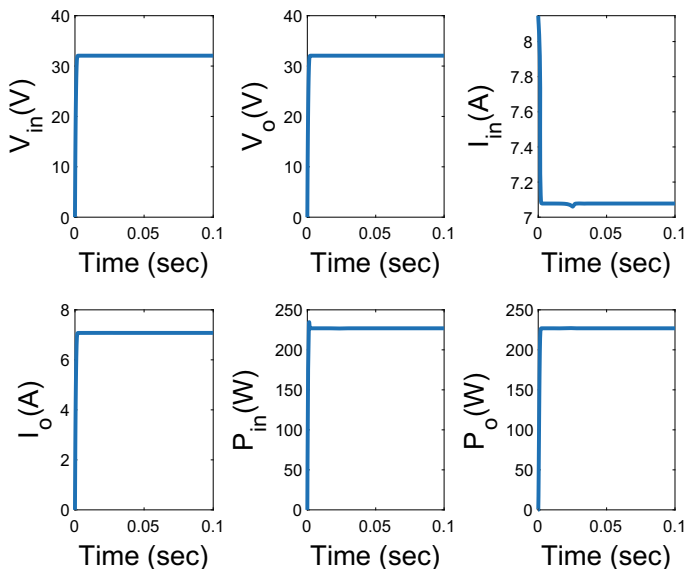
Fig. 3 Voltage, current, and power graph for PV panel connected with resistive load

3.2 Impedance Matching with Converter

Table 2 provides the comparative analysis of characteristics of basic DC-DC converter for integration to PV source. Different parameters such as output voltage and input resistance in both CCM as well as DCM condition of PV-fed DC-DC converter have been evaluated.

Where V_r is the ripple voltage of DC-DC converter.

Considering the PV panel specification discussed in Table 1, sizing of DC-DC converter components has been carried out. The related mathematical expression for sizing of components of DC-DC converter is summarized in Table 2. Table 3 provides the simulation parameters of different DC-DC converters. It is assumed that the PV panel is working in Standard Test Condition (STC), i.e., solar irradiation of 1 kW/m^2 and cell temperature of 25 °C. For design of DC-DC converter, the parasitic elements of passive components are neglected and ideal switch is considered. The converter is assumed to be working in continuous conduction mode. For design purpose, inductor current ripple and output voltage ripple has been assumed to be 10% and 5%, respectively.

Impedance Matching with Buck Converter Figure 4a represents circuit diagram of PV-fed buck converter. Figure 4b illustrates the simulation results for voltage, current, and power of PV-fed buck converter. As buck converter is a step-down converter, the input power and output power is around 100 W. Figure 4c shows the relation between duty cycle and power delivered by the buck converter.

Impedance Matching with Boost Converter Circuit diagram for PV-fed boost converter has been presented in Fig. 5a. Figure 5b illustrates the simulation results

Table 2 Comparison of characteristics of basic DC-DC converter for integration to PV source

Parameters	Buck	Boost	Buck-boost
V_o (CCM)	$V_{\text{pv}}d$	$V_{\text{pv}}\left(\frac{1}{1-d}\right)$	$V_{\text{pv}}\left(\frac{d}{1-d}\right)$
V_o (DCM)	$\frac{2V_{\text{pv}}}{1+\sqrt{1+\frac{8L}{Rd^2T_s}}}$	$\frac{V_{\text{pv}}}{2}\left(1+\sqrt{1+\frac{2Rd^2T_s}{L}}\right)$	$D\,|V_{\text{pv}}|\,\sqrt{\frac{RT_s}{2L}}$
I_o	$\frac{I_{\text{pv(avg)}}}{d}$	$I_{\text{pv}}(1-d)$	$I_{\text{pv(avg)}}\left(\frac{1-d}{d}\right)$
R_o	$R_{\text{pv}}d^2$	$R(1-d)^2$	$\frac{R(1-d)^2}{d^2}$
R_{in} (CCM)	$\frac{R}{d^2}$	$R(1-d)^2$	$\frac{R(1-d)^2}{d^2}$
R_{in} (DCM)	$\frac{R}{4}\left(1+\sqrt{1+\frac{8L}{Rd^2T_s}}\right)^2$	$\frac{4R}{\left(1+\sqrt{1+\frac{2Rd^2T_s}{L}}\right)^2}$	$\frac{2L}{d^2T_s}$
R_{in} (Range)	R to ∞	0 to R	0 to ∞
I_{in}	Discontinuous	Continuous	Discontinuous
L	$L_{\min}=\frac{(1-d)R}{2f_{sw}}$	$L_{\min}=\frac{(1-d)^2dR}{2f_{sw}}$	$L_{\min}=\frac{(1-d)^2R}{2f_{sw}}$
C	$C_{\min}=\frac{(1-d)V_o}{8V_rLf_{sw}^2}$	$C_{\min}=\frac{dV_o}{V_rRf_{sw}}$	$C_{\min}=\frac{dV_o}{V_rRf_{sw}}$

Table 3 Simulation parameters of DC-DC converter

Parameters	Buck converter	Boost converter	Buck-boost converter
L	1 mH	$228\,\mu$H	$150\,\mu$H
C (μF)	220	156.10	150
R (Ω)	10	9.97	10.92
d	0.9	0.39	0.6
C_{in} (μF)	250	250	250
f_{sw} (kHz)	25	25	25

(a)

(b)

(c)

Fig. 4 Impedance matching of PV panel with buck converter. **a** Circuit diagram. **b** Voltage, current, and power. **c** Change of duty cycle to power for PV-fed buck converter

for current, voltage, and power for PV-fed boost converter. From simulation results it is observed that at $d = 0.39$, $P_{in} = 231.5$ W and $P_o = 226.2$ W. This proves that maximum power has been transferred from PV panel to load via boost converter. This also validates the impedance matching of PV panel and boost converter. Figure 5c shows the relation between change in duty cycle to power for PV-fed DC-DC boost converter which clearly shows that the maximum power transfer from PV panel to load via boost converter at a moderate duty ratio of $d = 0.39$.
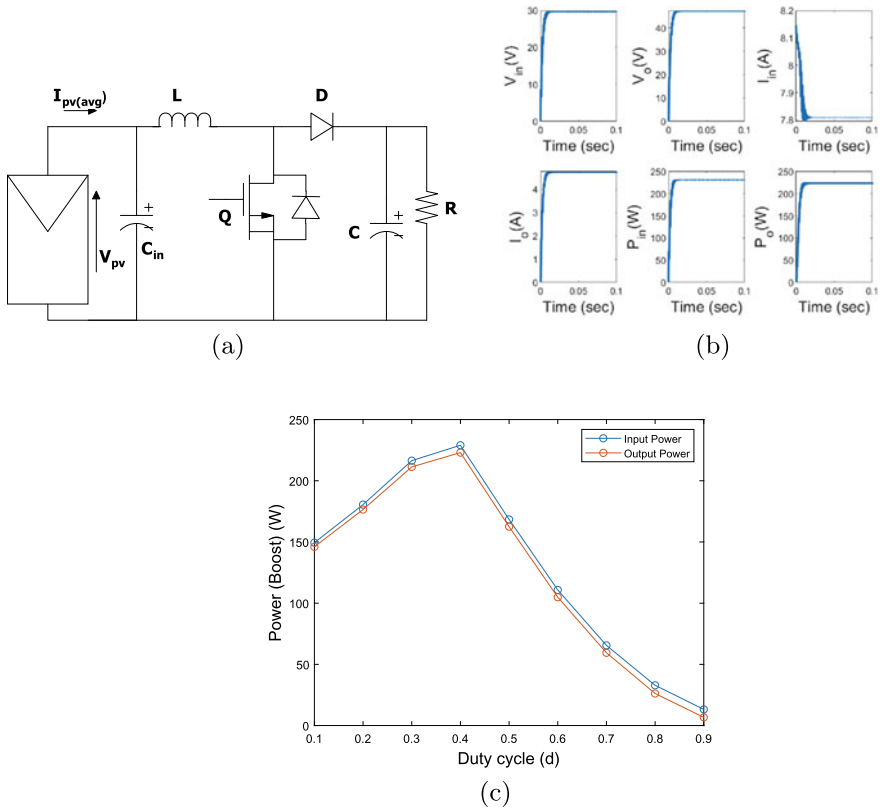
Fig. 5 Impedance matching of PV panel with boost converter. **a** Circuit diagram. **b** Voltage, current, and power. **c** Change of duty cycle to power for PV-fed boost converter

Boost converter has lower component counts and the practical conversion efficiency of boost converter is limited to 5. For conversion efficiency of more than 5, reverse recovery problem of diode is encountered.

Impedance Matching with Buck-Boost Converter An inverting type buck-boost converter is connected to PV panel as shown in Fig. 6a. PV-panel connected inverting buck-boost converter provides $P_{in} = 216.9\,\text{W}$ and $P_o = 203.6\,\text{W}$ at $d = 0.6$ as illustrated in Fig. 6b. The relation between change in duty cycle to power for PV-fed inverting buck-boost converter is shown in Fig. 6c. At $d=0.6$, maximum power transfer is transferred from PV panel to load via inverting buck-boost converter.
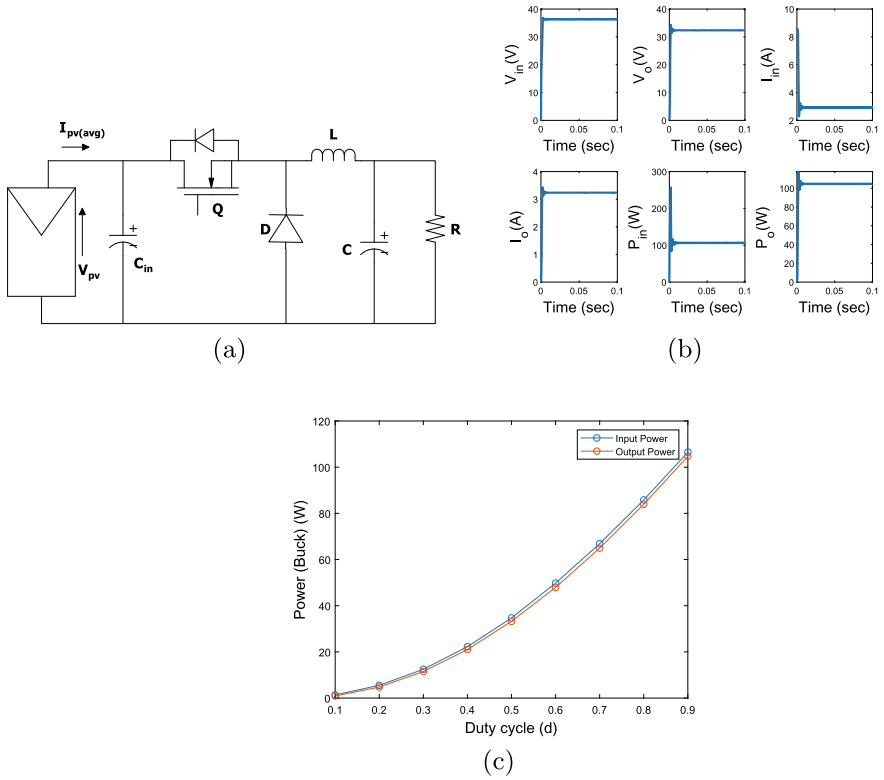

(a)   (b)

(c)
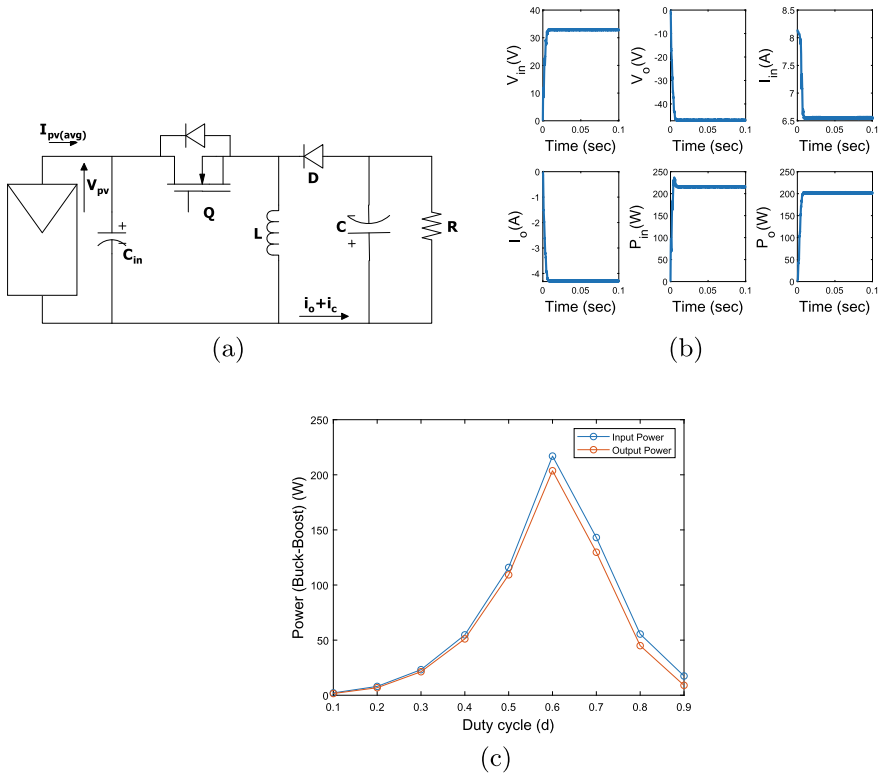
Fig. 6 Impedance matching of PV panel with buck-boost converter. **a** Circuit diagram. **b** Voltage, current, and power. **c** Change of duty cycle to power for PV-fed buck-boost converter

4 Conclusion

This paper provides an analysis of impedance matching of PV module with and without switching power converter. The necessary and sufficient condition for maximum power transfer has been derived with resistive load and with different classical DC-DC converter topologies (buck converter, boost converter, and inverting buck-boost converter). From the above theoretical and simulation analysis, it can be concluded that boost converter is the most suited converter for PV panel energy harvesting as it can achieve the maximum power transfer in moderate duty cycle of 0.39 and provides a power transfer efficiency of 97%. Buck converter and inverting buck-boost converter fed PV panel are used in specific applications.

References

1. G.R. Walker, P.C. Sernia, Cascaded DC-DC converter connection of photovoltaic modules. IEEE Trans. Power Electron. **19**(4), 1130–1139 (2004)
2. T.-P. Teng, H.-M. Nieh, J.-J. Chen, L. Yu-Cheng, Research and development of maximum power transfer tracking system for solar cell unit by matching impedance. Renew. Energy **35**(4), 845–851 (2010)
3. W. Li, T. Chen, X. Wilsun, On impedance matching and maximum power transfer. Electr. Power Syst. Res. **80**(9), 1082–1088 (2010)
4. D.P. Hohm, M. E. Ropp, Comparative study of maximum power point tracking algorithms. Progr. Photovolt.: Res. Appl. **11**(1), 47–62 (2003)
5. B. Bendib, H. Belmili, F. Krim, A survey of the most used MPPT methods: conventional and advanced algorithms applied for photovoltaic systems. Renew. Sustain. Energy Rev. **45**, 637–648 (2015)
6. H. Rezk, A.M. Eltamaly, A comprehensive comparison of different MPPT techniques for photovoltaic systems. Solar Energy **112**, 1–11 (2015)
7. T. Esram, P.L. Chapman, Comparison of photovoltaic array maximum power point tracking techniques. IEEE Trans. Energy Conversion **22**(2), 439–449 (2007)
8. R. Ahmad, A.F. Murtaza, H.A. Sher, Power tracking techniques for efficient operation of photovoltaic array in solar applications—A review. Renew. Sustain. Energy Rev. **101**, 82–102 (2019)
9. D. Verma, S. Nema, A.M. Shandilya, A different approach to design non-isolated DC–DC converters for maximum power point tracking in solar photovoltaic systems. J. Circ. Syst. Comput. **25**(08), 1630004 (2016)
10. B.S. Revathi, M. Prabhakar, Non isolated high gain DC–DC converter topologies for PV applications—A comprehensive review. Renew. Sustain. Energy Rev. **66**, 920–933 (2016)
11. E. Durán, J.M. Andújar, J.M. Enrique, J.M. Pérez-Oria, Determination of PV generator IV/PV characteristic curves using a DC–DC converter controlled by a virtual instrument. Int. J. Photoenergy **2012** (2012)
12. M.H. Taghvaee, M.A.M. Radzi, S.M. Moosavain, H. Hizam, M. H. Marhaban, A current and future study on non-isolated DC–DC converters for photovoltaic applications. Renew. Sustain. Energy Rev. **17**, 216–227 (2013)
13. M.G. Villalva, J.R. Gazoli, E.R. Filho, Comprehensive approach to modeling and simulation of photovoltaic arrays. IEEE Trans. Power Electron. **24**(5), 1198–1208 (2009)
14. M. Wolf, G.T. Noel, R.J. Stirn, Investigation of the double exponential in the current–voltage characteristics of silicon solar cells. IEEE Trans. Electron Dev. **24**(4), 419–428 (1977)

PQ Analysis of T-VSI and ICT-VSI with Their Impacts on 3-P 3-W Utility System

Mrutyunjaya Mangaraj, Rohan Vijay Thakur, Sanjoy Kumar Mishra, Jogeswara Sabat, and Anil Kumar Patra

Abstract This paper establishes inductor coupled T-type voltage source inverter (ICT-VSI) supported distribution static compensator (DSTATCOM) for enhancement of power quality (PQ). The ICT-VSI utilized a inductor network in between the two section of T-type voltage source inverter (T-VSI); for three-phase three-wire (3-P 3-W) electrical utility system, it is established as a power conditioner. The new topology produces a balanced voltage at point of common coupling (PCC) with good quality and low total harmonic distortion (THD) source currents, which improves the power quality (PQ) in 3-P 3-W traditional electrical utility system. The comparative evaluations of T-VSI with ICT-VSI are presented in the literature and the strength and effectiveness of the ICT-VSI is verified by simulations using MATLAB/Simulink environment. Finally, justified the advantages of the ICT-VSI on the base of PQ issues considering the standard value of IEEE-2030-7-2017 & IEC-61000-1 grid code.

Keywords ICT-VSI · DSTATCOM · PQ · T-VSI · 3-P 3-W · PCC · THD · PF · CSI · Icos control algorithm · EUS

M. Mangaraj · J. Sabat
Department of Electrical & Electronics Engineering, Lendi Institute of Engineering and Technology, Vizianagaram 535005, India

R. V. Thakur (✉) · S. K. Mishra
Department of Electrical Engineering, G H Raisoni University Amaravati, Maharashtra 444701, India
e-mail: rvt.prmceam@gmail.com

S. K. Mishra
e-mail: sanjoy.mishra@ghru.edu.in

A. K. Patra
Department of Electrical & Electronics Engineering, Kalam Institute of Technology, Berhampur 761003, Odisha, India

1   Introduction

Nowadays, the traditional electrical utility systems are suffering from several issues like, unavailability of expansion facility, increase in load demand, aging infrastructure, poor PQ due to load disturbance, and environmental issues. Among all these issues, the PQ issue is an emerging issue because numerous undesired effects such as poor voltage regulation, unbalanced voltage at PCC, and low power factor (PF) are produced by harmonic content of the load currents which results in increased electrical utility system losses and increased source current distortions. Therefore, this movement would mandate to design an improved inverters for reliable operation of utility system [1–3]. In specific, voltage source inverter (VSI) is referred to as a voltage buck inverter and current source inverter (CSI) is referred to as current buck inverter. Conversion using VSI and CSI, in different applications such as utility system, hybrid electric vehicles and photovoltaic systems, suffer from some severe drawbacks [4–6].

Consecutively to overcome the conventional inverter's demerits, T-VSI is proposed [7, 8]. T-type inverter has several advantages over two-level VSI like fault tolerant capability, flexible operation in drives, and high efficiency. But owing to its exclusive structure, it has some disadvantages. These disadvantages degrade the reliability of the electrical utility system (EUS). In T-VSI, common input is utilized to supply two sections. The total system current splits into two sections which reduced the filter rating. So, it results in reduced filter size. However, increment in number of switches results in growth in the budget of system. Compared with ICT-VSI, T-VSI shows less reactive power compensation in case of EUS. Hence, in this research work, reactive power compensation is achieved in 3-P 3-W ICT-VSI [8–10].

In this research work, reactive power compensation characteristics are achieved by designing a new model namely ICT-VSI which inserts an inductor network in between the two sections of T-VSI [11, 12]. The design of 3-P 3-W EUS can be used for three-phase balanced supply fed sensitive non-linear load. The performance of the proposed dual ICT-VSI-based DSTATCOM is justified by employing PQ attributes. In this research work, DSTATCOM-based $i\cos\phi$ control technique is suggested for PQ enhancement, power factor (PF) improvement, voltage balancing at point of common coupling (PCC), and enhancing reliability and system stability for increasing the efficiency of EUS. The proposed $i\cos\phi$ control has several benefits such as toughness, tracking, adaptive abilities, THD reduction, PF improvement, load balancing, and voltage regulation [10, 13–16].

This paper presents the simple circuit structure, operation, and principle of the planned inverter in Sect. 2. Here, $i\cos\phi$ control technique is presented in Sect. 3 and applied to both T-VSI and ICT-VSI-based DSTATCOM. Section 4 describes the simulation performance of the topologies by showing the effectiveness of the DSTATCOM. Lastly, the objective achievements are potted in Sect. 5.

2 Circuit Configuration

A 3-P 3-W EUS consisting of 3-phase balance source, DSTATCOM, and non-linear load is depicted in Fig. 1. Arrangement of T-VSI-based DSTATCOM and ICT-VSI-based DSTATCOM is shown in Figs. 2 and 3, respectively. Both T-VSI and ICT-VSI diminish the PQ issues. Each topology consists of two sections and each section contains 6 switches. As total of 12 switches are there, it attains 12^2 or 144 switching combination. Pulses for switches of inverters are estimated by using the $i\cos\phi$ control algorithm as shown in Fig. 4. The details of the control techniques are derived in the upcoming Sect. 3.
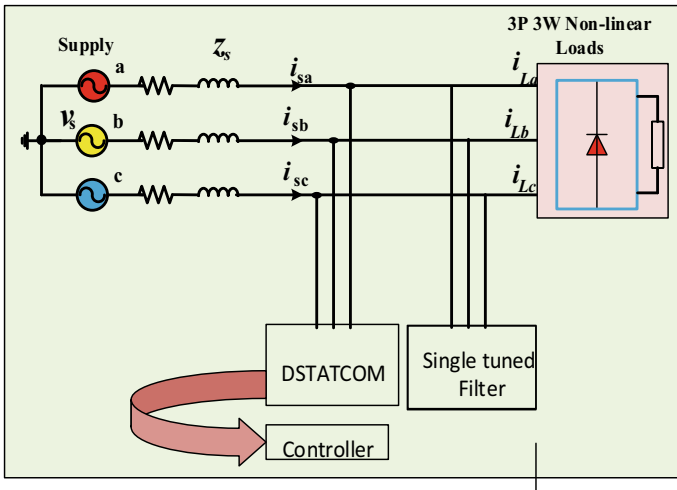
Fig. 1 Configuration of the proposed EUS
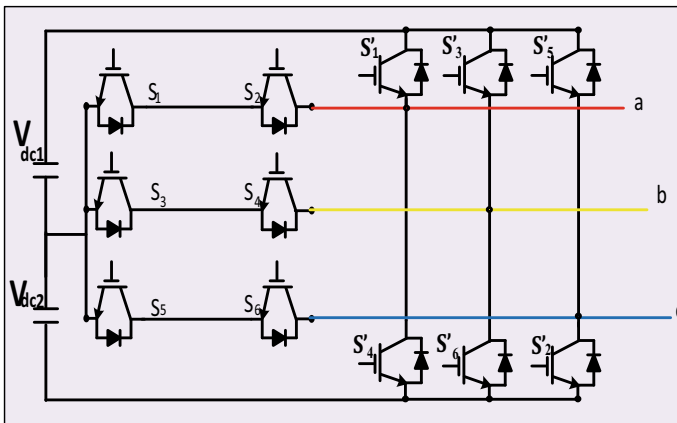
Fig. 2 Circuit structure for T-VSI-based DSTATCOM
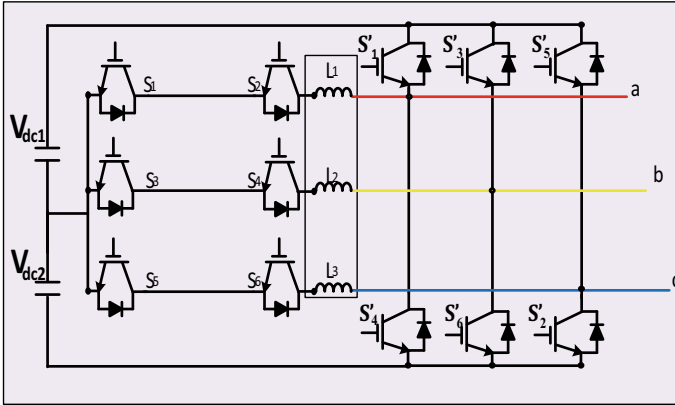
Fig. 3 Structural Diagram for Proposed ICT-VSI-based DSTATCOM
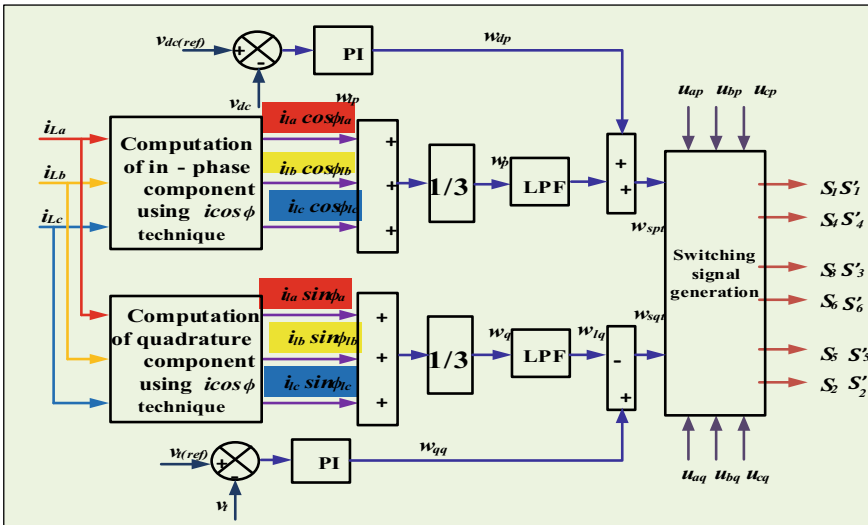
Fig. 4 Diagram of $i\cos\phi$ control technique

3 Control Algorithm

For inverter switches, the gate signals are produced by employing the $i\cos\phi$ controller. Also, this technique is adopted owing to its fast and robust dynamic response in case of steady-state as well as transient response. Reference source currents are derived by following several computational steps.

For fundamental load current, real power component is represented by i_{lap} and it can be represented as

$$\begin{bmatrix} i_{\text{lap}} \\ i_{\text{lbp}} \\ i_{\text{lcp}} \end{bmatrix} = \begin{bmatrix} \text{Re}(i_{\text{la}}) \\ \text{Re}(i_{\text{lb}}) \\ \text{Re}(i_{\text{lc}}) \end{bmatrix} = \begin{bmatrix} i_{\text{la}}\cos\phi_{\text{la}} \\ i_{\text{lb}}\cos\phi_{\text{lb}} \\ i_{\text{lc}}\cos\phi_{\text{lc}} \end{bmatrix} \tag{1}$$

For real power component, weighted average value w_p is represented as

$$w_p = \left(\frac{i_{\text{la}}\cos\phi_{\text{la}} + i_{\text{lb}}\cos\phi_{\text{lb}} + i_{\text{lc}}\cos\phi_{\text{lc}}}{3} \right) \tag{2}$$

In the same way, expression for reactive power component is

$$\begin{bmatrix} i_{\text{laq}} \\ i_{\text{lbq}} \\ i_{\text{lcq}} \end{bmatrix} = \begin{bmatrix} \text{Im}(i_{\text{la}}) \\ \text{Im}(i_{\text{lb}}) \\ \text{Im}(i_{\text{lc}}) \end{bmatrix} = \begin{bmatrix} i_{\text{la}}\sin\phi_{\text{la}} \\ i_{\text{lb}}\sin\phi_{\text{lb}} \\ i_{\text{lc}}\sin\phi_{\text{lc}} \end{bmatrix} \tag{3}$$

Similarly, for reactive power component, weighted average value w_q is

$$w_q = \left(\frac{i_{\text{la}}\sin\phi_{\text{la}} + i_{\text{lb}}\sin\phi_{\text{lb}} + i_{\text{lc}}\sin\phi_{\text{lc}}}{3} \right) \tag{4}$$

The DC supply (v_{de}) error to the PI controller and PI controller output is represented as below

$$w_{\text{dp}} = k_{\text{pdp}}v_{\text{de}} + k_{\text{idp}} \int v_{\text{de}}\text{dt} \tag{5}$$

The reference source current

$$w_{\text{spt}} = w_{\text{dp}} + w_{\text{lp}} \tag{6}$$

In the same way, computation of total reactive components is given as

$$w_{\text{sqt}} = w_{\text{qq}} - w_{\text{lq}} \tag{7}$$

A low-pass filter (LPF) with a 20 Hz cut-off frequency is used for filtration of active and reactive weighting factor for load current.

i_{sp} represents the instantaneous value for active source currents is computed as

$$\begin{bmatrix} i_{\text{sap}} \\ i_{\text{sbp}} \\ i_{\text{scp}} \end{bmatrix} = w_{\text{spt}} \begin{bmatrix} u_{\text{ap}} \\ u_{\text{bp}} \\ u_{\text{cp}} \end{bmatrix} \tag{8}$$

Instantaneous value of the reactive source currents i_{sq} is computed as

$$\begin{bmatrix} i_{\text{saq}} \\ i_{\text{sbq}} \\ i_{\text{scq}} \end{bmatrix} = w_{\text{sqt}} \begin{bmatrix} u_{\text{aq}} \\ u_{\text{bq}} \\ u_{\text{cq}} \end{bmatrix} \qquad (9)$$

Lastly, the reference source currents can be given as

$$\begin{bmatrix} i_{\text{sa}}^* \\ i_{\text{sb}}^* \\ i_{\text{sc}}^* \end{bmatrix} = \begin{bmatrix} i_{\text{sap}} \\ i_{\text{sbp}} \\ i_{\text{scp}} \end{bmatrix} + \begin{bmatrix} i_{\text{saq}} \\ i_{\text{sbq}} \\ i_{\text{scq}} \end{bmatrix} \qquad (10)$$

After the generation of the reference source currents i_{sa}^*, i_{sb}^*, and i_{sc}^*, it will be compared with actual source currents i_{sa}, i_{sb}, & i_{sc} and current error signals are fed to the hysteresis current control (HCC) and it operates when $i_{\text{sa}} < i_{\text{sa}}^*$, switch 1 is ON and switch 4 is OFF and similarly when $i_{\text{sa}} > i_{\text{sa}}^*$, switch 1 is OFF and switch 4 is ON.

4   MATLAB Results

In the MATLAB/Simulink environment, simulation using Simscape tool box has been accomplished for validating the feasibility of the proposed topology. With use of the listed parameters in Appendix A, the simulation is applied to the proposed topology. Firstly, the EUS performance is analyzing by connecting the three-phase non-linear load (uncontrolled rectifier with R and L load) only and DSTATCOM is not attached at the PCC. To verify the proposed selective compensation control method among distortion, unbalanced and reactive power of the DSTATCOM, simulation results are carried out to examine the system performance. The performance parameters of both T-VSI and ICT-VSI with DSTATCOM are shown in Table 1.

4.1   Simulation Results of T-VSI-Based DSTATCOM

The simulation model of T-VSI supported DSTATCOM contains, a non-linear load with $R = 10\ \Omega$ and $L = 20$ mH, 230 V (rms)/phase balanced source voltage, fundamental frequency 50 Hz and 600 V reference dc link voltage. The other specifications of parameters utilized to construct the model are organized in Appendix A.

Table 1 Comparison between T-VSI and ICT-VSI

Integrated DSTSTCOM	Source Current (A), % THD	Load Current (A), % THD	PF	PCC Voltage (V), % THD
T-VSI	59.6, 4.80	57.86, 35.23	0.961	299.3, 1.4
ICT-VSI	59.55, 4.57	58.53, 34.37	0.979	299, 1.03

The steady-state response of T-VSI current tracking characteristics were depicted in Fig. 5a.

The impact of distortion in the EUS is testified; Fig. 5d, e represents the THD analysis of source current 4.80%, magnitude 59.6A and load current 35.23%, magnitude 57.86A, respectively.
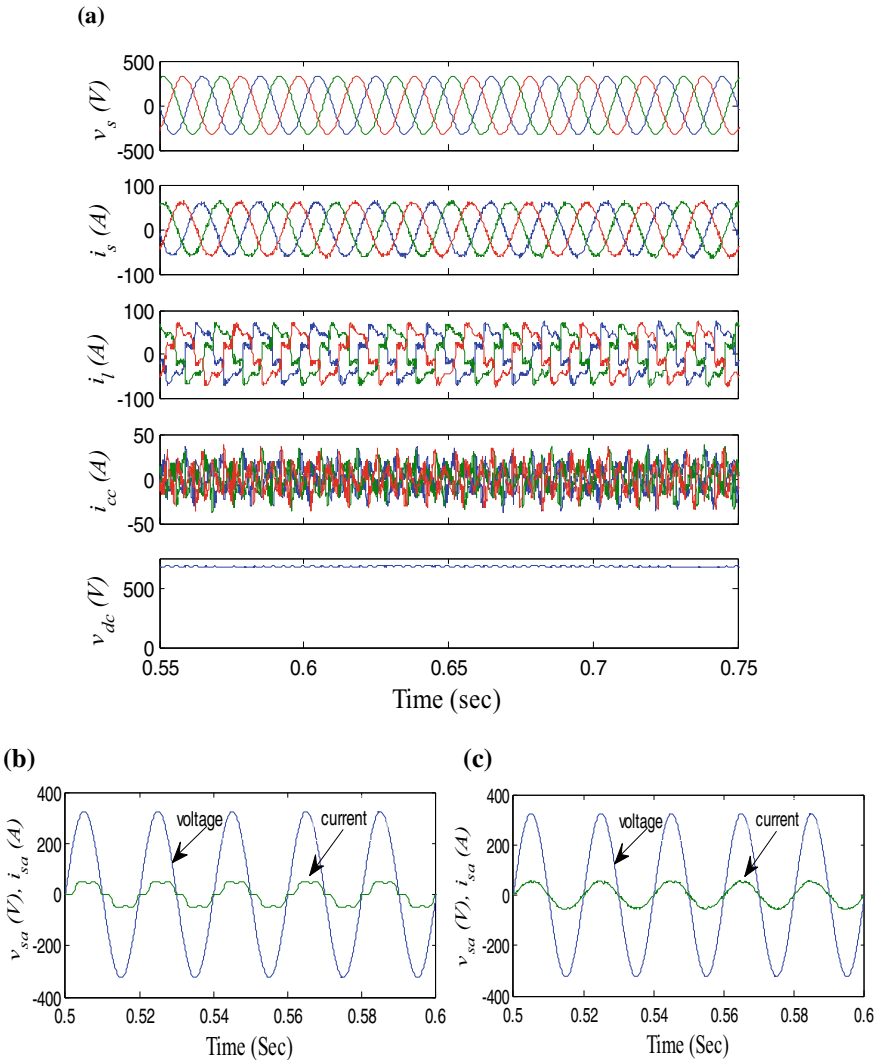
Fig. 5 **a** Simulation results for source voltage, source current, load current, compensating current & DC link voltage of T-VSI. **b** Phase angle between v_s and i_s. **c** Phase angle between v_s and i_s (DSTATCOM at PCC). **d** Source current THD. **e** Load current THD

(d)

Fundamental (50Hz) = 59.6, THD= 4.80%

(e)

Fundamental (50Hz) = 57.86, THD= 35.23%

Fig. 5 (continued)

(a)
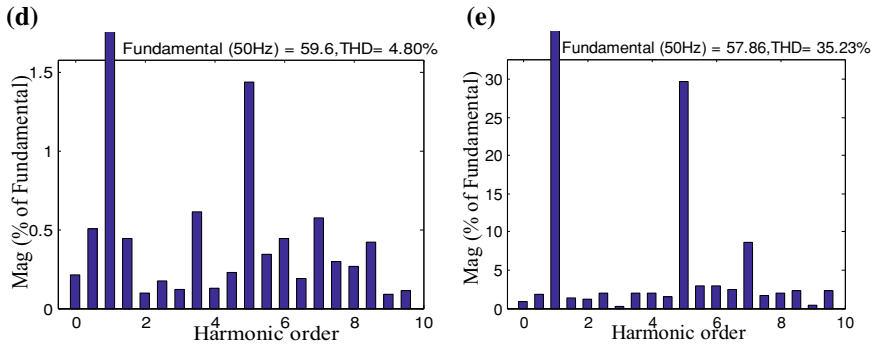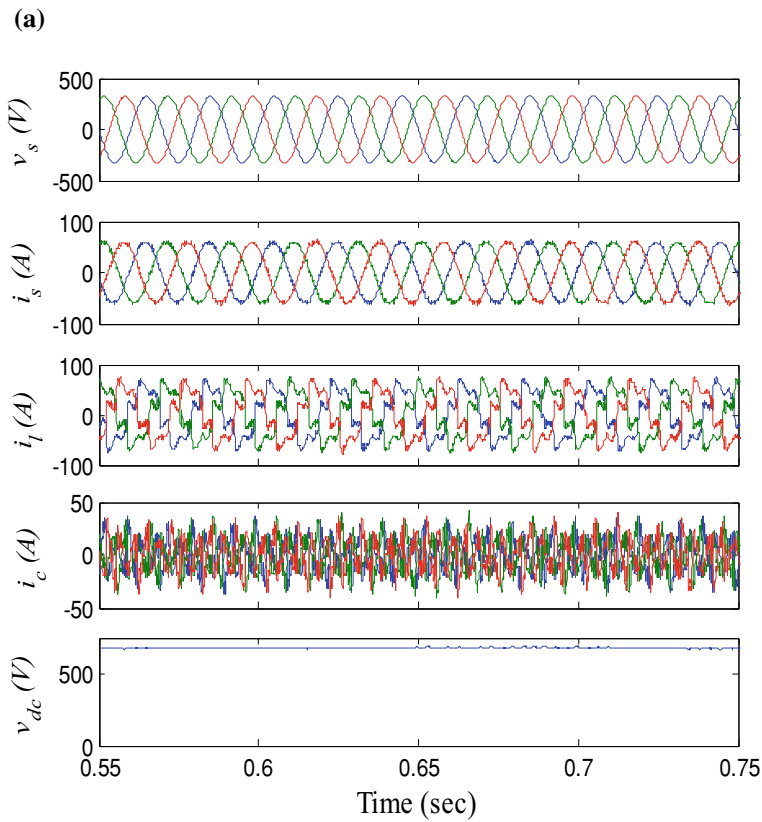
Fig. 6 **a** Simulation results for source voltage, source current, load current, compensating current, and DC link voltage of ICT-VSI. **b** Phase angle between v_s and i_s. **c** Phase angle between v_s and i_s (DSTATCOM at PCC). **d** Source Current THD. **e** Load Current THD

(b)

(c)

(d)

(e)
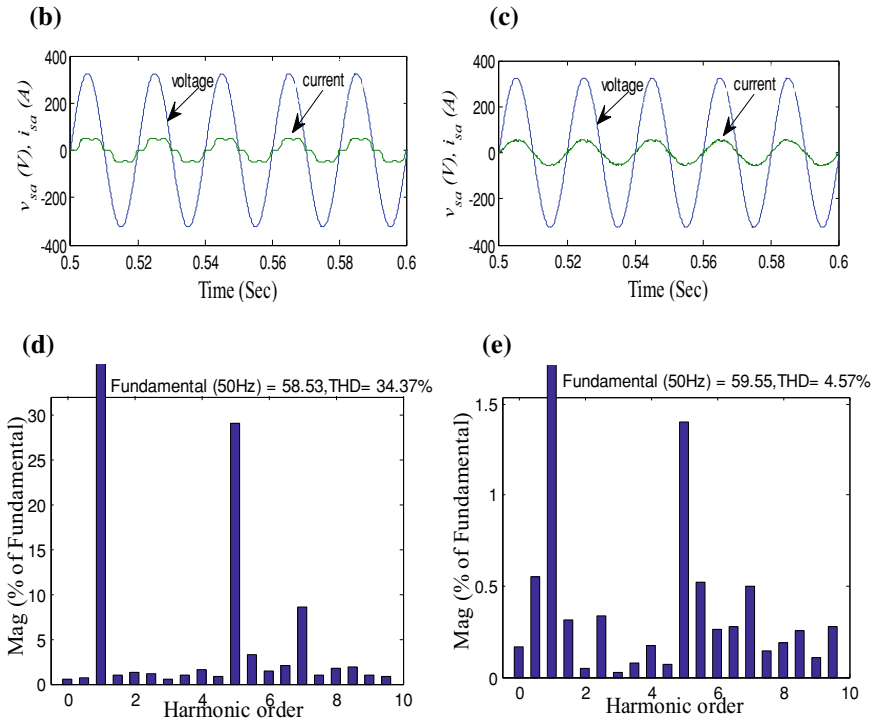
Fig. 6 (continued)

4.2 Simulation Results of ICT-VSI-Based DSTATCOM

The same parameters are used to build the proposed topology; instead of T-VSI here inductor network is connected in between two sections of T-VSI. The steady-state response of ICT-VSI current tracking characteristics was depicted in Fig. 6.

The impact of distortion in the EUS is testified; Fig. 6d, e represents the THD analysis of source current 4.57%, magnitude 59.55A and load current 34.37%, magnitude 58.53A, respectively. Source current THD reduction must be taken into account to compare these two DSATCOMs; this reduction in THD of EUS can lead to a better performance of DSATCOM and an increase in reliable and flexible operation of EUS with enhanced PQ. The performance parameters of ICT-VSI are shown in Table 1.

5 Conclusion

The PQ issues of EUS have been investigated in this paper. The proposed ICT-VSI topology has better reactive power compensation capability in comparison with

T-VSI. The justification of both the DSTATCOM is successfully examined through simulation results with the help of MATLAB/Simulink software. The superior performance of the ICT-VSI-based DSTATCOM is validated by the simulation results. The ICT-VSI achieves better harmonics reduction, PF improvement, acceptable voltage regulation and retains the balanced voltage at PCC. Also, the ICT-VSI is able to shrink the THD well below the limit of the IEEE-2030-7-2017 and IEC-61,000-1 grid code over T-VSI.

Appendix A

3-phase source voltage (v_s): 230 V/phase, Fundamental frequency (f_s): 50 Hz, Resistance of Source (R_s): 0.5 Ω, Inductance of Source (L_s): 2 mH, Resistance of Compensator (R_c): 0.25 Ω, Inductance of Compensator (L_c): 1.5 mH, AC Proportional controller (K_{pr}): 0.2, AC Integral controller (K_{ir}): 1.1, DC link voltage (v_{dc}): 600 V, Capacitance (C_{dc}): 2000 μF, DC Proportional controller (K_{pa}): 0.01, DC Integral controller (K_{ia}): 0.05, etc.

References

1. M.M. Mangaraj, A.K. Panda, Performance analysis of DSTATCOM employing various control algorithms. IET Gener. Transm. Distrib. **11**(10), 2643–2653 (2017)
2. S.R. Arya, R. Niwas, K.K. Bhalla, B. Singh, A. Chandra, K. Al-Haddad, Power quality improvement in isolated distributed power generating system using DSTATCOM. IEEE Trans. Ind. Appl. **51**(6), 4766–4774 (2015)
3. M. BarghiLatran, A. Teke, Y. Yoldaş, Mitigation of power quality problems using distribution static synchronous compensator: a comprehensive review. IET Power Electron. **8**(7), 1312–1328 (2015)
4. K.V. Singh, H.O. Bansal, D.A. Singh, Comprehensive review on hybrid electric vehicles: architectures and components. J. Modern Transp. **27**, 77–107 (2019)
5. T. Penthia, M.M. Mangaraj, A.K. Panda, S.K. Sarangi, Sparse LMS control algorithm for fuel cell based SAPF, in *2016 IEEE Uttar Pradesh Section International Conference on Electrical Computer and Electronics Engineering (UPCON)*, pp. 72–77 (2016)
6. V. Kamatchi Kannan, N. Rengarajan, Investigating the performance of photovoltaic based DSTATCOM using Icosϕ algorithm. Int. J. Electr. Power Energy Syst. **54**, 376–386 (2014)
7. M. Schweizer, J.W. Kolar, Design and implementation of a highly efficient three-level T-type converter for low-voltage applications. IEEE Trans. Power Electron. **28**(2), 899–907 (2013)
8. C. Kumar, M.K. Mishra, An improved hybrid DSTATCOM topology to compensate reactive and nonlinear loads. IEEE Trans. Industr. Electron. **61**(12), 6517–6527 (2014)
9. U. Choi, F. Blaabjerg, K. Lee, Reliability improvement of a T-type three-level inverter with fault-tolerant control strategy. IEEE Trans. on Power Electron. **30**(5), 2660–2673 (2015)
10. V.C. Sekhar, K. Kant, B. Singh, DSTATCOM supported induction generator for improving power quality. IET Renew. Power Gener. **10**(4), 495–503 (2016)
11. H. Myneni, G. Siva Kumar, Simple algorithm for current and voltage control of LCL DSTATCOM for power quality improvement. IET Gener. Transm. Distrib. **13**(3), 423–434 (2019)

12. M.M. Mangaraj, A.K. Panda, Modelling and simulation of KHLMS algorithm-based DSTATCOM. IET Power Electron. **12**(9), 2304–2311 (2019)
13. J. He, N. Weise, R. Katebi, L. Wei, N.A.O. Demerdash, A fault tolerant T-type multilevel inverter topology with soft-switching capability based on Si and SiC hybrid phase legs, in *IEEE 2016 Energy Conversion Congress and Exposition (ECCE)* (2016)
14. C. Kumar, M.K. Mishra, A Voltage-controlled DSTATCOM for power-quality improvement. IEEE Trans. Power Deliv. **29**(3), 1499–1507 (2014)
15. G. Bhubaneswari, M.G. Nair, Design, simulation and analog circuit implementation of a three phase shunt active filter using Icosϕ algorithm. IEEE Trans. Power Deliv. **23**(2), 1222–1235 (2008)
16. M.M. Mangaraj, J. Sabat, Comparative analysis of both three & fifth level based DSTATCOM using technique, in *2020 International Conference on Computational Intelligence for Smart Power System and Sustainable Energy (CISPSSE)*, Keonjhar, Odisha, India, pp. 1–6 (2020)

Dual Image-Based High Quality Digital Image Watermarking

V. Srinadh, Balajee Maram , **and T. Daniya**

Abstract   Digital image watermarking techniques are suitable for integrity authentication, watermark security, and copyright protection. Further, the number of embedding bits and the process of watermarking also play a crucial role in deciding the effectiveness of any watermarking process. In this regard, to achieve better security without producing noticeable artifacts in the watermarked image, this paper proposes a dual image-based watermarking technique using an exclusive-or (XOR) operation. The proposed technique utilizes a modified least significant bit (LSB) substitution strategy in the host image (HI) pixel to substitute the watermark bits with a maximum of ± 1 modification to each pixel. Each HI pixel embeds two watermark bits by producing two different watermarked pixels each. The proposed technique has better watermark bit embedding capacity, higher perceptual transparency, and security.

Keywords   Watermarking · Capacity · Authentication · LSB

1   Introduction

With the rapid growth of digital technology, image authentication is becoming a prime concern as it is quite easy to manipulate the image [1]. Thus, to alleviate this concern, researchers have produced various watermarking techniques. The process of digital watermarking is performed through two major phases, such as (1) watermark embedding and (2) watermark extraction. During embedding, the host image that is used to hold the watermark is usually pre-processed and then the watermark

V. Srinadh
Department of Computer Science and Engineering, GMR Institute of Technology, Rajam, Andhra Pradesh, India
e-mail: srinadh.v@gmrit.edu.in

B. Maram (✉)
Dept of CSE, Chitkara University Institute of Engineering and Technology, Chitkara University, Baddi, Himachal Pradesh, India
e-mail: maram.balajee@gmail.com

T. Daniya
Research Scholar, Sathyabama Institute of Science and Technology, Chennai, India

is embedded in the same [2]. Further, using different keys, the embedding process can be strengthened. At the opposite end, the watermark can be extracted using the watermark extraction technique and the same key. Watermarking can be visible or invisible [3]. When the watermark is embedded in the host image and the watermark will be visible is called visible watermarking. On the other hand, invisible watermarking intelligently embeds the watermark in the host signal.

There are various applications of watermarking ranging from telemedicine, copyright protection, authentication, electronic health care, fingerprinting, and source tracking. Robust, fragile, and semi-fragile are the types of water marking techniques [4]. Robust watermarking techniques successfully prevent various attacks like geometric, scaling, cropping, and noise. Even after an attack, robust watermarking does not modify the watermark in the host signal [5]. Mostly, robust watermarking techniques are used in broadcast observation, fingerprinting, and copyright preservation, etc. The fragile watermarking techniques are very much susceptible to different kinds of attacks. Therefore, the watermark cannot be accurately extracted even with modest modification. Due to the feature of fragility, these techniques are suitable for multimedia authentication and integrity attestation. Finally, the Semi-fragile technique combines the feature of both robust as well as fragility.

2   Related Work

In [5], the image is partitioned into various 2×2 blocks and the recovery pixels are found using the average of the blocks. Zhang et al. [6] suggested a fragile watermarking technique using the concept of the local binary pattern (LBP). In this, the watermark is generated using the LBP operator. The suggested technique performs well in forgery detection as compared to existing techniques.

Wong et al. [7] introduced a digital watermarking technique using the public key algorithm. A fuzzy c-means clustering-based watermarking technique is proposed by Chen and Wang [8] to provide image authentication. Here, each block of the image is clustered and the authentication data is inserted in the last two LSBs. Teng et al.'s [9] fragile watermarking schema is based on chaotic map and exclusive-or operation. This technique successfully resists the content-based watermark attack, but issues with tampering coincidence problem. This problem occurs when the block is tampered with using various attacks and due to which recovery is not possible. Molina-Garcia et al. [10] suggested a novel fragile watermarking technique to achieve better authentication and recovery using color images. Here, the image is partitioned into blocks and each block performs both authentication and recovery using a permutation process. Further, the technique successfully avoids the tampering coincidence problem. A block-based compression technique to recover the watermark bits is suggested in [11]. In [13], author has proposed a LSB matching technique using random ± 1 modification to embed one bit in each pixel, which efficiently withstands different attacks. Further, the technique avoids the tampering coincidence problem. The technique proposed in [13] utilizes the logistic map-based embedding strategy

to embed the watermark information in the LSB bits. Further, the suggested technique successfully resists various image tampering attacks. Pal et al. [14] proposed LBP technique is suggested to protect from illegal modification. Here embedding is performed in 3×3 blocks. Authors in [15] proposed watermarking technique which achieves high tampering detection accuracy and low false-positive pixels. The authors [16, 17] proposed various security and privacy issues to solve the problems related to mining and intruder's problem. The authors have proposed the security algorithms using images and got good results comparatively existing algorithms [18–20].

3 Proposed Technique

Digital image watermarking techniques require higher imperceptibility, better capacity, and security. Most of the watermarking techniques suggested in the literature are highly inclined towards exploring the LSB bits in the pixel. In the process of achieving above mentioned requirements existing techniques fail to maintain a required balance among the measures. The proposed watermarking technique indirectly embeds the watermark bits in the LSB bits of each HI pixel using XOR feature of the HI pixel. It achieves all the aforementioned requirements of a better watermarking technique. The proposed technique is mainly implemented using two stages, such as (1) watermark embedding and (2) watermark extraction. During the embedding stage, the dual image of the HI is obtained. The dual image is the replica of the HI. The following section discusses them. Further, the working procedure is shown in Fig. 1.

3.1 Embedding Stage

Initially, the HI pixels are obtained from the image. The following steps are implemented to embed two bits of watermark information in each HI pixel.

Step 1   Since each HI is replicated, assuming P_1^1 and P_2^1 are the replicated pixel of one of the HI pixels.

Step 2   Considering w_1 and w_2 are the watermark bits that need to be embedded in P_1^1 and P_1^2.

Step 3   Let $p_1^1 p_1^2 p_1^3 p_1^4 p_1^5 p_1^6 p_1^7 p_1^8$ and $p_2^1 p_2^2 p_2^3 p_2^4 p_2^5 p_2^6 p_2^7 p_2^8$ be the eight-bit binary representation of P_1^1 and P_2^1.

Step 4   Then, applying XOR operation on the first seven individual bits of the obtained pixels the resulting bits r_1^1 and r_1^2 are obtained as below.

$$r_1^1 = p_1^1 \oplus p_1^2 \oplus p_1^3 \oplus p_1^4 \oplus p_1^5 \oplus p_1^6 \oplus p_1^7 \tag{1}$$

$$r_1^2 = p_2^1 \oplus p_2^2 \oplus p_2^3 \oplus p_2^4 \oplus p_2^5 \oplus p_2^6 \oplus p_2^7 \tag{2}$$

$$P_1^1 = p_1^1 p_1^2 p_1^3 p_1^4 p_1^5 p_1^6 p_1^7 p_1^8$$

$$P_2^1 = p_2^1 p_2^2 p_2^3 p_2^4 p_2^5 p_2^6 p_2^7 p_2^8$$

$$r_1^1 = p_1^1 \oplus p_1^2 \oplus p_1^3 \oplus p_1^4 \oplus p_1^5 \oplus p_1^6 \oplus p_1^7$$

$$r_2^1 = p_2^1 \oplus p_2^2 \oplus p_2^3 \oplus p_2^4 \oplus p_2^5 \oplus p_2^6 \oplus p_2^7$$

$$c_1^1 = r^1 \oplus w^1$$

$$c_1^2 = r^2 \oplus w^2$$

$$P_1^{1*} = p_1^1 p_1^2 p_1^3 p_1^4 p_1^5 p_1^6 p_1^7 c_1^2$$

$$P_2^{1*} = p_2^1 p_2^2 p_2^3 p_2^4 p_2^5 p_2^6 p_2^7 c_1^1$$

$$P_1^{1*} = p_1^1 p_1^2 p_1^3 p_1^4 p_1^5 p_1^6 p_1^7 c_1^2$$

$$P_2^{1*} = p_2^1 p_2^2 p_2^3 p_2^4 p_2^5 p_2^6 p_2^7 c_1^1$$

$$r_1^{1*} = p_1^1 \oplus p_1^2 \oplus p_1^3 \oplus p_1^4 \oplus p_1^5 \oplus p_1^6 \oplus p_1^7$$

$$r_2^{1*} = p_2^1 \oplus p_2^2 \oplus p_2^3 \oplus p_2^4 \oplus p_2^5 \oplus p_2^6 \oplus p_2^7$$

$$w^1 = r_1^{1*} \oplus c_1^2$$

$$w^2 = r_2^{1*} \oplus c_1^1$$
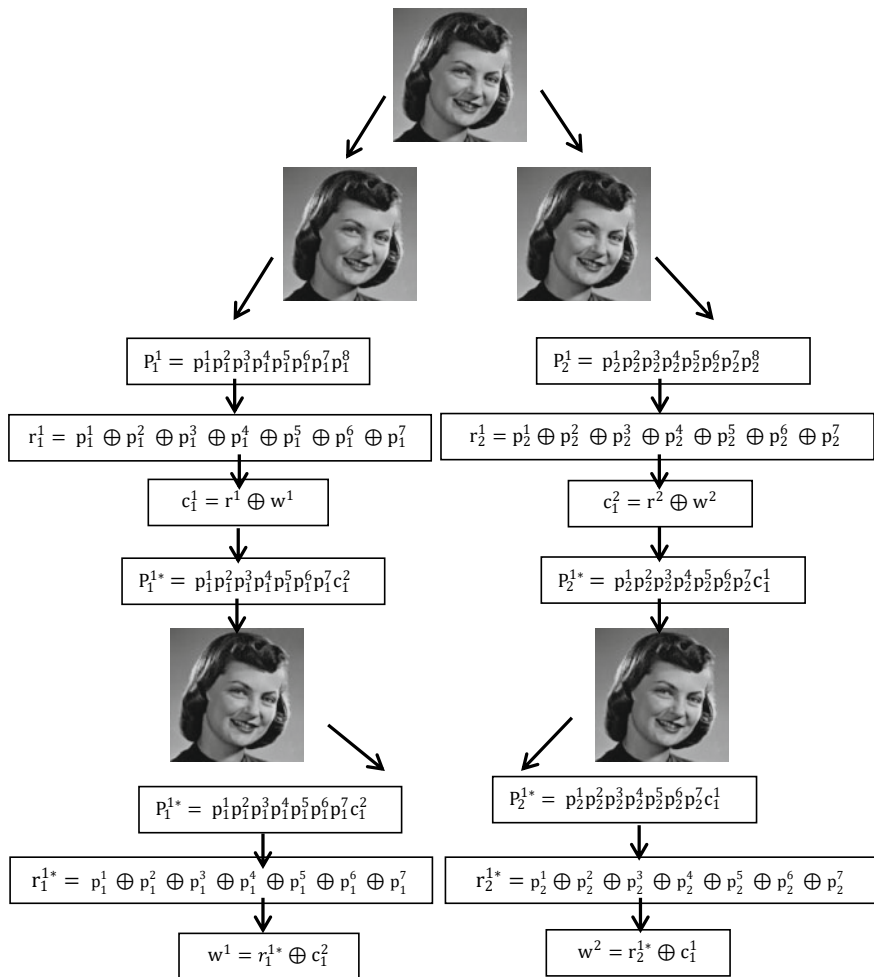
Fig. 1 Proposed technique-embedding and extraction technique for watermark

Step 5   Once again the obtained r_1^1 and r_1^2 bits are XORed with the watermark bits w_1 and w_2 using Eqs. (3) and (4) to find c_1^1 and c_1^2.

$$c_1^1 = r_1^1 \oplus w_1 \tag{3}$$

$$c_1^2 = r_1^2 \oplus w_2 \tag{4}$$

Step 6   The watermarking pixels are obtained by replacing the LSB bits of P_1^1 and P_2^1 with the obtained c_1^1 and c_1^2 as below.

$$P_1^{1*} = p_1^1 p_1^2 p_1^3 p_1^4 p_1^5 p_1^6 p_1^7 c_1^2 \tag{5}$$

$$P_2^{1*} = p_2^1 p_2^2 p_2^3 p_2^4 p_2^5 p_2^6 p_2^7 c_1^1 \tag{6}$$

Step 7   However, in Eqs. (5) and (6), to improve the security, c_1^1 is replaced with the LSB of P_2^{1*} and c_1^2 is replaced with the LSB of P_1^{1*}

Step 8   Finally, P_1^{1*} and P_2^{1*} are the updated watermarking pixels for P_1^1 and P_1^2. The above steps are followed for embedding the remaining watermark bits.

Step 9   Watermark embedding is completed.

3.2 Extraction Stage

At the receiving end, the embedded w_1 and w_2 bits are retrieved from the P_1^{1*} and P_2^{1*} pixels of the watermarked image using the following steps.

Step 1   At first, P_1^{1*} and P_2^{1*} are represented in its corresponding binary eight bits as $p_1^1 p_1^2 p_1^3 p_1^4 p_1^5 p_1^6 p_1^7 c_1^2$ and $p_2^1 p_2^2 p_2^3 p_2^4 p_2^5 p_2^6 p_2^7 c_1^1$.

Step 2   Then using Eqs. (7) and (8) r_1^{1*} and r_2^{1*} are obtained as below.

$$r_1^{1*} = p_1^1 \oplus p_1^2 \oplus p_1^3 \oplus p_1^4 \oplus p_1^5 \oplus p_1^6 \oplus p_1^7 \tag{7}$$

$$r_2^{1*} = p_2^1 \oplus p_2^2 \oplus p_2^3 \oplus p_2^4 \oplus p_2^5 \oplus p_2^6 \oplus p_2^7 \tag{8}$$

Step 3   Then, perform XOR of r_1^{1*} with c_1^1 to obtain w^1. Similarly, perform XOR of r_2^{1*} with c_1^2 to obtain w^2.

$$w^1 = r_1^{1*} \oplus c_1^2 \tag{9}$$

$$w^2 = r_2^{1*} \oplus c_1^1 \tag{10}$$

Step 4   Finally, w^1 and w^2 are the watermark bits obtained form P_1^{1*} and P_2^{1*}.

Step 5   Watermark extraction is completed.

4 Results and Analysis

In the proposed watermarking technique, the HIs of size 512×512 are considered for the experimentation purpose. Important watermarking parameters like PSNR, capacity, SSIM are taken for comparison. It is compared with 1LSB, 2LSB, 3LSB, and Mielikainen's [12] technique. Among the considered measures PSNR is an image quality measuring parameter. PSNR finds the distortion between the HI and watermarked image. PSNR is computed using the following Eq. (11).

$$\text{peak} - \text{signal} - \text{to} - \text{noise ratio (PSNR)} = 10 \times \log_{10} \frac{255 \times 255}{\text{MSE}} \quad (11)$$

where MSE is found from Eq. (12).

$$\text{MSE} = \frac{1}{i \times j} \sum_{a=1}^{i} \sum_{b=1}^{j} (\text{HI}_{ab} - \text{WI}_{ab})^2 \quad (12)$$

Here, HI_{ij} and WI_{ij} points to the ith and jth coordinates pixels.

Structural similarity index (SSIM) is the image quality evaluation parameter. Its values range between 0 and 1. Higher SSIM suggests better quality of the watermarked image. Equation (13) is used to compute the SSIM.

$$\text{SSIM} = \frac{(2\mu_H \mu_W + k_1)(2\sigma_{\text{HW}} + k_2)}{(\mu_H^2 + \mu_W^2 + k_1)(\sigma_H^2 + \sigma_W^2 + k_2)} \quad (13)$$

k_1 are k_2 are constants. $\sigma_{\text{HW}}, \mu_H, \mu_W, \mu_H^2, \mu_W^2, \sigma_H^2, \sigma_W^2$ covariance, mean, variance, and standard deviations for the HI and watermarked image (Fig. 2).

Tables 1 and 2 present the result of the proposed, Mielikainen's [12] technique, 1 LSB, 2LSB, and 3LSB techniques. It produces two different watermarked images from a single HI. Each watermarked image achieves a higher PSNR with above 51 dB. Further, each watermarked pixel embeds 1 bit of watermark information, therefore, two bits are hidden in each HI pixel. So the capacity is 524288 bits. Further, the SSIM values are also superior with above 0.99. When we compare the PSNR of the proposed work with Mielikainen's [12] technique, 1LSB, 2LSB, and 3 LSB technique, Mielikainen's [12] technique offers better PSNR. However, the capacity of the technique is 262144 bits only. Similarly, PSNR for 1LSB, 2LSB,

(a) Baboon, (b) Airfield, (c) Zelda, (d) Crowd, (e) House, (f) Baby, (g) Boat, (h) Lena, (i) Houses, (j) Clown

Fig. 2 Host images (**a–j**). **a** Baboon, **b** Airfield, **c** Zelda, **d** Crowd, **e** House, **f** Baby, **g** Boat, **h** Lena, **i** Houses, **j** Clown

Table 1 Results for the proposed work, Mielikainen's [12] technique, and 1LSB technique

	Proposed technique					Mielikainen's [12] technique			1LSB		
	PSNR1	PSNR2	Capacity	SSIM1	SSIM2	PSNR	Capacity	SSIM	PSNR	Capacity	SSIM
Baboon	51.13	51.14	524,288	0.99	0.99	52.02	262,144	0.99	51.12	262,144	0.99
Tank	51.15	51.13	524,288	0.99	0.99	52.02	262,144	0.99	51.13	262,144	0.99
Zelda	51.14	51.15	524,288	0.99	0.99	52.01	262,144	0.99	51.13	262,144	0.99
Crowd	51.16	51.14	524,288	0.99	0.99	52.02	262,144	0.99	51.12	262,144	0.99
House	51.16	51.15	524,288	0.99	0.99	52.02	262,144	0.99	51.13	262,144	0.99
Baby	51.16	51.16	524,288	0.99	0.99	52.03	262,144	0.99	51.13	262,144	0.99
Boat	51.15	51.15	524,288	0.99	0.99	52.04	262,144	0.99	51.13	262,144	0.99
Lena	51.17	51.16	524,288	0.99	0.99	52.04	262,144	0.99	51.12	262,144	0.99
Houses	51.16	51.14	524,288	0.99	0.99	52.06	262,144	0.99	51.11	262,144	0.99
Clown	51.17	51.17	524,288	0.99	0.99	52.05	262,144	0.99	51.10	262,144	0.99
Avg	51.16	51.15	524,288	0.99	0.99	52.03	262,144	0.99	51.12	262,144	0.99

Table 2 Results for the 2LSB and 3LSB technique

	2LSB			3LSB		
	PSNR	Capacity	SSIM	PSNR	Capacity	SSIM
Baboon	44.05	524,288	0.97	37.91	786,432	0.94
Tank	44.05	524,288	0.97	37.90	786,432	0.94
Zelda	44.06	524,288	0.98	37.93	786,432	0.95
Crowd	44.06	524,288	0.97	37.92	786,432	0.96
House	44.07	524,288	0.97	37.93	786,432	0.95
Baby	44.05	524,288	0.98	37.94	786,432	0.95
Boat	44.08	524,288	0.97	37.94	786,432	0.96
Lena	44.06	524,288	0.97	37.95	786,432	0.95
Houses	44.05	524,288	0.98	37.93	786,432	0.96
Clown	44.08	524,288	0.97	37.92	786,432	0.96
Average	44.06	524,288	0.97	37.93	786,432	0.95

and 3LSB techniques are lower as compared to the proposed technique. At the same time, the capacity of 1LSB is less than the proposed work. Also, the LSB-based technique directly replaces the watermark bits in the HI pixels and therefore, these techniques are highly susceptible to various watermarking attacks. On the other hand proposed technique expertly embeds the watermark bits without giving any indication of the presence of secret information inside the watermarked image. Additionally, the right balance among the three required measures is achieved successfully using the proposed work.

5 Conclusion

This paper proposes a highly imperceptible dual image-based digital watermarking technique using the XOR feature and modified LSB substitution technique. The watermark bit embedding is performed using dual images of the HI. Each host image pixel is further partitioned into two new pixels. The watermark bits are embedded using the XOR feature of the individual bits of the HI pixels. Later the bits are extracted from the LSB position of each pixel by applying the reverse process of the embedding. Results achieved from the experiment are encouraging with respect to the watermarked image quality and capacity. Further, in the future, we are extending the work to achieve complete reversibility as well as fragility.

References

1. K. Sreenivas, V.K. Prasad, Fragile watermarking schemes for image authentication: a survey. Int. J. Mach. Learn. Cybern. **9**(7), 1193–1218 (2018)
2. L. Rakhmawati, W. Wirawan, S. Suwadi, A recent survey of self-embedding fragile watermarking scheme for image authentication with recovery capability. EURASIP J. Image Video Process. **2019**(1), 61 (2019)
3. C. Rey, J.L. Dugelay, A survey of watermarking algorithms for image authentication. EURASIP J. Adv. Signal Process. **2002**(6), 1–9 (2002)
4. M. Begum, M.S. Uddin, Digital image watermarking techniques: a review. Information **11**(2), 110 (2020)
5. W.L. Tai, Z.J. Liao, Image self-recovery with watermark self-embedding. Signal Process.: Image Commun. **65**, 11–25 (2018)
6. H. Zhang, C. Wang, X. Zhou, Fragile watermarking based on LBP for blind tamper detection in images. J. Inf. Process. Syst. **13**(2), 385–399 (2017)
7. P.W. Wong, A public key watermark for image verification and authentication, in *Proceedings 1998 International Conference on Image Processing. ICIP98 (Cat. No. 98CB36269)*, Vol. 1, pp. 455–459. IEEE (1998)
8. W.C. Chen, M.S. Wang, A fuzzy c-means clustering-based fragile watermarking scheme for image authentication. Expert Syst. Appl. **36**(2), 1300–1307 (2009)
9. L. Teng, X. Wang, X. Wang, Cryptanalysis and improvement of a chaotic system based fragile watermarking scheme. AEU-Int. J. Electron. Commun. **67**(6), 540–547 (2013)
10. J. Molina-Garcia, B.P. Garcia-Salgado, V. Ponomaryov, R. Reyes-Reyes, S. Sadovnychiy, C. Cruz-Ramos, An effective fragile watermarking scheme for color image tampering detection and self-recovery. Signal Process.: Image Commun. **81**, 115725 (2020)
11. T.Y. Lee, S.D. Lin, Dual watermark for image tamper detection and recovery. Pattern Recogn. **41**(11), 3497–3506 (2008)
12. J. Mielikainen, LSB matching revisited. IEEE Signal Process. Lett. **13**(5), 285–287 (2006)
13. P. Pal, B. Jana, J. Bhaumik, Watermarking scheme using local binary pattern for image authentication and tamper detection through dual image. Secur. Priv. **2**(2), e59 (2019)
14. A.K. Sahu, M. Sahu, Digital image steganography techniques in spatial domain: a study. Int. J. Pharm. Technol. **8**(4), 5205–5217 (2016)
15. S. Trivedy, A.K. Pal, A logistic map-based fragile watermarking scheme of digital images with tamper detection. Iran. J. Sci. Technol. Trans. Electr. Eng. **41**(2), 103–113 (2017)
16. T. Daniya, K. Suresh Kumar, B. Santhosh Kumar, C. Sekhar Kolli, A survey on anomaly based intrusion detection system. Mater. Today Proc. (2021)
17. B.S. Kumar, T. Daniya, N. Sathya, R. Cristin, Investigation on privacy preserving using K-anonymity techniques. Int. Conf. Comput. Commun. Inform. (ICCCI) **2020**, 1–7 (2020)
18. B. Maram, S.K. Gorripati, N. Supriya, A framework work for data security using cryptography and video steganography. Int. J. Sci. Technol. Res. **9**(4), 56–60. ISSN 2277-8616 (2020)
19. B. Maram, G.K.D. Gopisetty, P.S. Rao, A framework work for data security using cryptography and image steganography. Int. J. Innov. Technol. Explor. Eng. **8**(11), 1066–1070. ISSN:2278-3075 (Online) (2019)
20. B. Maram, J.M. Gnanasekar, G. Manogaran, M. Balaanand, Intelligent security algorithm for unicode data privacy and security in IoT. Serv. Orient. Comput. Appl. (SPRINGER) (2018). ISSN:1863-2386 (Print) 1863-2394 (Online)

Role of Controller Zeroes in Stabilizing an Unstable System

Shradha Kishore

Abstract A controller is an integral component in any process. An unstable system can be paired with a PID controller in a closed-loop feedback configuration to obtain a desired response. Insertion of a controller results in adding a pole at origin and two zeroes into the transfer function at a location determined by the tuning strategy employed. If placed suitably, the zeroes of the controller can pull the root locus starting at an unstable pole and terminating at a stable zero towards the stable left half. This paper presents the suitability of a tuning technique not only from the response of the output but also by graphical depiction of the change in the pole-zero patterns caused by the tuning technique. The system chosen for the demonstration is an open-loop unstable Maglev system which is gaining prominence in green and environment-friendly transportation and the tuning techniques chosen are Zeigler–Nichols and pole placement techniques.

Keywords PID controller · Maglev · Feedback · Tuning · Root Locus

1 Introduction

It is a normal perception that a controller is required to modify the response and only the poles of a system play a significant role in determining the stability of a system. This paper effectively highlights the actual task done by a PID controller in inserting the zeroes at appropriate locations which can bring about the desired modification in the response, and thus help in giving a clear understanding of the reasons behind the nature of response obtained [1]. These zeroes can pull the poles from an unstable region to a stable region as has been done for an open-loop unstable and highly sensitive Maglev system in the present work. The location of the zeroes is evaluated by the algorithm of the tuning technique used, some of which are general in nature while some are specific to the system taken. The root locus plot depicts the location of the poles and zeroes and its effect on the stability of the system and hence

S. Kishore (✉)
Birla Institute of Technology, Patna Off-Campus, Patna Extension Centre, Mesra, India
e-mail: skishore@bitmesra.ac.in

the suitability of the tuning technique chosen. The concept of levitation is widely gaining momentum in the transportation sector as it does not use biofuel, is free from hazardous environmental pollution with high efficiency due to absence of frictional losses.

The organization of the paper has been done sequentially with the PID Controller Tuning in Sect. 2, description of the chosen Maglev system in Sect. 3, application of Zeigler–Nichols (Z-N) technique in Sect. 4, Pole placement (PP) in Sect. 5, Root Locus analysis in Sect. 6, and the conclusion in Sect. 7.

2 PID Controller Tuning

The choice of tuning strategy to estimate the values of the parameters of a controller plays a very crucial role in the effective working of any system. These poles and zeroes of the controller can nullify the destabilizing effect of the unstable pole of the system if placed at a suitable location [2]. The choice of any tuning technique from a vast multitude of existing techniques is crucial to obtain the desired response such that the deviation between the actual response and the desired response is as meager as possible.

2.1 Parameters of a Controller

A PID control has three components, the proportional term, K_P, the derivative term, K_D, and the integral term K_I which can tackle the error occurring at any instance or that might occur at a future instance or that has already occurred in the past. So by taking all the terms the transfer function of a parallel form of PID controller is given by

$$G_c(s) = K_P + K_I/s + sK_D = \frac{s^2 K_D + s K_P + K_I}{s} \qquad (1)$$

It can be seen from the transfer function of this controller that it has a pole at the origin and two zeroes Z_c at a location given by the formula,

$$Z_c = \frac{-K_P \pm \sqrt{K_P^2 - 4K_I K_D}}{2K_D} \qquad (2)$$

Therefore, the strategic locations of these zeroes of the controller depend on the values of K_P, K_D, and K_I which can be determined by the tuning technique applied. The controller pole and zeroes along with the poles and zeroes of the process in the

feedback configuration can stabilize even an unstable system and a desired response can be obtained [3].

2.2 Tuning Techniques

Evaluation of components of the controller directly leads to the location of zeroes so choice of tuning strategy is important in getting the desired response. Some techniques are general in nature and can be applied safely on most of the industrial systems as the formula is based on the experimental inference of a wide variety of systems. These techniques are not specific to the system and require lesser assumptions. They are necessary in complex cases where derivation of mathematical transfer function is difficult. One such popular tuning technique has been derived by Zeigler–Nichols (Z–N).

Some tuning techniques require the mathematical model of the system for evaluation of the parameters of the controller [4]. These techniques are specific to the system and require validation and most of the times give better tuned values. Pole placement (PP) is one such technique.

Figure 1 depicts the nature of the working methodology of the tuning techniques.
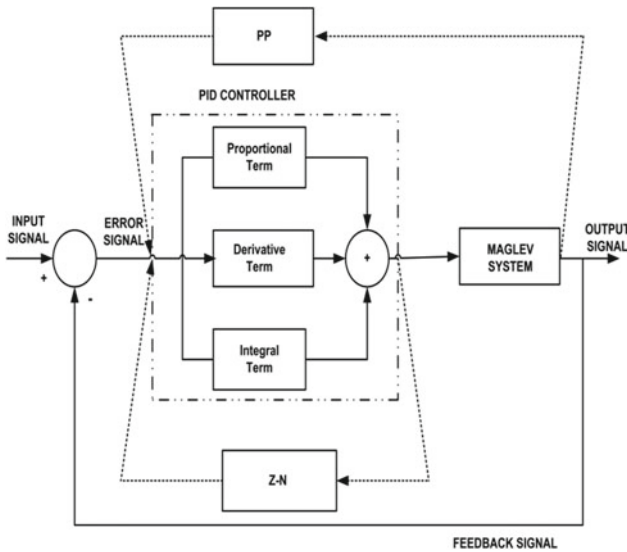
Fig. 1 Nature of the tuning techniques

3 Unstable Maglev System

The concept of magnetic levitation causes an object to rise from ground and hove in air based on the force balance conditions. This technique is widely applied in various fields due to absence of energy losses caused due to friction leading to high efficiency. Maglev trains can run at super high speeds and do not cause adverse effect on the environment.

One such model based on the concept of magnetic levitation system has been developed by The Feedback Instruments Limited, U.K. The objective of the model is to cause levitation of a hollow steel ball at an equilibrium position which requires an accurate current supply to the electromagnet so that the required attractive force can be generated. There are certain assumptions made for the linearization of the model and also due to presence of computational and rounding off errors there are vibrations in the levitated state which cause the ball to drop out of levitation [5]. The task of the controller is to constantly manipulate the supply of current to the electromagnet based on the position of the ball and keep it in levitated state. This is regulated by the setting of the parameters of the controller which has been tuned by the above-mentioned techniques.

3.1 Hardware Setup

The hardware setup of the Maglev system as shown in the actual photograph in Fig. 2 consists of three separate units, namely, Hardware Unit, 33–210, Interface Unit, 33–301, and Computerized Control Unit.

Fig. 2 Photograph of the actual hardware layout
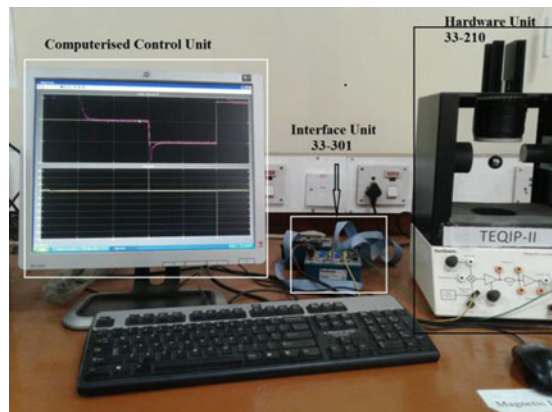
3.2 Transfer Function

The derivation of transfer function of the linearized model is based on force balance of upward attractive force, fe and the downward gravitational force.

After applying Taylor's expansion formula, Laplace transform and substituting the system data provided by the manufacturer, the transfer function of the Maglev system can be evaluated as (detailed derivation in [6, 7]),

$$M(s) = \frac{-3653.3575}{s^2 - 2180} \tag{3}$$

Analysis of the transfer function of the model shows that it is an unstable system in open loop due to the presence of one of the quadratic poles in the right side of the s-plane at a location of +46.69. It is the effect caused by this unstable pole which has to be negated by the zeroes of the controller.

4 Zeigler–Nichols Method

Ziegler–Nichols tuning strategy is the most popular and widely used tuning technique for the evaluation of the parameters of a PID controller in most industrial process control applications. The ease of application and cost effectiveness are the advantages of this method. The initial setting of the controller requires the removal of the integral and derivative actions. The gain of the controller is then only the proportional action, K_P. This gain, K_P, is increased till the output response shows oscillations due to the shifting of the location of the poles at the imaginary axis. The value of the gain at this instance is called the critical gain, K_u and the corresponding time between oscillations is called critical time, T_u [8].

4.1 Calculation of Parameters of the Controller

The calculations have been done for damping ratio, $\xi = 0.8$ and a settling time, $t_S = 2$ s.

The natural frequency of oscillation, ω_n can be calculated as

$$\omega_n = 4/\xi * t_S = 2.5 \tag{4}$$

The critical gain, K_u, can be calculated from a closed-loop response by setting K_P as K_u to obtain limited stability for this value of ω_n.

$$K_u = 0.59 \tag{5}$$

Table 1 Controller parameters by Z-N method

K_P	K_I	K_D
−0.36	−0.28	−0.12

The critical time period can be calculated as

$$T_u = 2\pi/\omega_n = 2.513 \tag{6}$$

The parameters of the controller can now be calculated as shown in Table 1.

4.2 Response by Z-N Tuning

The closed-loop response obtained from the simulated model for these controller settings has been shown in Fig. 3. The nature of the response clearly shows that the system has not been tuned properly as the uneven square input wave has not been tracked by the response.

5 Pole Placement Technique

Some tuning strategies need model of the system for evaluation of the tuning parameters (K_P, K_I, and K_D) of the controller. Modeling of the real system requires certain assumptions to be made for linearization around an equilibrium position, rounding off, and computational simplification. These techniques cannot be applied in all cases and need experimentation to check if the linearized model is a true representation of the system. Pole placement technique is mostly applied to place a system pole at any desired location to achieve a performance goal. In this method, the desired response
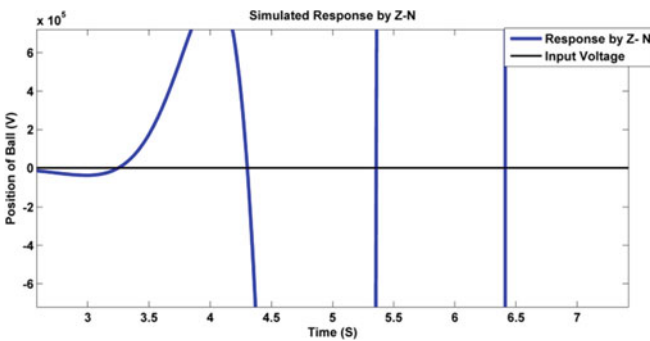
Fig. 3 Response by Z-N

Table 2 Controller parameters by PP method

K_P	K_I	K_D
-2.33	-2.66	-0.43

is compared with the actual response and subsequently the three parameters of the controller can be evaluated [9].

5.1 Calculation of Parameters of the Controller

Assuming the same parameters, the desired response of any second order system can be obtained as

$$R(s) = \frac{\omega_n^2}{\left(s^2 + 2\xi\omega_n s + \omega_n^2\right)} = \frac{6.25}{s^2 + 4s + 6.25} \tag{7}$$

The characteristic equation of the actual closed-loop response with PID controller and Maglev system as shown in Fig. 2 can be written as

$$(1 + G_C G_P) = s\left(s^2 - 2180\right) - 3653.3575(sK_P + K_D s^2 + K_I) \tag{8}$$

Now equating the actual and the desired response, we get the parameters of the controller evaluated for an assignment at $-750\ \xi\omega_n$ has been shown in Table 2.

5.2 Response by PP Tuning

The closed-loop response for these controller settings has been shown in Fig. 4. It can be seen that the simulated response is able to track the uneven square input waveform satisfactorily.

Fig. 4 Simulated response by PP
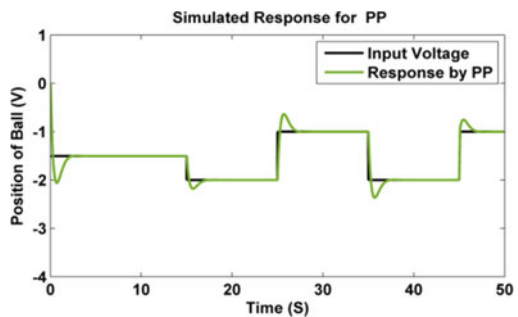
Fig. 5 Root Locus of an open-loop Maglev system
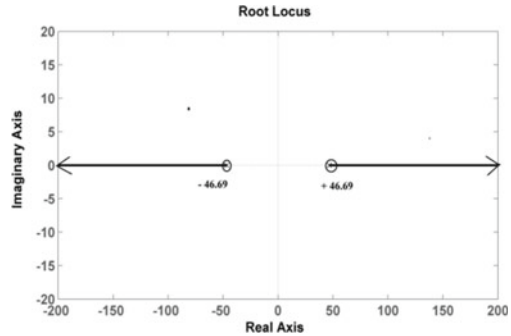
6 Root Locus Analysis

Root locus is graphical tool which has been used to represent the pole-zero trajectory of Maglev system under present consideration, the effect of both the tuning techniques on re-location of the poles and zeroes and the stability of the system [10]. The system poles and zeroes are based on the differential equations governing the system and give sufficient information about the system [11]. The location of a pole directly indicates the nature of stability of a system. The location of zeroes does not affect the system stability directly but if they lie on the left half of the stable s-plane then the system is called a non-minimum phase system and can be realized physically [12]. The poles are attracted by the zeroes and if the zeroes are located in the unstable portion then the poles might have a tendency to move towards the zero and make the system unstable eventually [13].

6.1 Root Locus of the Open-Loop Maglev System

The root locus of the open-loop Maglev system is shown in Fig. 5. The transfer function of the Maglev system as shown in Eq. (3) indicates that the system has two real poles, $P_1 = +46.69$, $P_2 = -46.69$, and Gain $= -3653.3575$. The root locus clearly shows the divergent nature of the branch towards unstable right half due to the presence of an unstable pole at $+46.69$.

6.2 Change in Root Locus Due to Z-N Method

The complex zeroes of the controller, Z_c, evaluated by Zeigler–Nichols method in Table 3 can be evaluated from Eq. (2) as

$$Z_c = -1.5 \pm j0.28 \tag{9}$$

Table 3 Compilation of poles and zeroes

System	Poles			Zeroes	
Open-loop Maglev	−46.69	+46.69	−	−	−
closed loop tuned by Z-N	−440.4	0.985 + j 1.16	0.985 − j 1.16	−1.5 + j 0.294	−1.5 − j 0.294
closed loop tuned by PP	−1557	−2.03 + j 1.46	−2.03 − j 1.46	−3.805	−1.638

The transfer function of the feedback system with the PID controller tuned by the values the Maglev system shows the value of gain, location of poles and zeroes of the configuration by this technique can be evaluated as $P_1 = -440.4$, $P_{2,3} = 0.985 \pm j\,1.16$, and $Z_{1,2} = -1.5 \pm j\,0.294$ with Gain $= 438.4$.

As a result of this application, there is a real pole in the stable region and a pair of complex dominant poles in the unstable region which tends to shift towards a pair of complex zeroes in the stable region as shown in Fig. 6.

These stable complex zeroes do attract the unstable poles but as they are not placed at an accurate location so they are unable to avoid the region of instability. This effect can also be seen in the simulated response of Fig. 3 due to which the response is unable to track the input voltage for this tuning strategy. The zoomed response of the region encircled near the origin can be better seen in Fig. 7.

Fig. 6 Root Locus by Z-N Tuning
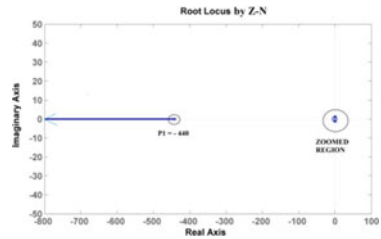
Fig. 7 Enlarged view of zoomed region by Z-N
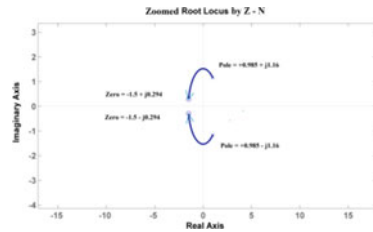
6.3   Change in Root Locus Due to PP Technique

The controller zeroes Z_c in this case may be evaluated as

$$Z_c = -3.77 \text{ and } -1.64 \tag{10}$$

Application of this technique relocates the poles and zeroes of the entire configuration. The shifting of location of poles and zeroes becomes $P_1 = -1557$, $P_{2,3} = -2.03 \pm j\,1.46$ and $Z_{1,2} = -3.805, -1.638$ with Gain $= 1570.9$.

In this case, all the poles and zeroes are in the stable region and the system is a minimum phase system. The zeroes have shifted from complex plane to real axis, whereas the complex poles have shifted from unstable region to stable region. The effectiveness of this relocation of poles and zeroes can be seen in the simulated response in Fig. 4. Figure 8 shows the root locus of the closed-loop configuration for the controller tuned by this method.

Figure 9 shows the zoomed root locus of the dominant poles and zeroes. In this case, none of the poles or zeroes lie in the unstable region and the tuning parameters are appropriate. The compiled pole-zero locations of the unstable open-loop Maglev system as well as that obtained by the tuning strategies of Zeigler–Nichols (Z-N) and Pole Placement (PP) have been shown in Table 3.

Fig. 8 Root Locus by PP tuning
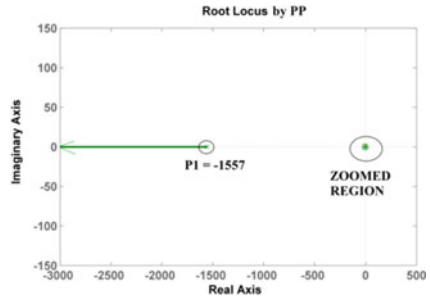
Fig. 9 Zoomed region by PP
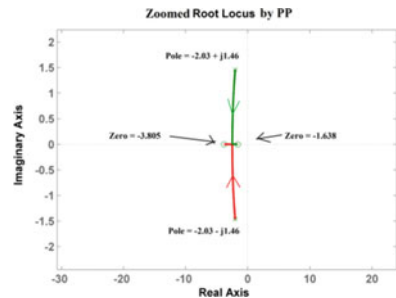
7 Conclusion

The evaluation of the poles and zeroes from the closed-loop feedback transfer function with a tuned PID controller, and the Maglev system gives a fair idea about the behavior of the system. The root locus plot makes it evident that strategic positioning of the controller zeroes can attract the unstable poles towards a more stable position such that the system can operate in a desired way. The choice of tuning strategy plays a vital role as the parameters of the controller directly control the location of placing of these zeroes. This kind of pole-zero analysis is instrumental in judging the reasons behind the failure or success of the tuning strategy employed. It can be concluded that Zeigler–Nichols method is unsuitable as compared to Pole Placement method for this sensitive and unstable system. This paper clearly demonstrates the important role played by the controller and specifically the location of zeroes in getting the desired response.

References

1. C.B. Schrader, M.K. Sain, Research on system zeros: a survey. Int. J. Control **50**(4), 1407–1433 (1989)
2. B.F. Wyman, M.K. Sain, G. Conte, A.-M. Perdon, On the zeros and poles of a transfer function. Linear Algebra Appl. **122–124**, 123–144 (1989)
3. Q.-G. Wang, T.-H. Lee, H.-W. Fung, Q. Bi, Y. Zhang, PID tuning for improved performance. IEEE Trans. Control Syst. Technol. **7**(4), 457–465 (1999)
4. S. Tavakoli, M. Safaei, Analytical PID control design in time domain with performance-robustness trade-off. Electron. Lett. **54**(13), 815–817 (2018)
5. R.K.H. Galvao, T. Yoneyama, F.M.U. de Araujo, R.G. Machado, A simple technique for identifying a linearized model for a didactic magnetic levitation system. IEEE Trans. Educ. **46**(1), 22–25 (2003)
6. Magnetic Levitation: Control Experiments, Feedback Instruments Limited, UK (2011)
7. S. Kishore, V. Laxmi, Modeling, analysis and experimental evaluation of boundary threshold limits for Maglev system. Int. J. Dynm. Control **9**, 707–716 (2020)
8. J.G. Ziegler, N.B. Nichols, *Optimum settings for automatic controllers* (Am. Soc. Mech. Eng., N. Y., 1941), pp. 1–5
9. Q.-G. Wang, Z.Zhang, K.J. Astrom, L.S. Chek, Guaranteed dominant pole placement with PID controllers. J. Process Control **19**(2), 349–352 (2009)
10. A.M. Lopes, J.A. Tenreiro Machad, *Root Locus Practical Sketching Rules for Fractional-Order Systems*. Hindawi Publishing Corporation, Article ID 102068, vol. 2013
11. G. Conte, A.M. Perdon, B.F. Wyman, Zero/pole structure of linear transfer functions, in *24th IEEE Conference on Decision and Control*, USA, pp. 529–530 (1985)
12. J. Salt, A. Sala, P. Albertos, A transfer-function approach to dual-rate controller design for unstable and non-minimum-phase plants. IEEE Trans. Control Syst. Technol. **19**(5), 1186–1194 (2011)
13. H.H. Rosenbrock, The zeros of a system. Int. J. Control **18**(2), 297–299 (1973)

Intelligent Optimization Techniques for Controlling Load Frequency of Interconnected Multiple Source Power Systems Including Renewable Energy Sources

Bijaya Kumar Mohapatra, Deepak Kumar Gupta, and Chinmoy Kumar Panigrahi

Abstract Controlling the system frequency under load variation of multiple source power systems (MSPS), including renewable energy sources (RES), is a very difficult task for power system engineers. The LFC acts as a dynamic role in evaluating the performance of a MSPS. The system's complexity has been exacerbated by the use of several power generation sources, including RES. The paper presents a performance investigation of a two-area system that includes RES. Hydro, thermal, wind, and diesel power stations have been modeled and used in the test system. The algorithms set the constraints of a PID controller to provide controlling load frequency in an automatic manner of MSPS with RES. Intelligent optimization techniques are used to fine-tune the controller's parameters with constraints. The ITAE is used as an objective function. The PID Controller kept the deviation of frequency and tie-line power of the MSPS within acceptable limits. A two-area power system comprising of different energy sources was designed using the Simulink tool of MATLAB.

Keywords Renewable energy sources · Load frequency control · Multiple source power system · Optimization techniques

1 Introduction

An interconnected power network controls the interchange of electricity and regulates the frequency to keep it within the nominal range. With the dynamic change in load, both active and reactive power demands change continuously. With the Automatic Generation Control (AGC), the oscillations can be quickly adjusted in a normal range. Due to system losses and generation charge mismatch, the frequency of the power supply is fluctuating. The power of the tie-lines between the test system's sections can also be altered. Controlling the generators and tie-line power can help keep the

B. K. Mohapatra (✉) · D. K. Gupta · C. K. Panigrahi
School of Electrical Engineering KIIT, Deemed to Be University, Bhubaneswar, India
e-mail: bijaya87@gmail.com

system dynamics steady. The area control error (ACE) is commonly known for this control.

Sandhya et al. [1] the LFC of an MSPS was proposed with a cascade tilting-integral-tilt-derivative control. Topno et al. [2] introduced a tilt-in derivative controller for a two-area power system. Tavakoli et al. [3] the nonlinear optimization approaches is to be utilized to optimize controller tuning for efficient power system operation in the framework of LFC. Lu et al. [4]. developed a population extremely optimization strategy with a PI controller. Sahoo et al. [5] the Multi-Verse Optimization methodology was recently proven to offer enhanced fine tuning of the fractional-order PDPI controller for LFC with and without the HVDC link. Guha et al. [6] developed a nature-inspired stochastic evolutionary method to attain the best LFC KOM et al. [7] designed an interphase power controller and Ahmed et al. [8] designed a FACTS controller to improve the power quality of a MAPS.

A two-area power system with multiple sources is considered in this work. By minimizing ITAE, the proposed methodology was used to modify the parameters of the PID controller. For optimally tuning the parameter of PID controller and problems on LFC, two well-known optimization techniques such as GSA and Firefly Algorithm (FA) have been used. Comparative analysis for the dynamic behavior of frequency and tie-line power of the system for both the techniques has been done. The performance of the system was evaluated in both domains while considering the perturbation step load change.

The following is a summary of how the rest of the article is organized. Section 2 defines the Proposed Power System and the PID Controller in depth. Section 3 describes the development of intelligent optimization methodologies. In Sect. 4, the case study is explained together with the discussion, and in Sect. 5, the proposed work's conclusion is discussed. The Appendix A section contains the various parameters of the algorithms.

2   The Proposed Power System and the PID Controller

The proposed work introduces an intelligent optimization methodology based on heuristics for the automatic LFC of a two-area MSPS. The PID controller is one of the most extensively utilized controllers in today's modern industries. Furthermore, it is extensively applicable in systems with a single input and single output. The output of the PID controller can be denoted by Eq. (1).

$$u(t) = K_P e(t) + K_I \int e(t)dt + K_D \frac{de(t)}{dt} \tag{1}$$

The PID controller's input and output are denoted by e (t) and u (t). In addition, the proportional, integral, and derivative gains are also represented by KP, KI, and KD.

As an objective function, the ITAE was chosen. The PID controller parameters were tuned by minimizing this objective function. The objective function can be described by Eq. (2).

$$ITAE = \int_0^{t_{sim}} t \times |e(t)| dt \tag{2}$$

For the LFC study, a test system with two areas was used. Power was generated by various sources including thermal, hydro, diesel, and wind power station in the test system. Figure 1 shows the model for this test system, which was created in MATLAB/SIMULINK using a linearized technique. The test system's specifications are listed in Appendix A. Thermal and hydropower stations were connected in each region, wind and diesel power stations were connected in area1 and area2, respectively, and the AGC was controlled with a PID controller. The dynamic behavior of the tie-line power, frequency, and the ACE was captured and used to assess performance. For both areas of the power system, perturbation with step load was taken into account.
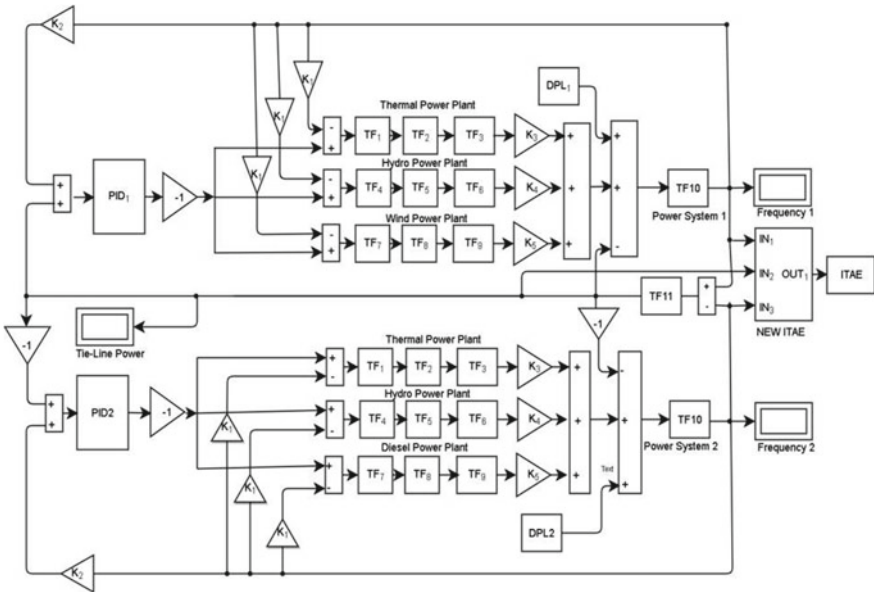
Fig. 1 Designed simulation model implementation of a two-area MSPS

3   Objective Function for Controlling Load Frequency

The correct tuning of the controllers connected to the system is critical for the proper operation of the power system under varied operating conditions. The controllers' parameters must be fine-tuned to make them resistant to model uncertainty and dynamical changes. It should be capable of tracking the desired point for all variables and responsive to load perturbation fluctuations. In terms of overshoot and settling time, however, ITAE was proven to provide satisfactory results for parametric optimization concerning LFC. As a result, we used ITAE as an objective function in our current research.

$$J = ITAE = \int_{0}^{t_{sim}} (|\Delta F_1| + |\Delta F_2| + |\Delta P_{tie}|).t.dt \tag{3}$$

where ΔP_{tie} ΔP_{12} denotes tie-line power variation and ΔF_1 and ΔF_2 denote frequency variation corresponding to regions 1 and 2, respectively.

4   Intelligent Optimization Techniques

4.1   *Gravitational Search Algorithm (GSA*

GSA is implemented by Newton's Gravitational law.In this algorithm, agents are considered as objects. Object performance is measured by its masses, i.e., heavy masses mean good solution. Gravitational force is used by an object to attract each other. The gravitational force causes the movement of objects toward heavier masses.

If there are N objects having d dimensions, then each agent position 'i' is determined as

$$X_i = (X_i^1, ..., X_i^{d-1}, X_i^d, ..., X_i^m)\forall_i \in \{1, 2, ..., N\} \tag{4}$$

The force applied by mass 'j' on mass 'i' is

$$F_{ij}^d(t) = G(t)\frac{M_{pi}(t).M_{aj}(t)}{R_{ij}(t)+ \in}(X_j^d(t) - X_i^d(t)) \tag{5}$$

$$F_i^d(t) = \sum_{j=1:j\neq i}^{N} rand_j F_{ij}^d(t), a_i^d(t) = \frac{F_i^d(t)}{M_{ii}(t)} \tag{6}$$

The velocity and agent's position are simplified by

$$v_i^d(t+1) = rand_i \times v_i^d(t) + a_i^d \tag{7}$$

$$x_i^d(t+1) = x_i^d(t) + v_i^d(t+1) \tag{8}$$

where

Rij   the Euclidian distance between agents i and j.
G(t)   the gravitational constant.
M_{aj} the active gravitational mass of agent j.
M_{pi} the passive gravitational mass of agent i.
ε   small constant

4.2 Firefly Algorithm (FA)

The FA is a metaheuristic algorithm inspired by firefly flashing activity. The following assumptions are used to construct this algorithm: (1) Fireflies are attracted to each other, (2) Attractiveness is related to brightness, (3) A brighter firefly attracts a less bright firefly, (4) Attractiveness reduces as the distance between two fireflies increases, (5) If the brightness of both is the same, fireflies will move at random, and (6) The random walk and the attraction of fireflies generate new solutions. The following is the formula for the attractiveness function used for firefly:

$$\beta = \beta_0 e^{-\gamma r^2} \tag{9}$$

Distance between two fireflies at positions x_i and x_j can be computed as

$$r_{ij} = \sqrt{\sum_{k=1}^{d}(x_{i,k} - x_{jk})^2} \tag{10}$$

The movement of firefly 'i' toward firefly 'j' is represented by

$$x_i(t=1) = x_i(t) + \beta_0 e^{-\gamma r_{ij}^2}(x_j - x_i) + \alpha \in \tag{11}$$

Here, $x_i(t=1)$ represents the new solution, $x_i(t)$ shows the current position, $\beta_0 e^{-\gamma r_{ij}^2}$ represents the attractiveness, and $\alpha \in$ represents the step size, in which, $\propto$ is the randomization parameter and ε is the random number vector.

5   Discussion of the Finding Results

The MSPS model has been developed based on the theories of control systems. The equivalent transfer functions of different plants, such as thermal, hydro, diesel, and wind turbine were used to represent them. With these power plants, two separate areas were examined. On an i3-6006U CPU at 2.00 GHz with 4 GB RAM, the test system was developed as a Simulink model using the MATLAB (R2016a) software. In addition, MATLAB was used to implement various optimization techniques such as GSA and FA. To get a comparative performance evaluation between these two algorithms were connected with the test system's MATLAB Simulink model. In Appendix A of the article, certain other essential parameters of the test system and parameters related to optimization strategies are detailed. The PID controller parameters were optimized by reducing the ITAE using the two optimization strategies. The optimization approaches were utilized to identify the ideal PID controller parameters, which are employed for the MSPS' LFC. We selected two scenarios to demonstrate the efficacy of the proposed optimization strategies, which are discussed below.

The First Case Study: A load increment of up to 0.01 p.u. was applied to both sections of the test system. For the parametric tuning of the PID controller, the intelligent optimization algorithms GSA and FA were applied. For the ΔP_{12} $\Delta P_{12}, \Delta F_1$ ΔF_1, and ΔF_2 ΔF_2 variables, where ΔP_{12} ΔP_{12} represents variation in tie-line power and ΔF_1 and ΔF_2 ΔF_2 reflect variation in frequency corresponding to designed power system area 1 and 2, respectively, their performances were compared in terms of overshoot and settling time. The tuned PID controller parameters are shown in Table 1. For the variables of interest, Table 2 shows the settling time and the peak overshoot. Figure 2 illustrates the dynamic responses. Finally, the FA algorithm's efficacy was assessed as to settling time. The settling times for Case Study I of ΔF_1,

Table 1 PID controller parameters being fine-tuned utilizing various optimization techniques—case study I

Optimization technique	K_{P1}	K_{I1}	K_{D1}	K_{P2}	K_{I2}	K_{D2}	ITAE
FA	3.8885	4.9999	2.2505	3.1142	2.7464	1.2471	0.0724
GSA	1.4920	5.0000	1.6811	1.1192	0.001	0.001	0.0792

Table 2 shows the impact of various optimization approaches on system state variables in case study I

Optimization technique	States variables	Over-shoot	Settling time
FA	ΔF_1	−0.0105	14.5
FA	ΔF_2	−0.08	14.5
FA	ΔP_{12}	−0.0009	16
GSA	ΔF_1	−0.011	16
GSA	ΔF_2	−0.03	16
GSA	ΔP_{12}	−0.0011	19

(a)   (b)

(c)
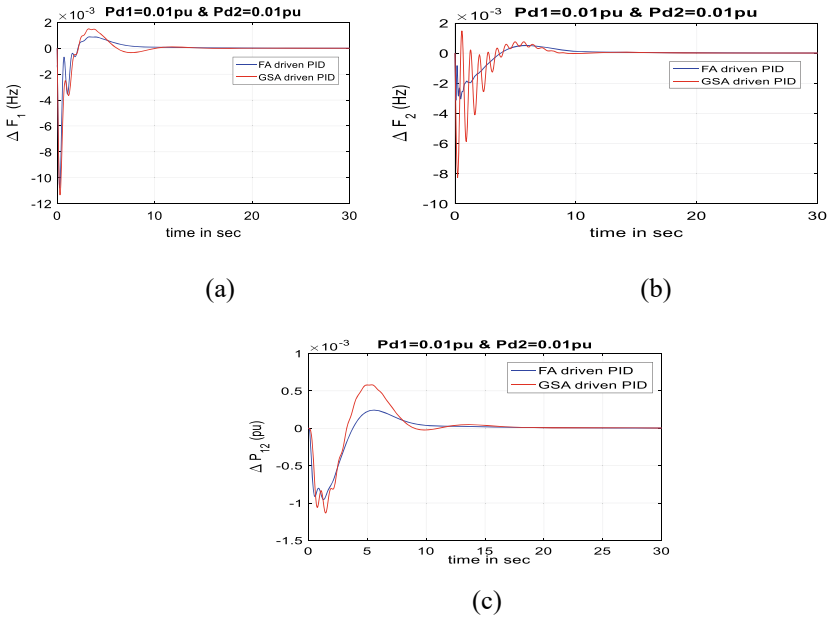
Fig. 2 Dynamic behaviors of the for case study I. **a** Δf1, **b** Δf2, and **c** ΔP12

ΔF_2, and ΔP_{12} obtained using the FA algorithm were 14.5 s, 14.5 s, and 19.0 s, which was better than the results of 16 s, 16 s, and 19 s using GSA.

The Second Case Study: We looked at area 1 with load increments up to 0.01 p.u. and area 2 with load increments for up to 0.02 p.u. The PID controller tuned parameters were obtained using these two strategies. The performance of the three system variables ΔF_1, ΔF_2, and ΔP_{12} was evaluated by utilizing the proposed approaches in response to the perturbation step load change. Table 3 summarizes the PID controller's tuned parameters. Table 4 also summarizes the settling time and peak overshoot for system variables. Figure 3 depicts the dynamic response to perturbation step load for each system variable.

The settling times for Case Study II of ΔF_1, ΔF_2, and ΔP_{12} obtained using FA were 12 s, 12 s, and 15 s, which were better than the results of 13 s, 13 s, and 17 s obtained using GSA. In terms of settling times, it can be seen that the FA optimization methodology outperformed the GSA optimization methodology.

Table 3 PID controller parameters being fine-tuned utilizing various optimization techniques—case study II

Optimization technique	K_{P1}	K_{I1}	K_{D1}	K_{P2}	K_{I2}	K_{D2}	ITAE
FA	4.2471	5.000	0.7984	1.2245	3.9482	1.2358	0.0686
GSA	5.0000	5.00	0.0010	0.0010	2.6407	0.0010	0.0830

Optimization technique	States variables	Over-shoot	Settling time
FA	ΔF_1	−0.012	12
FA	ΔF_2	−0.006	12
FA	ΔP_{12}	−0.0009	15
GSA	ΔF_1	−0.013	13
GSA	ΔF_2	−0.019	13
GSA	ΔP_{12}	0.0015	17

Table 4 shows the impact of various optimization approaches on system state variables in case study II

Fig. 3 Dynamic behaviors of the system case study II. **a** ΔF_1, **b** ΔF_2, and **c** ΔP_{12}

6 Conclusions

The work looked at the difficulties of using the LFC in MAPS with various sources. We explored a multi-source, two-area power system. By minimizing ITAE performance indices, the optimization methodologies were used to optimize the parameters of PID controller. In both sections, the performance of the system was assessed with perturbation step load modification. The settling times for Case Study I obtained using the FA were 14.5 s, 14.5 s, and 16 s, compared to 16 s, 16 s, and 19 s using GSA. Similarly, the settling times for Case Study II obtained using the FA were 12 s, 12 s, and 15 s, compared to 13 s, 13 s, and 17 s for GSA; even though the settling

time is a more desirable statistic than overshoot/undershoot, the FA for tie-line power flow was determined to have the least overshoot/undershoot for a case study I and II. Finally, it was found that the FA outperformed the GSA. In contrast to the current study, which used a PID controller, the authors are interested in investigating the effects of various controllers on the performance of the MSPS in the future.

Appendix A

The following are typical values for the system under consideration:

FA Parameters:– No. of fireflies: 25, α(randomness) = 0.5, β0 = 0.2, γ(absorption) = 1, No. of Iteration: 30.

GSA Parameters:– No. of populations: 25, G0 (gravitational constant) = 100, α = 20, No. of iterations: 30.

References

1. S. Kumari, G. Shankar, Maiden application of cascade tilt-integral–tilt-derivative controller for performance analysis of load frequency control of interconnected multi-source power system. IET Gener. Transm. Distrib. **13**(23), 5326–5338 (2019)
2. P.N. Topno, S. Chanana, Load frequency control of a two-area multi-source power system using a tilt integral derivative controller. J. Vib. Control **24**(1), 110–125 (2018)
3. M. Tavakoli et al., Load-frequency control in a multi-source power system connected to wind farms through multi terminal HVDC systems. Comput. Oper. Res. **96**, 305–315 (2018)
4. K. Lu et al., Constrained population extremal optimization-based robust load frequency control of multi-area interconnected power system. Int. J. Electr. Power Energy Syst. **105**, 249–271 (2019)
5. P.K. Sahoo et al., Multi-verse optimized fractional order PDPI controller for load frequency control. IETE J. Res. 1–14 (2020)
6. D. Guha, P.K. Roy, S. Banerjee, Whale optimization algorithm applied to load frequency control of a mixed power system considering nonlinearities and PLL dynamics. Energy Syst. **11**(3), 699–728 (2020)
7. K.O.M Charles Hubert, Understanding interphase power controller: a description. J. Electr. Eng. Electron. Control Comput. Sci. **6**(3), 19–24 (2020)
8. S.A. Ahmed, Mohamed, Performance analysis of power quality improvement for standard IEEE 14-bus power system based on FACTS controller. J. Electr. Eng. Electron. Control Comput. Sci. **5**(4), 11–18 (2019)

Random Forest Regression-Based Fault Location Scheme for Transmission Lines

Maanvi Bhatnagar, Anamika Yadav, and Aleena Swetapadma

Abstract The location of the fault is a very important issue with electric power systems, as it allows the system to be isolated as soon as possible, and to be recovered as quickly as probable. This allows electric equipment to function without an overload and ensures that buyers are satisfied. This paper proposes a random forest (RF) and Teager-Kaiser energy operator (TKEO)-based fault location scheme tested using an IEEE 14-bus system. The Teager energy of both voltage and current signals of pre- and post-fault signals has been evaluated and given as an input to the RF regressor modules. For different types of faults, four regressor models were developed. Testing of the proposed scheme under a variety of fault conditions has demonstrated the ability of the scheme to accurately determine the fault site. This fault location scheme retains its accuracy even if there are changes in fault characteristics such as fault initiation angle and fault resistance. Another advantage of this scheme is its ability to determine the location of high impedance faults (HIF) accurately. The absolute error in fault location estimation is well within 1 km for most of the test cases.

Keywords Random forest regressor (RFR) · Teager-Kaiser energy operator (TKEO) · High impedance faults (HIF) · Fault location estimation

1 Introduction

It is becoming more common for transmission grids to operate close to the limits of their stability. Due to the large topographical area covered by transmission lines, they are susceptible to faults because of short circuits, bird strikes, thunderstorms and lightning. There are times when a fault lasts a short time before the system returns to

M. Bhatnagar (✉) · A. Yadav
Department of Electrical Engineering, National Institute of Technology, Raipur, India
e-mail: maanvib93@gmail.com

A. Yadav
e-mail: ayadav.ele@nitrr.ac.in

A. Swetapadma
School of Computer Engineering, KIIT Deemed to Be University, Bhubaneswar, India

normal operating conditions. These types of faults are temporary in nature. Another type of fault occurs when a short circuit remains for a longer period of time until it is recognized and repaired. The failure to clear temporary faults eventually makes them permanent in nature sooner or later. In addition to these faults, other types of faults, including high impedance faults (HIFs), are a common phenomenon in these lines. The system can be seriously affected if these faults go undetected [1]. Protective relays ensure that if a transmission line is faulted, it will separate the faulted area. Because of this, the rest of the grid comes under immense stress. In such a situation, the maintenance team should be able to determine the malfunctioning component and repair the damages associated with the fault as rapidly as possible [2]. A precise and timely fault location thus plays a key role in power system stability and operation. This is also essential for the well-being of power paraphernalia and for customer satisfaction.

There have been several studies conducted that used a variety of methods for detecting fault locations within the transmission system. The traveling wave-based technique determines the fault location as a result of the propagation time of the traveling wave following a fault in the transmission line [3, 4]. Despite the fast response time and high precision of this method, the accuracy is dependent on the exact estimation of when a surge arrives. For detecting fault location, impedance-based methods require voltage and current signals as well as sequence impedance (positive, negative, zero). These algorithms can be classified as one-ended [5] or two-ended [6] depending on the nature of the input signals. There are several reasons for errors in using this technique, including zero-sequence mutual effects, parameter uncertainty in transmission lines, unbalanced load flows, the influence of FACT devices, and measurement errors in transmission lines. A variety of artificial intelligence methods also exist, including radial basis function neural network (RBFNN) [7], wavelet transforms (WT) [8], Kalman filtering [9], artificial neural network (ANN) [10] and support vector machine (SVM), [11] among many others. These approaches are based on analyzing voltage and current variations. A lot of advancement has been made in this field due to improvements in digital technologies. All of the above-stated methods necessitate large training data and training time. This increases the computational burden on the system. These methods also depend on the changes in system frequency.

Upon detailed investigation of the previously reported literature work, it has been observed that it is not easy to locate faults in transmission networks because of their long length. Also, the research conducted in the field of detection of fault location in the case of HIFs is also limited. It has also been observed that none of the authors has considered the effect of changes in transmission line parameters, fault resistance and fault inception angle while estimating the fault locations. Moreover, the error in locating the faults is very large in a few case studies. A system that circumscribes these disadvantages has been developed in this work in order to overcome these difficulties. In this study, a Teager-Kaiser energy operator (TKEO) and Random Forest regressor (RFR)-based approach have been proposed for the identification of fault location which takes into consideration all the previously stated disadvantages.

2 Design of Fault Location Estimation Method

RFR-based fault location estimation algorithm in case of low impedance fault (LIF) and high impedance faults (HIF) has been designed with the help of the steps discussed in Fig. 1. The three-phase voltage and current signals are recorded from the designated buses as discussed later in the subsequent sections. The features from these signals are then computed with the help of TKEO. The energy features are then given as an input to the RFR which gives the final decision about the estimated fault location.

2.1 Power System Network

A 14-bus IEEE transmission system has been used for validation and testing of the proposed scheme as shown in Fig. 2. The 14-bus test case is an approximate model of the American Electric Power system [12]. From [13], the 14-bus system data has been taken. MATLAB/Simulink has been used to simulate the IEEE bus system, while the Python platform has been used to implement the fault location algorithm. On the lines that connect Bus 1 and Bus 5, all fault simulation studies have been
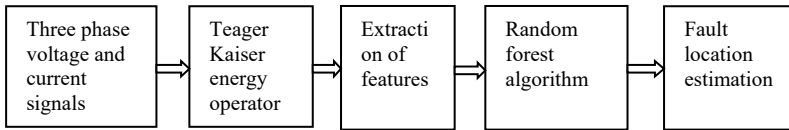

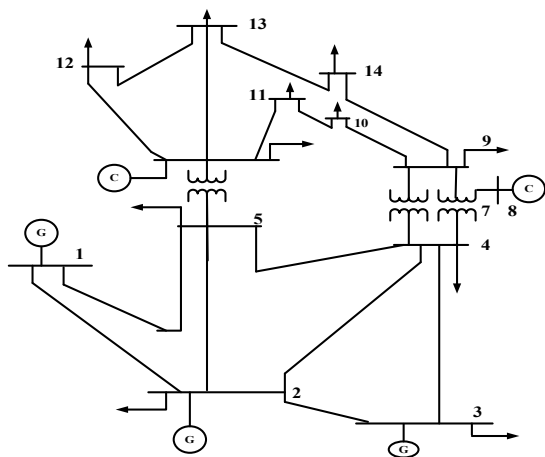**Fig. 1** Flowchart of the proposed methodology

Fig. 2 IEEE 14-bus test system

Table 1 Fault parameters for generating training and testing dataset

Parameter variation	Training dataset	Testing dataset
HIF (LG, LLG, LLLG)	Fault resistance varied in the range 40–140Ω with steps of 10 Ω	Fault resistance varied in the range 45–145Ω with steps of 10 Ω
LIF (LG, LLG, LLLG, LL)	Fault resistance varied in the range 0–40Ω with steps of 2Ω	5Ω,15Ω, 25 Ω, 35Ω
Fault inception angle (FIA)	Random angles between 21° and 357° at even kms of fault location	63°, 105° and 315° at odd kms of fault location km
Change in power flow angle (PFA) (°)	±1, ±3, ±5, ±7, 9, 11, 13	−2, −4, 6, 10

performed, and the corresponding voltage and current signals are analyzed for the development of the scheme.

2.2 Feature Extraction Using Teager-Kaiser Energy Operator

Current and voltage signals were subjected to TKEO to obtain discriminatory features. The TKEO expression estimates the energy associated with a given sample. Hence instantaneous energy of the discrete signals is obtained using TKEO. The Teager energy of signals has been calculated for one cycle of post- and pre-fault signal data. The 14-bus system operates on a 60 Hz power frequency. The sampling frequency used for the proposed algorithm is 1 kHz. For the purpose of testing and training data generation, various types of LIFs and HIFs have been simulated the details of which are presented in Table 1.

2.3 Design of Random Forest Regression

In RFRs, sets of decision trees (DT) are used to perform an ensemble average to obtain the finest estimation outcomes. The DTs are created by focusing on the feature column that optimizes the objective function, for instance, information gain or Gini index at every split. The splits are repeated at each node until the number of samples in each node falls below a predefined threshold. This is regarded as a form of bagging. The final nodes in DT represent the outcome of the DT. RF estimates are then calculated by averaging the estimations from every decision tree. The RF regression schematic is shown in Fig. 3.
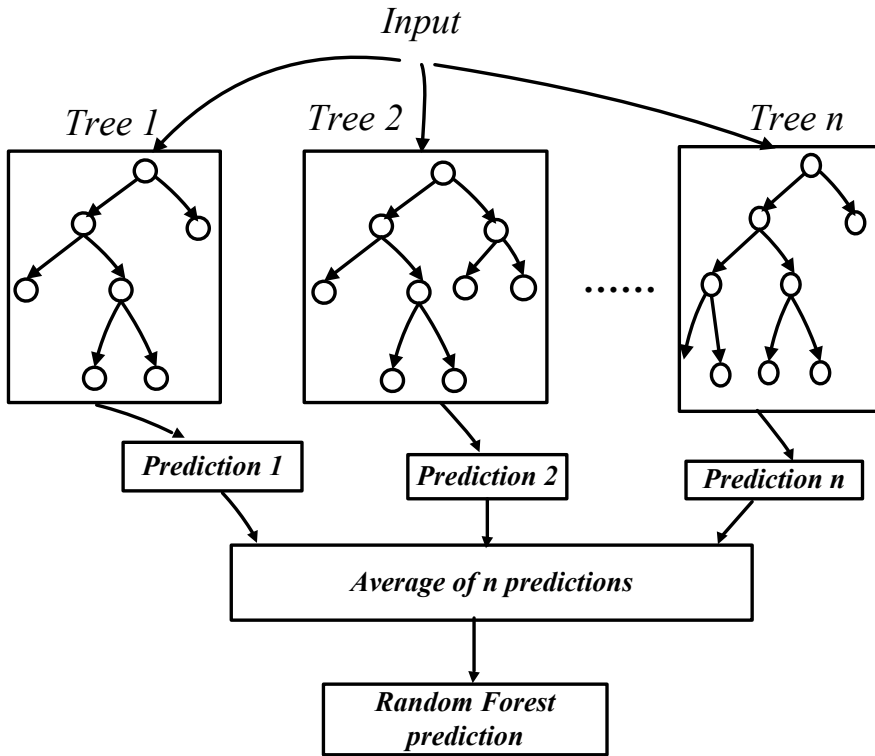
Fig. 3 RFR schematic diagram

2.3.1 Fault Location Estimation Scheme

The location estimation of faults is carried out by four types of RF modules, i.e., one each for LG, LLG, LLLG and LL fault types. The RF algorithm used in this article is performed as a regression technique to assist in locating fault locations, and it entails two phases: training and testing. A set of input datasets is given to the RF-based location module to learn hidden relationships between the feature vectors. By comparing with the input feature space, it predicts the fault location of unknown fault samples in the test stage. For training fault data, signals captured at even kilometers have been analyzed, and for testing fault data, data obtained at odd kilometers have been investigated for the total line length. The various hyperparameters used for the generation of fault location modules are given in Table 2. The performance of these modules is evaluated with the help of an absolute error and R-Squared (R^2) value**.**

Table 2 Hyperparameters for different fault location modules

Module	Hyperparameters
LG	Number of trees = 300, max_features = auto
LLG	Number of trees = 200, max_features = log2
LLLG	Number of trees = 200, max_features = sqrt
LL	Number of trees = 100, max_features = sqrt

3 Results and Discussion

Various fault cases are examined with the proposed RFR method. Based on Eq. (1), the absolute fault location error is calculated.

$$Absolute\ Error(km) = |\text{Actual fault location} - \text{Predicted fault location}| \quad (1)$$

Another parameter used for justifying the efficacy of the modules is the R^2 value. It characterizes the fraction of variance of response variables apprehended by the module used for regression. It is given as

$$R^2 = 1 - \frac{SSE}{SST} \quad (2)$$

Here, SSE is the sum of squared residual error and SST represents the sum of squares total.

3.1 High Impedance Fault Detection

During a HIF, an electrical conductor accidentally comes in contact with a highly resistive medium. The resulting fault current is extremely small in magnitude. A fault current of such magnitude would be relatively close to the normal current drawn by the load. This condition causes conventional overcurrent relays to become blind to HIFs. These faults are highly dangerous and may cause harm to the people or result in undesired fire hazards. Therefore, it is imperative to know the location of these faults in order to ensure the healthy operation of the system. Because they are directly linked to human safety, detection of HIF faults involving the ground is of utmost importance. Table 3 demonstrates the results for location estimation during HIFs. Different types of faults such as LG (CG), LLG (ABG) and LLLG (ABCG) have been considered for demonstration of results. The absolute error as observed in most of the cases is well within 1 km. Therefore, it can be concluded that the proposed scheme is able to locate the HIF locations effectively.

Table 3 Fault location estimation and corresponding absolute error for HIFs

Fault type	Actual location (km)	Estimated location (km)	Absolute error (km)
CG	17	17.9	0.9
	29	29.8	0.8
ABG	9	8.78	0.22
	25	24.10	0.9
ABCG	17	18.356	1.356
	77	77.299	0.299

Table 4 Fault location estimation changing resistance values for LIFs

LIF fault type	Resistance (Ω)	Actual location (km)	Estimated location (km)	Absolute error (km)
AG	5	3	3.953	0.953
ACG	25	13	13.39	0.61
ABCG	35	25	23.91	1.09
BG	15	19	18.34	0.66

3.2   Low Impedance Fault Detection

LIFs are normally short circuits resulting from bolted faults. To validate the proficiency of the scheme, different fault cases have been discussed in the subsequent sections.

3.2.1   Fault Resistance

LIFs give rise to very high currents due to the small resistance path offered by them to the current signals. To study the effect of varying fault resistances on the detection of fault location, different case studies have been conducted the result of some of which are tabulated in Table 4. The resistance values have been varied between 5 and 35 Ω. It is clearly seen from the results obtained that the variation in fault impedance does not affect the system performance, and it is still able to accurately determine the fault location with the least amount of error. The value of absolute error is well within 1 km for different cases.

3.2.2   Power Flow Angle

Changes in power system operating conditions occur periodically. Consequently, PFAs fluctuate. In order to evaluate the proposed scheme, its ability to locate faults in the event of a change in PFA has been scrutinized. The original PFA of the system

Table 5 Fault location estimation and absolute error evaluation for changing PFAs

Fault type	PFA (°)	Actual location (km)	Estimated location (km)	Absolute error (km)
AG	−2	3	2.433	0.567
ABG	−4	5	4.629	0.37
AB	4.7	7	6.259	0.74
ABCG	10	27	26.73	0.269

Table 6 Fault location estimation in case of different inception angles

LIF fault type	Inception angle $(\varnothing_i^\circ)$	Actual location (km)	Estimated location (km)	Absolute error (km)
AB	63	5	5.98	0.02
ACG	105	31	30.33	0.67
ABCG	105	5	4.08	0.92
BC	315	21	20.4	0.6

under study is 3.778 degrees. As can be seen in Table 5, power flow angles were changed to −2, −4, +4.7 and +10° in comparison to the initial value, and the results were evaluated. It is evident from the attained results that the absolute error in different cases as mentioned in the table is well under 1 km thus proving and confirming that the scheme doesn't get affected by changes in PFA either.

3.2.3　Fault Inception Angle

There is no way to know ahead of time, or to put it another way, the angle at which the fault will begin in transmission lines. Ideally, the fault location algorithm should be capable of estimating the location of faults arising at any fault initiation time or angle Therefore, considering this, the system is tested for shunt faults occurring at various inception angles. Some of the results are illustrated in Table 6. The value of absolute error in each of the exemplified cases is found to be less than 1 km thereby justifying the efficiency of the scheme for locating faults in the system. A further advantage of this RFR-based scheme is that it is robust to changes in fault inception angles.

3.3　Overall Performance of the System

The overall performance of the RF- and TKEO-based fault location estimation technique has been evaluated with the help of R^2 value. R^2 is a statistic that measures how closely the data match the fitted regression line. In simple words, it describes

Table 7 R^2 value for different RF modules

Module	LG	LLG	LLLG	LL
R^2 value	0.994	0.991	0.979	0.999

the goodness of fit for any regression model. This measure gives an estimation of the magnitude of the association between the model and the response variable. It indicates how closely the regression predictions correspond to the actual data points. The different values of R^2 for various RFR modules is shown in Table 7. It can be observed that all the models exhibit a R^2 value between 0.97 and 0.99. Regression models with a higher R^2 value are generally more accurate. An R^2 value of 0.97 indicates that 97% of the data fit the regression model. Hence, all the regression models are fairly efficient in estimating the location of the fault.

4 Conclusion

For an IEEE 14-bus transmission network, this paper describes TKEO and RFR fault location estimation techniques. The scheme is set up to test a variety of shunts and phases to phase faults of low impedance and high impedance types. The performance of the proposed scheme is analyzed based on the dataset generated by changing transmission line parameters, location and angle of fault initiation and changes in fault resistance for LIF along with HIF. RF fault location identification modules are fed by energy operator features of the voltage and current signals. Training and testing of the RF modules have been conducted with one cycle of post- and pre-fault data. All the tested fault cases showed an absolute error within 1 km in fault location estimation. This scheme is able to identify HIF location with much ease, and its accuracy is not affected by changes in fault parameters. In addition, the proposed method uses current and voltage signals obtained from a single bus terminal to locate the fault without having to know the fault type, offering another advantage over other methods requiring the fault type to be known beforehand.

References

1. M. Bhatnagar, A. Yadav, Fault detection and classification in transmission line using fuzzy inference system, in *5th IEEE International Conference on Recent Advances and Innovations in Engineering (ICRAIE)*, pp.1–6. IEEE, India (2020)
2. A. Swetapadma, A. Yadav, Fuzzy based fault location estimation during unearthed open conductor faults in double circuit transmission line, in *Information Systems Design and Intelligent Applications,* pp. 445–456. Springer, New Delhi (2016)
3. M. Khalili, F. Namdari, E. Rokrok, Traveling wave-based protection for TCSC connected transmission lines using game theory. Int. Trans. Electr. Energy Syst. **30**(10), 12545 (2020)

4. A. Abu-, M.I. Mosaad, S. Mir, Voltage–current technique to identify fault location within long transmission lines. IET Gener. Transm. Distrib. **14**(23), 5588–5596 (2020)
5. A. Abu-, S. Mir, A new on-line technique to identify fault location within long transmission lines. Eng. Fail. Anal. **105**, 52–64 (2019)
6. S. Mishra, S. Gupta, A. Yadav, A novel two-terminal fault location approach utilizing traveling-waves for series compensated line connected to wind farms. Electr. Power Syst. Res. **198**, 107362 (2021)
7. K.H. Mallick, B. Patel, P. Bera, WPD and RBFNN based fault location estimation on TCSC based series compensated transmission line, in *International Conference on Computational Intelligence.* Communications, and Business Analytics. (Springer, Singapore, 2018), pp. 425–433
8. M. Dashtdar, Fault location in the transmission network using a discrete wavelet transform. Am. J. Electr. Comput. Eng. **3**(1), 30–37 (2019)
9. R. Fan, Y. Liu, R. Huang, R. Diao, S. Wang, Precise fault location on transmission lines using ensemble Kalman filter. IEEE Trans. Power Deliv. **33**(6), 3252–3255 (2018)
10. A. Swetapadma, A. Yadav, An artificial neural network-based solution to locate the multilocation faults in double circuit series capacitor compensated transmission lines. Int. Trans. Electr. Energy Syst. **28**(4), e2517 (2018)
11. C. Fei, G. Qi, C. Li, Fault location on high voltage transmission line by applying support vector regression with fault signal amplitudes. Electr. Power Syst. Res. **160**, 173–179 (2018)
12. http://www.ee.washington.edu/research/pstca/pf14/pg_tca14bus.html. Accessed 9 Sept 2020
13. I.I. Alnaib, O.S. Alyozbaky, A. Abbawi, A new approach to detecting and classifying multiple faults in IEEE 14-bus system. Eastern-Eur. J. Enterpr. Technol. **5**(8), 107 (2020)

Islanding Detection in Distributed Generation System Using MLPNN and ELPID Methods

Sushree Shataroopa Mohapatra [ID], **Manoj Kumar Maharana, Abhilash Pradhan, P. K. Panigrahi, and R. C. Prusty**

Abstract Renewable energy generation techniques have received a lot of attention and development in recent years. As a key source of renewable energy, distributed generation (DG) is effective. These contrasting assets are able to combine as a hybrid energy system with a micro-grid, delivering electric power with the option of cooling or heating. The biggest issue with this type of DG is islanding. When DG deliveries power to loads once severing from the grid, islanding occurs. For islanding detection of distributed generation, the Eradicate Liability Passive Islanding Detection (ELPID) methodologies of Point of Common Coupling (PCC), Rate of Change of Frequency (ROCOF), and Rate of Change of Frequency (ROCOF) are utilized in this study.

Keywords Distributed generation (DG) · Eradicate liability passive islanding detection (ELPID) · Micro-grid · Islanding detection · Non-detection zone · Threshold · Artificial neural network · Decision tree · Multilayer perceptron neural network

S. S. Mohapatra (✉) · M. K. Maharana
School of Electrical Engineering, KIIT Deemed to Be University, Bhubaneswar, India
e-mail: mshataroopa@gmail.com

M. K. Maharana
e-mail: mkmfel@kiit.ac.in

A. Pradhan
GIET University, Gunupur, Odisha, India

P. K. Panigrahi
School of Engineering and Technology, GIETU, Gunupur, Odisha, India
e-mail: pkpanigrahi@giet.edu

R. C. Prusty
Department of Electrical Engineering, VSSUT, Burla, Odisha, India

1   Introduction

Renewable energy production techniques have received a lot of attention and development in recent years. Greenhouse gas emissions from renewable energy are lower than those from fossil fuels [1]. Distributed generation (DG) is an efficient source of renewable energy. These diverse assets can be linked together to form a hybrid energy system with a micro-grid, giving both electric power and cooling or heating alternatives [2]. The efficiency of renewable energy has greatly improved. DG approaches are also encouraged in a micro-grid. DG allied unswervingly to the main grid has a substantial adverse impact as most distributed resources are spasmodic [3]. On the one hand, these complementarities allow the micro-grid to compensate for the main grid's negative effects. On the other hand, different types of scattered resources, governable load, and overall load can be blended to reduce grid reliability [4, 5]. As a result, the micro-grid is gaining popularity and rapidly expanding. To put it another way, the micro-grid is an important part of long-term energy development. Different tactics are employed when a micro-grid is grid-connected or islanding [6].

Islanding is the most serious problem with this sort of DG. When DG delivers power to loads after severing from the grid, this is referred to as islanding. Islanding poses a risk to field personnel and equipment because service personnel are unaware that the frame-up is linked and provided with DG close by [7]. Grid failures, the inadvertent germinal of circuit breakers (CB) at the grid, the premeditated germinal of CB for preservation, human error, and natural occurrence are the primary causes of inadvertent islanding. It is vital that the DG source be turned off within 2 s, as fluctuations in voltage (V), frequency (f), current (I), THD, Active power, and Reactive powers that exceed the requirements may be harmful to the consumer loads as well as the DG source [8].

Local and remote techniques are used to detect islanding; techniques used locally are further categorized as Passive, Active, or Hybrid [9, 10]. Phase Angle difference, Rate of change of voltage (ROCOV), Rate of change of reactive power (ROCORP), Over-under voltage/over-under frequency (OUV/OUF). Certain Passive techniques have a high NDZ and when the power imbalance is modest or absent, it is difficult to identify islanding [11]. When a PID technique bombs to sense islanding, the NDZ is the range of values. A combination of two passive parameters, such as ROCOF and Power Output, ROCOV and THD, ROCOV and power factor, ROCOV and ROCOF, and ROCOAP in conjunction with ROCORP, is used to reduce NDZ. These solutions will reduce the NDZ to a lower level than single-parameter passive techniques [12].

SCADA, on the contrary, detected islanding using data from CB auxiliary links [4]. Alternative monitoring devices, transmitters, and receivers are more expensive and require more effort, making them difficult to implement. Active methods identify islanding by introducing a fracas at PCC for a few sequences and analyzing the output signal variations. Local shocks are absorbed by the grid-connected system, so substantial fluctuations aren't visible. The output signal, on the other hand, shows larger changes once the system is landed. Although Active methods are more proficient than Passive methods, they have a negative impact on power quality [13].

Machine learning detection strategies use huge data samples from non-islanding and islanding occurrences to detect islanding. Common techniques like ANN, DTM, and SVM are utilized to discriminate between islanding and non-islanding occurrences. Regional properties like voltage, frequency, current, phase angle, and THD are scrutinized at the PCC, and islanding is perceived if deviations surpass a specific threshold. These methods have a higher NDZ than active and hybrid methods [14].

In recent years, several different forms of IDMs for DG units have been proposed. The onset of an islanding state should be noticed within 2 s, according to IEEE Std. 1547. The three forms of IDMs are passive detection techniques (PDTs), active detection techniques (ADTs), and hybrid detection techniques (HDTs). Voltages, currents, and frequency readings from the Point of Common Coupling are used by the PDMs (PCC) [15]. To identify the islanding operating condition, several passive procedures have been developed, including over/under voltage and frequency deviation, rate of change of frequency (ROCOF), over system power, harmonic monitoring, phase jump detection (PJD), and voltage vector shift. In the case of a high utility voltage, a low grid impedance ensures that the required THD limits are met. This can lead to incorrect detections in balanced load and power settings, as well as during significant load/generation variations [16].

2 Modeling of the Problem

2.1 Proposed Algorithm

Integrating distributed generation (DG) capacity into electric power systems can improve energy security and reliability while decreasing environmental impact. Inadvertent islanding is one of the most serious problems with DG integrations. A novel approach to detecting liability passive islanding was presented, which takes dynamic load behavior into account. It is computed for the observed voltage signal in the presence of noise, and the corresponding derivative of resistance is taken as the index for frequency-controlling islanding detection. As a result, the calculations for this study cover three major areas: Data Generation, Feature Extraction, and Islanding Detection. In the Distributed Generation system, classifications are utilized to perceive and organize islanding and non-islanding events.

Data Generation

Solar photovoltaic (PV) power that is distributed and grid-connected has its own set of advantages and disadvantages. PV cells are used as a basis for dispersed generation in this study. Small PV systems (5–25 KW) generate power for on-site use and link to low-voltage transformers on the electric utility system in distributed solar applications. Distributed PV can help reduce transmission line losses, improve grid resilience, reduce generation costs, and lessen the need for new utility generation capacity. When correctly equipped and calibrated, distributed PV systems can also

help to reduce the reliability issues that come with providing standby power during electric utility disruptions or outages.

Feature Extraction

The technique of obtaining the threshold amount of dispersed generation to grid connection parameters is known as feature extraction. The suggested islanding detection technique's threshold amount is determined by examining various power system operating circumstances. The threshold resolution is established on the notion that it must recognize the islanding situation while ignoring non-islanding events that occur frequently. The research embraces the islanding situation with a zero-power imbalance amid DG and load. The power system experiences a variety of non-severe disturbances for which islanding is not possible. A 50% surge in RL load, a disparity in grid frequency between 49.5 Hz and 50.2 Hz, a disparity in the grid's X/R ratio between 5 and 15, and PQ conflicts (e.g., a 20% rise/decline in rated voltage in swell/sag conditions), among other things, are all taken into account. Because the unbalanced load is always varying, it is critical to evaluate the system's usual level of voltage unbalance. As a result, for DG's autonomous operation, a maximum of 3% load unbalance is allowed. All of the aforementioned conditions are taken into account when determining the threshold value. The threshold voltage in the negative sequence is 2 V, and the threshold voltage in zero-sequence is 0.2 V, after which the pattern sends a trip signal to the CB. The threshold situation in ELPID techniques needs to be prudently determined to avoid mal operation in the course of network interruptions. When the threshold is set too low, nuisance tripping occurs, while islanding may go unnoticed if the threshold is set too high. In these methods, a trade-off should be established in order to have a sufficient threshold (Fig. 1).

Islanding Detection using ELPID

Eradicate Liability is a scheme that purposes to exclude liability. Indigenous parameters like voltage and frequency are censored at the PCC using passive methodologies, and if deviations exceed a particular threshold islanding is identified. Passive IDMs are required for grid-connected PV inverters, which bases the PV inverter to discontinue delivering power to the grid if the voltage amplitude or frequency of the PCC between the local load and the grid deviates from prescribed limits.

The over-under voltage and over-under frequency protection (OUV/OUF) procedure is an ELPID that identifies islanding when the system's voltage or frequency overdoes a certain range. The NDZ of the OUV/OUF approaches presently employed for protection in recent PV inverters was chosen for all of the simulated islanding instances. The frequency is computed in this paper using the PCC voltage. The zero-crossing slant is used to estimate the frequency range first. It is then precisely estimated using the least-squares error (LSE) approach.

Artificial Neural Network

The ANN approach is employed in this study to diagnose voltage and frequency coupling that was observed by ELPID. The discovered islanding issue was diagnosed

Fig. 1 Flowchart of proposed methodology
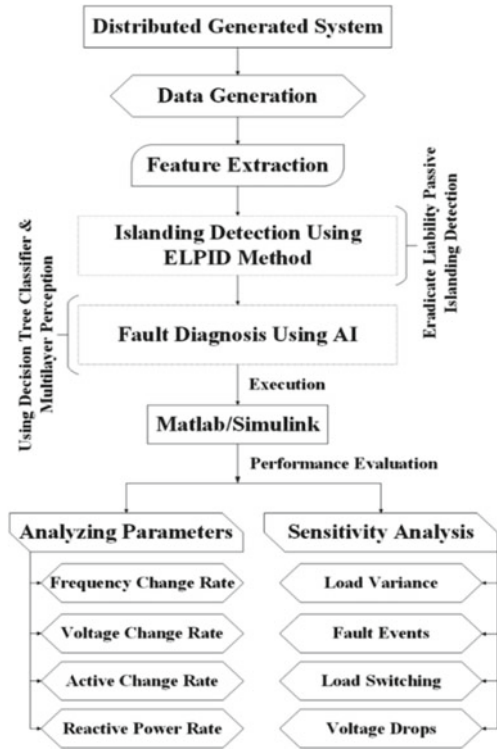
using an Artificial Neural Network (ANN). Decision Tree Classifier and Multilayer Perceptron are two classification models that are employed. Decision trees classify information along numerous branches and organize it in a tree-like shape. Each branch represents a different path. This structure may be used to anticipate the values of data attributes. A multilayer perceptron (MLP) feedforward artificial neural network (ANN) is a form of ANN where MLP is an ambiguous term which specifically refers to networks composed of several layers of the perceptron (Fig. 2).

2.2 Mathematical Model

The equation for the main signal can be considered as

$$V(t) = V_p \sin(wt)[wt + \theta) \tag{1}$$

where V(t) is a Measured voltage (V); ω is an Angular speed (rad/s); V_p is a Peak voltage (V); Θ is an Angle (rad); t is Time (s).

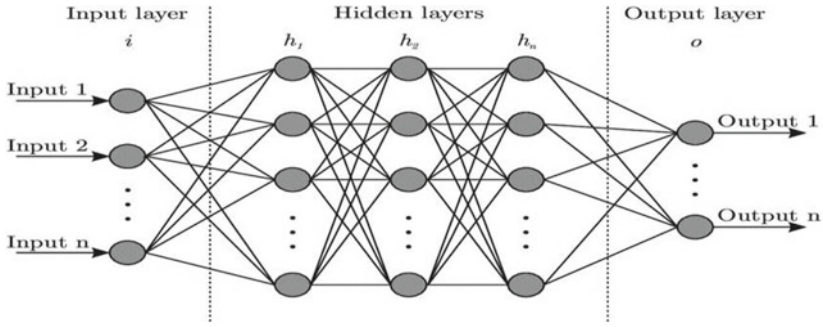Using sinusoidal extension followed by Taylor's series extension

Fig. 2 Architecture of an artificial neural network

$$V(t) = V_p \cos \theta \sin \omega t + V_p \cos \omega t \sin \theta \qquad (2)$$

$$
\begin{aligned}
V(t) = {}& \sin(\omega t) V_p \cos \theta + (\Delta \omega) t \cos[(\omega t)] V_p \cos \theta + \cos \omega t \, V_p \sin \theta \\
& - (\Delta \omega) t \sin(\omega t) V_p \sin \theta \\
& - \frac{t^2}{2} \sin(\omega t)(\Delta \omega^2) \cos \theta - \frac{t^2}{2} \cos(\omega t)(\Delta \omega^2) \sin \theta
\end{aligned} \qquad (3)
$$

where $\Delta \omega =$ change in angular speed.

Since in the above equation a total of 6 unidentified measures are there, at least 7 equations are required to calculate the unidentified measures using the LSE method. Angular speed variation can be estimated by separating the identified and unidentified measures of Eq. (5). So the equation can be rewritten as

$$V(t) = S_{11}X_1 + S_{12}X_2 + S_{13}X_3 + S_{14}X_4 + S_{15}X_5 + S_{16}X_6 \qquad (4)$$

$$\Delta \omega = \frac{X_2 + X_4}{X_1 + X_3} \qquad (5)$$

After adding the change in frequency achieved from the zero-crossing to the basic frequency, the final frequency can be calculated using the formula

$$f = f_{zero} + \frac{\Delta \omega}{2\pi f_0} \qquad (6)$$

At the Point of Common Coupling (PCC), Voltage (V) and Current (I) have been dignified with the help of a capacitor voltage transformer (CVT) and current transformer (CT). The LSE algorithm used above measures Voltage (V) and Current (I) phase angle (Θ) and frequency (F) of the DG.

Power/Voltage/Frequency Misalliance boundaries along with their inception values can be found using the below equations

$$\left(\frac{V}{V_{\max}}\right)^2 - 1 \le \frac{\Delta P}{P} \le \left(\frac{V}{V_{\min}}\right)^2 - 1 \tag{7}$$

$$Q_f\left(1 - \left(\frac{f}{f_{\min}}\right)^2\right) \le \frac{\Delta Q}{P} \le Q_f\left(1 - \left(\frac{f}{f_{\max}}\right)^2\right) \tag{8}$$

where $V_{\max}$, $V_{\min}$, $f_{\max}$, and $f_{\min}$ represent the extreme and least values of Voltage (V)/Frequency (F) with their threshold limits of the relay in the DG; ΔP and ΔQ characterize the power misalliances earlier than the main grid suspension; Q_f is the load quality factor generally measured to outline parallel RLC load. The marginal limits of Non-Detection Zone (NDZ) can be demarcated as well as the zone of acute and non-acute operating conditions can be favored using the equations defined.

The recommended Islanding detection method can be embodied using the Decision tree classifier model as follows:

$$X = \{X_1, X_2, \ldots, X_n\}^T \tag{9}$$

$$X_i = \left\{X_{i_1}, X_{i_2}, \ldots, X_{i_j}, \ldots, X_{i_m}\right\} \tag{10}$$

$$Y = \{y_1, y_2, \ldots, y_n\} \tag{11}$$

$$E = \{(X_k, y_k), \quad k = 1, 2, \ldots, N\} \tag{12}$$

where X is a dimensional pattern vector. Xi is pattern vector of X; I is an feature variable of the pattern vector *xi*; *m* represents numbder of independent variables; Y is a dependent vector associated with X; $y1, y2, \ldots yn$ are dependent class variables of the vector Y; (X, Y) are jointly distributed random variables with dimensional vector denoting pattern vector and denoting the associated class vector; E is a vector of labeled credible events with a total number of N events.

3 Experimental Exploration

With the threshold values of each parameter, the suggested approach detects islanding. The previously indicated threshold values are the only values that may be used to identify islanding; if the standards are inside the threshold value, it perceives as non-islanding; if the values surpass the threshold value, the detection of islanding is conceded out. It was discovered with the help of the MATLAB/SIMULINK software tools.

Fig. 3 Irradiance-graph of 4 different PV cells
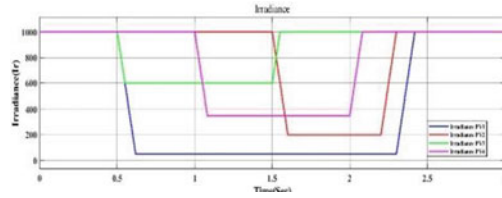
Result and Discussion

Islanding was identified with the help of the ANN technique, i.e., decision tree and multilayer perceptron to obtain the accuracy of islanding and anti-islanding in DG within the simulation time of 124.13 s in MATLAB with the help of 4 PV cells. As per IEEE 1547 standard, the islanding and re-closer setting should be noticed in less than two seconds. The time of detection is a crucial aspect in differentiating islanding prior to the re-action because the re-constant closer's time is often shorter than 500 ms. Furthermore, according to various grid codes, the DG should be able to operate in autonomous islanded mode indefinitely. As a result, the islanding is detected, allowing the DG to be disconnected or prepared to run in the new controller mode once the islanding has occurred (Figs. 3, 4, 5, 6, 7, 8, and 9).

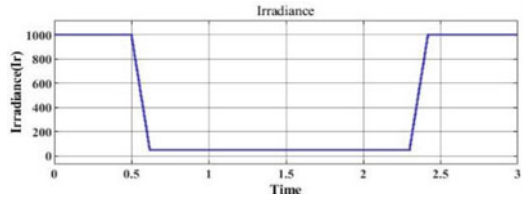**Fig. 4** Irradiance-graph of a photovoltaic cell
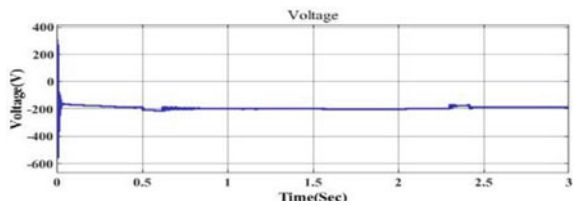

Fig. 5 Voltage-graph of a PV cell
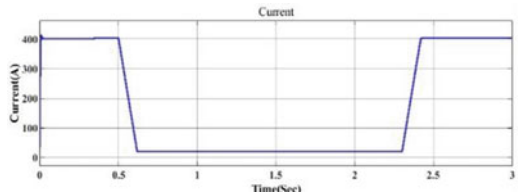

Fig. 6 Current-graph of a PV cell

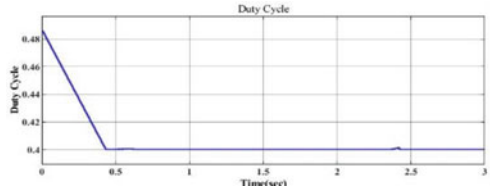**Fig. 7** Duty Cycle-graph for the PV cell

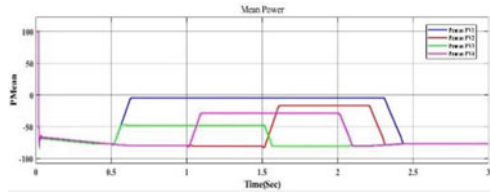**Fig. 8** Mean power-graph of 4 different PV cells

Fig. 9 Mean power-graph of a photovoltaic cell
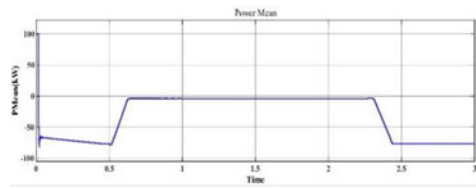
3.1 Research Highlights

The proposed method works well for active power mismatches (Fig. 10) and reactive power mismatches (Fig. 11), but it may fail to identify islanding for bigger mismatches, thus it's believed that it'll be used in conjunction with the PCC's Over/Under Voltage (OUV) and Over/Under Frequency (OUF) relays. The voltage
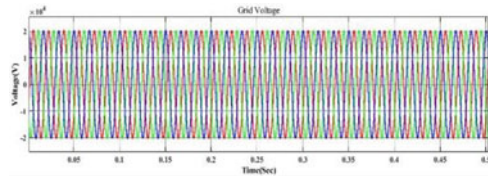
Fig. 10 Voltagegraph of a grid

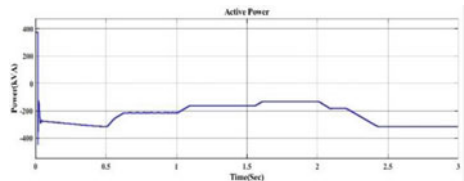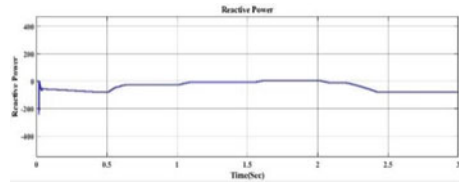**Fig. 11** Active power mismatch-graph

Fig. 12 Reactive power mismatch-graph

or frequency change in PCC is determined by the active and reactive power mismatch levels shortly before the utility circuit breaker. The result of active and reactive power mismatch with greater or smaller mismatches was obtained using a combination of OUF/OUV, ROCOF, ROCOV, and ROCPAD in the ELPID method. The previously mentioned threshold quantities are the restricted quantities used to sense islanding events; if the quantities are within the threshold limits, anti-islanding is diagnosed; nonetheless, if the readings surpass the thresholds, the islanding detection process is passed out (Fig. 12).

4 Conclusion

With the integration of micro-grid, scattered generating systems, renewable energy efficiency has skyrocketed. Because of its intermittent nature, distributed generation (DG) is an effective source of renewable energy. Because they are connected to a larger-scale electricity grid, the distributed energy resources (DERs) within the DG system serve a specific load and permit the sharing of abundant electricity. When a section is relocated, the DER may control the detachable portion; in this scenario, an "island" is created. When a segment of the electric power system is removed from the main power grid, this is known as islanding. The proposed technique in this work combines ELPID with several methodologies such as ROCOF, ROCOV, PCC, OUF/OVV, and ROCPAD to detect islanding and reduce the Non-Detection Zone. The proposed result for islanding detection using ELPID includes a flaw. To diagnose the frequency and voltage coupling identified by Artificial Neural Network, ELPID approaches such as Decision tree and Multilevel perceptron neural network are applied. MLP will diagnose the error based on the choice made by the decision tree classifier.

References

1. M.R. Alam, M.T.A. Begum, B. Mather, Islanding detection of distributed generation using electrical variables in space vector domain. IEEE Trans. Power Deliv. **35**(2), 861–870 (2019)
2. E.C. Pedrino, T. Yamada, T.R. Lunardi, de Melo Vieira Jr, J.C., Islanding detection of distributed generation by using multi-gene genetic programming-based classifier. Appl. Soft Comput. **74**, 206–215 (2019)

3. A. Shrestha, R. Kattel, M. Dachhepatic, B. Mali, R. Thapa, A. Singh, D. Bista, B. Adhikary, A. Papadakis, R.K. Maskey, Comparative study of different approaches for islanding detection of distributed generation systems. Appl. Syst. Innovat. **2**(3), 25 (2019)

4. A. Rostami, A. Jalilian, S. Zabihi, J. Olamaei, E. Pouresmaeil, Islanding detection of distributed generation based on parallel inductive impedance switching. IEEE Syst. J. **14**(1), 813–823 (2019)

5. M. Mishra, P.K. Rout, Fast discrete s-transform and extreme learning machine based approach to islanding detection in grid-connected distributed generation. Energy Syst. **10**(3), 757–789 (2019)

6. M.S. Kim, R. Haider, G.J. Cho, C.H. Kim, C.Y. Won, J.S. Chai, Comprehensive review of islanding detection methods for distributed generation systems. Energies **12**(5), 837 (2019)

7. A.A. Chandio, J.A. Laghari, S. Khokhar, S.A. Almani, A new islanding detection technique based on rate of change of reactive power and radial basis function neural network for distributed generation. J. Intell. Fuzzy Syst. **37**(2), 2169–2179 (2019)

8. B. Pancha, R. Shrestha, A.K. Jha, Islanding detection in distributed generation integrated Thimi-Sallaghari distribution feeder using wavelet transform and artificial neural network. J. Inst. Eng. **15**(2), 55–61 (2019)

9. C.R. Reddy, K.H. Reddy, Passive islanding detection technique for integrated distributed generation at zero power balanced islanding. Int. J. Integr. Eng. **11**(6), 126–137 (2019)

10. C.R. Reddy, K.H. Reddy, A new passive islanding detection technique for integrated distributed generation system using rate of change of regulator voltage over reactive power at balanced islanding. J. Electr. Eng. Technol. **14**(2), 527–534 (2019)

11. A.T. Kolli, N. Ghaffarzadeh, A novel phaselet-based approach for islanding detection in inverter-based distributed generation systems. Electr. Power Syst. Res. **182**, 106226 (2020)

12. M. Gholami, Islanding detection method of distributed generation based on wavenet. Int. J. Eng. **32**(2), 242–248 (2019)

13. C. Darab, R. Tarnovan, A. Turcu, C. Martineac, Artificial intelligence techniques for fault location and detection in distributed generation power systems, in *2019 8th International Conference on Modern Power Systems (MPS)*, pp. 1–4. IEEE (2019)

14. P. Nayak, A. Avilash, R.K. Mallick, Faster islanding detection of microgrid based on multiscale mathematical morphology. Int. J. Renew. Energy Res. (IJRER) **10**(2), 1005–1011 (2020)

15. C.R. Reddy, K.H. Reddy, K.V.S. Reddy, Recognition of islanding data for multiple distributed generation systems with ROCOF shore up analysis, in *Smart Intelligent Computing and Applications* (Springer, Singapore, 2019), pp. 547–558

16. H. Samet, F. Hashemi, T. Ghanbari, Minimum non detection zone for islanding detection using an optimal Artificial Neural Network algorithm based on PSO. Renew. Sustain. Energy Rev. **52**, 1–18 (2015). https://doi.org/10.1016/j.rser.2015.07.080

17. P.P. Mishra, C.N. Bhende, A passive islanding detection technique with reduced complexity for distributed generations, in *2017 7th International Conference on Power Systems (ICPS)*, pp. 830–835 (2017). https://doi.org/10.1109/ICPES.2017.8387404

18. S.S. Mohapatra, M.K. Maharana, S.B. Pati, Comprehensive review to analyze the islanding in distributed generation system, in *2021 1st International Conference on Power Electronics and Energy (ICPEE)*, pp. 1–7 (2021). https://doi.org/10.1109/ICPEE50452.2021.9358542

19. B. Matic-Cuka, M. Kezunovic, Islanding detection for inverter-based distributed generation using support vector machine method. IEEE Trans. Smart Grid **5**(6), 2676–2686 (2014). https://doi.org/10.1109/TSG.2014.2338736

20. M.-S. Kim, R. Haider, G. Cho, C.-H. Kim, C.-Y. Won, J.-S. Chai, Comprehensive review of islanding detection methods for distributed generation systems. Energies **12**, 837 (2019). https://doi.org/10.3390/en12050837

21. F. Hashemi, M. Mohammadi, Islanding detection approach with negligible non-detection zone based on feature extraction discrete wavelet transform and artificial neural network. Int. Trans. Electr. Energ. Syst. **26**, 2172–2192 (2016). https://doi.org/10.1002/etep.2197

Simulation and Analysis of Medium-Voltage Low-Speed Cyclo-Converter Synchronous Motor Drive and Issues with on-Load Speed Trimming

Ashok K. Wankhede, Archana Sharma, and B. G. Fernandes

Abstract Medium-voltage cyclo-converter drives are commonly used for low-speed salient pole synchronous motors in mines. Cyclo-converters give very reliable, efficient and simple solution because they use rugged thyristor devices. Generally, the mines are located at remote locations and the availability factor is very important to minimize Business Interruption loss. However, a cyclo-converter drive has the drawback of generation of sub-harmonics and inter-harmonics along with high-order harmonics. These harmonics are harmful to transformers and weak supply networks and may cause saturation and instabilities. The sub-harmonic frequencies are a function of output frequency and change with output frequency. To mitigate these frequencies, huge passive filters are employed. If the output frequency is fixed, the filter designs are relatively simple but with the variable frequency it becomes complicated. For operational requirements in a mill, on-load output frequency trimming is required. This creates additional problems in terms of MVA sizing of equipment and the requirement of additional filter banks. This paper simulates the fixing and trimming of operating speed of medium-voltage cyclo-converter driven, low-speed, salient pole synchronous motor and brings out issues related to equipment sizing, harmonic mitigation, etc.

Keywords MV drive · Synchronous motor · Cyclo-converter

A. K. Wankhede (✉)
HBNI Anushaktinagar, Mumbai 400094, India
e-mail: ashokkw@barc.gov.in

A. Sharma (✉)
Bhabha Atomic Research Centre, Trombay, Mumbai 400085, India
e-mail: arsharma@barc.gov.in

B. G. Fernandes
Department of Electrical Engineering, IIT Bombay, Mumbai, India

1   Introduction

Medium-voltage low-speed, salient pole synchronous motors (SM) are used in numerous applications like grinding mills, ball mills, conveyor belts in mines, etc. Many of these applications work at low speed and have a requirement of tuning the speed for optimizing the performance under different loading conditions. The required speed trimming range is generally small but essential to operate the system in a safe and cost-effective manner. Medium-voltage induction motors have established themselves as variable speed drives using either cyclo-converters or modern multi-level converters [1]. But they suffer from certain drawbacks like relatively low efficiency and more MVA consumption because of the lagging power factor [2, 3]. Moreover because of the slip, achieving speed within acceptable tolerance demands a more complex control design. Medium-voltage low-speed, salient pole SM offers good efficiency and has the capability of operation at lagging, leading and unity power factor. Unity power factor operation reduces required MVA significantly thereby reducing losses and cooling requirements [1]. The medium-voltage low-speed SMs in mines are designed for a certain operating speed and are driven by cyclo-converters because of rugged construction and good efficiency of thyristors. However, their operation has got issues like the direct injection of harmonics in the supply network, generation of sub-harmonics, inter-harmonics and limited speed resolution capability [4]. For fixed speed operation, sub-harmonic frequencies are fixed and accordingly filters are employed for mitigation. Since sub-harmonics are a function of output frequency, the filter requirement changes with speed. This makes filter design more complex. Injecting harmonics in a weak supply network needs to be mitigated to take care of THD requirements as per guidelines issued by IEEE standard 519. Medium-voltage passive filter banks for lower frequency are bulky and proper designing is required to avoid problems like resonance, etc. [4, 5]. In the case of applications like grinding mills and ball mills, frequency trimming is required in the range of about 2 Hz on load. The operation of SM on load is simulated in MATLAB Simulink for establishing the sizing of equipment, finding the nature of sub-harmonics and THD, etc. Smooth transition of on-load speed from a fixed value to the desired one is simulated, and operating parameters and issues are discussed.

2   The Methodology of Operation

Figure 1 shows the block diagram of a cyclo-converter drive for salient pole, 3.125 MVA, 2400 V, 48 pole SM. The motor is driven with a three-phase, 6 pulse cyclo-converter. At the input side, phase shifting transformers are used for stepping down grid supply to medium voltage and also providing certain harmonic cancellation. The Excitation control block controls the field voltage for reactive power control. Load is connected to motor shaft directly or through gearboxes, and power varies proportionally to operating speed. The motor is started with a minimum load on the
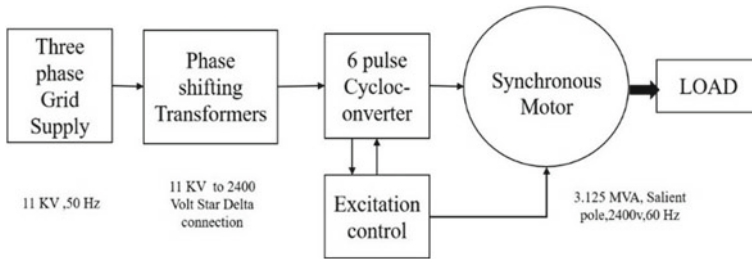
Fig. 1 Block diagram of synchronous motor cyclo-converter drive

shaft to represent an empty mill. Once the system is put into operation and achieves the desired speed, the charge is loaded till a full load is achieved. With the change in density and ingot size of the ore, the system needs retuning on lower side of present operating speed. This is done by changing the speed on load and observing parameters like vibration and instabilities. Assuming that the motor is running at synchronous speed and excitation control is set to control for unity power factor, change of speed is bound to affect the operating parameters. The operating philosophy is simulated using MATLAB Simulink to study the behaviour of the system.

2.1 The Major System Component Specifications

Tables 1, 2 and 3 list the specifications for the motor, transformers and supply system. SM is a salient pole, with low speed with the number of poles as 48. Friction factor and inertia are considered for the motor. Saturation of the motor core is considered when parameters exceed the limits. The transformer is used as a zigzag connection in the primary and delta D11 in the secondary having a 30° phase shift for third and multiple harmonic cancellations. The transformer leakage reactance values are considered along with the saturation of the core. Supply system components are

Table 1 Motor specifications

1	Rating	3.125 MVA, 2400 V, 60 Hz
2	Reactance's: Xd, Xd', Xd", Xq, Xq", Xl (pu)	1.56, 0.296, 0.177, 1.06, 0.177, 0.052
3	Time constants: Td', Td", Tqo" (s):	3.7, 0.05, 0.05
4	Stator resistance: Rs (pu)	0.0036
5	Inertia coefficient, friction factor, pole pairs H (s), F (pu), p()	1.07, 0.05, 48
6	Initial conditions: dw (%), th (deg), ia, ib, ic (pu), pha, phb, phc (deg), Vf (pu)	0, 0, 0, 0, 0, 0, 0, 0, 1
7	Saturation is considered	Yes

Table 2 Phase-shifting transformer specifications

1	Nominal power and frequency: Pn (VA), fn (Hz)	5 MVA, 50 Hz
2	Primary (zigzag) nominal voltage Vp: VrmsPh-Ph	11 kV
3	Secondary nom. Ph Voltage, phase shift degree	2400/1.73, 30
4	Winding 1 zigzag [R1, L1] (pu)	0.001, 0.001
5	Winding 2 zigzag [R2, L2] (pu)	0.001, 0.001
6	Winding 3 secondary [R3, L3] (pu)	0.0025, 0.06
7	Magnetizing branch [Rm, Lm] (pu)	200, 200
8	Magnetizing resistance Rm (pu)	500
9	Initial fluxes	0,0,0
10	Saturation considered	Yes

Table 3 Supply system specifications

1	Supply rating	11 kV, 50 Hz, 3 ph
2	Line-to-neutral volts Va, Vb, Vc	11 kV/$\sqrt{}$ 3 Vrms each
3	3-phase short-circuit VA at base voltage V	500 MVA,11 kV
4	X/R ratio	10

considered as per weak supply network having a short circuit MVA of 500 and X/R ratio of 10.

3   MATLAB Simulink Modelling of a Complete Drive

Figure 2 shows the complete modelling of the drive. Three-phase, 11 kV supply is connected to three phase-shifting transformers. Secondary of each transformer is stepped down to 2400 V to obtain rated voltage for six pulse thyristor-based cyclo-converter. Three single-phase cyclo-converter module output is obtained using sinusoidal voltage modulation and phase-shifted 120° and 240°, respectively, from the first phase. A series element with 0.1 Ω resistance and 200 µH inductance is connected to smoothen the output current. Field excitation circuit block takes vd and vq components as feedback from SM and computes field voltage correction using PID control system so as to stabilize the power factor towards unity and is tuned for critical damping. Starting of the motor is achieved by connecting 20 Ω resistance to the field winding and applying a low frequency of 5 Hz to the motor. The SM model selected does not have a speed reset, so it is done by applying 5 Hz to bring the speed to zero and then applying the next frequency of 10 Hz to move further. At the same time, field control is transferred to the excitation control block. The simulation is done in a discrete domain with a step size of 100 µS with the trapezoidal robust
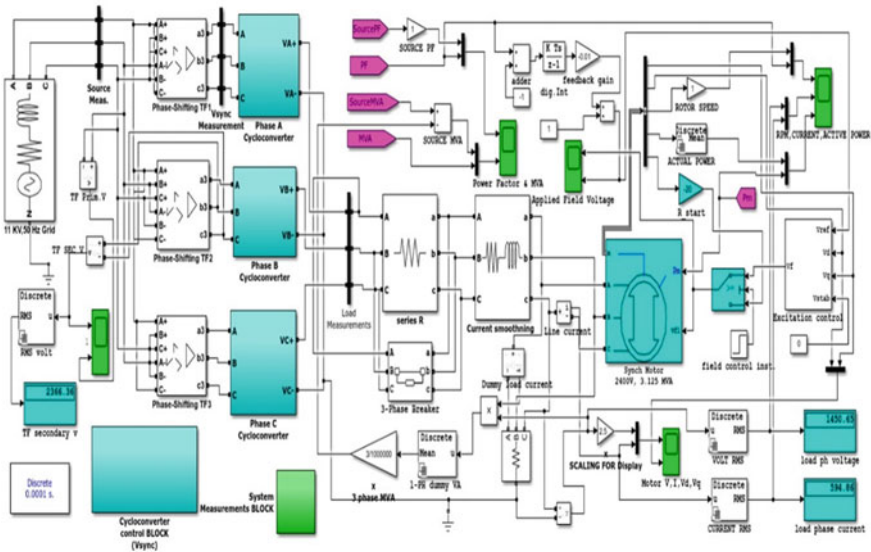
Fig. 2 Simulation of cyclo-converter driven SM with field control block

model for SM. Input and output power factor, MVA, harmonic content in voltage and current are recorded and shown in the measurement block in Fig. 3. The speed set at different simulation intervals with corresponding load power is simulated in Fig. 4. Figure 5 shows 6 pulses per phase thyristor connection for each limb and cyclo-converter pulse generation using reference for a given set output frequency.
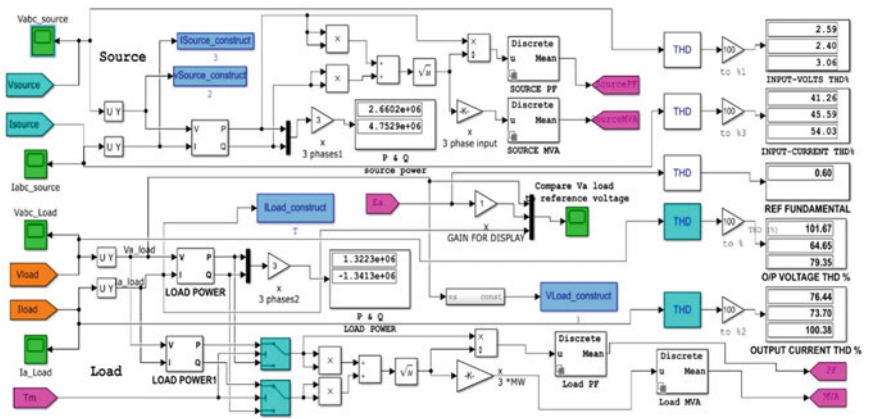

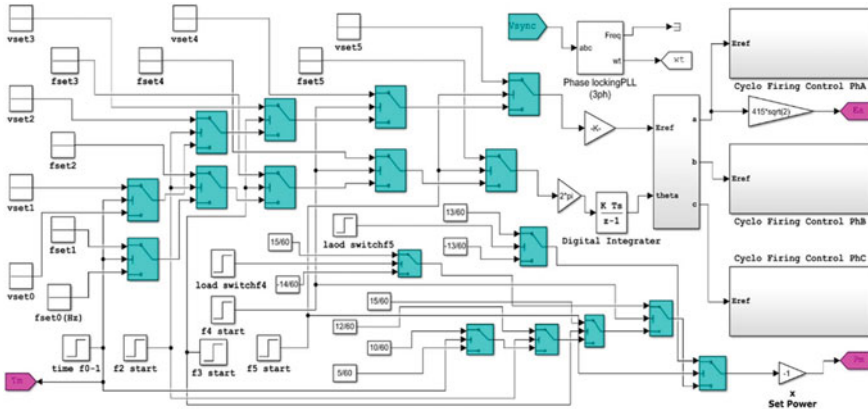**Fig. 3** Measurement of various parameters and THD

Fig. 4 Generation of cyclo-converter control signals and speed setting module
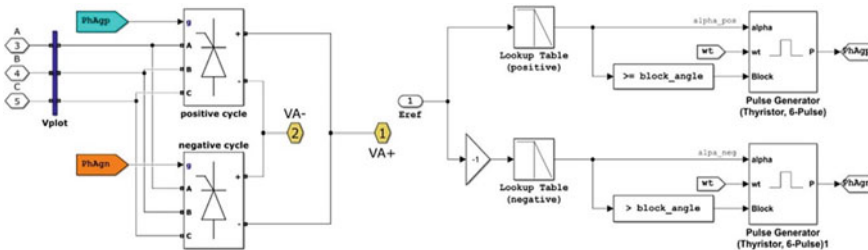
Fig. 5 Six-pulse cyclo-converter per phase module and gate pulse generation

3.1 Operation Philosophy

The drive operation is intended for 15 Hz (37.5 RPM) for SM on load. This speed is achieved by starting the motor at 5 Hz (12.5 RPM) for resetting the SM model to zero speed and accelerating to 10 Hz (25 RPM) and then taking it to 15 Hz. As per the required strategy of operation, speed needs to be finally reduced and stabilized to 13 Hz. This is done by reducing the speed to 14 Hz first and taken to 13 Hz (32.5 RPM) and operating with load. This operation is performed with optimized voltage to frequency ratio and exciter control parameters to achieve critical damping for stabilization of speed. Figure 6 shows recorded parameters like speed, power factor, voltage, current, MVA consumed and active power at different frequencies.

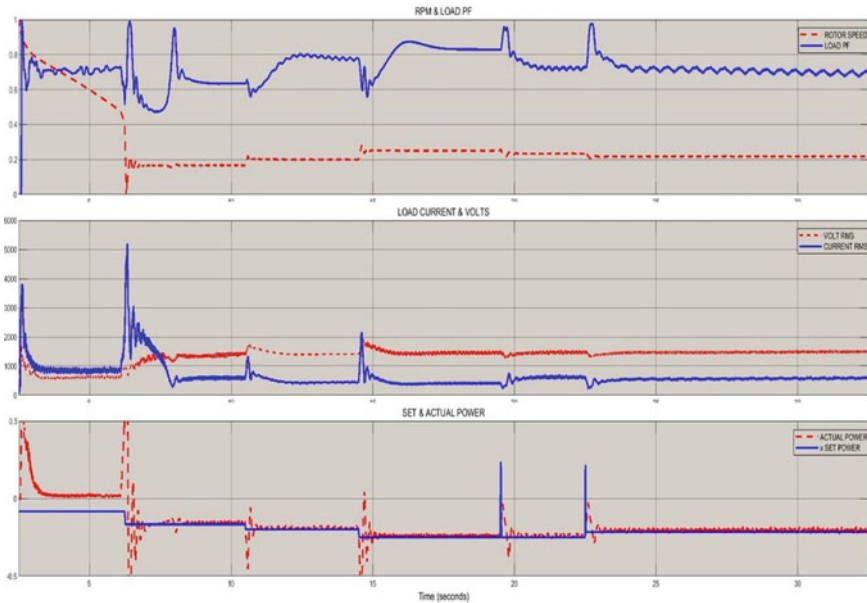**Fig. 6** Simulation result for motor at 15 Hz and then taken to 13 Hz on full load

4   Results and Findings

The basic objective of the simulation is to establish the sizing of equipment, decide the sequence of operation and study the difficulties with sub-harmonics, power factor and overshoots for change in output frequency on load. A high rate of rise of voltage and currents affects significantly motor insulations and is critical in generating EMI which may disturb the control circuits and also affect equipment connected to the same supply network. This issue needs to be addressed and established in simulation runs. Also, the requirement of sub-harmonic filters for various frequency operations is understood to ensure trouble-free and cost-effective solutions.

4.1   Study of Parameters

Figure 6 shows simulation results corresponding to the operation of the drive for grinding mill where speed is required to be brought down from 15 to 13 Hz on load so as to achieve efficient operation for a particular charge to be processed in case of grinding operation in mines. For each frequency switching, the system encounters overshoot in the speed and correspondingly in the currents and power. This needs to be corrected by tuning excitation controller parameters. For simulation and establishing the behaviour, the system is tuned for critical damping here. While increasing the
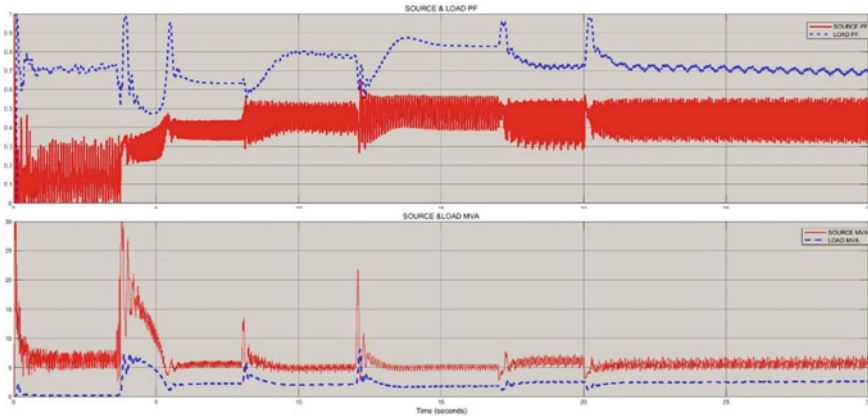
Fig. 7 Simulation result for power factor and MVA at various speeds

speed, the motor does not encounter major issues but while decreasing the speed, it goes into generator mode. It is therefore reduced in finer speed steps to avoid jerks and overshoots in current, speed, etc. [6]. The speed is reduced from 15 to 14 Hz first and then to 13 Hz. While decelerating from running speed to lower speed, the existing load on the shaft will supply power till it reaches to lower set speed. To take care of generation mode, load value corresponding to previous frequency is applied as generating load till speed stabilizes to new set value. Once the desired speed is achieved, again full motoring load is applied. The same sequence of operation is shown in the figure by plotting speed, power factor, current, voltage and active power. It is evident that the maximum current required is for starting and is coming out as 3000 Amps for a short duration of a few milliseconds. After starting and changing the speed to the desired value, the current remains below 1000 Amps for all speeds which are close to the rated current for SM except for small spikes during changeover which can be taken care of by field control parameter tuning. MVA consumed was also observed as 5 MVA for all the speeds except starting. MVA required for starting can be optimized by putting suitable filters and soft-starting of the motor. This value of MVA will be used for sizing transformers, series element and cyclo-converter devices. The steady-state power factor for input and output of cyclo-converter is 0.5 and 0.7, respectively. The field control is not able to correct further because of sub-harmonics and inter-harmonics. Further improvement of the power factor may be achieved with suitable harmonic filters on input and output sides (Fig. 7).

4.2 Sub-Harmonics and Related Issues

Figure 8 shows the sub-harmonics injected in the source current while operating at full load for various output frequencies. Harmonic component values for various
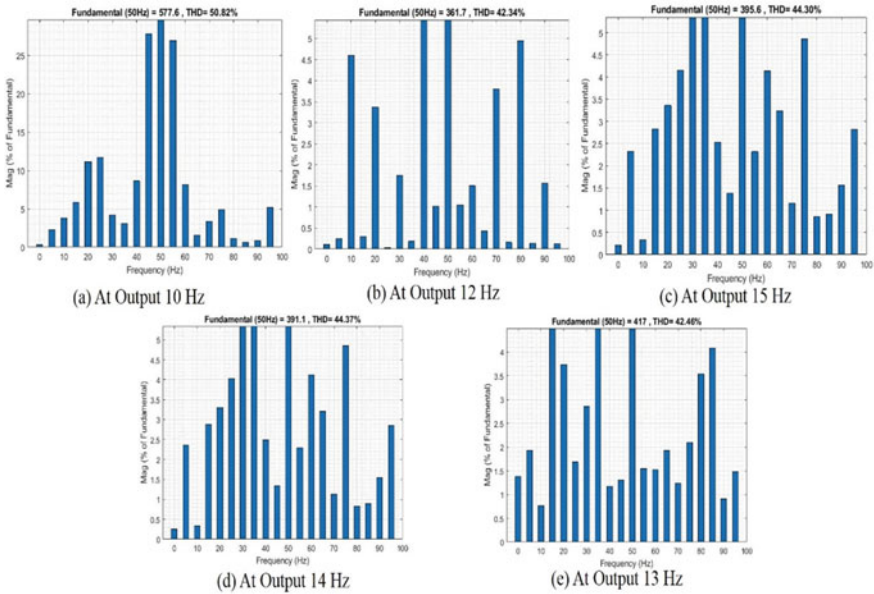
Fig. 8 Sub-harmonics at various output frequencies

output frequencies are summarized in Table-4. It can be seen that as the operating frequency is increased from 10 to 15 Hz and then down to 13 Hz, the dominant harmonic frequency changes for each operating frequency. Hence, the requirement for sub-harmonic mitigation filter also changes. For example, for output of 10 Hz, 12 Hz, 15 Hz, 14 Hz and 13 Hz, the dominant harmonic is 45 Hz, 40 Hz, 35 Hz, 30 Hz and 30 Hz, respectively. It can be observed that THD for 12 Hz, 15 Hz, 14 Hz and 13 Hz is almost the same as about 44%, but the filter requirement for sub-harmonic mitigation is different. The only measurement of THD may be misleading for filter requirement assessment. This change in harmonic frequency throws more challenges to designing optimum filters [7, 3]. Harmonic frequency component in between frequencies appears to be not important but definitely, it can create problems of resonances and dangerous situation for the overall system by resonating with the critical frequency of certain mechanical parts of the installation. Hence, a holistic approach needs to be adopted for filter design for a full operation range of frequencies. The harmonics higher than 50 Hz is also present but it can be taken care of in a suitable low pass filter design (Table 4).

Table 4 Dominant sub-harmonic components for various operating speeds

(Hz) Sub-harmonic	% Harmonic at 10 Hz o/p	% Harmonic at 12 Hz o/p	% Harmonic at 15 Hz o/p	% Harmonic at 14 Hz o/p	% Harmonic at 13 Hz o/p
45	**27.79**	1.05	1.30	1.34	1.38
40	**8.63**	**10.21**	1.17	2.49	2.53
35	3.08	0	**14.54**	**6.04**	**6.12**
30	**4.20**	1.75	2.86	**13.01**	**13.23**
25	**11.7**	0	1.68	**4.04**	**4.15**
20	**11.5**	3.37	3.74	3.30	3.36
15	**5.87**	0	**5.62**	2.88	2.83
10	3.81	**4.6**	0	0	0
5	2.28	0	1.93	2.36	2.32
% THD	50.82	42.34	42.46	44.33	44.30

5   Conclusions

Medium-voltage, salient pole Synchronous Motor with a cyclo-converter drive is extensively used in mines because of its good efficiency and reliability. SM can be operated at a unity power factor, so the MVA requirement is low compared to an induction motor. The operating requirement of speed trimming on load for optimum operation is simulated with MATLAB Simulink. The operating parameters like speed overshoot, MVA consumption and sub-harmonic generation are studied. With change in speed, change in dominant sub-harmonic frequency demands filter design for wide frequency range to avoid saturation of equipment and resonance effects. It also put an additional MVA burden on transformers. SM drive of 3.125 MVA is simulated and sub-harmonic components are recorded for various speeds of interest for the typical operation of grinding mills in mines. The control over overshoot in speed and currents is established for critical damping in exciter control. The SM exciter control set is operated for unity power factor but could not get corrected beyond 0.7, which may be because of the lack of filters at the input side. Simulation of the drive for intended operation for 15 Hz and trimming down to 13 Hz on load give good insight for designing an actual MV drive system for similar applications.

References

1. G. Seggewiss, J. Dai, M. Fanslow, Rockwell automation and TECO-Westinghouse motor co, 'evaluation of synchronous motors on grinding mills', in *IEEE conference* (2014)
2. J. Pontt, J. Rodryguez, W. Valderrama, G. Sepulveda, G. Alzamora, Resonance effects, power quality and reliability issues of high-power converters-fed drives employed in modern SAG circuits. Miner. Eng. **17**, 1125–1134 (2004)

3. H. Miranda, L. Moran, G. Alzamora, Technical evaluation and practical experience of high-power grinding mill drives in mining applications. IEEE Trans. Ind. Appl. **41**(3) (2005)
4. B. Wu, J. Rodriguez, 'Current-source converter and cyclo-converter topologies for industrial medium-voltage drives. IEEE Trans. Ind. Electron. **55**(7) (2008)
5. J. Pontt, J. Rodr´ıguez, W. Valderrama, G. Sepilveda, P. Chavez, B. Cuitino, P. Gonzalez, G. Alzamora, Current_issues_on_high-power_cycloconverter_Fed Gearless motor drives for grinding mills', in *IEEE conference* (2003)
6. J. Pontt, J. Rodrıguez, K. Tischler, N. Becker, J. Rebolledo, Operation of high power cycloconverter-fed gearless drives under abnormal conditions. IEEE Trans. Ind. Appl. (2007)
7. D. Basic, V.S. Ramsden, P.K. Muttik, University of Technology, Sydney, Australia; GEC ALSTHOM (Australia) Ltd, 'Performance of combined power filters in harmonic compensation of high power cycloconverter drives', in *IEEE Conference Paper* (1998)

Optimal Sudoku Static Reconfiguration Technique for Power Enhancement of PV Array Under Partial Shading Conditions

Praveen Kumar Bonthagorla, Suresh Mikkili, and Kanjune Akshay Bapurao

Abstract From the beginning of electrical energy generation, maximum amount of energy is generated from fossil fuel. Demerits of fossil fuel is, it creates greenhouse gases. Fossil fuel is not available in all the parts of earth. It has to import and export. The cost of energy depends on global market. Solar energy available in large amount, and free of cost. This solar energy extraction depends on environmental condition. Partial shading effect on power generation. In TCT model Partial shading causes the current to reduce and hence the output power. Sudoku and Optimal sudoku techniques cause this demerit to eliminate. It helps in power enhancement as compared to TCT arrangement under shading condition. Also due to shading condition there is a greater number of power peaks. Using Sudoku and optimal sudoku techniques, the multiple power peaks are also to be reduced.

Keywords Sudoku arrangement · Optimal Sudoku arrangement · Reconfiguration techniques

1 Introduction

Electricity is one of the important factors in development of nation. Day by day whole world is facing problem of Energy demand and supply [1]. Energy demand and energy production planning is the main task for the power regulating board [2]. AC system has various factors such as Skin effect, Copper loss, Inductance effect, Capacitance effect. Generation and transmission of DC is good alternative to AC system. As DC doesn't have skin effect, hence whole conductor is used efficiently [3]. For generating electricity thermal, nuclear power plants are used. This creates large amount of pollution. Using renewable resources this pollution is reduced. Indian grid is divided into 5 regions. NORTH, EAST, WEST, SOUTH, NORTH-EAST. To

P. K. Bonthagorla (✉) · S. Mikkili · K. A. Bapurao
Department of EEE, NIT Goa, Ponda 403401, Goa, India
e-mail: praveennitgoa2017@gmail.com

S. Mikkili
e-mail: mikkili.suresh@nitgoa.ac.in

achieve ONE-NATION-ONE-GRID, all this region is connected and One single Grid is formed. North- East and East grid connected in 1991. Then in 2003 west region is connected to these two regions. In 2006 North region is connected to these three regions and all four regions are interconnected. In 2013 South region is connected to the all central grid using Solapur- Raichur line [4]. India is a tropical country. It receives large amount of solar energy. In INDIA solar power plant are divided into three categories: 1. Small (Range less than 99 MW) 2. Medium (From 100 to 400 MW) 3. Large (Greater than 400 MW) [5]. Government of India launch a program of National Solar Mission. In recent years there is a great development in Renewable energy uses. It was planned to achieve 100 GW of solar energy by 2022. Partial shading conditions are the main threat to the PV system to reduce output power. In terms of maximum power, the TCT configuration is superior to other systems, but the horizontal and wide structure gives very little power output [6]. [7] Proposes a switched matrix-based dynamic PV array reconfiguration method to reduce the PSC effect for water pump application. It is also known as electric array reconfiguration (EAR). Experimental analysis of dynamic array reconfiguration has been done in [8].

In EAR, through power loss has been minimized, sensors switch and complex algorithms for switching control increase the cost and complexity of the PV system. To overcome this issue, [9] proposes a Sudoku based improvised, physical reconfiguration. [10] offers a magic square method of reconfiguration to reposition the PV panel. [11] Proposes a clue based, skyscraper method of physical reconfiguration. Different reconfiguration methods have been reviewed in the literature [12, 13]. Limitation of array size and power dependence on logic, clue dependency, complex reasoning, implementation complexity etc., are the main significant limitations of these methods. Under partial shade conditions, this article demonstrates a strategy for reconfiguring the modules in an array to maximize the power provided by the array. It has been designed to spread the shade effect throughout a total cross-tied (TCT) linked PV array by placing modules according to the proposed novel shade dispersion (NSD) pattern by applying simple, effective, and less costly solutions to minimize the PSC effect and enhance the power extraction. In this paper analysis of TCT, Sudoku and optimal sudoku technique is done on basis of MATLAB simulation. Parameter for comparison used are Mismatch power loss (%), Fill Factor (%), Efficiency (%).

2   Modelling of Sudoku and Optimal Sudoku Static PV Array Reconfiguration Techniques

The shadow falling on panel reduces the energy generated from solar PV. The shadow causes less current generation. To increase the output power, reconfiguration techniques are used which helps in reducing the effect of shadow. In reconfiguration techniques, either the panel are changed from their location or the electrical connection of the panel are changed. Changing panel from their location is called static reconfiguration. Changing electrical connection of PV panel is called Dynamic reconfiguration. There are various types of static and dynamic techniques.

2.1   Basic Sudoku Reconfiguration Technique

Sudoku puzzle is used to form sudoku reconfiguration arrangement. Sudoku puzzle is a logic based on numbers. It consists of digit 1–9. It uses of a 3×3 sub matrix There are 9 matrices in 9×9 array. To form this arrangement some rules, have to be considered [14].

Rule 1   Each Row and column includes number 1–9.
Rule 2   Not a single number is repeated in row or column or sub array.
Rule 3   Each 3×3 sub array consist number 1–9.
Rule 4   1st digit represents the row; the 2nd digit represents column.

When shadow falls on solar array then some of panel gets shades. This causes the output power of PV to decrease. To increase this power and reduce the shading effect sudoku reconfiguration helps. In sudoku technique the solar PV are placed from one place to another place. This will disperse the shade from one part to overall array. So, the partial shading effect is minimized. But note that in sudoku method electrical connection is kept constant. Figure 1 shows the TCT array for 9×9 arrangement. For this corresponding arrangement sudoku array is shown in Fig. 2. In figure the panel of panel 42 i.e. fourth row second column is relocated at to row one column second. This helps in dispersing shadow over array.

2.2   Proposed Optimal Sudoku Reconfiguration Technique

Reconfiguration technique disperse shadow effect. But while relocating the connection is kept constant. While relocating the location are changed. This increases the cable required for connection. As the length increases then resistance of cable increases. This causes Voltage drop I^2R loss to increase. Optimal sudoku technique provides optimum relocation of solar PV so that the length of wire required is reduced [15]. This reduces the I^2R loss and voltage drop as compare to sudoku method.

Fig. 1 Total cross tied 9 × 9 array

11	12	13	14	15	16	17	18	19
21	22	23	24	25	26	27	28	29
31	32	33	34	35	36	37	38	39
41	42	43	44	45	46	47	48	49
51	52	53	54	55	56	57	58	59
61	62	63	64	65	66	67	68	69
71	72	73	74	75	76	77	78	79
81	82	83	84	85	86	87	88	89
91	92	93	94	95	96	97	98	99

Fig. 2 Sudoku arrangement 9 × 9 array

11	42	53	94	25	76	87	68	39
21	92	73	84	35	66	57	18	49
31	82	63	44	55	16	97	78	29
41	32	13	54	85	96	77	28	69
51	22	93	64	75	46	17	38	89
61	72	83	24	15	36	47	98	59
71	12	23	34	45	56	67	88	99
81	62	43	74	95	26	37	58	19
91	52	33	14	65	86	27	48	79

Figure 3 shows the optimal sudoku array arrangement. Consider column two the length of wire required in optimal sudoku technique is less as compare to sudoku technique as shown in Fig. 4. From figure it can be observed that wire length is minimized. Steps for optimal sudoku technique [16]:

Fig. 3 Optimal Sudoku
Arrangement 9 × 9 array

11	72	43	24	85	56	37	98	69
21	82	53	34	95	66	17	78	49
31	92	63	14	75	46	27	88	59
41	12	73	54	25	86	67	38	99
51	22	83	64	35	96	47	18	79
61	32	93	44	15	76	57	28	89
71	42	13	84	55	26	97	68	39
81	52	23	94	65	36	77	48	19
91	62	33	74	45	16	87	58	29

Fig. 4 Connection diagram
for **a** Sudoku, **b** optimal
Sudoku
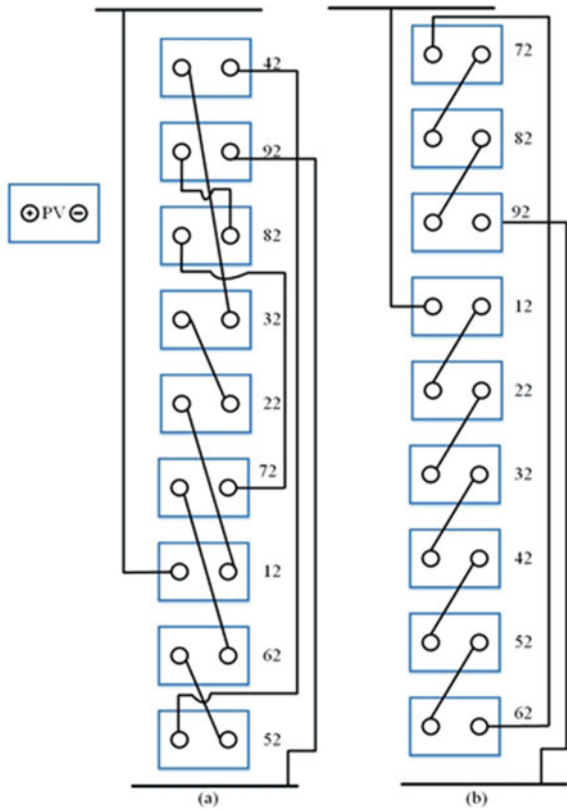
Step 1   For first column fill number from 1–9 in ascending manner.
Step 2   For the next column two and three special pattern is followed, in which
               the numbers from previous column are displaced by six. This special
               pattern is used for the Second and third column till the number in column
               completes sequence up to 9.
Step 3(a) For fourth column if the shifting done again by six, it will be exactly
               same as first column. As this will not follow sudoku pat- tern rules (No
               number repetition). Hence, for fourth column new rule is used.
Step 3(b) Then put Second (Middle) digit is on first number, first digit on third
               number and Third digit on second number.
Step 4   For column fifth and sixth the numbers in the previous column are shifted
               by Six (Refer Step 2).
Step 5   For column seventh again use step 3.
Step 6   For 8 and 9 columns refer step 2.

3   Partial Shading Conditions

In this study six different types of shading conditions are used. The shading conditions
are bottom of right corner (BORC), bottom of left corner (BOLC), top of right corner
(TORC), top of left corner (TOLC), Centre all this five are 4×4 matrix and last one
is two sub arrays of 3×3 matrix. In the first five shading condition the shading was
4×4 size. The solar insolation levels consider are 100–700 W/m^2 and 1000 W/m^2
respectively. The shading conditions are shown in Fig. 5.

4   Simulation Results and Discussion

In this section the TCT, Sudoku and Optimal Sudoku technique is analyzed and
compared. The analysis is based on Matlab simulation based on parameters such as
Mismatch power loss (%), Fill Factor (%), Efficiency (%). The parameters can be
calculated as

$$Powerloss(\%) = \frac{P_{GMP(unshaded)} - P_{GMP(Shaded)}}{P_{(Shaded)}} \tag{1}$$

$$FillFactor = \frac{P_{GMP(Shaded)}}{V_{Oc} \times I_{Sc}} \tag{2}$$

$$Efficiency = \frac{P_{GMP(Shaded)}}{SolarInsolation\left(\frac{W}{m^2}\right) \times AreaofPanel(m^2)}$$
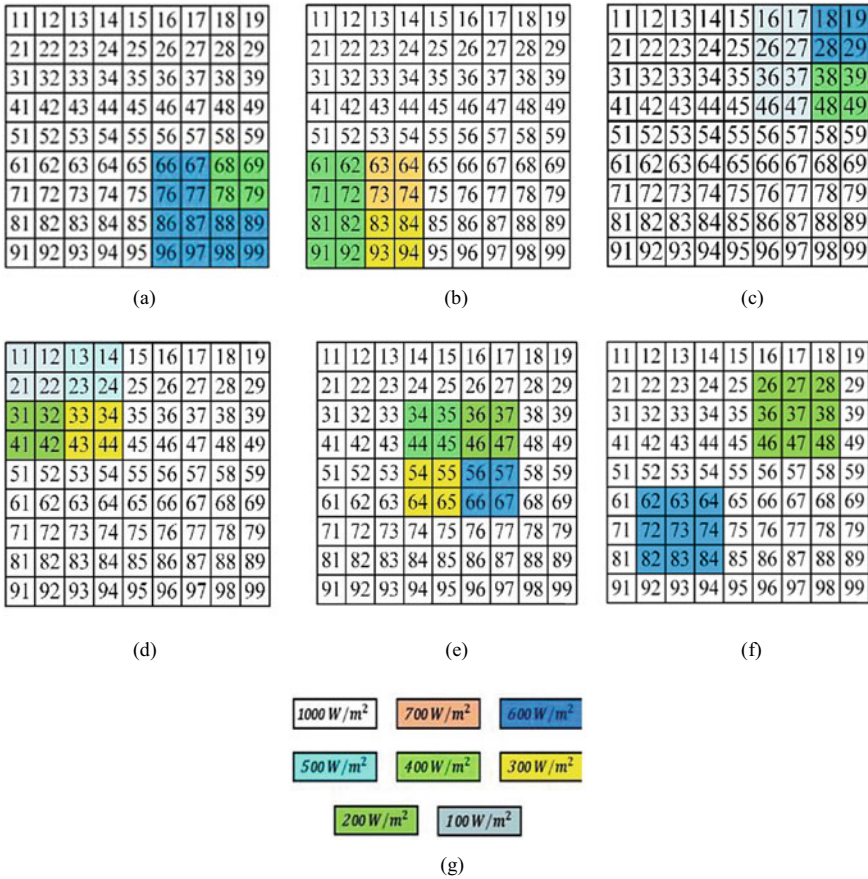
Fig. 5 Shading conditions **a** BORC, **b** BOLC, **c** TORC, **d** TOLC, **e** center, **f** two sub arrays of 3 × 3, **g** solar insolation levels

4.1 Uniform Condition:

In uniform condition each solar PV receives same solar insolation level 1000 W/m^2. Under this shading, the GMPP, I_{GMP}, V_{GMP} is mentioned in Table 1.

Table. 1. Performance factors under uniform shading

V_{OC} (V)		I_{SC} (A)	P_{GMP} (W)	V_{MP} (V)	I_{MP} (A)
397.8		46.9539	13,773	321.4876	42.8414

4.2   Under Type 1 Shading: Right Corner Bottom Side of 4 × 4 Sub-Array

In this type the right corner bottom side 4 × 4 Sub-array shading condition is considered and comparison between TCT, Sudoku and Optimal Sudoku techniques is carried out on basis of factors such as Mismatch power loss (%), Fill Factor (%), Efficiency (%) as shown in Table 2. From Table 2 it can be observed that optimal sudoku gives better performance, as compared to Sudoku and optimal sudoku. From the results it can be noted that, the Optimal sudoku produces 0.1779% more power than sudoku and 6.1691% than TCT arrangement. Also, it can be observed that the Optimal sudoku has fill factor 69.6825 which is more than sudoku i.e.69.5379 and TCT arrangement i.e. 62.4231. Optimal sudoku has Power loss (%) 10.2011 which is less than sudoku i.e.10.3608 and TCT arrangement i.e. 15.7409. Figure 6 shows P-V characteristic for various configuration in Type-1 shading condition (Tables 3, 4, 5, 6 and 7).

Table 2 Power enhancement comparison of static reconfiguration methods under type-1 shading

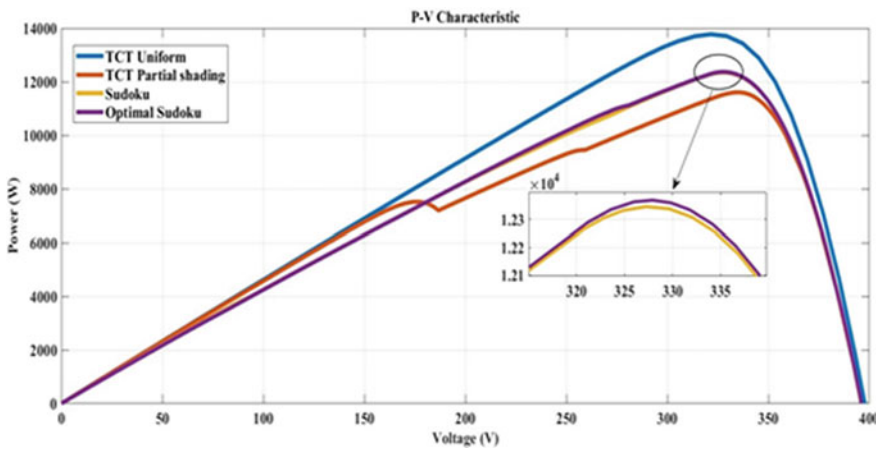| Method	GMPP (W)	Power loss (%)	Fill factor	Efficiency (%)
TCT	11,605	15.7409	62.4231	11.11
Sudoku	12,346	10.3608	69.5379	11.80
Optimal Sudoku	12,368	10.2011	69.6825	11.82

Fig. 6 P-V curve for type-1 shading

Table 3 Power enhancement comparison of static reconfiguration methods under type-2 shading

Method	GMPP (W)	Power loss (%)	Fill factor	Efficiency (%)
TCT	10,794	21.6463	58.137	10.41
Sudoku	11,810	14.2711	68.1606	11.30
Optimal Sudoku	12,038	12.6161	67.2241	11.48

Table 4 Power enhancement comparison of static reconfiguration methods under type-3 shading

Method	GMPP (W)	Power loss (%)	Fill factor	Efficiency (%)
TCT	10,104	26.6550	54.5310	9.74
Sudoku	11,087	19.5195	62.6525	10.69
Optimal Sudoku	11,332	17.7409	64.1389	10.93

Table 5 Power enhancement comparison of static reconfiguration methods under type-4 shading

Method	GMPP (W)	Power loss (%)	Fill factor	Efficiency (%)
TCT	10,043	27.0978	54.2228	9.68
Sudoku	11,095	19.4613	63.5559	10.70
Optimal Sudoku	11,106	19.3814	65.1616	10.73

Table 6 Power enhancement comparison of static reconfiguration methods under type-5 shading

Method	GMPP (W)	Power loss (%)	Fill factor	Efficiency (%)
TCT	10,458	24.0854	56.3887	10.67
Sudoku	11,677	15.2366	66.0436	11.38
Optimal Sudoku	11,703	15.0479	66.1792	11.41

4.3 Under Type 2 Shading: Bottom of Left Corner 4 × 4 Sub-Array

In type-2 shading, the Bottom left corner 4 × 4 sub array is considered. Under this condition different parameters are compared between Sudoku, Optimal Sudoku and TCT arrangement as shown in Table 3. From Table 3 it can be observed that optimal sudoku gives better performance, as compared to Sudoku and optimal sudoku. The

Table 7 Power enhancement comparison of static reconfiguration methods under type-6 shading

Method	GMPP (W)	Power loss (%)	Fill factor	Efficiency (%)
TCT	10,892	20.9349	58.7683	10.95
Sudoku	11,102	19.4106	62.6894	11.29
Optimal Sudoku	11,546	16.1875	65.3256	11.32

Table 8 Comparison all reconfiguration methods in terms of maximum power and power improvement:

Type of shading	TCT GMPP (W)	Sudoku GMPP (W)	Optimal Sudoku GMPP (W)	% Power improved using Sudoku method compare to TCT under PSC	% Power improved using Optimal Sudoku method compare to TCT under PSC	% Power improved using Optimal Sudoku method compare to Sudoku under PSC
1	11,605	12,346	12,368	6.0019	6.1691	0.1779
2	10,794	11,810	12,038	8.6029	10.3339	1.894
3	10,104	11,087	11,332	8.8662	10.8366	2.162
4	10,043	11,095	11,106	9.4817	9.5714	0.0990
5	10,458	11,677	11,703	10.4393	10.6382	0.2221
6	10,892	11,102	11,546	1.89	5.6643	3.845

optimal sudoku generated 1.894% more power than sudoku and 10.3339% than TCT arrangement. Also, it can be observed that the Optimal sudoku has efficiency 11.48 which is more than sudoku i.e.11.30 and TCT arrangement i.e. 10.41. Optimal sudoku has Power loss (%) 12.6161 which is less than sudoku i.e.14.2711 and TCT arrangement i.e. 21.6463. Figure 7 shows P-V characteristic for various configuration in Type-2 shading condition and uniform TCT configuration.
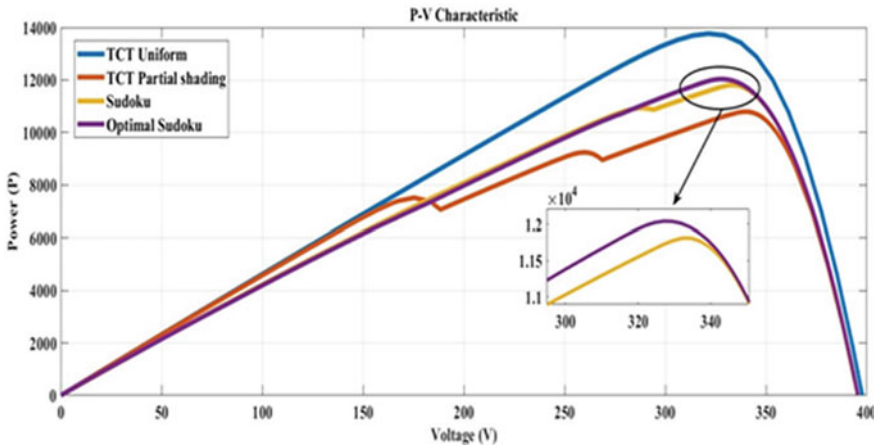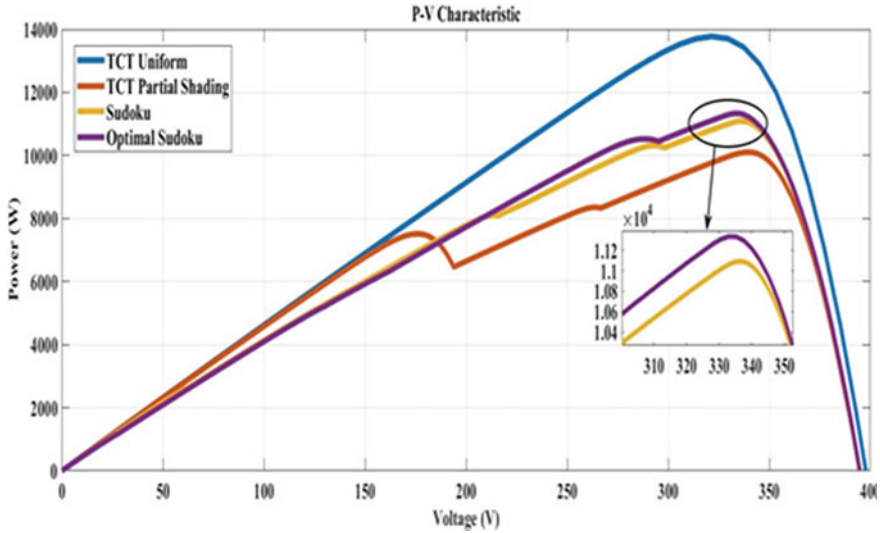

Fig. 7 P-V curve for type-2 shading

Fig. 8 P-V curve for type-3 shading

4.4 Under Type 3 Shading: Top Right Corner 4 × 4 Sub-Array

In this type of shading, the Top of Right Corner 4 × 4 Sub-array shading condition is considered. Under this condition different parameters are compared between Sudoku, Optimal Sudoku and TCT arrangement as shown in Table 4. Figure 8 shows P-V characteristic for various configuration in Type-3 shading condition and uniform TCT configuration.

From Table 4, it can be observed that optimal sudoku gives better performance, as compared to Sudoku and optimal sudoku. Optimal sudoku generated 2.162% more power than sudoku and 10.8366% than TCT arrangement. Also, it can be observed that the Optimal sudoku has fill factor 64.1389 which is more than sudoku i.e.62.6525 and TCT arrangement i.e. 54.5310. Optimal sudoku has Power loss (%) 17.7409 which is less than sudoku i.e.19.5195 and TCT arrangement i.e. 26.6550.

4.5 Under Type 4 Shading: Top Left Corner 4 × 4 Sub-Array

In type-4 shading the Top Left corner 4 × 4 sub array is considered. Under this condition different parameters are compared between Sudoku, Optimal Sudoku and TCT arrangement as shown in Table 5. From Table 5 it can be observed that optimal sudoku gives better performance, as compared to Sudoku and optimal sudoku. Optimal sudoku generated 0.0990% more power than sudoku and 9.5714% than
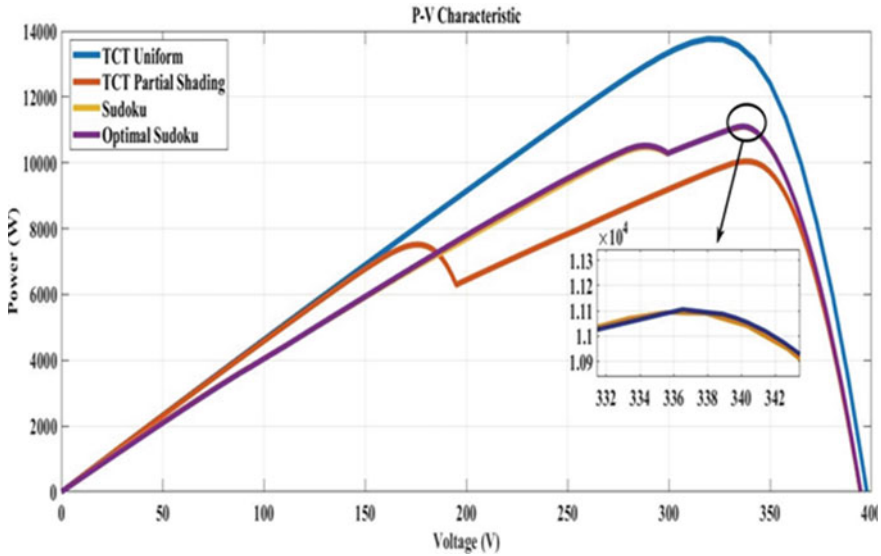
Fig. 9 P-V curve for type-4 shading

TCT arrangement. Also, it can be observed that the Optimal sudoku has fill factor 65.1616 which is more than sudoku i.e.63.5559 and TCT arrangement i.e. 54.2228. Opti- mal sudoku has Power loss (%) 19.3814 which is less than sudoku i.e.19.4613 and TCT arrangement i.e. 27.0978. Figure 9 shows P-V characteristic for various configuration in Type-4 shading condition and uniform TCT configuration.

4.6 Under Type 5 Shading:4 × 4 Sub-Array at Center

In type-5 shading the Centre 4 × 4 sub array is considered. Under this condition different parameters are compared between Sudoku, Optimal Sudoku and TCT arrangement as shown in Table 6. From Table 6 it can be observed that optimal sudoku gives better performance, as compared to Sudoku and optimal sudoku. Optimal sudoku generated 0.2221% more power than sudoku and 10.6382% than TCT arrangement. Also, it can be observed that the Optimal sudoku has fill factor 66.1792 which is more than sudoku i.e.66.0436 and TCT arrangement i.e. 56.3887. Optimal sudoku has Power loss (%) 15.0479 which is less than sudoku i.e.15.2366 and TCT arrangement i.e. 24.0854. Figure 10 shows Type-5 shading condition for various configuration.
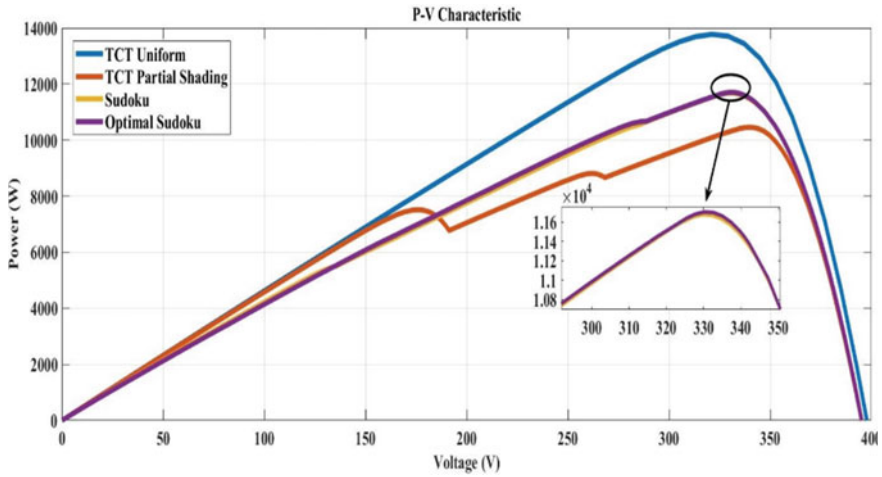
Fig. 10 P-V curve for type-5 shading

4.7 Under Type 6 Shading: Two 3 × 3 Sub-Arrays

In type-6 shading the Two 3 × 3 Sub-array shading condition is considered at center. Under this condition different parameters are compared between Sudoku, Optimal Sudoku and TCT arrangement as shown in Table 7. From Table 7 it can be observed that optimal sudoku gives better performance, as compared to Sudoku and optimal sudoku. Optimal sudoku generated 3.845% more power than sudoku and 5.6643% than TCT arrangement. Also, it can be observed that the Optimal sudoku has fill factor 65.3256 which is more than sudoku i.e. 62.6894 and TCT arrangement i.e. 58.7683. Optimal sudoku has Power loss (%) 16.1875 which is less than sudoku i.e. 19.4106 and TCT arrangement i.e. 20.9349. Figure 11 shows P-V characteristic for various configuration in Type-6 shading condition and uniform TCT configuration.

Figure 12 shows GMPP generated by various configuration under all Six types of shading condition.

% Power improved using Sudoku method compare to TCT under PSC, % Power improved using Optimal Sudoku method compare to TCT under PSC, %Power improved using Optimal Sudoku method compared to Sudoku under PSC are given in Table 8. In Type-1 GMPP value for TCT is 11605 W, Sudoku is 12346 W and 12,368 W in this shading condition. In Type-2 GMPP value for TCT is 10794 W, Sudoku is 11810 W and Optimal sudoku is 12038 W in this shading condition. InType-3 GMPP value for TCT is 10104 W, Sudoku is 11087 W and Optimal sudoku is 11332 W in this shading condition. In Type-4 GMPP value for TCT is 11605 W, Sudoku is 12346 W and Optimal sudoku is 12368 in this shading condition. In Type-5 GMPP value for TCT is 10458 W, Sudoku is 11677 W and Optimal sudoku is 11703 W in this shading condition. In Type-6 GMPP value for TCT is 10892 W, Sudoku is 11102 W and Optimal sudoku is 11546 W in this shading condition.
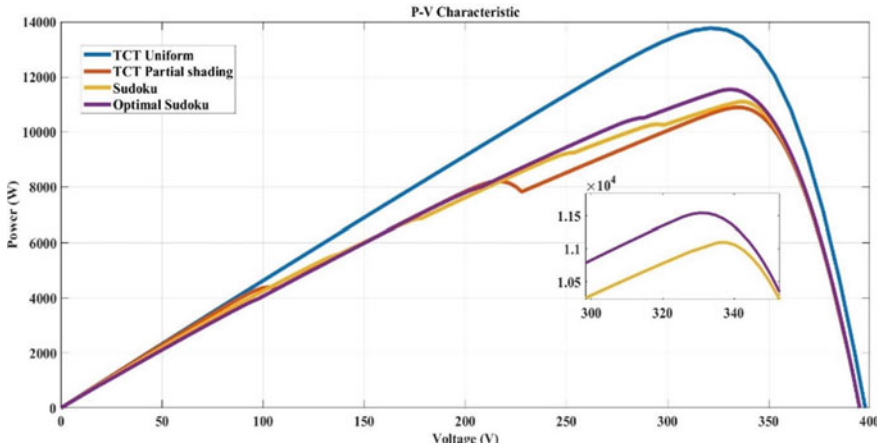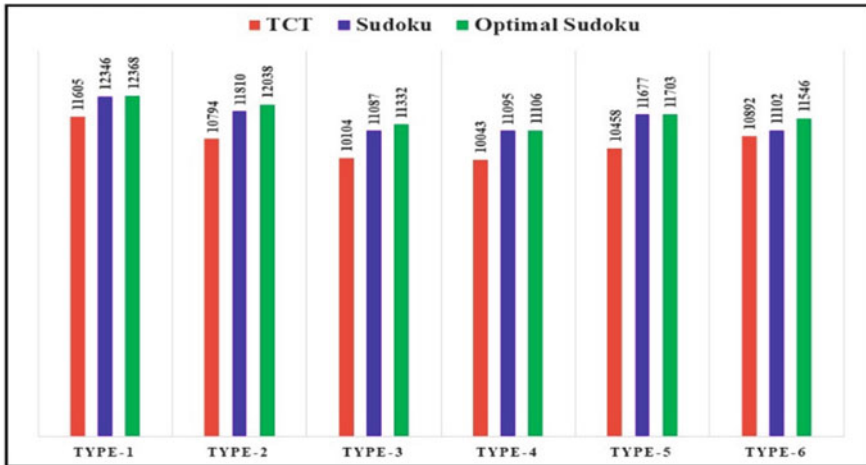
Fig. 11 P-V curve for type-6 shading

Fig. 12 GMPP value for various configuration under different type of shading condition

5 Conclusion

This paper discusses sudoku and optimal sudoku reconfiguration techniques. Power enhancement using Sudoku and optimal sudoku technique is analyzed using MATLAB simulation Simulink model. Solar energy conversion into electricity depends on efficiency and environmental factors. Shading condition effects to reduce the power output of an array. This power loss has to be mitigated. Reconfigure- ration techniques help in mitigating the power loss due to partial shading. Sudoku tech- nique enhances the power as compare to TCT arrangement under partial shading

Table A.1 PV module parameters

Parameter	Value
Power	170 W
V_{OC}	44.2 V
I_{SC}	5.2 A
V_{mp}	35.8 V
I_{mp}	4.75 A
No. of cells	72

condition. But in sudoku arrangement the cable losses are more due to relocation. Optimal sudoku arrangement helps in reducing the loss in cable. Also, it helps in power enhancement as compare to TCT and Sudoku arrangement.

Appendix

See Table A.1.

References

1. P.K. Bonthagorla, S. Mikkili, Optimal PV array configuration for extracting maximum power under partial shading conditions by mitigating mismatching power loss. CSEE J. Power Energy Syst. https://doi.org/10.17775/CSEEJPES.2019.02730
2. A. Negi, A. Kumar, Long-term electricity demand scenarios for India: implications of energy efficiency, in *2018 International Conference on Power Energy, Environment and Intelligent Control (PEEIC),* Greater Noida, India, 2018, pp. 462–467. https://doi.org/10.1109/PEEIC.2018.8665452
3. R.K. Chauhan, K. Chauhan, Performance analysis of power distribution systems with weakly grid connected rural homes in Indian. Energy Build. (2018). https://doi.org/10.1016/j.enbuild.2018.05.003
4. V. Boddapati, A.S.R. Nandikatti, Salient features of the national power grid and its management during an emergency: a case study in India. Energy Sustain. Dev. **59**, 170–179 (2020). ISSN 0973-0826. https://doi.org/10.1016/j.esd.2020.10.010
5. N. Kumar, M.M. Tripathi, Solar power trading models for restructured electricity market in India, 1 Jan. 2020, pp. 49–54
6. P.K. Bonthagorla, S. Mikkili, A novel fixed PV array configuration for harvesting maximum power from shaded modules by reducing the number of cross-ties. IEEE J. Emerg. Sel. Topics Power Electron.
7. H.K. Varma Gadiraju, V. Reddy Barry, I. Maraka, Dynamic photovoltaic array reconfiguration for standalone PV water pumping system, in *2019 8th International Conference on Power Systems: Transition towards Sustainable, Smart and Flexible Grids, ICPS 2019,* pp. 2932 (2019). https://doi.org/10.1109/ICPS48983.2019.9067606
8. R. Pachauri, R. Singh, A. Gehlot, R. Samakaria, S. Choudhury, Experimental analysis to extract maximum power from PV array reconfiguration under partial shading conditions. Eng. Sci. Technol. Int. J. **22**(1), 109130 (2019). https://doi.org/10.1016/j.jestch.2017.11.013

9. G. Sai Krishna, T. Moger, Improved SuDoKu reconfiguration technique for total-cross-tied PV array to enhance maximum power under partial shading conditions. Renew. Sustain. Energy Rev. **109**, 333348 (2019). https://doi.org/10.1016/j.rser.2019.04.037

10. S.M. Samikannu, R. Namani, S.K. Subramaniam, Power enhancement of partially shaded PV arrays through shade dispersion using magic square configuration. J. Renew. Sustain. Energy **8**(6) (2016). https://doi.org/10.1063/1.4972285

11. G. Meerimatha, B.L. Rao, Novel reconfiguration approach to reduce line losses of the photo-voltaic array under various shading conditions. Energy **196**, 117120 (2020). https://doi.org/10.1016/j.energy.2020.117120

12. C.V. Chandrakant, S. Mikkili, A typical review on static reconfiguration strategies in photo-voltaic array under non-uniform shading conditions. CSEE J. Power Energy Syst. (2020). https://doi.org/10.17775/cseejpes.2020.02520

13. M. Etarhouni, C. Benjamin, L. Zhang, Review of PV array interconnection schemes for maximum power operation under partial shading, *36th European Photovoltaic Solar Energy Conference and Exhibition REVIEW*, no. September, 2019.

14. B.I. Rani, G.S. Ilango, C. Nagamani, Enhanced power generation from PV array under partial shading conditions by shade dispersion using SuDoKu configuration. IEEE Trans. Sustain. Energy **4**(3), 594–601 (2013). https://doi.org/10.1109/TSTE.2012.2230033

15. S.R. Potnuru et al., Positioning of PV panels for reduction in line losses and mismatch losses in PV array, in *Renewable Energy* (vol. 78, 2015), pp. 264–275. https://doi.org/10.1016/j.renene.2014.12.055

16. S.G. Krishna, T. Moger, Optimal SuDoKu reconfiguration technique for total-cross-tied pv array to increase power output under non-uniform irradiance. IEEE Trans. Energy Convers. **34**(4), 1973–1984 (2019). https://doi.org/10.1109/TEC.2019.2921625

Power Enhancement of Total-Cross-Tied Configured PV Array During Dynamic Irradiance Change Using Metaheuristic Algorithm-Based MPPT Controllers

Praveen Kumar Bonthagorla and Suresh Mikkili

Abstract Partial shading condition (PSC) is the major threat to the building-integrated PV systems as they are sorely affected in terms of drastic reduction in PV output power and efficacy. To enhance the maximum power production capability and efficacy, the PV system needs a robust maximum power point tracking (MPPT) controller capable of tracking global maximum power peak (GMP) under PSCs. Many conventional algorithms, i.e., incremental conductance (Inc) , perturb and observe (P&O), etc., are reported in literature, but they are failed to track GMP and also create significant power oscillations in steady state during PSCs. Hence, this paper proposes metaheuristic algorithms-based TCT-configured PV MPPT system. In this, metaheuristic algorithms such as artificial bee colony (ABC), grey wolf optimization (GWO), and particle swarm optimization (PSO) techniques are applied to TCT-configured PV array to operate at GMP under four dynamic PSCs. All the metaheuristic algorithm-based MPPT methods are simulated in MATLAB/Simulink platform and their performances are compared with each other and also with conventional P&O and Inc techniques with respect to achieved GMP, tracking speed/convergence time, efficiency, and oscillations at GMP. The presented simulation results confirm that PSO algorithm outperforms other methods by achieving the highest GMP, efficiency, less convergence time, and reduced oscillations around GMP.

Keywords TCT configuration · Global maximum power · Artificial bee colony · Grey wolf optimization · Particle swarm optimization

1 Introduction

The world's expanding energy demand and diminishing conventional energy resources are driving a shift towards renewable energy sources. Among all energy sources, solar is the most promising because it is inexpensive, widely available, and

P. K. Bonthagorla (✉) · S. Mikkili
Department of EEE, NIT Goa, Ponda ,, Goa 403401, India
e-mail: praveennitgoa2017@gmail.com

eco-friendly [1]. The Indian energy revolution will be mostly powered by solar photo-voltaics (PV). Currently, for the vast majority of uses, including residential, commercial, and agricultural, as well as for charging electric vehicles, solar power generation is the best option. But the power generation under PSCs is somewhat complicated. To enhance the power output from PV panel, several MPPT techniques are reported in literature such as Conventional, Intelligence, Optimization, and Hybrid methodologies. But among these, classical techniques are less effective during partial shading conditions (PSCs) [2]. Recently, a good amount of research has been done in the area of MPPT control strategies for photovoltaic systems operating during PSCs. The environment which regularly sees non-uniform radiation changes the P–V curve in a matter of seconds, results in multiple peaks. The day-to-day emerging nature-based metaheuristic algorithms became the vital development in this PV MPPT-based research. Many techniques are emerged based on biological inspiration [3]. The MPPT is the most developing area in this era and it is emerging from conventional techniques [4–6] to intelligence techniques [7–9]. The nature-based metaheuristic methodologies are an advancement in intelligence techniques.

The optimization techniques [10–20] are inspired by nature and are most promising in regard to their performance. The drawback of both P & O and InC techniques is, unable to show a better performance, especially during PSCs [4, 5]. Research towards the enhancement in MPPT performance lead to the invention of intelligence-based techniques namely ANN and FLC. ANN [21], an intelligence technique replica of human brain, first acts well on the sample data to get the optimum point thereby can easily track the maximum point in real-time changing environment with the help of efficient training. Also, FLC [22] technique utilizes the mathematical approach of fuzzification, rule base, and de-fuzzification for reliable performance. These evolutionary techniques are well developed to handle all non-linear objective functions. Metaheuristic-based optimization technologies such as PSO [13], GWO [23], and ABC are getting used extensively in all sorts of applications, especially in the stream of engineering. Novel techniques of optimization came into existence most recently [21, 22].

The organization of this paper is presented as Stand-alone TCT-configured PV system is briefed in Sect. 2, followed by the implementation of metaheuristic algorithm-based MPPT techniques in Sect. 3. Results and Discussion is clearly discussed in Sect. 4. Finally, Sect. 5 deals with the conclusion.

2 Description of the Stand-Alone TCT-Configured PV System

The schematic diagram of the TCT configured stand-alone PV system architecture is presented in Fig. 1. It mainly comprises of TCT configuration of 4×4 PV array, boost converter as power optimizer, MPPT controller, and a resistive load.
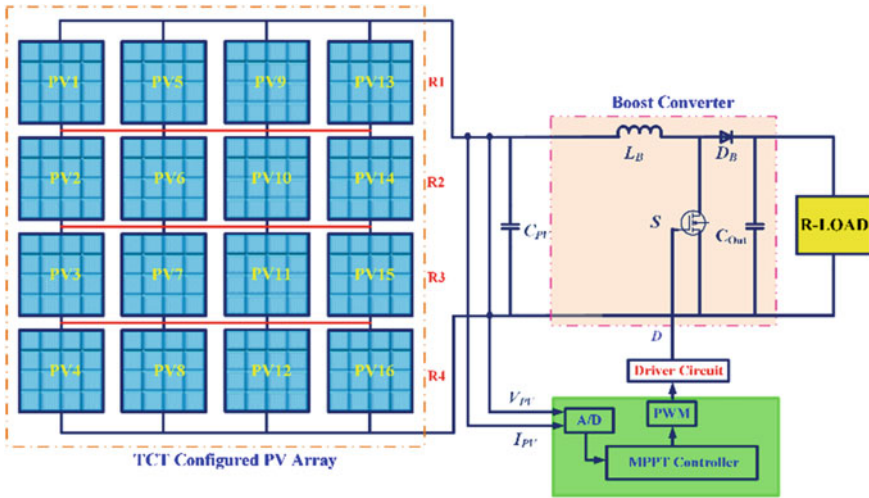
Fig. 1 Block diagram of the TCT-configured PV MPPT system

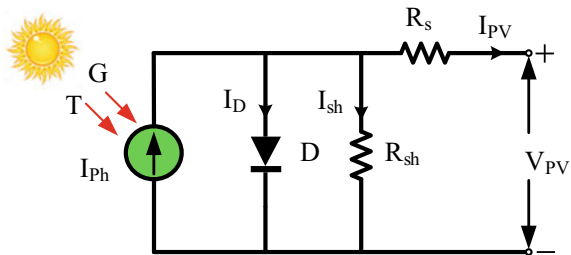## 2.1 Model of a Single-Diode PV Cell

Solar PV modeling is a significant area of research in which the accuracy of photo-voltaic characteristics is highly valued [8]. The model of an equivalent circuit-based PV cell is shown in Fig. 2. One way to approximate the ideal equivalent PV cell is to use a diode in parallel with a current source.

By applying KCL, the PV cell output current equation is expressed as

$$I_{PV} = I_{PH} - I_O\left(e^{\frac{V_{PV} + I_{PV}R_s}{\eta V_T}} - 1\right) - \frac{V_{PV} + I_{PV}R_s}{R_{sh}} \tag{1}$$

where $V_T = \frac{KT}{q}$ is the thermal voltage, the generated current at the output of PV cell is I_{PV} and the voltage generated at the output of PV cell is V_{PV}, the generated current by photons is I_{PH}, the reverse leakage current is Io, approximated practical cell parameters are series and shunt resistances (R_S and R_{Sh}). The PV panel output power is estimated as
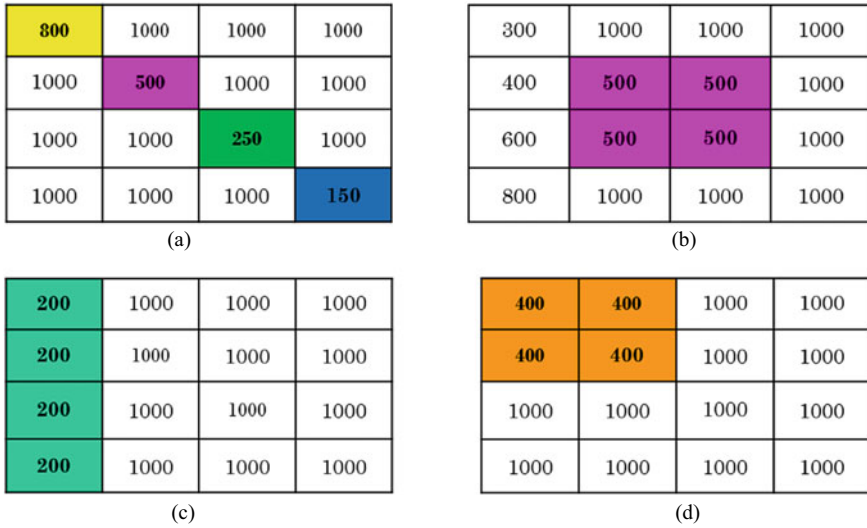
Fig. 2 Model of a single diode PV cell

800	1000	1000	1000
1000	500	1000	1000
1000	1000	250	1000
1000	1000	1000	150

(a)

300	1000	1000	1000
400	500	500	1000
600	500	500	1000
800	1000	1000	1000

(b)

200	1000	1000	1000
200	1000	1000	1000
200	1000	1000	1000
200	1000	1000	1000

(c)

400	400	1000	1000
400	400	1000	1000
1000	1000	1000	1000
1000	1000	1000	1000

(d)

Fig. 3 Models of partial shadings on TCT-configured PV array. **a** Diagonal; **b** center; **c** one column; **d** corner shading

$$P_{PV} = V_{PV} \times I_{PV} \qquad (2)$$

For simulation study, KC-200 GT PV module parameters ($P_{mp} = 200$ W, $V_{mp} = 26.3$ V, and $I_{mp} = 7.61$ A) were used.

2.2 Partial Shading Models on TCT-Configured PV Array

The energy output generation and efficacy of a PV system are greatly dominated by PSCs. To examine the performance of maximum power tracking capability of MPPT methods, some realistic partial shading conditions are created on a PV array of TCT configuration. The TCT configured PV array is having 16 PV modules and those are arranged in 4×4 array form. The created realistic partial shading patterns are diagonal, center, one column, and center. The shading models and the corresponding irradiation levels (W/m^2) on PV array are presented in Fig. 3.

2.3 Importance of Boost Converter

The boost converter is the main component of the PV MPPT system. It behaves as a power optimizer and is installed between TCT-configured PV source and the connected load. Its function is to boost the voltage of the PV array to some extent and

alter the system impedance by changing the duty ratio for operating the system at MPP point. The input and output relations (voltage and current) of the boost converter with reference to duty ratio (D) are described as

$$\left.\begin{array}{c} \frac{V_{Out}}{V_{PV}} = \frac{1}{1-D} \\ I_{Out} = (1-D)I_{PV} \end{array}\right\} \tag{3}$$

where V_{Out} and V_{PV} are the voltages at the output and input, and I_{Out} and I_{PV} are the output and input currents of the boost converter, respectively.

3 Metaheuristic Algorithms-Based MPPT Techniques

The MPPT controller is the most vital part of the PV MPPT system to operate at GMPP in the P–V curve under PSCs. In general, two methods are using often, namely P&O and InC. But these methods were trapped at local maximum peaks under dynamic varying irradiation conditions and also generates significant power losses in steady state in terms of power oscillations. Hence, metaheuristic algorithm-based MPPT techniques are evolved to overcome the weaknesses of conventional [4–9] and intelligence-based MPPT techniques [10–16].

3.1 Artificial Bee Colony (ABC)

This method is a metaheuristic approach based on honeybee colony foraging behavior. The foraging behavior of honeybee colonies [23]. It consists of three types of honeybees termed as employed, onlooker, and scouts. This optimization is carried out in four phases as given below. The flowchart of ABC MPPT method is given in Fig. 4.

Phase 1—Initialization phase: Initially, ABC generates a swarm size of SN solutions. *Phase 2—Employed Bee's phase:* Let each employee bee be $X_i = \{x_{i,1}, x_{i,2}, x_{i,3,\dots} \dots x_{i,D}\}$ which generated a new candidate solution V_i having components

$$v_{i,j} = x_{i,j} + \emptyset_{i,j}(x_{i,j} - x_{k,j}) \tag{4}$$

where i is the swarm's solution, D is the size of dimension, j is the dimension index selected randomly from $\{1, 2 \dots \dots D\}$, x_k is the randomly selected solution for all $i \neq j$, and $\emptyset_{i,j}$ is the number chosen randomly between [-1, 1].

Phase 3—Onlooker Bee's phase: Now using the greedy selection method, the fitness value of both V_i and X_i are calculated and X_i is updated with V_i. This knowledge is then shared with the onlooker bees who form the objective function as follows:
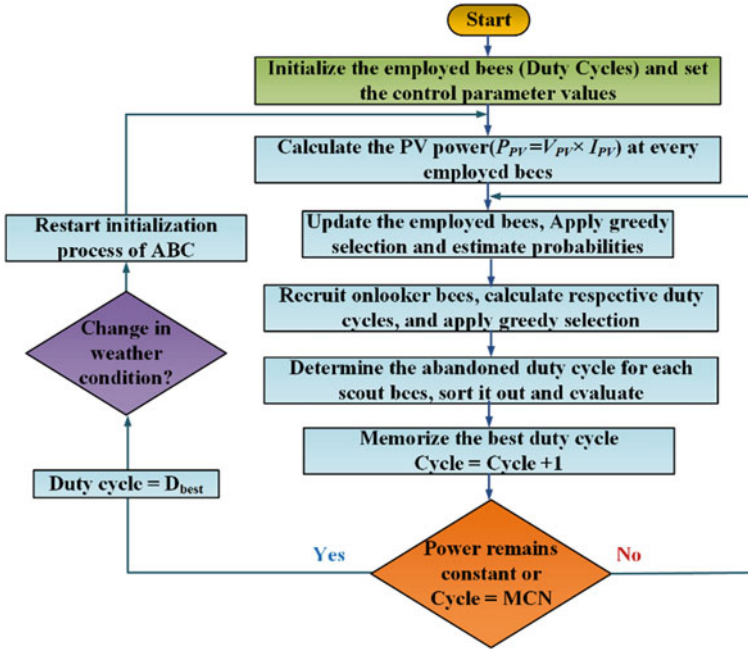
Fig. 4 Flowchart of ABC MPPT method

$$P_i = \frac{fit_i}{\sum_{j=1}^{SN} fit_j} \tag{5}$$

where fit_i is the value of the fitness solution X_i. The better the food source, the higher the probability of selection.

Phase 4—Scout Bee's Phase: If the position cannot be better further after a predetermined number of cycles, the location is discarded and the employed bee turns into a scout bee who discovers a new source of food and replaces X_i through the equation:

$$x_{i,j} = lb_j + rand(0, 1)(ub_j - lb_j) \tag{6}$$

where rand (0, 1) is chosen based on normal distribution, ub_j—interval of upper limit, and lb_j—interval of lower limit of jth dimensions.

3.2 Grey Wolf Optimization (GWO)

The grey wolf pack's hunting mechanism served as an inspiration for the development of the GWO algorithm. [23]. Based on their fitness and strength, the wolves are sorted into four different types as α, β, δ, and ω. The most dominant wolf in the pack, known

as the α, is responsible for the majority of the pack's decisions followed by β and δ. Afterward, the pack use this structure to locate the prey, encircle it, and finally attack the prey. To represent this wolf social hierarchy analytically, we use the best-fitting solutions in the order as α, β, δ, and ω. The GWO MPPT method flowchart is given in Fig. 5.

The mathematical model of encircling a prey during the hunt by search agents is described as

$$\vec{D} = \vec{C} \, \vec{X}_{p}(t) - \vec{X}_{p}(t) \tag{7}$$

$$\vec{X}(t + 1) = \vec{X}_{p}(t) - \vec{A} \, \vec{D} \tag{8}$$

Fig. 5 Flowchart of the GWO MPPT method
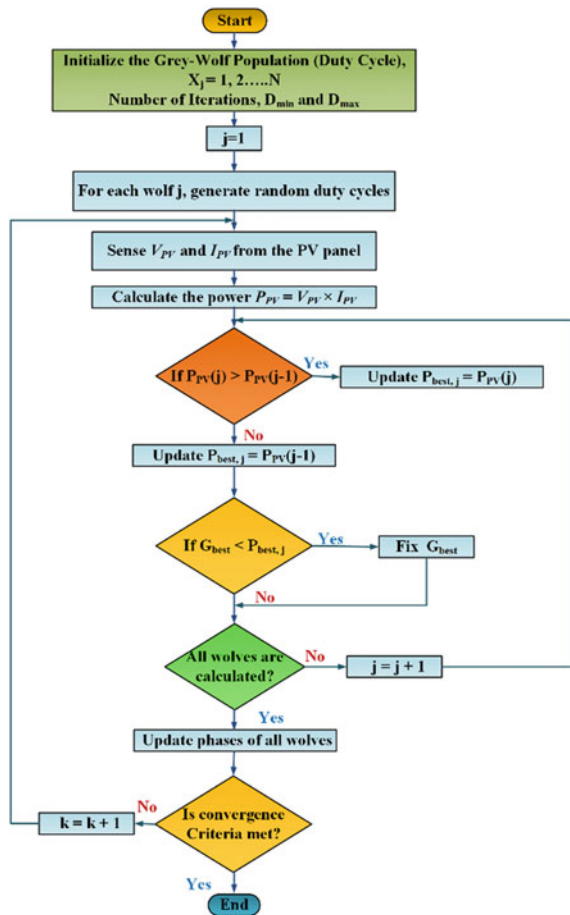
where the iteration is denoted by t at the present instant; coefficient vectors are denoted by D, A, and C; Xp and X denote the position vectors of prey and grey wolf.

The estimation of A and C vectors are given by

$$\left.\begin{array}{l} \overrightarrow{A} = 2\overrightarrow{a}.\overrightarrow{r_1} - \overrightarrow{a} \\ \overrightarrow{C} = 2.\overrightarrow{r_2} \end{array}\right\} \tag{9}$$

where $\overrightarrow{a}$ is the vector ranging from (2 to 0) and $\overrightarrow{r_1}$ and $\overrightarrow{r_2}$ are the vectors randomly selected in between [0, 1].

3.3   Particle Swarm Optimization (PSO)

This method is very popular in recent times for especially single-dimensional problems. It took inspiration from the flocking behavioral patterns of birds [23]. It works by generating a population of N particles, each starting with a random position x_i, and initial random velocities of v_i. Each particle remembers its best position (denoted as P_i) and its cost function (Value associated) with that position denoted as J_i. The best positions attained by the whole swarm are pointed to as the global best position designated by g_{best} or x_{best} with corresponding cost function J_{best}. The PSO algorithm memorizes all the best positions of each individual particle along with the global best obtained by the swarm. The flowchart of PSO MPPT method is given in Fig. 6.

The positions and velocities after each iteration are updated as follows:

$$v_i(t+1) = \omega.v_i(t) + C_1 r_1(P_i - x_i) + C_2 r_2(g_{best} - x_i) \tag{10}$$

Here, the newly updated velocity is denoted by $v_i\,(t+1)$, ω is inertial weight, current velocity is denoted by $v_i(t)$, C_1 is the coefficient of cognitive acceleration (pushes particle to local best), C_2 is the coefficient of social acceleration (pushes particle to global best), r_1 and r_2 are the numbers chosen randomly in [0, 1], x_i is the position at current instant, and P_i is the particles best position.

The updating of positions of the particles is as

$$x_i(t+1) = x_i(t) + v_i(t+1) \tag{11}$$

We follow the velocity updating function Eq. (10) and the position updating function Eq. (11) for each particle present in the swarm.
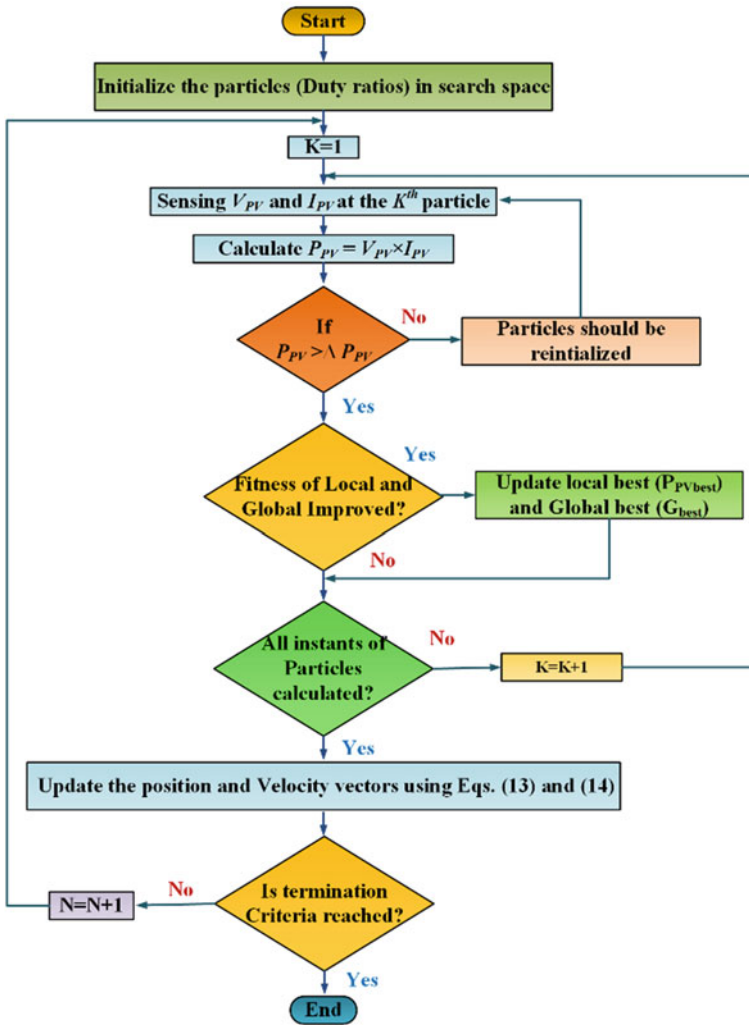
Fig. 6 Flowchart of the PSO MPPT

4 Results and Discussion

To investigate the effectiveness of conventional MPPT methods (P&O; Inc) and metaheuristic algorithm-based MPPT methods (ABC; GWO; PSO) four partial shading patterns are considered which are already detailed in Sect. 2. The above-mentioned MPPT methods were coded and simulated in MATLAB environment. The performance of all methods under each shading pattern is explained as follows:
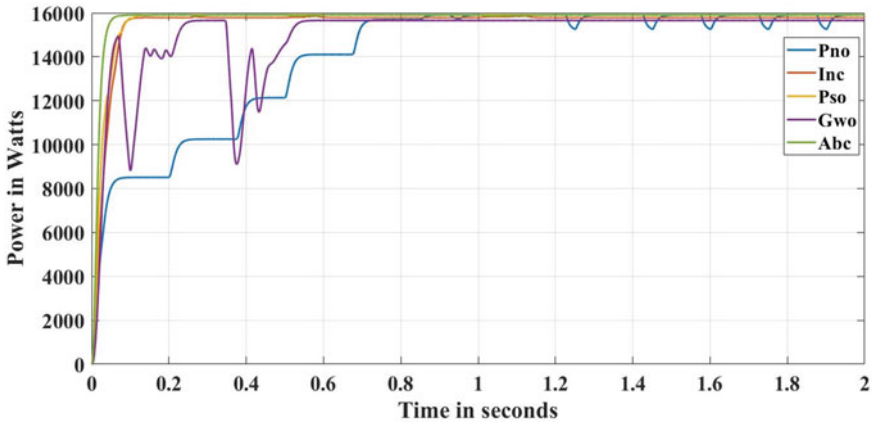
Fig. 7 Simulated power tracked with MPPT methods for uniform shading

Under uniform shading: During this shading pattern, all 16 modules in the TCT-configured PV array receives even irradiation of 1000 W/m². Because of the consistent irradiation, the *P–V* characteristics show only one global peak at 16000 W. The simulated power tracked from the PV array of all methods is presented in Fig. 7. From the obtained results from the simulation, it is observed that all the methods are efficiently tracking the GMP.

Under diagonal shading: In this kind of shading, due to the non-uniform irradiations on PV modules, the P–V characteristic of TCT-configured array constitutes four MPPs at 3900 W, 7200 W, 10,500 W, and 13,200 W, respectively. Though the P–V curve is having four MPPs, a significant amount of difference is there among the MPP points.

The simulated power tracked from the PV array of all methods is presented in Fig. 8. From the simulation study, it is clearly noticed that, due to the fixed perturbation in duty cycle, conventional methods are trapped at local peaks instead of global peaks. The optimization-based algorithms such as ABC, GWO, and PSO come close to the global maximum of 13200 Watts. Even though the algorithms come closer to the global MPP in this case, only the PSO method managed to arrive at the global MPP.

Under center shading: Due to this condition, TCT-configured PV array exhibits only two MPPs at 8000 W and 13,800 W, respectively, in the P–V curve. The simulated power tracked from the PV array of all methods is presented in Fig. 9. From the simulation study, it is evident that the PSO MPPT method significantly reaches around the global peak of 13,000 W. The GWO and ABC algorithms track the maximum power at 11,000 and 10,600 W, respectively. The conventional methods also track the global peak along with PSO, but these methods produced significant ripples in the steady state with longer convergence time.

Under one column shading: Due to this condition, TCT-configured PV array exhibit only one global peak in the P–V curve at 13,800 W. The simulated power
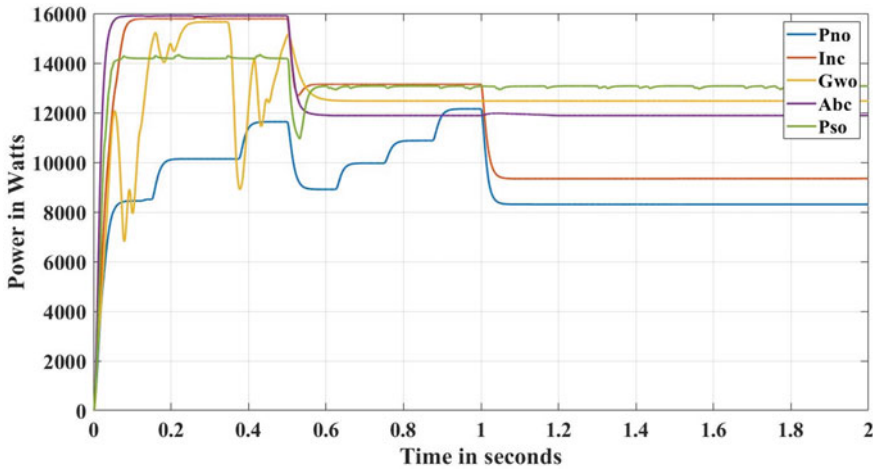
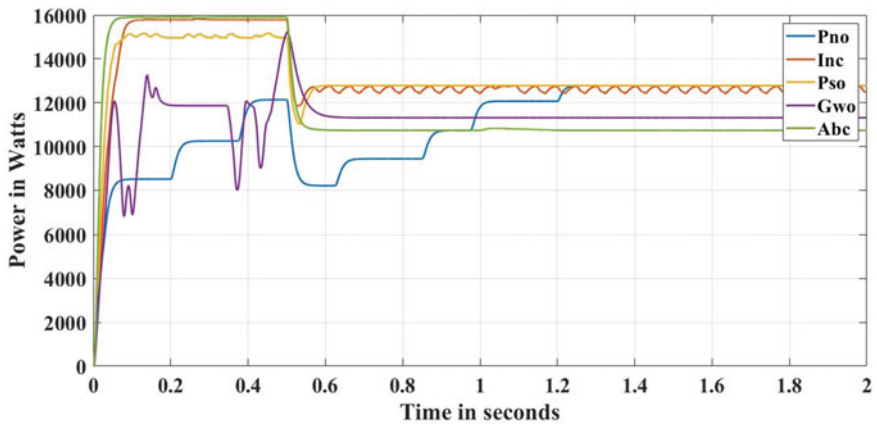**Fig. 8** Simulated power tracked with MPPT methods for diagonal shading

Fig. 9 Simulated power tracked with MPPT methods for center shading

tracked from the PV array of all methods is presented in Fig. 10. As the PV curve is having only one peak, hence all the algorithms could manage to reach the global peak. But the convergence time is different. From the simulation study, both classical algorithms, P&O and InC, are managed to do well in this case as there were no local maximums for the algorithms to get trapped in. The GWO algorithm is managed to reach closer to global maximum at 12459.2 W successfully in the steady state and the other algorithms PSO and ABC are trapped at 11903.6 W and 11903.5 W, respectively.

Under corner shading: Due to this condition, TCT-configured PV array displays only two MPPs in the P–V curve at 8000 W and 10,800 W, respectively. The simulated
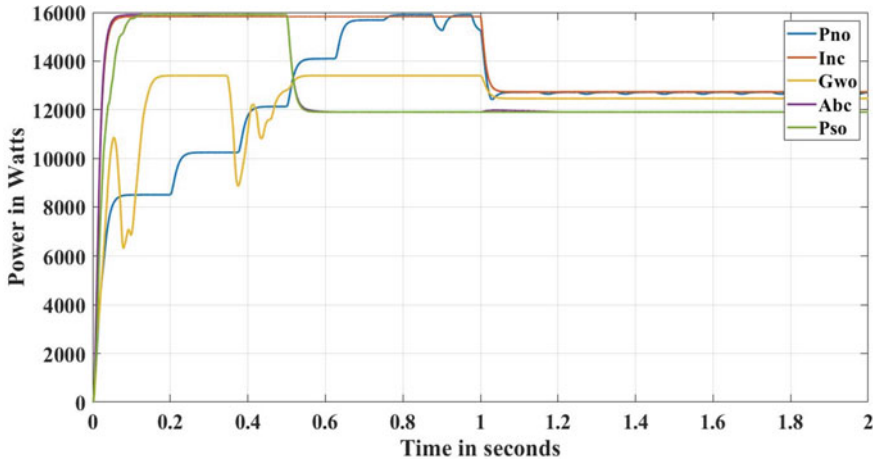
Fig. 10 Simulated power tracked with MPPT methods for one column shading

power tracked of all methods is presented in Fig. 11. From the obtained simulation results, it is noticed that the GWO MPPT algorithm significantly reaches around the GMP of 10,368 W. But the drawback is that it took more time to converge over other metaheuristic algorithms. The PSO and ABC algorithms track the maximum power at 6980 W and 6982 W, respectively. The conventional methods could not manage to reach global with significant ripples in the steady state and longer convergence time.

The performance of all metaheuristic and conventional algorithm-based MPPT methods are discussed with respect to tracked GMP, time of convergence, and tracking efficiency. The tracked GMP under PSCs is shown in Fig. 12, and from that, PSO MPPT method achieves the highest GMP under most shading conditions.
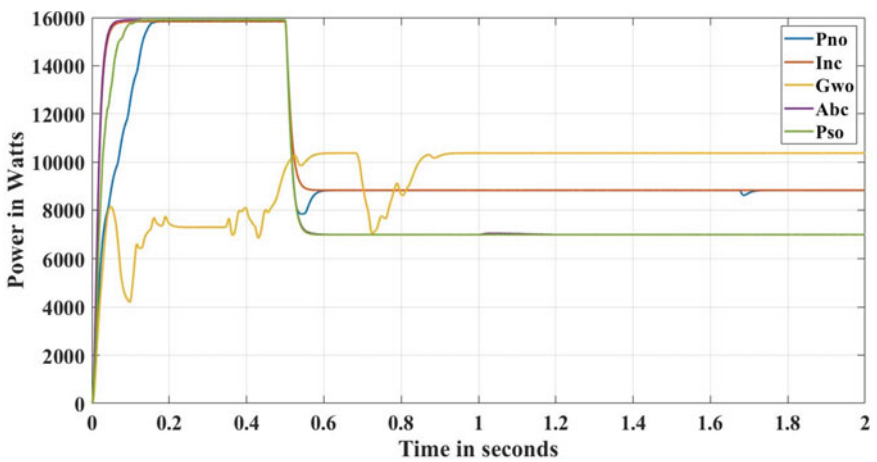

Fig. 11 Simulated power tracked with MPPT methods for corner shading
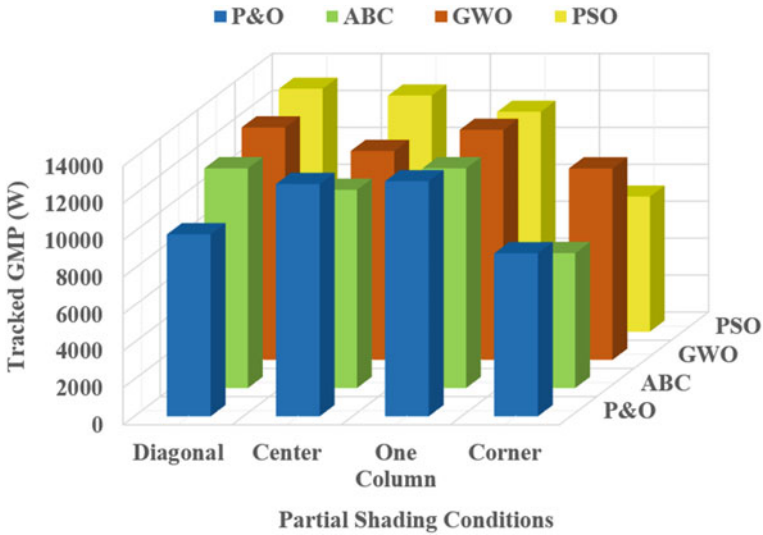
Fig. 12 Tracked GMPs of all MPPT methods during PSCs

Table 1 Performance factors of MPPT methods under four PSCs

Type of shading	Method	GMP at STC (W)	GMP under PSCs (W)	Tracking time (s)	Tracking Efficiency (%)
Diagonal	P&O	13,200	9854.2	**0.045**	74.65
	ABC		11,900	0.05	90.15
	GWO		12,589	0.13	95.37
	PSO		**13,150**	0.058	**99.62**
Center	P&O	13,800	12,580	0.78	91.15
	ABC		10,738	0.072	77.811
	GWO		11,312	0.11	81.97
	PSO		**12,783.5**	**0.07**	**92.63**
One column	P&O	13,800	**12,731**	0.12	**92.25**
	ABC		11,903.5	0.042	86.25
	GWO		12,459.2	0.06	90.284
	PSO		11,903.6	**0.04**	86.257
Corner	P&O	10,800	8824.0	0.085	81.70
	ABC		7309	0.045	67.67
	GWO		**10,368**	0.43	**96.00**
	PSO		7312	**0.04**	67.70

Here, we are not considering the Inc method in Fig. 12, because the performance of P&O and Inc methods are very similar.

The parameters for performance evaluation of the above-mentioned MPPT methods are tabulated in Table 1.

5 Conclusion

This paper clearly explains the metaheuristic algorithm-based TCT-configured PV MPPT system. For this system, conventional (P&O, InC) and metaheuristic (ABC, GWO, and PSO) MPPT algorithms were implemented to operate the TCT configured PV array at GMPP under dynamic PSCs. The comprehensive performance of the above-mentioned MPPT methods was examined and compared under four shading patterns. From the simulation results, P&O and Inc algorithms are not capable of tracking the GMP and produce oscillations in the steady state under most of the dynamic shading conditions, while the metaheuristic-based algorithms are capable of finding the GMPP. The metaheuristic algorithms, GWO and ABC, sometimes could not reach the global maximum and managed to evade to trap into local maximum. But, the PSO MPPT method was outperformed in the majority of PSCs in comparison with the other methods by reaching GMPP with less convergence time, high tracking efficiency, and less steady-state oscillations.

References

1. P.K. Bonthagorla, S. Mikkili, Performance analysis of PV array configurations (SP, BL, HC and TT) to enhance maximum power under non-uniform shading conditions. Eng. Reports (2020). https://doi.org/10.1002/eng2.12214
2. R. Bollipo, S. Mikkili, P. Bonthagorla, Critical review on PV MPPT techniques: classical, intelligent and optimisation. IET Renew. Power Gener. **14**(9), 1433–1452 (2019)
3. M.A. Mohamed, A.A.Z. Diab, H. Rezk, Partial shading mitigation of PV systems via different meta-heuristic techniques. Renew. Energy **130**, 1159–1175 (2019)
4. M.A.G. de Brito, L. Galotto, L.P. Sampaio, G.d.A.e Melo, C.A. Canesin, Evaluation of the main MPPT techniques for photovoltaic applications. IEEE Trans. Ind. Electron. **60**(3), 1156–1167 (2013). https://doi.org/10.1109/TIE.2012.2198036
5. R.B. Bollipo, S. Mikkili, P.K. Bonthagorla, Critical review on PV MPPT techniques: classical, intelligent and optimization. IET Renew. Power Gener. **14**(9), 1433–1452 (2020). https://doi.org/10.1049/iet-rpg.2019.1163
6. D. Casadei, G. Grandi, C. Rossi, Single-phase single-stage photovoltaic generation system based on a ripple correlation control maximum power point tracking. IEEE Trans. on Energy Convers. **21**(2), 562–568 (2006). https://doi.org/10.1109/TEC.2005.853784
7. B.J. Choi, S.W. Kwak, B.K. Kim, Design and stability analysis of single input fuzzy logic controller. IEEE Trans. Syst., Man, and Cybern., Part B (Cybern.) **30**(2), 303–309 (2000). https://doi.org/10.1109/3477.836378
8. R.B. Bollipo, S. Mikkili, P.K. Bonthagorla, Application of radial basis neural network in MPPT technique for stand-alone PV system under partial shading conditions. IETE J. Res. (2021). https://doi.org/10.1080/03772063.2021.1988874

9. T. Hiyama, S. Kouzuma, T. Imakubo, Identification of optimal operating point of PV modules using neural network for real time maximum power tracking control. IEEE Trans. Energy Convers. **10**(2), 360–367 (1995). https://doi.org/10.1109/60.391904

10. R.B. Bollipo, S. Mikkili, P.K. Bonthagorla, Hybrid, optimal, intelligent and classical PV MPPT techniques: a review. CSEE J. Power Energy Syst. **7**(1), 9–33 (2021). https://doi.org/10.17775/CSEEJPES.2019.02720

11. S. Mohanty, B. Subudhi, P.K. Ray, A new MPPT design using grey wolf optimization technique for photovoltaic system under partial shading conditions. IEEE Trans. Sustain. Energy **7**(1), 181–188 (2016). https://doi.org/10.1109/TSTE.2015.2482120

12. S. Mohanty, B. Subudhi, P.K. Ray, A grey wolf-assisted perturb observe MPPT algorithm for a PV system. IEEE Trans Energy Convers. **32**(1), 340–347 (2017). https://doi.org/10.1109/TEC.2016.2633722

13. H. Rezk, A. Fathy, Simulation of global MPPT based on teaching–learning based optimization technique for partially shaded PV system. Elect. Eng. **99**(3), 847–859 (2017)

14. A. Fathy, H. Rezk, A novel methodology for simulating maximum power point trackers using mine blast optimization and teaching learning-based optimization algorithms for partially shaded photovoltaic system. J. Renew. Sustain. Energy **8**(2), (2016), Art. no. 023503

15. Y. Wan, M. Mao, L. Zhou, Q. Zhang, X. Xi, C. Zheng, A novel nature inspired maximum power point tracking (MPPT) controller based on SSA-GWO algorithm for partially shaded photovoltaic systems. Electronics **8**(6), (2019), Art. no. 680.

16. A. Mellit, A.M. Pavan, A 24-h forecast of solar irradiance using artificial neural network: application for performance prediction of a grid-connected PV plant at Trieste, Italy. Sol. Energy **84**(5), 807–821 (2010)

17. R. Rajesh, M.C. Mabel, Efficiency analysis of a multi-fuzzy logic controller for the determination of operating points in a PV system. Sol. Energy **99**, 77–87 (2014)

18. S. Mirjalili, S.M. Mirjalili, A. Lewis, Grey wolf optimizer. Adv. Eng. Software **69**, 46–61 (2014)

19. A.F. Mirza, M. Mansoor, Q. Ling, B. Yin, M. Yaqoob Javed, A salp-swarm optimization based MPPT technique for harvesting maximum energy from PV systems under partial shading conditions. Energy Convers. Manag. **209** (2020). https://doi.org/10.1016/j.enconman.2020.112625

20. A.F. Mirza, M. Mansoor, Q. Ling, A novel MPPT technique based on Henry gas solubility optimization. Energy Convers. Manag. **225** (2020). https://doi.org/10.1016/j.enconman.2020.113409

21. J. Basil, B. Karthik, T. Sudhakar Babu, A.S. Mohammed, N. Rajasekar, Solar PV modelling and parameter extraction using artificial immune system. Energy Proc. **75**, 331e6 (2015)

22. J.P. Ram, T.S. Babu, T. Dragicevic, N. Rajasekar, A new hybrid bee pollinator flower pollination algorithm for solar PV parameter estimation. Energy Convers Manage **1**(135), 463–476 (2017)

23. J. Muhammad Yaqoob, A. Mirza, H. Rizvi, Hussain, Q. Lin, M.M. Gulzar, Safder, M. Mansoor, A comprehensive review on a PV based system to harvest maximum power. Electronics **8**, 1480 (2019). https://doi.org/10.3390/electronics8121480

Analysis and Controlling of Distribution Transformer Parameter using AVR Microcontroller IoT System

Aditya Virat, Apurva Ashish, Ranjeeta Patel, and Rudra Narayan Dash

Abstract Distribution transformers are among the foremost important equipment in power network. As the massive number of transformers distributed over a wide range in power electric systems, the information acquisition and condition monitoring are the crucial issue. Distribution transformers can not be operated at 100% efficiency in non rated condition, as the load is user dependent and it is not possible to control the user load. The main focus of this research work is the monitoring and controlling of distribution transformer using Internet of Things (IoT). If the transformer gets affected due to any of the reason that is voltage, current, temperature or humidity, it can be monitored and the necessary requisites can be provided to the distribution transformer within the appropriate time. The monitoring and controlling of temperature, humidity, voltage and current of distribution transformer is performed based on the AVR micro-controller ATMEGA 328P. After interfacing the specified components such as AVR microcontroller, sensors, Wi-Fi module and relay the proposed application programming in embedded-C is implemented in AVR microcontroller ATMEGA 328P. The sensing of relay with continuous reading of temperature, humidity, voltage, current values and same has been displaced on the LCD(16 × 2) screen and sending all the data of transformer to the web-server of ThingSpeak in real time using a Wi-Fi module commonly known as ESP 8266.

Keywords Transformer · Monitoring parameters · AVR micro-controller · ESP 8266 Wi-Fi module · ThingSpeak web server · IoT

A. Virat (✉) · A. Ashish · R. Patel · R. N. Dash
Kalinga Institute of Industrial Technology Deemed to Be University, Bhubaneswar, India
e-mail: adityavirat@gmail.com

A. Ashish
e-mail: 1803011@kiit.ac.in

R. Patel
e-mail: ranjeeta.patelfel@kiit.ac.in

R. N. Dash
e-mail: dash.rudranarayan@gmail.com

1 Introduction

The Internet of Things (IoT) can be said very safely that it creates the another industrial revolution. IoT is the network of physical objects with the characterization of an IP address concerned for internet connectivity. The physical objects like Industrial and utility components, sensors, and other everyday objects amalgamate with Internet connectivity. There are significant data analytic capabilities of IoT that promise to transform the way we work. The ever so growing network of physical objects will rival the marvels of past technology. IoT also refers to places where network connectivity and computing capability expands to objects and sensors, allowing these devices to generate, exchange and consume data with minimal human intervention. IoT implementations use disparate technical communications prototypes, each with its unique characteristics [1].

The distribution transformer can have 100% efficiency only under rated conditions. It also ensure that transformer will have longer life under rated condition. If the transformer is operated in overloading condition then it might be possible that the transformer gets damaged as a result unexpected power cut will be there in nearby areas, which will affect the large number of consumers of that particular area [2]. Due to overloading, that is in terms of voltage, current and power, the transformer will have lesser life. Increase in temperature and humidity also affects the life of transformer. The catastrophe in the transformer is mainly caused due to increase in load and natural climatic condition. This will affect the system's reliability to a great extent. The ineffective cooling of transformers under overloaded condition are the major reasons of power failure in all the distribution transformers. Generally faults occurs in transformer due to the following reasons [3, 4]:

i. Overloading of transformer, means that when the transformer is operating beyond the rated capacity, for a short period of time. As a result the protection relay cut off the power supply.
ii. During overloading condition of the transformer, temperature will also rise inside the body of transformer (Winding temperature and Oil temperature). As a result insulation failure due to both over voltage and over Current occurs.
iii. Oil inside the transformer is used for the cooling and insulation purpose but the break down voltage (BDV) value of the oil gets reduce due to the rise in temperature, mean there is a high chance of insulation failure inside the core of the transformer. As result the oil inside transformer will be less effective.
iv. Effect of humidity: Moisture is one of the dangerous enemy of Transformer which will affect the life cycle of transformer which as a result leads to deterioration of Transformer's material with very quick time. When there is any exposed part of the main tank to the environment, this will lead the oil of

the transformer to absorb the moisture from the air and accumulate it in the oil. Some of this moisture will be dropped down to the base of the transformer which results in corrosion, that we can see from outside and some of the moisture will be absorbed and accumulated again in the insulation papers between each winding turns. By this time insulation paper will be deteriorated and broken into pieces and cause short between turns this short will reduce the number of turns. When turns are connected together and number of turns reduced, this will cause the output voltage to be changed and the ratio of N_1/N_2 will be changed too. This will give a different output voltage [15–17].

The distribution transformer using Internet of Things (IoT) which monitors all the system parameters like voltage, current, temperature and humidity, oil level and send the same data to the ThingSpeak web server in real time for the accurate monitoring, so that the needful can be done. The selected parameters of the distribution transformer is being monitored online so that it will give all the useful information (in the form of data) about the transformer's health which will help us to optimally use transformer and keep the transformer in operation for longer time or period [5–11]. All this data which gets accessed through the ThingsSpeak web server will help to identify problem in the transformer before any serious fault occur, which results in avoiding huge expenditure and provide greater reliability to the power electrical system [12, 13].

Recently developed AVR microcontroller ATMEGA 328P being used in IoT due to its own advantage. The advantages can be depicted as: Microcontroller ATMEGA 328P readily usable without additional computing components with 32 KB of onboard self-programmable flash program memory as well as 23 programmable I/O lines. Code Efficient, all 31 registers are directly connected to the arithmetic logic unit (ALU), making it 10 times faster than conventional CISC microcontrollers [14].

The ATMEGA 328P microcontroller used on the Arduino has an analog-to-digital conversion (ADC) module, which has the ability of converting an analog voltage to a 10-bit number from 0 to 1023 or an 8-bit number from 0 to 255. The input to the module can be chosen from any one of six inputs on the chip. Micro-controller ATMEGA 328P stores all the input and output commands.

The intense motivation behind the research is to (i) Maintain uninterrupted power availability; (ii) To take precautionary measure for the transformers to protect or safeguard from breakdown or permanently damage, resulting in saving of huge expenses; (iii) To monitor parameters of number of transformers at a time of different loction, remotely and (iv) Preventative measure can be taken against any minor fault in time.

The main objective of this research work is to read and record the transformer parameters as temperature, humidity, voltage and current with all the possible information about the transformer in order to keep the transformer in good health condition. Once the information about the transformer is recorded the same data or information is sent through a wireless communication using the Wi-Fi module (ESP-8266) to the web-server of ThingSpeak. The web-server of ThingSpeak presents all the data in a systematic way, so that the information comes in organized manner, such that one can find the fault very easily if occurred at any point of time. As it is difficult for one to visit every transformer and note down all the readings, due to the large number of transformer present in a given area or radius. Using this IoT based system the data operator or workmen availed all the parameters information easily through mobile, computer, laptop etc. having internet facility in the real time, so that action can be taken before any serious fault occurs.

The paper has been arranged in the manner that Sect. 1 presents Introduction. Section 2 depicts the working principle of IoT based transformer along with circuit diagram, and in Sect. 3 the hardware implementation and results are presented following the conclusion.

2   IoT Based Transformer

Here the proposed IoT based transformer is analyzed in detail. The prototype of distribution transformer is used here for analysis is an air core isolation transformer. The monitoring of the parameters such as voltage, current, humidity and temperature is being tracked of the prototype transformer. The k.V.A. rating of the used prototype transformer is 0.115 k.V.A.

2.1   Analysis of IoT Based Prototype Transformer

Figure 1 depicts the IoT based transformer with voltage, current, temperature and humidity sensors to sense the parameters value concerned. The circuit diagram consists of transformer of 0.115 k.V.A as TR-1, potential transformer (PT) as TR-2, current transformer (CT) as TR-3, bridge rectifier, voltage regulator IC 7805, Wi-Fi module (ESP-8266), DHT-11 temperature and humidity sensor, relay, micro-controller ATMEGA 328P, LCD (16 × 2) screen.
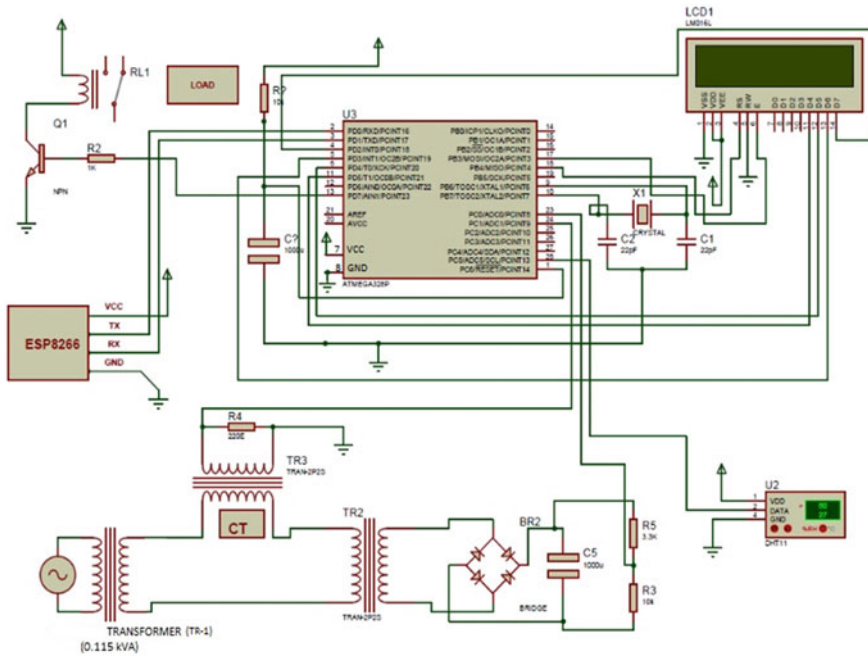
Fig. 1 IoT based transformer with sensors and microcontroller

ATMEGA 328P utilized all the sensed parameters value and processed. For processing the programming embedded in C (Programming Language) is performed here. For programming the analog sensed parameters value have been used with the output in digital form. The voltage gets sensed by PT(TR-2) but there is no set limit, as here it is considered within the range of 215–230 V. The other parameters value in the programming are as follows:

i.   350 mA < Current < 0 mA
ii. 40 °C < Temperature < 0 °C
iii. 70% < Humidity < 0%

If the parameters value concerned is more than the set values then the relay gets tripped. In case of any abnormal condition the micro-controller will give command to relay to trip or switch off the transformer load and start the buzzer for safety point of view and for smooth identification of the transformer. The transformer load will not get the supply until unless the problem is attended. All this data will also be reflected to the web server also. This abnormal condition can be due to any of the following reasons.

i.   Overloading
ii. Temperature rise
iii. Humidity rise
iv. Over-current
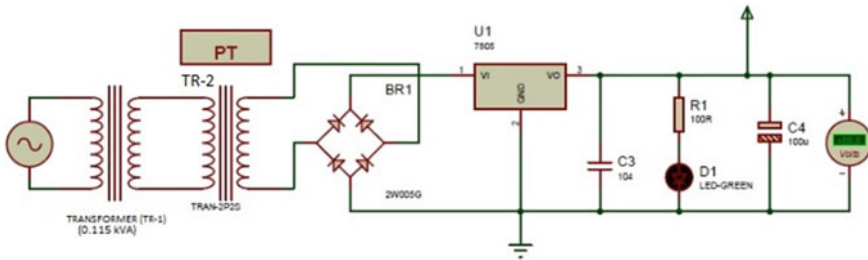
Fig. 2 Calibrated DC voltage sensing system

When the problem is attended (or fault resolved), then the transformer is again ready for normal operation until unless the reset switch is pressed.

The Wi-Fi module ESP-8266 sends the sensed parameters value of voltage, current, temperature, humidity to the web server of ThingSpeak in real time. So that parameters value can be monitored and take proper action before any serious fault occurs. The data can be accessed by using Internet through mobile, laptop, tablet, etc.

The prototype transformer (TR-1) 0.115 k.V.A is used here for the analysis of its different parameters such voltage, current, temperature and humidity. The primary and secondary voltage of transformer are rated same as 230 V that is 1:1 turn ratio. The secondary side of the transformer (TR-1) is connected to the PT(TR-2). The PT(TR-2) is the step-down voltage transformer which reduces supply voltage to low voltage for the purpose of measuring. The PT(TR-2) is being used here to sense the voltage of the transformer (TR-1). Along with this the PT(TR-2) secondary voltage is also utilized to provide supply for ESP 8266 (Wi-Fi module) and microcontroller ATMEGA 328P. To run the ESP 8266 Wi-Fi module, the PT(TR-2) primary voltage 230 V being step down to 12 V. The 12 V AC of PT(TR-2) secondary is then rectified through the single phase bridge rectifier. After this an IC 7805 is used to convert this 12–5 V DC. The calibrated value of 12 V AC of PT(TR-2) secondary is 5 V. In other words it can be said that 230 V of TR-1 is calibrated to 5 V as can be seen in Fig. 2. After that two resistors are placed in order to get 3.3 V to power up the ESP 8266 Wi-Fi module the rest 1.7 V is drop across the resistor as can be seen in Fig. 1. In the same way the microcontroller ATMEGA 328P is supplied from the IC 7805 based voltage regulated circuit in pin number 7 as shown in Fig. 1 clearly. Again the same 5 V analog DC supply from IC 7805 is being used by the micro-controller ATMEGA 328P for the programming calculation with digital output. The same digital output is displayed in LCD(16 × 2) screen. The components involved in Fig. 2 for voltage sensing is intentionally not kept in Fig. 1 to reduce the complexity, otherwise Fig. 2 is a part of Fig. 1.

The secondary side of the transformer (TR-1) is connected to the primary of the current transformer (CT TR-3). The CT(TR-3) is a step down current transformer which is used to measure the high value of current in calibrated form. Here the CT(TR-3) measures the amount of current flowing through the transformer (TR-1). After measuring the value of current, the data is being used by the microcontroller ATMEGA 328P for programming purpose. The processed data of microcontroller ATMEGA 328P is sent to the web server of ThingSpeak through Wi-Fi module (ESP 8266) for continuous monitoring by the user. The same processed data of current through microcontroller ATMEGA 328P is also displayed in LCD(16 × 2) screen. The maximum set value of current for prototype model is 350 mA. The fault at which the current increased beyond this set value the relay trips and the same reflects on LCD(16 × 2) screen and web server (ThingSpeak).

To measure the temperature and humidity for the transformer (TR-1), a commonly known sensor DHT-11 is used. The sensed parameters value are send to microcontroller for processing and monitoring purpose. The microcontroller ATMEGA 328P monitors the temperature and humidity as per set values. The maximum set value for temperature is 40 °C and 70% for humidity. If temperature and humidity are more then the set values concerned then the relay gets tripped and the same is reflected in the LCD(16 × 2) screen and web server of ThingSpeak.

Apart from this the location of the transformer (TR-1) is also important, therefore location is entered manually using Google Maps in longitude and latitude, this can be seen in the hardware implementation and results section.

2.2 Program Code

Here only the main part of the program has been shown. All programming is performed in Arduino IDE 1.8.16 [18] and the same program is installed in microcontroller ATMEGA 328P. The same microcontroller ATMEGA 328P is placed in the project which is used for research work. There are some set point installed in the microcontroller ATMEGA 328P for monitoring purpose such the current should be less then 350 mA, temperature below 40 °C, humidity less then 70% this means that the transformer is in normal condition. In case if the value is deviated beyond the set point values that means the transformer is in abnormal condition in this case microcontroller ATMEGA 328P will send command to relay to trip the power supply. As a result the transformer life is increased.

```
Program (Output)
void loop()
{
    int chk = DHT.read11(DHT11_PIN);
    /////////////////////////////////////
    average=0;
    for(i=0;i<AV_Value;i++){
      CurrentValue = analogRead(CT);
      average=average+CurrentValue;
      delay(1);
    }
    Phase1=average/AV_Value;
    Phase1=(Phase1/73.86);
    /////////////////////////////////////
    int sensorValue = analogRead(VOLT);
    float voltage = sensorValue * (5.0 /
1023.0);
    voltage=73.43*voltage + 20;
                      lcd.setCursor(0,    0);
    lcd.print(DHT.temperature);lcd.print("C'
    ");
    lcd.print(DHT.humidity);lcd.print("%");
                      lcd.setCursor(0,    1);
    lcd.print(voltage);lcd.print("V");
    lcd.print(Phase1);lcd.print("Amp");
    if(Phase1>0.35){
                  digitalWrite(Relay,HIGH);
digitalWrite(Buzzer,HIGH);
```

```
        while(1);

    }

            else   if(DHT.temperature>40   ||
DHT.humidity>70){

                    digitalWrite(Relay,HIGH);
digitalWrite(Buzzer,HIGH);

        while(1);

    }

    else{

                    digitalWrite(Relay,LOW);
digitalWrite(Buzzer,LOW);

    }

    INC++;

    if(INC==10){

     ThingSpeakWrite(DHT.temperature,DHT.hum
idity,Phase1,

        voltage);

    INC=0;

    }

    delay(1000);

    lcd.clear();

}
```

3 Hardware Implementation and Result

The Fig. 3 represents the experiential set up of IoT based transformer. The prototype transformer (TR-1) model being used here is of 0.115 kVA the primary and secondary voltage is set as same as 230 V. The other equipment used here are potential transformer (PT) as TR-2, current transformer (CT) as TR-3, bridge rectifier, voltage regulator IC 7805, Wi-Fi module (ESP-8266), DHT-11 temperature and humidity sensor, relay, micro-controller ATMEGA 328P, LCD(16 × 2) screen.

The Wi-Fi module (ESP 8266) is sending all the parameters such as voltage, current, temperature, and humidity value to the web-server of Things-Speak which is being updated in every 15 s, and the same is displayed on the LCD screen in real-time. This proposed project reduces the manpower requirement and will also
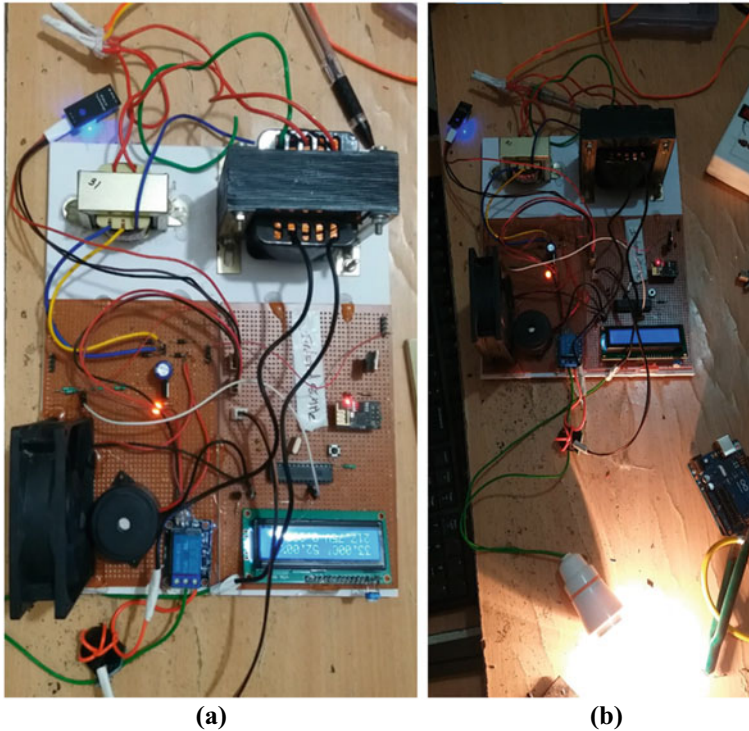
Fig. 3 Hardware implementation of IoT based transformer **a** and **b** at different conditions

provide an effective and accurate reading. As all the parameter values which getting updated in web server of ThingSpeak are in real-time, so that the safety measures can be taken within time. This project will also ensure that safety, and does not cause any harm to our surroundings and environment. The results presented here are taken from HP laptop.

Here the experimental set up figure has been shown for normal and abnormal condition. The Fig. 3a represents the normal condition that is all parameters value are satisfying the maximum point of set values as 350 mA current, 40 °C temperature and 70% humidity.

For normal condition the LED bulb of 12 W is implemented with the prototype IoT based transformer experimental set up. The reading for current is 52 mA by considering the voltage as 230 V.

The Fig. 3b represents the prototype experimental set up of IoT based transformer during abnormal condition. Here the load as incandescent lamp of 100 W is employed with the IoT based transformer and the fault current is created artificially. The calculated current for the used 100 W incandescent lamp is 434 mA which is more then the maximum set value 350 mA. As soon as the bulb glows as can be seen in Fig. 3b the relay gets tripped and the same result is reflected in the experimental
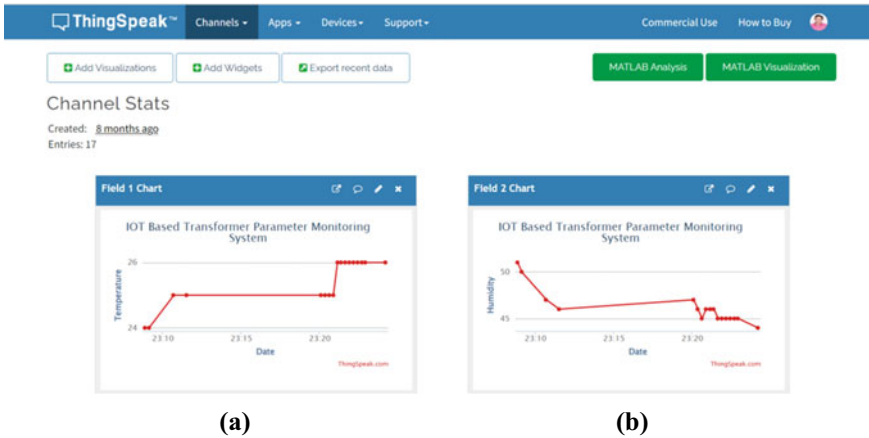
Fig. 4 Web-server result of **a** temperature results w.r.t date and time; **b** humidity results with respect to date and time
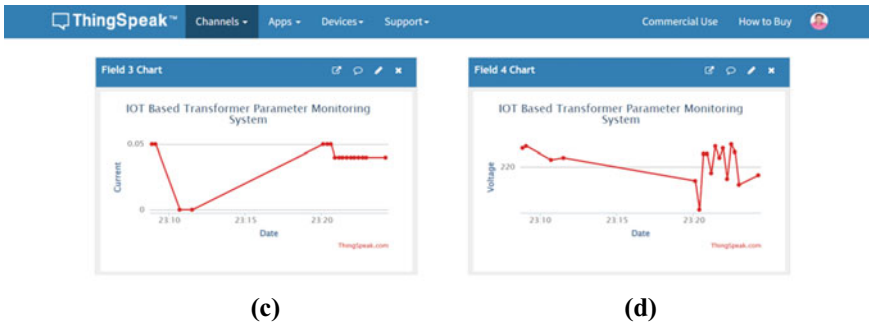

Fig. 5 Web-server result from ThingSpeak of **c** current results with respect to date and time; **d** voltage results with respect to date and time

results depicted in Fig. 5c. The current reading in Fig. 5c is 0 A due to tripped in relay taken from web server ThingSpeak. In the same way the result for voltage, temperature, and humidity are shown in Figs. 5d and 4a, b in abnormal condition respectively. Figure 6e depicts the location of the prototype IoT based transformer. Figure 6f represent the current in the form of odometer.

(e) **(f)**
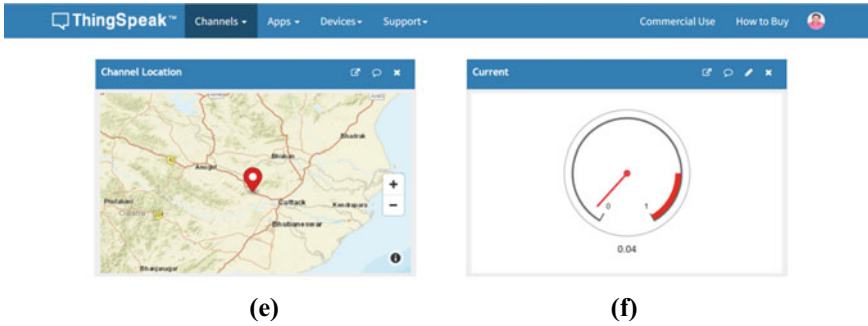
Fig. 6 Web-server result from ThingSpeak of **e** location of the transformer; **f** current results with respect to date and time (odometer)

4 Conclusion

The transformers play a significant role in the distribution part of the power system. Therefore the monitoring and protection of the transformer are eminently crucial. Here the prototype experimental setup for IoT based transformer using microcontroller ATMEGA 328P and Wi-Fi module (ESP 8266) is designed successfully. The parameters voltage, current, temperature and humidity are sensed and uploaded to web server of ThingSpeak with success. Those data can be sent and accessed using the HTTP protocol. The uploaded parameters value tracked from laptop as presented in the experimental setup and results section. The prototype experimental setup gets tripped with 434 mA as it is more then the maximum set value of 350 mA. Therefore, the real-time data collection, storage, and monitoring of the transformer parameters are feasible with the system.

4.1 Future Scope

- An artificial intelligence can be comprised to this system for receiving and storing transformer parameters information occasionally about all the distribution transformers.
- In future, user can have on board computer or the display system on which user can set the parameters of distribution transformers.
- In future, more number of sensor can be used in order to find more faults.
- All the parameters data which are stored in the web server can be used for the purpose of machine learning algorithms.

References

1. T.D. Poyser, An on-line microprocessor based transformer analysis system to improve the availability and utilization of power transformers. IEEE Trans. Power Appar. Syst. **PAS-102**(4), 957–962, (1983). https://doi.org/10.1109/TPAS.1983.317809

2. Y. Han, Y.H. Song, Condition monitoring techniques for electrical equipment-a literature survey. IEEE Trans. Power Deliv. **18**(1), 4–13 (2003). https://doi.org/10.1109/TPWRD.2002.801425

3. S. Apte, R. Somalwar, A. Wajirabadkar, Incipient fault diagnosis of transformer by DGA using fuzzy logic, in *2018 IEEE International Conference on Power Electronics, Drives and Energy Systems (PEDES)* (2018), pp. 1–5. https://doi.org/10.1109/PEDES.2018.8707928

4. G. Wang, Y. Liu, X. Chen et al., Power transformer fault diagnosis system based on Internet of Things. J. Wireless Com. Network **2021**, 21 (2021). https://doi.org/10.1186/s13638-020-01871-6

5. W.K.A. Hasan, A. Alraddad, A. Ashour, Y. Ran, M.A. Alkelsh, R.A.M. Ajele, Design and implementation smart transformer based on IoT, in *2019 International Conference on Computing, Electronics & Communications Engineering (iCCECE)* (2019), pp. 16–21. https://doi.org/10.1109/iCCECE46942.2019.8941980

6. K. Hazarika, G. Katiyar, N. Islam, IOT based transformer health monitoring system: a survey, in *2021 International Conference on Advance Computing and Innovative Technologies in Engineering (ICACITE)* (2021), pp. 1065–1067. https://doi.org/10.1109/ICACITE51222.2021.9404657

7. C.J. Mozina, Impact of smart grids and green power generation on distribution systems, IEEE Trans. Ind. Appl. **49**(3), 1079–1090 (2013). doi: https://doi.org/10.1109/TIA.2013.2253292

8. P. Bodke, A.A. Kalage, Design of an IoT based system for monitoring and controlling the sub-station equipment. in *Techno-Societal 2020*, ed. by P.M. Pawar, R. Balasubramaniam, B.P. Ronge, S.B. Salunkhe, A.S. Vibhute, B. Melinamath (Springer, Cham, 2021). https://doi.org/10.1007/978-3-030-69921-5_14

9. Y. Cai, X.Q. Huang, J. He, High-voltage equipment monitoring system based on IOT. in: *Wireless Communications and Applications. ICWCA 2011. Lecture Notes of the Institute for Computer Sciences, Social Informatics and Telecommunications Engineering*, vol. 72, ed. by P. Sénac, M. Ott, A. Seneviratne (Springer, Berlin, Heidelberg, 2012). https://doi.org/10.1007/978-3-642-29157-9_5

10. H.N. Sen, A. Srivastava, M.V. Reddy, V. Singh, IoT-integrated voltage monitoring system, in *Control Applications in Modern Power System. Lecture Notes in Electrical Engineering*, vol. 710, ed. by A.K. Singh, M. Tripathy (Springer, Singapore, 2021). https://doi.org/10.1007/978-981-15-8815-0_16

11. C. Bengtsson, Status and trends in transformer monitoring. IEEE Trans. Power Deliv. **11**(3), 1379–1384 (1996). https://doi.org/10.1109/61.517495

12. L. Thangiah, C. Ramanathan, L.S. Chodisetty, Distribution transformer condition monitoring based on edge intelligence for industrial IoT, in *2019 IEEE 5th World Forum on Internet of Things (WF-IoT)* (2019), pp. 733–736. https://doi.org/10.1109/WF-IoT.2019.8767272

13. M.M. Ahmed, M.O. Qays, A. Abu-Siada, S.M. Muyeen, M.L. Hossain, Cost-effective design of IoT-based smart household distribution system. Designs, **5**, 55 (2021). https://doi.org/10.3390/design5030055

14. H. Jamal, M. Waseem, I.A. Sajjad, A. Anjum, M.S. Khan, Low-cost feedback control thermal protection system for 3-phase distribution transformer using microcontroller, in *2018 IEEE International Conference on Smart Energy Grid Engineering (SEGE)* (2018), pp. 200–204. https://doi.org/10.1109/SEGE.2018.8499489

15. Y. Lin, R. Liao, Y. Liu, H. Zhao, J. Li and Z. Zhao, in Effects of moisture on furfural distribution and aging estimation of transformer cellulose insulation, in *2018 12th International Conference on the Properties and Applications of Dielectric Materials (ICPADM)* (2018), pp. 447–450. https://doi.org/10.1109/ICPADM.2018.8401051

16. Z. Jiang, W. Chen, L. Jin, H. Zhang, F. Cui, X. Li,Effect of humidity on the detection of dissolved gases in transformer oil for tin oxide based gas sensor, in *2018 IEEE International Conference on High Voltage Engineering and Application (ICHVE)* (2018), pp. 1–4. https://doi.org/10.1109/ICHVE.2018.8642030

17. L. Naranpanawe, T. Saha, C. Ekanayake,Moisture and temperature effects on power transformer winding clamping pressure, in *2016 IEEE PES Asia-Pacific Power and Energy Engineering Conference (APPEEC)* (2016), pp. 74–78. https://doi.org/10.1109/APPEEC.2016.7779473

18. O.E. Amestica, P.E. Melin, C.R. Duran-Faundez, G.R. Lagos, An experimental comparison of Arduino IDE compatible platforms for digital control and data acquisition applications, in *2019 IEEE CHILEAN Conference on Electrical, Electronics Engineering, Information and Communication Technologies (CHILECON)* (2019), pp. 1–6. https://doi.org/10.1109/CHILECON47746.2019.8986865

A Comparison of PSO, GA and FA-Based PID Controller for Load Frequency Control of Two-Area Hybrid Power System

Ajay Kumar, Deepak Kumar Gupta, Sriparna Roy Ghatak, and Soubhagya Ranjan Prusty

Abstract This paper presents a comparative study between three different optimization techniques such as Particle Swarm Optimization (PSO), Genetic Algorithm (GA) and Firefly Algorithm (FA) for tuning the parameters of proportional-integral-derivative (PID) controller in load frequency control (LFC) of a two-area hybrid power system. In this paper, Power systems are composed of renewable and non-renewable sources along with battery energy storage (BES) and superconducting magnetic energy storage (SMES) as energy storage systems. The integral time absolute error (ITAE) was selected as the objective function. Additionally, the controllers are likewise regulated to confirm that the tie-line power and frequency of the hybrid power system are inside the adequate limits. Comparison of the optimization technique is done on the basis of settling time, objective function and convergence characteristics, and their results illustrate the best performance of the proposed method PSO.

Keywords ITAE · Renewable energy sources · Hybrid energy storage system (HESS) · Settling time · Convergence characteristics · PID controller component · Load frequency control

A. Kumar (✉) · D. K. Gupta · S. R. Ghatak · S. R. Prusty
School of Electrical Engineering KIIT Deemed to Be University Bhubaneswar, Bhubaneswar, India
e-mail: 0631ajay@gmail.com

D. K. Gupta
e-mail: Dpkgpt214@gmail.com

S. R. Ghatak
e-mail: Sreeparna.ghatak@gmail.com

S. R. Prusty
e-mail: soubhagya.prustyfel@kiit.ac.in

1   Introduction

With the global energy crisis and environmental pollution, other sources such as solar, wind, bio-mass and hydro are being employed mainly to produce electricity in modern times. A hybrid system consisting of renewable and non-renewable sources proposes a better choice than a single-source-based system in terms of efficiency, economy and reliability [1]. In this paper, we concentrated especially on photovoltaic (PV) and wind-based hybrid systems. Due to their complementary natural advantages, wind and PV are the most promising power generating sources [2]. As these renewable energy sources are intermittent in nature, we use BES along with SMES for the reliable operation of the system. The SMES has higher power density and lower energy density in comparison to other energy storage systems, whereas the battery has higher energy density. So, the overall HESS can be improved in terms of power and energy density by combining SMES and batteries [3]. In an interconnected power system, besides control of frequency, the generation within each area has to be also controlled to maintain power exchange. This control of generation and frequency is known as LFC [4]. Further, it is observed that the system complexity increases as we add renewable energy sources [5]. As the penetration of intermittent solar and wind power is increasing day by day in power systems and load also varies in a random way, it results in frequency and system voltage fluctuations [6].

In this paper, two different cases are considered. In case one, a load variation of 3% in area one and 6% in area two are considered, whereas in case two both the areas of the test system are subjected to a load increment of up to 3%.

Together, frequency along with tie-line power errors becomes zero by adjusting the area control error (ACE) to zero by the automatic generation control (AGC) [7]. For the minimization of frequency variation balancing of the flow of real power inside the system is main task [8]. For this purpose, our main task in this paper is the selection of an efficient controller as the system which is a combination of renewable and conventional sources.

Researchers all over the world proposed numerous approaches [9–11] related to LFC for interconnected power systems to preserve the frequency and tie-line power during normal as well as load variation condition. The method of PID perception is instigated on a hybrid arrangement to analyze the behavior of AGC by choosing appropriate optimal gains throughout perturbations [12]. Some of them also proposed a hybrid technique with the combination of different optimization techniques [13]. PSO tuned PID controller [14], GA tuned PID controller [15] and FA tuned PID controller [16] are studied separately, and then they are compared in this paper.

In this paper, PID1 and PID2 in area one, and PID3 and PID4 in area two are tuned and optimized by PSO, GA and FA. A hybrid energy system along with hybrid energy storage with different load changes is applied with a comparative optimization to tune the PID controller for the systems. Many of the previous research works used PSO, GA and other optimization techniques, but a very few research were done on the comparative study [13–16] that will help researchers to choose the optimization technique for a controller in future.

In this paper, the major contribution is as follows:

1. Modeling of the hybrid test system with renewable, non-renewable resources, and storage like PV, wind turbine generators (WTG), DEG, SMES and BES.
2. PSO, GA and FA are applied to adjust and tune the parameters of the PID controller realized in the considered system, and a comparative study of the behavior of the system in respect of settling time, objective function and convergence characteristics is done.
3. Authenticating the robustness of the intended system by changing the load of the system in both areas with two different cases.

2 System Investigated

A hybrid power system model is designed that comprises of WTG, SMES along with DEG in area one and in area two, PV, BES in conjunction with DEG. The arrangement of different components is depicted in Fig. 1. The modeling of the above-debated systems is explained below.
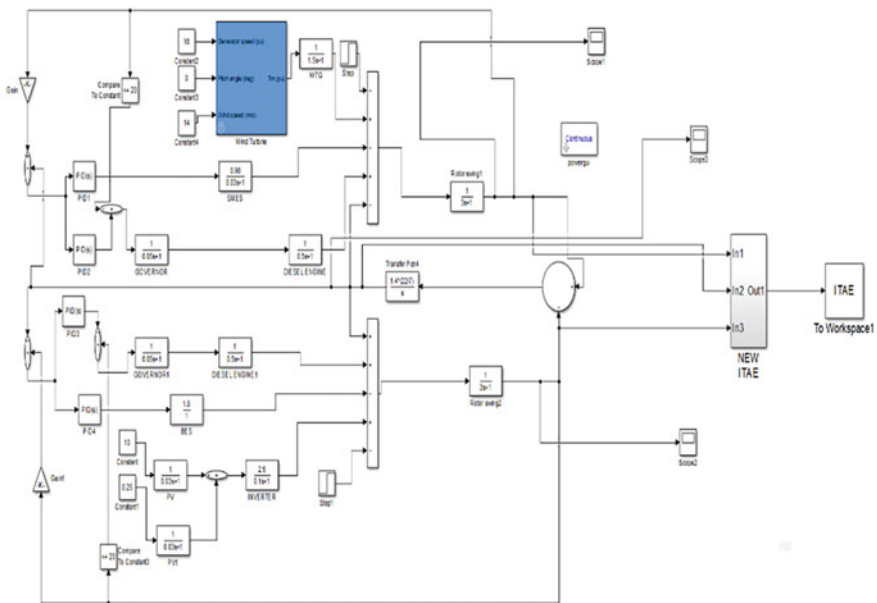
Fig. 1 Model of a two-interconnected-area hybrid renewable energy system

2.1 WTG Model

Mechanical power extracted as of wind system is [17]

$$P_{Wt} = 0.5\rho A_R v_w^3 C_p(\beta, \lambda) \tag{1}$$

where P_{wt} is power taken from wind, ρ is air density (kg/m^3), A_R is brushed area of the blade, V_ω is rapidity of the wind and C_p is power constant, which can be explained mathematically as

$$C_p = \frac{1}{2}(\lambda - 0.022\beta^2 - 5.6)e^{-0.17} \tag{2}$$

2.2 Solar PV System

The power produced by the photovoltaic system:

$$P_{solar} = P_{pv} \times \frac{G}{G_{ref}} \times [1 + K_t(T_{amb} + 0.0256 \times G - T_{ref})] \tag{3}$$

where P_{solar} is output photovoltaic power, P_{pv} is rated power and G is solar-irradiance (W/m^2).

2.3 Battery Energy Storage System

As the renewable sources are intermittent in nature, a large amount of energy is stored with the help of BESS, and it can supply at the load side during peak demand time. In this way, BESS acts as a complementary for these types of PV and WTG [18].

2.4 Diesel Engine Generatorn

The shortage of power is provided by the DEG once WTG/PV fails to accomplish the generating-load demand balance situation. DEG always acts as a backup.

2.5 SMES Model

SMES is one system which stores direct electrical energy with specific power density, infinite discharge and charge cycles, and it discharges the electrical power within milli-seconds with an energy conversion efficiency of above 95% [19, 20].

3 PID Controller and Power System

The comparative study is done using three different optimization techniques, namely PSO, GA and FA. The output of PID can be written as

$$u(t) = K_{pr}e(t) + K_i \int e(t)dt + K_d \frac{de(t)}{dt} \tag{4}$$

4 Objective Function for Automatic Generation Control (AGC)

Under varying operation conditions, the optimal tuning of controllers connected to the system is very important for the proper operation test power system. ITAE is selected as an objective function for the designed test model which is given as follows:

$$J = ITAE = \int_0^{t_{sim}} (|\Delta F_1| + |\Delta F_2| + |\Delta P_{tie}|).t.dt \tag{5}$$

where ΔF_1 and ΔF_2 are variations in frequency in area one and area two. ΔP_{tie} is variation in tie-line power. Tuning parameters of the PID controller are achieved by minimizing this objective function.

5 Different Optimization Techniques

In this paper, we used three types of optimization techniques and compared their performance with each other.

5.1 Particle Swarm Optimization (PSO)

PSO is a biologically motivated computational search and optimization process proposed in 1995 by Ebehart and Kennedy, established on the social behaviors of birds flocking or fish schooling, where particle is nothing but a simple object which has some physical properties like mass, etc. It can be considered as a possible solution to the given problem. Swarm is nothing but a collection of those objects, and optimization is a simple object to make the best utilization of the resources [21]. The particle's position and its velocity are updated:

$$V_i(t+1) = w.v_i(t) + c_1\phi_1(P_{ibest} - x_i) + c_2\phi_2(P_{gbest} - x_i)$$

$$(6)$$

$$X_i(t+1) = X_i(t) + V_i(t+1) \tag{7}$$

where c_1 and c_2 are defined as position constant. W is the inertia weight [22].

5.2 Genetic Algorithm

The genetic algorithm belongs to the evolutionary algorithm. This genetic algorithm is an adaptive heuristic search algorithm. Its adaption depends upon the environment or change in the environment [23]. It basically depends on genetics and natural selection like what is gene, genotype, chromosome, etc. There are different operators of GA: (i) Selection, (ii) Crossover and (iii) Mutation.

5.3 Firefly Algorithm

The above algorithm was suggested by Xin-She Yang in late 2007. FA is a bio-inspired metaheuristic algorithm for optimization problems [24].

If any firefly located at X_j is more attractive (brighter) than another firefly located at X_i, the firefly located at X_i will move toward X_j by the following equation:

$$X_i^{t+1} = X_i^t + \beta_0 e^{-\gamma r_{ij}^2}(X_j^t - X_i^t) + \alpha_t \in_i^t \tag{8}$$

where t is iteration counter, X_i is position of firefly, $\in_i^t$ is random number from uniform distribution, α_t is randomization parameter and value of β_0 is consider 1.

6 Result and Discussion

In this paper, the model for load frequency control is developed using the concepts of the control system. Different energy sources such as WTG, PV, DEG and ESS are represented using their equivalent transfer functions. Two different areas were considered with these energy sources. The test system is developed to estimate the performance of the proposed concept. Mathematical modeling of different energy sources is given in "(1–8)". The hybrid test system was implemented as a Simulink model using the MATLAB 2016a software on an i3-7020 CPU@2.30 GHZ with 8 GB RAM. Different optimization techniques such as PSO, GA and FA are used for tuning the parameters of the PID controller. All these algorithms are used to obtain a comparative performance evaluation. The gains of all four different controllers are optimized by PSO, GA and FA. In the first case, area one and area two are put to separate load changes of 0.03 pu and 0.06 pu, respectively. In the second case, both areas are put a separate load changes of 0.03 pu. Preliminary parameters: population size kept 20 along with maximum iteration kept at 70 for all the optimization techniques used here. The lower and upper ranges of K_{pr}, K_i and K_d are 0 and 10, respectively. The overshoot condition cannot be avoided in a hybrid power system with perturbation step load change. However, for the proper operation of a hybrid power

Table 1 Tuned PID parameter's values

| | Step load change of 3% in area one and 6% in area two | | | | | | | | |
| | PSO | | | GA | | | FA | | |
	K_p	K_i	K_d	K_p	K_i	K_d	K_p	K_i	K_d
PID1	6.00	9.96	0.39	6.47	6.00	6.27	6.56	8.54	5.86
PID2	4.78	0.07	0.66	1.14	0.67	2.98	3.66	2.78	2.56
PID3	0.10	9.92	1.25	7.92	9.92	4.08	4.74	9.99	5.24
PID4	0.10	10.0	0.10	3.14	9.17	2.83	3.67	9.99	1.74
ITAE	1.2296			1.6618			1.5014		

Table 2 Effect of different optimization techniques (O.T.) on system state variables—case study I

O.T.	State variables	Over-shoot (Pu)	Settling time (s)
PSO	ΔF_1	0.00810	8.4781
	ΔF_2	0.00301	1.5219
	ΔP_{12}	0.00757	8.3194
GA	ΔF_1	0.00337	10.3241
	ΔF_2	0.00710	6.6670
	ΔP_{12}	0.00365	9.7034
FA	ΔF_1	0.00106	10.9120
	ΔF_2	0.00679	3.9738
	ΔP_{12}	0.00380	9.6511

system, our main consideration is minimum settling time. Therefore, the minimum settling time is a more desirable parameter in comparison to the overshoot. Thus, the efficiency of the proposed technique is measured in terms of settling time.

Case Study 1: We considered area 1 with increments in load up to 0.03 pu. (3%) and in area 2 increments of load up to 0.06 pu. (6%). PSO, GA and FA tuned the parameters of PID. Table 1 represents the tuned value obtained by using PSO, GA and FA considering load change of 3% in area one and 6% in area 2. Table 2 reports the peak overshoot and the settling time for this corresponding to case study one. The lowest settling times of ΔF_1, ΔF_2 and ΔP_{tie} are found to be 8.4781 s, 1.5219 s and 8.3194 s, respectively, from PSO tuned PID. The value of ITAE in respect of PSO, GA and FA are 1.2296, 1.6618 and 1.5014, respectively. It is observed that all three optimization techniques provide stability and robustness. However, the PSO technique gives the best performance in respect of settling time and objective function as observed in Fig. 2.

Fig. 2 Dynamic response of hybrid power system related to case study. **a** Δf_1; **b** Δf_2 and **c** ΔP_{tie}
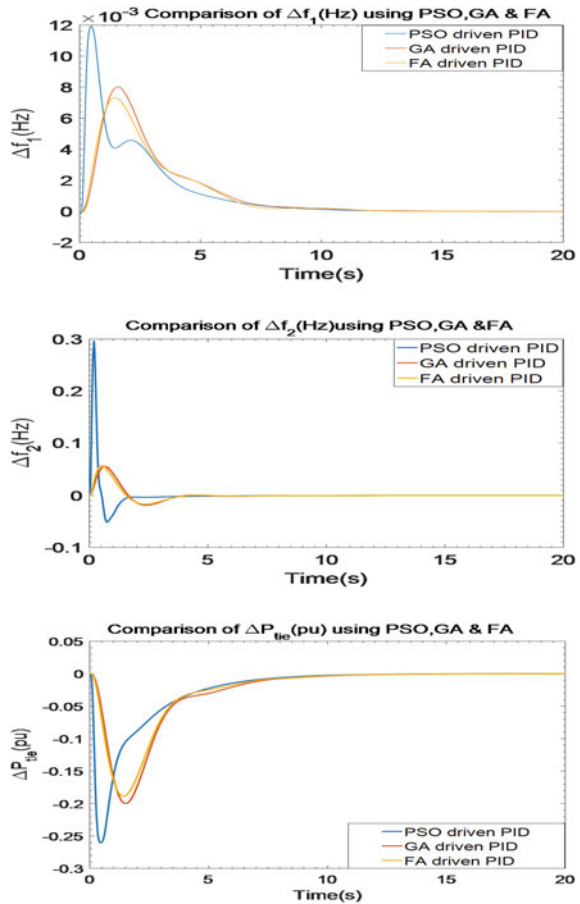
Case Study 2: Both the areas of the test system are subjected to a load increment of up to 0.03 pu. PSO, GA and FA tuned the parameters of PID.

Table 3 represents the tuned value obtained by using PSO, GA and FA considering a load change of 3% in both areas. Table 4 reports the peak overshoot and the settling time for this corresponding to case study two. The lowest settling times of ΔF_1, ΔF_2 and ΔP_{tie} are found to be 8.4567 s, 1.5212 s and 8.3192 s, respectively, from PSO tuned PID. The values of ITAE in respect of PSO, GA and FA are 1.2309, 1.6646 and 1.5074, respectively. It is observed that all three optimization techniques provide stability and robustness. However, the PSO technique gives the best performance in respect of settling time and objective function as observed in Fig. 4.

Optimization methods are also compared on the basis of convergence characteristics. Figures 3 and 5 clearly specify the superior convergence characteristics of the PSO method when compared with other methods.

Table 3 Tuned PID Parameter's values

| | Step change of 3% for both areas | | | | | | | | |
| | PSO | | | GA | | | FA | | |
	K_p	K_i	K_d	K_p	K_i	K_d	K_p	K_i	K_d
PID1	6.00	9.96	0.39	7.10	7.37	6.31	6.69	8.75	5.76
PID2	4.78	0.07	0.62	1.14	0.67	4.24	3.69	2.42	2.61
PID3	0.10	9.92	1.25	7.92	9.76	4.16	5.10	10.0	4.93
PID4	0.10	10.0	0.10	1.02	9.21	2.98	3.88	9.99	1.93
ITAE	1.2309			1.6646			1.5074		

Table 4 Effect of different optimization techniques (O.T.) on system state variables—case II

O.T.	State variables	Overshoot (Pu)	Settling time (s)
PSO	ΔF_1	0.00307	8.4567
	ΔF_2	0.00173	1.5212
	ΔP_{12}	0.00745	8.3192
GA	ΔF_1	0.00396	9.7523
	ΔF_2	0.00383	6.7746
	ΔP_{12}	0.00431	9.4403
FA	ΔF_1	0.00293	10.7003
	ΔF_2	0.00620	3.9943
	ΔP_{12}	0.00350	9.5947

Fig. 3 Convergence
characteristics for case 1
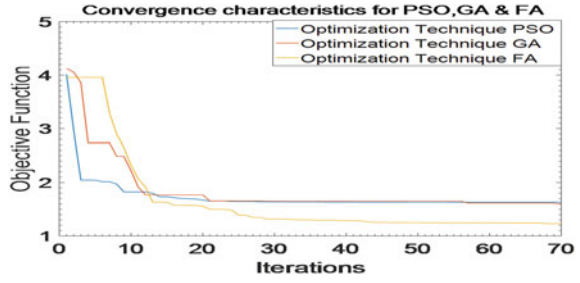
Fig. 4 Dynamic response of
hybrid power system related
to case study 2. **a** Δf_1, **b**
Δf_2 and **c** ΔP_{tie}
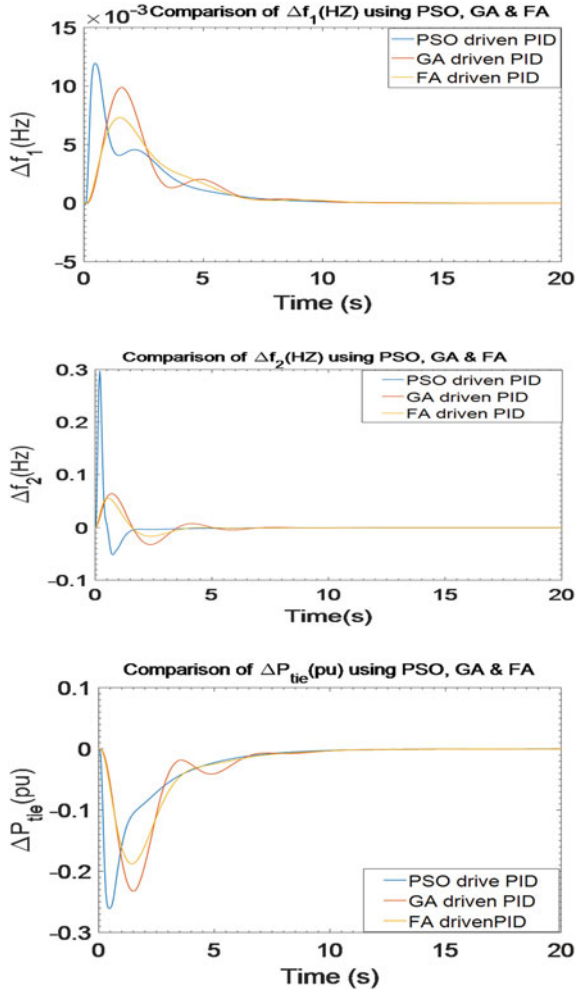
Fig. 5 Convergence characteristics for case 2
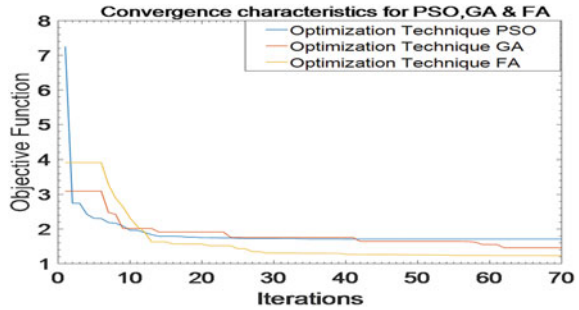
7 Conclusion

The challenges related to the LFC in a hybrid renewable-based power system are addressed in the test proposed work. A comparative analysis of three different optimization techniques, the PSO, the GA and the FA, is carried out. These methods tuned PID controller's parameters by minimizing ITAE which is considered as the objective function in this paper. Performance indices are settling time, objective function and convergence time.

Results express the effectiveness of all three (PSO, GA and FA) tuned PID controllers regarding settling time, ITAE and convergence characteristics. It was found that the case study verified that PSO has overall the least settling time. Convergence time of PSO is also faster than GA and FA in both cases of perturbation of step load. Furthermore, the work can be extended to obtain the system performance in a deregulated environment with power contracts between many generation stations and the consumers.

References

1. M.D.A. Al-Falahi, S.D.G. Jayasinghe, H.J.E.C. Enshaei, A review on recent size optimization methodologies for standalone solar and wind hybrid renewable energy system. Energy Convers. Manag. **143**, 252–274 (2017)
2. F. Giraud, *Analysis of a utility-interactive wind-photovoltaic hybrid system with battery storage using neural network* (University of Massachusetts Lowell, 1999)
3. K.C. Omran, Ali Mosallanejad, SMES/battery hybrid energy storage system based on bidirectional Z-source inverter for electric vehicles. IET Electr. Syst. Transp. **8**(4), 215–220 (2018)
4. P. Kundur, Power system stability and control, in ed. by N.J. Balu, M.G. Lauby 4.2 (1994)
5. A. Kumar et al., A review of multi criteria decision making (MCDM) towards sustainable renewable energy development. Renew. Sustain. Energy Rev. **69**, 596–609 (2017)
6. Y. Mi et al., The sliding mode load frequency control for hybrid power system based on disturbance observer. Int. J. Electr. Power & Energy Syst. **74**, 446–452 (2016)
7. P. Kumar, D.P. Kothari, Recent philosophies of automatic generation control strategies in power systems. IEEE Trans. Power Syst. **20**(1), 346–357 (2005)

8. R. Shah et al., Stability and control of mixed AC–DC systems with VSC-HVDC: a review. IET Gener., Transm. Distrib. **12**(10), 2207–2219 (2018)
9. S. Kumari, G. Shankar, Novel application of integral-tilt-derivative controller for performance evaluation of load frequency control of interconnected power system. IET Gener. Transm. Distrib. **12**(14), 3550–3560 (2018)
10. M. Ma, X. Liu, C. Zhang, LFC for multi-area interconnected power system concerning wind turbines based on DMPC. IET Gener. Transm. Distrib. **11**(10), 2689–2696 (2017)
11. R. Shankar et al., A comprehensive state of the art literature survey on LFC mechanism for power system. Renew. Sustain. Energy Rev. **76**, 1185–1207 (2017)
12. A. Khodabakhshian, R. Hooshmand, A new PID controller design for automatic generation control of hydro power systems. Int. J. Electr. Power Energy Syst. **32**(5), 375–382 (2010)
13. D.K. Gupta et al., Load frequency control using hybrid intelligent optimization technique for multi-source power systems. Energies **14**(6), 1581 (2021)
14. M.H. Qais et al., Output power smoothing of grid-tied PMSG-based variable speed wind turbine using optimal controlled SMES, in *2019 54th International Universities Power Engineering Conference (UPEC)* (IEEE, 2019)
15. G. Konar, K.K. Mandal, N. Chakraborty, Two area load frequency control using GA tuned PID controller in deregulated environment, in *Proceedings of the International MultiConference of Engineers and Computer Scientists*, vol. 2 (2014)
16. S. Padhan, R.K. Sahu, S. Panda, Application of firefly algorithm for load frequency control of multi-area interconnected power system. Electr. Power Compon. Syst. **42**(13), 1419–1430 (2014)
17. K. Nour EL Yakine et al., Optimal load frequency control in interconnected power system using PID controller based on particle swarm optimization, in *2014 International Conference on Electrical Sciences and Technologies in Maghreb (CISTEM)* (IEEE, 2014)
18. T. Uma, R. Pilla, Design and analysis of redox flow battery for load frequency control of power system. *Intelligent Computing in Control and Communication* (Springer, Singapore, 2021), pp. 23–33
19. A.Z.A. Shaqsi, K. Sopian, A. Al-Hinai, Review of energy storage services, applications, limitations, and benefits. Energy Reports (2020)
20. R.S. Dondapati, *High temperature superconducting devices for energy applications*, 1st edn. (CRC press, Boca Raton, FL, 2021)
21. R. Eberhart, J. Kennedy, Particle swarm optimization, in *Proceedings of the IEEE International Conference On Neural Networks*, vol. 4 (Citeseer, 1995), pp. 1942–1948
22. A. Lazinica (ed.) *Particle Swarm Optimization* (BoD–Books on Demand, 2009)
23. D. Sharma, P. Gaur, A.P. Mittal, Comparative analysis of hybrid GAPSO optimization technique with GA and PSO methods for cost optimization of an off-grid hybrid energy system. Energy Technol. & Policy **1**(1), 106–114 (2014)
24. X.-S. Yang, Firefly algorithms for multimodal optimization. *International Symposium On Stochastic Algorithms* (Springer, Berlin, Heidelberg, 2009)

Enhancement of Power System Stability and Damping Oscillation in a Multi-Machine System Using SSSC

Badri Narayan Behera, Kamalesh Chandra Rout, and Rudra Narayan Dash

Abstract These days the power framework is vigorously stacked, because of the steady interest for power which causes shakiness. There might be lacking and successful energy. This paper discloses the appropriate method for making up for the productive and successful power and decreases the motions in the multi-machine framework with four machines and six transport devices. The Static Synchronous Series Compensator (SSSC) can be contemplated as the main remuneration for the series utilized by the FACT family in transmission frameworks. This paper has examined the mistake of three stages. Reenactment is accomplished in the MATLAB/SIMULINK programming program in four cases: test the gadget without mistake, with issue, with the SSSC without control, and SSSC with Power Oscillation Damper (POD). The recreation result shows that without SSSC, the framework becomes temperamental during blunders. While the SSSC is feeling the squeeze inside the organization, the framework will settle. Inside the case, while the SSSC has a POD, then, at that point, the framework boundaries will be significantly more vigorous in a quicker way than without a regulator. So with POD, the entire machine execution is significantly refined and the power framework motions are delivered rapidly.

Keywords Facts controllers · Power oscillation damper (POD) · Static synchronous series compensator (SSSC)

B. N. Behera (✉)
Department of Electrical Engineering, CET, Bhubaneswar, India
e-mail: badrinarayanbehera@ymail.com

K. C. Rout (✉)
Department of Electrical Engineering, VNIT, Nagpur, India
e-mail: rout.kamalesh@gmail.com

R. N. Dash
School of Electrical Engineering, KIIT University, Bhubaneswar, India
e-mail: dash.rudranarayan@gmail.com

1 Introduction

Later breathtaking turn upward and improvement, the adaptable AC transmission framework contraptions are viewed as presently to be an adult and set up innovation. The controllability and the power that the gadgets are chosen to supply the most environmental elements lovely and reliable options regarding the matter of power frameworks. The adaptable AC transmission structures (information) would then be able to be portrayed as the transmission structures of rotating flow day that fuses them gadgets explicitly dependent on electrical energy and exact regulators which may ameliorate the presentation of solidarity exchange and controllability. Probably, the major objective with outfit receptive strength that is each capacitive or inductive, at a similar time as working on the dynamite of transmission and power figuring gadget balance every unique and impermanent equilibrium, voltage steadiness, loads tons less complete of presence and responsive electrical power misfortune, and voltage guideline. An SSSC can be remotely overseen by means of the utilization of a planned power gadget regulator that extensively further develops the dynamic and normal state conventional execution in huge scope strength framework. It's far from the powerful idea of the SSSC; this is related to the help of thyristor gadgets, including GTO and IGCT. The potential of an SSSC machine to work each inside the modes which can be capacitive and inductive makes it environmental elements charming in controlling the float along with strength within that device. In both the modes of operation, i.e., inductive and capacitive, the voltage stays quadrature in the present day in the line due to which may be inductive or capacitive reactance may be produced in the transmission line. The quadrature component of the infused voltage can be significant or slacking the line contemporary day through 90° with the end goal that the receptive strength is consumed or created [1–3].

2 Control Technique of SSSC

In case of SSSC, it is not the energetic stock of power, and the implanted voltage and the line current are quadrature with each other. As the voltage Vq is quadrature with the current, the SSSC performs as a reactance compensator either an inductive or a capacitive compensator. The Voltage-Sourced Converter (VSC) with the help of a coupling transformer delivers the injective voltage. Similarly, the VSC uses constrained commutate energy-progressed gadgets to coordinate a voltage from a stock of DC voltage (Fig. 1) [4].

Diagram of
transmission Line with SSSC

Fig. 1 Diagram of transmission Line with SSSC
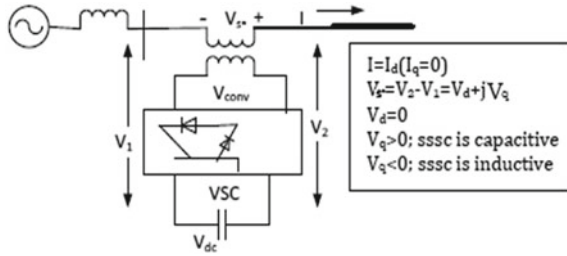
3 Damping Controller with SSSC

To regulate the SSSC-infused voltage, the shape utilized in this paper is the lead–slack shape as demonstrated in Fig. 2. In the wake of sifting or clammy through wavering, it moreover offers a mistake sign and eventually two blunder signs have been added (Fig. 3) [5].
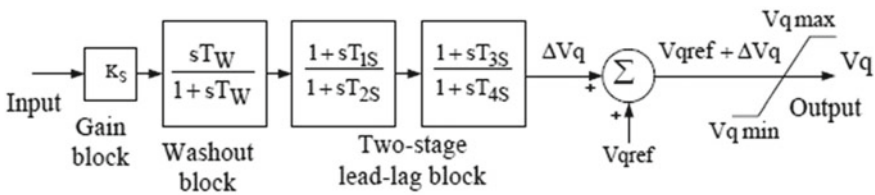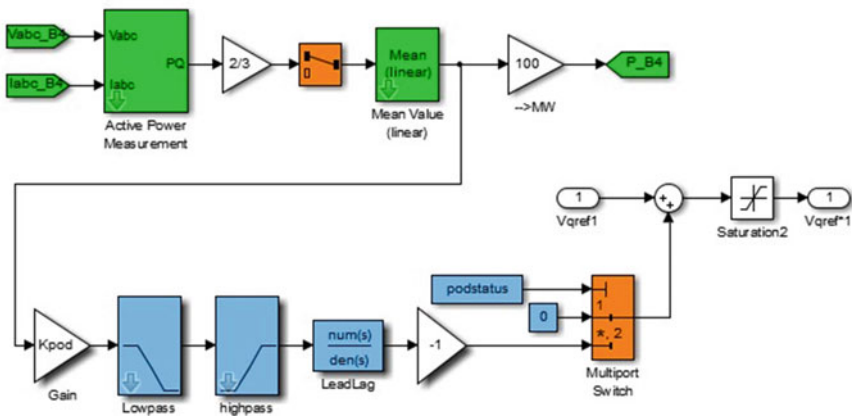

Fig. 2 Block diagram of POD controller

Fig. 3 POD controller design structure

4 Simulation Results and Study Cases

4.1 Case 1. A Test System Without SSSC Under Normal Condition

For this situation, SSSC is avoided from the energy framework. The voltage profile, fiery energy, and receptive energy are shown in the figure below under normal condition (Figs. 4, 5, 6, 7) [6].

4.2 Case 2. Test System with a Three-Phase Fault

For the product program execution purposes, we had taken a four-generator six-transport device with 500 kV line and 1,000 MVA generators. A three-stage shortcoming made for a length of 0.01–0.05 s is assessed (Fig. 8) [7].

4.3 Case 3. A Test System with SSSC

The SSSC is set at transport B4 in arrangement with line L2, and it has a positioning of 100 MVA and is fruitful for infusing up to 10% of the ostensible gadget voltage.
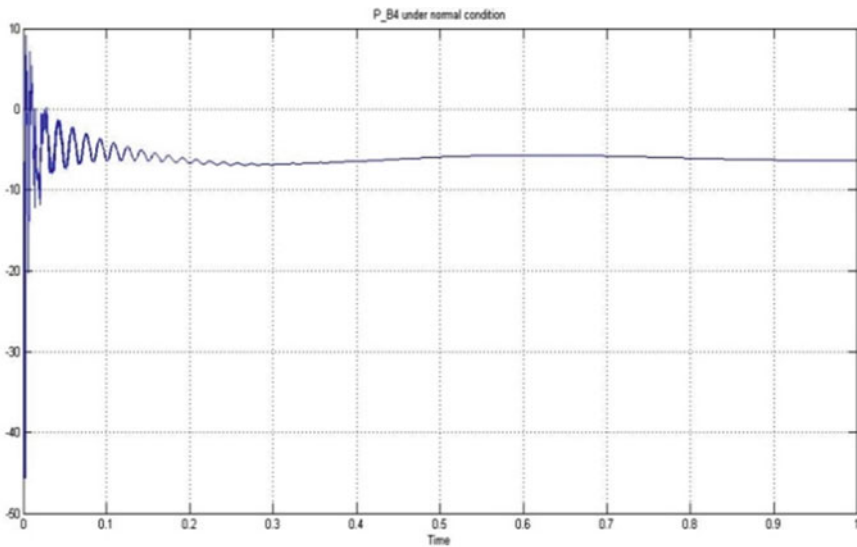
Fig. 4 Active power under normal condition
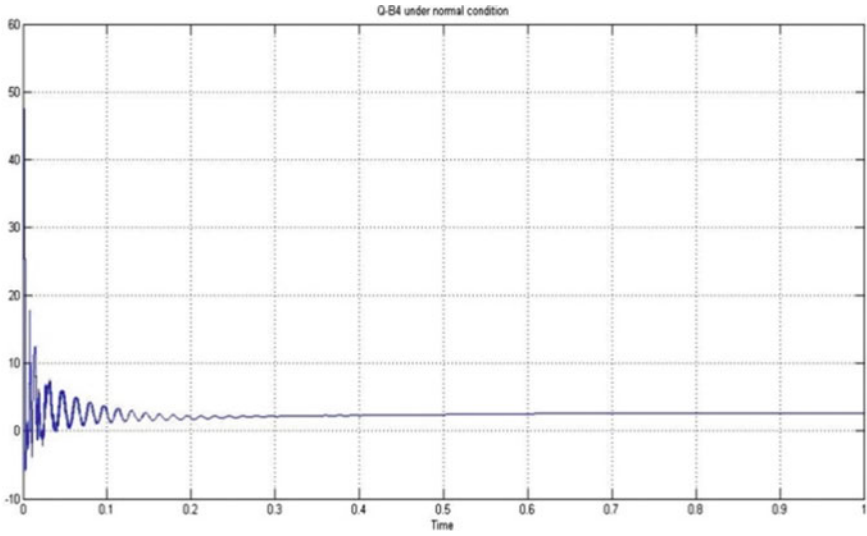
Fig. 5 Reactive power under normal condition
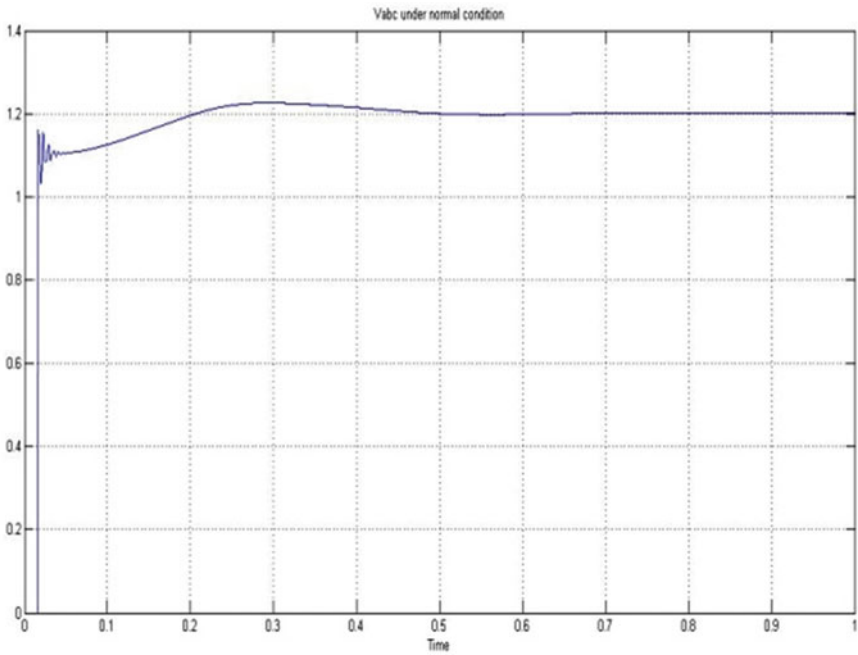
Fig. 6 Voltage at bus 4 under normal condition
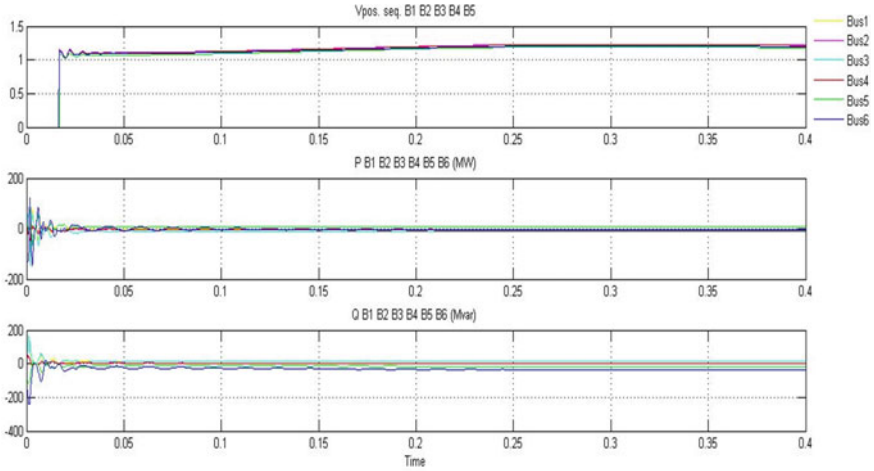
Fig. 7 Waveforms at different buses under normal condition
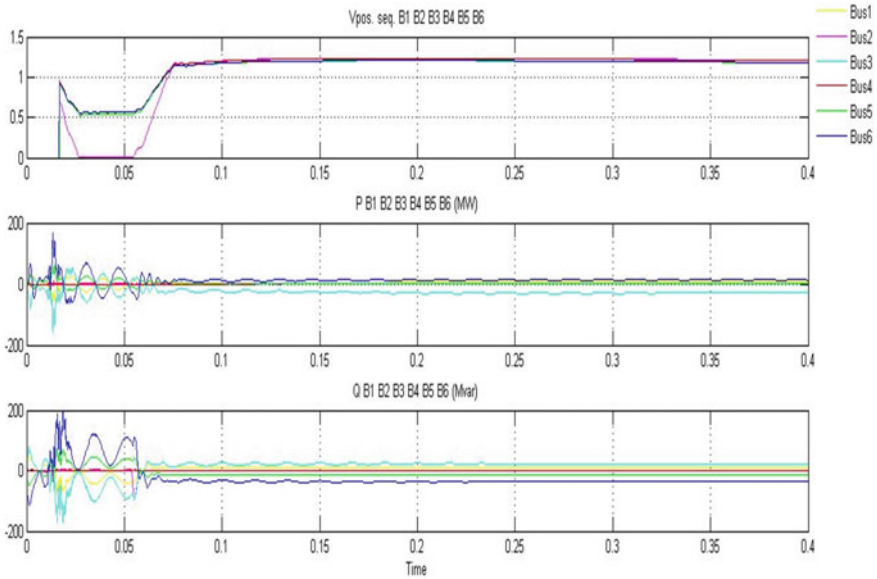
Fig. 8 Waveforms at different buses after fault

The reproduction configuration comprises a four-machine six-transport structures with SSSC. Unmistakably, the SSSC keeps the float of force, steady over the span of the shortcoming. Likewise, the voltage in transport 4 is practically 1 pu. The SSSC infuses the necessary voltage to protect transport voltage at 1 pu (Figs. 9, 10, 11, 12) [8].
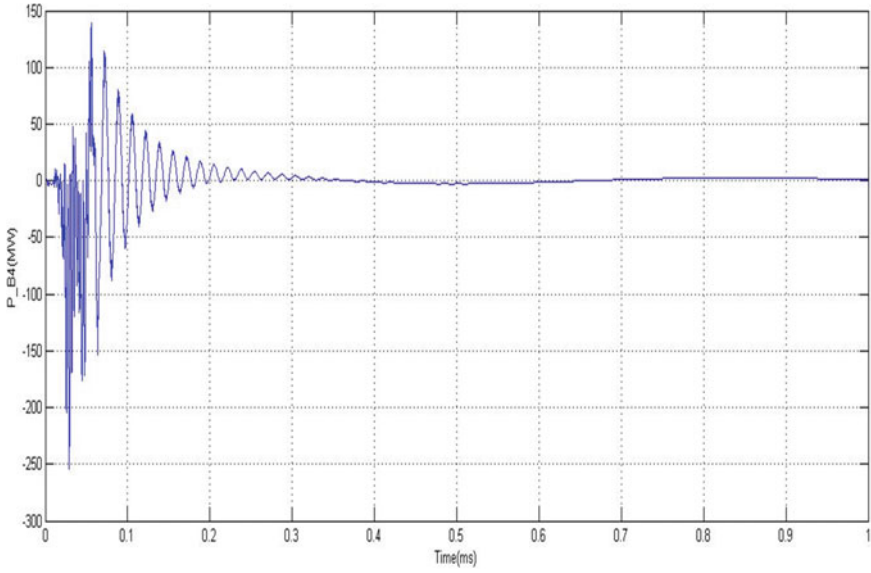
Fig. 9 Real power at bus 4 after SSSC
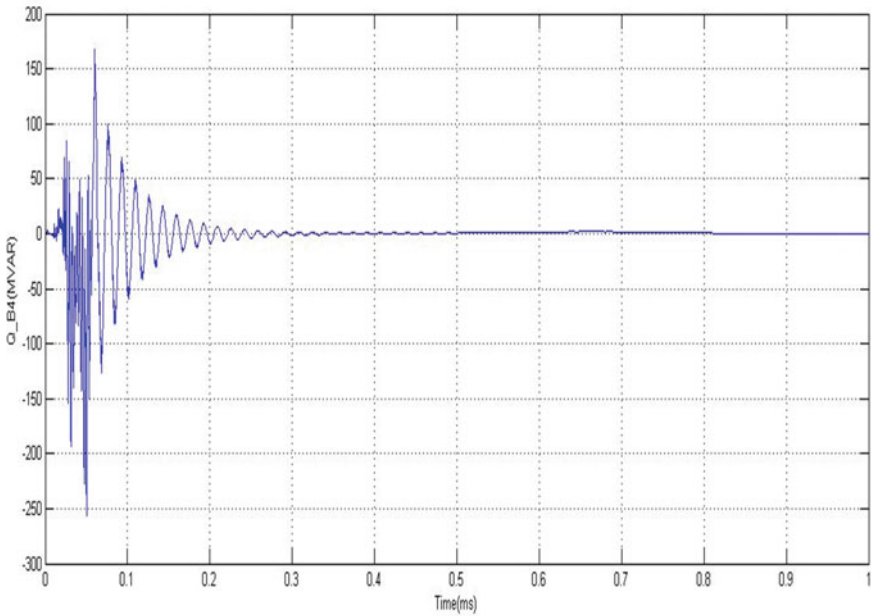
Fig. 10 Reactive power at bus 4 after SSSC
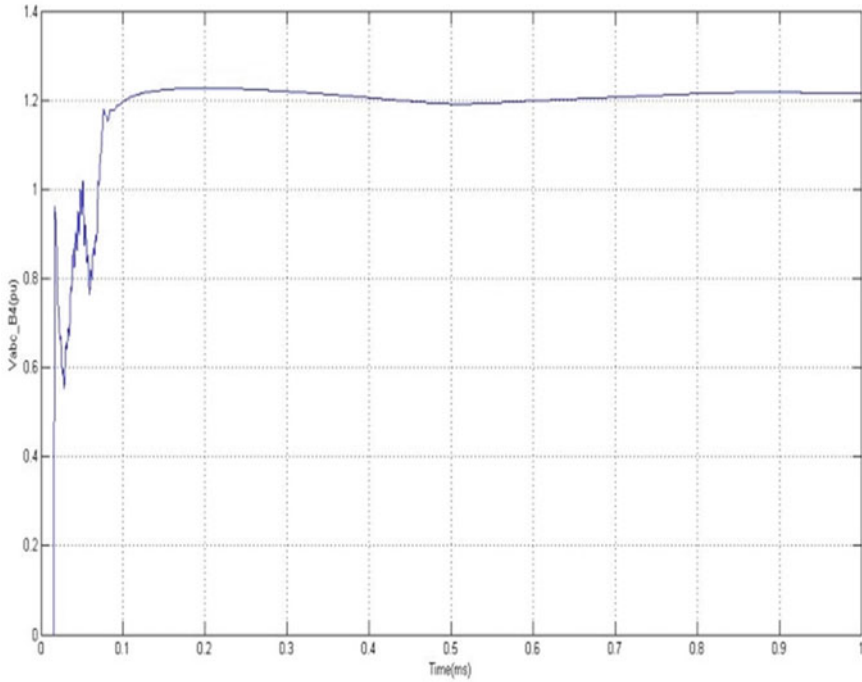
Fig. 11 Voltage waveform at bus 4 after SSSC

4.4 Case 4. A Test System with SSSC and POD

On the off chance that no shortcomings have happened, then, at that point, change will stay open. However, when the issue happened, then, at that point, the change is shut & subsequent to sifting or sodden through wavering, it moreover offers a mistake sign and at last two blunder signs have been brought & this is Vq_{ref}. In this lead–lag switch, trademark block is utilized (Fig. 13).

By placing the SSSC with POD, the voltage-consistent quality has been upgraded and energy motions are damped immaculately when in contrast to the four-PC gadget excepting POD [9–10]. The reenactment results show that this regulator offers the top of the line in general execution to the contraption for the term of ordinary and issue conditions. Case regulators can achieve wavering damping, rapid reaction, and, in the end, balancing out the strength framework (Fig. 14, 15, 16, 17).
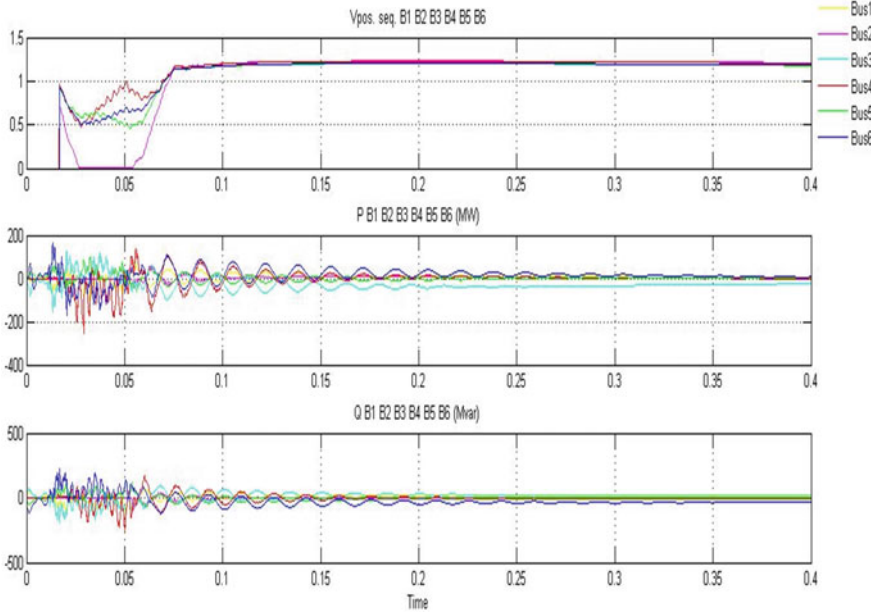
Fig. 12 Waveforms at different buses after SSSC
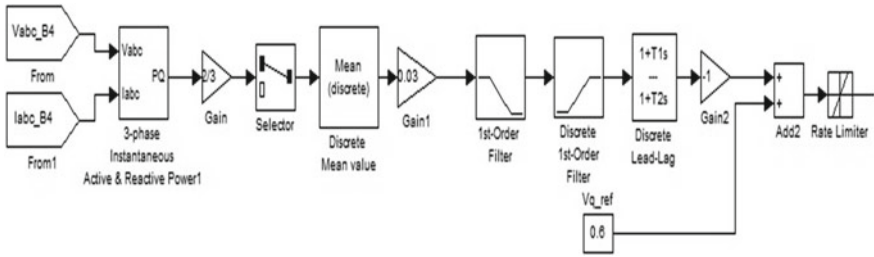
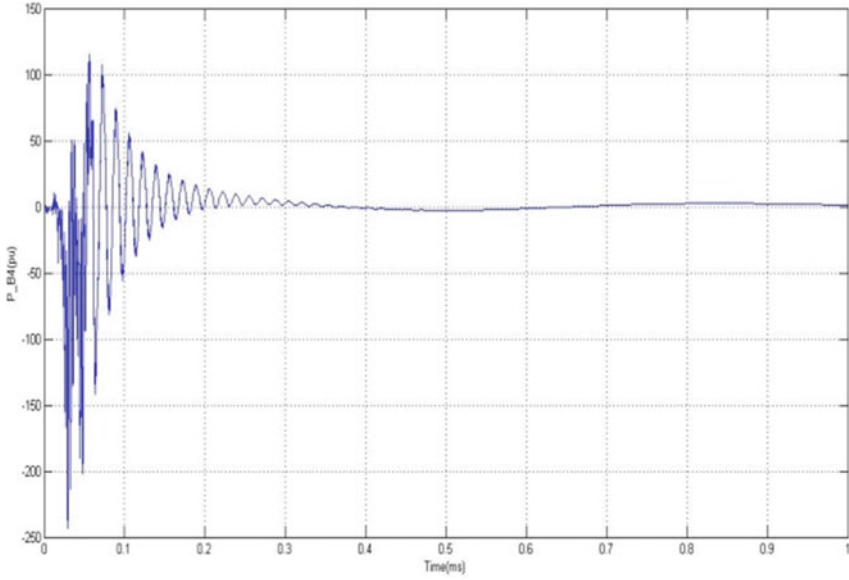**Fig. 13** Simulink model of POD controller

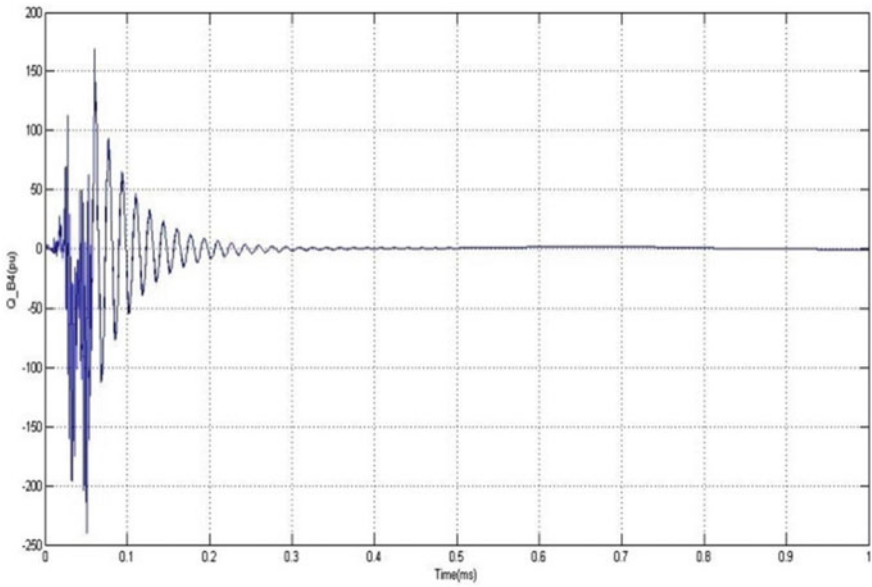**Fig. 14** Real power at bus 4 after SSSC with POD

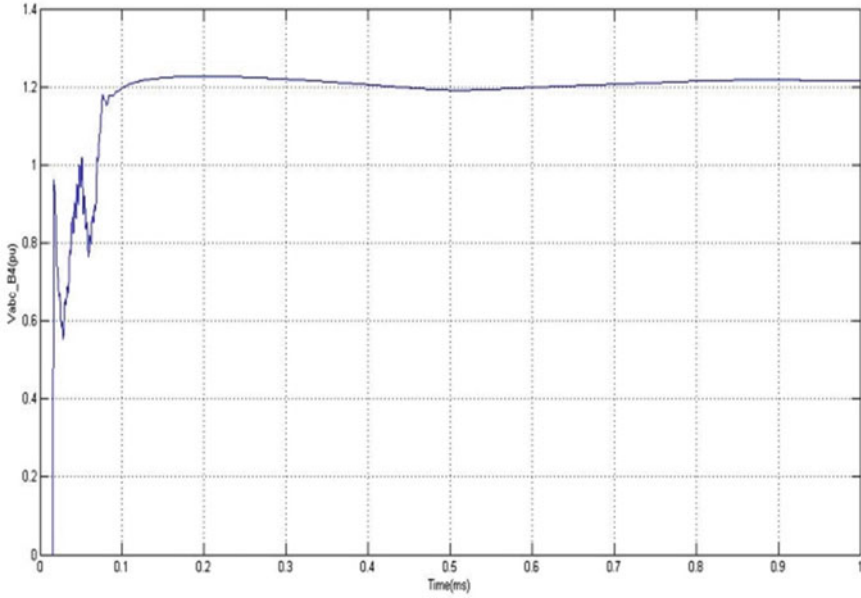**Fig. 15** Reactive power at bus 4 after SSSC with POD

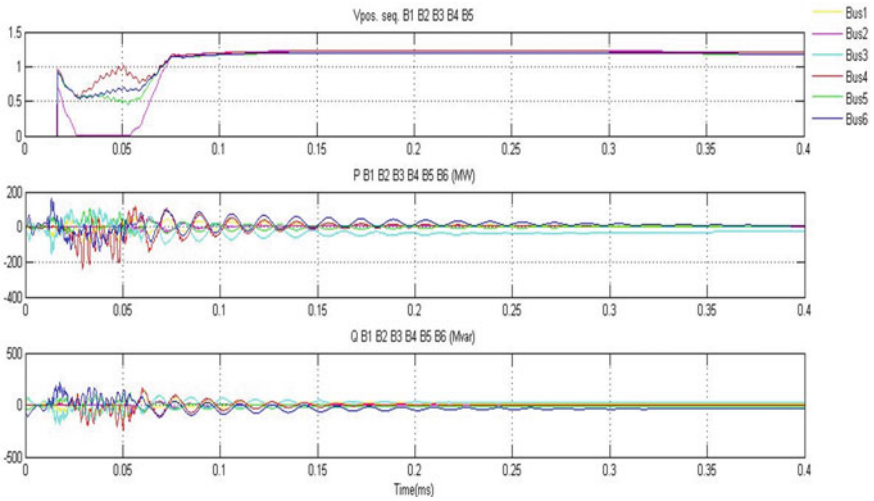**Fig. 16** Voltage waveform at bus 4 after SSSC with POD

Fig. 17 Waveforms at different buses after SSSC with POD

5   Conclusion

In this paper, the simulation results of six-bus four-machine strength gadget mannequin with the help of SSSC-based totally damping controllers are performed. This lookup suggests that multi-computer gadgets subjected to energy machine disturbances and transient steadiness of strength gadget analyzed the usage of FACTS machine SSSC. From the results, it shows that the SSSC is successfully minimizing the waft of electricity at a preferred factor on the references transmission line via injecting a quickly altering voltage in collection with the line and it continues the steady-strength waft under the fault conditions. SSSC can function and compensate for voltage at the bus controller hastily and efficiently.

References

1. S. Akter, A. Saha, P. Das, Modelling, simulation and comparison of various FACTS devices in power system. Int. J. Eng. Res. Technol. (IJERT) **1**(8) (2012). ESRSA Publications
2. R.A. Ali, E. Ercelebi, Improve power stability & damping oscillation in multi machine system using (SSSC) with POD controller. Int. J. Comput., Commun. & Instrum. (IJCCIE) **3**(2) (2016)
3. H. Taheri, S. Shahabi, Sh. Taheri, A. Gholami, Application of synchronous static series compensator (SSSC) on enhancement of voltage stability and power oscillation damping. IEEE Explore (2009)
4. M.R., Ravi, Analysis of power system oscillation damping & voltage stability improvement using SSSC in a multimachine system. Int. J. Eng. Res. Technol. **3**(7) (2014). ESRSA Publications
5. Fawzi A.L. Jowder, Influence of mode of operation of the SSSC on the small disturbance and transient stability of a radial power system. IEEE Trans. Power Syst. **20**(2): 935–942 (2005)
6. S. Panda, Modelling, simulation and optimal tuning of SSSC-based controller in a multi-machine power system. World J. Model. Simul. **6**(2), 110–121 (2010)
7. B.M. Naveen Kumar Reddy, G.V. Rajashekar, H. Goyal, *Power System Stability Enhancement Using Static Synchronous Series Compensator (SSSC)* (2013)
8. C.N. Sangeetha, Enhancement of stability in multibus system using static synchronous series compensator (SSSC). Int. J. Eng. Science (2013)
9. S.U. Bharatbhai, S.M. Govindbhai, K.G. Chamanbhai, Enhancement of power quality and stability in power system using FACTS device with controller. Int. Res. J. Eng. Technol. (IRJET) **1**(4) (2017)
10. N.G. Hingorani, L. Gyugi, *Understanding FACTS: "concepts and technology of flexible AC transmission systems* (IEEE Press, New York, 2000)

Squirrel Search Algorithm (SSA)-Driven Optimal PID-FOI Controller for Load Frequency Control of Two-Area Multi-Source Power System

Geetanjali Dei, Deepak Kumar Gupta, and Binod Kumar Sahu

Abstract This work presents the control concept for dealing with the load frequency control problem of hybrid multi-source power system under different system operating conditions. For diversity, different energy sources are considered in both areas. In area 1, the thermal power plant is used along with hydro and wind power plants. Similarly in area 2, diesel-based plant is considered along with hydro and thermal power plants. Because of the superior convergence characteristic, tuning of different controller's parameters is optimally tuned with the newly developed Squirrel Search Algorithm (SSA). Proportional Integral Derivative (PID) controller and proposed PID-Fractional Order Integral (PID-FOI) controller are used for minimizing Area Control Error (ACE) along with frequency variation and tie-line power deviation. Parameters of both the controllers have been optimally tuned with the SSA optimization technique. Integral Time multiplied by Absolute Error (ITAE) performance index is used as the objective function for tuning the controller's parameters with the SSA optimization technique. The performance of both the controllers tuned with the SSA technique is compared at various system operating conditions. Finally, the effectiveness of the proposed SSA-driven PID-FOI controller has been evidenced at different operational shifts in the system.

Keywords Area control error (ACE) · Load frequency control (LFC) · Fractional order integral (FOI) · PID controller · Squirrel search algorithm (SSA)

G. Dei (✉) · D. K. Gupta
School of EE, KIIT Deemed to Be University, Bhubaneswar, India
e-mail: geetanjaalidei@gmail.com

B. K. Sahu
SOA Deemed to Be University, Bhubaneswar, India
e-mail: binoditer@gmail.com

1   Introduction

To avoid malfunctioning the power system, it is essential to maintain a real power balance. Load variation generates problems that reduce the power quality of the power system [1]. The main goal of load frequency control is to sustain the frequency variation as well as inter tie-line power variation within the prescribed limit [2]. This variation occurs due to random load disturbances. In a two-area hydrothermal system, a fuzzy-PIDF controller is introduced by Mohanty et al. [3]. A hybrid technique combining PSO with PS is implemented by Sahu et al., in a non-reheat thermal power system [4]. A fuzzy PI controller is implemented to analyze the system response. Debbarma et al. suggested a 2DOF-PIDD controller for automatic generation control of a three-area system [5]. Two-area hybrid system incorporating a dish-Stirling solar thermal system and wind turbine system is analyzed by Rahman et al. [6]. In a hybrid power system, DE-based PID controller has been analyzed for AGC [7]. A TLBO-optimized cascaded PD-PID controller for a two-area system is analyzed by Debnath et al. [8]. Patel et al. [9] proposed a fractional order fuzzy PID controller. ALO optimization technique is implemented to optimize the controller parameters. Dual-mode proportional-integral (PI) controller is implemented [10]. Vrdoljak et al. implemented PI controller for a hydro system [11]. Sahu et al. [12] used ITSE as the objective function to optimize the controller gains using the TLBO algorithm. Ray et al. used the small-signal analysis for a hybrid system to design a PI controller [13]. Fini et al. used the Integral of absolute error (IAE) as the objective function to analyze the performance of AGC of a multi-area system [14]. Arya et al. [15] investigated the performance of a hydrothermal gas power system using a novel FOFPID controller. Redox flow batteries are used to analyze the system performance. Bhatt et al. [16] analyzed two-area multi-source units by two different optimization techniques. A comparative analysis is made using GA and Craziness-based particle swarm optimization (CRPSO). CRPSO gives better performance. As compared to the GA technique, Arya et al. [17] implemented a fuzzy-based PID controller. BFOA optimization technique is implemented in a multi-area multi-source system. To enhance the dynamic performance, SMES-TCPS unit is integrated with the system. Sahu et al. [19] investigated the system response of a deregulated power system with two different energy storage systems like UPSC and RFB. A Hybrid DE-PSO optimization technique is implemented for the analysis.

The proposed work presented the application of the SSA optimization technique to optimize the PID controller and PID-FOI controller for maintaining the deviation of power in the tie-line between the two areas and frequency deviation in each area within the prescribed limits. SSA is implemented to find the best optimal gains of the controllers for the hybrid system. Section 2 shows the description of the PID-FOI controller whereas Sect. 3 describes two-area system. Section 4 gives the information about the SSA technique. Section 5 shows the result and analysis and Sect. 6 concludes the work. The appendix has been given in Sect. 7.

2 Controllers for LFC

2.1 PID-FOI Controller

A proportional plus integral plus derivative (PID) controller is a controller which is simple, reliable, and popular. This controller is used mainly in the industries. It is analyzed from different research that PID controller output response is better than the response of PI and I controllers.

A PID-FOI controller is implemented to improve the system performance Eq. (1).

$$\frac{U(s)}{R(s)} = \left(K_p + \frac{Ki}{s} + K_d s \right) \frac{K_I}{S^\lambda}$$ (1)

Equation (1) represents the transfer function of a PID-FOI controller.

3 System Investigated

In this study, two-area multi-machine power system has been developed as shown in Fig. 1. For diversity, different energy sources are considered in both areas. In area 1, the thermal power plant is used along with hydro and wind power plants. Similarly, in area 2, diesel-based plant is considered along with hydro and thermal power
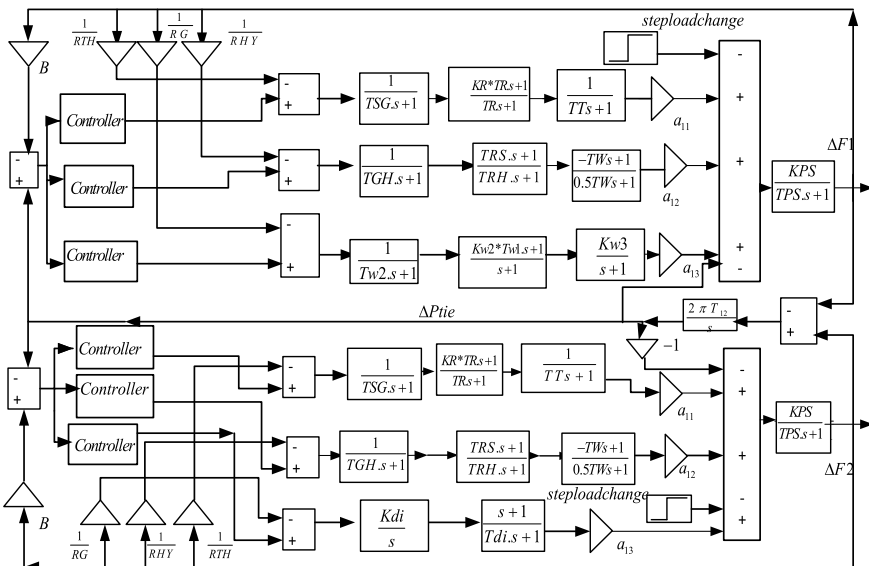

Fig. 1 Block diagram of two-area multi-source hybrid power system

plants. To validate the proposed work, a complete hybrid test system is developed in MATLAB/SIMULINK platform. Different controllers (such as PID and PID-FOI controllers) are used in each area for maintaining the frequency and tie-line power variation to the minimum values. These controllers try to minimize the Area Control Error (ACE) for each area of the system.

3.1 Objective Function for LFC

For maintaining the load frequency control of the hybrid system, optimal tuning of controllers connected in each area is very essential. A newly proposed PID-FOI controller is used for the managing LFC problem and a comparison is made with the traditional PID controller. Tuning of both controller's parameters has been done with the recently developed Squirrel search algorithm (SSA) optimization technique. Among different performance indices reported in the research work such as Integral of Time multiplied Absolute Error (ITAE), Integral Time weighted Squared Error (ITSE), and Integral Absolute Error (IAE), the ITAE index showed the best performance in terms of improved damping and less oscillation in the system. For tuning of parameters of PID-FOI and PID controllers, ITAE is used as the objective function in this research work.

$$J = ITAE = \int_0^{t_{sim}} (|\Delta F_1| + |\Delta F_2| + |\Delta P_{tie}|).t.dt \tag{2}$$

where change in frequency in areas 1 and 2 is given by $\Delta F1$ and $\Delta F2$, respectively, and tie-line power variation is given by ΔP_{tie}.

4   SSA Intelligent Optimization Technique

Mohit Jain represents the squirrel search algorithm in 2019 [19]. The dynamic sliding behavior of the squirrels is described by three different mathematical models.

Initialization of population:

The initial position of each squirrel is expressed as

$$FS_i = FS_L + U(0, 1) \times (FS_U - FS_L) \tag{3}$$

where FS_L and FS_U are the lower limit value and the upper limit value of the of ith squirrel in jth dimension, respectively, and $U(0, 1)$ is an evenly assigned random number in the range [0, 1].

Classification of the Population:

Assuming 'N' no. of trees in the forest. There is only one hickory tree out of N trees in the forest. No. of acorn trees is N_{fs} ($1 < N_{fs} < N$) and the rest are normal trees without food. Depending upon the rank of the fitness values of the squirrels, squirrels are classified into three categories, squirrels on hickory trees (F_h), squirrels on acorn trees (F_a), and squirrels located on normal trees (F_n). F_h represent the squirrels with the lowest fitness value; depending on better food requirements, the desired location of F_a is F_h, and the target locations of F_n are randomly decided as either F_a or F_h.

Updating the Location of squirrels:

Considering a random number R between 0 and 1, the predator appearance probability is denoted by P_{dp}. P_{dp} is assumed as 0.1. If $R > P_{dp}$, then there is no predator, the squirrels are free to search food in the forest; if $R \leq P_{dp}$, the squirrels are bound to limit the searching work due to presence of predator, they are not safe, and they change their locations in random. The current iteration is denoted as t; the value of G_c is 1.9; $F_{ai}(i = 1, 2, \ldots\ldots N_{fs})$ is the population obtained in random from F_a, where h_g is assumed as 8; the value of sf is 18; and the gliding angle is $\tan(\phi)$.

Case 1 FS_{at} represent the location of individuals who may progress toward the hickory nut tree. If $R_1 \geq P_{dp}$,

Then apply

$$FS_{at}^{t+1} = FS_{at}^{t} + \left[dg \times Gc \times \left(FS_{ht}^{t} - FS_{at}^{t}\right)\right] \qquad (4)$$

else update the new location at random.

Case 2: FS_{nt} represent the location of individuals proceeding to acorn nut trees for the food requirement. If $R_2 \geq P_{dp}$, then renew the location of the squirrel on the normal trees else update the position at random.

$$FS_{nt}^{t+1} = FS_{nt}^{t} + \left[d_g \times G_c \times \left(FS_{at}^{t} - FS_{nt}^{t}\right)\right] \qquad (5)$$

Case 3: FS_{nt}^{t} is the location of individuals who already consumed acorn nuts and may drift toward the hickory nut tree to store nuts in case of food scarcity. If $R_3 \geq P_{dp}$, determine the squirrels on the hickory tree. Then apply equation

$$FS_{nt}^{t+1} = FS_{nt}^{t} + \left[d_g \times G_c \times \left(FS_{ht}^{t} - FS_{nt}^{t}\right)\right] \qquad (6)$$

to renew the position of the squirrel on normal trees. If $R_3 \geq P_{dp}$ is not satisfied, then renew the position at random.

Monitoring of Seasonal Transformation

After modification, the season changes can be decided [19].

$$S_c^t = \sqrt{\sum_{k=1}^{D}\left(F_{ai,k}^t - F_{h,k}^t\right)^2}, i = 1, 2, \ldots, Nfs \qquad (7)$$

If $S_c^t < S_{min}$, winter season becomes summer, else, it is winter. When the season changes to summer, squirrels that move toward F_h remain at the new position, and other squirrels that shift toward F_a without facing predators renew their locations.

$$FS_{inew}^{t+1} = FS_L + Le'vy(n) \times (FS_U - FS_L) \qquad (8)$$

5 Result and Discussion

The proposed concept of optimal tuning of PID-FOI controller's parameters with SSA optimization technique for dealing with the problems associated with load frequency control has been developed and performed in MATLAB/SIMULINK environment with 5-6200 CPU@ 2.30 GHz with 8 GB RAM. A hybrid model is developed in the SIMULINK platform while the SSA optimization technique is implemented in MATLAB coding. To demonstrate the effectiveness of the proposed concept for dealing with the load frequency control problem, different case studies have been considered.
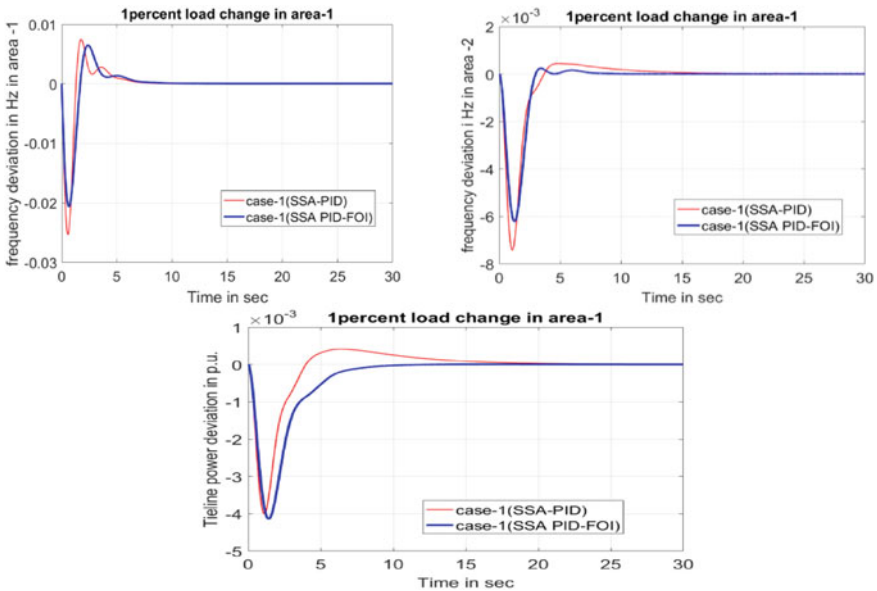
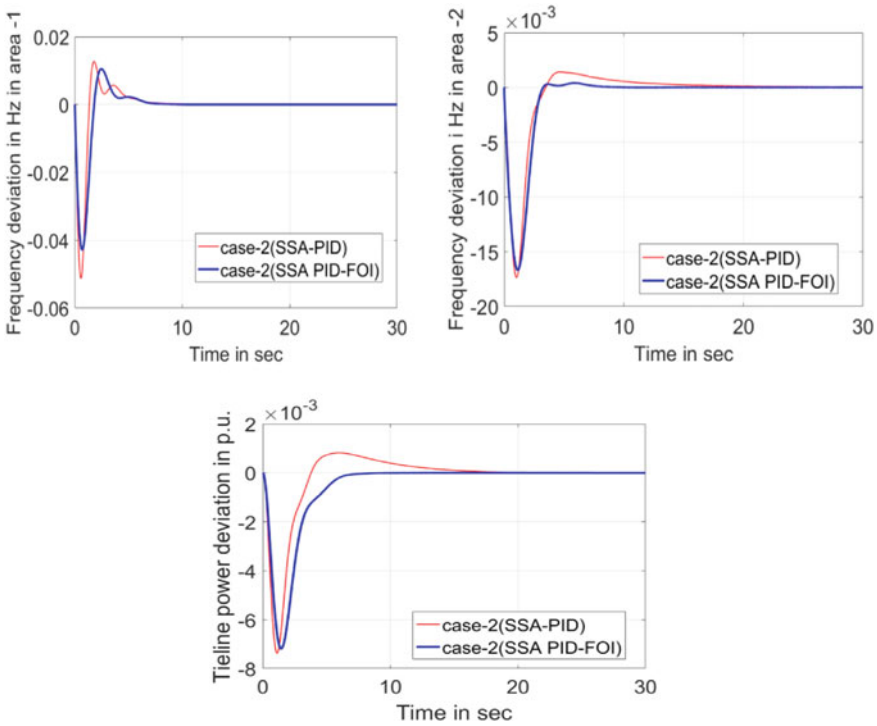**Fig. 2** Perturbation response of two-area multi-source system for Case 1

Fig. 3 Perturbation response of two-area multi-source system for case II

Case Study 1: 1 percentage step load change is considered in area 1 and parameters of PID-FOI and PID controllers are tuned with the SSA optimization technique keeping the ITAE performance index to a minimum value. Perturbed response of change in frequencies of both areas along with variation in tie-line power exchange is given in Fig. 2. Optimally tuned parameters for both controllers are given in Table 1 and values of settling time and overshoot/undershoot are given in Table 2. From Fig. 1, it is clear that the proposed SSA-driven PID-FOI controller improves the damping much more along with less oscillation and less settling time and overshoot as compared to the PID controller.

Case Study II: In this study, load change of 1 percentage has been considered in both areas. For the given load variation in the system, tuning of different controller's parameters is done by the SSA optimization technique, and values of all the parameters are given in Table 3. Perturbed responses of all the variables are shown in Fig. 3. From the figure, it can be concluded that the response of the PID-FOI controller is better as compared to the PID controller in terms of overshoot and settling time. Table 4 validates the same by giving values of settling time and overshoot for all the state variables.

Case III: For validating the robustness of the concept under the dynamic mode of system operation, various load changes have been taken into consideration at

Table 1 Optimally tuned PID controller's parameter—case study I

Optimization technique	Controller	Kp	Ki	Kd	K_I	Λ	ITAE
SSA-driven cascaded PID-FOI controller	PID-FOI	0.01	0.01	0.01	1.998	0.0119	0.1081
	PID-FOI2	1.6866	0.01	0.01	0.010	0.1815	
	PID-FOI3	1.9986	2.0000	1.9979	1.997	0.0113	
	PID-FOI4	1.989	0.01	1.9994	0.2861	0.0117	
SSA-driven PID controller	PID1	1.6610	2	1.2382			0.1321
	PID2	2	0.3558	2			
	PID3	1.3941	0.1354	0.8944			
	PID4	0.01	2	0.5975			

Table 2 Overshoot and settling time for all the states variables—case study I

Optimization technique	States variables	Case Study I		
		Under-shoot in Hz (*e−3)	Overshoot in Hz (*e−3)	Settling time in sec
SSA driven cascadedPID-FOI controller	Δf_1	−20.36	6.471	8.141
	Δf_2	−6.206	0.245	3.64
	ΔP_{12}	−4.134	0.03	6.305
SSA-driven PID controller	Δf_1	−25.2	7.3	7.206
	Δf_2	−7.39	0.440	9.794
	ΔP_{12}	−3.941	0.415	11.2

Table 3 Optimally tuned PID controller's parameter—case study II

Optimization technique		Kp	Ki	Kd	K_I	Λ	ITAE
SSA-driven PID-FOI controller	PID-FOI	0.01	0.01	0.01	2	0.01	0.1939
	PID-FOI	1.6866	0.01	0.01	0.01	0.1815	
	PID-FOI	1.998	1.989	2	2	0.01	
	PID-FOI	1.998	0.01	2	0.2861	0.01	
SSA-driven PID controller	PID1	1.6610	2	1.2382			0.3283
	PID2	2	0.3588	2			
	PID3	1.3941	0.1354	0.8944			
	PID4	0.01	2	0.5975			

different time stamps as shown in Fig. 4(a). Dynamic load change is considered in both the areas and tuning of the PID-FOI controller has been done with Squirrel Search Algorithm (SSA) optimization technique. Perturbed responses of the change in frequency in areas 1 and 2 are shown in Fig. 4(b) & 4(c) respectively along with the variation of tie-line power exchange between both the areas (Fig. 4(d)).

Table 4 Overshoot and settling time for all the states variables—case study II

| Optimization technique | States variables | Case Study II | | |
		Under-shoot in Hz (*e−3)	Overshoot in Hz (*e−3)	Settling time (s)
SSA-driven cascaded PID-FOI controller	Δf_1	−37.1	5.3	9.639
	Δf_2	−16.66	0. 22	4.136
	ΔP_{12}	−4.14	0.004	7.19
SSA-driven PID controller	Δf_1	−41.01	7.126	8.049
	Δf_2	−14.99	2.197	14.64
	ΔP_{12}	−6.078	1.002	12.99

(a)

(b)

(c)

(d)
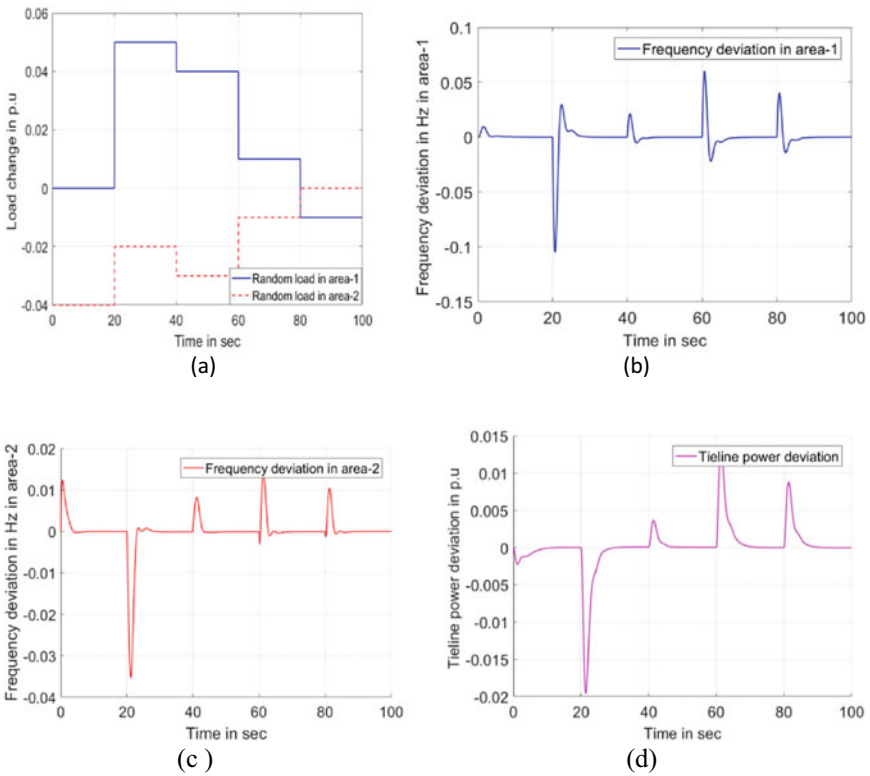
Fig. 4 **a** Variation of dynamical load change—Case III; **b, c,** and **d** perturbed response of Δf_1, Δf_2, and ΔP_{tie} under dynamical load change-Case III, respectively

6 CONCLUSION

The work reported in this paper compares the performance of the proposed PID-FOI controller with the PID controller for load frequency control of multi-area multi-source power system. In area 1, the thermal power plant is used along with hydro and wind power plants. Similarly, in area 2, diesel-based plant is considered along with hydro and thermal power plants. Because of the superior convergence characteristic, tuning of different controller's parameters is optimally tuned with the newly developed Squirrel Search Algorithm (SSA). For optimal tuning of parameters, the ITAE performance index is used which gives the improved performance of the system. To check the robustness of the proposed SSA-based PID-FOI controller, various operational shifts have been considered and a comparison is made in terms of settling time and overshoot/undershoot. From the results, it can be observed that the proposed work is more effective in dealing with different uncertainties of the system.

7. APPENDIX

Typical values for the system parameters are as follows:

$P_R = 2000$ MW (rating); Frequency (f) = 50 Hz; $B_1 = 0.4312$ pu MW/Hz; $B_2 = 0.4312$ pu MW/Hz; $P_L = 1840$ MW; $T_t = 0.3$ s; $K_r = 0.3$; $T_r = 10$ s; $T_{sg} = 0.08$; $K_T = 0.543478$; $R_1 = R_2 = R_3 = 2.4$ Hz/pu MW; $T_{rh} = 28.75$ s; $T_{gh} = 0.2$ s; $K_G = 0.130438$; $K_H = 0.326084$; $Y_c = 1$ s; $X_c = 0.6$ s; $c_g = 1$; $b_g = 0.5$; $T_W = 1$ s; $T_{rs} = 5$ s; $T_{ps} = 11.49$ s; $T_{cd} = 0.2$ s; $T_{fc} = 0.23$ s; $T_{cr} = 0.01$ s; $K_{ps} = 68.9566$ Hz/pu MW; $T_{12} = 0.0433$ pu; $a_{12} = -1$.

Squirrel Search Algorithm: No. of Iterations: 50, No. of particles: 30.

References

1. K. Prabha, Power system stability and control. in ed. by N.J. Balu, M.G. Lauby, Vol. 7 (McGraw-hill, New York, 1994)
2. S. Hadi, *Power System Analysis* (WCB, McGraw-Hill, 1999)
3. P.K. Mohanty et al., Design and analysis of fuzzy PID controller with derivative filter for AGC in multi-area interconnected power system. IET Gener., Transm. & Distrib. **10**(15), 3764–3776 (2016)
4. R.K. Sahu, S. Panda, G.T. Chandra Sekhar, A novel hybrid PSO-PS optimized fuzzy PI controller for AGC in multi area interconnected power systems. Int. J. Electr. Power Energy Syst. **64**, 880–893 (2015)
5. D. Sanjoy, L.C. Saikia, N. Sinha, Robust two-degree-of freedom controller for automatic generation control of multi-area system. Int. J. Electr. Power Energy Syst. **63**, 878–886 (2014)
6. R. Asadur, L.C. Saikia, N. Sinha, Automatic generation control of an interconnected two-area hybrid thermal system considering dish-stirling solar thermal and wind turbine system. Renew. Energy Elsevier **105**(C), 41–54

7. B. Mohanty, S. Panda, P.K. Hota, Controller parameters tuning of differential evolution algorithm and its application to load frequency control of multisource power system. Int. J. Electr. Power Energy Syst. **54**, 77–85 (2014)
8. M.K. Debnath, N.C. Patel, R.K. Mallick, Optimal base PD-PID controller for automatic generation control of multi-source tuned by teaching learning base optimization algorithm. IEEE Conference (2016), pp. 77–85
9. N.C. Patel, B.K. Sahu, D.P. Bagarty, P. Das, M.K. Debnath, A novel application of ALO-based fractional order fuzzy PID controller for AGC of power system with diverse sources of generation. Int. J. Electr. Eng. Educ. (2019). https://doi.org/10.1177/0020720919829710
10. K. Chatterjee, Design of dual mode PI controller for load frequency control. Int. J. Emerg. Electr. Power Syst. **11** (2011)
11. K. Vrdoljak, N. Peri´c, D. Šepac, Optimal distribution of load-frequency control signal to hydro power plants. in Proceedings of the 2010 IEEE International Symposium on Industrial Electronics (ISIE) (Bari, Italy, 2010), pp. 286–291
12. R.K. Sahu, T.S. Gorripotu, S. Panda, Automatic generation control of multi-area power systems with diverse energy sources using teaching learning based optimization algorithm. Eng. Sci. Technol. **19**, 113–134 (2016)
13. P.K. Ray, S.R. Mohanty, N. Kishor, Proportional–integral controller based small-signal analysis of hybrid distributed generation systems. Energy Convers. Manag. **52**, 1943–1954 (2011)
14. M.H. Fini, G.R. Yousefi, H.H. Alhelou, Comparative study on the performance of many-objective and single-objective optimisation algorithms in tuning load frequency controllers of mlti-area power systems. IETGener. Transm. Distrib. **10**, 2915–2923 (2016)
15. Y. Arya, AGC performance enrichment of multi-source hydrothermal gas power systems using new optimized FOFPID controller and redox flow batteries. Energy **127**, 704–715 (2017)
16. P. Bhatt, R. Roy, S. Ghoshal, GA/particle swarm intelligence based optimization of two specific varieties of controller devices applied to two-area multi-units automatic generation control. Int. J. Electr. Power Energy Syst. **32**, 299–310 (2010)
17. Y. Arya, N. Kumar, BFOA-scaled fractional order fuzzy PID controller applied to AGC of multi-area multi-source electric power generating systems. Swarm Evol. Comput. **32**, 202–218 (2017)
18. R.K. Sahu, T.S. Gorripotu, S. Panda, A hybrid DE–PS algorithm for load frequency control under deregulated power system with UPFC and RFB. Ain Shams Eng. J. **6**, 893–911 (2015)
19. M. Jain,V. Singh, A. Rani, A novel nature-inspired algorithm for optimization: squirrel search algorithm, Swarm Evol. Comput. **44**, 148–175 (2019)

Parameter Estimation of Photovoltaic Module Using Sine Cosine Algorithm

Alivarani Mohapatra, Chidurala Saiprakash, Byamakesh Nayak, Sarita Samal, and Usharani Raut

Abstract The increasing demand for electrical energy has made it inevitable to bring forth an environment-friendly energy resource which has to be robust as well as economic. Solar energy fulfils these criteria significantly, and to cultivate such energy, a reliable photovoltaic (PV) model is required. But most of the typical PV system undergoes a low energy conversion ratio because of improper choice of PV parameters. To build a proficient PV model, the estimation of precise and accurate parameters is mandatory. This paper portrays the Sine Cosine Algorithm (SCA) for the estimation of photovoltaic (PV) module parameters. Unknown parameters of the PV model of a single diode PV module are estimated under the standard test condition (STC). PV parameter estimation using SCA has shown a significant minimum value of the fitness function hence maximizing the convergence. A comparative study has been done between SCA and other existing popular techniques named as the nonlinear least square (NLS) method and the modified Newton–Raphson (N-R) method. From the power–voltage (P-V) and current–voltage (I-V) characteristics, it's found that the SCA model matches more accurately with the datasheet values.

Keywords Renewable energy · Photovoltaic · Single diode model · Sine cosine algorithm · Parameter estimation

A. Mohapatra (✉) · C. Saiprakash · B. Nayak · S. Samal
School of Electrical Engineering, KIIT Deemed to be University, Bhubaneswar, Odisha 751024, India
e-mail: aliva.priti@gmail.com

C. Saiprakash
e-mail: saiprakash.ace@gmail.com

B. Nayak
e-mail: electricbkn11@gmail.com

S. Samal
e-mail: ssamalfel@kiit.ac.in

U. Raut
Department of Electrical Engineering, IIIT Bhubaneswar, Bhubaneswar, Odisha, India
e-mail: usharani@iiit-bh.ac.in

1 Introduction

Solar energy has become one of the most popular resources of energy today because they are environment-friendly, economic as well as are abundantly available in nature. Sunlight is directly converted into electricity using the photovoltaic (PV) effect and the device used to do that is the PV cell. Numerous cells are gathered together in series and parallel to make a PV array for meeting the load voltage and current demand [1]. As PV arrays show nonlinear I-V characteristics and are also affected by changing temperature and other environmental conditions, the output power mainly depends on the nature of the load that is connected to the Photovoltaic system [2]. The efficiency of the Photovoltaic system further decreases if the load is directly connected to the PV system. Therefore, maximum power point tracking (MPPT) controller is incorporated between the PV array and load. Before practical execution of PV MPPT, it is required to confirm through simulation. Hence, designing a precise PV model is inevitable. The important task in designing a PV MPPT controller is to learn the model of the PV panel that is integrated with the converter [3, 4].

In previous works, a different mathematical model of PV cell is available. Among all, the single diode model (SDM) is found to be less complex and more accurate [5]. To do PV modelling, all the required system parameters should be available to us. However, all the model parameters are not available in the datasheet. Hence, unknown model parameters are needed to be estimated by various extraction procedures [6]. Usually, all manufacturers provide the PV cell parameters such as power at maximum power point (P_{mp}), open-circuit voltage (V_{oc}), and short circuit current (I_{sc}) at standard test condition (STC).

There are numerous techniques portrayed in previous literature for estimating the module parameters. Among them, iterative techniques [7, 8] and evolutionary algorithms [9–12] play an important role. In this paper, a newly evolved optimization algorithm is utilized to estimate unknown parameters such as resistance in series (R_{se}), resistance in shunt (R_{sh}), and ideality factor of diode (a) of the PV module. The extracted parameters are utilized in PV modelling, and model characteristics are compared with two popular methods such as the Nonlinear Least Square (NLS) [13] and the modified Newton–Raphson (N-R) method [14].
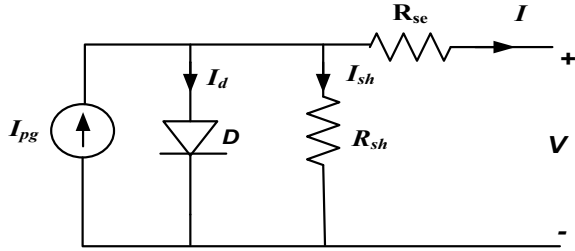
2 PV Modelling

Single diode model (SDM) as shown in Fig. 1 is a simple and accurate model. Therefore, in this paper, SDM has been utilized for parameter estimation and performance comparison [15].

By Kirchhoff's current law, we can write the output current (I) of the PV module as follows:

$$I = I_{pg} - I_d - I_{sh} \tag{1}$$

Fig. 1 Single diode model of PV module

where I_{sh} represents the leakage current of the PV module, I_d represents the diode current, *and* I_{pg} describes the light-generated current. Considering the values of I_d and I_{sh}, Eq. (1) can be written as follows:

$$I = I_{pg} - I_0\left[\exp\left(\frac{q(V + R_{se}I)}{N_s K T a}\right) - 1\right] - \frac{(V + R_{se}I)}{R_{sh}} \qquad (2)$$

where q is the electron charge, T is the module temperature, N_s is the number of cells of the module, and K is the Boltzmann constant. The current across the diode is described by Eq. (3).

$$I_d = I_0\left[\exp\left(\frac{q(V + R_{se}I)}{N_s K T a}\right) - 1\right] \qquad (3)$$

3   Problem Formulation

Single diode model comprises of five unknown model parameters namely I_{pg}, I_0, R_{se}, R_{sh}, *and a*. Among these parameters, I_{pg} and I_0 can be calculated analytically using Eqs. (4) and (5). Therefore, three unknown model parameters R_{se}, R_{sh}, and *a* are estimated in this paper.

$$I_{pg} = \left[I_{pg,STC} + K_I dt\right]\frac{G}{G_{STC}} \qquad (4)$$

$$I_0 = \frac{I_{sc,STC} + K_I dt}{\exp\left(\frac{q(V_{oc,STC} + K_v dt)}{N_s K T a}\right) - 1} \qquad (5)$$

For the estimation of three unknown parameters, three equations are needed. Rewriting Eq. (2) at MPP, we can get Eq. (6). At I_{sc}, $dI/dV = -1/R_{sh}$, and at MPP, $dP/dV = 0$. Solving these, two more Eqs. (7) and (8) can be obtained.

$$I_{mp} = I_{pg} - I_0 \left[\exp\left(\frac{V_{mp} + R_{se}I_{mp}}{N_s V_t a} \right) - 1 \right] - \frac{V_{mp} + R_{se}I_{mp}}{R_{sh}} \quad (6)$$

$$I_{mp} = V_{mp} \left[\frac{\frac{I_0}{N_s V_t a} \exp\left(\frac{V_{mp} + R_{se}I_{mp}}{N_s V_t a} \right) + \frac{1}{R_{sh}}}{1 + \frac{R_{se} I_0}{N_s V_t a} \exp\left(\frac{V_{mp} + R_{se}I_{mp}}{N_s V_t a} \right) + \frac{R_{se}}{R_{sh}}} \right] \quad (7)$$

$$\frac{1}{R_{sh}} = \frac{\frac{I_0}{N_s V_t a} \exp\left(\frac{R_{se}I_{sc}}{N_s V_t a} \right) + \frac{1}{R_{sh}}}{1 + \frac{R_{se} I_0}{N_s V_t a} \exp\left(\frac{R_{se}I_{sc}}{N_s V_t a} \right) + \frac{R_{se}}{R_{sh}}} \quad (8)$$

V_t is the thermal voltage defined as $V_t = \frac{KT}{q}$. The best solution is achieved using a particular objective function called the fitness function. The fitness function is evaluated at each iteration and the set of values of R_{se}, R_{sh}, and a are evaluated. The objective functions $f_1(x)$, $f_2(x)$, and $f_3(x)$ are now built up using Eqs. (6), (7), and (8) as Eqs. (9), (10), and (11), respectively [16].

$$f_1(x) = 0 = I_{pg} - I_0 \left[\exp\left(\frac{V_{mp} + R_{se}I_{mp}}{N_s V_t a} \right) - 1 \right] - \frac{V_{mp} + R_{se}I_{mp}}{R_{sh}} - I_{mp} \quad (9)$$

$$f_2(x) = 0 = V_{mp} \left[\frac{\frac{I_0}{N_s a V_t} \exp\left(\frac{V_{mp} + R_{se}I_{mp}}{N_s a V_t} \right) + \frac{1}{R_{sh}}}{1 + \frac{R_{se} I_0}{N_s a V_t} \exp\left(\frac{V_{mp} + R_{se}I_{mp}}{N_s a V_t} \right) + \frac{R_{se}}{R_{sh}}} \right] - I_{mp} \quad (10)$$

$$f_3(x) = 0 = \frac{\frac{I_0}{N_s a V_t} \exp\left(\frac{R_{se}I_{sc}}{N_s V_t a} \right) + \frac{1}{R_{sh}}}{1 + \frac{R_{se} I_0}{N_s a V_t} \exp\left(\frac{R_{se}I_{sc}}{N_s V_t a} \right) + \frac{R_{se}}{R_{sh}}} - \frac{1}{R_{sh}} \quad (11)$$

To simplify the problem, a single objective function $f(x)$ is considered as Eq. (12) for the proposed SCA for parameter estimation.

$$f(x) = \left(f_1(x)^2 + f_2(x)^2 + f_3(x)^2 \right) \quad (12)$$

4 Sine Cosine Algorithm

Sine cosine algorithm (SCA) is a physics-based optimization algorithm used for solving nonlinear optimization problems as discussed in [17]. For exploration and exploitation phases, the following position updating equations are used.

$$X_i^{n+1}(j+1) = \begin{cases} X_i^n(j) + r_1 \times \sin(r_2) \times \left| r_3 P_i^n - X_i^n(j) \right|, r_4 < 0.5 \\ X_i^n(j) + r_1 \times \cos(r_2) \times \left| r_3 P_i^n - X_i^n(j) \right|, r_4 \geq 0.5 \end{cases} \quad (13)$$

$X_i^n(j)$ is the position of jth search agent of the current solution in ith dimension at nth iteration and P_i is the position of the destination point along the ith dimension. The four parameters of SCA are r_1, r_2, r_3, and r_4 are the random numbers. The parameter r_1 is calculated as Eq. (14).

$$r_1 = A - n\frac{A}{N} \tag{14}$$

where n stands for recent iteration, N is the highest iteration value, and A represents a constant quantity. The factor r_2 is random in nature with a value within $[0,2\pi]$, and r_3 represents weightage for the destination to emphasize ($r_3 > 1$) or deemphasize ($r_3 < 1$). Parameter r_4, which is a random number within $[0,1]$, is used to switch over from sine to cosine as defined in Eq. (13.1) and (13.2). The flowchart of SCA for parameter estimation is shown in Fig. 2.

5 Results and Discussion

The methods discussed in previous literature have some disadvantages. The unknown parameters of the PV model X $= [a, R_{se}, R_{sh}]$ are extracted by the N-R method as described in [14] which requires initial values of parameters to be selected properly to reach the best possible solution. Choices of initial parameters are very important to avoid the singularity. NLS method as described in [13] is also dependent on initial parameter values and the lower and upper limit of the parameter values. If these parameter values are not selected properly, it may give an inaccurate solution. For the given SCA method, the selection of the initial parameters is also very essential as the optimization of the function depends on it. In SCA, initial parameters are arbitrarily chosen in accordance with their physical emphasis. The values of series resistance, R_{se}, are quite small and taken in the limit [0.1-1]. The shunt resistance R_{sh} has a higher value and is chosen within [80–2000]. The diode ideality factor "a" is chosen in the limit [1-1.6]. To reduce the calculation complexity, unknown parameters, namely diode ideality factor (a), shunt resistance (R_{sh}), and series resistance (R_{se}) are extracted by the considered sine cosine algorithm.

The fitness function is evaluated using Eq. (12) as shown in Fig. 3. It is seen that as arbitrarily selected initial parameters values the fitness function value converges rapidly starting from fitness value 0.2 to 0.00090488 and then from 0.00090488 to 0.00085639 in 50 iterations. After 200 iterations, it becomes 0.00084578, and then after 450 iterations, it becomes 0.00051963. Finally, it becomes a very small value of 1.4240e−04 after 900 iterations. From the convergence curve for the fitness value, it is observed that in 50 iterations it becomes very small and after 900 iterations it becomes nearly 0. Therefore, the SCA method can be utilized suitably where initial parameter values are not known beforehand. The accuracy and robustness of the
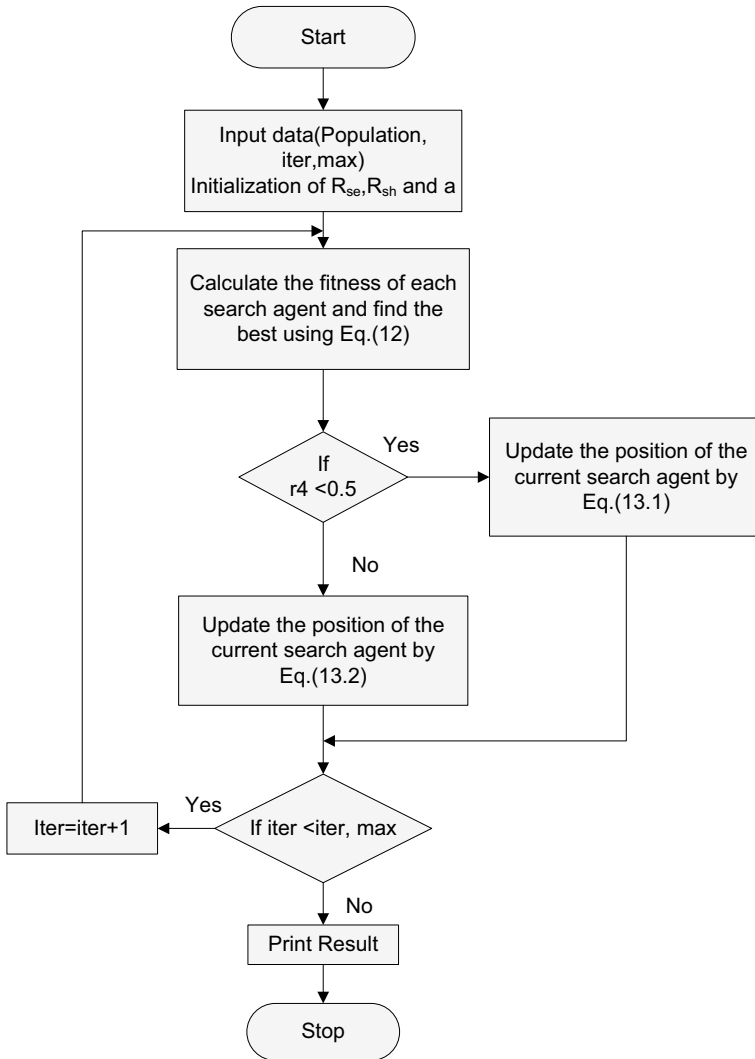
Fig. 2 Flowchart of SCA algorithm for parameter estimation

SCA model have been compared with the modified N-R and NLS methods and with experimental values by the P-V and I-V curves.

The datasheet values of the KC200GT PV module as given in Table 1 are used under STC to draw the characteristics as shown in Figs. 4 and 5. It is noticed that the suggested method gives improved results as it provides very less fitness value and, hence, portrays maximum convergence.
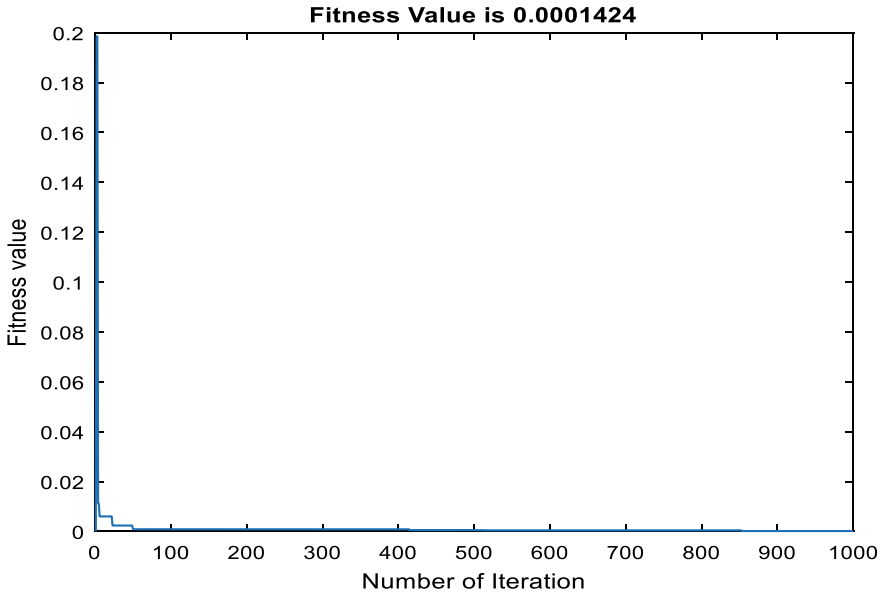
Fig. 3 Fitness function variation of for Sine Cosine method

Table 1 Datasheet parameters values of KC200GT PV module at STC

Parameters	Values
$V_{oc, STC}$	32.9 V
$I_{sc, STC}$	8.21 A
K_V	−0.1230 V/°K
K_I	0.0032 A/°K
Q	1.60e−19 C
K	1.380e-23 J/°K
G_{STC}	1000 W/m^2
T_{STC}	25 + 273 °K
V_{mp}	26.3 V
I_{mp}	7.61 A

5.1 Attainment Calculation and Error Evaluation

The model performance is discussed and evaluated by considering the P-V and I-V characteristics which are shown in Figs. 4 and 5 and compared with different techniques, such as the modified N-R and NLS methods as well as with the experimental values. From the characteristics curves for P-V and I-V, it is clear that the given model is more accurate with less absolute error in power and current.
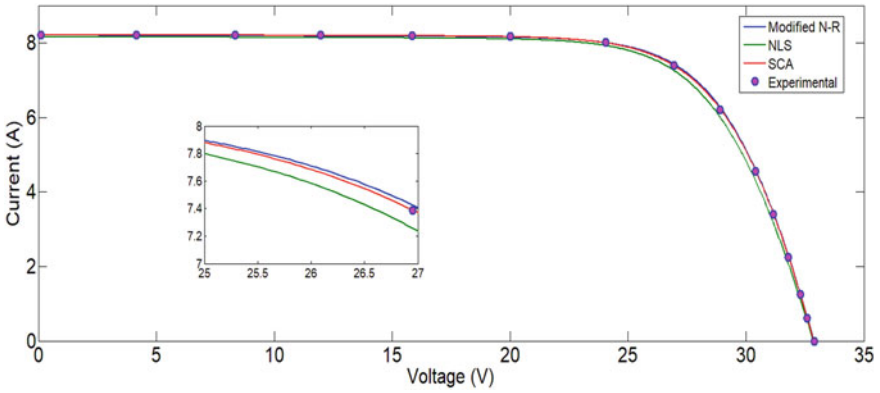
Fig. 4 Evaluation of I-V characteristic of datasheet values and model parameters extracted by different methods at STC
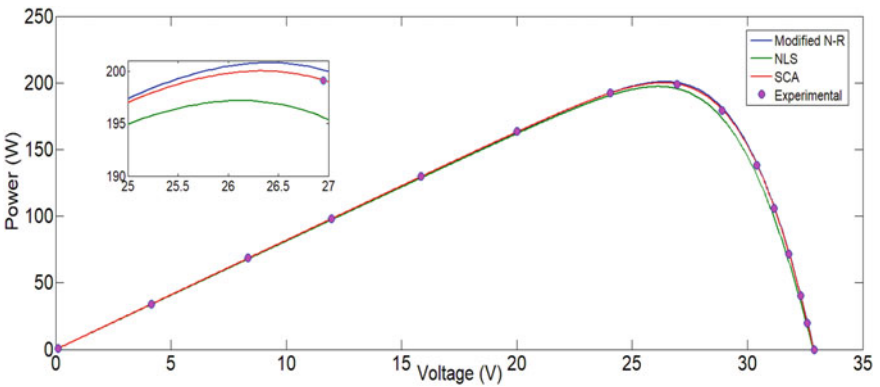
Fig. 5 Evaluation of P-V characteristic of datasheet values and model parameters extracted by different methods at STC

To understand the suitability of the discussed method, the current error (*CE*) is calculated for all three methods at STC. The *CE* at STC is shown in Fig. 6. Usually, in lower voltage regions where the current is almost constant, the error is less. But

Fig. 6 Absolute error for current at STC
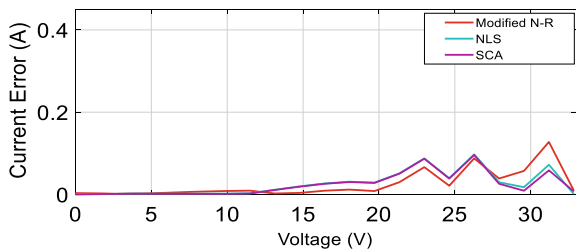
Table 2 KC200GT module parameters at STC using SCA

Parameters	NLS [11]	Modified N-R [12]	SCA
a	1.98	1.34	1.22
R_{se} (Ω)	0.2256	0.2172	0.2543
R_{sh} (Ω)	411.47	951.931	433.53
RMSD (%)	0.0082	0.0278	0.0038

in higher voltage regions where the current changes substantially, the error becomes more and it decides the accuracy of the method. Compared to the modified N-R and NLS methods, CE of the SCA method is quite less. Equation (15) is used to calculate current error (CE).

$$CE = |I_{datasheet} - I_{calculated}| \tag{15}$$

where $I_{datasheet}$ and $I_{calculated}$ are the datasheet and calculated current values, respectively. Root mean square deviation (RMSD) is calculated as Eq. (16). Here, N represents the number of data points of current–voltage curve.

$$RMSD = \sqrt{\frac{1}{N}\sum_{i=1}^{N}(|I_{datasheet} - I_{calculated}|)} \tag{16}$$

It is seen that, compared to NLS and the Modified N-R methods, the RMSD of SCA is very small which proves the superiority of the SCA method in comparison to NLS and the Modified N-R methods. The Estimated Parameter values using SCA for KC200GT at STC are given in Table 2.

6 Conclusion

Three unascertained parameters of a single diode PV module have been extracted using the SCA algorithm and are compared with some existing methods in the literature. The methods discussed in previous literature have some limitations. In the modified N-R method, there is a chance of premature convergence or it may happen that there is no convergence at all if the selected initial values of the parameters are not proper. If initial parameters are suitably not chosen, the singularity problem may occur. Chosen initial parameter values and upper and lower limit of parameters play a vital role in the NLS method. It may converge to local minima with the wrong choice of initial parameter values. It is found that there is maximum convergence in SCA with fitness value 1.4240e-04 after 900 iterations. In this paper, the performance of SCA is compared with NLS and the modified N-R method based on current error (CE) and root mean square deviation (RMSD). It is found that both CE and RMSD

are very small in the SCA method in comparison to the modified N-R and NLS methods.

References

1. S. Bhattacharjee, B. J. Saharia. 2014. A comparative study on converter topologies for maximum power point tracking application in photovoltaic generation. J. Renew. Sustain. Energy 6. https://doi.org/10.1063/1.4900579

2. B. Nayak, A. Mohapatra, K.B. Mohanty, Selection criteria of dc-dc converter and control variable for MPPT of PV system utilized in heating and cooking applications. Cogent Eng **26**, 1–16 (2017). https://doi.org/10.1080/23311916.2017.1363357

3. A. Mohapatra, B. Nayak, B. Misra (2014) Model validation and maximum power point tracking of photovoltaic module. 2014 Power Energy Syst Conf Towar Sustain Energy, PESTSE 2014 0–3. https://doi.org/10.1109/PESTSE.2014.6805314

4. Mohapatra A, Nayak B, Mohanty KB (2016) Performance improvement in MPPT of SPV system using NN controller under fast changing environmental condition. 2016 IEEE 6th Int Conf Power Syst ICPS 2016 0–4. https://doi.org/10.1109/ICPES.2016.7584159

5. Villalva MG, Gazoli JR, Filho ER (2009) modeling and circuit-based simulation of photovoltaic arrays

6. P.A. Kumari, P. Geethanjali, Parameter estimation for photovoltaic system under normal and partial shading conditions : A survey. Renew Sustain Energy Rev **84**, 1–11 (2018). https://doi.org/10.1016/j.rser.2017.10.051

7. M.G. Villalva, J.R. Gazoli, E.R. Filho, Comprehensive Approach to Modeling and Simulation of Photovoltaic Arrays. IEEE Trans Power Electron **24**, 1198–1208 (2009). https://doi.org/10.1109/TPEL.2009.2013862

8. D. Sera, R. Teodorescu, P. Rodriguez, PV panel model based on datasheet values. IEEE Int Symp Ind Electron **2007**, 2392–2396 (2007). https://doi.org/10.1109/ISIE.2007.4374981

9. D.H. Muhsen, A.B. Ghazali, T. Khatib, I.A. Abed, Extraction of photovoltaic module model's parameters using an improved hybrid differential evolution/electromagnetism-like algorithm. Sol Energy **119**, 286–297 (2015). https://doi.org/10.1016/j.solener.2015.07.008

10. D.F. Alam, D.A. Yousri, M.B. Eteiba, Flower Pollination Algorithm based solar PV parameter estimation. Energy Convers Manag **101**, 410–422 (2015). https://doi.org/10.1016/j.enconman.2015.05.074

11. Moldovan N, Picos R, Garcia-Moreno E (2009) Parameter extraction of a solar cell compact model usign genetic algorithms. Proc 2009 Spanish Conf Electron Devices, CDE'09, Spain 379–382. https://doi.org/10.1109/SCED.2009.4800512

12. M.U. Siddiqui, M. Abido, Parameter estimation for five- and seven-parameter photovoltaic electrical models using evolutionary algorithms. Appl Soft Comput J **13**, 4608–4621 (2013). https://doi.org/10.1016/j.asoc.2013.07.005

13. Nayak BK, Mohapatra A, Mohanty KB (2013) Parameters estimation of photovoltaic module using nonlinear least square algorithm: A comparative study. 2013 Annu IEEE India Conf INDICON 2013. https://doi.org/10.1109/INDCON.2013.6726120

14. A. Mohapatra, B.K. Nayak, K.B. Mohanty, Comparative study on single diode photovoltaic module parameter extraction methods. Proc 2013 Int Conf Power. Energy Control ICPEC **2013**, 30–34 (2013). https://doi.org/10.1109/ICPEC.2013.6527619

15. F.J. Toledo, J.M. Blanes, Geometric properties of the single-diode photovoltaic model and a new very simple method for parameters extraction. Renew Energy **72**, 125–133 (2014). https://doi.org/10.1016/j.renene.2014.06.032

16. A. Mohapatra, B. Nayak, K.B. Mohanty, Parameter estimation of single diode PV module based on Nelder-Mead optimization algorithm. World J Eng **15**, 70–81 (2018). https://doi.org/10.1108/WJE-04-2017-0093
17. S. Mirjalili, SCA: A Sine Cosine Algorithm for solving optimization problems. Knowledge-Based Syst **96**, 120–133 (2016). https://doi.org/10.1016/j.knosys.2015.12.022

Parametric Design and Analysis of Ferrite PMaSynRM for EV Application

Subhendu Mishra, B. K. Nayak, and B. G. Fernandes

Abstract Increasing demand of electric traction motors and the limited availability of rare-earth elements have accelerated the research for new motor design topologies. Ferrite permanent magnet-assisted synchronous reluctance motor (ferrite PMaSynRM) can prove to be a viable solution. This paper discusses a new parametric model for designing the rotor of ferrite PMaSynRM. The proposed motor is optimized for FreedomCar 2020 specifications. Finite element method is used to analyse the average torque, torque ripple and stress in the proposed design. The proposed motor is evaluated over complete torque-speed profile. Further, use of asymmetric flux barrier and odd slots per pole pair is proposed to reduce the torque ripple and improve efficiency.

Keywords PMaSynRM · Ferrite PMaSynRM · Traction motors · Electric vehicles · Rotor design · Flux barrier

1 Introduction

Climate change has pushed governments to restrict greenhouse emissions and promote electric vehicles (EVs) and hybrid electric vehicles (HEVs). Various motor options are available for use in EVs and HEVs. These include Induction Motors (IM), Synchronous Reluctance Motors (SynRM), Switched Reluctance Motors (SRM), Permanent Magnet Synchronous Machines (PMSM) and Permanent Magnet-Assisted Synchronous Reluctance Motors (PMASynRM). Typical traction application requires these motors to have high staring torque, low torque ripple, high power factor, high power density, high efficiency and low cost.

The main limitation of PMSMs is that with field weakening, operation in the constant power region, including torque capability, also decreases. Safety and fault-

S. Mishra (✉) · B. K. Nayak
Kalinga Institute of Industrial Technology, Bhubaneswar, India
e-mail: subhendu.mishra20@gmail.com

S. Mishra · B. G. Fernandes
Indian Institute of Technology, Bombay, India

tolerant operation are important considerations for PMSMs. PM-Assisted Synchronous Reluctance Motors (PMaSynRM) prove to be a good alternative to PMSMs. PMaSynRM have lower amounts of PMs as compared to PMSM. Magnetic torque is the main contributor towards total torque in case of PMSM; however, it is reluctance torque in case of PMaSynRM. Thus, PMaSynRM provide good power factor along with a high reluctance torque.

The use of rare-earth magnets in PMaSynRM do provide a viable solution. However, the cost of rare-earth magnets like NdFeB has been increasing over the years due to the limited availability of rare-earth elements. This has motivated researchers to study rare-earth free design topologies like ferrite PMaSynRM. However, the optimized design of the rotor becomes very critical for ferrite PMaSynRM. The reason is the fact that maximum energy product ($B_m H_m$) for NdFeB is about 300 kJ/m^3 versus 30 kJ/m^3 for ferrite PMs. Intrinsic coercivity H_c of rare-earth magnets is also greater than ferrite magnets.

2 Theory and Background

Typical synchronous reluctance motors (SynRM) and PM-Assisted (PMaSynRM) can be seen in Fig. 1a, b, respectively. Saliency ratio and the power factor are given in (1) and (2). In PMaSynRM, PM is added along the q-axis. Thus, q-axis inductance is reduced due to the saturation of rotor iron bridges, resulting in an increase in saliency ratio and an improved power factor.

$$k_{sr} = L_d/L_q \tag{1}$$

$$cos\phi = \frac{k_{sr} - 1}{k_{sr} + 1} \tag{2}$$

Flux linkage $L_q I_q$ is compensated by the permanent magnet flux, as shown in Fig. 2. The voltage vector shifts near the current vector, thus improving the power factor. The addition of permanent magnets leads to addition of magnetic torque to the reluctance torque, thus increasing the total torque.

The torque equation for SynRM is shown in (3).

$$T_{syncRM} = \frac{3}{\omega_{sync}} \left(\frac{X_d - X_q}{2X_d X_q} V_t \sin 2\delta \right) = \frac{3}{2} \frac{P}{2} (L_d - L_q) i_q i_d \tag{3}$$

The main flux of the machine flows along the D-axis. Hence, D-axis path generally has minimum reluctance and maximum inductance (L_d). Further, to increase the saliency ratio, Q-axis reluctance is increased. Hence, L_q (q-axis inductance) is designed to be as small as possible. The torque equation for PMaSynRM is shown
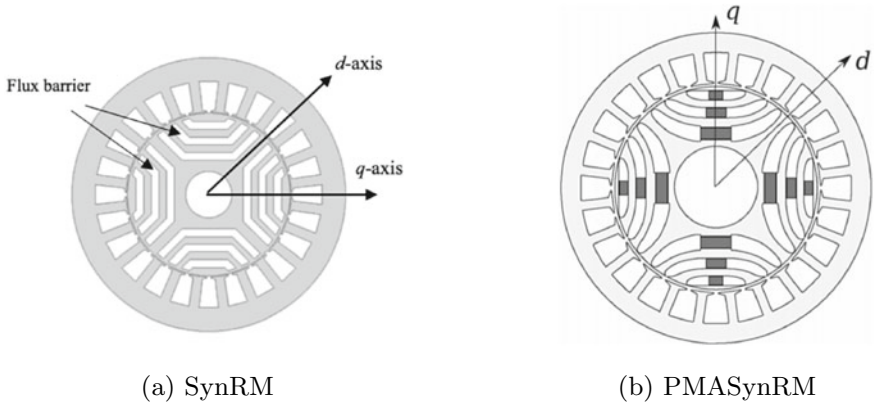
(a) SynRM

(b) PMASynRM

Fig. 1 Design Topology for SynRM and PM-Assisted SynRM [1]

(a) SynRM
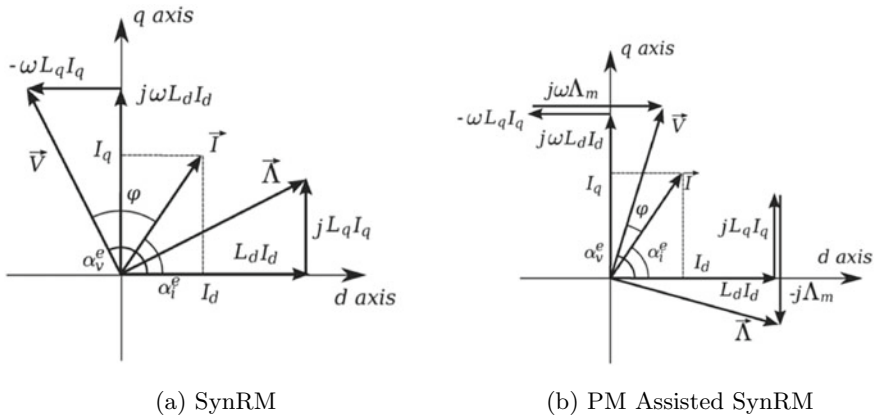
(b) PM Assisted SynRM

Fig. 2 Phasor diagrams for SynRM and PM-assisted SynRM [1]

in (4). The additional term $\lambda_m i_d$ represents the magnetic torque component.

$$T_{PMAsyncRM} = \frac{3}{2}\frac{P}{2}(\lambda_m i_d + (L_d - L_q)i_q i_d) \tag{4}$$

3 Motor Topology

The proposed motor is designed for electric four wheeler traction application. FREE-DOMCAR 2020 was an initiative of the US Department of Energy (DOE), where they proposed the design targets of electric motors that could push the current research in EV motor drive design. The speed-torque profile can be seen in Fig. 3. A detailed
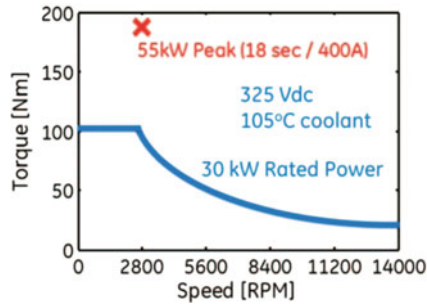
Fig. 3 Torque versus speed profile [2]

Table 1 Design Targets

Machine specification	Value
Power (Rated)	30 kW
Power (Peak)	55 kW
Speed (Rated)	2800 rpm
Speed (Peak)	14000 rpm
Voltage at DC Link	200–450 (325 rated) V
Line-line back EMF (Maximum limit)	600 V
Peak phase current	400 A
Maximum motor outer diameter	250 mm
Maximum motor stack length	200 mm
Motor volume	< 9.7 L
Motor mass	< 35 Kg
Coolant temp.	< 105 Deg C, Liquid Cooled
Motor efficiency	> 95% for 10% - 100% speed
Motor cost	< $275 per unit

analysis of the targets has been discussed in [2]. The motor specifications can be seen in Table 1. These specifications are very stringent. In this paper, first the stator design is discussed, taking into consideration the rated conditions. Then the rotor design is discussed along with the approach taken towards optimization.

4 Stator Design for Ferrite PMASynRM

Table 2 shows the machine parameters for the designed PMaSynRM and Fig. 4a shows the finite element model using Ansys Maxwell.

Various studies have been carried out to determine the best slot-pole combination for the desired torque-speed profile. It is verified in [2] that distributed winding reduces the weight and back emf as compared to concentrated winding design. The

(a) Designed motor 2D FEM Model   (b) Winding pattern
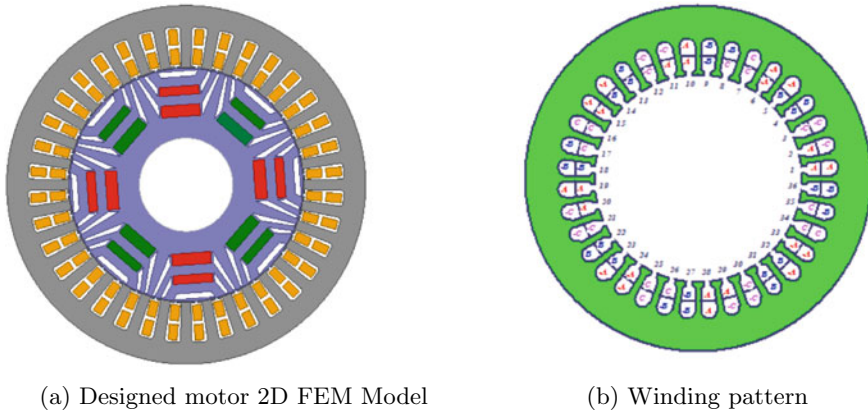
Fig. 4 Proposed motor

study in [3] proved that if an odd value for slots per pole-pair (n_s) is considered, we can reduce the stator-rotor mutual harmonic interactions. This further leads to reduction in torque ripple.

Considering the odd value of n_s we choose the number of slots to be 36 and number of poles to be 8. Thus, the n_s value taken is 9. The winding pattern can be seen in Fig. 4b. With four conductors in each slot and two-layer distributed winding, stator current density considered for rated condition is 9 A/mm^2. Motor specifications can be seen in Table 2. The peak current is taken as 400 A with the current density of 16 A/mm^2. Thermal analysis has not been included in the paper, which will be done in further research. With proper thermal management, the current density can be further increased. However, with the current density of 16 A/mm^2 the peak torque obtained is 184 Nm at rated speed.

4.1 Rotor Topology

Ideally high saliency is preferred to increase the percentage of reluctance torque in the motor. Thus, a simple salient rotor is not suitable as its saliency ratio is very poor. The multi-barrier rotor is also not used due to its complicated construction. For the proposed design, we use transversally laminated multi-barrier rotor with a lamination thickness of 0.75 mm. The various parameters considered for rotor design can be seen in Fig. 5. The paper concentrates on analysing the rotor design for three objectives—optimizing the flux barrier to increase torque and reduce torque ripple, optimizing design to reduce demagnetization at peak output power and designing for minimizing stress on the rotor ribs.

Table 2 Proposed Design

Proposed	Parameters		
Design	Value		Units
Outer diameter of stator	250		mm
Inner diameter of stator	163.56		mm
Air gap	0.595		mm
Stack length	130		mm
Shaft diameter	65		mm
Stator slots	36		–
Rotor poles	8		–
Current density (Rated)	9		A/mm^2
Current density (Peak)	16		A/mm^2
Current (Rated)	226		A
Current (Peak)	400		A
Turns per coil	2		–
Slot fill factor	45 %		–
Mass of ferrite magnets	1.81		Kg
Iron mass of stator	19.19		Kg
Iron mass of rotor	11.91		Kg
Effective mass of copper	4.18		Kg
Combined mass	37.1		Kg
Combined volume	6.4		L

Fig. 5 One-pole ferrite PMASynRM with three flux barriers per pole

(a) Average Torque   (b) Torque Ripple
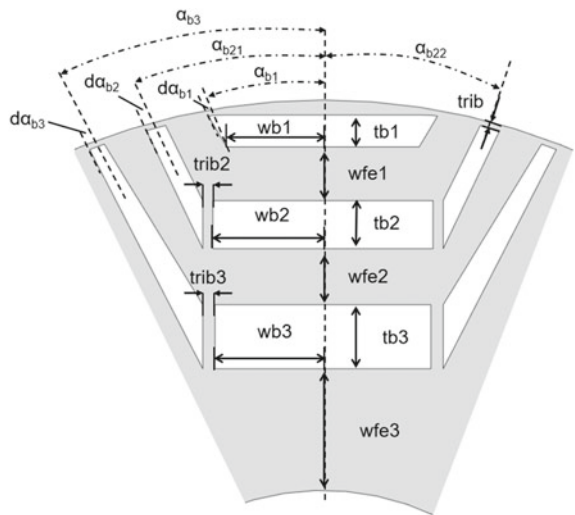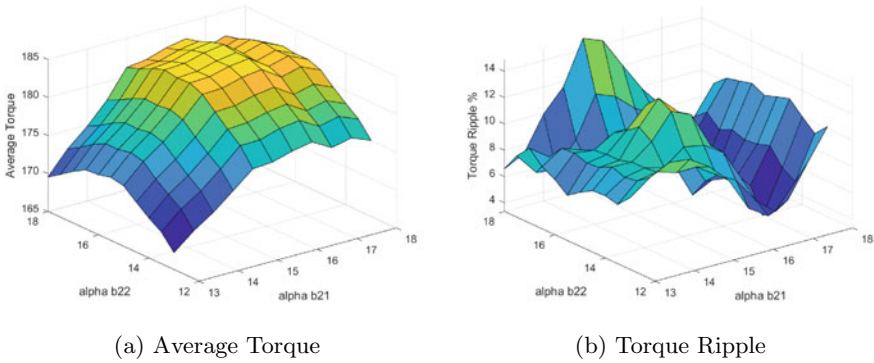
Fig. 6 Optimization of α_{b21} and α_{b22}

4.2 Design of Flux Barrier

In the literature review, traction motors with comparable power output tend to have three flux barriers. Further increasing the number of barriers generally leads to saturation of the steel [4, 5].

Flux barrier angle affects both D- and Q-axis inductance and thus the saliency ratio. The average torque and the torque ripple are also significantly affected by the flux barrier angle. It is found in the study that the ends of the second barrier should be asymmetric in order to reduce the torque ripple and increase average torque. α_{b21} and α_{b22} are optimized at peak power operating point so as to have the maximum average torque as shown in Fig. 6a and minimum torque ripple in Fig. 6b. The optimized flux barrier angles can be seen in Table 3.

4.3 Demagnetization Analysis

For the machine, ferrite magnets (Y33BH) are considered. The intrinsic coercivity (H_c) for these magnets is 247 kA/m. However, these ferrite magnets should not get demagnetized beyond knee point. At peak load conditions, it is necessary to avoid possible demagnetization. The $B - H$ curve and permeability of Y33BH-grade ferrite can be seen in Fig. 7 [6].

The H magnitude plot is shown in Fig. 8a. The greatest amount of magnetic field intensity is at the first barrier. It is proposed here to remove the PMs from the first barrier to avoid demagnetization. Magnets inserted in the second barrier have the peak H magnitude of 140 kA/m, which is an acceptable operating point for ferrite magnets at all temperatures.

Table 3 Optimized parameters for the rotor

First barrier half angle	α_{b1}	10	deg
Second barrier upper half angle	α_{b21}	16.5	deg
Second barrier lower half angle	α_{b22}	16	deg
Third barrier half angle	α_{b3}	20.5	deg
Thickness of the first barrier	t_{b1}	4	mm
Second barrier thickness for ferrite magnet	t_{b2}	6	mm
Third barrier thickness for ferrite magnet	t_{b3}	8	mm
First barrier width	w_{b1}	12	mm
Second barrier width	w_{b2}	15	mm
Third barrier width	w_{b3}	15	mm
Distance between barriers 1 and 2	w_{fe1}	6.7	mm
Distance between barriers 2 and 3	w_{fe2}	7	mm
Distance between barriers 3 and shaft	w_{fe3}	15.2	mm
Rib thickness	t_{rib}	0.75	mm
Rib thickness at barrier 2	t_{rib2}	1.261	mm
Rib thickness at barrier 3	t_{rib3}	1.526	mm
Barrier 1 end half angle	$d\alpha_{b1}$	0.2251	deg
Barrier 2 end half angle	$d\alpha_{b2}$	0.8877	deg
Barrier 3 end half angle	$d\alpha_{b3}$	0.6964	deg
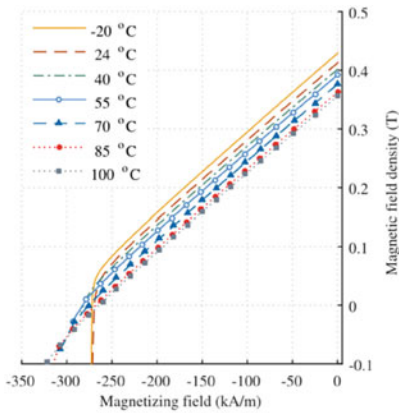
(a) Demagnetisation Characteristics   (b) Permeability Variation
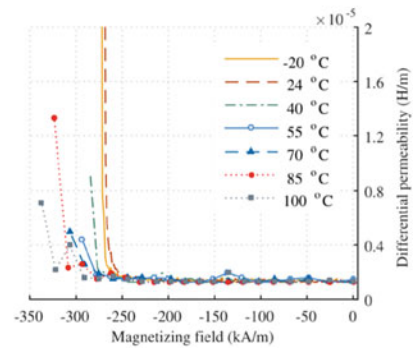
Fig. 7 Demagnetization Analysis at different temperatures [6]

(a) H Magnitude Plot (b) Demagnetization curve
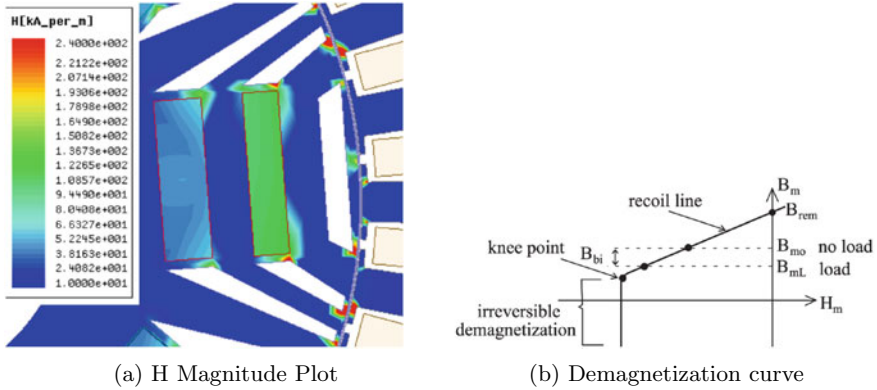
Fig. 8 Demagnetization analysis at peak load

4.4 Stress Consideration at Peak Speed

In this section, the mechanical stress on the rotor lamination is analysed. In the literature review, various studies have been done for stress analysis of PMaSynRM [7]. The rotational speed of the rotor is considered to be 16,600 RPM, which is 18% above the maximum operating speed. The yield strength of the rotor core material used is 800 MPa. A limit of 720 MPa is set as the peak stress allowed for the rotor, with a safety margin of 10%. Figure 9 shows the von Mises stress for the rotor lamination. The ends of barrier 1 suffer from maximum stress; however, it is less than the calculated limit of core material.
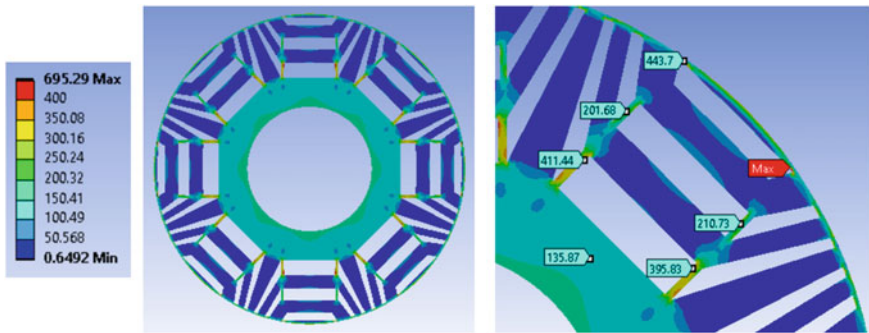
Fig. 9 Von Mises stress of the rotor for 16600 rpm

5   FEM Analysis Results

Ansys Maxwell software is used for the finite element analysis of the machine. Table 2 shows the various parameters for the machine. We obtain a torque of 152 Nm for the SynRM model at the maximum current density (16 A/mm^2). This torque value is 75% of the peak torque for PMaSynRM model. The torque-speed profile for the proposed machine is presented in Fig. 3.

In Fig. 10, the FEM results obtained for the proposed motor over the complete speed range and along the rated power envelope can be seen. The rated mechanical power is a constant value of 30 kW. The current angle calculated for each operating point is along maximum torque per ampere (MTPA) trajectory. Figure 11 shows the core loss for the proposed design at various operating speeds. In order to achieve better efficiency at maximum speed, further research is needed.
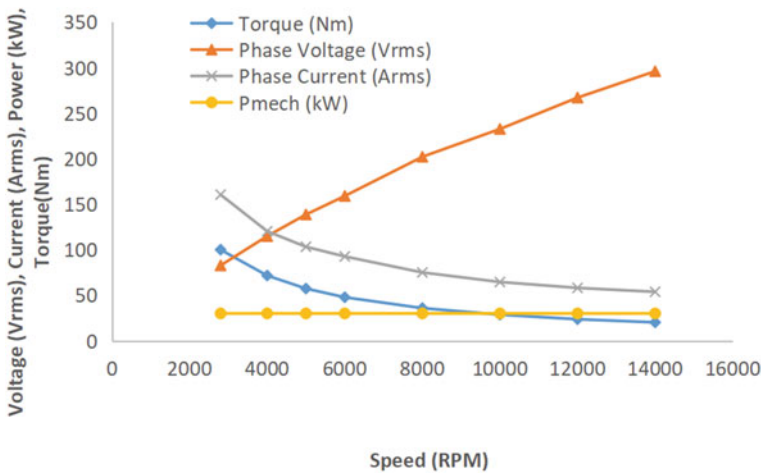
Fig. 10 Motor performance over complete power envelope
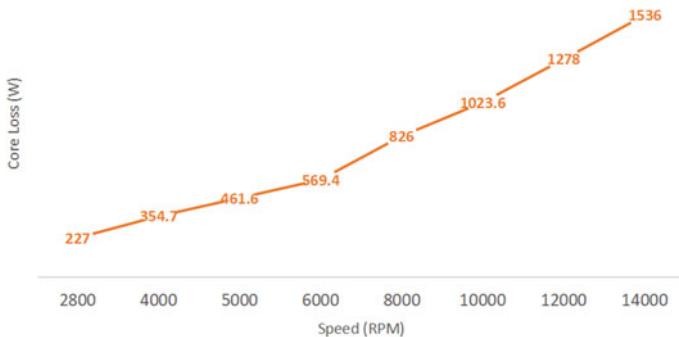
Fig. 11 Machine core loss

5.1 Rated Speed Operation

2800 RPM is the rated speed considered for the machine. Magnetic field density plots for rated torque and peak torque conditions can be seen in Fig. 12. It is observed that the magnetic flux density in the stator teeth does not exceed 1.9 T at any operating point.

The rated torque operation in Fig. 13a shows that torque ripple is 5.5% with peak back emf of 117 V when supplied with a phase current of 160 A(rms) at 60° current angle. The peak torque operation is shown in Fig. 13b. The peak torque obtained is 184 Nm. The peak back emf is 137 V when supplied with a phase current of 283 A(rms) at a 60° current angle.

(a) Rated Torque   (b) Peak Torque
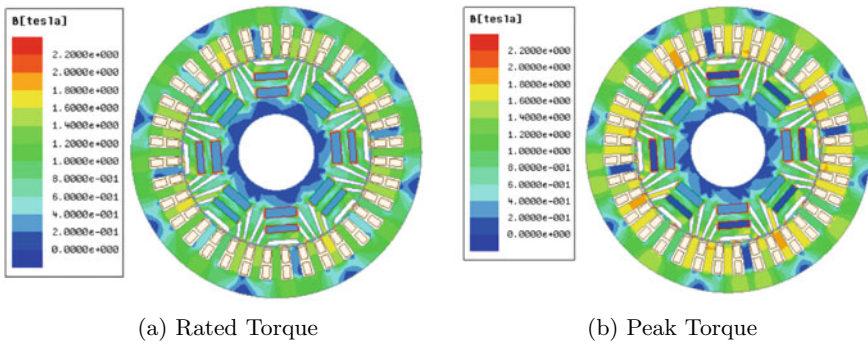
Fig. 12 Flux density plot at rated speed

(a) Rated Torque Operation   (b) Peak Torque Operation
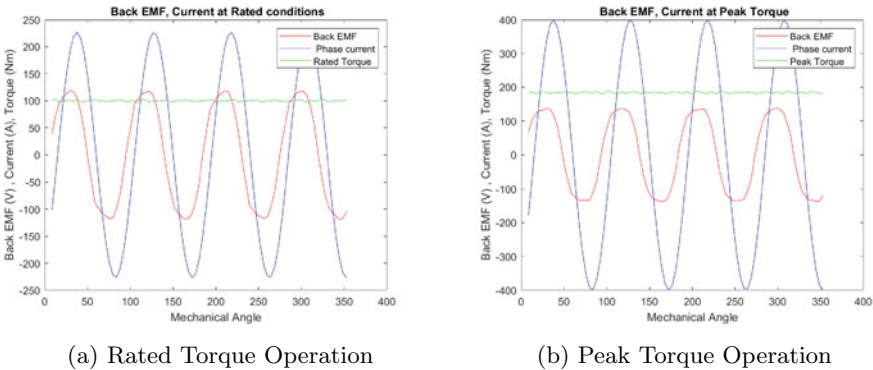
Fig. 13 Simulation results for the rated speed
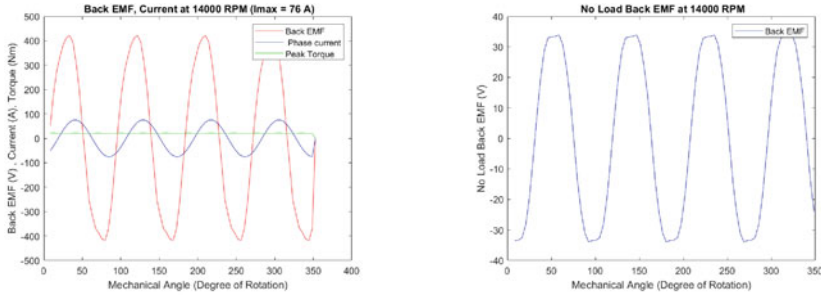
(a) Maximum speed performance   (b) No load Back-EMF at maximum speed

Fig. 14 **a** Maximum speed performance **b** No-load back EMF at maximum speed

5.2 *Maximum Speed Operation*

The back emf increases with operating speed. However, the rated DC link voltage is maintained at 325 V. A constant mechanical power of 30 kW is maintained at the maximum speed of 14000 RPM as well. The peak speed operation is shown in Fig. 14a. At the no-load condition, the back emf obtained at peak speed is 34 V. With electrical loading of 54 A(rms) at a current angle of 76°, the back emf obtained is 296 V(rms) as shown in Fig. 14a.

6 Conclusion

A parametric rotor design for ferrite PMaSynRM has been proposed in this paper. It is verified that the torque ripple can be reduced by using an odd value of n_s (slots per pole pair). The flux barrier shape is optimized for minimum torque ripple and maximum average torque.

Further, the proposed model is used to study demagnetization of ferrite magnets at peak loading. The proposed design shows promise as the ferrite magnets do not get demagnetized at any operating point. Stress analysis of the rotor lamination is presented which shows that maximum rotor stress is under the specified limit while taking a safety factor of 10%.

While the proposed model shows reduced torque ripple, the efficiency at max speed can be further improved. In this paper, the thermal analysis has not been shown. Further research will look into the thermal management and improvement in high-speed efficiency of the motor.

References

1. N. Bianchi, E. Fornasiero, W. Soong, Selection of pm flux linkage for maximum low speed torque rating in a pm assisted synchronous reluctance machine. IEEE Trans. Indus. Appl. **51**(5)
2. A. Walker, M. Galea, C. Gerada, A. Mebarki, D. Gerada, Design considerations for high performance traction machines: aiming for the freedomcar 2020 targets, in *International Conference on Electrical Systems for Aircraft, Railway, Ship Propulsion and Road Vehicles (ESARS)* (IEEE, 2015)
3. S.-H. Han, T.M. Jahns, W.L. Soong, Torque ripple reduction in interior permanent magnet synchronous machines using the principle of mutual harmonics exclusion, in *IEEE Industry Applications Annual Meeting* (2007)
4. Z. Zhang, Design and experimental verification of low cost ferrite pm-assisted synchronous reluctance motor, in *IEEE Transportation Electrification Conference and Expo* (2020)
5. E.E. Montalvo-Ortiz, S.N. Foster, J.G. Cintron-Rivera, E.G. Strangas, Comparison between a spoke-type pmsm and a pmasynrm using ferrite magnets, in *International Electric Machines and Drives Conference* (2013)
6. M. Fasil, N. Mijatovic, B.B. Jensen, J. Holboll, Performance variation of ferrite magnet pmbldc motor with temperature. IEEE Trans. Mag. **51**(12): 1–6 (2015)
7. M. Al-Ani, S. La Rocca, A. La Rocca, A. Walker, R. Ramanathan, T. Zou, G. Vakil, D. Gerada, C. Gerada, K. Paciura, et al., Design of rare-earth-free pm-assisted synchronous reluctance machine for heavy-duty automotive application (2021)

Comparative Analysis of Different Signal Processing Schemes for Islanding Detection in Microgrid

Prajna Parimita Mishra, Chandrashekhar Narayan Bhende, and Akshaya Kumar Pati

Abstract In this paper, islanding detection in a microgrid scenario is analyzed by using the signal processing techniques such as the S-transform method (ST), Sparse S-transform (SST), variational mode decomposition method (VMD) and total variation filtering method (TVF). To get a clear picture of the comparison, all the detection schemes are evaluated in the standard 13-bus distribution system. In this paper, the PCC voltage of a three-phase system is utilized for further signal processing and subsequent feature selection procedure. The extracted voltage is also called as modal voltage. Various monitoring parameters have been considered to check the effectiveness of the selected threshold and subsequent islanding detection. Further, the detailed overview of above-mentioned methods has been thoroughly discussed.

Keywords Distributed generations (DGs) · Islanding detection · Signal processing schemes · Modal voltage signal

1 Introduction

In recent decades, the eco-friendly nature of renewable source leads to increase uses distributed generation systems (DGs) in the power system network. Mostly the photovoltaic and wind turbine system are widely used as renewable energy sources. The integration of renewable sources with the grid arises several issues. In general, the islanding condition arises when one or more DGs continue to energize the loads even though the power from the utility is under a cutoff state. If such island conditions are not identified at right time, it may cause serious harm to the equipment and working personnel. So it needs an accurate and timely detection of the islanding

P. P. Mishra (✉)
School of Electrical Engineering, KIIT Deemed to be University, Bhubaneswar, India
e-mail: prajnaelect@gmail.com

C. N. Bhende
School of Electrical Sciences, IIT Bhubaneswar, Bhubaneswar, Odisha, India

A. K. Pati
School of Electronics Engineering, KIIT Deemed to be University, Bhubaneswar, India

343

states. According to the IEEE 1547-2003 standard, the islanding must be detected within 2 s [1].

Generally, the islanding detection approaches are categorized as active, passive, and communication-based techniques. Among the methods, the passive islanding method of detection requires monitoring of the system parameters such as voltage, frequency, and total harmonic distortion of the signal. It is also convenient for implementation, however, the major disadvantage of this technique is the large non-detection zone (NDZ) which depends on the accurate selection of the threshold value. Some of the commonly used passive methods are: Over/Under voltage protection (OVP/UVP), rate of change of voltage (ROCOV), rate of change of power (ROCOP), Over/Under frequency protection (OFP/UFP), and rate of change of frequency (ROCOF), etc. [2]. The active method is based on monitoring the system's response by injecting an intentional disturbance. In this method, the NDZ is negligible in width, but due to the injection of the external disturbance, power quality deteriorates [3]. Some other active methods such as Sandia frequency shift, slip-mode frequency shift, and active frequency drift are also reported in the literature [4]. The drawbacks of both active and passive methods are overcome by the communication method. In this method, direct communication between the utility and DG exists [5]. But, practical implementation of this method costs more. Another method called the hybrid approach which is the combination of both active and passive islanding methods, is reported in the literature [6, 7]. But, it increases the overall complexity of the system. From the above-mentioned overview, as compared to other existing methods, the passive techniques have more advantages in terms of cost-effectiveness, detection speed, and also it doesn't have any impact on power quality. Therefore, the passive detection scheme equipped with an effective NDZ reduction feature is a promising solution to the islanding detection problem.

Further, various signal process tools are applied to the test signal to overcome the drawbacks of the passive method, i.e. large NDZ issues. In an islanding detection method, extracting the hidden characteristics of the signal plays an important role in the accurate detection of the islanding. This can be done by using powerful weapons like different signal processing techniques which are very much versatile, stable, and also cost-effective. Some of the important signal processing tools are Fast Fourier transform (FFT), TT-transform, Kalman filtering, Hilbert Huang transform, Wavelet transform (WT), S-transform, etc. [8]. Further, some other signal processing methods such as wavelet packet transform and backpropagation neural network for island detection are presented in [9]. Another study that uses the artificial neural network and its synchronized phasor data for islanding detection is described in [10]. In this study, the signal processing schemes such as the S-transform method (ST), Sparse S-transform (SST), Variational Mode Decomposition method (VMD) and total variation filtering method (TVF) are used for islanding detection. The effectiveness of these detection schemes has been discussed.

This paper is organized as follows. The description of the system considered for the proposed comparative analysis is discussed in Sect. 2. The details of these signal processing schemes have been discussed in Sect. 3. Section 4 shows the comparative

results of the studied observation along with the complete overview of the methods. The overall conclusion is presented in Sect. 5.

2 Test System Configuration

This section presents a detailed description of the system considered for the proposed study of the effectiveness of various signal processing-based islanding detection schemes. In this study, a standard test system of photovoltaic system integrated into a standard IEEE 13-bus distribution network is considered as shown in Fig. 1. The test system contains a substation, 13 numbers of nodes or buses with 11 line sections and many loads. Different types of loads such as balanced, unbalanced, nonlinear and dynamic loads are considered. The substation rating is taken as 115 kV, further, it stepped down to a level of 4.16 kV by using a distribution transformer. The PV system of 14,1 kW rating is connected to the network. The PV system is integrated into the bus through an inverter and transformer, the transformer T2 is used to step
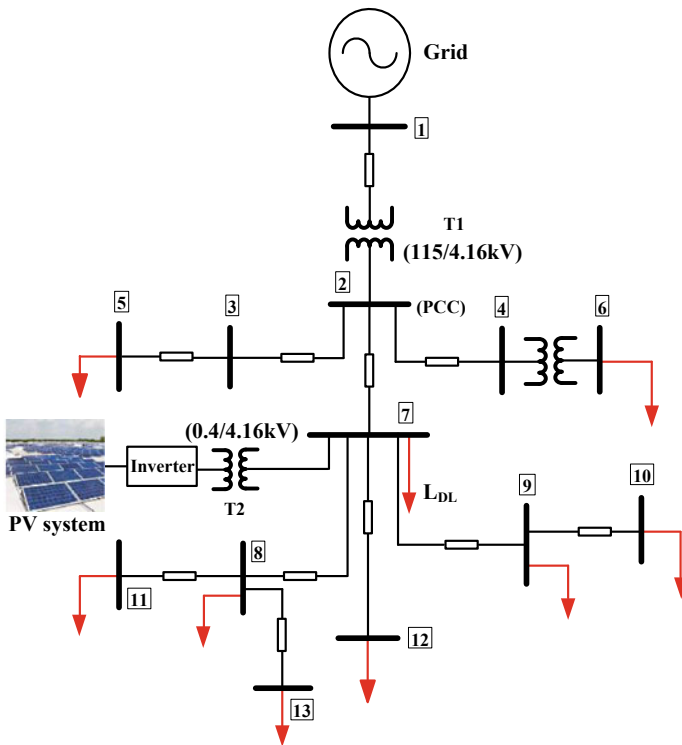
Fig. 1 Grid interactive 13-bus distribution network for islanding detection

Table 1 PV system parameters

Parameter	Value
Short circuit current (I_{SC})	8.01A
Open circuit voltage (V_{OC})	36.90 V
Number of series connected PV module	22
Power rating of the series connected PV array	4.7 kW
Number of such series connected PV array	3
Maximum power rating of the PV array	14.1 kW

down the voltage to 400 V. The parameters of data of the IEEE 13-bus system are taken from [11] and the PV system parameter is given in Table 1.

The voltage at PCC (as shown in the Fig. 1) of the three-phase system is measured, and then, by applying a linear combination of the three-phase voltages, the modal voltage signal is obtained. This parameter is used as the test signal for the detection schemes.

3 Signal Processing-Based Islanding Detection Schemes

The contribution of various signal processing techniques for efficient passive islanding detection is well documented in the literature. The NDZ is a significant parameter of the passive islanding detection method. Due to the advancement of signal processing tools (as the method reported in recent literature) [12–19], which have been applied to the passive islanding method to reduce the NDZ. Many such widely accepted advanced tools for signal decomposition are: wavelet singular entropy [12], data mining [14], Bayesian classification [15], pattern recognition [13], artificial neural network [16] and S-Transform (ST) [17]. The advantages, as well as shortcomings of these methods, are outlined in [18]. In this paper, the detection scheme based on S-transform, Sparse S-transform (SST), Variational Mode Decomposition method (VMD) and Total Variation Filtering method (TVF) are discussed. The details of these signal processing schemes are given in references [17, 19, 20] and [18], respectively (Fig. 2).

In the islanding detection scheme based on signal processing techniques, the first step is considered as extraction of three-phase voltage signal from the PCC of the system. In the second step, to get the corresponding modal voltage, the PCC voltage signal is computed through the modal voltage transformation. In the third step, the obtained modal voltage signal is passed through the processing algorithms for further signal processing. To characterize the decomposition, suitable features are extracted from the decomposed signal. To evaluate the behaviour of the signal, it is further monitored by comparing it with pre-specified threshold values. The threshold value for the islanding detection techniques is calculated by considering the signal behaviour under various network disturbances conditions. The logic behind
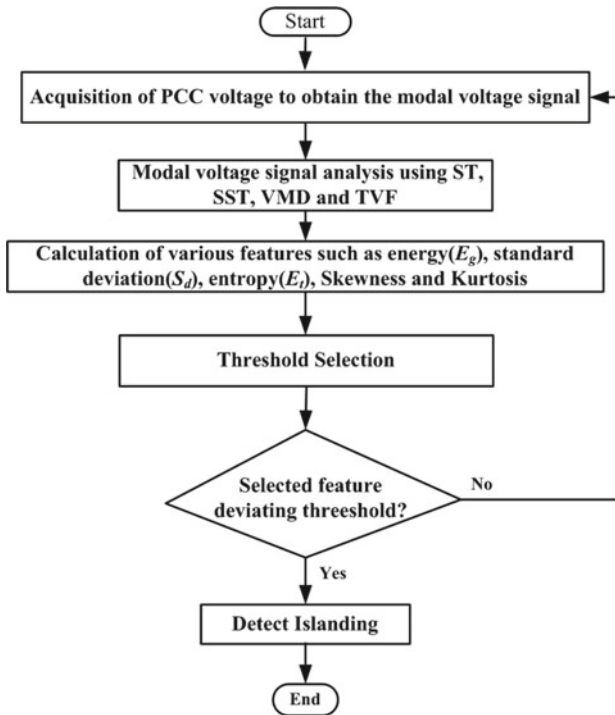
Fig. 2 Flowchart of the signal processing based islanding detection method

the selection of threshold is that the islanding condition should be accurately identified and the other normally occurring non-islanding events should be ignored by the island detection method. While calculating the threshold, the following disturbances are considered such as grid's X/R ratio variation between the range of 5 to 15, grid frequency variation between 49.5 Hz to 50.2 Hz, power quality disturbances, i.e. variation in swell/sag conditions, zero power mismatch between distributed generation and the load and increase of *R-L* load value by 50%,

4   Results and Discussion

All the schemes discussed above detect the islanding condition very effectively. However, in order to get a comparative analysis of different decomposition schemes, various performance measures are considered. To evaluate the effectiveness of various islanding detection techniques, various criteria such as the detection time taken by the schemes, the minimum number of statistical parameters required for accurate detection and the effectiveness of the selected threshold are considered. To get a clear picture of the comparison among the signal decomposition methods,

all the schemes are evaluated on the same system of Fig. 1 with the introduction of 20 dB noise into the PCC voltage. This performance of the system is analyzed on the computer processor of Intel i3 with 2.8 GHz, 8 GB RAM computer and in MATLAB/SIMULINK platform. The input voltage signal to the algorithm in case of all the detection schemes contains three cycles of data (600 samples).

4.1 Detection Time

The accuracy of the islanding detection time is of prime importance. As per the IEEE Std. 929-2000, the DG should be disconnected after detection of islanding. Similarly as per the IEEE Std. 1547-2003, the islanding condition should be identified within 2 s of its formation. However, in case of power system protection, the detection should be always faster so that decision-making for further remedial action can be better. In this section, in order to get a comparative analysis of different decomposition schemes, the islanding detection time is treated as an important parameter. The islanding detection time consists of the algorithm time (time taken by the algorithm) and the execution time (time interval between the receiving of the input signal and the generating of the trip signal). The details of the time taken by various decomposition methods are presented in Table 2.

As noticed in Table 2, all the decomposition methods are able to achieve fast detection. However, among the schemes, TVF-based detection scheme is the fastest to detect islanding in a noisy environment.

Table 2 Comparative analysis of different signal decomposition based islanding detection algorithms in a noisy environment

Events		Algorithm time (ms)	Islanding detection time/execution time (ms)
S-Transform [69]		15.32	32
SST with	Automatic Scaling	7.3	26
	Harmonic Scaling	6.49	23
	Dyadic Scaling	4.67	21
Variational mode decomposition (VMD) based scheme		3.357	17
Total variation (TV) based filtering scheme		2.562	16

4.2 Number of Statistical Parameters

In case of passive islanding detection algorithms, the selection of powerful moni-
toring parameters plays an important role in successful islanding detection. For the
analysis of signals, various statistical parameters were used. The statistical param-
eters such as energy, standard deviation (SD), variance, energy, entropy, kurtosis
and skewness are used in signal decomposition-based algorithms. In case of TVF-
based detection approach, along with the statistical parameters, the rate of change of
positive sequence phase angle (ROCOPSA) is also considered in order to enhance
the reliability of the islanding detection scheme. In many of the detection schemes,
reported in the literature, these statistical parameters are efficient in detecting the
disturbances. But, for the accurate islanding detection, those parameters that demon-
strate maximum changes to the disturbance are considered more suitable. So in this
context, the most suitable and efficient parameters are selected for the proposed
detection schemes for the successful islanding detection. Then the parameters are
compared with the pre-defined threshold value. If the value of the parameter devi-
ates from the pre-specified threshold value, then the islanding detection method will
generate a trip signal to the corresponding relay for the isolation purpose. The number
of parameters required for the proposed detection schemes are given in Table 3.

As observed from Table 3, SST-based scheme required three statistical parameters,
whereas the VMD and TVF-based schemes can detect islanding accurately with two
numbers of statistical parameters.

Table 3 Comparative analysis of different islanding detection algorithms in terms of statistical parameters

Detection scheme	No. of statistical parameters required
Sparse S-Transform (SST)	3
Variational mode decomposition (VMD)	2
Total variation filtering (TVF)	2

Table 4 Comparative analysis of different islanding detection algorithms in terms of their effectiveness in threshold selection

	Threshold	Value of parameters for islanding with load $Q_f = 2$	Percentage difference (%)
SST (Dyadic Scaling)	Energy > 150	212.87	29.53
VMD	Kurtosis < 7	3.6339	48.08
TVF	ROCOPSA > 7	18	61.11

Table 5 Overall comparative analysis of different signal processing algorithms

Description	S-Transform	SST	VMD	TVF
Property	A variable and scalable localizing Gaussian window is used while decomposing the signal	Advanced version of S-transform in which sparsity can be incorporated	Signal is decomposed into a group of band limited IMFs (intrinsic mode functions)	Effective algorithm for signal decomposition under noisy environment, whose derivation is based on minimax property
Distinct feature	Provide frequency dependant resolution	Introduction of sparsity	Signal separation is accurate and robust to noise	Effective enough while preserving the sharp edges of the given signals during noise removal
Technique	Time–frequency resolution	Time–frequency Resolution	Analysis of signal is an adaptive and non-recursive method	The objective function is described in terms of a Convex optimization problem
Methodology	Feature extraction and then detection	Feature extraction and then detection	Feature extraction and then detection	Feature extraction and then detection
Islanding Detection	Yes	Yes	Yes	Yes
NDZ	Low, since detection is degraded to some extent under harmonic condition [21]	Negligible	Negligible	Negligible
Advantage	Dilation and translation of localizing scalable Gaussian window with absolute phase spectrum	Less memory requirement, Fast computation	Faster as compared to SST	Faster as compared to VMD
Disadvantage	Calculation requirement and computational burden are quite high	Possibility of selected frequency band may not be always having vital information	VMD requires the number of modes to be pre-defined. Convergence is sensitive to noise	Proper selection of Regularization parameter (λ) is highly essential in order to retain vital signal information

(continued)

Table 5 (continued)

Description	S-Transform	SST	VMD	TVF
Efficiency	Low	High	High	High
Reliability	Yes	Yes	Yes	Yes
Scope for improvement	Possible through other variants of S-transform such as SST	More analysis to select the relevant frequency band for sparsity	Criteria for automatic determination of the number of modes	Automatic selection of λ

4.3   Effectiveness of Selected Threshold

In case of passive islanding detection schemes, proper threshold selection plays a crucial role in the success of the detection scheme. Therefore, there is a necessity to have a comparative study of the effectiveness of the selected threshold for different algorithms. Thus, to compare the effectiveness of various islanding detection algorithms, the percentage difference between the specified threshold value and the monitoring parameter value is considered. In order to get the comparison, the critical case of islanding with a load having a quality factor equal to 2 is taken into account for all the three algorithms. For each algorithm, the percentage difference between the specified threshold and the monitoring parameter value during the high load quality factor event is presented in Table 4.

As observed from the above table, all the proposed passive islanding detection schemes are efficient enough to detect the critical case of islanding along with accurate threshold selection. However, among all the algorithms, the percentage difference between the algorithm's threshold and the corresponding monitoring parameter value is large in case of TVF as compared to other algorithms. Apart from all the above analyses, a complete analysis of different signal processing techniques used in this work is presented in Table 5. From the above analysis, it is observed that the TVF-based detection scheme is the most effective one among the other specified algorithms.

5   Conclusion

This paper has presented a comparative analysis of a plethora of signal processing-based islanding detection techniques which include S-transform (ST), Sparse S-transform (SST), Variational Mode Decomposition (VMD) and Total Variation Filtering (TVF). In order to compare the effectiveness of these algorithms, various monitoring parameters such as detection time, number of statistical parameters required and effectiveness of threshold are evaluated in the studied system. The test system includes a standard IEEE 13-bus distribution system with the introduction of noise. From the analysis, it is concluded that in a noisy environment, although all signal decomposition schemes are effective for successful islanding detection, the TVF-based decomposition scheme outperforms other schemes in successful islanding detection. This analysis will help the power engineer to choose the most effective tool for effective islanding detection in a microgrid scenario.

References

1. IEEE Std. 1547–2003: IEEE standard for interconnecting distributed resources with electric power systems (2003)
2. F. De Mango, M. Liserre, A. Dell'Aquila, A. Pigazo (2006)Overview of anti-islanding algorithms for pv systems. Part I: Passive methods, in *12th International Power Electronics and Motion Control Conference* (2006), pp. 1878–1883
3. P.P. Mishra, C.N. Bhende, Islanding detection scheme for distributed generation systems using modified reactive power control strategy. IET Gener. Transm. Distrib. **13**(6), 814–820 (2019 May 6)
4. F. De Mango, M. Liserre, A. Dell'Aquila, Overview of anti-islanding algorithms for pv systems. Part II: Activemethods, in *2006 12th International Power Electronics and Motion Control Conference*, (IEEE, 2006 Aug 30), pp. 1884–1889
5. A. Timbus, A. Oudalov, C.N. Ho, Islanding detection in smart grids, in *2010 IEEE Energy Conversion Congress and Exposition* (IEEE, 2010 Sep 12), pp. 3631–3637
6. M. Khodaparastan, H. Vahedi, F. Khazaeli, H. Oraee, A novel hybrid islanding detection method for inverter-based DGs using SFS and ROCOF. IEEE Trans. Power Deliv. **32**(5), 2162–2170 (2015 Feb 24)
7. D. Mlakić, H.R. Baghaee, S. Nikolovski, Gibbs phenomenon-based hybrid islanding detection strategy for VSC-based microgrids using frequency shift, THDu, and RMSu. IEEE Trans. Smart Grid **10**(5), 5479–5491 (2018 Nov 27)
8. S. Raza, H. Mokhlis, H. Arof, J.A. Laghari, L. Wang, Application of signal processing techniques for islanding detection of distributed generation in distribution network: a review. Energy Convers. Manag. **15**(96), 613–624 (2015 May)
9. H.T. Do, X. Zhang, N.V. Nguyen, S.S. Li, T.T. Chu, Passive-islanding detection method using the wavelet packet transform in grid-connected photovoltaic systems. IEEE Trans. Power Electron. **31**(10), 6955–6967 (2015 Dec 7)
10. D. Kumar, P.S. Bhowmik, Artificial neural network and phasor data-based islanding detection in smart grid. IET Gener. Transm. Distrib. **12**(21), 5843–5850 (2018 Nov 29)
11. W.H. Kersting, Radial distribution test feeders. IEEE Trans. Power Syst. **6**(3), 975–985 (1991 Aug)
12. A. Samui, S.R. Samantaray, Wavelet singular entropy-based islanding detection in distributed generation. IEEE Trans. Power Deliv. **28**(1), 411–418 (2012 Dec 4)
13. N.W. Lidula, A.D. Rajapakse, A pattern recognition approach for detecting power islands using transient signals—Part I: design and implementation. IEEE Trans. Power Deliv. **25**(4), 3070–3077 (2010 Aug 12)
14. K. El-Arroudi, G. Joos, I. Kamwa, D.T. McGillis, Intelligent-based approach to islanding detection in distributed generation. IEEE Trans. Power Deliv. **22**(2), 828–835 (2007 Apr 2)
15. W.K. Najy, H.H. Zeineldin, A.H. Alaboudy, W.L. Woon, A Bayesian passive islanding detection method for inverter-based distributed generation using ESPRIT. IEEE Trans. Power Deliv. **26**(4), 2687–2696 (2011 Jul 19)
16. V.L. Merlin, R.C. dos Santos, A.P. Pavani, D.V. Coury, M. Oleskovicz, J.C. de Melo Vieira, Artificial neural network based approach for anti-islanding protection of distributed generators. J. Contr. Autom. Electr. Syst. **25**(3), 339–348 (2014 June 1)
17. P.K. Ray, N. Kishor, S.R. Mohanty, Islanding and power quality disturbance detection in grid-connected hybrid power system using wavelet and $ S $-transform. IEEE Trans. Smart Grid **3**(3), 1082–1094 (2012 May 31)
18. P.P. Mishra, C.N. Bhende, M.S. Manikandan, Islanding detection using total variation-based signal decomposition technique. IET Energy Syst. Integr. **2**(1), 22–31 (2020 Mar)

19. P.P. Mishra, C.N. Bhende, Islanding detection using sparse S-transform in distributed generation systems. Electr. Eng. **100**(4), 2397–2406 (2018 Dec)
20. P. Parimita Mishra, C. N. Bhende, Islanding detection based on variational mode decomposition for inverter based distributed generation systems. IFAC-PapersOnLine **52**(4), 306–311 (2019 Jan 1)
21. S.R. Mohanty, N. Kishor, P.K. Ray, J.P. Catalo, Comparative study of advanced signal processing techniques for islanding detection in a hybrid distributed generation system. IEEE Trans. Sustain. Energy **6**(1), 122–131 (2014 Nov 4)

Gamma Band: A Bio-Marker to Detect Epileptic Seizures

Sunanda Das, Mohammad Jabirullah, Neda Afreen,
Amarana Prabhakara Rao, and K. V. S. H. Gayatri Sarman

Abstract The Electroencephalogram (EEG) signal is made up of several frequency bands that describe human behaviours such as emotion, attention, sleep state, and so on. It is necessary to do categorization on the basis of distinct EEG segments in order to detect epileptic seizures. Short-Time Fourier Transform (STFT) is used to analyze the performance of the gamma band in an EEG signal. It also compares various classification approaches and shows that some classification algorithms attain very high accuracy. The analysis was carried out in stages, including STFT, gamma frequency band extraction, statistical feature extraction, and at last classification is performed using an ANN classifier. This work uses STFT to extract statistical properties from collected two-dimensional data and classify epilepsy in the high-frequency region. The proposed Artificial Neural Network (ANN) classifier got 91.3% accuracy rate.

Keywords ANN classifier · EEG · Gamma band · Short-time fourier transform · Seizures

S. Das
Department of Computer Science and Engineering, Jain University, Bangalore 562112, India

M. Jabirullah
Department of ECE, Lords Institute of Engineering and Technology Hyderabad, Telangana 500091, India
e-mail: jabir.ullah@gmail.com

N. Afreen (✉)
Department of Computer Engineering, Jamia Millia Islamia, New Delhi 110025, India
e-mail: afreenneda1@gmail.com

A. Prabhakara Rao · K. V. S. H. Gayatri Sarman
Department of ECE, Vishnu Institute of Technology, Bhimavaram, Andra Pradesh 534202, India
e-mail: prabhakararao.a@vishnu.edu.in

K. V. S. H. Gayatri Sarman
e-mail: gayatrisarman.k@vishnu.edu.in

1   Introduction

Epilepsy is a peripheral nervous system or neurological disturbance in which the brain starts to act abnormally and a serious injury may occur while driving or during some work. Sometimes this even leads to death. According to the World Health Organization report, 50 million people around the world are afflicted by epileptic seizures, and among them, more than 80% of patients are residing in developing countries [1]. This disease occurs due to some defects in the brain, so for proper treatment, it is important to detect this disease on time. EEG waveforms are generally used by clinicians for epilepsy diagnosis because of their high temporal resolution and minimal cost. Information in the EEG signal waveforms is gathered by setting a reasonable number of electrodes at a specified area on the scalp of patients [2]. International Standard 10–12 has been decided for electrode placement on the human scalp. Neurons' electrical activity is measured using these electrodes. Epileptical seizures detection is a difficult job for neurologists by only visualization of the EEG signal from epileptic patients as there are more chances of wrong prediction or human error possibility. So an automated diagnostic system is needed to assist the neurologist in the process of recognizing seizure patients [3].

The behaviour of the EEG signal is non-stationary, with various frequency bands such as δ (0.4–4 Hz), θ (4–8 Hz), α (8–12 Hz), β (12–30 Hz), and γ (30–60 Hz) [4]. High-frequency oscillations (HFO) with frequencies of 40 Hz or above might be utilized as an epileptogenicity biomarker, according to research conducted on human and animal epilepsy models. HFO can be classified as ripples (100–250 Hz), gamma (30–100 Hz) or rapid ripples (250 Hz and above) depending on the frequency characteristics [5]. In this paper, the gamma band is extracted from the time–frequency plane using STFT, as well as statistical time–frequency characteristics and an ANN classifier to classify the data.

The paper is organized in the following order. Section 2 examines some of the linked literature. The details of the functioning model are described in Sect. 3. The findings of our experiments are presented in Sect. 4, and the conclusions are presented in Sect. 5.

2   Related Work

Research on epilepsy detection based on EEG recording had already begun three to four decades ago. It had reached an advanced level with great precision and accuracy. Analysis based on the computer is now extensively employed, and it is commonly used to solve problems such as detection of an event in between two consecutive seizures and seizure analysis. Different algorithms have previously been provided to assist us in doing so.

Short-time Fourier transform (STFT) is used to convert EEG data into the time–frequency (t–f) plane [6]. The t–f plane of the alpha band yielded four statistical

properties. Using tenfold cross-validation, the detection achievement of alpha-band characteristics was examined on six classifiers, revealing that the Random Forest (RF) technique provides the greatest results compared to other classifiers for the majority of the tests done. And the study had the highest classification accuracy, with a maximum Area Under Curve (AUC) of 1 to discriminate seizures from normal people. The statistical characteristics of the alpha band suggest that it could be used as a biomarker in a real-time detection system. Another paper uses a short-time fourier transform to analyze the performance of the gamma band in an EEG signal (STFT) [7]. It also compares various classification approaches and shows that some classification algorithms attain very high accuracy. The analysis was carried out in stages, including STFT, gamma frequency band extraction, statistical feature extraction, and application to a classifier.

Using Haralick characteristics, the study uses the beta sub-band to differentiate between ictal and interictal states [8]. Short-time Fourier Transform was used to turn one-dimensional EEG data into a picture (STFT). Haralick features are input into the decision tree classifier after the beta sub-band is removed from the time frequency (t-f) plane. The maximal area under the curve (AUC) for distinguishing between interictal and ictal has been discovered using receiver operating characteristic (ROC) analysis. For seizure identification using picture descriptors [9], this study solely uses the high-frequency electroencephalogram (EEG) sub-band. The superiority of this work is that instead of using the entire frequency spectrum, it uses only a portion of it, which minimizes computation load and also demonstrates the importance of the gamma band in seizure detection. This article uses [10] picture descriptors to analyze electroencephalograms (EEGs) and sub-bands (delta, theta, alpha, beta, and gamma) for epileptic seizure identification. The 1D EEG data was converted into a picture with the help of a short-time Fourier transform (STFT). The time–frequency (t-f) matrix is divided into sub-bands, and the Haralick characteristics of each sub-band are given into the Naive Bayes (NB) classifier. The need for creating a reliable approach for detecting automatic seizures is expanding all the time. For seizure categorization, a lightweight CNN architecture is developed [11]. High accuracy is attained for binary classification with few trainable parameters and in only 20 epochs.

3 Dataset

The dataset given in [12] was used in this study to meet the goal of epilepsy identification using the more advanced frequency band of EEG signals gathered from patients. This dataset contains information from both epilepsy and non-epilepsy patients. The authors collected EEG data from an epileptic patient and a healthy person. The data was obtained using 128 channels and is divided into five different data classes: A, B, C, D, and E. This dataset class consists of hundred segments gathered over the course of 23.6 s from a single channel, or in different words, each class of data has 4097 samples/pulses with a 173.61 Hz sampling frequency and a 12 bit resolution.

Table 1 shows that in the above-named dataset, data from the A and B classes were collected on healthy people. For data collection, an electrode was put on the person's scalp using the global standard 10–20 system, and it was recorded with the eye closed and open process. The remaining two classes, C and D, contain epileptic patients' data who were seizure-free at the time. Those data were obtained using intracranial EEG signals, data from the hippocampus formation for class C, and data from the epileptogenic zone for class D. During convulsions, epileptic patients provide additional data for class E.

Figure 1 shows the signal traces of EEG data. Signal traces of class A data is shown in figure (a), signal trace of class B data is shown in figure (b), signal trace of class C data is shown in figure (c), signal trace of class D data is shown in figure (d) while signal trace of class E data is shown in figure (e), respectively. The horizontal axis in this diagram indicates the data points number in the time domain of 23.6 s, while the vertical axis indicates the amplitude of EEG data.

4   Methodology

Here, the technique shown in Fig. 2 is used to detect epileptical seizures, as well as a dataset that is existing to perform this research work. The database is open to the public and is hosted at the University of Bonn in Germany. Because the available data has already been pre-processed, no noise removal techniques have been utilized and the dataset is used as it is.

4.1   Time–Frequency Analysis of EEG Data

To perform analysis, a variety of time–frequency approaches are available. STFT is further desirable to wavelet transform algorithms for actual-time processing [13]. STFT is utilized here for EEG data to perform time–frequency analysis. The approach can be used to locate frequency on the time axis and time on the frequency axis. STFT is a technique for converting one-dimensional (time series) data to two-dimensional (time–frequency) data.

Suppose x(t) is a (EEG) signal message, which is also referred to as a pre-window function, and h be the short duration window employed in STFT (t). The following expression (1) is used to calculate STFT:

$$STFT(t, f) = \int_{-\infty}^{\infty} x(\tau)h(\tau - t)e^{-if\tau}d\tau \tag{1}$$
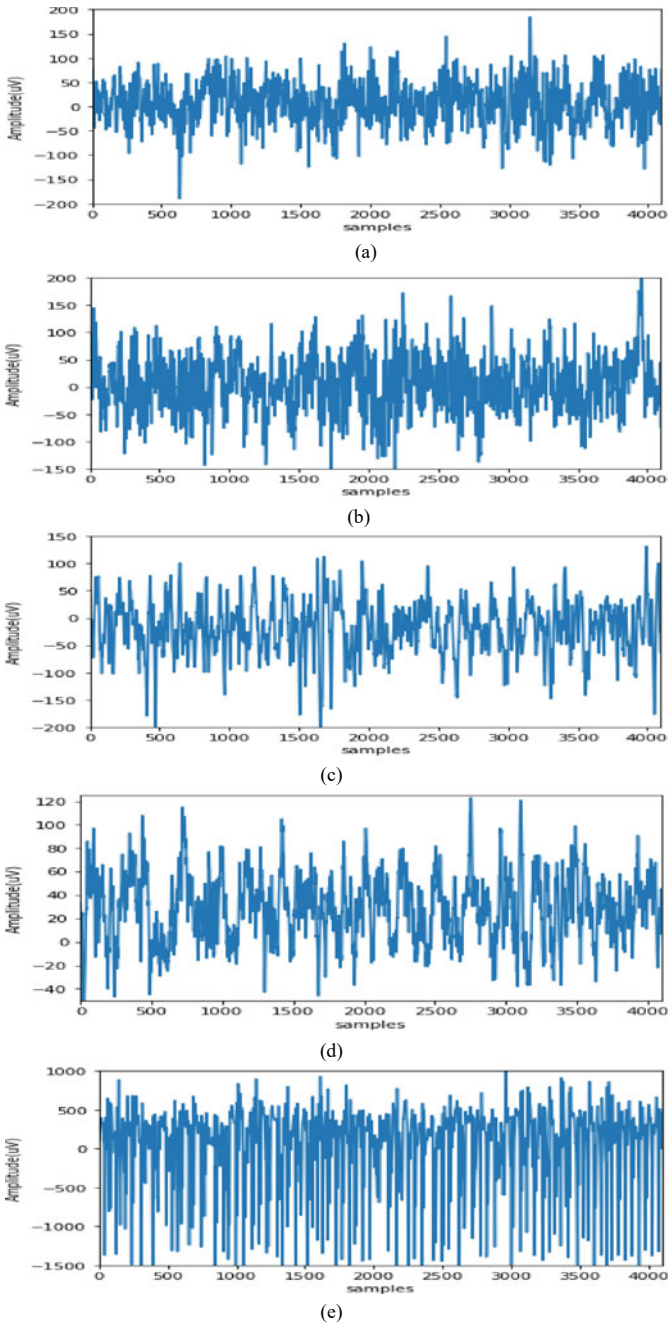
Fig. 1 Bonn EEG data: **a** A class, **b** B class, **c** C class, **d** D class, and **e** E class

Table 1 Descriptions of dataset

EEG data collection subjects	Class	Numbers of signal	Data acquisition
Healthy person	A (Normal)	100	EEG waveform obtained with open eye
	B (Normal)	100	EEG waveform obtained with closed eye
Epileptic patients	C (Seizure free)	100	EEG waveform via the hippocampal development
	D (Seizure free)	100	EEG waveform via epileptogenic area
	E (Seizure)	100	EEG waveform obtained during seizure phase
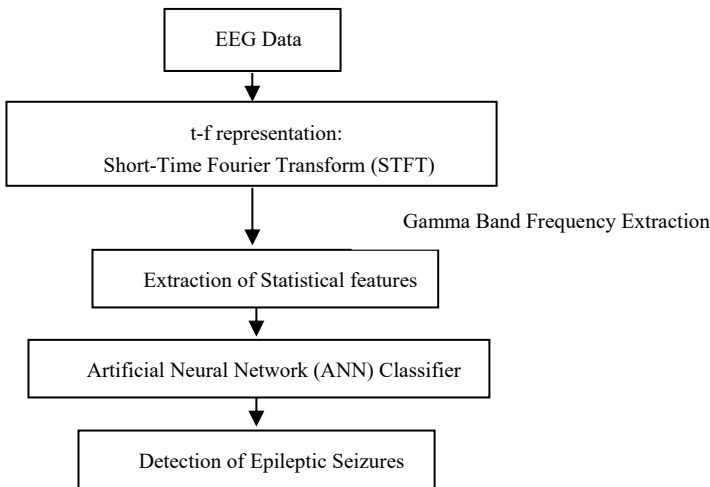
Fig. 2 Epileptical seizures detection steps

4.2 Extracting Features in Accordance with Time– Frequency Analysis

Extraction of features has been carried out after time–frequency analysis. After completing the STFT for this study, high-frequency statistical characteristics (Gamma band) EEG data components have been taken out. The gamma bands are actually found in the frequency range of 30–60 Hz, and a specific collection of statistical characteristics has been extracted.

Many time-series data characteristics with statistical qualities of signals can be constituted in an extended type to illustrate features in time–frequency domain. During epileptic seizures, there is a change in brain rhythm. As a result, statistical changes can be a distinguishing feature from a healthy normal state to an epileptic

seizure state [14]. The following is a list of statistical traits that have been retrieved for studies: variance, mean, kurtosis, and skewness from (2)–(5) are the time–frequency domain representations of these in terms of numerical expressions.

$$m_{(t,f)} = \frac{1}{NM} \sum_n \sum_k \rho[n,k] \tag{2}$$

$$\sigma^2_{(t,f)} = \frac{1}{NM} \sum_n \sum_k (\rho[n,k] - m_{(t,f)})^2 \tag{3}$$

$$\gamma_{(t,f)} = \frac{1}{(NM-1)\sigma^3_{(t,f)}} \sum_n \sum_k (\rho[n,k] - m_{(t,f)})^3 \tag{4}$$

$$k_{(t,f)} = \frac{1}{(NM-1)\sigma^4_{(t,f)}} \sum_n \sum_k (\rho[n,k] - m_{(t,f)})^4 \tag{5}$$

The EEG waveform x(t) is gathered in the domain of time; next, this signal is translated into the time–frequency domain, which is denoted as a q[n, k] matrix of order N by M and can be used to find a variety of additional features.

4.3 Classification Method to Detect Epileptical Seizures

A variety of classification techniques have already been suggested by researchers for performance evaluation or accuracy detection. The classifier is trained using the retrieved time–frequency domain information. There are several methods for separating training and testing data. Cross-validation is one of the most effective methods for doing it. Cross-validation is carried out with k = 10 in this study. The number of subsets of the feature vector is represented by k. K-fold cross-validation is another name for this method. Data from the train and test can be analyzed further. It is viable to transfer test data and assess accuracy after successful completion of training. There have been several classification algorithms used for classifying time–frequency domain EEG signals and provide a concise explanation of them.

- *Classification Using Artificial Neural Network(ANN)*
  ANN (artificial neural network) can be used for the classification of normal and epileptical EEG signals [15, 16]. Because of its self-adaptation and natural way of organizing and implementing redundancy, ANN has proven to be a successful approach for a wide range of EEG signal applications. Classifier performance can be seen by evaluating epileptic seizures detection accuracy and its performance. The training of a network depends on the number of neurons present in the layer. The summary of the ANN model is shown in Fig. 3.

Layer (type)	Output Shape	Parameters
dense_1 (Dense)	(None, 1000)	5000
batch_normalization_1	(None, 1000)	4000
dense_2 (Dense)	(None, 750)	750750
batch_normalization_2	(None, 750)	3000
dense_3 (Dense)	(None, 500)	375500
batch_normalization_3	(None, 500)	2000
dense_4 (Dense)	(None, 250)	125250
batch_normalization_4	(None, 250)	1000
dense_5 (Dense)	(None, 100)	25100
dense_6 (Dense)	(None, 1)	101

Total parameters: 1,291,701
Trainable parameters: 1,286,701
Non-trainable parameters: 5,000

Fig. 3 ANN model summary

5 Results and Discussion

The dataset reported was used in this study. The chosen classes of data (A, B, C, D, and E) were selected, where class A and B data is associated with healthy people, but class C, D, and E data is associated with epileptic patients at the time of seizure activity/ictal phase. The study in this paper was done with data from each class, which included 200 EEG segments. Finally, epilepsy detection was done using these data segments, and the accuracy was obtained using the ANN classifier as shown in Table 2.

Before we go into the results, let's take a look at this document that briefly describes the work that was done. To begin, 200 segments of EEG time-series data were transformed into time–frequency domain using STFT. A section of the advanced

Table 2 Accuracy obtained using gamma band	Classifier	Dataset	Accuracy in percentage
	ANN	A-E	91.3
		B-E	90.0
		C-E	89.67
		D-E	90.67

order frequency band, gamma band (30–60 Hz) was utilized for statistical parameters extraction such as mean, variance, skewness, and kurtosis in this study.

In [7], authors have achieved 90% accuracy, while our proposed method has achieved 91.3% to classify between healthy and seizures, and in [9], a 77% detection rate was shown by authors between interictal and ictal states, while here, the authors have achieved 90.67%.

Here, ANN is employed as a classification algorithm to categorize EEG data and detect epileptical seizures based on time–frequency-based features and compared the accuracy attained.

6 Conclusion

In this study, an accuracy comparison reveals that the system attained a high percentage of accuracy utilizing STFT. It shows that the time domain EEG data has been successfully transformed into the time–frequency domain. The required statistical features were easily extracted. Various classifiers can be integrated in the future utilizing various optimal features to improve seizure detection accuracy. The proposed work will be helpful for clinicians to diagnose seizures.

Disclosure Statement The authors report no conflict of interest.

References

1. F. Mormann, R.G. Andrzejak, C.E. Elger, K. Lehnertz, Seizure prediction: the long and winding road. Brain **130**, 314–333 (2007)
2. Y. Paul, Various epileptic seizure detection techniques using biomedical signals: a review. Brain Inform. **5**, 1–19 (2018)
3. A. Mahajan, K. Somaraj, M. Sameer, Adopting artificial intelligence powered ConvNet to detect epileptic seizures, in *2020 IEEE-EMBS Conference on Biomedical Engineering and Sciences (IECBES)* (2021), pp. 427–432
4. M. Sameer, B. Gupta, Time-frequency statistical features of delta band for detection of epileptic seizures. Wirel. Pers. Commun. (2021). https://doi.org/10.1007/s11277-021-08909-y
5. S.M. Beeraka, A. Kumar, M. Sameer, S. Ghosh, B. Gupta, Accuracy enhancement of epileptic seizure detection: a deep learning approach with hardware realization of STFT. Circuits, Syst. Signal Process. (2021). https://doi.org/10.1007/s00034-021-01789-4
6. M. Sameer, B. Gupta, Detection of epileptical seizures based on alpha band statistical features. Wirel. Pers. Commun. **115**, 909–925 (2020). https://doi.org/10.1007/s11277-020-07542-5
7. M. Sameer, A.K. Gupta, C. Chakraborty, B. Gupta, Epileptical seizure detection: performance analysis of gamma band in EEG signal using short-time fourier transform, in *2019 22nd International Symposium on Wireless Personal Multimedia Communications (WPMC)* (2019), pp. 1–6
8. M. Sameer, B. Gupta, Beta band as a biomarker for classification between interictal and ictal states of epileptical patients, in *2020 7th International Conference on Signal Processing and Integrated Networks (SPIN)* (2020), pp. 567–570

9. M. Sameer, A.K. Gupta, C. Chakraborty, B. Gupta, ROC analysis for detection of epileptical seizures using Haralick features of Gamma band, in *2020 National Conference on Communications (NCC)* (2020), pp. 1–5
10. M. Sameer, B. Gupta, ROC Analysis of EEG subbands for epileptic seizure detection using naive bayes classifier. J. Mob. Multimed. 299–310 (2021)
11. S. Gupta, M. Sameer, N. Mohan, Detection of epileptic seizures using convolutional neural network, in *2021 International Conference on Emerging Smart Computing and Informatics (ESCI)* (2021), pp. 786–790
12. R.G. Andrzejak, K. Lehnertz, F. Mormann, C. Rieke, P. David, C.E. Elger, Indications of nonlinear deterministic and finite-dimensional structures in time series of brain electrical activity: dependence on recording region and brain state. Phys. Rev. E **64**, 61907 (2001)
13. M.K. Kiymik, G. Inan, A. Dizibüyük, M. Akin, Comparison of STFT and wavelet transform methods in determining epileptic seizure activity in EEG signals for real-time application. Comput. Biol. Med. **35**, 603–616 (2005)
14. L. Cohen, Time-frequency distributions-a review. Proc. IEEE **77**, 941–981 (1989)
15. S.P. Kumar, N. Sriram, P.G. Benakop, B.C. Jinaga, Entropies based detection of epileptic seizures with artificial neural network classifiers. Expert Syst. Appl. **37**, 3284–3291 (2010)
16. M. Sameer, P. Agarwal, Coplanar waveguide microwave sensor for label-free real-time glucose detection. Radioengineering **28**, 491–495 (2019)

Experimental Validation and Performance Analysis of a DER-Supported DVSI-Based DSTATCOM in Three-Phase Three-Wire Distribution System

Mrutyunjaya Mangaraj and Jogeswara Sabat

Abstract This paper demonstrates the control and operation of dual voltage source inverter (DVSI)-based distribution static compensator (DSTATCOM) in a three-phase three-wire distribution system. In this paper, a neural network-based control algorithm known as the Sparse Least Mean Square (SLMS) technique is employed to enhance the power quality (PQ) of the system. The proposed topology is built using a two-level two-voltage source inverter (VSI), where one inverter is marked as VSI-1 supported by distributed energy resource (DER) DC link. The other one is represented as VSI-2 supplied by self-supported capacitor DC link. The proposed system automatically senses the DER power generation and performs multi-operation such as PQ as well as optimal active power flow. The observations of the DVSI and VSI are carried out using an FPGA SPARTAN-6 controller-based experimental setup where the solutions are taken into consideration of the permissible standard grid code.

1 Introduction

A major part of electrical power generated in the power industry is using conventional sources, where the generated power is supplied to the distribution system. But the negative aspects of the conventional sources are depletion of fossil fuels, environmental pollution and more transmission losses. So, these reasons divert the attention of the power industry toward the development of DER [1]. Moreover, the modern human society totally depends upon the semiconductor device in every aspect of life which causes instability and PQ issues in the distribution system. Hence, the distribution system requires a DSTATCOM which enhances the PQ like voltage balancing at the point of common coupling (PCC), distortion free source currents, reactive power compensation and unity power factor (P.F), etc.

M. Mangaraj · J. Sabat (✉)
Department of EEE, LIET, Vizianagaram 535005, India
e-mail: jogesh.electrical@gmail.com

The proper design of the shunt compensator for a three-phase distribution system is a challenge to obtain maximum benefits [2]. Among different configurations, two-level VSI-supported DSTATCOM is the popular inverter used as a shunt compensator in the distribution system. But it suffers from some drawbacks such as reduced output voltage, high rating of filter inductor, higher switching frequency, high DC link voltage and limited compensation capability [3, 4]. Hence, researchers are focusing on DVSI to overcome the drawbacks of VSI because of high reliability, easy-to-identify fault position, no neutral point fluctuation, etc. [3–5], and the main reason for the above benefit is the simple decoupled control method [6]. In the DVSI configuration, each VSI is fed by an independent DC source. It is engaged to minimize the total harmonic distortion (THD), lower EMI emission and lower voltage rating of switches [7]. Also, it possesses the capability of optimal power flow under the DER power generation [6].

In this paper, the proposed DVSI topology configuration consists of the DER-supported VSI-1 along with shunt compensation capability. Similarly, the VSI-2 is supported by a self-supported capacitor DC link. The proposed system functions into two approaches: DER supports DVSI-based DSTATCOM and single VSI-based DSTATCOM. It automatically changes the approaches by sensing the DER power generation. The proposed topology is the advanced version of DSTATCOM, enhancing the source current shaping and injecting real power to the nonlinear load, decreasing the dependency of conventional energy generations and avoiding power cut possibilities of the distribution system. The surplus power generated by DER supplies power to the distribution system. However in normal DSTATCOM operation and power generation by the DER is zero, the power flow from the source of the distribution system to the load, here both VSI-1 and VSI-2 are compensating the reactive power for enhancing the PQ.

In recent years, different neural network (NN)-based control algorithms [8] are developed such as Kernel Hebbian least mean square (KHLMS) [9], Naïve back propagation-based *icosφ* [10], GLMS control strategy [11] and Sparse Least Mean Square technique [12]. The SLMS control technique has been utilized in this proposed system to operate the DSTATCOM because it has several advantages as follows:

- The proposed technique is very simple and has the abilities of generalization and learning.
- It provides error-free computation and has the abilities to fast response on dynamic condition.

This paper is structured in a total of five sections. Section 1 describes the DVSI-based DSTATCOM using the SLMS control technique. The discussion in Sect. 2 gives the details of circuit configuration of DVSI and power flow control. In Sect. 3, the SLMS control technique is presented. The experimental results are presented in Sect. 4. Finally, the conclusion is oppressed in Sect. 5.

2 Circuit Description and Power Flow Analysis

The proposed system consists of a 1.6 kW DER-supported distribution system as shown in Fig. 1. A self-supported capacitor is connected to the DER for maintaining DC link voltage. Consequently, the higher frequency component is filtered. The proposed SLMS control strategy is shown in the below part of Fig. 1.

2.1 Power Flow Analysis

This DVSI-based DSTATCOM comprises two VSIs; both VSI-1 and VSI-2 are interfaced to 230 V/phase (RMS), and 50 Hz three-phase distribution system. The power rating of each VSI is 2 kVA, and both VSIs can eliminate harmonic, reactive power compensation and unity P.F during normal operation of the system. During the operation, when DER power generation equals zero, it operates as conventional
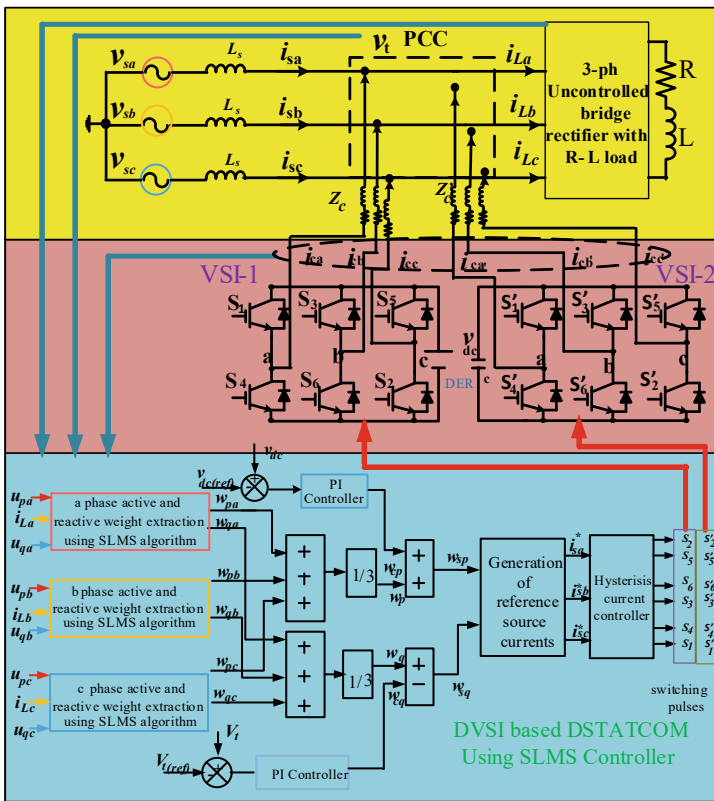
Fig. 1 Circuit configuration of proposed system

DSTATCOM and the power flows from a distribution system to load and the main function is to provide quality power. When power generation by DER is greater than zero, the VSI-1 supplies the generated power from the DER to the variable nonlinear loads and the excess power is injected to the distribution system.

3   SLMS Control Strategy

The objective of the SLMS technique is to correct the source current profile and provide finest real power control in a DER-supported three-phase distribution system. It reduces the computation error and follows a simple process, which includes several steps of the technique, as derived below.

From three-phase load currents, the fundamental active components are extracted and can be expressed as

$$w_{pa}(n+1) = \left[\mu_k e_k i_{La} u_{pa} - \sigma_k \gamma_k \frac{sgn\{w_{pa}(n)\}}{\xi_k + |w_{pa}(n)|} \right] + w_{pa}(n) \tag{1}$$

$$w_{pb}(n+1) = \left[\mu_k e_k i_{Lb} u_{pb} - \sigma_k \gamma_k \frac{sgn\{w_{pb}(n)\}}{\xi_k + |w_{pb}(n)|} \right] + w_{pb}(n) \tag{2}$$

$$w_{pc}(n+1) = \left[\mu_k e_k i_{Lc} u_{pc} - \sigma_k \gamma_k \frac{sgn\{w_{pc}(n)\}}{\xi_k + |w_{pc}(n)|} \right] + w_{pc}(n) \tag{3}$$

To achieve the (w_{qa}, w_{qb}, w_{qc}) fundamental reactive component of load current, which can be written as

$$w_{qa}(n+1) = \left[\mu_k e_k i_{La} u_{qa} - \sigma_k \gamma_k \frac{sgn\{w_{qa}(n)\}}{\xi_k + |w_{qa}(n)|} \right] + w_{qa}(n) \tag{4}$$

$$w_{qb}(n+1) = \left[\mu_k e_k i_{Lb} u_{qb} - \sigma_k \gamma_k \frac{sgn\{w_{qb}(n)\}}{\xi_k + |w_{qb}(n)|} \right] + w_{qb}(n) \tag{5}$$

$$w_{qc}(n+1) = \left[\mu_k e_k i_{Lc} u_{qc} - \sigma_k \gamma_k \frac{sgn\{w_{qc}(n)\}}{\xi_k + |w_{qc}(n)|} \right] + w_{qc}(n) \tag{6}$$

The mean value 'w_p' is expressed as follows:

$$w_p = \frac{w_{pa} + w_{pb} + w_{pc}}{3} \tag{7}$$

The mean value 'w_q' is expressed as follows:

$$w_q = \frac{w_{qa} + w_{qb} + w_{qc}}{3} \tag{8}$$

The 'v_t' is computed as follows:

$$u_{pa} = \frac{v_{sa}}{v_t}, u_{pb} = \frac{v_{sb}}{v_t}, u_{pc} = \frac{v_{sc}}{v_t} \tag{9}$$

The unit voltage templates 'u_{qa}, u_{qb}, u_{qc}' are computed as follows:

$$u_{qa} = \frac{u_{pb} + u_{pc}}{\sqrt{3}}, u_{qb} = \frac{3u_{pa} + u_{pb} - u_{pc}}{2\sqrt{3}}, u_{qc} = \frac{-3u_{pa} + u_{pb} - u_{pc}}{2\sqrt{3}} \tag{10}$$

where v_t can be expressed as

$$v_t = \sqrt{\frac{2(v_{sa}^2 + v_{sb}^2 + v_{sc}^2)}{3}} \tag{11}$$

The error in DC voltage v_{de} is expressed as follows:

$$v_{de} = v_{dc(ref)} - v_{dc} \tag{12}$$

The output of the Proportional-Integral (PI) controller is expressed as

$$w_{cp} = k_{pa}v_{de} + k_{ia} \int v_{de}dt \tag{13}$$

The active component of reference source current can be computed as

$$w_{sp} = w_{ap} + w_{cp} \tag{14}$$

The AC voltage error (v_{te}), which can be computed as

$$v_{te} = v_{t(ref)} - v_t \tag{15}$$

where $v_{t(ref)}$ is the reference AC voltage and v_t is the peak AC voltage. The output of PI controller at AC side can be expressed as

$$w_{cq} = k_{pr} v_{te} + k_{ir} \int v_{te} dt \qquad (16)$$

The total reactive components of the reference source current, this can be computed as

$$w_{sq} = w_{rq} - w_{cq} \qquad (17)$$

$$i_{aa} = w_{sp} u_{pa}, i_{ab} = w_{sp} u_{pb}, i_{ac} = w_{sp} u_{pc} \qquad (18)$$

In the same way, to achieve the (i_{ra}, i_{rb}, i_{rc}) instantaneous reference reactive component (i_{ra}, i_{rb}, i_{rc})

$$i_{ra} = w_{sq} u_{qa}, i_{rb} = w_{sq} u_{qb}, i_{rc} = w_{sq} u_{qc} \qquad (19)$$

The $(i_{sa}^*, i_{sb}^*, i_{sc}^*)$ reference source currents can be obtained as

$$i_{sa}^* = i_{aa} + i_{ra}, i_{sb}^* = i_{ab} + i_{rb}, i_{sc}^* = i_{ac} + i_{rc} \qquad (20)$$

The (i_{sa}, i_{sb}, i_{sc}) actual source currents and the generated $(i_{sa}^*, i_{sb}^*, i_{sc}^*)$ reference source currents are compared, and after that the errors are fed to HCC.

4 Experimental Validation

The overall experimental setup and connection diagram are shown in Fig. 2. A balanced three-phase source voltage 230 V/phase and source current rating of 10A are connected to the nonlinear load through distribution impedance Z_S. The DVSI-based DSTATCOM output, i.e., VSI-1 and VSI-2 outputs are connected at PCC through two MCBs rated 10A as primary protection of the system. A MCB rated 10A controls the source of the distribution system. The multifunction meters (MFMs) made by SELEC and its model no-MFM384 are used to measure different parameters of source and load by MFM-1 and MFM-2, respectively. As the connected load shows nonlinear characteristic, it injects harmonics to the distribution system and the system suffers the PQ issues.

4.1 Performance of VSI-Based DSTATCOM System Under PQ Analysis

The performance of VSI-based DSTATCOM shows the waveform of source voltages, load voltages, load currents, source currents, compensating currents and DC
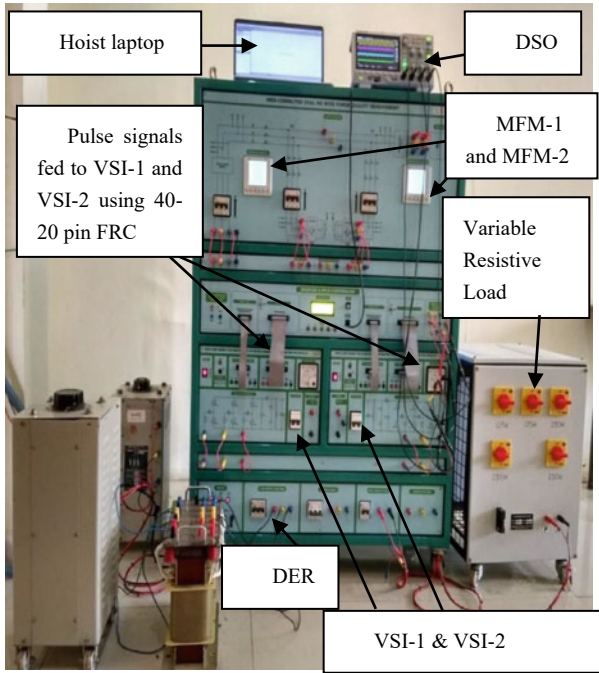
Fig. 2 Hardware setup of the DVSI topology

link voltage and current of single VSI as shown in Fig. 3. It is found that the SLMS controller is able to compensate the source current harmonics as per suggested IEEE standard grid code. The experimental waveforms are under nonlinear load conditions; at the start, the VSI-based DSTATCOM is not in operation, and therefore, whatever load current is drawn is supplied from the distribution system shows in Fig. 3a–c. The Figure 3d–e shows the waveforms of source currents, it is found from the waveform that initially the distribution system is supplying the nonlinear load demand and when the compensator turns on the source currents become perfectly sinusoidal. After compensation, the source current in phase with source voltages is shown in Fig. 3f. The compensating currents are shown in Fig. 3g. Figure 3h shows the DC link voltage and currents, where it is observed that initially there is some disturbance in DC link voltage for a transient period but after that it becomes stable and constant at 640 V. The distortion percentage found in supply voltage 1.7% and load voltage 5.2% are measured using MFM-1 and MFM-2 as shown in Fig. 4a, b. The distortion in load current 29.8% and source current 27.8% are displayed in Fig. 4c, d. It is observed from Fig. 4e, after compensation, the three-phase source current THDs are reduced to 4.5%. The average P.F after compensation is 0.982 which is shown in Fig. 4f.
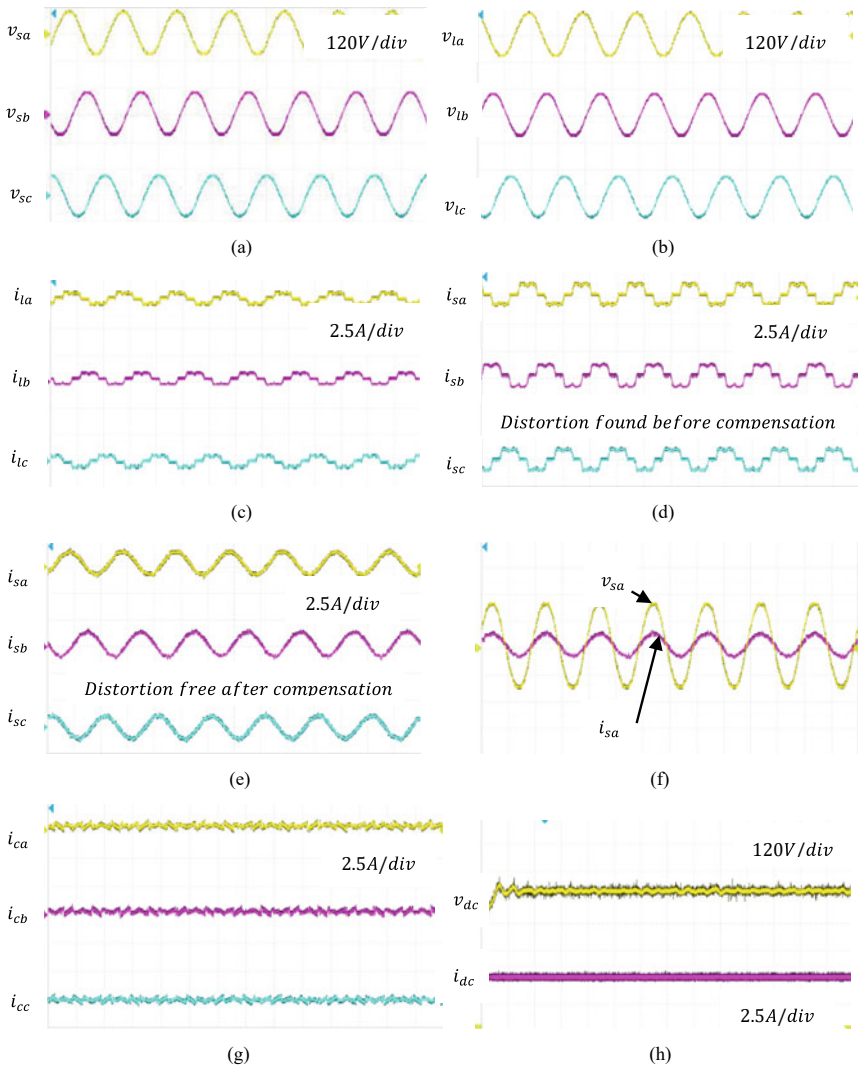
Fig. 3 Experimental performance of VSI topology, **a** three-phase supply voltage, **b** three-phase load voltage, **c** three-phase loads current, **d** three-phase supply current before DSTATCOM is switched on, **e** three-phase source current after DSTATCOM is switched on, **f** phase-1 source voltage and current after compensation, **g** three-phase compensator current and **h** DC link voltage and current

4.2 Performance of DVSI-Based DSTATCOM System Under PQ Analysis

In this scenario, when the DVSI is switched on, the source current becomes sinusoidal as shown in Fig. 5a and compensating current looks like a sine wave structure, not
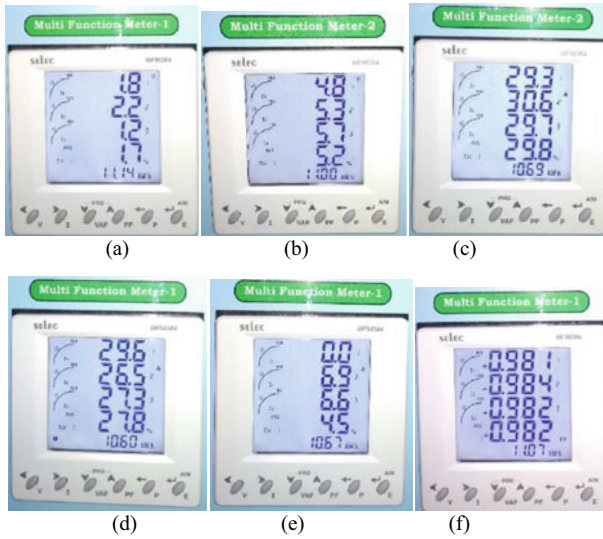
Fig. 4 Measured parameter of VSI topology, **a** THD of source voltage, **b** THD of load voltage, **c** THD of loads current, **d** THD of source current before compensation, **e** THD of source current after compensation, and **f** P.F
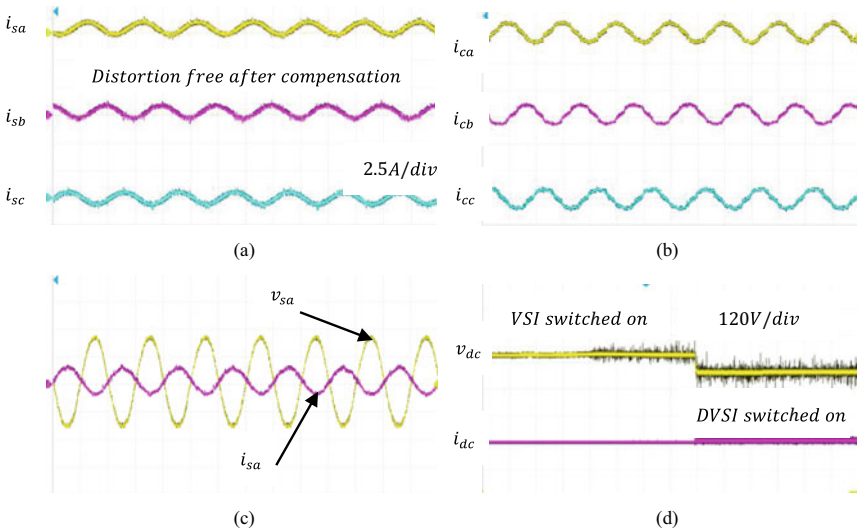
Fig. 5 Experimental performance of DVSI topology, **a** three-phase source current after compensation, **b** three-phase compensating current, **c** phase-a source voltage and current after compensation and **d** DC link voltage and current of both VSI and DVSI topology
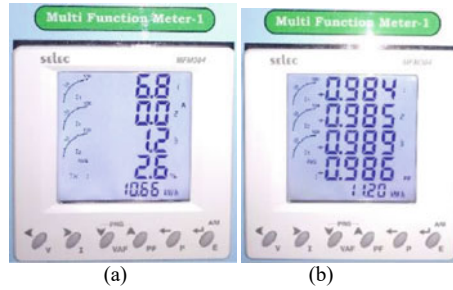
Fig. 6 Measured parameter of DVSI topology after compensation, **a** THD of source current and (b) improved P.F
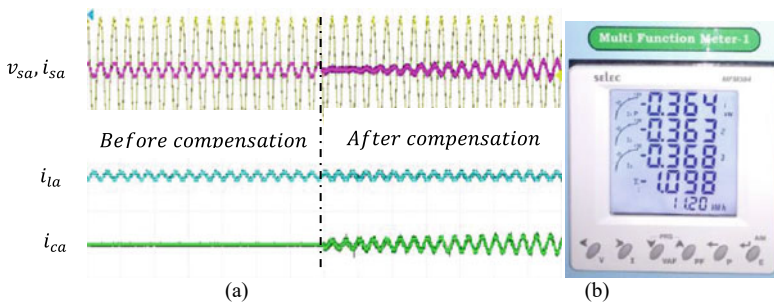
Fig. 7 Dynamic performance, **a** phase-a source voltage, source current, load current and compensating current and **b** MFM-1 measures the source side kW power measurement

a pure sine wave as it contains both active and reactive parts as shown in Fig. 5b. Figure 5c shows that the source voltage and current are out of phase after switching on the DVSI; here, we can conclude that the proposed topology has dual operation ability, i.e., active power injection and reactive power compensation. The inherent merits of the DVSI topology reduce the DC link voltage; Fig. 5d shows the DC link voltage of VSI and DVSI; it is found that during operation, the stable voltage of VSI is 640 V and DVSI is 540 V. It is observed from Fig. 6a, after compensation, the three-phase source current THDs are reduced to (average) 2.6%. The average P.F after compensation is 0.986 as shown in Fig. 6b. The proposed DVSI exhibits excellent dynamic performance, phase-1 source voltage, phase-1 source current, load current and compensating current waveforms as shown in Fig. 7a, b.

5 Conclusion

In this paper, the SLMS control algorithm is employed in several steps to compute the reference supply component, and this is further used to generate the firing pulses. The

experimental waveforms and measured parameters have verified the dual capability of the proposed system. The novelties of the DVSI-based DSTATCOM are explained point wise as follows:

- The concept of dual current pathway is utilized by the proposed configuration. Hence, the total load current is divided by VSI-1 and VSI-2. Therefore, the rating of the filter inductor is decreased.
- The power rating of inverter is utilized better as compared to conventional VSI, so the efficiency of the whole system is increased.
- Round the clock power supplies to the client of the distribution system are maintained even when power variation occurs in the distribution system.
- The DVSI topology provides better shunt compensation as compared to VSI-based DSTATCOM.

References

1. T. Meng, Z. Lin, Y. Wan, Y.A. Shamash, State-of-charge balancing for battery energy storage systems in DC microgrids by distributed adaptive power distribution. IEEE Contr. Syst. Lett. **6**, 512–517 (2022). https://doi.org/10.1109/LCSYS.2021.3082103
2. A.F. Zobaa, Optimal multiobjective design of hybrid active power filters considering a distorted environment. IEEE Trans. Industr. Electron. **61**(1), 107–114 (2014 Jan)
3. M.V. Kumar, Manoj, M.K. Mishra, C. Kumar, A grid-connected dual voltage source inverter with power quality improvement features. IEEE Trans. Sustain. Energy **6**(2) 482–490 (2015 Apr)
4. M. Mangaraj, J. Sabat, MVSI and AVSI-supported DSTATCOM for PQ analysis. IETE J. Res. (2021). https://doi.org/10.1080/03772063.2021.1920850
5. A.D. Kiadehi, K.E.K. Drissi, C. Pasquier, Voltage THD reduction for dual-inverter fed open-end load with isolated DC sources. IEEE Trans. Industr. Electron. **64**(3), 2102–2111 (2017 Mar)
6. K. Chen, M. Hsieh, Generalized minimum common-mode voltage PWM for two-level multiphase VSIs considering reference order. IEEE Trans. Power Electron. **32**(8), 6493–6509 (2017). https://doi.org/10.1109/TPEL.2016.2615111,Aug
7. S. Srinivas, J. Kalaiselvi, Pulse width modulation schemes enabling single DC power source driven dual two-level voltage source inverter with single voltage source inverter switching. IET Power Electron. **7**(5), 1181–1191 (2014 May)
8. A.K. Panda, M. Mangaraj, DSTATCOM employing hybrid neural network control technique for power quality improvement. IET Power Electron. **10**(4), 480–489 (2017 Mar)
9. M. Mangaraj, A.K. Panda, Modeling and simulation of KHLMS algorithm-based DSTATCOM. IET Power Electron. **12**(9), 2304 – 2311 (2019 Aug)
10. M. Mangaraj, A.K. Panda, NBP-based icosϕ control strategy for DSTATCOM. IET Power Electron. **10**(12), 1617 Sparse LMS algorithm for two-level DSTATCOM 1625 (2017 Oct)

11. J. Sabat, M. Mangaraj, GLMS control strategy based DSTATCOM for PQ enhancement: modeling and comparative analysis. Energy Syst. (2021). https://doi.org/10.1007/s12667-021-00489-x
12. M. Mangaraj, A.K. Panda, Sparse LMS algorithm for two-level DSTATCOM. IET Gener. Transm. Distrib. **15**, 86–96 (2021). https://doi.org/10.1049/gtd2.12014

Hardware Testing of the Effect of MPPT on the Performance of Photovoltaic Panels

Arjyadhara Pradhan, Soubhagya Ranjan Prusty, Lipika Nanda, Babita Panda, Chitralekha Jena, and Rudra Narayan Dash

Abstract Solar energy finds its application mainly in the form of thermal energy and electrical energy. Solar concentrator systems use thermal energy whereas electrical energy is obtained from solar photovoltaics. In comparison to the conventional method of using fossil fuels for electricity generation, photovoltaic is a clean and efficient way of generating electricity. Studies show that the conversion efficiency of PV modules decreases due to several factors like the presence of dust, insufficient irradiance and various other weather conditions. The system performs better only if the point of operation is always the maximum point under all environmental factors. MPPT trackers are used to track the knee point and help in load matching in order to ensure efficient utilization of the PV module. In this paper, MATLAB/Simulation of a PV system is done connected with a Boost converter and MPPT controller. The system is compared with Perturb and Observance Controller and the direct method found that efficiency increases by using maximum power point tracking. The efficiency of the PV system by using an MPPT controller is found to be 95% under standard operating conditions by using simulation and by testing with hardware, it was found to be 98% under maximum irradiance conditions.

Keywords Photovoltaics · Converter · Concentrator · Tracking · Performance

A. Pradhan (✉) · S. R. Prusty · L. Nanda · B. Panda · C. Jena · R. N. Dash
School of Electrical Engineering, KIIT Deemed to be University, Bhubaneswar, Odisha, India
e-mail: arjyadhara.pradhanfel@kiit.ac.in

S. R. Prusty
e-mail: soubhagya.prustyfel@kiit.ac.in

L. Nanda
e-mail: lnandafel@kiit.ac.in

B. Panda
e-mail: babitapfel@kiit.ac.in

C. Jena
e-mail: chitralekha.jenafel@kiit.ac.in

R. N. Dash
e-mail: dash.rudranarayan@gmail.com

1   Introduction

An intermediate power electronic device is used between the PV system and load for load matching, noise isolation and power bus regulation. To reduce the consumption of fossil fuels, switching to a non-conventional source of energy is required [1]. Coupling the PV panel with load directly, it is found that the operating point mismatches with the maximum point [2, 3]. Hence, the PV panel is not efficiently utilized. Mostly, directly coupled solar PV systems are used for agricultural processes where the modules are directly connected for running the pump [4]. In these cases, surge arresters are connected between positive and negative supply for protection against lightning surges [5, 6]. By using an MPPT controller along with a DC-DC converter, load matching can be carried out. Each time, the MPPT controller extracts maximum power from the module and the input given to the converter is also the maximum voltage rating of the PV module and maximum current rating [7–9]. Even while battery sizing, the controller ensures adequate DC power output from the PV system to sustain the connected load. The perturb and observance method is the most commonly used method for commercial application [10, 11]. It determines the system control commands considering the power output difference as per the present and past system state. When the system utilizes a fixed perturbation size the time taken to track MPP and remain in the steady condition is for a small period but at the same time, perturbation causes more loss of power. Thus to decrease the power loss, the perturbation size must be reduced which at the same time reduces the tracking speed. An intermediary considering both speed and accuracy is considered [12]. The efficiency of a PV system depends on several factors like cell fabrication, materials used, inverter efficiency and the maximum power point tracking method. By enhancing cell material technology, the efficiency does not exceed more than 15–20% [13–16]. Increasing inverter efficiency is also not easy due to complex technology and cost involvement. Hence, choosing an appropriate maximum power point tracking algorithm is economic and convenient. The P and O method is more effective under constant irradiance conditions [17–19]. But even in changes in weather conditions, the three-point weight method is considered. Now, a day modified and the adaptive p and o method are used to remove the constraints of the traditional method, and the problem of oscillation around the MPP point [20]. In this work, both simulation and hardware methods are used to see the effect of MPPT on the performance of the PV panel. In the hardware method, current and voltage act as input to the boost converter and the MPPT controller circuit. Thus, in Fig. 1, as shown below current and voltage sensor is used to sense current and voltage from the PV panel and give the signal to the converter. The same voltage and current signal are also fed to the micro-controller where the MPPT program runs and by the use of perturb and observance algorithm, the best duty cycle is fed to the converter switch. The converter output is connected with a resistive load and the maximum power is observed in the display LCD. Both the system with and without MPPT are tested by using a switch. From the various results, PV system performance is calculated in terms of efficiency.
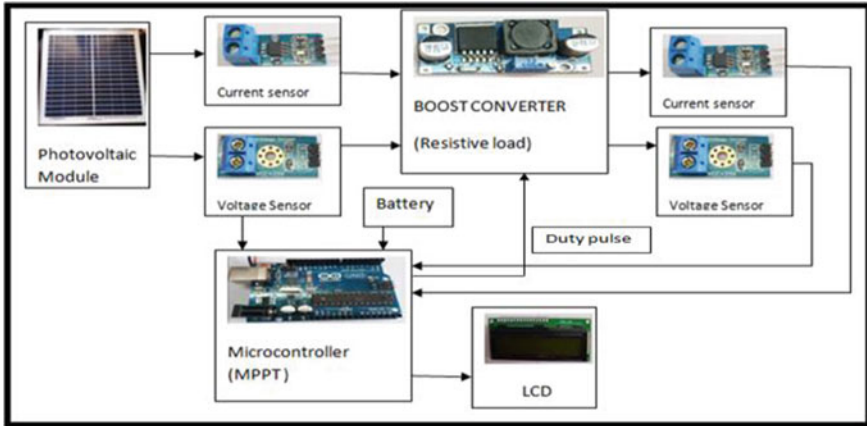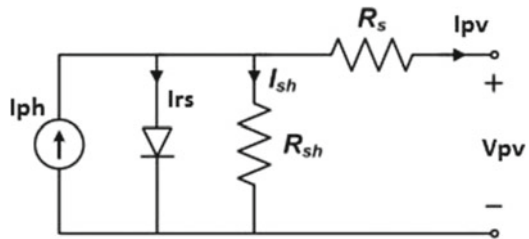
Fig. 1 Block diagram representation of hardware implementation of MPPT

Fig. 2 Solar cell with shunt
and series resistances

2 Photovoltaic System

A PV panel is made of a series and parallel arrangement of modules. Each module
consists of 32–36 solar cells which are mostly of crystalline type. When we draw
that point, the voltage and current of the cell at a particular condition is maximum.
Researchers have designed different types of PV cells. Considering the single diode
model, the diode is connected in the reverse direction and in parallel to the current
source. Practical solar cells consist of series and parallel connection of resistances.
The shunt branch resistance affects the output current (Fig. 2).

3 Load Matching

Load matching in a Photovoltaic system comes into the picture when PV is connected
with any type of load. Thus, we say that the operating point lies at the intersecting
point of the line of source and line of load. In the case of a directly coupled system,
the PV is not fully utilized. As per the power transfer theorem, maximum power
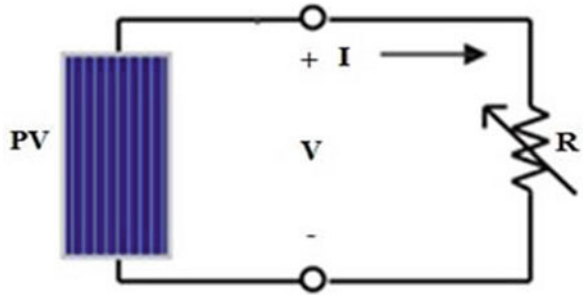
is transferred when the input impedance is equal to the output impedance. The PV module output can be efficiently utilized, and the performance can be improved by using tracking motors to track mechanically or using the electronic tracking system. MPPT uses a technique to track knee points for operating. With a change in resistance, the operating point moves from one point to another (Fig. 3).

4   Boost Converter

In this paper, we have considered a boost converter to get a higher output voltage in comparison to the input voltage. Below is shown the circuit of a simple step-up converter. The circuit consists of a single inductor, a capacitor in parallel with diode and a power switch to turn on the system. Generally, there are two modes of operation, i.e. ON state and OFF state. Here, N channel power MOSFET is used as a power switch (Fig. 4).

At mode 1 MOSFET is turned on, the current moves through the inductor with the circuit and at this stage, the storage of energy takes place. The parallel-connected capacitor supplies the load. At the second stage, i.e. Mode 2 begins the Turn off state. At this condition, the load receives energy from the inductor (Table 1).

Fig. 4 Boost converter
circuit with direction of
current flow
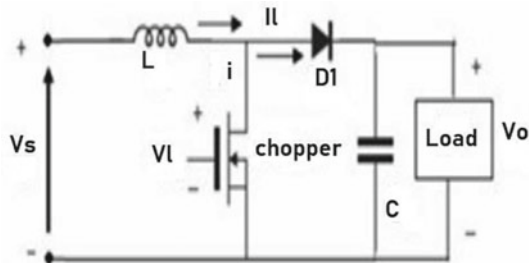
Table 1 Parameters calculated For Boost converter

Serial no.	Parameters	Value
1	Inductor value	7.5mH
2	Cin	250 microfarad
3	Cout	4400 microfarad
4	Load resistance	50 Ω

5 Maximum Power Point Tracking

MPPT controller operates the solar module to utilize the maximum power it is capable of generating. It is based on a tracking algorithm and a control system. Insolation and temperature are two inputs to the controller. As insolation varies, maximum point also varies. But the system can be said to be efficient if irrespective of any change in climatic condition, the module operates at the maximum power point. Studies show that there are various techniques used to track MPP. They differ in various aspects like sensor requirement, cost, effectiveness, convergence speed, hardware implementation, complexity, etc. In this paper, the Perturb and Observance method is considered. It is also called the Hill climbing method. During constant irradiance, this method is easy to implement and shows good performance. It has low computational power also. But one of the main drawbacks of this method is during rapidly changing weather conditions, oscillations occur around MPP and tracking is also done in the wrong direction.

In Fig. 5, the algorithm starts taking PV voltage and PV current into account. Then it calculates the power and change in power. On satisfying this condition, it checks whether current voltage is greater than the past voltage. If the condition holds true, the new voltage is raised, or else it is decremented. By generating the control voltage and using a comparator, duty pulse is generated. Incrementing the duty cycle is done

Fig. 5 Flowchart of P and O MPPT method
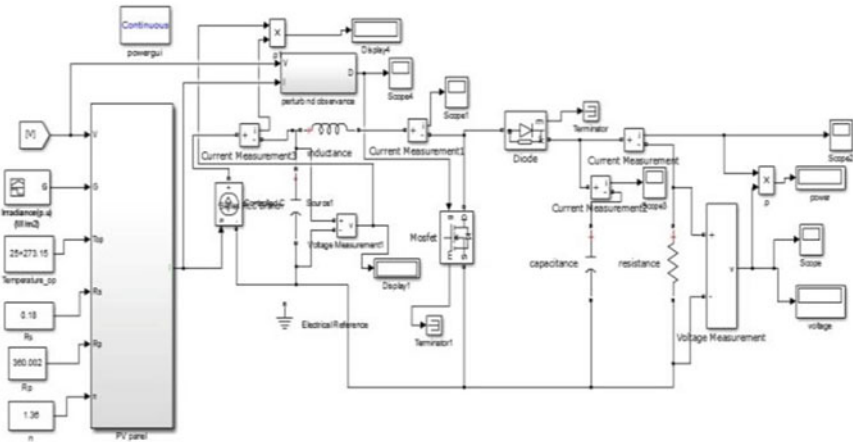
Fig. 6 The proposed system where the PV module is connected with DC-DC converter, and the duty cycle to the power switch is obtained by using the MPPT technique

by adjusting the voltage between the PV module and the converter. For finding the next perturbation sign of the last perturbation and the sign of the last increment of power are considered. On the left of MPP when the voltage is incremented, power increases whereas on the right power decreases.

6 Simulation

The proposed work is carried out in MATLAB/SIMULINK. A 60 W solar module is considered for the simulation. Taking into account the basic equations of solar cell, PV and IV curves are drawn. Then boost converter is simulated using the values of inductor, capacitor and load resistance. Firstly, the system is connected directly, i.e. without using MPPT. Then the PV module is connected with the converter by adjusting the duty pulses from the MPPT controller. In the simulation of the p and o algorithm, the limit of saturation is fixed to remove oscillation while tracking the MPP (Fig. 6).

7 Hardware Implementation

The effect of MPPT on the photovoltaic system is tested by using a hardware setup. The experiment is carried out on a real time basis at the terrace of the electrical department of Kalinga Institute of Industrial Technology, Bhubaneshwar. The setup was exposed to direct radiation of the sun from morning 10 am to 4 pm noon. Wires

Fig. 7 Hardware setup for the experiment
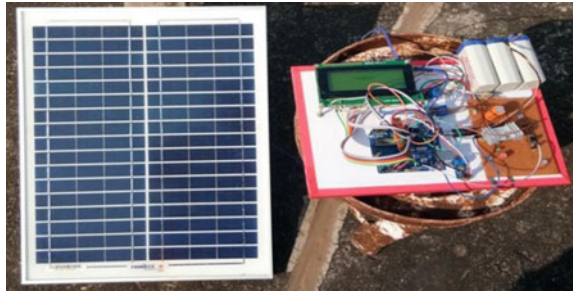
are used to connect the PV panel with the accessory system. A monocrystalline silicon panel is used for the testing.

Figure 7 shows the hardware setup for the experiment. It consists of one single monocrystalline 20 W solar module of make FRONTECH as a source for the system. A resistive load is considered for testing. The circuit consists of a step-up converter with a micro-controller unit where a simple P and O MPPT algorithm is used. A 16-bit LCD display unit is used along with two voltage and two current sensors. Three batteries each of rating 4 V are used to give supply to the display unit.

8 Results and Discussion

The simulation conducted for PV system with load and by the use of MPPT is shown here. We find the Current versus Voltage graph and PV graph for the simulation work carried out. IV graph is represented in Fig. 8. In this figure, the open-circuit voltage is taken as 21.2 V and the short-circuit current as 3.7 amp. The PV curve is represented in Fig. 9 with maximum power corresponding to 60 W.

Fig. 8 IV curve of solar module
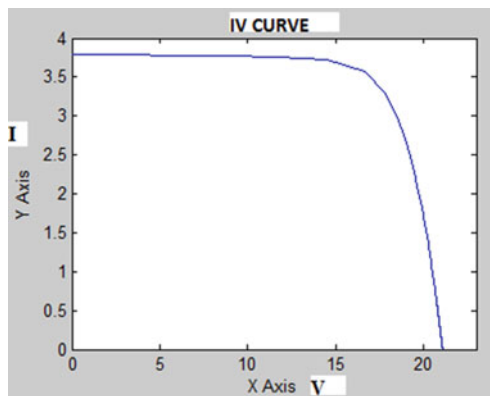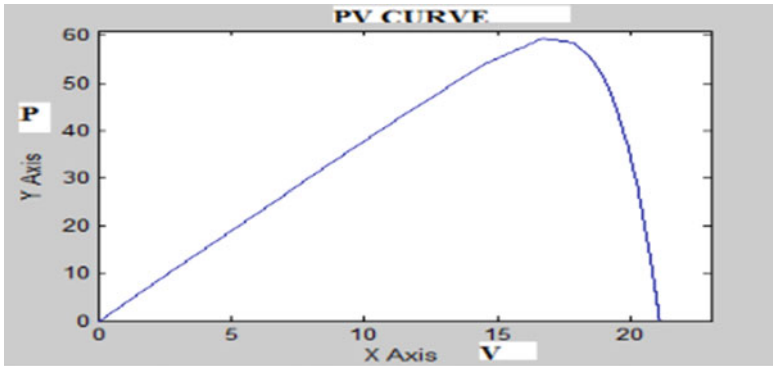
Fig. 9 PV curve of solar module

Fig. 10 Output voltages for system with and without MPPT
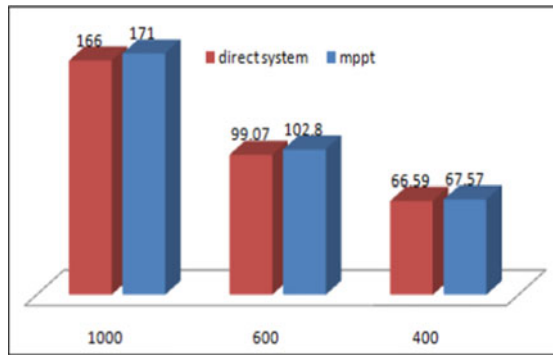
Figure 10 shows the values of output voltages for two systems, one directly connected without using MPPT and the other using MPPT for three different values of irradiance in watt/m^2. Figure 11 shows the value of the efficiency of the PV system both with and without MPPT for three different irradiances.

From Fig. 13, it is found that the maximum power is highest for the system with MPPT, i.e. 1.584 W at irradiance level 930 W/m^2 whereas the maximum power for the system without MPPT at the same irradiance is 1.395 W. The difference is marginal as the system considered is a small prototype but for a large array, the result will be better. From Fig. 12, efficiency is also more at high irradiance for the MPPT method, i.e. 97.9% than that without MPPT.
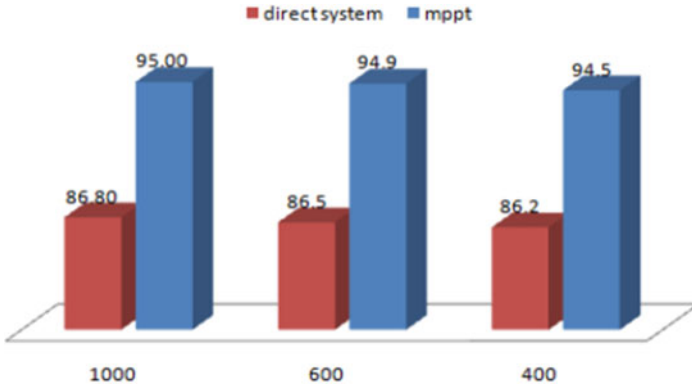
Fig. 11 Efficiency for PV system with and without MPPT at different irradiance level
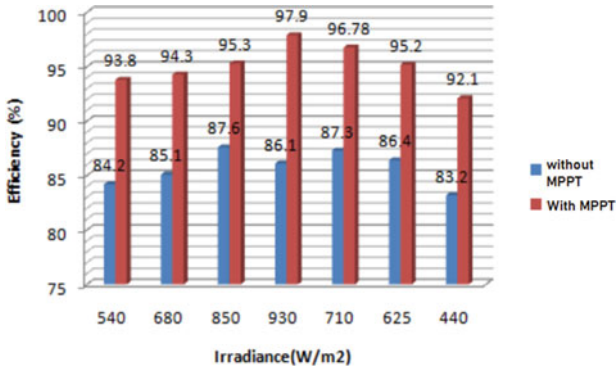
Fig. 12 Efficiency for PV system with and without MPPT
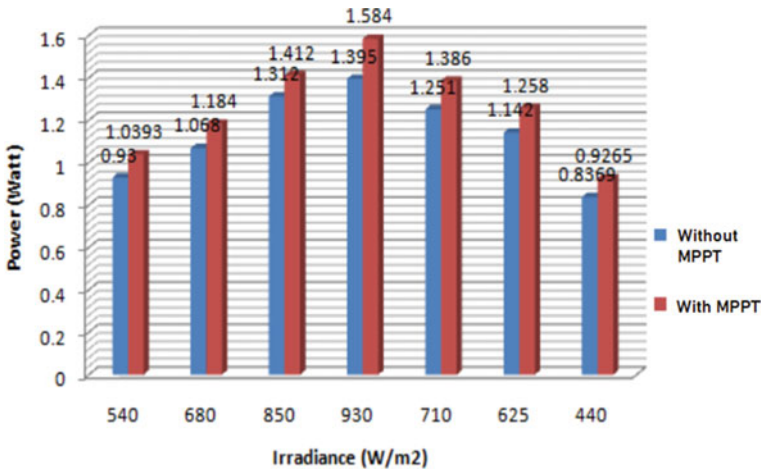
Fig. 13 Maximum power for PV system with and without MPPT

9   Conclusion

A PV system works more efficiently when it is operated at maximum power point under all weather and environmental conditions. For irradiance 1000 W/m^2, the output voltage of the converter is 166 V for a directly connected PV system without MPPT and 171 V for the system considering MPPT. It is also seen that in Fig. 10, the output voltage varies with the change in irradiance but it is always higher for the system with MPPT. Even the efficiency calculated for PV system with MPPT is found to be 9–10% more for various irradiance than that of the system without MPPT. At standard condition, the efficiency of the system by using MPPT controller is found to be 95%. Similarly, the hardware results show that both efficiency and maximum power are more with an MPPT controller than that without MPPT. A reduced PV system with 20 W is considered for ease of experimentation. Hence, it is suggested that for designing large PV systems, MPPT must be taken into account with any of the best suiting algorithms which can track the peak point very quickly.

References

1. O. Wasynezuk, Dynamic behavior of a class of photovoltaic power systems. Power Appar. Syst. IEEE Trans. PAS-102, 3031–3037 (1983)
2. G. Walker, Evaluating MPPT converter topologies using a MATLAB PV model. J. Electr. Electron. Eng. Aust. **21**, 49–56 (2001)
3. M.G. Villalva et al., Comprehensive approach to modeling and simulation of photovoltaic arrays. Power Electron. IEEE Trans. **24**, 1198–1208 (2009)
4. T. Huan-Liang, Insolation-oriented model of photovoltaic module using Matlab/Simulink. Sol. Energy **84**, 1318–1326 (2010)
5. M.H. Rashid, Power electronics - circuits, devices, and applications (3rd Edition Pearson Education: Academic Press, 2004)
6. S. Jain, V. Agarwal, A new algorithm for rapid tracking of approximate maximum power point in photovoltaic systems. IEEE Trans. Power Electron. **2**, 16–19 (2004)
7. P.E. Kakosimos, A.G. Kladas, Implementation of photovoltaic array MPPT through fixed step predictive control technique. Renew. Energy (2011)
8. A. Pandey, N. Dasgupta, A.K. Mukerjee, High-performance algorithms for drift avoidance and fast tracking in solar MPPT system. IEEE Trans. Energy Convers. **23**, 681–689 (2008)
9. V. Salas, E. Olı́as, A. Barrado, A. Lázaro, Review of the maximum power point tracking algorithms for stand-alone photovoltaic systems. Solar Energy Mater. Solar Cells **90**, 1555–1578 (2006)
10. D. Sera, R. Teodorescu, J. Hantschel, M. Knoll, Optimized maximum power point tracker for fast-changing environmental conditions. IEEE Trans. Ind. Electron. **55**, 2629–2637 (2008)
11. M. Sokolov, D. Shmilovitz, A modified MPPT scheme for accelerated convergence. IEEE Trans. Energy Convers. **23**, 1105–1107 (2008)
12. T. Esram, P.L. Chapman, Comparison of photovoltaic array maximum power point tracking techniques. Energy Conver. IEEE Trans. **22**, 439–449 (2007)
13. J. Zeng, W. Qiao, L, Qu, A single-switch isolated DC-DC converter for photovoltaic systems. Energy Convers. Congress Expo. (ECCE), 3446–3452 (2012)
14. K.V. Kryukov, M.M. Valiev, Residential photovoltaic power conditioning system with module integrated DC-DC converters, in *15th Power Electronics and Motion Control Conference (EPE/PEMC)* (2012), pp. DS3b.9-1–DS3b.9-4

15. V. Vekhande, B.G. Fernandes, Module integrated DC-DC converter for integration of photovoltaic source with DC micro-grid, in *38th Annual Conference on IEEE Industrial Electronics Society* (2012), pp. 5657–5662
16. D. Sera et al., Improved MPPT method for rapidly changing environmental conditions, in *Industrial Electronics, 2006 IEEE International Symposium on* (2006), pp. 1420–1425
17. A. Pradhan, B. Panda, Performance analysis of photovoltaic module at changing environmental condition using MATLAB/Simulink. Int. J. Appl. Eng. Res. **12**(13), 3677–3683 (2017). ISSN 0973–4562
18. A. Pradhan, B. Panda, A simplified design and modeling of boost converter for photovoltaic sytem. Int. J. Electr. Comput. Eng. **8**(1), 141–149 (2018). https://doi.org/10.11591/ijece.v8i1.pp141-149
19. A. Pradhan, B. Panda, Experimental analysis of factors affecting the power output of the PV module. Int. J. Electr. Comput. Eng. **7**(6), 3190–3197 (2017). https://doi.org/10.11591/ijece.v7i6.pp3190-3197. LNCS Homepage, http://www.springer.com/lncs, Last Accessed 2016 Nov 21
20. N. Mohan, T.M. Undeland, Power electronics: converters, applications, and design. Wiley-India (2007) J. Clerk Maxwell, A Treatise on Electricity and Magnetism, 3rd ed., vol. 2. (Clarendon, Oxford, 1892), pp. 68–73

Demand-Side Load Management Using Grey Wolf Optimization

Ashok Muthria and Lini Mathew

Abstract Demand-Side Management (DSM) is one of the methods that tries to understand customer behaviour and put it into a strategy that maintains network stability. Recently, a large number of load scheduling algorithms were developed by various experts, however these methods were not providing accurate results because of their high complexity and utilization of static datasets. To overcome these issues, an improved load scheduling method is proposed in this paper, in which loads are optimized by using the meta-heuristic Grey Wolf Optimization (GWO) algorithm. In addition to this, a real-time dataset is used that is collected from the Chandigarh Region. The information about the total demand felt and met initially is extracted from the available dataset. In addition to this, the minimum hour of electricity that must be provided to the six sectors (AP, PAT, RDS, MGJG, urban and industrial) is also defined. The loads are optimized by the proposed GWO model and later on its performance is evaluated in the MATLAB software. The performance outcomes were delineated by observing the total demand felt by the providers for the month of May, June and July and the total demand met by the proposed scheme. The results proved the efficiency of the proposed GWO model as it was able to provide electricity to every sector as per the demand.

Keywords Demand-side management (DSM) · Optimization algorithm · Renewable energy resources (RERs)

A. Muthria (✉) · L. Mathew
Department of Electrical Engineering, National Institute of Technical Teachers Training & Research, Chandigarh, India
e-mail: ashokmuthria1976@gmail.com

L. Mathew
e-mail: lini@nitttrchd.ac.in

1   Introduction

Energy efficiency, dependability, economic restrictions and integration of renewable energy resources (RERs) are considered as major factors when it comes to enhance the consistency in the power systems. The conventional grid that has served mankind for generations is now drained with the increase in population and energy consumption. The existing systems also become unstable because of the use of significant number of electric equipment's. The steep peak in the demand curve of a typical power system is created by aggregating heavy loads during peak time. As a result of this circumstance, power suppliers are forced to confide on costly Peaker facilities to meet peak demand. The Peaker power plants are basically thermal power plants that result in exorbitant greenhouse gas (GHG) emission [1]. Smart Grids (SGs) are now recognized as next major technology innovation in the power systems for both commercial and government organizations. The significance and need for SGs will rise with time and will be used for solving key concerns such as power constraint, carbon dioxide emissions, fossil fuel depletion and so on [2]. This will not only help power grids to conserve energy, reduce costs, increase sustainability and efficiency but will also benefit the user through Demand-Side Management (DSM) that is considered as one of the key elements in smart grids. However, the major challenge for both, i.e. utility centres and customers, is the continuously growing electricity demand that demands attention. According to the report given by National Institute for Transforming India (NITI) Ayog, India's home power demand is expected to climb 6–13 × by 2047 [3].

1.1   Demand-Side Management (DSM)

Demand-side management (DSM) means any activity that is performed by the utility centres at the users end in order to improve the profitability and efficiency. By managing and controlling the loads, both the user and the utility centres are getting benefitted [4]. The main purpose of DSM is to effectively manage loads so that the efficiency of the power grid is improved, cost and extra pressure are reduced and reliability and resilience are improved. This is accomplished by increasing system throughput without altering the structure of power system [5]. DSM programmes are commonly used in manufacturing and commercial sectors, while just a few DSM programmes are used by residential users [6]. According to studies, the power usage in industries and residential organizations will increase by around 20–40%. Therefore, it is necessary to effectively manage loads at residential side in order to offer sustainable and inexpensive power supply in the coming years without a significant increase in the number of new power plants [7].

In brief, we can say that strategies like DSM make sure that the electrical appliances follow the available generation patterns which will reduce the capital costs and increase the efficacy of the power system. As indicated in Fig. 1, DSM can be
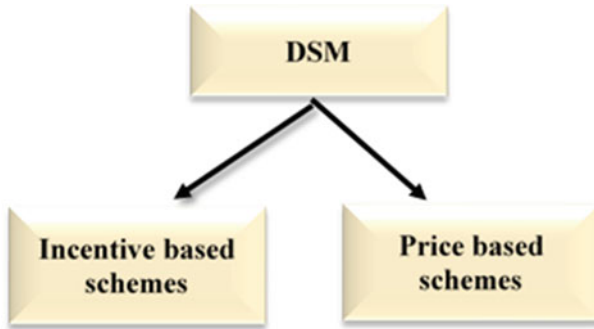
Fig. 1 DSM types

broadly classified into two types, one is incentive based and the other is price based. Incentive-based systems are the systems in which both parties, i.e. utilities and users, agree to provide full control of specific loads in exchange for some incentives. The biggest downside of this particular scheme is that users may complain over privacy issues because once the control is given in utility companies, the customers can no longer operate them according to their needs. While as in price-based systems, different rates will be offered to customers depending on the projected generation and load. Generally, the price of power will be higher in peak hours and lower at off hours of the day. In this type, the users can directly control the electrical equipment's on the basis of electricity price and their needs.

1.2 Architecture and Components of DSM Frameworks

Demand-Side Management (DSM) systems are developed in order to manage customer's loads as efficiently as possible via a specific architecture, which consists of several essential components, as shown in Fig. 2.

Local generators: Local generators are power plants such as photovoltaic (PV) plants, which produce electricity that can be consumed directly or pumped into the power grid.

Smart devices: These are the intelligent devices that can track themselves and provide statistics like power usage and can be managed remotely.

Sensors: Sensors are used to track wide range of data which include location of user in house, heat and illumination. Additionally, power meters were also utilized to track and regulate classic electrical equipment [8].

Energy storage systems: These are the data storing devices which enable DSM to manage electric loads more efficiently and effectively [9].

Energy Management Units (EMUs): EMU is responsible for transferring data to other components and regulates electric loads of user by using an intelligent DSM
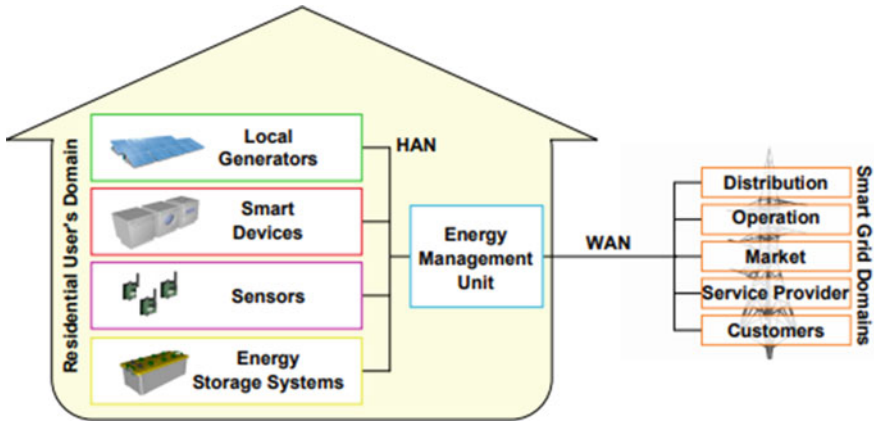
Fig. 2 DSM architecture

process. This technique must establish the device scheduling, the ESS operation plan and the supply-side profiles, among many other things.

Smart grid domains: It includes transmission, operational, marketplace, service provider and client in smart grids. A utilities corporation in the market realm provides electrical power to customers in exchange for payments based on energy prices. In the long run, a profit-neutral body known as an independent system operator (ISO) can be formed to act as a buffer among suppliers and clients. With the purpose of balancing supply and demand, the ISO purchases power from providers and sells it to customers. Customers are linked to a centralized server that controls their actions.

1.3 DSM Techniques

DSM adjusts the power usage to attain the ideal load profile at the utility side. DSM focuses on power management strategies, energy tariffs, incentives and eco-friendly government regulations to minimize load demand during peak hours. Due to the continuous rise in energy demand, the power system becomes unstable and unreliable. In order to overcome these instabilities, DSM can be used that changes the configuration of load curve by decreasing and moving entire demand load to the utility side sequentially at peak hours, which in return reduces the electricity costs. Peak clipping, load shifting, valley filling, load growth, strategic conservation and flexible load curve are six main approaches that can be used for changing the load designs which indicate the daily power requirements at domestic, commercial and industrial users during peak and off-peak hours. Figure 3 depicts the six demand-side management structures. Peak clipping and valley filling strategies aimed to balance peak and valley load levels in order to alleviate smart grid risk fears. A direct load control (DLC) technique is the peak clip approach. Moreover, load shifting curve is
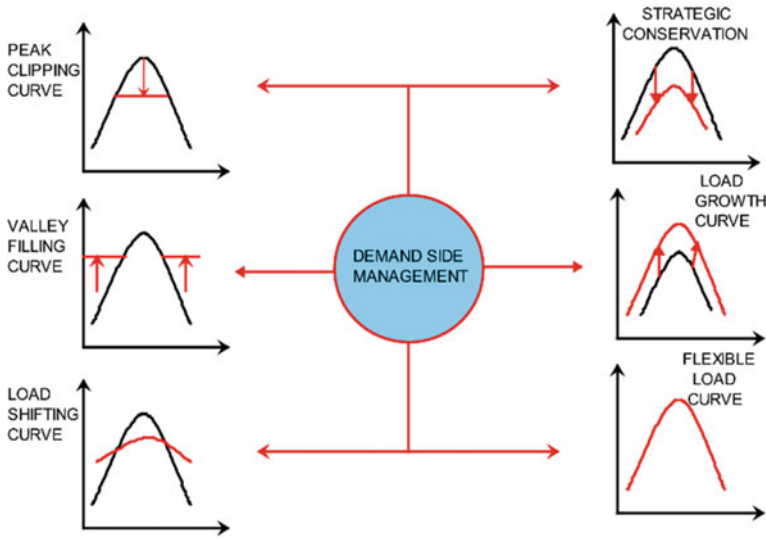
Fig. 3 DSM techniques

a load management approach in which loads are adjusted during peak and off-peak hours. On the other hand, strategic conservation seeks to employ demand curtailment measure directly at consumers' homes in order to attain load shape optimization. Strategic load expansion is similar to the valley fill strategy, except that it is used to optimize the day responses in cases of high demand. Furthermore, the reliability of smart grids is mostly linked to the flexible load curves. The main job of the smart grid management systems (SGMS) is to find users with flexibly managed loads at peak hours in exchange for different economic rewards [10].

To tackle the issues related to DSM, different strategies that are different linear and non-linear programming methods were utilized. However, the problem with these programming techniques is that they are unable to handle large number of controlled devices with a variety of computational patterns. When dealing with non-convex computing, mixed integer non-linear programming or non-deterministic polynomial time (NP-hard) issues, they may not be able to discover an ideal solution or the computing time is too long.

In such scenarios, heuristic-based evolutionary algorithms can give rapid and optimum solution. Heuristic algorithms like particle swarm optimization (PSO), ant colony optimization (ACO), genetic algorithm (GA) and so on have the ability to search a large area for an ideal solution in polynomial time. The following portion of this paper describes several DSM strategies that have been presented by specialists for improved optimization over the years.

2 Literature Survey

In order to optimize the performance of DSM techniques, several methods were proposed by researchers, some of them are explained here; Gaur et al. [11] studied the application of DSM in smart grids (SGs) and suggested a novel scheduling approach for managing loads that is based on genetic algorithm. The suggested algorithm proved out to be effective in minimizing PAR and electricity usage costs. Babu and Kumar [12] examined different sorts of DSM initiatives that help utility companies to minimize their energy demand. Also, the authors of this paper analysed various current power utility centres to demonstrate how they are working to forecast the load demands in future which resulted in reduced power cost. Hossain et al. [13] suggested a novel DSM approach for residential customers in which the main focus was to decrease the peak-to-average ratio (PAR), so that the efficacy can be enhanced and electricity usage cost can be minimized. Raju and Laxmi [14], the authors of this paper, developed a new and unique method for managing loads in SG's energy management unit (EMU). To do so, a number of DSM strategies which include peak clipping, load priority techniques by utilizing artificial neural network (ANN) were implemented so that conventional and non-conventional energy resources can be integrated. Babu et al. [15] analysed the behaviour of power system when neural network and different DSM techniques are implemented to industrial users. The results received showed that efficacy of the system is improved in terms of load factor. Also, the tariffs for electricity consumption were also minimized because of the decrease maximum demand (MD). Philipo et al. [16] suggested a fuzzy logic-based load balancing DSM strategy to account for consumers who have little impact on power systems during peak hours. This was done by utilizing the k-means clustering technique which selects the suitable candidates for DSM. In addition to this, a controlling strategy that is based on power usage and load priority is also implemented. Nasir et al. [17], the authors of this paper, reviewed different DSM optimization techniques and highlighted few DSM techniques like peak shaving and load shifting. Hammou Ou Ali et al. [18] considered the time-varying devices and power generated by solar panels as two important factors and proposed a branch-and-bound (B&B) method for DSM that is based on three postulates which enables quantification of time-varying devices as per their time and load attributes. Nawaz et al. [19] demonstrated the application of hybrid bacterial foraging and particle swarm optimization (HBF-PSO) approach to determine the DSM technique that can fulfill all the four objectives which include minimized cost, peak-to-average ratio (PAR), carbon emissions and customer's discomfort. A fresh DSM structure was also developed in this work in which four components, i.e. DISCO, multi-layer perceptron (MLP)-based forecast engine, AMI and DSM modules were built effectively. Ahmad and Abrar [20], the authors of this paper, utilized the optimization techniques to propose an optimal energy management algorithm in order to minimize the tariffs and rebound peaks while satisfying the needs of the user. For productive solutions, optimization algorithm was utilized and to decrease the computational complexity sub-optimal solutions were proposed. Uzoechi et al. [21] explained different concepts of DSM

along with the challenges faced by it and suggested how these techniques could be implemented to solve the power issues of Oda community which is basically a residential area of Benin Electricity Distribution company (BEDC). The suggested techniques not only proved out to be good for utility centres and customers, but it benefitted the entire country when implemented effectively. Mahin et al. [22] implemented the three techniques of DSM which are solar system, load limiting and planned load reduction on the domestic consumers of Dhaka, Bangladesh. The results obtained were compared with the classic approaches in terms of energy efficiency and load control. After analysing the results, it was proved that a large amount of electric power can be conserved by utilizing the solar system in residential homes.

From the literature survey conducted, it was observed that a large number of load scheduling algorithms were developed in the past few years in order to schedule loads effectively and efficiently. However, the performance of these methods was not up to the mark because of various underestimated reasons which lead to inefficiency, complexity and inaccurate results. One of the main reasons for low performance was that, in majority of cases, loads were scheduled manually by the experienced persons on the basis of their knowledge. Since the humans are prone to errors and mistakes, the scheduling decisions made by them were not accurate which lead to inefficiency and inaccuracy. Furthermore, traditional load management systems typically used static datasets which were available online which significantly reduced their usefulness, as such systems are not recommended in real-world scenarios. As a result, it is advised that the dataset gathered from the real world be used to improve the system's efficiency. Furthermore, it was discovered that optimization algorithms can produce efficient outcomes; however, the challenge is that there are number of optimization and it is difficult to choose one, to produce the greatest results. Another key flaw with today's load scheduling systems was that they were ineffective due to their poor convergence rate, large complexity and tendency to become caught in local minima. Inspired from these findings, an enhanced load scheduling method will be proposed in this paper to solve these issues.

3   Proposed Work

In order to mitigate the issues of traditional load scheduling methods, an improved version of load scheduling method is proposed, in which optimization is done through Grey wolf Optimization (GWO) algorithm. The main objective of the proposed work is to schedule loads automatically and efficiently without human intervention, which ultimately will increase the efficiency and effectiveness of the models. Also, it was analysed that the optimization methods can enhance the performance of scheduling algorithms but the techniques used by the authors also faced some issues like high complexity, slow convergence rate and gets usually stuck in the local minima, which is not the case in proposed GWO algorithm, as it has faster convergence rate when compared with other meta-heuristic algorithms and simple structure. Another main objective of using the GWO in the proposed work is that it doesn't get stuck in the local

minima and needs only few parameters to make the decisions. Furthermore, prior load scheduling systems were based on static data, which made them unsuitable for use in real-world circumstances. As a result, in the current effort, a real-time dataset gathered from the Chandigarh Region is used. By using the real-time dataset, the application of the proposed model can be demonstrated in the real-world scenario as well. The detailed description of the attained dataset is given below.

3.1 Dataset Utilized

In the proposed work, a real-time dataset has been utilized that is gathered from the Chandigarh Region and contains information about the total demand felt and demand met after a time slot of 15 min by six sectors, i.e. AP, PAT, RDS, MGJG, urban and industrial areas. With each time slot of 15 min, a total of 96 time slots are formed during the 24 h. The sample dataset is obtained for the month of May, June and July 2021 and is given in Table 1.

Because the statistics in the database pertains to total demand felt and total demand satisfied over the course of 3 months (May, June and July). As a result, in order for the data obtained to be more productive and relevant, we must determine the individual proportion of demand felt for every area throughout each month. This is done by dividing the dataset into two sections: UHBVN and DHBVN. The percentage of the demand felt by each sector in the month of May under the two given sections is

Table 1 Dataset sample of month May 2021

Time	Actual demand met	Demand felt
0:15	4172	4172
0:30	4115	4115
0:45	4041	4041
1:00	3984	3984
1:15	3938	3938
1:30	3908	3908
1:45	3903	3903
2:00	3880	3880
2:15	3877	3877
2:30	3896	3896
2:45	3971	3971
3:00	3983	3983
3:15	4058	4058
3:30	4137	4137
3:45	4204	4204
4:00	4269	4269

Table 2 Share of individual sections under UHBVN and DHBVN

Sector	Share May 21 under UHBVN (%age)	Share May 21 under DHBVN (%age)
AP	14.562	14.157
RDS	8.5920	7.6860
PAT	1.618	1.5730
MGJG	20.048	17.934
Urban	33.63	37.090
Industrial	21.55	21.560

represented in Table 2. The overall load demand felt by each sector, i.e. AP, RDS, PAT, MGJG, urban and industrial under UHBVN and DHBVN sections in the month of May 2021 is the sum of all sector contributions and is given in Table 2. In the same way, the percentage share of load is obtained for the month of June and July under UHBVN and DHBVN sections. In addition to this, we also extracted information about the minimum electricity running hours required by each sector. The minimum electricity hours needed in AP, PAT, RDS, MGJG, urban and industrial areas are 8 h, 16 h, 16.5 h, 16.5 h, 24 h, and 24 h, respectively. All this initial information is extracted from the Chandigarh Region to form a final information set. This information is then utilized in the proposed scheme to achieve the desired results. The detailed discussion about how the model works is given in the following section.

3.2 Methodology

A number of steps must be followed in the proposed GWO load scheduling model, so that desired results can be achieved. The detailed description about every step is given below:

Step 1: At the very beginning, data or information is collected from the datasets that are available online or obtained from the real world. A variety of databases are accessible online; however, we used a dataset obtained from the real life to improve the efficiency of the suggested system. The information available in the dataset was gathered from the Chandigarh area. As previously stated, the used dataset provides statistics on the overall load demand experienced by the six sectors as well as their minimum running hours.

Step 2: Once all the necessary information is extracted from the available dataset, the next step is to initialize the GWO parameters. The various attributes defined here are population size, total number of iterations, dimension, etc. In addition to this, the upper limit and lower limit are also defined which determine the minimum power cuts that need to be scheduled in each sector. Table 3 illustrates the defined GWO parameters and their respective values.

Step 3: The next phase of the proposed model is to calculate the fitness value that is evaluated by calculating the difference between the actual total demand felt and

Table 3 GWO initialization parameters

Parameters	Values
Population	10
Iterations	1000
Dimensions	2
Lower limit	[1,64]
Upper limit	[96,72]

total demand met by the proposed GWO model.

$$\text{Fitness} \ = \ \text{Total demand felt} \ - \ \text{Total demand met}$$

The fitness value should be as minimum as possible because the higher the fitness value, lesser is the efficiency of the system and vice versa. This process is repeated continuously for given number of iterations. For every iteration, the power slots are varied continuously for each sector and the best fitness value is stored.

Step 4: Once all of the rounds have been completed, the best fitness value is chosen from among all of the possible fitness values, and then loads are planned based on this fitness, with power being given to each sector according to their need and requirements.

Step 5: Finally, the performance of the proposed GWO model is analysed in the MATLAB software for a period of 3 months, i.e. May, June and July 2021.

4 Results and Discussions

In order to evaluate the efficacy of the proposed GWO load scheduling method, its performance is analysed in the MATLAB software. The performance outcomes were determined in terms of the total demand felt by the electricity providers and the total demand met by the proposed GWO model. The results are obtained for the 3 months, i.e. May, June and July and are described below.

4.1 Performance Evaluation

The effectiveness of the proposed GWO load scheduling algorithm is firstly analysed by comparing the total demand felt by the electricity providers and the total demand met by the suggested model in the month of May 2021. The graph obtained for the same is given in Fig. 4. The blue bars given in the graph reflect total demand felt by the electricity providers at a specific slot, whereas the orange bars depict demand satisfied by the suggested GWO system. After examining the graph, it is observed that the load requirement for the month of May 2021 is fulfilled effectively
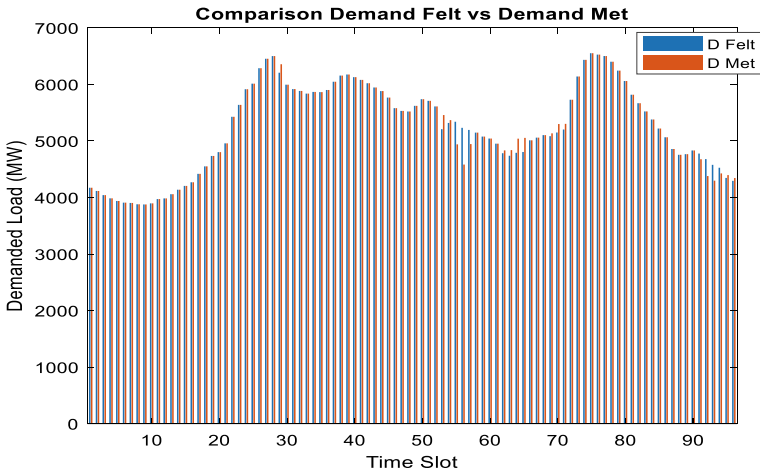
Fig. 4 Comparison graph for demand felt and met during May 2021

by the proposed GWO model. This showed that the suggested approach is effectively matching the current load demand, hence improving its performance.

Moreover, the performance of the proposed GWO model is analysed in terms of the fitness function reduced. The comparison graph obtained between the initial fitness and the optimized fitness for the month of May 2021 is shown in Fig. 5.

The above figure illustrates the comparison graph for the fitness value initially and when it was optimized by using the GWO algorithm. Upon closely examining the graph, it is apparent that the normal fitness value attained previously was 4199.051; however, the value of fitness achieved after optimizing was 4198.8951. This indicates
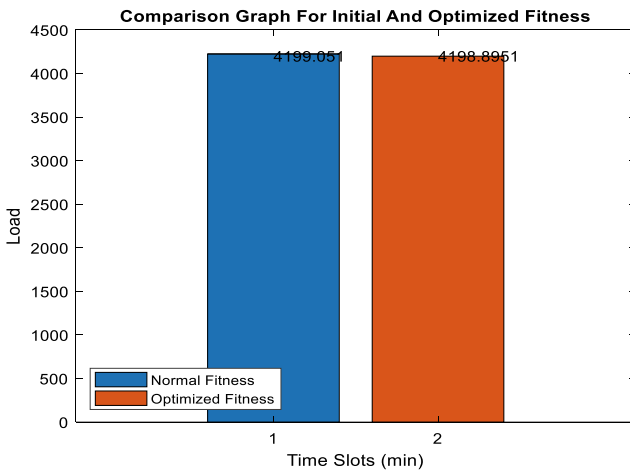
Fig. 5 Comparison graph for initial and optimized fitness for the month of May 2021

that the fitness value has decreased by 0.1559. On the basis of this data, a proper and optimized schedule is proposed for every sector, i.e. AP, PAT, RDS, MGJG, urban and industrial areas as per their required running hours for the month of May 2021. The graph obtained for each sector is given in Fig. 6.
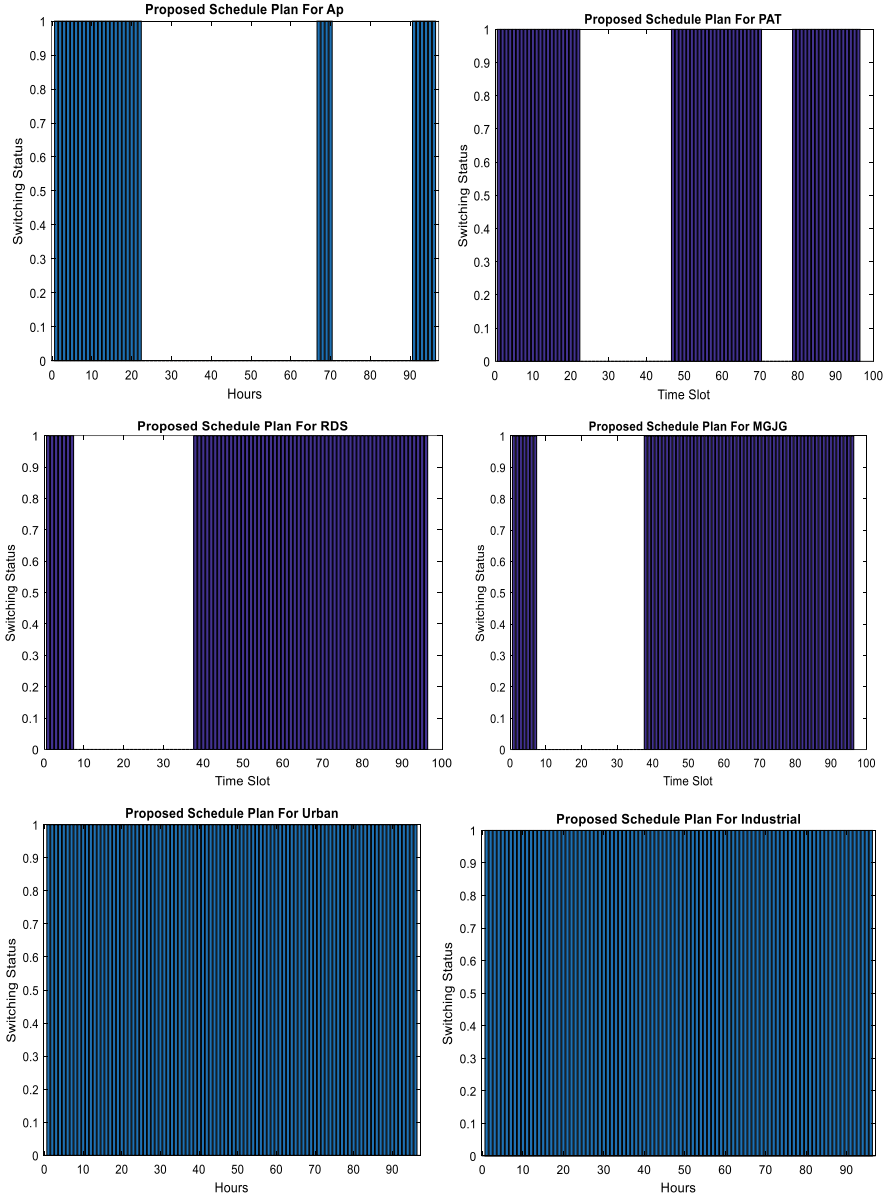
Fig. 6 Proposed schedule for six sectors the month of May 2021

Figure 6 illustrates the timetable for scheduling the electricity in every sector as per their needs and demands. The x-axis and the y-axis of the graph correspond to the hours and switching status, respectively. After thoroughly examining the graph, it is clear that every sector receives power for the lowest amount of time required. The coloured bars in the graph show the time intervals during which each area receives electricity, while the unfilled spaces represent power outages. In the same way, the load demand felt by the electricity providers and the demand met by the proposed
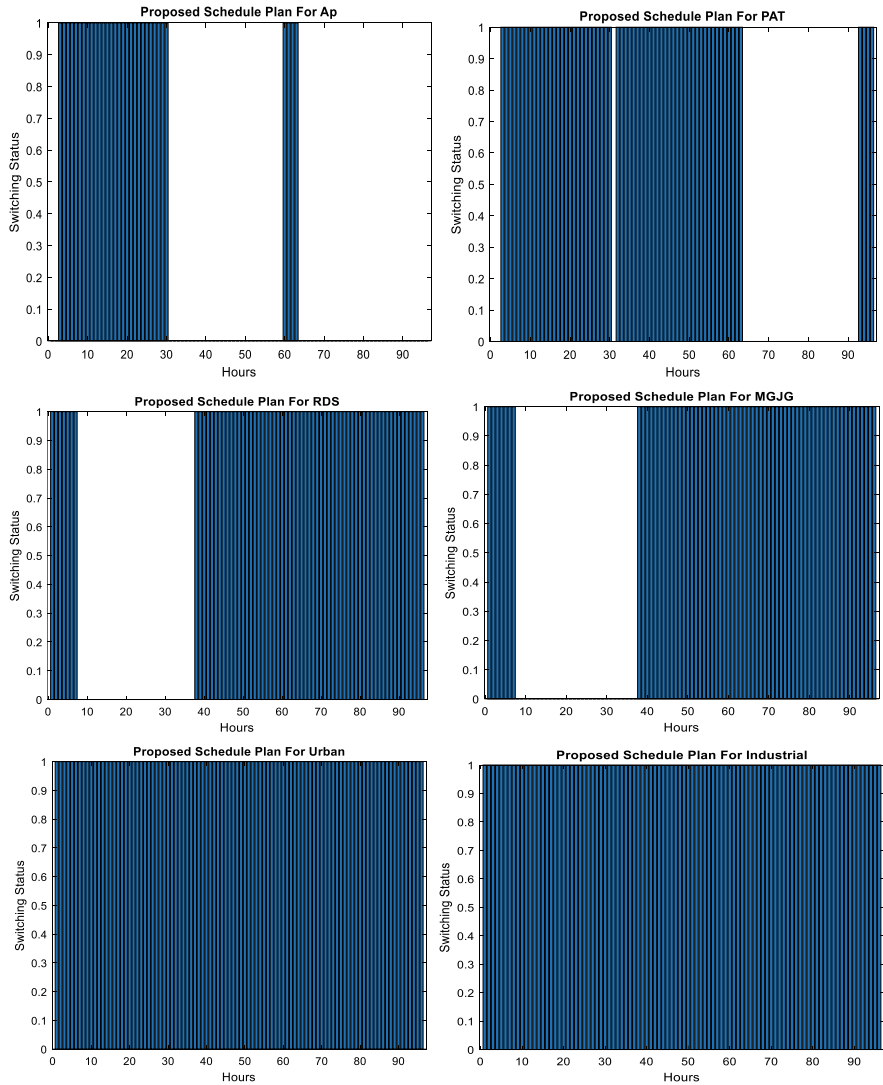
Fig. 7 Electricity scheduled for the month of June 2021
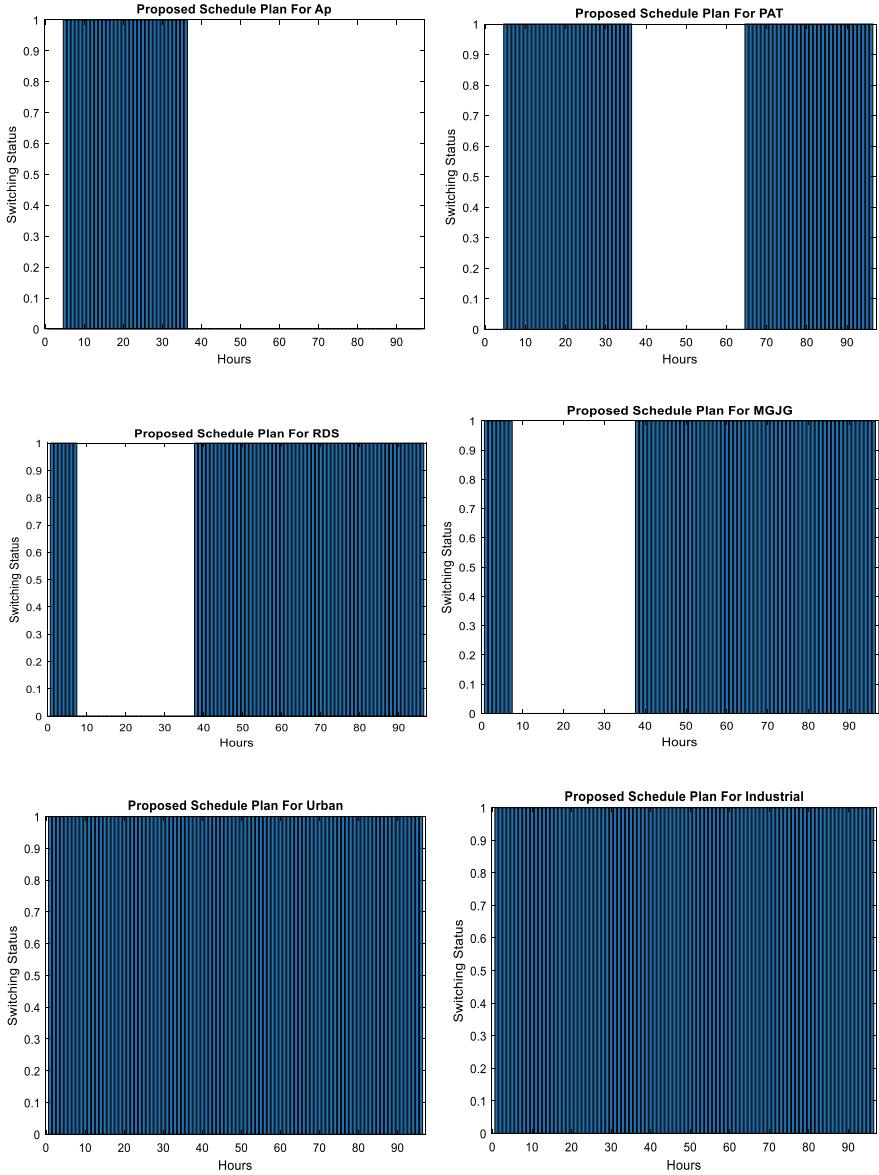
Fig. 8 Electricity scheduled for the month of July 2021

GWO approach in the month of June and July 2021 were also analysed and compared. The results came out to be satisfactory again for both months (June and July 2021) as the demand felt was effectively satisfied and met by the proposed GWO model. In addition to this, the value of fitness reduced after optimizing it by the GWO is also analysed. The value of fitness achieved initially was 3280.4072 for the month of June 2021 that was decreased to 3277.6306 when the loads are optimized by the GWO algorithm, which means that the fitness value is reduced by around 2.7766 in the month of June 2021. Moreover, the fitness is reduced up to 12.6569 in the month of July 2021, where initial fitness was 5658.0802 which later on was reduced to 5645.4233. This reduced fitness value represents that the demand felt by electricity providers and the total demand met by the model in the month of June and July 2021 is very less which in turn depicts the efficiency of the proposed GWO load scheduling approach. The electricity scheduled for the six sectors (Ap, PAT, RDS, MGJG, urban and industrial) for the month of June and July 2021 is represented in the graphical form and is shown in Figs. 7 and 8, respectively.

Figures 7 and 8 represent the electricity schedules for the month of June and July 2021, respectively. The x-axis and the y-axis of the given explicate the number of hours and switching status, respectively. From the graph, it is observed that all the six sectors are provided electricity as per its minimum requirement. The filled spaces represent the total number of hours in which electricity is provided and the blank spaces in the graph represent the electricity power cuts, respectively. These graphs are proof that the proposed GWO model is able to meet the demands and provides electricity to every sector of the area.

5 Conclusion

In this paper, an improved technique for optimizing the loads was proposed, in which the optimization is done using the Grey Wolf Optimization (GWO) algorithm. The efficacy of the proposed GWO-based load scheduling algorithm is analysed in the MATLAB software by examining the total load felt by the electricity providers and total load met by the proposed technique for the month of May, June and July 2021. After evaluating the data, it was discovered that the demand felt by the suppliers and the demand satisfied by the proposed GWO model over the course of 3 months were sufficient, because every sector, i.e. AP, PAT, RDS, MGJG, urban and industrial received power during their minimal operational hours. Furthermore, the fitness values of the load scheduling model were also analysed. The initial fitness value and the optimized fitness value attained in the month of May 2021 were 4199.051 and 4198.8951, respectively. Whereas, the fitness value achieved for the month of June and July 2021 came out to be 3280.4072 and 5658.0802 initially, which was later on reduced by the GWO algorithm and the final optimized values were 3277.6306 and 5645.4283, respectively. These findings support the efficacy and dependability of the proposed GWO method, which optimizes load scheduling based on demand while reducing complexity.

References

1. A. Mahmood, M.N. Ullah, S. Razzaq, A. Basit, U. Mustafa, M. Naeem, N. Javaid, A new scheme for demand side management in future smart grid networks. Procedia Comput. Sci. **32**, 477–484 (2014). ISSN 1877-0509

2. P.A. Pattanaik, N.C. Sahoo, S. Mishra, Implementation of demand side management using microcontroller and wireless communication, in *2017 Second International Conference on Electrical, Computer and Communication Technologies (ICECCT)* (2017), pp. 1–6. https://doi.org/10.1109/ICECCT.2017.8117935

3. S. Iqbal, M. Sarfraz, M. Tariq, R.K. Chakrabortty, M.J. Ryan, B. Alamri, A comprehensive review on residential demand side management strategies in smart grid environment. Sustainability **13**, 7170 (2021). https://doi.org/10.3390/su13137170

4. P.A. Pattanaik, N. Sahoo, S. Mishra, Demand side management in smart grid: a laboratory-based educational perspective. Int. J. Electr. Eng. Educ. **58**(2), 331–356 (2019)

5. H.O. Alwan, S. Abdelwahed, Demand side management- literature review and performance comparison, in *2019 11th International Conference on Computational Intelligence and Communication Networks (CICN)* (2019), pp. 93–102. https://doi.org/10.1109/CICN.2019.8902364

6. R. Mehta, P. Verma, D. Srinivasan, Smart load control strategy for residential demand side management, in *2018 IEEE Innovative Smart Grid Technologies - Asia (ISGT Asia)* (2018), pp. 1227–1232. https://doi.org/10.1109/ISGT-Asia.2018.8467947

7. S.H. CharanCherukuri, B. Saravanan, G. Arunkumar, An overview of residential demand side management strategies, in *2019 Innovations in Power and Advanced Computing Technologies (i-PACT)* (2019), pp. 1–6. https://doi.org/10.1109/i-PACT44901.2019.8960143

8. T.A. Nguyen, M. Aiello, Energy intelligent buildings based on user activity: a survey. Energy Build. **56**, 244–257 (2013)

9. S. Lanzisera, S. Dawson-Haggerty, H. Cheung, J. Taneja, D. Culler, R. Brown, Methods for detailed energy data collection of miscellaneous and electronic loads in a commercial office building. Build. Environ. **65**, 170–177 (2013)

10. A.K. Sharma, A. Saxena, A demand side management control strategy using Whale optimization algorithm. SN Appl. Sci. **1**, 870 (2019). https://doi.org/10.1007/s42452-019-0899-0

11. G. Gaur, N. Mehta, R. Khanna, S. Kaur, Demand side management in a smart grid environment, in *2017 IEEE International Conference on Smart Grid and Smart Cities (ICSGSC)* (2017), pp. 227–231. https://doi.org/10.1109/ICSGSC.2017.8038581

12. P.R. Babu, K.A. Kumar, Application of novel DSM techniques for industrial peak load management, in *2013 International Conference on Power, Energy and Control (ICPEC)* (2013), pp. 415–419. https://doi.org/10.1109/ICPEC.2013.6527692

13. M.M. Hossain, K.R. Zafreen, A. Rahman, M.A. Zamee, T. Aziz, An effective algorithm for demand side management in smart grid for residential load, in *2017 4th International Conference on Advances in Electrical Engineering (ICAEE)* (2017), pp. 336–340. https://doi.org/10.1109/ICAEE.2017.8255377

14. M.P. Raju, A.J. Laxmi, A novel load management algorithm for EMU by implementing demand side management techniques using ANN, in *2017 International Conference on Electrical and Computing Technologies and Applications (ICECTA)* (2017), pp. 1–6

15. P.R. Babu, V.P.S. Divya, P. Srikanth, B.D. Singh, K. Varun, Neural network and DSM techniques applied to a industrial consumer a case study, in *2007 Compatibility in Power Electronics* (2007), pp. 1–4. https://doi.org/10.1109/CPE.2007.4296503

16. G.H. Philipo, Y.A.C. Jande, T. Kivevele, Clustering and fuzzy logic-based demand-side management for solar microgrid operation: case study of Ngurudoto microgrid, Arusha, Tanzania. Adv. Fuzzy Syst. **2021**, 6614129 (2021)

17. T. Nasir, S.S.H. Bukhari, S. Raza, H.M. Munir, M. Abrar, H. Abd ul Muqeet, K.L. Bhatti, J.-S. Ro, R. Masroor, Recent challenges and methodologies in smart grid demand side management: state-of-the-art literature review. Math. Probl. Eng. **2021**, 5821301 (2021)

18. I. Hammou Ou Ali, M. Ouassaid, M. Maaroufi, Dynamic time- and load-based preference toward optimal appliance scheduling in a smart home. Math. Probl. Eng. (2021)
19. A. Nawaz, G. Hafeez, I. Khan, K.U. Jan, H. Li, S.A. Khan, Z. Wadud, An intelligent integrated approach for efficient demand side management with forecaster and advanced metering infrastructure frameworks in smart grid. IEEE Access **8**, 132551–132581 (2020)
20. J. Ahmad, M. Abrar, Demand side management based optimal energy management technique for smart grid. Iran J. Sci. Technol. Trans. Electr. Eng. **41**, 81–91 (2017)
21. L. Uzoechi, C.U. Eze, D.D. Agwu, A new proposed demand side management technique (2016)
22. A.U. Mahin, F. Ahmed, S.M. Ishraqul Huq, N.U.R. Chowdhury, Role of demand side management techniques in reducing electricity demand of residential users. EJECE, Eur. J. Electr. Comput. Eng. **3**(4) (2019)

Modeling and Tracking of Underground Cable Fault Using Genetic Algorithm

Sanhita Mishra, Subhadeep Roy, Sarat Chandra Swain, and Aurobinda Routray

Abstract In this paper, the genetic algorithm has been implemented to track the fault signals generated in an underground cable. In addition, GA has also been implemented for estimating the parameters such as amplitude, phase, and frequency of the fault signals. Several faults have been simulated to study the consistency of genetic algorithm for tracking the signals. The robustness of the algorithm has been validated by tracking a fault signal with additive white Gaussian noise. It reveals that GA performs better and can reliably estimate the fault signal in a noisy environment.

Keywords Underground cable · Genetic algorithm · Parameter estimation

1 Introduction

Underground cables (UG) are having multiple advantages compared to overhead transmission systems. For UG cable design and insulation studies, transient analysis is highly essential. Transients mostly occur for a very small period, slowly settle down to steady-state conditions. During this small period, the system may get subjected to a high amplitude of current and voltage, which may affect the cable insulation. Hence, transient studies in the underground cable are highly essential.

S. Mishra (✉) · S. C. Swain
KIIT Deemed to Be University, BBSR, India
e-mail: sanhita.mishra@gmail.com

S. C. Swain
e-mail: scs_132@rediffmai.com

S. Roy
IISC, Bangalore, India
e-mail: subhadeeproy2000@gmail.com

A. Routray
IIT, Kharagpur, India
e-mail: aroutray@ee.iitkgp.ac.in

The abrupt change in the current and voltage signal during transient condition creates changes in the amplitude, phase, and frequency of the signal. Hence, for transient detection, the signal modeling and parameter estimation are essential. A minor change in any of the parameters once detected, will be helpful for fault diagnosis and cable health monitoring of the system.

There are several algorithms already reported by many researchers for tracking the generic power system signals, but very few algorithms have been developed for tracking and estimating the parameters of the transient signal of a UG cable. A few of them are discussed below.

The parameters can be estimated by both parametric and non-parametric approaches. Non-parametric approach like FFT is mentioned in [1], and it has the major demerits of result approximation. As in the real-time signals, noise is present, hence parametric approaches perform better even in the noisy environment. Few parametric approaches are discussed below.

Chen et al. have implemented an extension [2] version Kalman filter for tracking the signals having harmonic components. Here, the harmonic amplitude and phase angles of the power signals are measured accurately. Apart, as frequency plays a vital role in the power system, hence authors in [3] implemented a novel EKF algorithm for estimating the frequency of a distorted signal. Furthermore, for frequency estimation, an improvised version of the Complex Kalman Filter (ECKF) is implemented in [4], which performs better while estimating the frequency. For tracking the signals in UG cable, the literature is very limited. A Kalman-based approach is implemented for the detection of an incipient fault in UG cable. A two-stage process has been proposed in [5] for detection and discrimination of incipient fault by putting forward the Kalman filter algorithm. Similarly, a Kalman filter algorithm-based [6] algorithm is proposed for the detection of the incipient fault. Nonetheless, an improvised wavelet transform named DTCWT [7] has been used for feature extraction and sparse representation-based classification (SRC) approach to identify power system transients like capacitor switching, inrush current, motor switching, and short circuit fault. Apart, a superimposed damped sinusoid (SDS) [8] model has been implemented for transient modeling as well as parameter estimation.

Hence, for proper monitoring of UG cable during transient conditions, accurate modeling and estimation of parameters are highly essential. In this work, an evolutionary optimization technique genetic algorithm has been implemented for tracking the fault signals in a UG cable. The estimated parameters will help in detecting the various faults like L-G, L-L, L-L-G, and L-L-L-G faults.

2 System Studied

The system as in Fig. 1 is simulated on PSCAD/EMTDC, which adopts a frequency-dependent model. The system implemented for simulation is a 95 mm^2 XLPE unbranched cable.
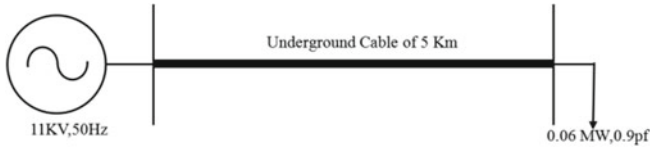
Fig. 1 System studied

3 Genetic Algorithm

Genetic algorithm [9, 10] (GA) is a method that can be used for solving nonlinear equations and complex optimizing problems. This algorithm is an evolutionary search method [9] and is adapted by the evolutionary strategy in nature, in which stranger and compatible people win in survival struggle and create next generation. According to this, genetic algorithm is not only strict mathematics, which is based on complex mathematical formulas for getting optimum; but the optimum point is evolved generation to generation using some operators. Figure 2 represents the flowchart of GA.

Implementation of GA for Optimizing Error

The following steps describe the implementation [11] of the GA algorithm for minimizing the error function. This is shown with the flowchart in Fig. 2.

Step 1: Initialize all the GA parameters and specify the lower and upper limits of each variable.

Fig. 2 Flowchart of genetic algorithm [12]
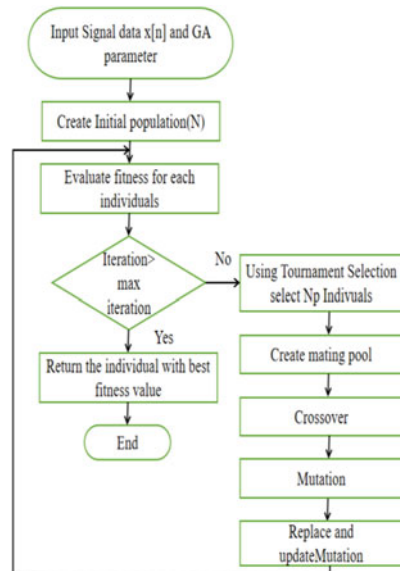
Step 2: Randomly initialize the initial population generation of Chromosomes.

Step 3: Evaluate the fitness value for each of the decoded strings using the error function. Store the information about the string with the highest fitness value.

Step 4: If stopping criteria are satisfied, go to Step 9; otherwise proceeds.

Step 5: From the selected parents' pool, we select pairs in order and apply a uniform crossover to obtain a new chromosome.

Step 6: Apply mutation on the mated chromosome strings with a small pre-assigned mutation probability.

Step 7: Replace the chromosome with the least fitness value with the offspring so that the size of the population remains the same.

Step 8: Return to step 3 to repeat the evaluation process with the updated population.
Step 9: The optimal solution is the individual with the best fitness value.

4 Results and Discussion

So genetic algorithm has been implemented to track several faulty signals simulated in the cable. PSCAD 4.5 has been implemented for the simulation. Proper mathematical modeling of the fault signal has been performed, and the error function has been calculated by comparing the estimated signal with the true signal. Equation (2) represents the error function to be calculated, where $y(n)$ and $z(n)$ represent the true signal and the estimated signals evaluated at nth sample respectively. N is the total number of samples in the signal. We have minimized the squared error function to evaluate the required parameters of the transient signal. The fault signal can be modeled as represented in Eq. (1).

$$y(n) = \sum_{p=1}^{T} A_p \cos\left(2\pi f_p n T_s + \varphi_p\right) + B_p e^{-\left(\beta_p n T_s\right)} + e(n) \tag{1}$$

The total number of sinusoids present in the model is represented by T and $A_p, \varphi_p, f_p, and \beta_p$ are amplitude, phase, frequency, and damping factor [13], respectively. p represents the corresponding harmonics number present in the signal. The second term (B_p) signifies the decaying DC of the signal, $\epsilon(n)$ represents the Gaussian noise added to the signal.

The RMSE percentage error can be calculated as

$$\text{RMSPE} = \sqrt{\frac{\sum_{i=1}^{N} \left(\frac{(y(n)-z(n))}{y(n)}\right)^2}{N}} * 100 \tag{2}$$

Computational Time: The average computational time (i.e. the cell time comprising the optimization part) taken by the CPU is noted for individual algorithms.

An underground cable might face a slow fault before being converted to a permanent fault. During the occurrence of an incipient fault, the magnitude of the current is comparatively low and persists for a shorter period. In the worst scenario, this may continue for multiple cycles. Further, the multi-cycle fault is prone to permanent fault. Hence, fault analysis in a UG cable is highly essential for cable health monitoring. Here, the CUSUM algorithm [14] has been implemented for the detection of the fault and GA has been implemented for signal tracking and parameter estimation.

Table 1 represents the estimated parameters of the various fault signals generated in the UG cable. The computational time for GA is near about 290 s for the faulted signal but for noisy signal, GA took near about 390 s to converge. Figures 3, 4, 5, and 6 represent the tracking of the faults generated in the UG cable.

Table 1 Estimated parameters for fault signals

Fault types	Amplitude (A_1) (kA)	Freq. (f) (Hz)	Phase (φ) (in rad)	Decaying D.C. (in kA) (A_2)	Damping factor in s^{-1}	Error
LL	7.369	50.0079	0.3379	−4.2264	1000	0.4273
LLG	6.1624	50.2514	3.4589	1.9680	90.2031	0.011
LLLG	7.3893	50.0166	0.8446	0.4333	171.854	0.7828
LG	3.0098	50.0000	0.4718	−0.7862	31.7974	1.352

Fig. 3 Tracking of L-G fault
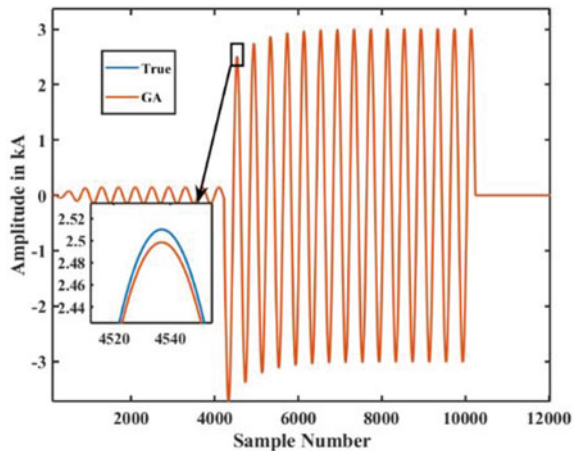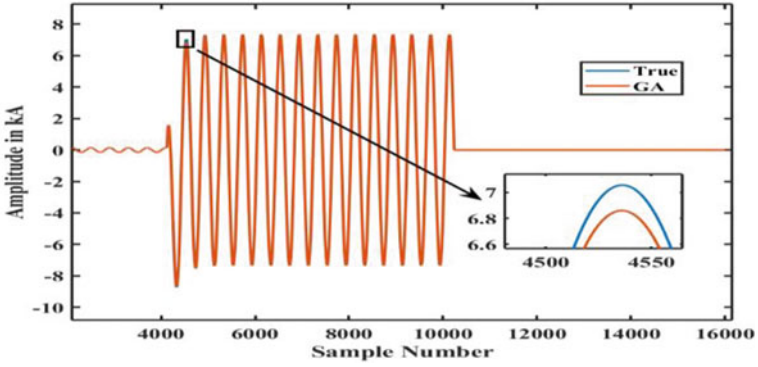
Fig. 4 Tracking of L-L fault

Fig. 5 Tracking of L-L-G
fault
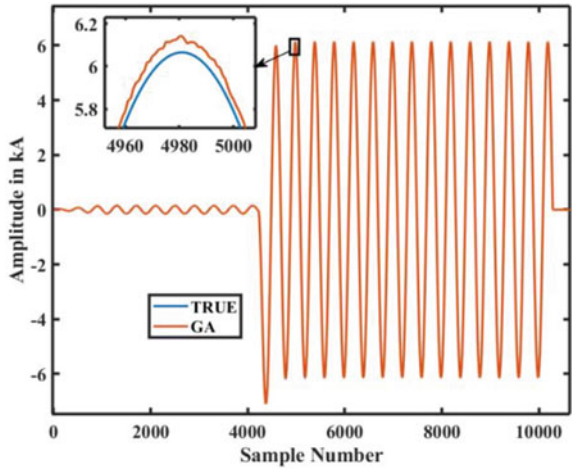
Fig. 6 Tracking of L-L-L-G
fault
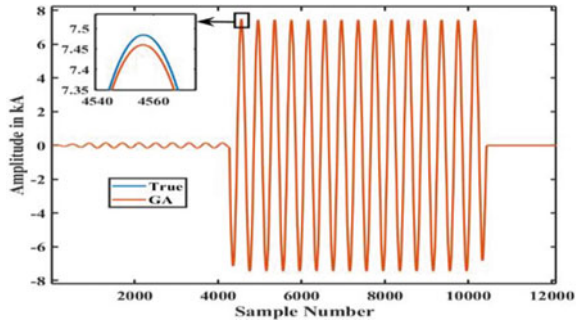
Fig. 7 LG fault with 30 dB noise
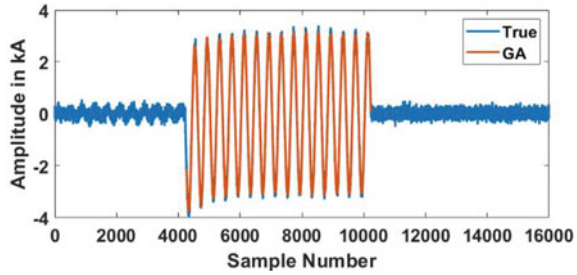
5 Analysis with Noisy Signal

To make the signal real-time noise is added to the LG fault signal and try to track the signal using genetic algorithm, we observe that if we add more noise, the genetic algorithm cannot track the signal. Then we should adopt some new hybrid optimization algorithm. But for 30 dB or more SNR, it can track well. Figure 7 represents the signal with Gaussian additive noise, it is clear that GA is able to track even in a noisy environment.

6 Conclusion

In this article, evolutionary optimization techniques such as the genetic algorithm are used to analyze underground cable defects. GA is one of the most effective methods for determining the root cause of challenging issues such as UG cable failures. GA runs effectively while tracking the fault signal and provides accurate and consistent findings under a set of simulated data. Furthermore, the GA approach takes less computer time, and this algorithm performs better in the noisy environment.

References

1. A.A. Girgis, F. Ham, A qualitative study of pitfalls in FFT. IEEE Trans. Aerosp. Electron. Syst. **16**(4), 434–439 (1980)
2. C.I. Chen et al., Extended real model of Kalman filter for time-varying harmonics estimation. IEEE Trans. Power Deliv. **25**(1), 17–26 (2010)
3. A. Routray, A.K. Pradhan, K.P. Rao, A novel Kalman filter for frequency estimation of distorted signals in power systems. IEEE Trans. Instrum. Meas. **51**(3), 469–479 (2002)
4. C.-H. Huang et al., Frequency estimation of distorted power system signals using a robust algorithm. IEEE Trans. Power Deliv. **23**(1), 41–51 (2008)
5. H. Samet et al., A statistical-based criterion for incipient fault detection in underground power cables established on voltage waveform characteristics. Electr. Power Syst. Res. **197**, 107303 (2021)

6. T. Ghanbari, Kalman filter based incipient fault detection method for underground cables. IET Gener. Transm. Distrib. **9**(14), 1988–1997 (2015)
7. S. Chakraborty, A. Chatterjee, S.K. Goswami, A sparse representation based approach for recognition of power system transients. Eng. Appl. Artif. Intell. **30**, 137–144 (2014). https://doi.org/10.1016/j.engappai.2014.01.009
8. M. Nait-Meziane, P. Ravier, K. Abed-Meraim, Electrical transient modelling for appliance characterization. EURASIP J. Adv. Signal Process. **55** (2019)
9. D.E. Goldberg, *Genetic Algorithms in Search, Optimization, and Machine Learning* (Addison Wesley, Boston, MA, 1989)
10. K.M. EL-Naggar, A genetic based fault location algorithm for transmission lines, in *16th International Conference and Exhibition on Electricity Distribution*, Amsterdam, Netherlands, 2001
11. A. Sanad Ahmed, M.A. Attia, N.M. Hamed, A.Y. Abdelaziz, Modern optimization algorithms for fault location estimation in power systems. Eng. Sci. Technol. Int. J. **20**(5), 1475–1485 (2017)
12. A. Niazi, R. Leardi, Genetic algorithms in chemometrics: genetic algorithms in chemometrics. J. Chemom. **26**(6), 345–351 (2012)
13. M. Pramanik, A. Routray, P. Mitra, Accurate real-time estimation of power system transients using constrained symmetric strong tracking square-root cubature Kalman filter. IEEE Access **7**, 165692–165709 (2019)
14. S.R. Mohanty, A.K. Pradhan, A. Routray, A cumulative sum-based fault detector for power system relaying application. IEEE Trans. Power Deliv. **23**(1), 79–86 (2008)

Obstacle Avoidance for a Swarm of AUVs

Sarada Prasanna Sahoo , **Bikramaditya Das** , **Bibhuti Bhusan Pati** , and **Rudra Narayan Dash**

Abstract This paper uses the bioinformatics-inspired technique for guiding a team of autonomous underwater vehicles (AUVs) towards the desired destination. Here, each AUV estimates the position of the neighbour AUVs while moving towards the destination. The proposed multi-AUV system constitutes a leader AUV and three follower AUVs. A distributed path consensus (DPC) is proposed that determines the distance constraint to ensure the neighbouring agent AUVs maintain a predefined distance between each other and are able to avoid static obstacles while moving towards the respective destinations. It is observed from MATLAB simulation that the co-operative motion control of multiple AUVs along the desired paths and obstacle avoidance is successively achieved. The proposed method solves coordination problems among multiple AUVs and increases the coverage of underwater missions like oceanographic surveys.

Keywords AUV · DPC · MAS · Path planning · Obstacle avoidance

1 Introduction

The underwater world is vast, and to cover a finite area requires the involvement of multiple AUVs as a team [1, 2]. The path planning of multiple AUVs using MAS is inspired by the team behaviour of humans working towards achieving a common

S. P. Sahoo · B. B. Pati
Department of Electrical Engineering, VSS University of Technology, Burla, Odisha, India

B. Das (✉)
Department of Electronics & Telecommunication Engineering, VSS University of Technology, Burla, Odisha, India
e-mail: adibik09@gmail.com

R. N. Dash
School of Electrical Engineering, KIIT DU, Bhubaneswar, Odisha, India
e-mail: dash.rudranarayan@gmail.com

goal within a defined time span. The MAS maintains relative positions and orientations deployed as a team while approaching the destination. The dynamic underwater environment and unavailability of GPS signals make path planning control tasks quite challenging. Thus, designing fewer complex controllers for path planning control is recently gaining research interest. The leader AUV decides the direction of advancement of the formation, while follower AUVs maintain the required angle of orientation and position with respect to the path of the leader.

Different consensus algorithms used for the networked multi-agent system (MAS) have been discussed. The MAS can be considered as a solution to the coordination problem for multi-AUV formation [3]. Hu et al. proposed an energy-efficient information exchange triggered by impulse signals between AUVs in a multi-AUV formation topology.

The efficient path planning of MAS is to determine the path of each agent between user-defined start and goal points. An efficient path planning method using Flow Annotation Replanning (FAR) on grid map is proposed which is still incomplete in terms of scalability and memory-efficiency. The decentralized multi-agent Rapidly exploring Random Tree (DMA-RRT) algorithm has been proposed to obtain a minimum cost path for MAS. Yu et al. solved the MAPP problem by reducing it to a network flow problem [4–7].

This research is concerned with path planning of coordinated multiple AUVs using switching topology based on the concept of bio-inspired MAS. The bio-inspired MAS is used to handle the position of the various AUVs in the underwater environment relative to each other, by considering their position [3, 8–11]. Here, each agent is represented by an AUV connected by a communication graph network. The proposed multi-AUV system constitutes of a leader AUV and three follower AUVs. All the AUVs are assumed to be identical [12–16]. The position estimation method is proposed for estimating the position of neighbour AUV and planning a path from starting point to the desired destination. The distributed path consensus (DPC) is proposed for path optimization by implementing a distance constraint that ensures a predefined distance between the neighbouring AUVs while moving towards the respective destinations. Due to the distance constraint, AUVs stay at a safe distance from each other while maintaining communication among the agents. Path optimization is performed for each AUV separately to find a minimum cost route between the desired start and destination points.

This research contribution as follows:

- Avoids inter-vehicle collision as well as obstacles while prevailing communication and provides an optimized path using the DPC algorithm.

2 Problem Formulation

This research is intended to solve a path planning problem [31] using bio-inspired MAS where each agent reaches their desired destinations using the position estimation technique. The MAS represent a system of identical AUVs deployed for the
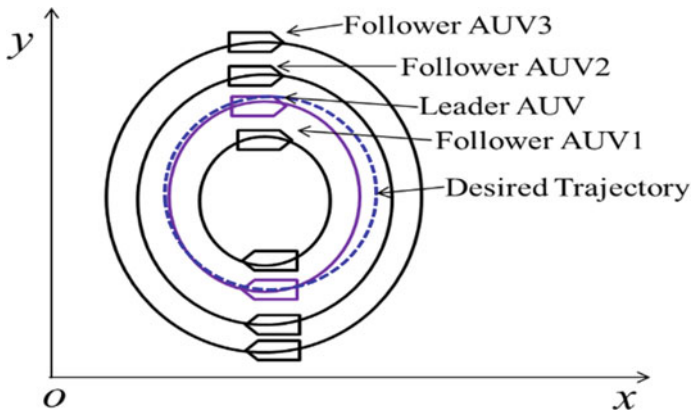
Fig. 1 Schematic presentation of flocking of four AUVs in 2D

mission. The AUVs travel from a different starting point to different predefined destinations while maintaining a coordinated shape. The DPC algorithm is proposed to implement a distance constraint that maintains a safe distance among neighbouring AUVs and helps in avoiding collision among them. The path cost is optimized by using distance constraint for each position of AUV along the path. Once the desired coordinated shape is obtained, the same is maintained by the agent AUVs while approaching their destinations as shown in Fig. 1.

The DPC algorithm is applied to the path of each agent separately to obtain an optimum position to maintain the coordinated shape. At the optimized position, the agent AUVs are at a safe distance from the neighbour AUVs without loss of communication among them. It intends to find K paths for K agent AUVs with optimized path cost defined as $\hat{P}_k$ for $(1 < k < K)$ through the defined directed graph $\mathcal{G}_k$ such that

$$\left\{ \hat{P}_1, \ldots, \hat{P}_K \right\} = \underset{\hat{P}_1, \ldots, \hat{P}_K}{\text{argmin}} \sum_{k=1 \ldots K} c_{\mathcal{E}} \left(\hat{P}_k \right) \qquad (1)$$

Equation (1) is subjected to the distance constraint given by

$$d \left(\hat{P}_k(t), \hat{P}_l(t) \right) \leq \pi_{kl}(t) \forall (1 \leq t \leq \tau), (1 \leq k \leq K), 1 \leq l \leq K, k \neq 1 \qquad (2)$$

The environment is modelled as a 2D grid map assuming that all the AUVs are at the same depth. The environment is free of obstacles. Thus, AUVs have to avoid collisions among them only.

3   Proposed Technique

A directed graph $\mathcal{G}_k = (N, \mathcal{E}, A)$, while $k = \{1, 2, \ldots, K\}$ with N set of nodes and $\mathcal{E} \subseteq (N \times N)$ set of edges can be used to represent an interaction topology of K agent AUVs connected through a communication network [17, 18]. Here, A represents a vector of non-negative values such that $A = [a_{kl}] \in R^{|\mathcal{E}| \times |\mathcal{E}|}$ and $|\mathcal{E}|$ is the cardinality of $\mathcal{E}$. The positive a_{kl} suggest that kth and lth AUVs are immediate neighbours with a communication edge, otherwise $a_{kl} = 0$. The degree of the kth node is given by $d_k = \sum_{l \in K_k} a_{kl}$. The Δ is the degree matrix of $\mathcal{G}_k$, which is a $(K \times K)$ diagonal matrix of d_k. The positive semi-definite Laplacian matrix of $\mathcal{G}_k$ is defined by

$$L = \Delta - A = \left[\updownarrow_{kl}\right], \text{ where} \updownarrow_{kl} \text{ is}$$

$$\updownarrow_{kl} = \begin{cases} \sum_{l \in K_k} a_{kl} \forall k = 1 \\ -a_{kl} \forall k \neq 1 \end{cases} \tag{3}$$

The $\mathcal{G}_k$ is formed by 'i' subspaces where $1 < i < K$. Target driven path planning of any kth agent AUV_k in a MAS can be described as finding a path with minimum path cost through $\mathcal{G}_k$. A time index can be added as an additional variable to $\mathcal{G}_k$ such that $\mathcal{G}_{tk} = \mathcal{G}_k \times \{0, 1, 2, \ldots \tau\}$ to obtain a time paramertized path [25]. Each node represents a state $\{s, t\}$ given by position coordinates of an agent AUV $\{x, y\}$ such that $s \in N(\mathcal{G}_{tk})$ at a time instant t. An agent AUV can only move from one state s to a next free state $\hat{s}$ along the edge represented by $\{s, t\} \rightarrow \{\hat{s}, t + 1\} \in \mathcal{E}(\mathcal{G}_{tk})$, such that $\hat{s} \in \mathcal{E}(\mathcal{G}_k)$ or $s \rightarrow \hat{s} \in \mathcal{E}(\mathcal{G}_k)$. This condition guarantees only the forward movement of AUVs with time. Each edge is associated with a positive cost factor $c_{\mathcal{E}}(s, \hat{s})$. The cost is represented by the Euclidean distances between the neighbouring cell centres. Each path from start to destination point is assumed to be accomplished in τ-time-steps. Thus, the path of kth AUV (AUV_k) can be given as $P_k = \{start_k, s_1, \ldots \ldots, target_k\}$. The path cost of path P_k can be defined as

$$c_{\mathcal{E}}(P_k) = \sum_{i=1\ldots\tau} c_{\mathcal{E}}(s_{i-1}, s_i) \tag{4}$$

The AUV system dynamics can be approximated as a second-order linear system as follows:

$$\begin{cases} \dot{\eta}_k = V_k \\ \dot{V}_k = \tau_k \end{cases} \tag{5}$$

where $V_k \in R^k$, $\eta_k \in R^k$, and $\tau_k \in R^k$. In real-world problems, it is difficult to find exact position η_k of the kth agent AUV. So the following assumptions are made as per [34]:

i. Each kth agent AUV estimates the relative position of the neighbouring lth AUV as it is unable to get the exact position. Thus, the relative position of lth AUV to kth AUV can be calculated as

$$\eta_{lk} = \eta_l - \eta_k \forall \forall (1 \le k \le K), 1 \le l \le K, k \ne l \tag{6}$$

ii. Each AUV is able to measure its own actual velocity and can also obtain its neighbour velocity information through a communication network.

Lemma 1 For any number $\sigma = {\gamma\mu - \beta \pm \sqrt{(\gamma h - \beta)^2 + 4\mu}}\Big/_2$, where $\sigma, \mu \in \mathbb{C}$.

If $\beta \ge 0$, $\mathrm{Re}(\mu) < 0$, $\mathrm{Im}(\mu) > 0$ and $\zeta(\mu) = \sqrt{2 \Big/ |\mu| \cos\left[\tan^{-1} \frac{\mathrm{Im}(\mu)}{-\mathrm{Re}(\mu)} \right]}$

then $\mathrm{Re}(\sigma) < 0$. Here, $\mathrm{Re}(.)$ and $\mathrm{Im}(.)$ are the real and imaginary parts of a number, respectively. For such condition

$$\gamma > \zeta(\mu) \tag{7}$$

Lemma 2 For the system given by Eq. (5), we can use a control law τ_{kl} as given in [34], such that

$$\tau_k = \sum_{l=1}^{K} a_{kl}(t)\left[(\eta_k - \eta_l) + \gamma(V_k - V_l) \right] \tag{8}$$

The MAS of AUVs obtains consensus asymptotically if and only if $\partial = \begin{bmatrix} 0_{K \times K} & I_K \\ -L_K(t) & \gamma L_K(t) \end{bmatrix}$ has two eigenvalues equal to '0' and rest with negative real parts. Here, $\eta_k(t) \to \sum_{k=1}^{K} \eta_k \eta_k(0) + \sum_{k=1}^{K} \eta_k V_k(0)$ and $V_k(t) \to \sum_{k=1}^{K} \eta_k V_k(0)$ for larger value of t, where $\eta = [\eta_1, \ldots, \eta_k]^T \ge 0$, $I_K^T \eta = 1$, $L_K^T \eta = 0$.

4 Results Analysis

The proposed path planner for a swarm of AUVs has been tested by simulation using MATLAB. This simulation shows a leader AUV and three follower AUVs. The follower AUVs are represented as AUV1, AUV2, and AUV3.

From Fig. 2, it is observed that there is no collision among AUVs as well as with obstacles arising during path planning.
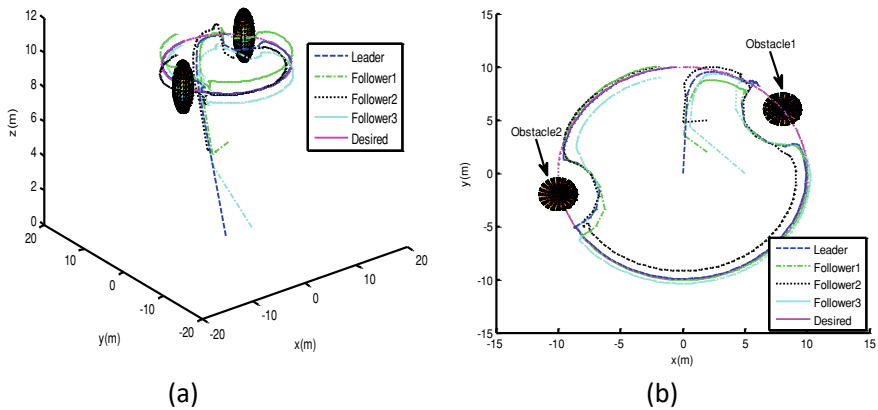
Fig. 2 Path planning of bio-inspired AUVs in a circular path and avoiding solid obstacles as well as inter-vehicle communication in **a** 3D space and **b** 2D plane

5 Conclusion

In this paper, a bio-inspired swarm of a team of AUVs is employed to address personal path planning problems to navigate towards their destination. During path planning of multiple AUVs, the desired safe distance among every pair of AUVs as well as avoiding obstacles are the motivation behind the paper using the DPC algorithm. The agent AUVs are identical and estimate the relative position with their neighbour AUVs while moving towards their respective destinations and assume full communication. From the simulation result, it can be observed that all the AUVs in path planning are able to reach their destination at the desired safe distance among every pair of AUVs as well as avoid static obstacles. The paper is useful for the surveillance of the underwater environment.

References

1. M. Panda, B. Das, B. Subudhi, B.B. Pati, A comprehensive review of path planning algorithms for autonomous underwater vehicles. Int. J. Autom. Comput. **17**(3), 321–352 (2020)
2. L. Durica, B. Micieta, P. Bubenik, V. Binasova, Manufacturing multi-agent system with bio-inspired techniques: codesa-prime. MM SJ **2015**(04), 829–837 (2015)
3. B. Das, B. Subudhi, B.B. Pati, Formation control of underwater vehicles using multi agent system. Arch. Control Sci. **30**(2), 365–384 (2020)
4. M. Panda, B. Das, B.B. Pati, Grey wolf optimization for global path planning of autonomous underwater vehicle, in *Proceedings of the Third International Conference on Advanced Informatics for Computing Research - ICAICR '19*, Shimla, India, 2019, pp. 1–6
5. B. Das, B. Subudhi, B.B. Pati, Employing nonlinear observer for formation control of AUVs under communication constraints. Int. J. Intell. Unmanned Syst. **3**(2/3), 122–155 (2015)

6. B. Das, B. Subudhi, B.B. Pati, Co-operative control of a team of autonomous underwater vehicles in an obstacle-rich environment. J. Mar. Eng. Technol. **15**(3), 135–151 (2016)
7. B. Das, B. Subudhi, B.B. Pati, Co-operative control coordination of a team of underwater vehicles with communication constraints. Trans. Inst. Meas. Control **38**(4), 463–481 (2016)
8. M. Panda, B. Das, B.B. Pati, Global path planning for multiple AUVs using GWO. Arch. Control Sci. **30**(1), 77–100 (2020)
9. M. Panda, B. Das, B.B. Pati, A hybrid approach for path planning of multiple AUVs, in *Innovation in Electrical Power Engineering, Communication, and Computing Technology* (Singapore, 2020), pp. 327–338
10. K.-H.C. Wang, A. Botea, MAPP: a scalable multi-agent path planning algorithm with tractability and completeness guarantees. J. Artif. Intell. Res. **42**, 55–90 (2011)
11. S. Bhattacharya, M. Likhachev, V. Kumar, Distributed path consensus algorithm. Technical Report MS-CIS-10-07 (University of Pennsylvania, 2010)
12. S. P. Sahoo, B. Das , B. B. Pati, Path planning of bio-inspired swarm of AUVs using distributed path consensus algorithm, J. Eng. Sci. Techno. Rev. **14**(5), 173–179 (2021)
13. B. Das, B. Subudhi, B.B. Pati, Cooperative formation control of autonomous underwater vehicles: an overview. Int. J. Autom. Comput. **13**, 199–225 (2016)
14. M. Chen, D. Zhu, A workload balanced algorithm for task assignment and path planning of inhomogeneous autonomous underwater vehicle system. IEEE Trans. Cogn. Dev. Syst. **11**(4), 483–493 (2019)
15. B. Das, B. Subudhi, B.B. Pati, Adaptive sliding mode formation control of multiple underwater robots. Arch. Control Sci. **24**(4), 515–543 (2014)
16. M. Panda, B. Das, B. Subudhi, B.B. Pati, Adaptive fuzzy sliding mode formation controller for autonomous underwater vehicles with variable payload. Int. J. Intell. Unmanned Syst. (2020)
17. K.M. Rizwan, D. Bikramaditya, P.B. Bhusan, A criterion based adaptive RSIC scheme in underwater communication. J. Syst. Eng. Electron. **32**(2), 408–416 (2021). https://doi.org/10.23919/JSEE.2021.000034
18. M.R. Khan, B. Das, Multiuser detection for MIMO-OFDM system in underwater communication using a hybrid bionic binary spotted Hyena optimizer. J Bionic Eng **18**, 462–472 (2021). https://doi.org/10.1007/s42235-021-0018-y

An Estimation-Based Sliding Mode Control Structure for High-Performance Control of Induction Motor

Swagat Pati, Abhijeet Choudhury, and Janmajaya Gantayat

Abstract This paper uses a sliding mode controller (SMC)-based vector control estimation for induction motor-based squirrel cage type. The performance of the entire system is subjected to a step change in speed and torque in order to observe the variation of different parameters. From the simulated results, the proposed SMC-based vector control strategy enhances the performance of the induction motor system. The entire system is modeled and simulated using the MATLAB/Simulink platform.

Keywords Cage induction motor · Sliding surface · Vector control

1   Introduction

In the large portion of electrical drives and control application, the standardized technique to control the squirrel cage induction machines/motors have been confined to field oriented principle so as to achieve robust and dynamic behavior [1]. In order to mitigate distortion issues of induction machines, indirect vector control schemes are preferred because of the independency between the unit vectors and terminal conditions as discussed in [2]. Thus, it helps in designing and implementing more precise control structures.

Moreover, induction machines are mostly preferred in terms of power generation or in any drive and control applications. Being the most rugged and maintenance-free machines, induction motors persist with drawbacks like torque and flux issues due to sluggish behavior. Hence, the use of a vector control algorithm has proved to mitigate the sluggish behavior of induction machines as discussed in [3]. Meanwhile, much research has been conducted on different schemes of vector control algorithms by using, for example, PI controllers [4], Fuzzy Logic controllers [5], hybrid controllers

S. Pati (✉) · A. Choudhury · J. Gantayat
Department of Electrical Engineering, Institute of Technical Education & Research, Siksha 'O' Anusandhan Deemed to Be University, Bhubaneswar, India
e-mail: swagatpati@soa.ac.in

A. Choudhury
e-mail: abhijeetchoudhury@soa.ac.in

[6], and sliding mode controllers [7]. Conventional PI controllers have indeed been implemented in various vector control schemes, but it lacks instability when there is a large disturbance, and the dynamic response is quite slow as compared to other controllers. Although fuzzy logic controllers are robust in nature, when it comes to the real-time application, it does not fit well rather the membership functions and rule base needs to be kept quite simple so as to reduce the computational burdens.

But in the present scenario, many hybrid controllers have already been implemented to acquire high-performance stability. Among these hybrid controllers, sliding mode controllers have proved to be highly efficient and precise, irrespective of any disturbances in induction machines, due to their simplicity, easy implementation, and nonetheless, the computational burdens are less as compared to Fuzzy controllers.

In this paperwork, an indirect vector controlled cage induction motor is studied. The indirect vector control algorithm is applied in order to improve the performance of the induction motor using a sliding mode controller. The entire system is subjected to step change in speed and torque and the results are analyzed. The entire system has been modeled in the Matlab/Simulink environment.

2 Control Structures

2.1 Control of Induction Motor Using SMC

The architectural representation of the induction motor using SMC-based vector control is shown in Fig. 1. Both transient and steady-state performance of induction
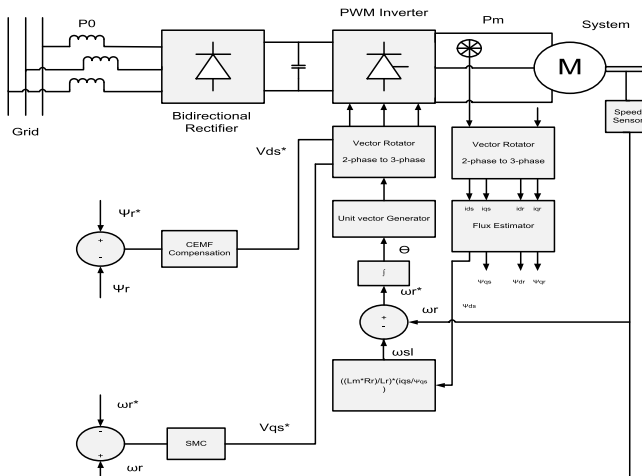
Fig. 1 Architectural representation of induction motor using SMC

motor can be improvised by speed and current controllers. With the assumption in order to get a better dynamic response, the mathematical model of induction motor is formulated using a synchronous reference frame as can be seen in Eqs. (1)–(5)

$$\omega_{sl} = \frac{R_r}{L_r} x \frac{i_{qs}}{i_{ds}} \tag{1}$$

$$T_e = \frac{3}{2} x \frac{P}{2} x \frac{L_m}{L_r} \psi_{dr} i_{qs} \tag{2}$$

The machine dynamics are given as

$$T_e + T_{Turbine} = J \frac{d\omega_m}{dt} + B\omega_m \tag{3}$$

The active and reactive power of the machine is given by

$$p = v_{ds} i_{ds} + v_{qs} i_{qs} \tag{4}$$

$$q = v_{qs} i_{ds} - v_{ds} i_{qs} \tag{5}$$

It can be clearly seen from Fig. 1 that the input to the sliding mode controller is the speed errors which moreover commands the quadrature axis voltage to be fed to the vector rotator block and the direct axis voltage is derived from the CEMF compensation block from flux errors and fed to the vector rotator block.

The sliding surface is defined as a scalar equation

$$s(e_w, \dot{e}_w, t) = 0 \tag{6}$$

where

$$e_w = w_m - w_w^*$$

The sliding variable s is given as $s = \dot{e}_w + \lambda e_w$ where λ is a positive constant and depends on the bandwidth of the system. The condition for sliding mode is given as

$$\frac{1}{2} \frac{d}{dt} s^2 = s \dot{s} \leq -n|s| \tag{7}$$

That is equivalent to $\dot{s} \, sgn(s) \leq -n$

$$\dot{s} \, sgn(s) \leq -n \tag{8}$$

Substituting $\dot{s}$, we get

$$(\ddot{w}_r - \ddot{w}_r^* + \lambda \dot{e}_w)\text{sgn}(s) \leq -n \tag{9}$$

$\ddot{w}_r$ is a constant

$$(\ddot{w}_r + \lambda \dot{e}_w)\text{sgn}(s) \leq -n$$

For the sliding mode controller to track the speed accurately

$$\dot{w}_m|_{w_m = w_m^*} = 0$$
$$\ddot{w}_m|_{w_m = w_m^*} = 0 \tag{10}$$

$$\dot{w}_m = \frac{-Bw_m}{J} + \frac{K_T}{J}i_{qs}\psi_{dr} + \frac{T_{Turbine}}{J} \tag{11}$$

$$\dot{w}_m = \frac{-Bw_m}{J} + bi_{qs} + noise \tag{12}$$

where $b = \frac{K_T}{J}\psi_{dr}$

$$\dot{w}_m = \frac{-Bw_m}{J} + bi_{qs} + noise$$
$$= f_1 + noise \tag{13}$$

where $f_1 = \frac{-Bw_m}{J} + bi_{qs}$

$$\ddot{w}_m = \frac{-B\dot{w}_m}{J} + b\dot{i}_{qs} + \dot{noise}$$
$$= -\frac{B}{J}\left(\frac{-Bw_m}{J} + bi_{qs} + noise\right) + b\dot{i}_{qs} + \dot{noise}$$
$$= \frac{B}{J}(f_1) + b\dot{i}_{qs} + \left(\dot{noise} - \frac{B}{J}noise\right) \tag{14}$$

$$Vqr = R_r i_{qr} + \frac{d}{dt}\Psi_{qr} + (w_e - w_r)\Psi_{dr}$$

$Vqr = 0$ for squirrel cage induction machine

so

$$\frac{d}{dt}\Psi_{qr} = -R_r i_{qr} - (w_e - w_r)\Psi_{dr}$$

$$= -R_r(\frac{\psi_{qr}}{l_r} - \frac{l_m}{l_r}i_{qs}) - (w_e - w_r)\Psi_{dr}$$

$$= -R_r\frac{\psi_{qr}}{l_r} + R_r\frac{l_m}{l_r}i_{qs} - (w_e - w_r)\Psi_{dr}$$

$$= R_s i_{qs} + \frac{d}{dt}(l_s i_{qs} + l_m i_{qr}) + w_e(l_s i_{ds} + l_m i_{dr})$$

$$= R_s i_{qs} + \frac{d}{dt}(l_s i_{qs} + \frac{l_m}{l_r}\psi_{qr} - \frac{l_m^2}{l_r}i_{qs}) + w_e(l_s i_{ds} + \frac{l_m}{l_r}\psi_{dr} - \frac{l_m^2}{l_r}i_{ds}) \qquad (15)$$

$$= R_s i_{qs} + \frac{d}{dt}(l_s i_{qs} + l_m i_{qr}) + w_e(l_s i_{ds} + l_m i_{dr})$$

$$= R_s i_{qs} + \frac{d}{dt}(l_s i_{qs} + \frac{l_m}{l_r}\psi_{qr} - \frac{l_m^2}{l_r}i_{qs}) + w_e(l_s i_{ds} + \frac{l_m}{l_r}\psi_{dr} - \frac{l_m^2}{l_r}i_{ds}) \qquad (16)$$

Substituting for $\ddot{w}_r$, we get

$$(G_w + d + \frac{b}{\sigma l s}V_{qs} + \lambda \dot{e}_w)\text{sgn}(s) \leq -n$$

$$\Rightarrow \frac{b}{\sigma l s}V_{qs}^* + (G_w + d + \lambda \dot{e}_w) = -K'\text{sgn}(s) \qquad (17)$$

These were the following equation for the proposed sliding mode controller using an indirect vector control strategy

$$\Rightarrow V_{qs}^* = \frac{-(G_w + d + \lambda \dot{e}_w) - K'\text{sgn}(s)}{\frac{b}{\sigma l s}}$$

$$\Rightarrow V_{qs}^* = \frac{(-G_w - \lambda \dot{e}_w)}{\frac{b}{\sigma l s}} - \frac{K'}{\frac{b}{\sigma l s}}\text{sgn}(s) \qquad (18)$$

$$\Rightarrow V_{qs}^* = \frac{(-G_w - \lambda \dot{e}_w)}{\hat{b}_w} - K_w \text{sgn}(s)$$

where $\hat{b}_w = \frac{b}{\sigma l s}$.

And $K_w = \frac{K'}{\frac{b}{\sigma l s}}$ is a constant which has to be tuned.

So

$$V_{qs}^* = \frac{(-G_w - \lambda \dot{e}_w)}{\overset{\wedge}{b_w}} - K_w \mathrm{sgn}(s) \tag{19}$$

3 Result Analysis and Discussions

The proposed control strategy has been evaluated using SMC for induction motor as can be seen in Fig. 1. The performance improvement of the induction motor was observed from the experimental results by varying the step inputs of both torque and speed.

3.1 Results During Step Change in Speed

There is a step change in different time intervals, namely at t = 2.5 to 2.7 s the Wref = 1100 rpm, when t = 2.9 to 3.1 s Wref = 900 rpm. Initially, the speed (Wref) was assumed to be '1000 rpm'.

The entire proposed control induction motor system is subjected to step change in ref speed. From Fig. 2a, it can be seen that the reference speed is taken to be 1100 rpm for a period of 0.2 s and the settling time is quite faster. The torque variation due to the change in speed is observed in Fig. 2b. The active and reactive power does not deviate much due to the speed change as can be seen from Fig. 2c. The minor deviation in d-axis current and voltages can be seen in Fig. 2d, e, whereas the q-axis current and voltages remain unchanged. The variation in d-axis and q-axis flux can be seen in Fig. 2f.

3.2 Results During Step Change in Torque

There is a step change in different time intervals, namely at t = 3 s the T = 2 N·m, when t = 3.1 s T = 8 N·m, when t = 3.2 s T = 5 N·m, and when t = 3.3 s T = 1 N·m. Initially, the torque (T) was assumed to be '0'. The settling time of the actual speed is minimum as can be noticed from Fig. 3a, similarly, the change in electromagnetic torque is observed in Fig. 3b. The active and reactive power of the IM system can be seen in Fig. 3c. Both the active and reactive power are positive as per the sign convention, and due to the motoring action, the power is drawn from the grid. Figure 3d and 3e shows the d-axis and q-axis current and voltages, respectively, where the limits are in the zone of tolerance. The independent control can be easily observed from the above two figures. Individual flux changes of the d-axis and q-axis can be observed in Fig. 3f.

(a)   (b)   (c)

(d)   (e)   (f)
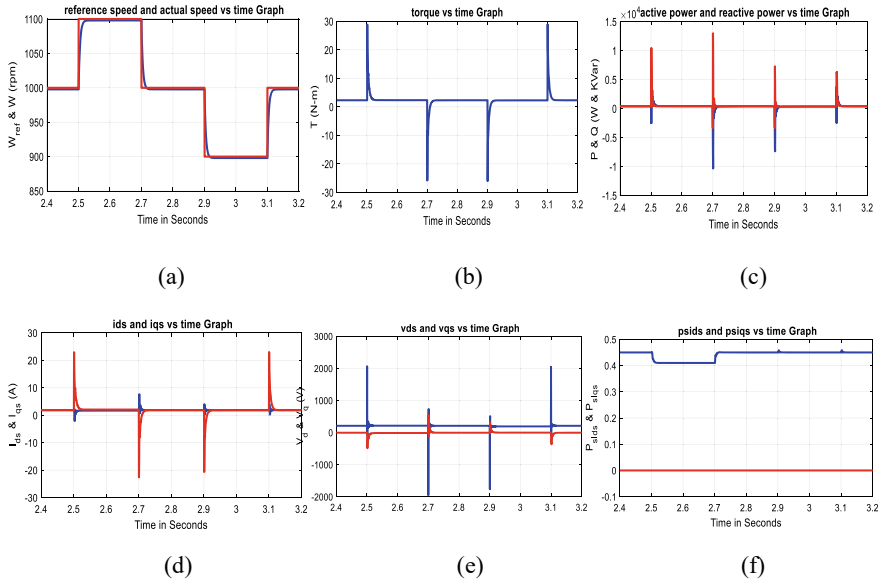
Fig. 2. Simulation responses with step change in reference speed **a** reference and actual speed, **b** electromagnetic torque, **c** active and reactive power, **d** d-axis and q-axis current, **e** d-axis and q-axis voltage, **f** d-axis and q-axis fluxes

(a)   (b)   (c)

(d)   (e)   (f)
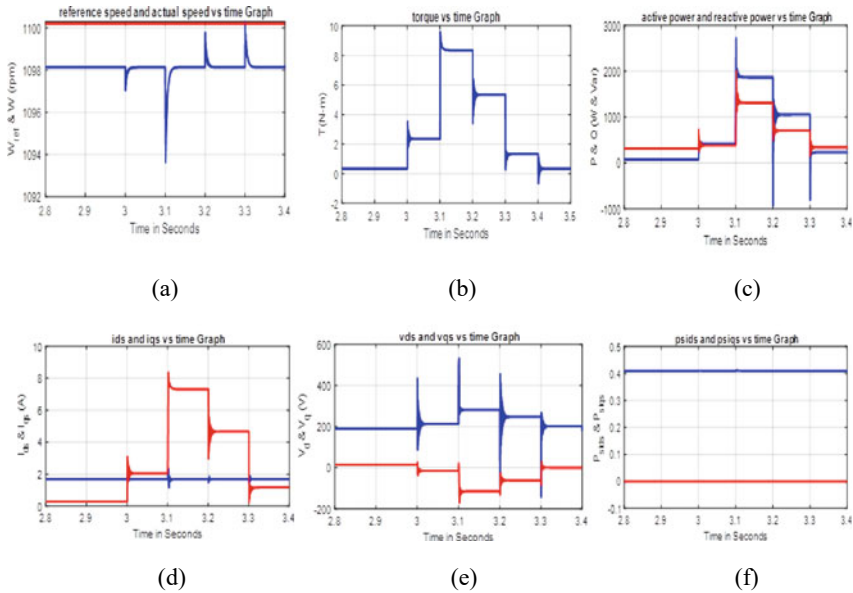
Fig. 3. Simulation responses with a step change in torque **a** reference and actual speed, **b** electromagnetic torque, **c** active and reactive power, **d** d-axis and q-axis current, **e** d-axis and q-axis voltage, **f** d-axis and q-axis fluxes

4 Conclusion

This paperwork focuses on the implementation of SMC-based vector controlled cage induction motor system with improved results during a step change in speed and torque. The system was observed to be robust and dynamic in nature irrespective of reference speed variation. The settling time of speed responses in both torque and speed change was experimentally proved to be minimum. Accordingly, the active and reactive power changes were observed as per the change in ref speed. The achievement of the entire system was assured to be better.

References

1. W. Leonhard, *Control of Electrical Drives* (Springer Science & Business Media, 2001)
2. B.K. Bose, *Power Electronics and AC Drives* (PH, 1986)
3. C.V. Nayar, J.H. Bundell, Output power controller for a wind-driven induction generator. IEEE Trans. Aerosp. Electron. Syst. **3**, 388–401 (1987)
4. R. Cárdenas, R. Peña, Sensorless vector control of induction machines for variable-speed wind energy applications. IEEE Trans. Energy Convers. **19**(1), 196–205 (2004)
5. M.G. Simoes, B.K. Bose, R.J. Spiegel, Fuzzy logic based intelligent control of a variable speed cage machine wind generation system. IEEE Trans. Power Electron. **12**(1), 87–95 (1997)
6. M. Masiala, B. Vafakhah, J. Salmon, A.M. Knight, Fuzzy self-tuning speed control of an indirect field-oriented control induction motor drive. IEEE Trans. Ind. Appl. **44**(6), 1732–1740 (2008)
7. T.G. Park, K.S. Lee, SMC-based adaptive input–output linearising control of induction motors. IEE Proc.-Control Theory Appl. **145**(1), 55–62 (1998)

Performance Analysis of a Nine Switch Converter During Partial Disconnection in an Isolated Multi-Source Generation System

Abhijeet Choudhury, Swagat Pati, Renu Sharma, Sanjeeb Kumar Kar, and Bruti Kumar Behera

Abstract In this paper, an isolated multi-source generation system is considered. The multi-source system consists of a 22 kW constant power-source self-excited induction generator, 7.5 kW WECS-based doubly fed induction generator and an 18 kW PV system equipped with BESS. This multi-source generation system consists of a nine switch converter that acts as an interface between these energy sources. The major focus of this work is to focus on the uninterruptible power supply to the load when multiple energy sources have been disconnected. Two different types of control algorithms have been designed, i.e. DFIG side control and real-reactive power compensation control algorithm. This control structure works efficiently to fulfill the load demand irrespective of source disconnection. The entire system is modeled and formulated using MATLAB 2018a.

Keywords Self-excited induction generator · Doubly fed induction generator · Multi-source generation system · Photovoltaic system · Battery energy storage system · Bidirectional switches · Induction generator

1 Introduction

In this fast-changing world, depletion of fossil fuels, population outburst and industrialization have created a large power demand. The present power generation scenario has been outmatched by the increasing power demand causing power shortages and

A. Choudhury (✉) · S. Pati · R. Sharma · S. K. Kar · B. K. Behera
Department of Electrical Engineering, Institute of Technical Education & Research, Siksha 'O' Anusandhan Deemed to be Univesity, Bhubaneswar, India
e-mail: abhijeetchoudhury@soa.ac.in

S. Pati
e-mail: swagatpati@soa.ac.in

R. Sharma
e-mail: renusharma@soa.ac.in

S. K. Kar
e-mail: sanjeebkar@soa.ac.in

blackouts. The environmental conditions such as global warming and pollution have created great concern for the utilization of renewable power generators, for clean power. In the last few decades, power generation from RPGs has been confronted by the researchers which mainly consists of solar, wind, biomass and micro-hydro systems.

Supplementary energy sources have become mandatory in order to generate green and clean power, and moreover, it helps in coping up with the industrial and environmental conditions to meet the energy demand. Though the only energy source, which does not have any boundary condition for power generation in PV, but it suffers from the cause of having lower efficiency upon the mostly used renewable energy sources. The detailed dynamic modeling of PV has been given in [1]. Due to its widespread nature, in remote locations, renewable power generators are emphasized where power grids are absent. There exist some lacunas as compared to conventional grids, i.e. the constant power supply is not possible in the case of RPGs due to random behavior. So maintaining a constant voltage and frequency in the case of an isolated system is a challenging issue. The challenge furthermore increases when a micro-hydro system-based self-excited IG is considered. SEIGs seem to be more appreciated for power generation at remote locations because of their advantages like brushless, maintenance-free, vigorous and furthermore for the excitation process they pose a capacitor bank which is easily available. Moreover, these SEIGs pose serious drawbacks, i.e. they operate in saturation region [2], which procures the system's frequency and voltage to get unstable easily. The detailed modeling and the capacitance requirement for SEIGs have been studied in [3].

Though both SEIGs and PV pose random behavior, wind energy systems have brought a huge phase shift in terms of renewable power generation. Increased economic and ecological issues have made researchers to discover new techniques to generate a cleaner form of electrical energy. A wind power conversion system poses equal potential as compared to a photovoltaic generation system in terms of economy and efficiency. Over the past two decades, more emphasis has been given to these wind energy systems as compared to other renewable power generation systems. Though induction generators are often used for WECS, doubly fed induction generators are preferred ones because of their advantages which encapsulate lower converter ratings and efficient power capture due to variable speed operation, the flexibility of power generation and higher efficiency. In [4], the comparison between variable speed wind generation system and fixed speed wind generation system is given. WECS integrated with a DFIG is an efficient option to harness the wind energy due to its capability for a broad range of operating speeds which makes generation possible in highly variable wind speeds. Improved efficiency can be observed in the case of DFIG-based WECS along with reduced converter cost and size, variable speed operation and better active and reactive power control capabilities as given in [5]. DFIG-based WECS employs a back-to-back (BTB) converter for the control of power flow in the system. The first part of the BTB converter is the machine side converter (MSC) which controls the stator side power flow. The second part is the grid side converter (GSC) which is used to control the dc-link voltage and also to compensate for the required active and/or reactive power as given in [6].

The back-to-back converters are a combination of 2 six switch converters connected back to back. These consist of 12-bidirectional switches, but the dc-link requirement is quite low. In order to enhance the cost of converters, matrix converters have been proposed but due to the absence of dc-link, independent power control is not possible. Hence, the authors in this work have given the major focus on nine switch converter which deploys 3-BD switches in each phase leg along with the presence of dc-link. Though the dc-link voltage requirement is quite higher as compared to the BTB converter, the stability as well as the reliability of the system is enhanced. The switching scheme for NSC is discussed in [7].

This paper work comprises of a hybrid multi-source generation system consisting of multiple renewable power generators. Basically, here a 22 kW SEIG is integrated with a 7.5 kW DFIG along with a 18 kW PV and battery storage system connected across the dc-link terminals of a nine switch converter. NSC acts as an interface between the multiple RPGs in order to control the power flow to the load. The proposed control algorithms hold beneficial for independent power control. Here, BESS plays a vital role in storing/supplying excess/deficit amount of power from/to the system. The flow of the paper work holds on after the introduction as system configuration where a brief description about the system is discussed. Then the control algorithm as well as the switching pulse generation for nine switch converter is discussed. The impact of partial disconnection of PV as well as DFIG for a period of 2 s has also been analyzed in the result section. The entire system is modeled and simulated using MATLAB-2018(a).

2   System Description and Control Strategies

2.1   System Description

The system considered here consists of a SEIG which is fed from a constant power-source and a doubly fed induction generator driven by a wind turbine. In the case of the DFIG-based wind system, both the converters, i.e. grid side converter and rotor side converter are replaced by a nine switch converter. This NSC controls the power flow of WECS and compensates both 'P' and 'Q' requirements of the system. Moreover, it also helps in affirming the system frequency and voltage at a fairly constant value. The system also houses a Photovoltaic system along with a battery bank connected to the dc side of NSC which helps in storing or supplying real power to the system. This hybrid MSG system is subjected to a base RL load. The power control of the entire system is analyzed by partial disconnection of the photovoltaic system and the wind energy conversion system. The schematic representation of the hybrid microgrid system is shown in Fig. 1. The system is modeled and simulated using Simulink/MATLAB environment.
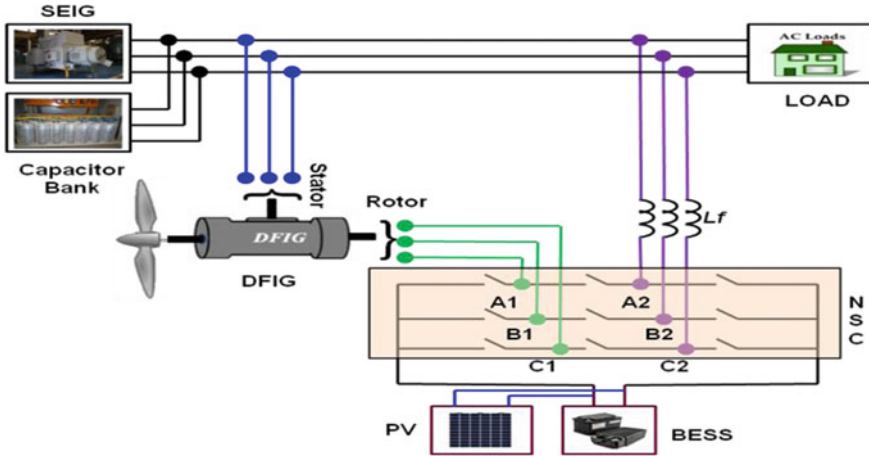
Fig. 1 Schematic representation of multi-source generation system

2.2 Control Algorithms

A SFOVC strategy is implemented for the control of the DFIG. The DFIG control structure consists of two loops to control the active and reactive power of the DFIG independently. The active power control loop, i.e. the quadrature axis loop generates the quadrature axis reference current from the speed error. The d-axis loop controls the flux of the machine otherwise controlling the stator side reactive power flow of the DFIG. In this proposed work, the stator side power factor of the DFIG is set to unity so the reference reactive power is taken to be zero. The controllers used in this work are conventional PI Controllers which are tuned by trial and error process to get near optimum results. The direct and quadrature axis currents are calculated and are transformed to their three-phase equivalent currents. The control signals for the A_1, B_1 and C_1 terminal output of the NSC are generated by subtracting the actual three-phase currents from the reference three-phase currents as shown in Fig. 2. The active and reactive power compensation is done through the terminals A_2, B_2 and C_2 of the NSC. NSC accumulates the excess real power in the BESS which can be utilized under power deficit conditions. The NSC also reimburses the required amount of reactive power to the system to maintain a constant voltage profile during load variations. The control structures for active and reactive power compensation are shown in Fig. 3. The authors in [8] have very well discussed about the configuration, switching sequence and structure of nine switch converter in detail.
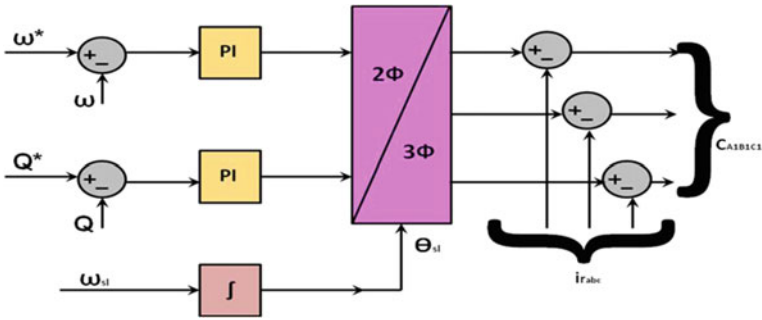
Fig. 2 Rotor side control
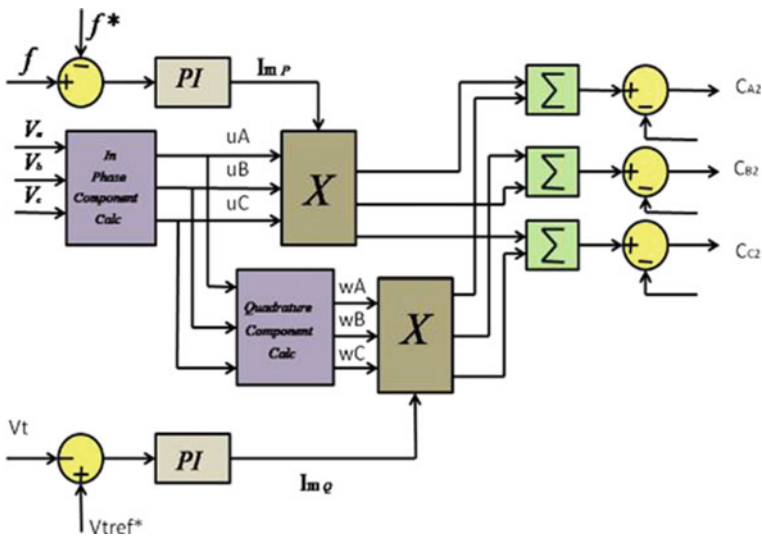
Fig. 3 Real-Reactive power compensation control structure

3 Result Analysis and Discussions

The multi-source generation system is subjected to partial disconnection of both photovoltaic system as well as wind energy conversion system in different time intervals. All the currents and voltages along with frequency are analyzed by subjecting them to variation in RL load.

The photovoltaic system is partially disconnected at a time interval of 4.5 s. In Fig. 4b when the PV is disconnected, the required amount of active power is managed by the battery energy storage system, which maintains the system's frequency and voltage to be at a steady value. The requirement of reactive power as well is compensated by the nine switch converter. Though a source, i.e. PV is disconnected, no

(a)   (b)
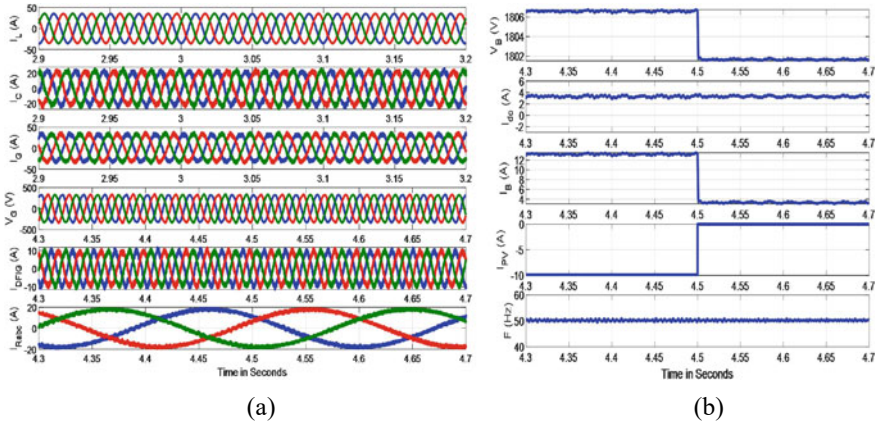
Fig. 4 **a** Alternating current parameters during partial disconnection of PV, **b** Direct current parameters during partial disconnection of PV

disturbance is observed either in SEIG's current or voltage or in DFIG's current or voltage as can be seen from Fig. 4a. The frequency of the system is 50 Hz as given in Fig. 4a. It can be clearly noticed from Fig. 5a that at a time interval of about 3 s, the wind energy conversion system is disconnected. The load current, SEIG current and voltage remain unchanged due to the robust control algorithm designed. The PV current gets negative; as per sign convention, the PV here supplies power to the load along with BESS as can be seen from Fig. 5b. Uninterrupted power supply capability is justified because of the real-reactive power compensation control algorithm used in nine switch converter. The frequency remains at a steady value of 50 Hz as can be seen from Fig. 5b.

(a)   (b)
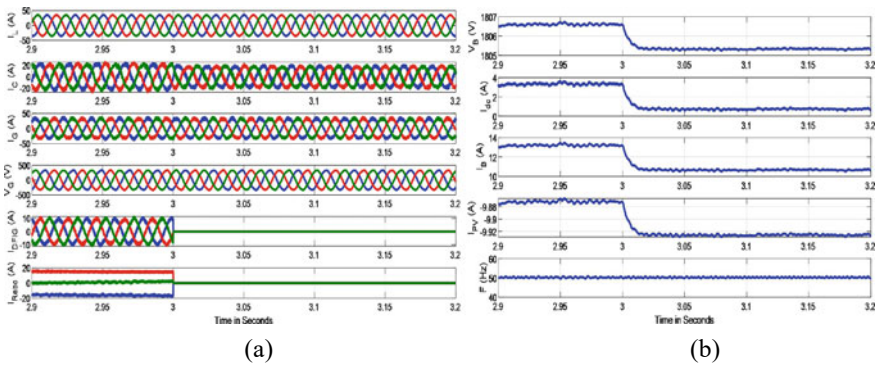
Fig. 5 **a** Alternating current parameters during partial disconnection of WECS, **b** Direct current parameters during partial disconnection of WECS

4 Conclusions

Here, a new topology of nine switch converter has been used to interface multiple generation system. The hybrid microgrid system consists of a micro-hydro system and a WECS which are integrated using a NSC along with a Photovoltaic system housing a BESS. The NSC acts as a compensator to manage the active and reactive power of the whole system. Although the NSC effectively manages the power of the system, there are very small fluctuations occurring in the voltage and frequency of the system and partial disconnection of PV and WECS. Although NSC efficiently manages the power flow but when it comes to dc-link voltage, the requirement of the dc-link voltage is higher as compared to BTB converters. Other than that the harmonic injection in the system current by the NSC is also a bit higher as compared to BTB converters. Despite these drawbacks, NSC can be considered as an efficient, reliable and robust alternative for conventional back-to-back converters in grid interfacing and microgrid power control operation.

References

1. B.K. Dey, I. Khan, N. Mandal, A. Bhattacharjee, Mathematical modelling and characteristic analysis of solar PV cell, in *2016 IEEE 7th Annual Information Technology, Electronics and Mobile Communication Conference (IEMCON)* (2016 October), pp. 1–5. IEEE
2. S.S. Murthy, O.P. Malik, A.K. Tandon, Analysis of self-excited induction generators, in *IEE Proceedings C-Generation, Transmission and Distribution* (1982 November), Vol. 129, No. 6, pp. 260–265 . IET
3. K. Charafeddine, K. Sangov, S. Tsyruk, Automatic voltage regulation and stability analysis of three-phase self-excited induction generator for wind energy, in *2017 2nd International Conference on the Applications of Information Technology in Developing Renewable Energy Processes & Systems (IT-DREPS)* (2017 December), pp. 1–6. IEEE
4. S.S. Murthy, B. Singh, P.K. Goel, S.K. Tiwari . A comparative study of fixed speed and variable speed wind energy conversion systems feeding the grid, in *2007 7th International Conference on Power Electronics and Drive Systems* (2007 November), pp. 736–743. IEEE
5. I. Boldea, *Variable Speed Generators* (CRC Press, 2015)
6. T. Ghennam, K. Aliouane, F. Akel, B. Francois, E.M. Berkouk, Advanced control system of DFIG based wind generators for reactive power production and integration in a wind farm dispatching. Energy Convers. Manag. **105**, 240–250 (2015)
7. A. Choudhury, S. Khatua, S. Pati, S.K. Kar, A reliable and efficient integration topology for autonomous hybrid systems using NSC, in *2019 International Conference on Electrical, Electronics and Computer Engineering (UPCON)* (2019 November), pp. 1–6. IEEE
8. A. Choudhury, S. Khatua, S. Pati, S.K. Kar, Power control of micro hydro-wind based hybrid autonomous system using nine switch converter, in *2019 International Conference on Electrical, Electronics and Computer Engineering (UPCON)* (2019 November), pp. 1–6. IEEE

Sliding Mode Control-Oriented Electric Spring for SEIG-Based Micro-Grid

Soumya Mohanty, Swagat Pati, Sanjeeb Kumar Kar, and Janmajaya Gantayat

Abstract Alternative power production is an ongoing research area both for power industries and researcher that developed interest in renewable energy sources (RESs) from more than two decades. But the integration of RES to power system leads to voltage fluctuation, which is well known to the operators as an unpredictable natural behavior of RES. In the recent past, an emerging technology known as 'Electric Spring' (ES) has been developed to resolve voltage stabilization problem especially in distributed network. In this paper, a novel 'in-phase control approach' for ES with sliding mode controller (SMC) is proposed for a wind-driven self-excited induction generator (SEIG) centric standalone system. The suggested approach is validated using MATLAB/SIMULINK environment under load change condition, and it is found that the approach is proven to be effective for voltage restoration across critical load. In addition, active and reactive power exchange has been studied.

Keywords Electric spring · Renewable energy sources · Self-excited induction generator · Sliding mode controller

1 Introduction

The demand side management process is becoming crucial day by day with large number of renewable energy source penetration [1]. This brings out the necessity of shifting the pattern of traditional centralized power control to decentralized power

S. Mohanty (✉) · S. Pati · S. K. Kar · J. Gantayat
Department of Electrical Engineering, Institute of Technical Education and Research, Siksha 'O' Anusandhan Deemed to Be University, Bhubaneswar, India
e-mail: soumyamohanty456@gmail.com

S. Pati
e-mail: swagatpati@soa.ac.in

S. K. Kar
e-mail: sanjeebkar@soa.ac.in

J. Gantayat
e-mail: janmajayagantayat@gmail.com

control. In this new pattern, the load demand balances the power generation, as RESs are unpredictable in nature. This creates two major questions in the exiting power system that are voltage and frequency stabilization. Several complicated techniques are already applied to address this particular problem but most of them associated with more or less limitations. In addition, the aforementioned issue becomes even serious when it comes to isolated system since there is no external prop up as of grid-connected mode. Further the existence of an intermittent generation source in a standalone network such as a wind-driven self-excited induction generator (SEIG) is even more challenging to tackle the fluctuation-related hurdles. Hence, there is a need for new technology that can come forward with a solution to eliminate the worry of voltage and frequency stability in low voltage networks.

Recently, 'Electric Spring' technology has come to limelight as the simplest solution to distributed voltage control and effectively contributing towards demand side management. The main concept of ES is derived from Hook's mechanical spring. It modulates the requirement of noncritical load in response to the fluctuation of RESs [2]. ES in series with noncritical load forms 'smart load' and whenever voltage fluctuates it inject a controllable voltage in series with noncritical loads to normalize voltage fluctuation across critical loads. ES regulates voltage as well as power, as it also modulates noncritical load power with input power, which results frequency stabilization. First of all, ES eliminates the worry of communication system [3] so as to monitor demand–supply balance, and secondly it also aids to reduction in energy storing device to boost up the system voltage at times [4]. Ref.[5] shows ES hardware implementation and control strategy for reactive power compensation, and Ref.[6] describes cumulative operation of ESs distributed along a transmission line. Refs[6] and [7] describe the comparison of ES with traditional SVC and STATCOM, respectively, which states that traditional compensation device adopts output voltage control, however, ES adopts input voltage control. Additionally, traditional compensating devices handle pure reactive power, on the other hand, ES can alter both active and reactive power [8].

This paper suggests a novel control strategy for ES that make use of in phase component of the current through the smart load that stabilizes the voltage across critical load by altering both real and reactive power. A sliding mode controller is adapted that exhibits best transient performance unlike a traditional PI (proportional-integral) controller. The capability of the control approach is tested with load variation and the results show appreciable outcomes. Moreover, the real and reactive power associated with critical load, non-critical load and electric spring are also presented in this paper to put forward better conviction to the reader.

2 System Description

In order to show the basic principle of ES, a simple system is taken into consider. The test system is illustrated in Fig. 1, it shows the single line diagram of three-phase, 22 KW, 230 V, 50 Hz SEIG system which is driven by wind energy. ES is
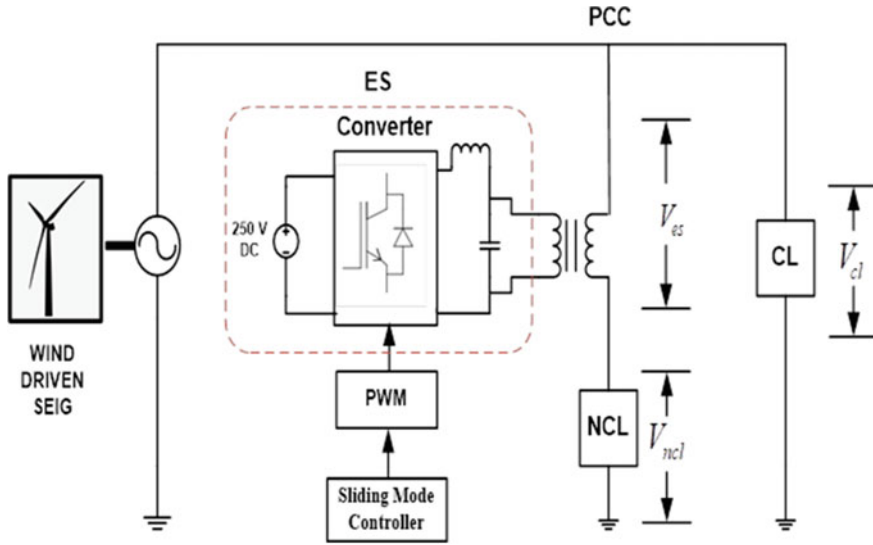
Fig. 1 Single line diagram of the test system

interfaced between source and divided loads, i.e., critical load and noncritical load, where critical load is connected in parallel and noncritical in series. The division is done by taking the voltage tolerance range of each load into consideration. For simplification both the loads are taken linear RL load. Voltage across Electric Spring, non-critical load, critical load is denoted by Ves, Vnc, Vc, respectively.

2.1 Structure of Electric Spring

From Fig. 1, if the dotted area is extracted, it gives the internal structure of Electric Spring. It is nothing but DC to AC converter with 250 V DC supply. The LC passive filter is connected to eliminate the DC component from the inverted signal. The passive filter is also used to compensate the higher order harmonics generated from the ES and provide disturbance eliminated signal to the system. Due to this purpose, the circuit efficiency as well as reliability are also improved (Fig. 2).

2.2 Control of Electric Spring

Figure 3 shows the control structure of ES, which further explains the determination of ES or noncritical current amplitude (I_t) and in-phase components (u_a, u_b, u_c). These are calculated as per Eqs. (1) and (2).
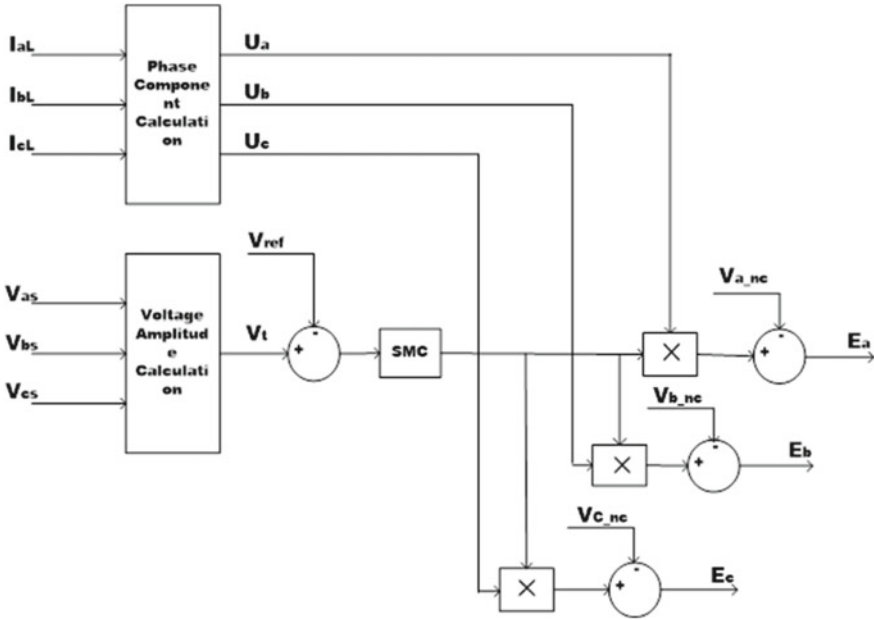
Fig. 2 Control structure of electric spring

$$I_t = \sqrt{\frac{2}{3}\left(I_a^2 + I_b^2 + I_c^2\right)} \tag{1}$$

$$u_a = \frac{I_a}{I_t}, u_b = \frac{I_b}{I_t}, u_c = \frac{I_c}{I_t} \tag{2}$$

Then the voltages of the SEIG are sensed, and the amplitude is calculated

$$V_t = \sqrt{\frac{2}{3}\left(V_a^2 + V_b^2 + V_c^2\right)} \tag{3}$$

The error signal is evaluated from the difference of obtained and reference voltage amplitude and further fed to SMC controller, which results in compensation voltage generation. In the next step, the product of compensation voltage and in phase components (u_a, u_b, u_c) is calculated. Further the noncritical voltage is eliminated, and the output reference voltage (E_a, E_b, E_c) is passed into pulse width modulation block to produce gating signal for the converter. In this way, ES produces desired voltage with respect to the difference of source to load power.

(a)

(b)
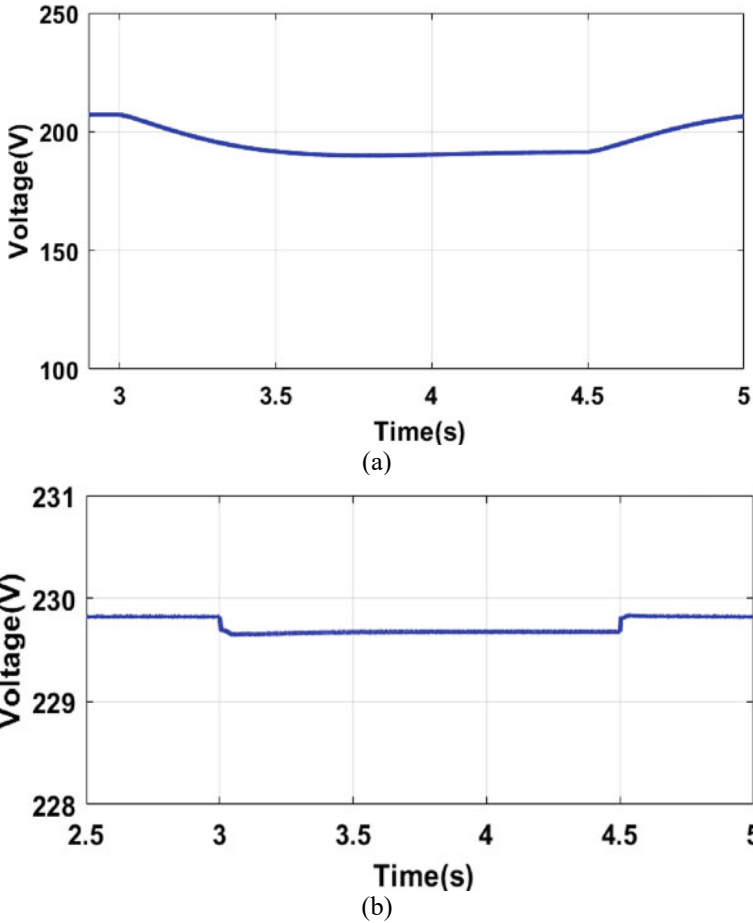
Fig. 3 Critical load voltage under load change **a** without ES, **b** with ES

2.3 Sliding Mode Controller

Sliding mode controller is a method of nonlinear control, which applies a discontinuous control signal that changes the dynamics of a nonlinear system. The discontinuous control signal makes the system to slide along a system's cross-section. Sliding mode controller has many advantages over other controllers such as improved stability, powerful control, rapid response, impassive to parameter changes.

The controllers, sliding surfaces are designed by the below equation

$$S(e, \dot{e}) = \alpha\dot{e} + \beta e = 0 \qquad (4)$$

where 'α' and 'β' are positive constants, 'e' and '$\dot{e}$' are error and its derivative, respectively.

Error is given by following equation

$$e = x - x* \qquad (5)$$

Again, x and 'x*' are the obtained and reference values. The general control law for the SMC is given as

$$u = -k.\text{sign}(s) \qquad (6)$$

Equation (6) when applied at steady state it causes chattering. For this reason, a modification is necessary. And the modified equation is given by,

$$u = -k.\text{sign}(\lambda) \qquad (7)$$

where 'λ' is defined as,

$$\lambda = \begin{cases} 1, \ s > \varphi \\ -1, \ s < -\varphi \\ \dfrac{s}{\varphi}, \ otherwise \end{cases} \qquad (8)$$

The parameters α, β, φ and k tuning are done by trial-and-error method to get required result. The values assigned to the parameters are: $\alpha = 1$, $\beta = 2500$, $\varphi = 44,000$, and k = 3800, $\lambda = 2880$.

3   Simulation and Result Analysis

This article is intended to determine the effectiveness of newly proposed in-phase sliding mode controller for operating the ES which can enable itself as an efficient voltage stabilizer. The system operations are described by intentional alteration of critical load at 3 s.

While the system is not equipped with ES, there is no discrimination of loads as critical and noncritical. When a load change is introduced to the system at 3 s the voltage drops, across it has deviated from nominal as a natural phenomenon of electrical circuitry. This behavior can be seen in Fig. 3a, by plotting a RMS voltage versus time curve. Further, the voltage has got back to its original value when the load change is occurred at 4.5 s.
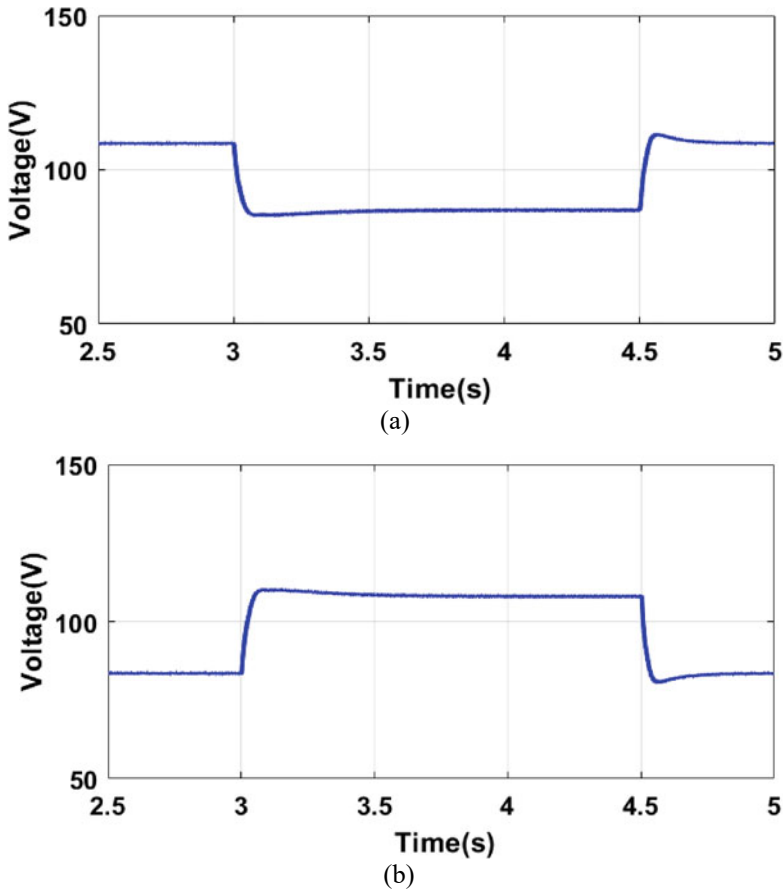
Fig. 4 Voltage profile under load change **a** non-critical load, **b** ES

The voltage drop during the load alteration can be restored with the help of ES. This is only possible when fluctuation retaining load (noncritical load) is present in the system, which are generally connected in series to the ES.

The critical load is initially requiring a real power demand of 6342 W. When there is a load increment at 3 s, the demand hiked to 8316 W as shown in Fig. 5a the impact of load change on critical voltage can be seen in Fig. 3a as a voltage dump from 230 to 191 V. But from Fig. 3b, it can be seen that in the presence of ES, the concerned voltage is not falling even below 229 V and maintaining its stability near to the nominal. The exceptional transient control is observed due to the presence of SMC. However, a traditional PI controller cannot guarantee such transient stability. Additionally, for the comprehensive study of SMC-based ES during load change, the voltage fluctuation across noncritical load and ES is displayed in Fig. 4a and b, respectively.

The power transfer between critical and noncritical loads via ES can be noticed during the load change condition in Fig. 5a and b, respectively. When the consumption of critical load is raised, ES tries to deliver the additional power by depleting the consumption of noncritical load. The same principle is equally applied for the trade-off in reactive power. The real and reactive power curve of the SEIG and ES is also shown in Fig. 5c and d for better reference.
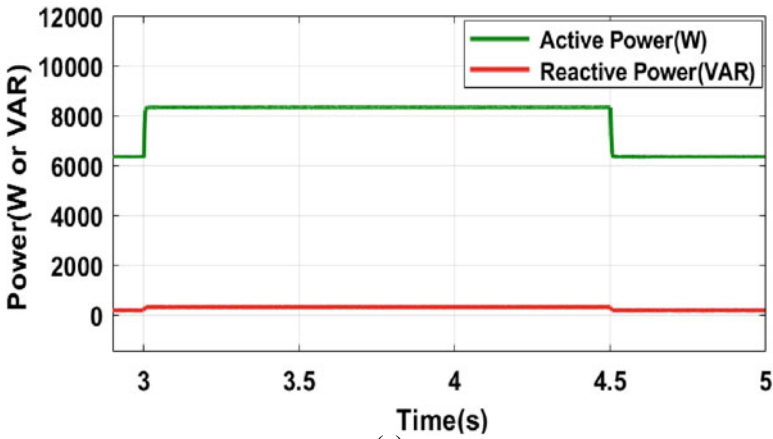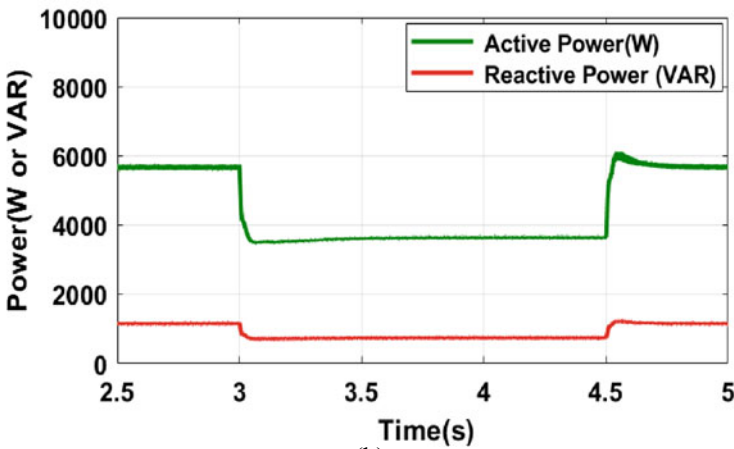
Fig. 5 Power consumption profile under load change **a** critical load, **b** non-critical load, **c** source, **d** ES

(c)

(d)
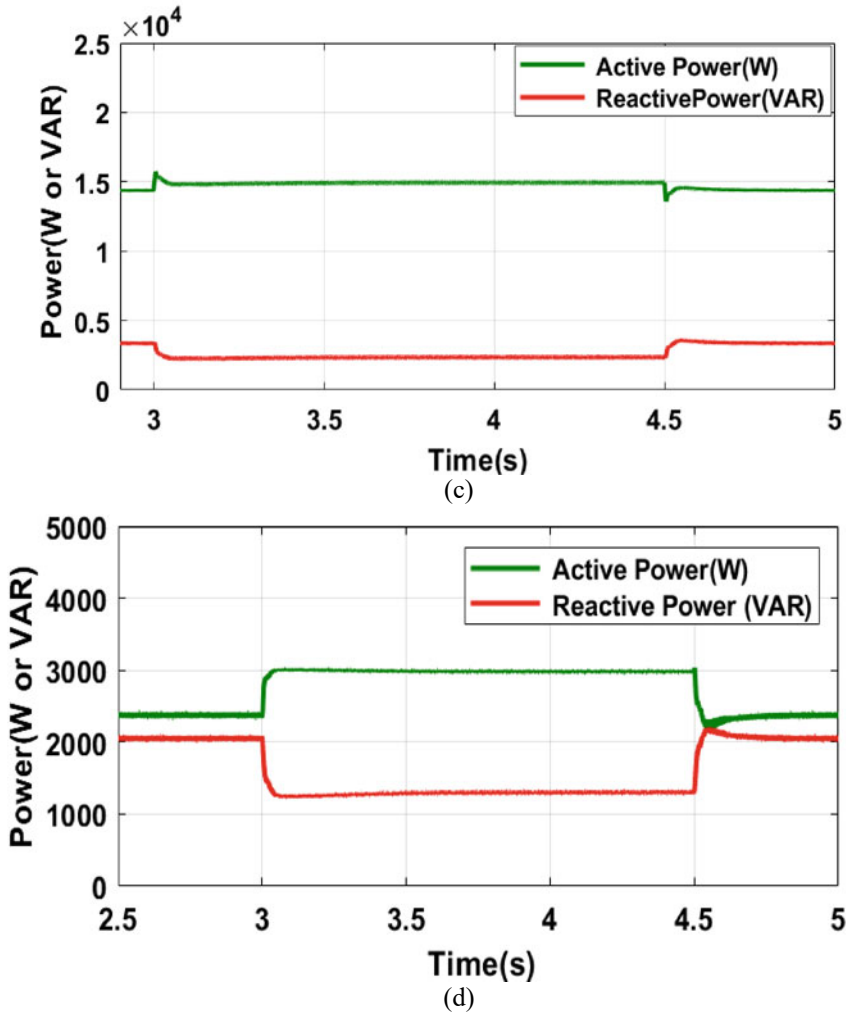
Fig. 5 (continued)

4 Conclusion

The undertaken standalone system with SEIG as primary source is analyzed under varying load conditions so as to determine the efficacy of the novel in-phase control approach for electric spring. It can be noted that, ES is successfully restoring the voltage across fluctuation restricting load (critical) with suitable power tradeoff between critical and non-critical load. During load change, the active power associated with non-critical load has gone down to support the critical loading. Moreover,

sliding more controllers is introduced to improve the transient behavior during the load transition.

References

1. P. Palensky, D. Dietrich, Demand side management: demand response, intelligent energy systems, and smart loads. IEEE Trans. Industr. Inf. **7**(3), 381–388 (2011)
2. S.Y. Hui, C.K. Lee, F.F. Wu, Electric springs—a new smart grid technology. IEEE Trans. Smart Grid **3**(3), 1552–1561 (2012)
3. D. Westermann, A. John, Demand matching wind power generation with wide-area measurement and demand-side management. IEEE Trans. Energy Convers. **22**(1), 145–149 (2007)
4. C.K. Lee, S.Y. Hui, Reduction of energy storage requirements in future smart grid using electric springs. IEEE Trans. Smart Grid **4**(3), 1282–1288 (2013)
5. C. K. Lee, B. Chaudhuri, S.Y. Hui, Hardware and control implementation of electric springs for stabilizing future smart grid with intermittent renewable energy sources. IEEE J. Emerg. Sel. Topics Power Electron. **1**(1), 18–27 (2013)
6. C.K. Lee, et al., Droop control of distributed electric springs for stabilizing future power grid. IEEE Trans. Smart Grid **4**(3), 1558–1566 (2013)
7. X. Che, et al., A general comparative analysis of static synchronous compensator and electric spring, in *2014 IEEE Conference and Expo Transportation Electrification Asia-Pacific (ITEC Asia-Pacific)*. IEEE (2014)
8. S.-C. Tan, C.K. Lee, S.Y. Hui, General steady-state analysis and control principle of electric springs with active and reactive power compensations. IEEE Trans. Power Electron. **28**(8), 3958–3969 (2012)

Author Index